

# **INTRODUCTION TO STRAPDOWN INERTIAL NAVIGATION SYSTEMS**

**Paul G Savage**

**Strapdown Associates, Inc.**

**January 10, 2010**

**(Twelfth Printing)**

The Material Presented In This Publication Was Prepared Exclusively And Independently By Paul G. Savage For Use As An Education Aid In Strapdown Inertial Navigation Tutorial Courses. Reproduction Of Any Part Of This Publication Without Permission From The Author Or Strapdown Associates, Inc., Is Prohibited.

© Strapdown Associates, Inc. 1981, 1985, 1990, 1991, 1996, 1997, 1999, 2005, 2007, 2010

All Rights Reserved

Strapdown Associates, Inc.  
4727 South Lake Sarah Drive  
Maple Plain, Minnesota 55359

Telephone: (763) 479-1981  
email: [pgs@strapdownassociates.com](mailto:pgs@strapdownassociates.com)

## FOREWORD

This book contains copies of the overhead slides used in my four and a half day Introductory Strapdown Inertial Navigation Systems course offered from 1981 to 2009 to the general public in Minneapolis-Minnesota and on-site at contracting host specified locations. Each slide is accompanied by a text describing the slide in much the same way I did verbally when presenting the course. This book was provided to all Introductory course attendees. Now that the Introductory course is no longer being offered, the book is available for purchase from my company Strapdown Associates, Inc (SAI) by telephone (763-479-1981) or by email (pgs@strapdownassociates.com).

The **Strapdown Inertial Navigation Lecture Notes** book referenced in this book and provided to Introductory course attendees as a source for inertial sensor details and analytical derivations, can also be purchased from SAI.

Paul G Savage

## **COURSE OBJECTIVES**

- **PROVIDE A BASIC UNDERSTANDING OF THE THEORY, OPERATION, AND PERFORMANCE CHARACTERISTICS OF STRAPDOWN INERTIAL NAVIGATION SYSTEMS**
- **PROVIDE A BASIC UNDERSTANDING OF THE DISTINCTION BETWEEN STRAPDOWN AND GIMBALED INERTIAL NAVIGATION SYSTEMS**
- **PROVIDE A BASIC UNDERSTANDING OF STRAPDOWN INERTIAL NAVIGATION SYSTEM AIDING THROUGH KALMAN FILTER BLENDING**

## **COURSE OBJECTIVES**

The objectives for this course are to provide a fundamental understanding of the theory, operation, and performance characteristics of strapdown as contrasted with gimbale inertial navigation systems, for both pure inertial and Kalman filter aided modes of operation.

The course is presented using viewgraph slides, each of which has been reproduced in this handout together with an accompanying text elaborating on the slide material. Sufficient background information is presented so that the course can be readily comprehended without requiring a background in inertial navigation or complex mathematics. Nevertheless, because strapdown inertial navigation is inherently analytical in nature, particular analytical relationships associated with system computer operations and error effects are an important part of the understanding of strapdown technology, hence, are treated in the course. Where presented, however, detailed derivations of equations are avoided, and the analytical material is described from an operational viewpoint. The second handout for the course, "Strapdown Inertial Navigation Lecture Notes", presents the derivations of all important strapdown analytical equations discussed.

The following slide lists the topics presented in the course with a Table of Contents indicating associated page numbers in this handout.

# **COURSE OUTLINE**

- **FUNDAMENTAL CONCEPTS**
- **INERTIAL NAVIGATION PRINCIPLES**
- **INERTIAL NAVIGATION POSITION/VELOCITY EQUATIONS**
- **INERTIAL NAVIGATION SYSTEM INITIALIZATION**
- **GIMBALED PLATFORM REFERENCE STABILIZATION**
- **STRAPDOWN REFERENCE OPERATIONS**
- **INERTIAL SENSORS**
- **SYSTEM MECHANICAL, THERMAL, PACKAGING DESIGN CONSIDERATIONS**
- **STRAPDOWN INERTIAL NAVIGATION SYSTEM ERROR CHARACTERISTICS**
- **AIDED INERTIAL SYSTEMS**
- **STRAPDOWN SYSTEM TESTING**
- **SUMMARY**
- **SUPPLEMENTAL MATERIAL**

## TABLE OF CONTENTS

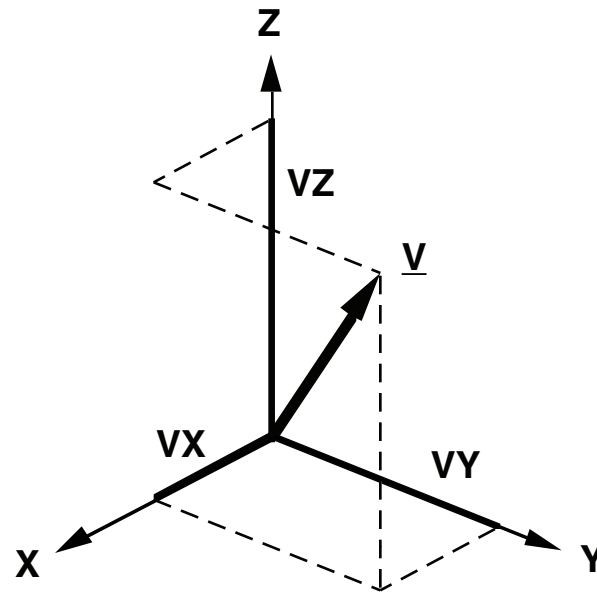
<b>TOPICS</b>	<b>PAGE NUMBER</b>
FUNDAMENTAL CONCEPTS .....	1
INERTIAL NAVIGATION PRINCIPLES .....	41
INERTIAL NAVIGATION POSITION/VELOCITY EQUATIONS .....	77
INERTIAL NAVIGATION SYSTEM INITIALIZATION .....	105
GIMBALED PLATFORM REFERENCE STABILIZATION .....	123
STRAPDOWN REFERENCE OPERATIONS .....	153
INERTIAL SENSORS .....	219
SYSTEM MECHANICAL, THERMAL, PACKAGING DESIGN CONSIDERATIONS .....	293
STRAPDOWN INERTIAL NAVIGATION SYSTEM ERROR CHARACTERISTICS .....	329
AIDED INERTIAL SYSTEMS .....	415
STRAPDOWN SYSTEM TESTING .....	489
SUMMARY .....	533
SUPPLEMENTAL MATERIAL .....	539

**NOTES**

# **FUNDAMENTAL CONCEPTS**

# VECTORS

- HAVE MAGNITUDE AND DIRECTION
- EXPRESSED AS COMPONENT PROJECTIONS ALONG COORDINATE FRAME AXES



$$\underline{V} = \begin{vmatrix} V_X \\ V_Y \\ V_Z \end{vmatrix}$$

## VECTORS

Vectors are parameters that have both magnitude and direction. A vector is typically expressed in terms of its components (or projections) on the axes of a three-axis right-handed coordinate frame. For this course (as in common usage), a vector will be represented analytically as a column matrix, each element in the column corresponding to the X, Y, and Z axis components of the vector in the particular coordinate frame in which it is represented.

## **EXAMPLES OF VECTORS**

- **LINEAR ACCELERATION**
- **ANGULAR RATE**
- **VECTOR COMPONENTS CAN BE MEASURED BY SENSORS ALONG MEASUREMENT COORDINATE AXES**
  - **GYROS – MEASURE ANGULAR RATE**
  - **ACCELEROMETERS – MEASURE LINEAR ACCELERATION**

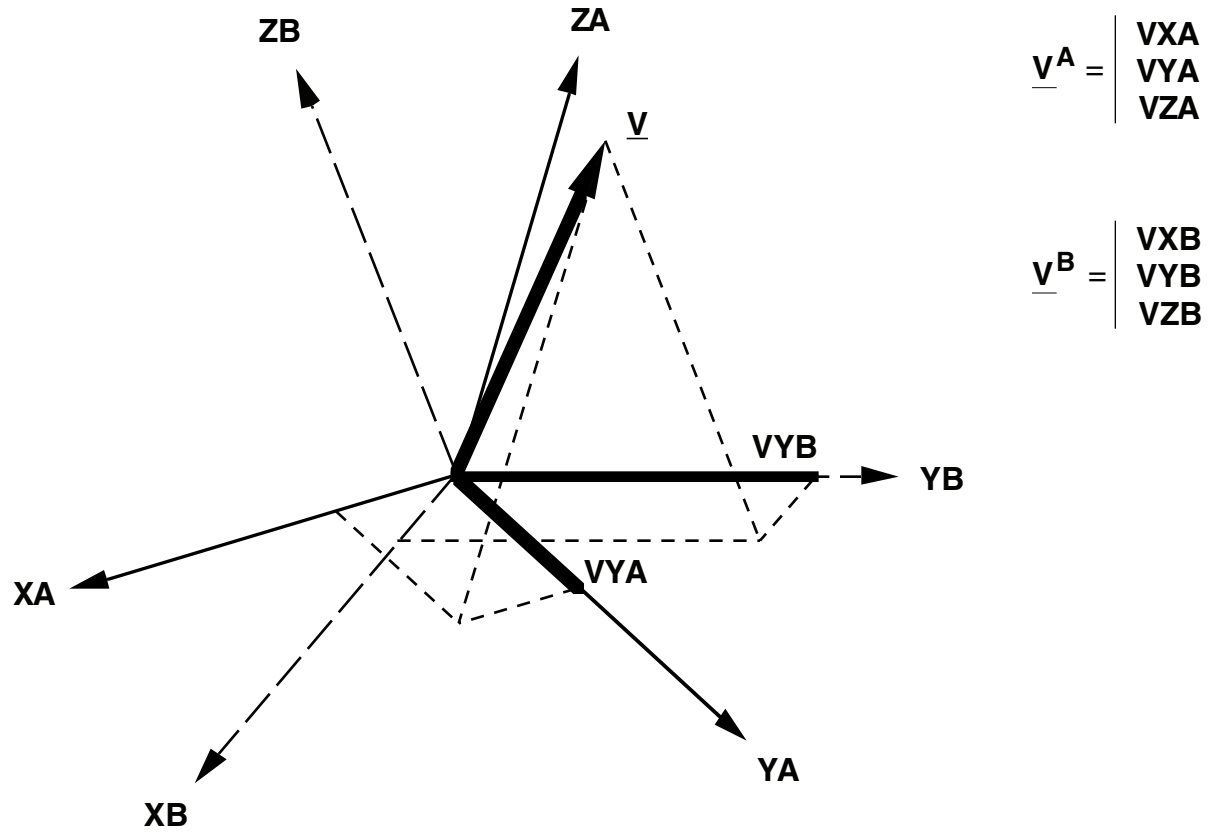
## EXAMPLES OF VECTORS

Physical vectors we will be dealing with in inertial navigation are linear acceleration and angular rotation rate. Each of these vectors can be measured in practice by instruments with their input axes directed along the axes of the coordinate frame in which the vector components are to be evaluated.

In the case of the angular rate vector, gyroscopes (or gyros) are used to measure each angular rate component. If the gyros utilized are single axis sensing instruments, three gyros would be needed to measure each of the three X, Y, Z angular rate components along the axes of the selected coordinate frame utilized.

In the case of the linear acceleration vector, accelerometers would be utilized to measure the acceleration components. Three accelerometers would typically be utilized to measure each of the three X, Y, Z components of the acceleration vector along the selected coordinate frame axes.

# A VECTOR LOOKS DIFFERENTLY IN DIFFERENT COORDINATE FRAMES



## A VECTOR LOOKS DIFFERENTLY IN DIFFERENT COORDINATE FRAMES

The values for the coordinate frame components of the vector being evaluated equals the projection of the vector on the coordinate frame axes. Consequently, the values for the vector components in a particular coordinate frame will depend on the angular orientation of the coordinate frame relative to the vector.

If the vector is projected along the axes of two different nonparallel coordinate frames (Frames A and B for example), the projections of the vector will in general look differently in the two frames. In Frame A, the vector components are  $V_{XA}$ ,  $V_{YA}$ , and  $V_{ZA}$ . For Frame B, the vector components are  $V_{XB}$ ,  $V_{YB}$ , and  $V_{ZB}$ .

A superscript is commonly used to indicate along which coordinate frame the vector components are projected (e.g.,  $\underline{V}^A$  or  $\underline{V}^B$  to indicate  $\underline{V}$  as projected along Frame-A or Frame-B axes).

**A VECTOR'S COMPONENTS IN ONE COORDINATE  
FRAME CAN BE COMPUTED FROM ITS COMPONENTS  
IN ANOTHER COORDINATE FRAME**

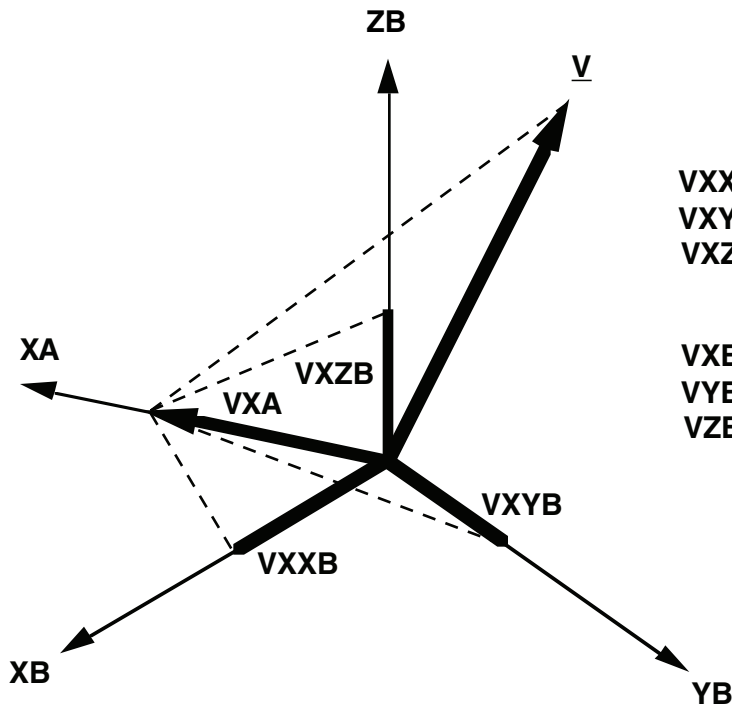
- **NEED TO KNOW THE RELATIVE ANGULAR ORIENTATION  
BETWEEN THE TWO COORDINATE FRAMES**

**A VECTOR'S COMPONENTS IN ONE COORDINATE FRAME CAN BE COMPUTED FROM IT'S COMPONENTS IN ANOTHER COORDINATE FRAME.**

A commonly encountered situation in inertial navigation is that a vector's components have been evaluated in one coordinate frame, and it is desired to calculate its components in another coordinate frame.

As we shall see in the next slide, the vector components in the second frame can be calculated from its components in the first frame if the relative angular orientation is known between the two frames.

# VECTOR TRANSFORMATION



$$\begin{aligned} V_{XXB} &= V_{XA} \cos(XB, XA) = C_{11} V_{XA} \\ V_{XYB} &= V_{XA} \cos(YB, XA) = C_{21} V_{XA} \\ V_{XZB} &= V_{XA} \cos(ZB, XA) = C_{31} V_{XA} \end{aligned}$$

$$\begin{aligned} V_{XB} &= C_{11} V_{XA} + C_{12} V_{YA} + C_{13} V_{ZA} \\ V_{YB} &= C_{21} V_{XA} + C_{22} V_{YA} + C_{23} V_{ZA} \\ V_{ZB} &= C_{31} V_{XA} + C_{32} V_{YA} + C_{33} V_{ZA} \end{aligned}$$

$$\underline{V}^A = \begin{bmatrix} V_{XA} \\ V_{YA} \\ V_{ZA} \end{bmatrix}$$

$$\underline{V}^B = \begin{bmatrix} V_{XB} \\ V_{YB} \\ V_{ZB} \end{bmatrix}$$

$$\underline{V}^B = C_A^B \underline{V}^A$$

DIRECTION COSINE MATRIX (DCM)

$$C_A^B = \begin{bmatrix} C_{11} & C_{12} & C_{13} \\ C_{21} & C_{22} & C_{23} \\ C_{31} & C_{32} & C_{33} \end{bmatrix}$$

## VECTOR TRANSFORMATION

The process of calculating a vector's components in one coordinate frame from its components in another coordinate frame is known as a "vector transformation" operation. In order to see how this is accomplished analytically, it is convenient to think of the vector as being composed of the sum of three individual vectors, each equal to the vector components along the axes of one of the coordinate frames (say Frame A) with direction along each A-Frame axis. Thus, vector  $\underline{V}$  can be considered to be composed of the sum of vectors  $\underline{VXA}$ ,  $\underline{VYA}$ , and  $\underline{VZA}$ , equal to the components of  $\underline{V}$  along the A-Frame axes. Let's look at one of these components of  $\underline{V}$  (say  $\underline{VXA}$ ) and determine its components in another coordinate Frame B.

The figure illustrates that the B-Frame components of  $\underline{VXA}$  equal the projections of  $\underline{VXA}$  onto Frame B. These equal the magnitude of  $\underline{VXA}$  times the cosines of the angles between the Frame-A X-axis (i.e.,  $\underline{XA}$ ) and the Frame-B X, Y, and Z axes (i.e.,  $\underline{XB}$ ,  $\underline{YB}$ , and  $\underline{ZB}$ ). Thus, the YB component of  $\underline{VXA}$ , denoted as  $VXYB$  equals  $VXA$  times the cosine of the angle between  $\underline{YB}$  and  $\underline{XA}$  (denoted as  $\text{COS}(\underline{YB}, \underline{XA})$ ). The X and Z B-Frame components of  $\underline{VXA}$  are denoted as  $VXXB$  and  $VXZB$ .

As shown in the figure, the cosines of the angles between the  $\underline{XB}$  axis and the A-Frame axes, are denoted by the shorthand notation  $C11$ ,  $C21$ , and  $C31$ . The first numeral denotes the B-Frame axis, and the second numeral denotes the A-Frame axis.

The latter development can be extended to also include the Y and Z A-Frame components of  $\underline{V}$  as viewed in the B-Frame. These results, when summed with the  $\underline{VXA}$  components yield the desired B-Frame axis components of  $\underline{V}$  in terms of the A-Frame components ( $\underline{VXA}$ ,  $\underline{VYA}$ ,  $\underline{VZA}$ ) and the cosines of the angles between the A and B frames ( $C_{IJ}$ 's representing the cosines of the angles between the  $I^{\text{th}}$  B-Frame axis and  $J^{\text{th}}$  A-Frame axis).

The sum of products expression for obtaining the B-Frame components from the A-Frame components is usually represented by the more compact notation indicated in the box. The  $C_A^B$  array is denoted as the direction cosine matrix that transforms vectors from Frame A to Frame B. The shorthand notation is consistent with standard matrix multiplication conventions.

# MATRIX PRODUCT

## GENERAL CASE

$$\begin{bmatrix} A_{11} & A_{12} & A_{13} \\ A_{21} & A_{22} & A_{23} \\ A_{31} & A_{32} & A_{33} \end{bmatrix} = \begin{bmatrix} B_{11} & B_{12} & B_{13} \\ B_{21} & B_{22} & B_{23} \\ B_{31} & B_{32} & B_{33} \end{bmatrix} \begin{bmatrix} C_{11} & C_{12} & C_{13} \\ C_{21} & C_{22} & C_{23} \\ C_{31} & C_{32} & C_{33} \end{bmatrix}$$

$$\overset{\Delta}{A_{23}} = B_{21} C_{13} + B_{22} C_{23} + B_{23} C_{33}$$

$$\overset{\Delta}{A_{IJ}} = B_{I1} C_{1J} + B_{I2} C_{2J} + B_{I3} C_{3J}$$

$$\mathbf{A} = \mathbf{B} \mathbf{C}$$

## SQUARE TIMES COLUMN MATRIX

$$\begin{bmatrix} A_1 \\ A_2 \\ A_3 \end{bmatrix} = \begin{bmatrix} B_{11} & B_{12} & B_{13} \\ B_{21} & B_{22} & B_{23} \\ B_{31} & B_{32} & B_{33} \end{bmatrix} \begin{bmatrix} C_1 \\ C_2 \\ C_3 \end{bmatrix}$$

$$\overset{\Delta}{A_2} = B_{21} C_1 + B_{22} C_2 + B_{23} C_3$$

$$\overset{\Delta}{A_I} = B_{I1} C_1 + B_{I2} C_2 + B_{I3} C_3$$

$$\underline{\mathbf{A}} = \underline{\mathbf{B}} \underline{\mathbf{C}}$$

## MATRIX PRODUCT

The slide indicates the standard convention for matrix products (such as utilized in the vector transformation slide). The rule is that for a matrix  $A$  equal to the matrix product of matrix  $B$  with  $C$ , the element in  $A$  corresponding to the  $I^{\text{th}}$  row and  $J^{\text{th}}$  column, equals the sum of products of the  $I^{\text{th}}$  row elements of  $B$  with the  $J^{\text{th}}$  column elements of  $C$ . An example is shown for the case where  $I=2$  and  $J=3$ .

Examples are shown for the general matrix product case, and for the simpler case of the product of a square matrix with a column matrix (such as used with a vector transformation operation).

## TRANSFORMATION MATRIX PRODUCTS

$$\underline{v}^B = C_A^B \underline{v}^A$$

$$\underline{v}^D = C_B^D \underline{v}^B$$

THEREFORE:  $\underline{v}^D = C_B^D C_A^B \underline{v}^A$

BUT:  $\underline{v}^D = C_A^D \underline{v}^A$

THEREFORE:  $C_A^D = C_B^D C_A^B$

## TRANSFORMATION MATRIX PRODUCTS

Given direction cosine matrices  $C_A^B$  and  $C_B^D$  (relating Frames A and B, and Frames B and D), it is frequently desired to calculate the direction cosine matrix relating Frames A and D. The development shows that the desired matrix  $C_A^D$  equals the matrix product of  $C_B^D$  with  $C_A^B$

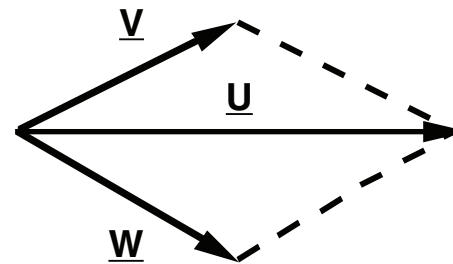
## VECTOR SUM

$$\underline{U} = \underline{V} + \underline{W}$$

- THE VECTOR DEFINED AS THE SUM OF TWO OTHER VECTORS HAS COMPONENTS EQUAL TO THE SUM OF THE COMPONENTS OF THE TWO VECTORS

$$\underline{U} = \begin{bmatrix} VX + WX \\ VY + WY \\ VZ + WZ \end{bmatrix}$$

OR GEOMETRICALLY:



WHERE

$$\underline{V} = \begin{bmatrix} VX \\ VY \\ VZ \end{bmatrix}$$

$$\underline{W} = \begin{bmatrix} WX \\ WY \\ WZ \end{bmatrix}$$

## VECTOR SUM

The vector defined as the sum of two other vectors has components equal to the sum of the components of the other vectors. The geometric construction shown in the figure is equivalent to this definition. The  $\underline{V}$  sum vector is constructed geometrically from  $\underline{W}$  and  $\underline{V}$  as the vector along the diagonal of the parallelogram formed with  $\underline{V}$  and  $\underline{W}$  as its sides.

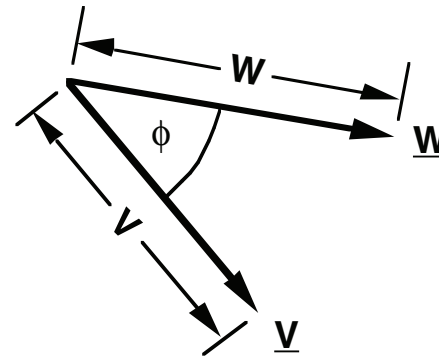
When calculating the vector sum, both vectors must be defined in the same coordinate frame. This implies that a vector transformation operation may be required to transform the vector components to a common coordinate frame before the vector summing operation is executed.

## VECTOR DOT PRODUCT

$$U = \underline{V} \cdot \underline{W}$$

- DOT PRODUCT OF  $\underline{V}$  WITH  $\underline{W}$  IS A SCALAR QUANTITY  $U$  EQUAL TO THE MAGNITUDE OF  $\underline{V}$  TIMES THE MAGNITUDE OF  $\underline{W}$  TIMES THE COSINE OF THE ANGLE BETWEEN  $\underline{V}$  AND  $\underline{W}$

$$U = V W \cos(\phi)$$



OR

$$U = V_X \times W_X + V_Y \times W_Y + V_Z \times W_Z$$

WHERE

$$\underline{V} = \begin{bmatrix} V_X \\ V_Y \\ V_Z \end{bmatrix} \quad \underline{W} = \begin{bmatrix} W_X \\ W_Y \\ W_Z \end{bmatrix}$$

## VECTOR DOT PRODUCT

Frequently it is desired to calculate a scalar quantity equal to the product of the magnitudes of two vectors times the cosine of the angle between them. It is easily verified that this product is equivalent to the magnitude of one vector times the projection of the other vector on the first. Such an operation is denoted as a "vector dot product".

The slide shows how the dot product is evaluated from the component projections of the two vectors ( $\underline{V}$  and  $\underline{W}$ ) along the axes of a selected coordinate frame, as the sum of the products of the X, Y, Z components of the vectors.

When calculating the vector dot product, both vectors must be defined in the same coordinate frame. This implies that a vector transformation operation may be required to transform the vector components to a common coordinate frame before the vector dot product operation is executed. It is also interesting to note that the numerical value of the vector dot product is identical for any coordinate frame in which it is computed.

# VECTOR CROSS-PRODUCT

$$\underline{U} = \underline{V} \times \underline{W}$$

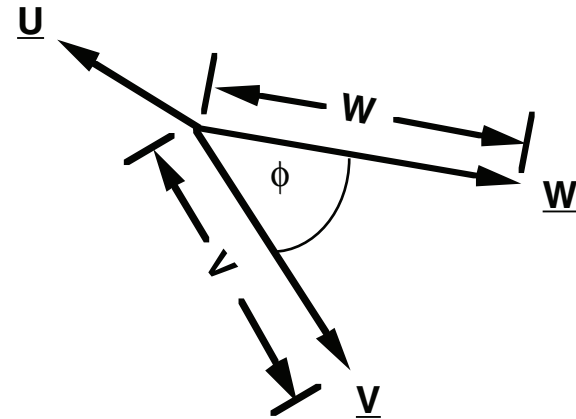
- CROSS PRODUCT OF  $\underline{V}$  WITH  $\underline{W}$  IS A VECTOR QUANTITY  $\underline{U}$  WITH MAGNITUDE EQUAL TO THE MAGNITUDE OF  $\underline{V}$  TIMES THE MAGNITUDE OF  $\underline{W}$  TIMES THE SINE OF THE ANGLE BETWEEN  $\underline{V}$  AND  $\underline{W}$ , WITH DIRECTION PERPENDICULAR TO THE PLANE DEFINED BY  $\underline{V}$  AND  $\underline{W}$

$$\underline{U} = [V W \text{SINE}(\phi)] \underline{n}$$

$$\underline{n} = \text{UNIT VECTOR ALONG } \underline{U}$$

OR

$$\underline{U} = \begin{bmatrix} VY \times WZ - VZ \times WY \\ VZ \times WX - VX \times WZ \\ VX \times WY - VY \times WX \end{bmatrix}$$



WHERE

$$\underline{V} = \begin{bmatrix} VX \\ VY \\ VZ \end{bmatrix} \quad \underline{W} = \begin{bmatrix} WX \\ WY \\ WZ \end{bmatrix}$$

## VECTOR CROSS-PRODUCT

Frequently it is desired to calculate a vector quantity equal in magnitude to the product of the magnitudes of two vectors times the sine of the angle between them, with direction perpendicular to the plane formed by the two vectors. Such an operation is denoted as a "vector cross-product". It is easily verified that the cross-product magnitude is equivalent to the magnitude of one vector times the magnitude of the component of the other vector perpendicular to the first.

The slide show how the cross-product  $\underline{U}$  is evaluated from the component projections of the two vectors ( $\underline{V}$  and  $\underline{W}$ ) along the axes of a selected coordinate frame.

When calculating the vector cross-product, both vectors must be defined in the same coordinate frame. This implies that a vector transformation operation may be required to transform the vector components to a common coordinate frame before the vector cross-product operation is executed.

## SKEW SYMMETRIC OR CROSS-PRODUCT OPERATOR FORM OF A VECTOR

$$(\underline{V} \times) \triangleq \begin{bmatrix} 0 & -V_Z & V_Y \\ V_Z & 0 & -V_X \\ -V_Y & V_X & 0 \end{bmatrix}$$

SKEW SYMMETRIC OR CROSS-PRODUCT  
OPERATOR  
FORM OF VECTOR V

WHERE

$$\underline{V} = \begin{bmatrix} V_X \\ V_Y \\ V_Z \end{bmatrix}$$

- THE SKEW SYMMETRIC FORM OF VECTOR V IS SOMETIMES DENOTED AS THE CROSS-PRODUCT OPERATOR FORM BECAUSE ITS MATRIX PRODUCT WITH ANOTHER VECTOR GENERATES THE CROSS-PRODUCT BETWEEN THE TWO VECTORS

$$(\underline{V} \times) \underline{W} = \begin{bmatrix} 0 & -V_Z & V_Y \\ V_Z & 0 & -V_X \\ -V_Y & V_X & 0 \end{bmatrix} \begin{bmatrix} W_X \\ W_Y \\ W_Z \end{bmatrix} = \begin{bmatrix} V_Y \times W_Z - V_Z \times W_Y \\ V_Z \times W_X - V_X \times W_Z \\ V_X \times W_Y - V_Y \times W_X \end{bmatrix} \triangleq \underline{V} \times \underline{W}$$

## **SKEW SYMMETRIC OR CROSS-PRODUCT OPERATOR FORM OF A VECTOR**

The skew symmetric or cross-product operator matrix form of a vector  $\underline{V}$  is defined as the skew symmetric square matrix arrangement of the components of  $\underline{V}$ , and is denoted as  $(\underline{V} \times)$ . Note that the matrix product of  $(\underline{V} \times)$  with another vector  $\underline{W}$  equals the cross-product of  $\underline{V}$  with  $\underline{W}$ . Hence, the terminology "cross-product operator" to identify  $(\underline{V} \times)$ .

## MATRIX OR VECTOR TRANSPOSE

- DEFINED AS MATRIX (OR VECTOR) WITH ROWS AND COLUMNS INTERCHANGED

$$\mathbf{C} = \begin{bmatrix} \mathbf{C11} & \mathbf{C12} & \mathbf{C13} \\ \mathbf{C21} & \mathbf{C22} & \mathbf{C23} \\ \mathbf{C31} & \mathbf{C32} & \mathbf{C33} \end{bmatrix} \quad \underline{\mathbf{V}} = \begin{bmatrix} \mathbf{V1} \\ \mathbf{V2} \\ \mathbf{V3} \end{bmatrix}$$
$$\mathbf{C}^T = \begin{bmatrix} \mathbf{C11} & \mathbf{C21} & \mathbf{C31} \\ \mathbf{C12} & \mathbf{C22} & \mathbf{C32} \\ \mathbf{C13} & \mathbf{C23} & \mathbf{C33} \end{bmatrix} \quad \underline{\mathbf{V}}^T = [ \mathbf{V1}, \mathbf{V2}, \mathbf{V3} ]$$

$\mathbf{C}^T, \underline{\mathbf{V}}^T =$  TRANSPOSE OF  $\mathbf{C}, \underline{\mathbf{V}}$

## MATRIX (OR VECTOR) TRANSPOSE

The transpose of a matrix or vector (denoted by a superscript T) is another matrix obtained from the first by interchanging rows and columns. Note that the vector dot product operation of  $\underline{V}$  with  $\underline{W}$  defined in another slide could also have been written as the matrix product of  $\underline{V}^T$  with  $\underline{W}$ .

## IDENTITY MATRIX

THE IDENTITY MATRIX IS A SQUARE MATRIX WITH ONES ALONG THE DIAGONAL AND ZEROES ELSEWHERE

$$I = \begin{bmatrix} 1 & 0 & 0 \\ 0 & 1 & 0 \\ 0 & 0 & 1 \end{bmatrix}$$

## **IDENTITY MATRIX**

The identity matrix is defined as a matrix with ones along the diagonal and zeroes elsewhere. Note that the product of the identity matrix with another matrix (or vector) equals the other matrix (or vector).

# MATRIX INVERSE

$C^{-1}$  = INVERSE OF C SATISFIES:

$$C C^{-1} = I$$

## MATRIX INVERSE

The inverse of a matrix (denoted by superscript -1) is a matrix related to the original such that its product with the original equals the identity matrix. In general, the inverse of a matrix can be calculated from the components of the matrix through a set of fairly complicated matrix operations.

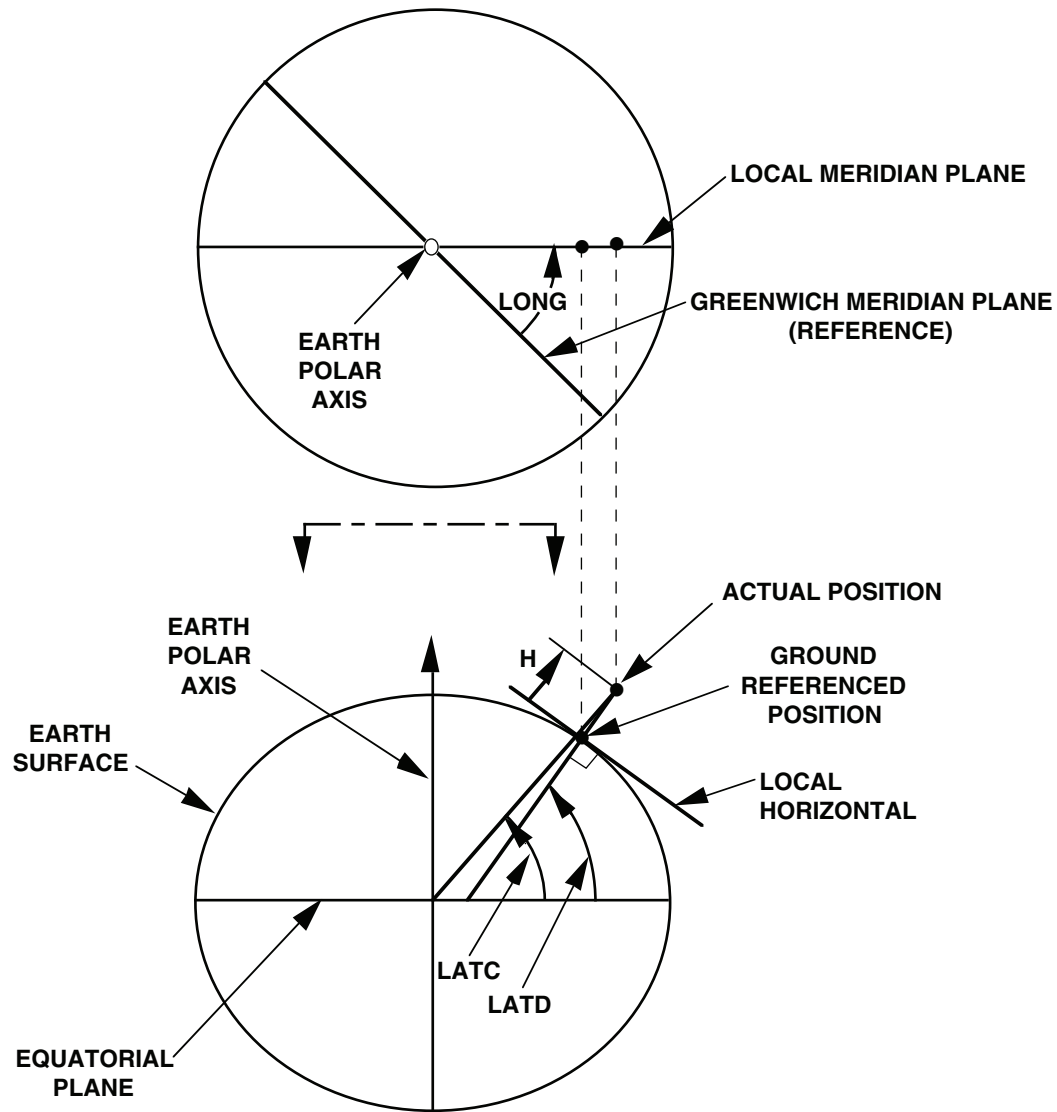
For the special case where the matrix is a direction cosine matrix, the matrix inverse equals the matrix transpose. This can be inferred by first recognizing from the definitions on page 10 that  $C_B^A$  is the inverse of the general direction cosine matrix  $C_A^B$  (i.e., a vector in the A Frame transformed to the B Frame through  $C_A^B$  and then back to the A Frame through  $C_B^A$  results in the original A Frame vector. This can only be true if the product of  $C_A^B$  with  $C_B^A$  is the identity matrix). Following the page 10 development approach, it then follows that  $C_B^A$  is the transpose of  $C_A^B$  because the cosine of the angle between two Frame A and B axes (i.e.,  $C_{ij}$ ) is the projection of a unit vector along A Frame axis j on B Frame axis i or the projection of a unit vector along B Frame axis i on A Frame axis j, and the axes of the A Frame are mutually orthogonal as are the axes of the B Frame.

# **NAVIGATION PARAMETERS**

## **NAVIGATION PARAMETERS**

The following slides define the navigation parameters typically utilized to describe the earth referenced position location of a vehicle, its linear translational movement over the earth, and its angular orientation with respect to the earth. These parameters would be typically calculated in an inertial navigation system aboard the vehicle based on the processing of vehicle acceleration data measured by a self-contained cluster of inertial sensing instruments (gyros and accelerometers). A discussion is included on the distinction between accelerations sensed by accelerometers and gravity acceleration.

# POSITION PARAMETERS



H = ALTITUDE

LATC = GEOCENTRIC LATITUDE

LATD = GEODETIC LATITUDE

LONG = LONGITUDE

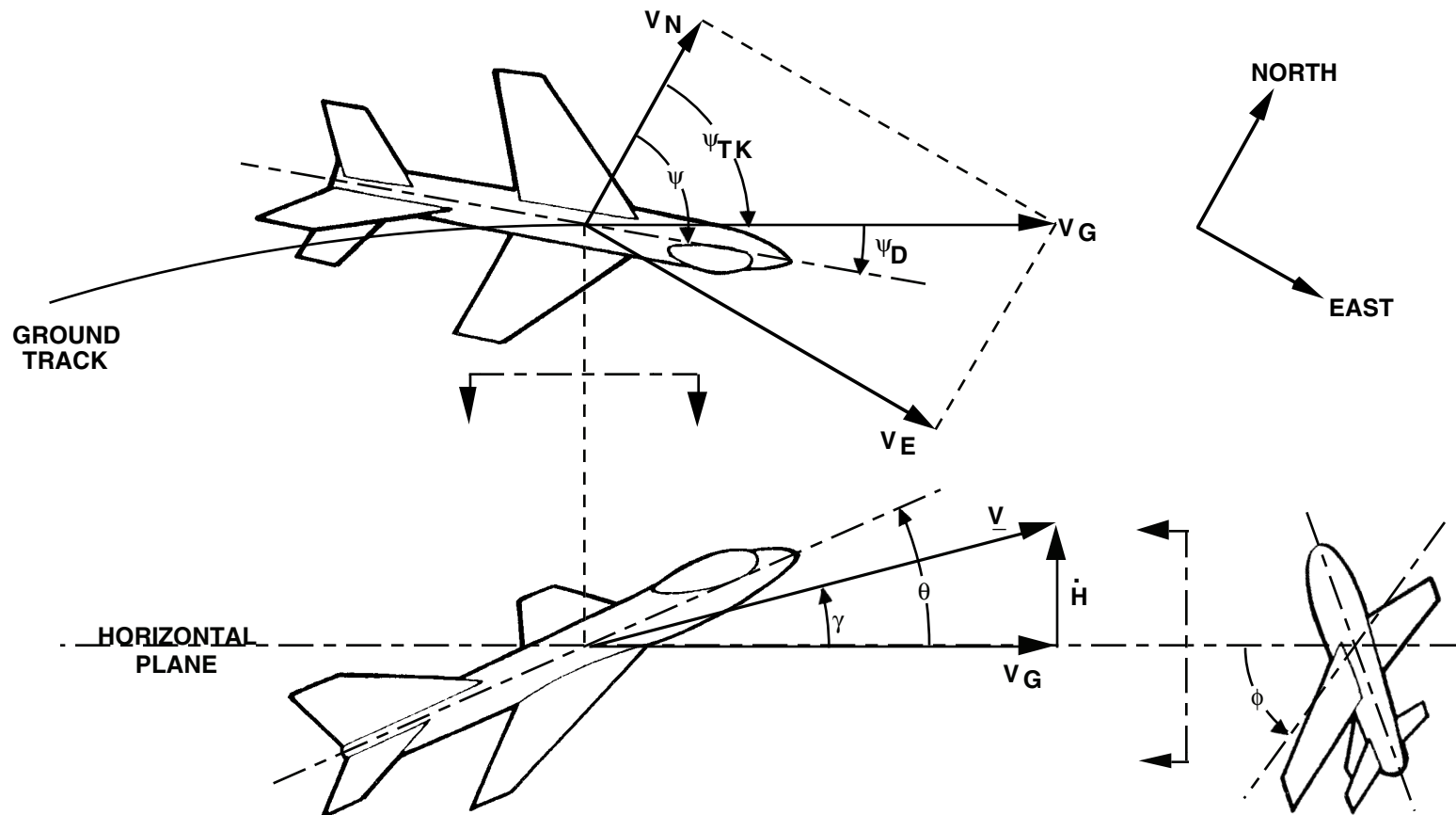
## POSITION PARAMETERS

In general, navigation deals with the calculation of position location. Terrestrial navigation with which we will be dealing in this course, involves the determination of position relative to the earth. Earth referenced position is typically defined in terms of latitude, longitude, and altitude.

Altitude is defined as the vertical distance above the earth (along a perpendicular to the earth surface). Longitude is defined as the angular distance, measured in the earth's equatorial plane, between the meridian plane corresponding to the actual position, and the earth reference meridian plane that passes through Greenwich, England. A meridian plane is defined as a plane containing the earth's polar axis, hence, is also perpendicular to the earth's equatorial plane.

Latitude is an angular measurement from earth's equatorial plane to the current position location. Latitude can be measured as geocentric or geodetic latitude. Geocentric latitude is the angle from earth's equatorial plane to a line drawn from earth's center to the position location. To describe geodetic latitude, we must first define a ground referenced position as the intersection with the earth surface of a perpendicular line to the earth surface dropped from the actual position location. If we extend the perpendicular line to the equatorial plane, geodetic Latitude is the angle from the equatorial plane to the extended perpendicular line. Geodetic latitude is the commonly used convention for defining earth referenced position. Typical maps are based on geodetic latitude.

# VELOCITY AND ATTITUDE PARAMETERS



- |                                   |                           |                              |
|-----------------------------------|---------------------------|------------------------------|
| $\underline{V}$ = VELOCITY VECTOR | $\psi$ = HEADING ANGLE    | $\theta$ = PITCH ANGLE       |
| $V_N$ = NORTH VELOCITY            | $\psi_D$ = DRIFT ANGLE    | $\phi$ = ROLL ANGLE          |
| $V_E$ = EAST VELOCITY             | $\psi_{TK}$ = TRACK ANGLE | $\gamma$ = FLIGHT PATH ANGLE |
| $\dot{H}$ = ALTITUDE RATE         | $V_G$ = GROUND SPEED      |                              |

## VELOCITY AND ATTITUDE PARAMETERS

Inertial navigation systems with which we shall be dealing, typically compute and output velocity and attitude parameters as well as latitude, longitude, altitude position.

Velocity parameters are typically expressed in terms of the vertical and horizontal components of aircraft translational movement relative to the earth. The vertical component of velocity is denoted as altitude rate. The horizontal component of velocity can be expressed in terms of North and East components or in terms of the net horizontal velocity component magnitude (called ground speed) and horizontal velocity vector direction relative to North (denoted as the track angle). True track angle is track angle referenced to true North (i.e., toward the earth North polar axis); magnetic track angle is track angle referenced to magnetic North. The magnetic variation (Mag Var) is the difference between true and magnetic North (which is available from the US National Oceanic and Atmospheric Administration as a surveyed function of latitude and longitude). Mag Var can be added to true track angle to convert it to magnetic track angle.

The trace of the point on the earth surface along a vertical line from the aircraft to the earth surface is called the ground track. The horizontal velocity of the aircraft is tangent to the ground track. Another velocity related parameter of interest is the flight path angle defined as the angle of the total velocity vector above the horizontal plane.

Aircraft convention defines the attitude parameters in terms of three "Euler" angles: heading, pitch, and roll. Heading is defined as the angle in the local horizontal plane measured clockwise about a downward vertical between North and a vertical plane containing the aircraft longitudinal (thrust) axis. True heading is heading referenced to true North. Magnetic heading is heading referenced to magnetic North. True heading can be converted to magnetic heading by adding Mag Var. The aircraft pitch angle is defined as the angle measured in the vertical plane between the aircraft longitudinal axis and the horizontal (positive for nose up). The roll angle is defined as the angle measured about the aircraft longitudinal axis that will rotate the aircraft from a wings horizontal orientation to the actual flight orientation. A climbing right hand turn from a level Northerly flight path direction generates a positive heading, pitch, and roll angle.

The drift angle is the angle measured in the horizontal plane between the horizontal velocity projection and the horizontal projection of the aircraft longitudinal axis. A drift angle is generated from cross-winds which cause the aircraft to point into the direction of the relative wind rather than along the ground referenced velocity direction.

# WIND RELATED PARAMETERS

NORTH



EAST



W = WIND VELOCITY

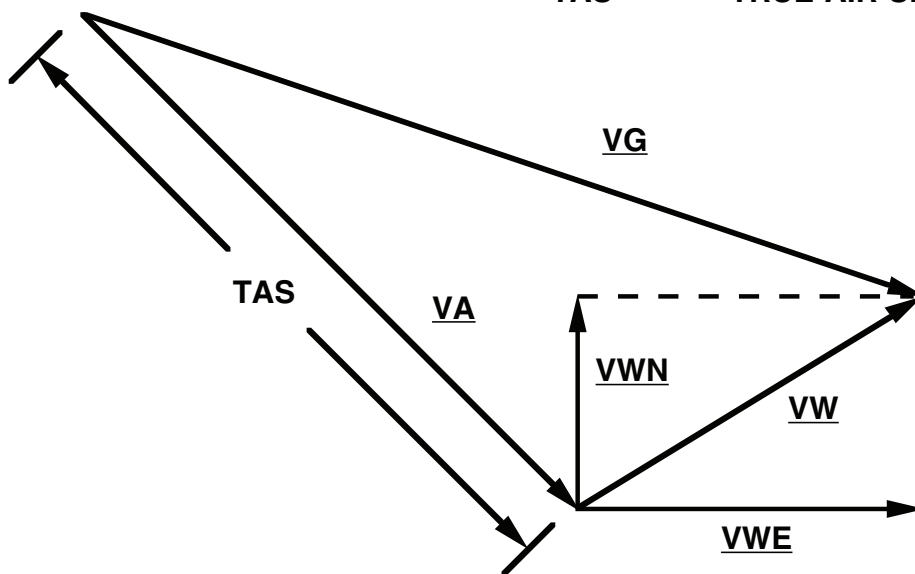
VWN = NORTH WIND VELOCITY

VWE = EAST WIND VELOCITY

VG = GROUND REFERENCED VELOCITY

VA = AIR VELOCITY

TAS = TRUE AIR SPEED



## **WIND RELATED PARAMETERS**

North and East wind velocity components are sometimes evaluated in an inertial navigation based on computed North/East ground velocity components, and input true air speed (provided from an air data computer).

Assuming that the aircraft is pointing into the relative wind, the true air speed and the aircraft attitude and true heading completely define the aircraft velocity vector (magnitude and direction) relative to the local air mass. The aircraft ground referenced velocity equals the vector sum of the velocity relative to the air mass and the velocity of the air mass relative to the ground (i.e., the wind). Conversely, then, the wind vector can be computed as the ground referenced velocity vector minus the true air speed vector. The slide illustrates this operation vectorially, showing the resulting North and East components of wind velocity as the projection of the wind velocity vector on the horizontal plane.

## GRAVITY AND SPECIFIC FORCE ACCELERATION

$$\left( \frac{d^2\mathbf{R}}{dt^2} \right)_I = \underline{\mathbf{A}} + \underline{\mathbf{G}}$$

**R** = VEHICLE POSITION VECTOR

**G** = LOCAL GRAVITATIONAL ACCELERATION

**A** = SPECIFIC FORCE ACCELERATION

( )<sub>I</sub> = DERIVATIVE AS VIEWED IN AN INERTIAL NON-ROTATING COORDINATE FRAME

- ACCELEROMETERS DO NOT SENSE THE GRAVITY COMPONENT OF TOTAL INERTIAL ACCELERATION
- THE **A** ACCELERATION COMPONENT THAT IS SENSED BY ACCELEROMETERS IS DENOTED AS “SPECIFIC FORCE ACCELERATION”

## **GRAVITY AND SPECIFIC FORCE ACCELERATION**

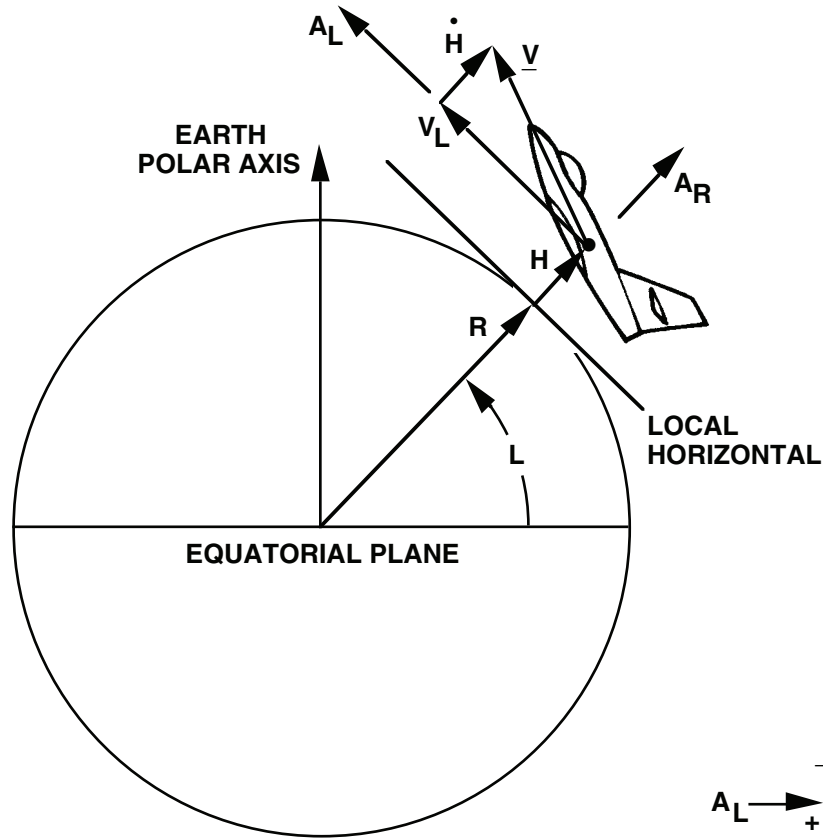
Inertial navigation systems utilize accelerometers to measure acceleration or the rate of change of velocity relative to inertial (non-rotating) space. Unfortunately, an accelerometer does not have the ability to measure the gravitational component of the total acceleration along its input axis. The "non-gravitational" portion of the acceleration that can be sensed (produced by contact forces) is denoted as "specific force acceleration". In order to determine the total acceleration, the gravity component must be calculated in the system computer and added to the accelerometer measured specific force acceleration.

As an example of the above statement, consider an accelerometer at rest on the earth's surface with its input axis directed upward. The accelerometer output under this condition would be 1 g. This conflicts with the reality of the situation which clearly is a nonaccelerating condition. The dilemma is resolved by correcting the accelerometer output for gravity (i.e., 1 g downward) which results in a net acceleration of zero, the proper answer.

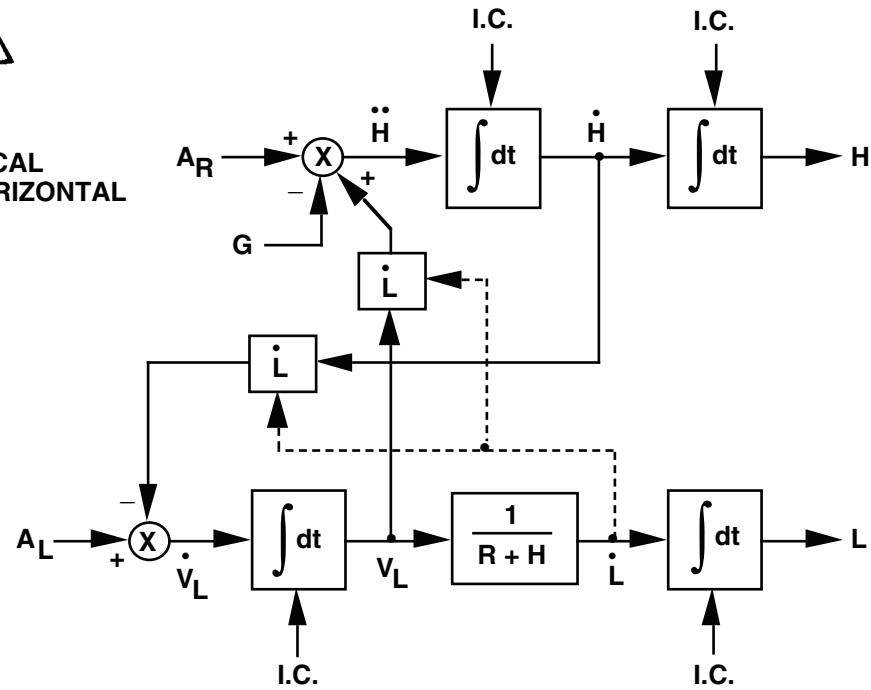
**NOTES**

# **INERTIAL NAVIGATION PRINCIPLES**

# SIMPLIFIED INERTIAL NAVIGATION CONCEPT (NORTH/SOUTH CHANNEL)



$$\begin{aligned} \ddot{H} &= A_R - G + \dot{L} V_L \\ \dot{V}_L &= A_L - \dot{L} \dot{H} \\ \dot{L} &= \frac{V_L}{R + H} \end{aligned}$$



- H = ALTITUDE
- L = LATITUDE
- $V_L$  = NORTH/SOUTH VELOCITY
- $A_R$  = RADIAL SPECIFIC FORCE ACCELERATION
- $A_L$  = NORTH/SOUTH SPECIFIC FORCE ACCELERATION
- G = GRAVITATIONAL ACCELERATION
- R = EARTH RADIUS

- I.C. = INITIAL CONDITION
- $\dot{\phantom{x}}$  = FIRST TIME DERIVATIVE
- $\ddot{\phantom{x}}$  = SECOND TIME DERIVATIVE

## SIMPLIFIED INERTIAL NAVIGATION CONCEPT (NORTH/SOUTH CHANNEL)

Inertial navigation is the process of calculating position and velocity based solely on inputs from self-contained acceleration sensing instruments. Accelerometers provide the acceleration magnitude sensing function. Gyroscopes (or gyros) provide the acceleration direction sensing function (i.e., define the direction of the accelerometer sensing axes). The basic inertial navigation concept is to integrate the sensed acceleration vector data (corrected for gravity) to determine vehicle velocity, and then integrate the velocity data to determine vehicle position. The slide illustrates the basic inertial navigation concept in the North/South direction over a simplified nonrotating spherical earth.

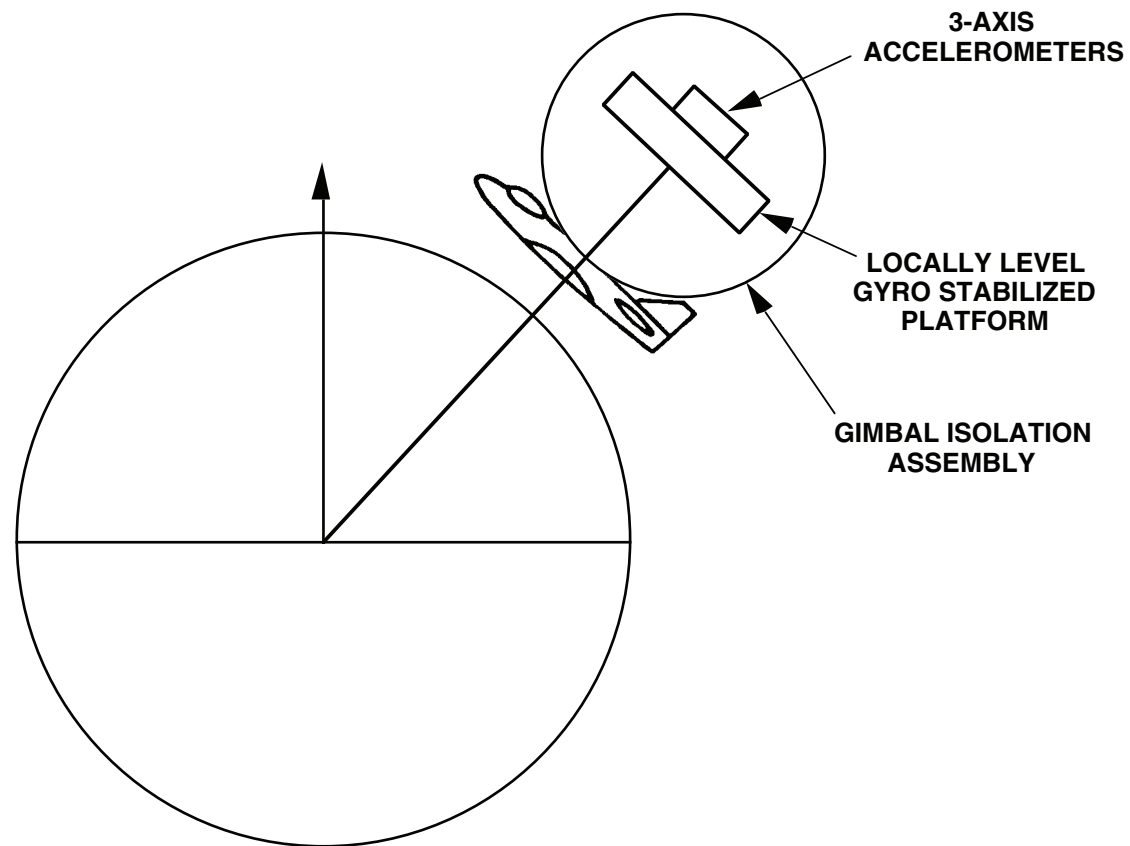
In the slide, an aircraft is shown traveling North and climbing. The horizontal acceleration of the aircraft (in the north direction) determines the change in its North velocity. Note, that because gravity has no horizontal component, the specific force acceleration of the aircraft in the North horizontal direction needs no gravity correction. Note also that an  $\dot{L} H$  term has been included as a North acceleration correction. This is a Coriolis term that accounts for the rotation rate of the local level reference frame and the associated rotation rate of the vertical velocity which appears as a North acceleration.

The vertical velocity change of the aircraft is caused by non-gravitational specific force acceleration along the vertical (or along a radial line from earth center to the aircraft), corrected for gravity acceleration directed downward, plus a Coriolis term  $\dot{L} V_L$  which accounts for the rotation rate of the North velocity in the local level reference frame (a vertical acceleration effect).

The slide shows that the second time derivative of altitude (vertical position) equals the vertical acceleration (specific force corrected for gravity), and that the rate of change of North horizontal velocity equals the North/South horizontal specific force acceleration. The slide also shows that the rate of change of latitude equals the North horizontal velocity divided by the radial arm from earth center to the aircraft.

An analog block diagram illustrates how the above relationships can be implemented through integrators to continuously compute altitude rate (the integral of vertical acceleration), altitude (the integral of altitude rate), North horizontal velocity (the integral of North horizontal acceleration), and latitude (the integral of latitude rate). Note that a key part of the integration process is the initialization of the integrators. As we shall see, initialization of inertial navigation systems is an important part of their mechanization configuration.

# GIMBALED LOCALLY LEVEL PLATFORM CONCEPT

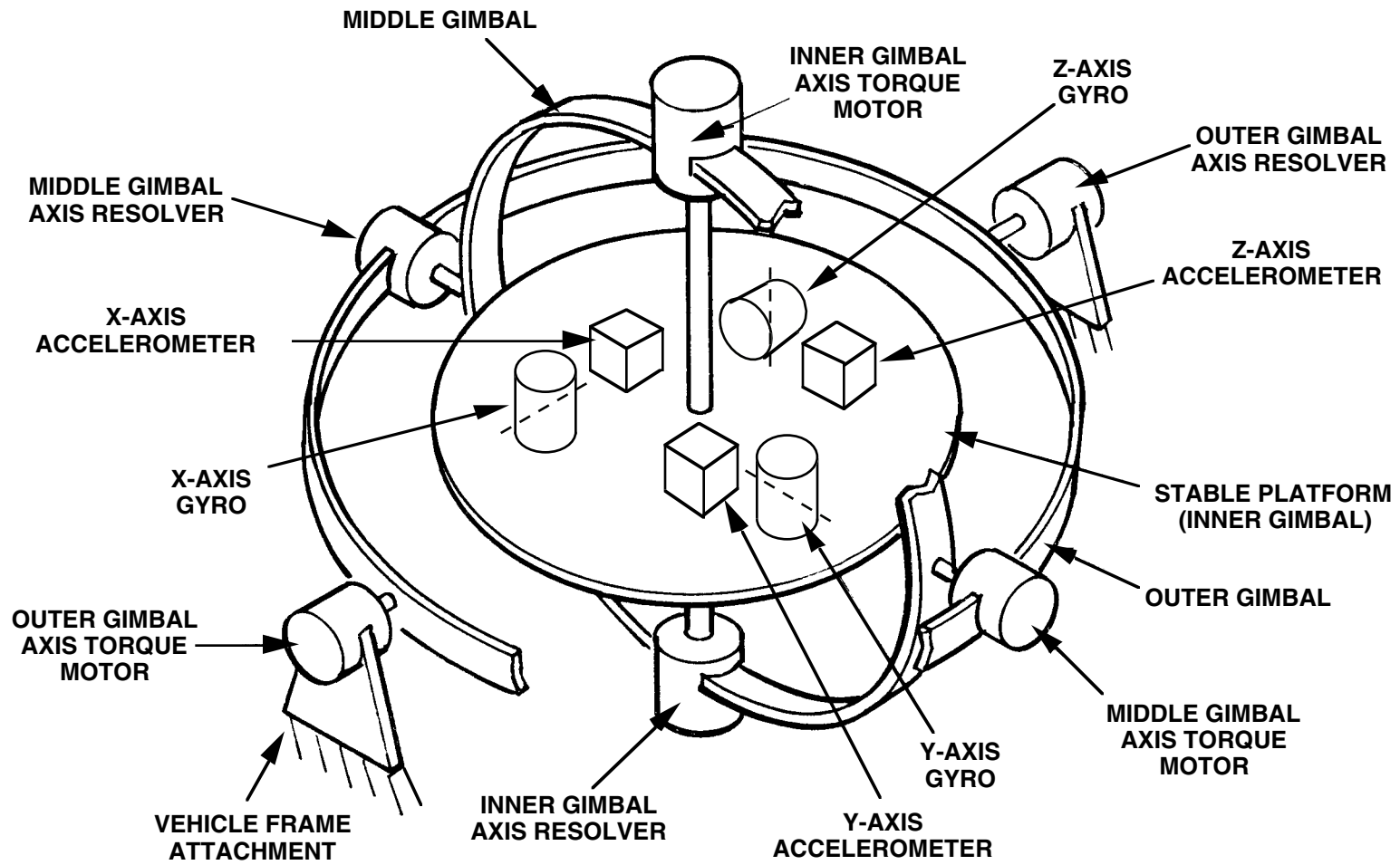


**ACCELEROMETERS DIRECTLY MEASURE HORIZONTAL AND VERTICAL ACCELERATION FOR INTEGRATION IN NAVIGATION COMPUTER**

## **GIMBALED LOCALLY LEVEL PLATFORM CONCEPT**

The previous slide illustrated how velocity and position could be generated from measured vertical and horizontal acceleration. One mechanization approach for realizing this concept has utilized a physical gyro stabilized platform to which the system accelerometers are mounted. With such an approach, the sensor platform is stabilized to remain horizontal. The platform is connected to the aircraft by a gimbal isolation assembly with appropriate motor drives to maintain the sensor platform horizontal. In this manner, the input axis of each accelerometer (horizontal and vertical) is physically directed along a known input axis direction. Thus, referring to the previous figure, a North accelerometer (for example) would provide the North specific force acceleration output while the vertical accelerometer would provide the vertical acceleration output. The integration of the acceleration data into velocity and position would be implemented in the inertial navigation system in a digital navigation computer.

# THREE GIMBAL GYRO STABILIZED PLATFORM



- TORQUE MOTORS DRIVEN BY GYRO OUTPUT AMPLIFIERS STABILIZE INNER ELEMENT

### **THREE GIMBAL GYRO STABILIZED PLATFORM**

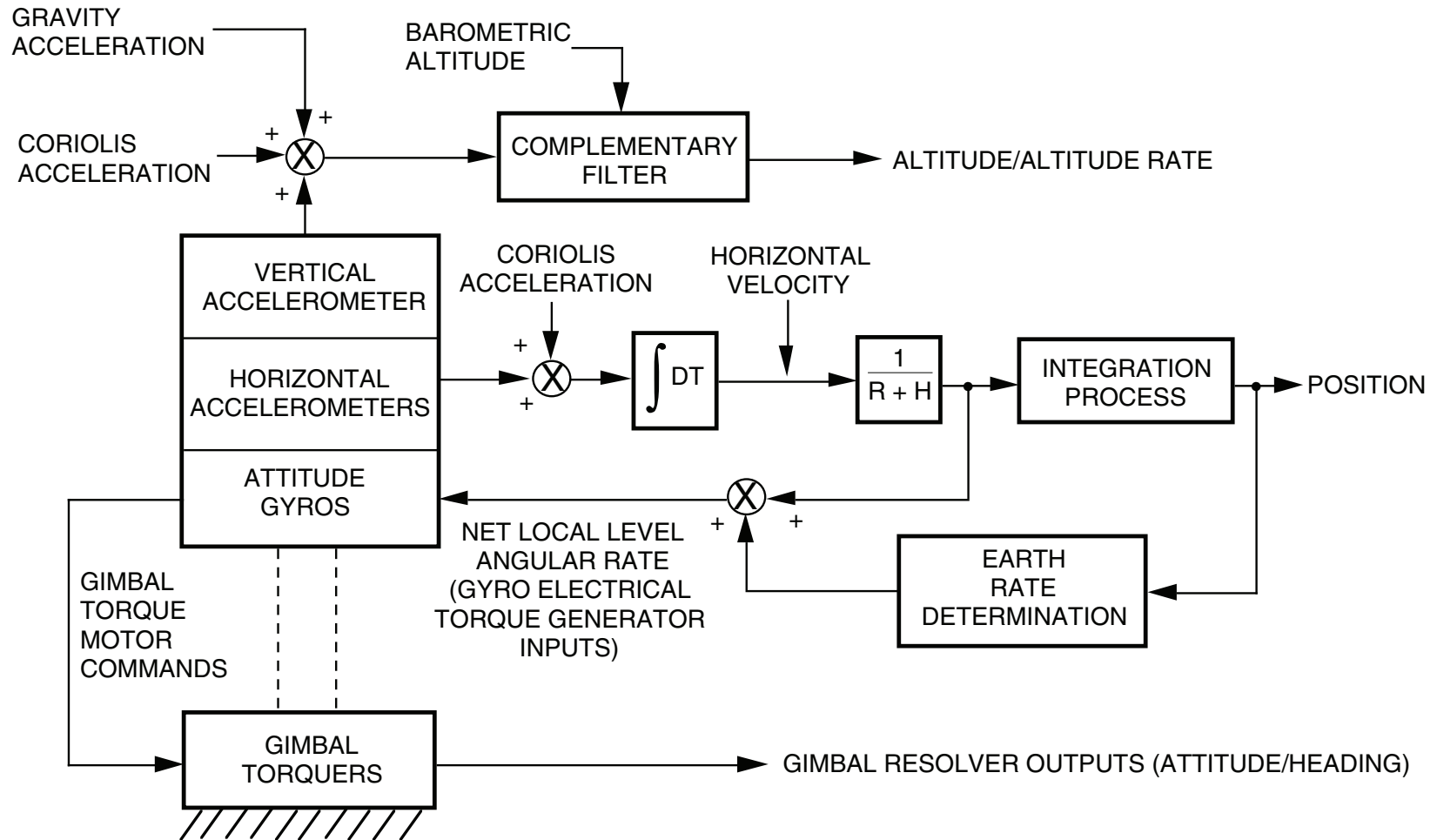
A typical gyro stabilized inertial platform consists of a platform (or stable element) to which are mounted a set of three-axis sensing gyros and accelerometers, a gimbal assembly connecting the platform to the user vehicle, torque motors for rotating the gimbals relative to one another, resolvers for sensing the relative gimbal angle orientations, and suitable bearings, slip rings, and electronics to operate the platform.

The gyros sense angular deviations of the platform from its inertial (non-rotating) orientation and provide drive signals to the platform gimbal torque motors to maintain the gyro outputs at null in each of the three orthogonal platform axes. In this manner, the platform is controlled to remain inertially stable in the presence of aircraft angular rotations. The gyros also contain electrical torque generators which can be utilized to create a fictitious input rate to the gyros.

Application of electrical input to the gyro torque generators causes the gimbal torque motor/servos to null the difference between the true gyro input rate and the electrically applied bias rate. Hence, the true rate becomes equal to the electrically applied rate. This mechanism is used by the system computer to produce platform angular rotation rates.

The accelerometers, being physically mounted to the gyro platform, sense input accelerations along gyro stabilized axes. Since the gyro platform orientation is known initially, and the platform rotation rate commands (applied through the gyro torque generators) are produced (hence also known) by the navigation computer, the platform orientation is known continuously following initialization. Therefore, the accelerometer orientations are also known, hence their outputs can be properly interpreted to determine velocity and position through suitable computerized integration algorithms.

# MAINTAINING A LEVEL PLATFORM



## MAINTAINING A LEVEL PLATFORM

In most gimballed inertial navigation systems, the sensor platform is maintained in a horizontal attitude as the vehicle containing the system travels over the earth. In this manner, the platform accelerometers provide direct measures of vertical and horizontal acceleration which can then be easily integrated to determine horizontal and vertical velocity/position (i.e., horizontal velocity, latitude/longitude position, altitude rate, and altitude).

The platform is maintained horizontal by causing it to rotate (by electrical gyro torque generator command) at an angular rate equal to earth's horizontal rotation rate plus the horizontal angular rotation rate of the vehicle position vector over the earth. The horizontal earth rate components are calculated based on computed vehicle position over the earth (latitude). The horizontal angular rate due to vehicle translation over the earth (also known as "transport rate") is calculated by dividing the computed horizontal velocity by the radial distance from the center of the earth to the vehicle (the sum of earth's radius  $R$  plus altitude  $H$ ). Note that position which is a measure of earth angle is calculated as an integrated function of the transport rate.

The gimbal torquer loops are illustrated in the slide to show the physical mechanism by which the platform is stabilized and made to rotate at the gyro torque generator input rate (i.e., by nulling the gyro outputs through platform rates generated by the gimbal torquer drive). The gimbal shaft resolver outputs are also shown in the slide providing measures of aircraft heading and attitude (pitch/roll). It is easily verified that for a three gimbal assembly oriented with the outer gimbal axis along the aircraft longitudinal axis, the outer gimbal angle measures aircraft roll, the middle gimbal angle measures aircraft pitch, and the inner gimbal angle measures aircraft heading relative to the heading orientation of the stable element.

The vertical acceleration from the platform (plus gravity) is shown being combined with a barometric altitude input signal (from an air data computer) in the integration process to generate altitude rate and altitude (using a complementary blending filter). As will be described later, the baro signal is required to stabilize vertical loop divergence created through the calculation of gravity (a function of altitude).

## **MAINTAINING A LEVEL PLATFORM (CONTINUED)**

Note that Coriolis acceleration terms are added to both the vertical and horizontal acceleration signals prior to velocity/position integration. Coriolis accelerations are corrections that account for the fact that the earth is rotating, and that the computed velocity is traditionally referenced to a locally horizontal coordinate frame that is also rotating relative to the earth surface at the aircraft transport rate. These angular rate effects rotate the vehicle velocity vector which is equivalent to an acceleration (acceleration is the rate of change of velocity, which includes velocity magnitude as well as direction changes). Since the system accelerometers measure velocity rate relative to nonrotating space, and since it is desired that the integrated acceleration represent velocity relative to the rotating earth, the Coriolis accelerations must be added to the sensed acceleration prior to velocity integration.

**NOTES**

## **GIMBALED SYSTEM ADVANTAGES**

- **LOCAL LEVEL GYRO ORIENTATION MINIMIZES G-SENSITIVE ERRORS**
- **LOCAL LEVEL STABILIZATION MINIMIZES GYRO ROTATION RATE REQUIREMENTS**
- **LOCAL LEVEL ACCELEROMETER OUTPUTS DIRECTLY IN FORM NEEDED FOR NAVIGATION CALCULATION – SIMPLIFIED COMPUTER REQUIREMENTS**
- **STABLE SENSOR AZIMUTH CANCELS ACCELEROMETER BIAS/MISALIGNMENT EFFECTS AND SOME EAST GYRO BIAS ERROR EFFECTS**
- **GIMBALED PLATFORM MAY BE USED AS AN ONBOARD TEST TABLE FOR SYSTEM SELF CALIBRATION OF SENSORS**

## GIMBALED SYSTEM ADVANTAGES

Mechanization of an inertial navigation system (INS) around a mechanically gimballed platform provides certain benefits that relax the performance requirements for the system sensors.

For gyros whose accuracy is sensitive to acceleration, maintaining a fixed orientation of the gyros relative to vertical can minimize G-sensitive error effects. For example, in instances where the G-sensitivity is lower along a particular gyro non-input axis, that axis can be oriented along the vertical (assuming that the input axis is still oriented along the proper platform axis direction). Since the average acceleration for cruise inertial systems is along the vertical, such an arrangement tends to minimize G-sensitive errors.

Because the gyros are mounted to the stabilized element, gyro rotation rate requirements are fairly minimal. For example, even in a Mach 3 aircraft, the rotational rates needed to maintain a level platform never exceed one degree per minute. This reduces the maximum torque generator rate requirement for platform mounted gyros. Since conventional spinning mass gyro accuracy degrades as torque generator rate requirements increase (e.g., due to torque generator heating or torque generator assembly mass unbalance), improved gyro performance results when maximum torque generator rate requirements are minimized.

As we will see during a later portion of the course, maintaining the gyros and accelerometers in the same orientation relative to the earth during flight as during system initialization alignment, can improve overall system accuracy. In the case of typical platform mounted sensors, the platform attitude and heading relative to the earth generally remain parallel to the ground initialization orientation by virtue of the platform stabilization loops, regardless of the aircraft flight path direction. In the case of the accelerometers, this causes platform tilt errors (created by the accelerometers during the INS initial alignment phase) to cancel the accelerometer errors during flight. East gyro bias errors during flight are similarly canceled by platform heading errors created by the East gyro bias during initial INS heading alignment.

Another benefit provided in high accuracy gimbaled systems is the built-in availability of the sensor platform for use as a rotation test table for the gyros and accelerometers on-board the aircraft. As a result, the inertial instruments can be rotated in a prescribed manner relative to the local vertical and earth rate vector during a selectable preflight sensor calibration mode. Measuring sensor outputs at these different orientations allows the sensor errors to be discriminated from actual specific force and earth rotation rate inputs, thereby, providing the required measurement for system self-calibration of the sensor errors. As a result of this built-in calibration capability, the long term stability requirements for the sensors (particularly the gyros) can be significantly reduced.

## **GIMBALED SYSTEM CONCERNS**

- **RELIABILITY/COST OF GIMBAL ASSEMBLY**
  - **TORQUE MOTORS**
  - **BEARINGS**
  - **SLIP RINGS**
  - **RESOLVERS**
  - **HIGH POWER DRIVE ELECTRONICS**
- **NO RATE SIGNALS AVAILABLE FOR OUTPUT TO OTHER AIRCRAFT SYSTEMS**
- **BODY ACCELERATION NOT DIRECTLY AVAILABLE**

## **GIMBALED SYSTEM CONCERNS**

On the other hand, utilization of a gimbal assembly to stabilize the inertial sensors also introduces significant penalties. The gimbal assembly is a fairly complex electromechanical assembly consisting of torque motors, gimbal bearings, slip rings, resolvers, and associated high power servo drive electronics. Such an assembly is fairly expensive, and the reliability of such devices in operational use (particularly in military environments) has been limited.

For advanced applications, alternative inertial systems (i.e., strapdown) provide airframe angular rate and linear acceleration outputs as an inherent part of their mechanization (for use as inputs to aircraft flight control or fire control systems). Such signals are not readily available from a gimbaled platform system, and if provided, the signal quality (particularly of the rate signals which must be derived from the platform resolver signals) is generally poor (noisy or with low bandwidth).

# **STRAPDOWN INERTIAL NAVIGATION CONCEPT**

- **ACCELEROMETERS MOUNTED DIRECTLY TO AIRFRAME (STRAPDOWN)**
  - **MEASURE “BODY” ACCELERATIONS**
- **HORIZONTAL/VERTICAL ACCELERATIONS COMPUTED ANALYTICALLY USING DIRECTION COSINE MATRIX (DCM) RELATING BODY COORDINATES AND LOCAL LEVEL NAVIGATION COORDINATES**
- **DIRECTION COSINE MATRIX COMPUTED USING STRAPDOWN BODY MOUNTED GYRO OUTPUTS**

## **STRAPDOWN INERTIAL NAVIGATION CONCEPT**

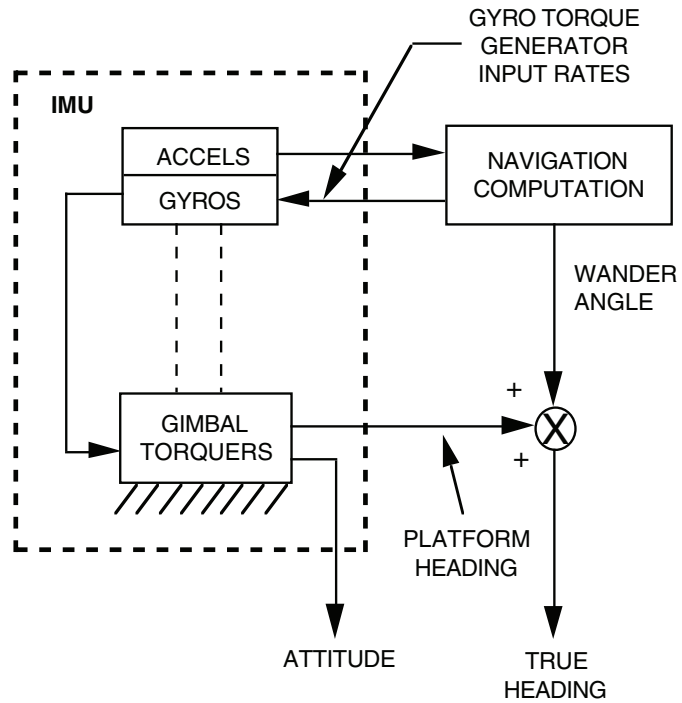
In a strapdown inertial navigation system, the system accelerometers are directly connected to the airframe, hence, the accelerometers measure the components of aircraft specific force acceleration in airframe (or "body") axes.

The horizontal and vertical acceleration components needed for the inertial navigation computer equations are obtained "analytically" in a strapdown system from the sensed body axis acceleration signals, using a vector transformation operation.

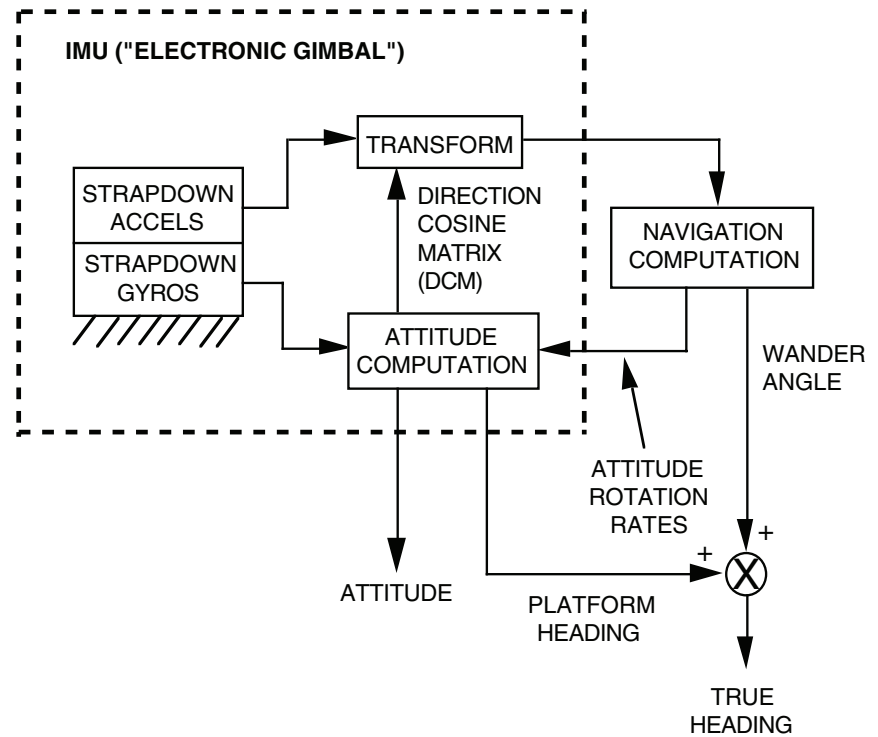
The required body axis to local vertical axis direction cosine matrix for the acceleration transformation operation is computed in a strapdown INS using the output data from a set of body mounted strapdown gyros.

# STRAPDOWN COMPARED TO GIMBALED INERTIAL NAVIGATION SYSTEMS

**GIMBALED SYSTEM**



**STRAPDOWN SYSTEM**



## STRAPDOWN COMPARED TO GIMBALED INERTIAL NAVIGATION SYSTEMS

The slide illustrates the basic functional differences between a strapdown and gimbaled INS. As can be seen, both concepts are equivalent with regard to the basic navigation (position/velocity) calculations implemented in the system computer. The systems differ in the manner in which the navigation computation inputs are generated.

In the case of the gimbaled system, the navigation computation inputs are typically obtained directly from the platform mounted accelerometers. A feedback loop is typically contained in a gimbaled system that commands the platform mounted gyro torque generators so that the accelerometers remain aligned at some desired orientation relative to the earth (e.g., horizontal and vertical). The gyro torque generator input signals are computed functions of navigation data (e.g., the sum of earth rate and aircraft transport rate for a local level platform mechanization).

In the strapdown system, the gimbaled platform stabilization and reference rotation rate functions are provided analytically in the system computer based on the outputs from the strapdown gyros and accelerometers. The attitude of the aircraft relative to the "navigation computation frame" is calculated as an integration process using strapdown gyro signals to measure the inertial aircraft rotation rate, and the feedback "platform rate signals" from the navigation computation as the measure of the rotation rate of the navigation reference frame (e.g., locally level) relative to inertial space. The aircraft attitude is computed in the form of a direction cosine matrix relating body to navigation coordinate axes. The direction cosine matrix (DCM) is utilized to transform the strapdown accelerometer output signals from body to navigation axes. The transformed strapdown acceleration signals thereby become identically equivalent to the accelerations measured by the gimbaled platform accelerometers. As with the gimbaled platform, the transformed accelerations are then input to the navigation position/velocity integration equations.

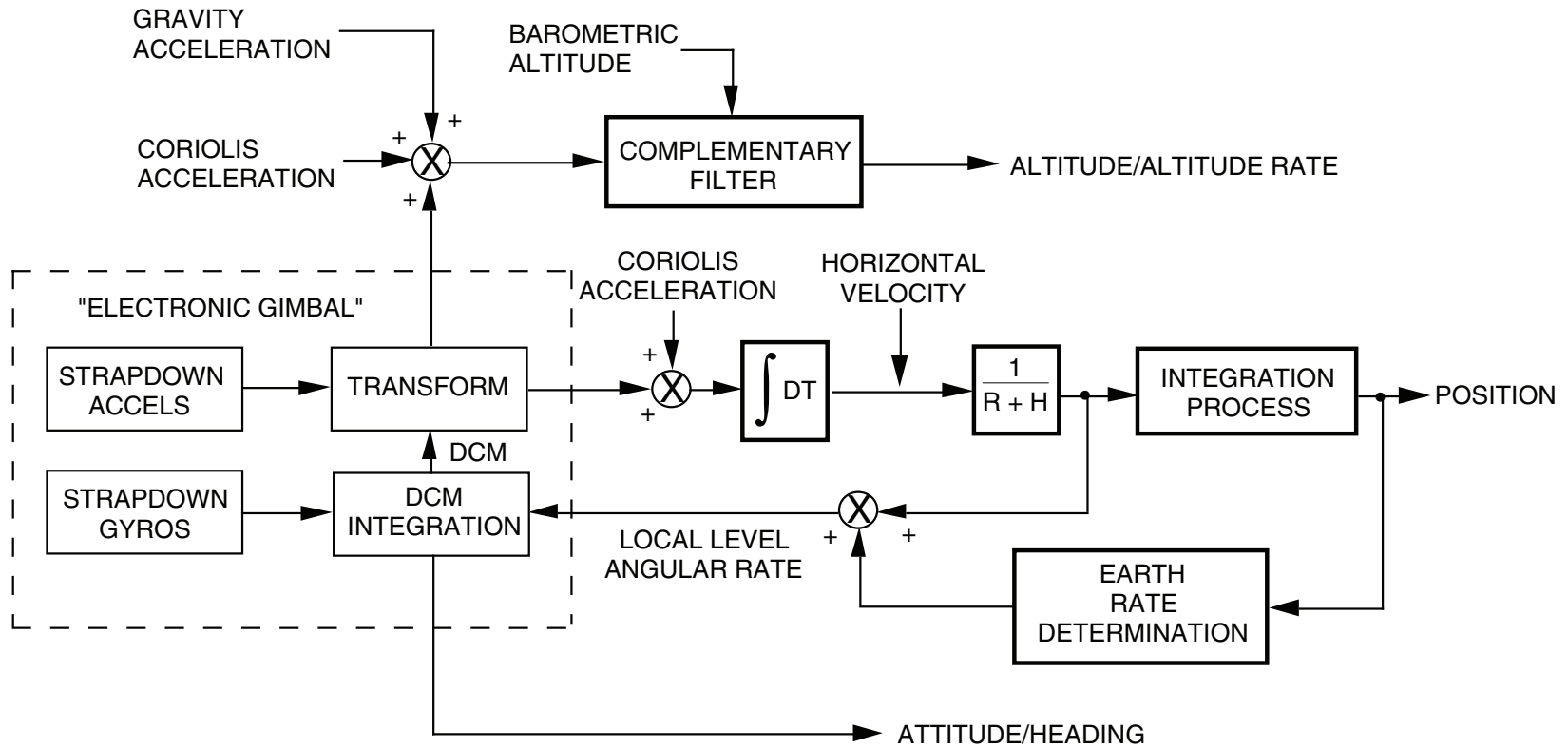
## **STRAPDOWN COMPARED TO GIMBALED INERTIAL NAVIGATION SYSTEMS (CONTINUED)**

The physical element represented by the gimbaled platform assembly has been referred to as an Inertial Measurement Unit (IMU). The comparable function performed by the strapdown sensors and analytical attitude/transformation operations has been referred to as an "Electronic Gimbal" because its inputs and outputs are directly equivalent to the mechanical IMU inputs and outputs.

Finally, it is to be noted that aircraft attitude and heading data are obtained from the gimbal platform shaft angle resolvers. The identically equivalent signals are obtained from the attitude data in the strapdown IMU by analytical conversion. In both the gimbaled and strapdown systems, the "platform heading" is shown to be corrected by the "wander angle" to determine the desired aircraft true heading output signal. The wander angle represents the azimuth angle (about the local vertical) between North/East axes and the navigation coordinate axes (assuming that navigation coordinates are horizontal/vertical). This is the first time we have alluded to the fact that navigation coordinates may not be North/East oriented. As we shall see later in the course, certain computational considerations generally dictate that a North/East navigation coordinate frame orientation is a poor choice for an inertial navigation system requiring a complete global navigation capability.

**NOTES**

# STRAPDOWN INERTIAL NAVIGATION SYSTEM CONFIGURATION

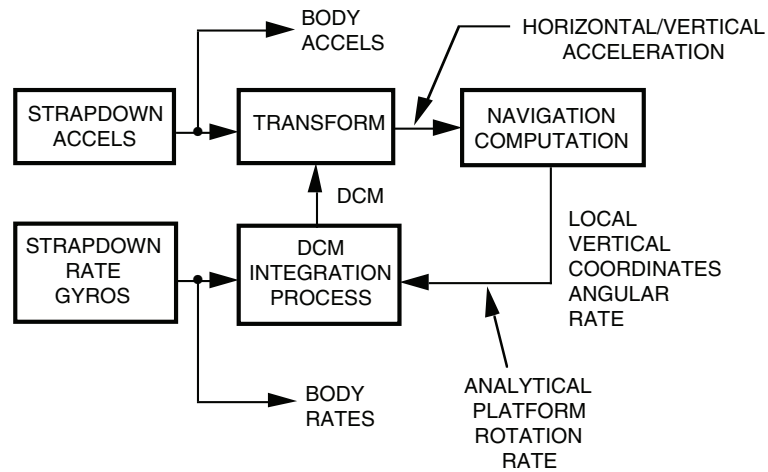


## **STRAPDOWN INERTIAL NAVIGATION SYSTEM CONFIGURATION**

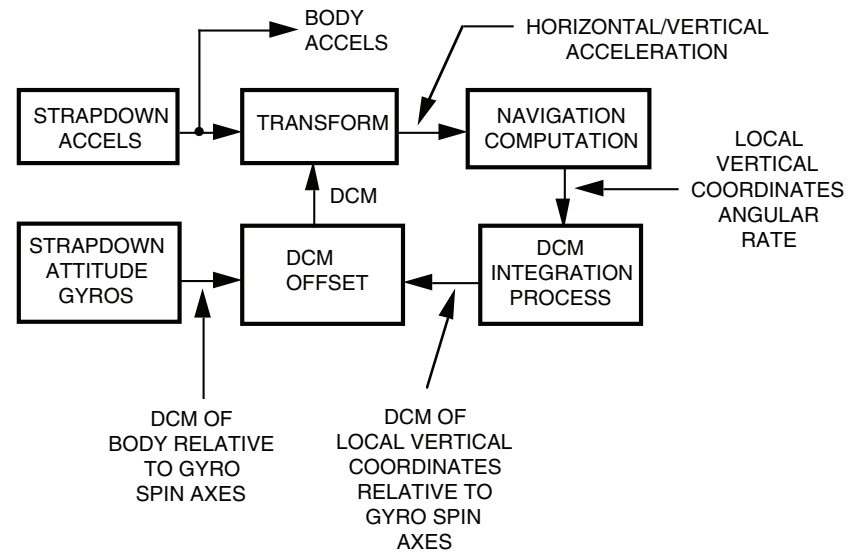
The chart depicts the inertial navigation system on page 48 with the gimbaled platform replaced by its strapdown functional equivalent (the "electronic gimbal"). The result is the general configuration of a strapdown inertial navigation system.

# STRAPDOWN INERTIAL IMPLEMENTATIONS

## RATE GYRO SYSTEM



## ATTITUDE GYRO SYSTEM



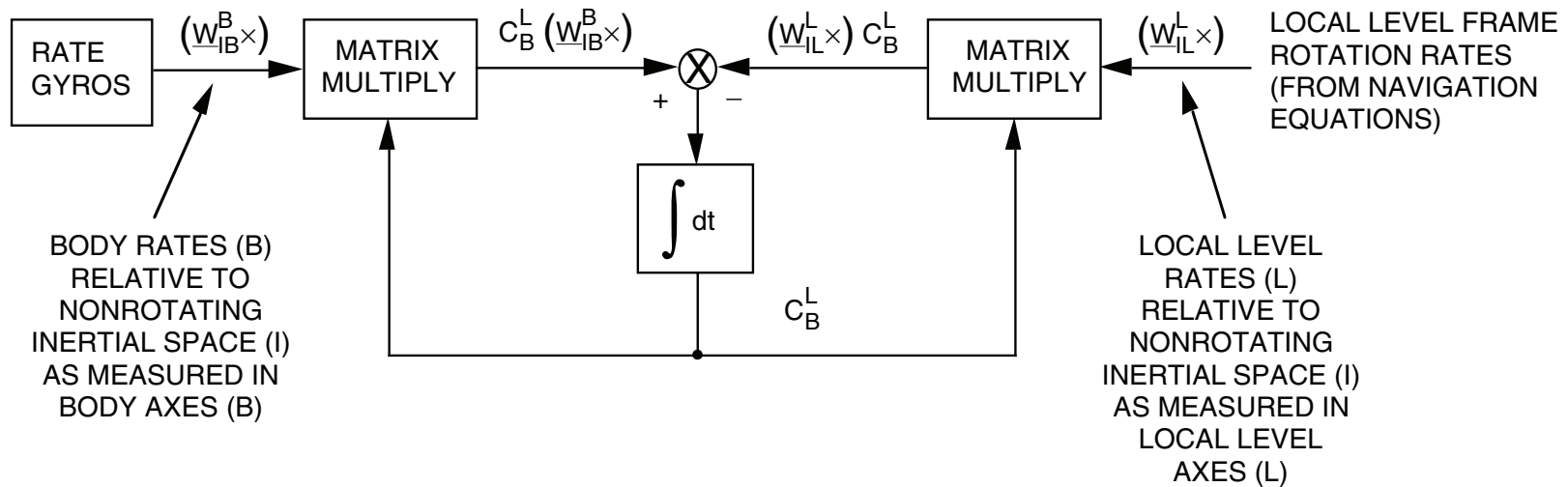
## STRAPDOWN INERTIAL IMPLEMENTATIONS

Thus far, we have implied that the gyros in a strapdown inertial system measure body rates which are then used through a suitable integration algorithm to calculate aircraft attitude. This is the "conventional" strapdown implementation approach.

In at least one system (using Electrostatic Gyros-ESGs), however, the strapdown gyros measure aircraft attitude relative to a nonrotating inertial gyro reference frame. In this alternate type of strapdown system, the attitude gyro signals represent the direction cosine matrix (DCM) relating body to gyro inertial coordinates. To calculate the desired body-to-navigation coordinate DCM, the gyro DCM must be multiplied by the DCM relating navigation to gyro inertial coordinates (the DCM offset operation indicated in the slide). The DCM relating navigation coordinates (denoted in the slide as "local vertical" coordinates) to gyro inertial coordinates, is calculated through an integration operation on the computed navigation frame rotation rates relative to inertial space ("local vertical angular rates" in the slide).

In other respects, the two strapdown implementation concepts shown are equivalent.

# DIRECT DCM COMPUTATION FROM STRAPDOWN RATE GYRO SIGNALS



$$(\underline{W}_{IB}^B \times) = \begin{bmatrix} 0 & -WBZ & WBY \\ WBZ & 0 & -WBX \\ -WBY & WBX & 0 \end{bmatrix}$$

$$(\underline{W}_{IL}^L \times) = \begin{bmatrix} 0 & -WLZ & WLY \\ WLZ & 0 & -WLX \\ -WLY & WLX & 0 \end{bmatrix}$$

## DIRECT DCM COMPUTATION FROM STRAPDOWN RATE GYRO SIGNALS

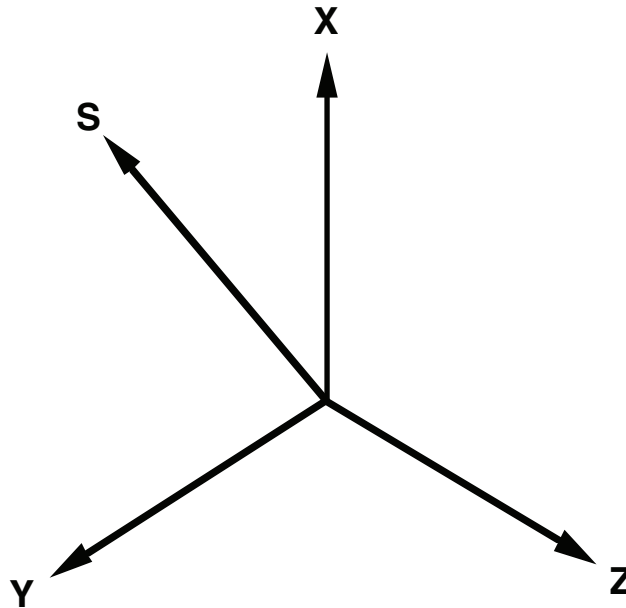
The slide indicates the form of the equations implemented in a rate gyro type strapdown inertial navigation system for directly calculating the direction cosine matrix (DCM) relating body-to-navigation (e.g., locally level) axes. The  $C_B^L$  DCM is computed as a continuous integration of scaled gyro body rates (relative to inertial space) and local level rates (relative to inertial space). The angular rate scale factors are the elements of the computed DCM.

In the slide, the  $(\underline{W} \times)$  matrices are the cross-product form of the body (B) and local level (L) frame angular rate vectors ( $\underline{W}_{IB}^B$  and  $\underline{W}_{IL}^L$ ) whose components are respectively, WBX, WBY, WBZ and WLX, WLY, WLZ.

## SKEWED STRAPDOWN SENSOR REDUNDANCY

### EXAMPLE

ORTHOGONAL  
TRIAD WITH  
ONE SKEWED  
AXIS



$$WS = A WX + B WY + C WZ$$

$$WX = \frac{1}{A} (WS - B WY - C WZ)$$

$$WY = \frac{1}{B} (WS - A WX - C WZ)$$

$$WZ = \frac{1}{C} (WS - A WX - B WY)$$

- ANY THREE SENSORS CAN BE USED TO DERIVE ORTHOGONAL 3-AXIS BODY RATE DATA
- FAILURE IN ANY SENSOR DETECTABLE BY:  
PARITY =  $A WX + B WY + C WZ - WS \neq 0$
- FAILURE ISOLATION TO PARTICULAR SENSOR REQUIRES ADDITIONAL REDUNDANCY LEVEL

## **SKEWED STRAPDOWN SENSOR REDUNDANCY**

By virtue of the strapdown mechanization that does not require a dedicated gimbal assembly for each cluster of inertial sensors, strapdown systems offer the potential of a unique low cost method for achieving redundancy. The concept is to utilize sensor input axis geometries that are skewed (rather than orthogonal) relative to one another.

For example, consider a conventional orthogonal three-axis sensor input-axis triad with a fourth sensor input axis skewed relative to the orthogonal set. The equations show that the X, Y, or Z axis sensor output can be calculated from a linear combination of the skewed sensor output and the outputs from the other two orthogonal sensors (e.g., WX can be calculated from WS, WY, and WZ). Thus, if either the X, Y, Z sensor outputs are unavailable directly (e.g., due to sensor failure), a redundant equivalent signal can be generated using WS and the remaining two orthogonal sensors. Hence, the one additional skewed sensor provides a single level of redundancy to protect failures in either the X, Y, or Z axis sensors. Conventional redundancy schemes typically require separate redundant X, Y, and Z sensors for the same level of redundancy protection.

The general skewed redundancy concept is based on the use of skew aligned tetrad (four-skew axis) sensor sets. The outputs from any three skewed sensors in such an array can be operated upon analytically to calculate the desired orthogonal three-axis sensor output equivalent. Thus, any one sensor in a tetrad can fail, leaving three to calculate a complete three-axis orthogonal output set.

In terms of redundancy management, three skewed sensors in a tetrad can be used to calculate the output from the fourth skewed sensor. The difference between the computed and actual sensor output defines a "parity" signal which should be zero if all four skewed sensors in the tetrad are operational. Failure of the parity signal (a non-zero value) indicates a failure in one of the four sensors.

## FAILURE ISOLATION IN SKEWED 5-AXIS (PENTAD) SENSOR ARRAY

- **CONFIGURATION – 5 SENSORS SKEWED RELATIVE TO EACH OTHER:  
NO 3 SENSING AXES COPLANAR**
- **PARITY EQUATIONS**

$$P1 = A1 W1 + A2 W2 + A3 W3 + A4 W4$$

$$P2 = B2 W2 + B3 W3 + B4 W4 + B5 W5$$

$$P3 = C3 W3 + C4 W4 + C5 W5 + C1 W1$$

$$P4 = D4 W4 + D5 W5 + D1 W1 + D2 W2$$

$$P5 = E5 W5 + E1 W1 + E2 W2 + E3 W3$$

- **FAULT ISOLATION MATRIX**

	W1	W2	W3	W4	W5
P1	X	X	X	X	
P2		X	X	X	X
P3	X		X	X	X
P4	X	X		X	X
P5	X	X	X		X

## **FAILURE ISOLATION IN A SKEWED 5-AXIS (PENTAD) SENSOR ARRAY**

To isolate a failed sensor in a tetrad, a fifth skewed sensor is needed. Five tetrads can be defined from such a five skewed axis array, each having a self monitoring parity equation. The parity equation that equals zero in such an arrangement identifies the four properly operating instruments. If the remaining four parity equations are nonzero, a failure is indicated (hence, isolated) to the fifth sensor (not contained in the parity OK tetrad).

Using this logic, it is readily evident that four skewed sensors provide a single failure detection capability, five skewed sensors provide the capability to isolate any one failure and indicate that any second failure has occurred (though not isolated), a six axis array (hexad) provides a two-failure isolation capability with the ability to detect the occurrence of a third failure, etc. The comparable capability using redundant sensors along each orthogonal input axis requires 6 sensors (for any single failure detection), 9 sensors for single failure isolation and a second failure detection (per channel), 12 sensors for double failure isolation and third failure detection (per channel), etc. The sensor savings becomes increasingly significant for the skewed sensor redundancy concept as the redundancy level requirement increases.

## **STRAPDOWN SYSTEM ADVANTAGES**

- **NO MECHANICAL GIMBAL ASSEMBLY (RELIABILITY/COST)**
  - **ADDITIONAL COMPUTER THROUGHPUT FOR STRAPDOWN ALGORITHMS NOT A PROBLEM FOR MODERN DAY MICROPROCESSORS**
- **BODY RATE/ACCELERATION SIGNALS DIRECTLY AVAILABLE FOR OUTPUT TO OTHER AIRCRAFT SYSTEMS**
- **SENSOR REDUNDANCY ADVANTAGES AVAILABLE**

## **STRAPDOWN SYSTEM ADVANTAGES**

By eliminating the complex gimbal isolation assembly, strapdown systems provide lower cost and higher reliability. In the 1960s when strapdown inertial navigation technology was in its early stages of development, the additional burden placed by the strapdown mechanization on computational speed and associated computer requirements, more than offset the cost advantages of eliminating the gimbal isolation assembly. Through the advent of the modern day high speed low cost microprocessor, the additional strapdown computational requirements can be achieved today for virtually no computer penalty.

Due to the nature of the strapdown body mounted sensor mechanization, strapdown systems provide three-axis body angular rate and acceleration signals as additional outputs for other aircraft system usage. As a result, separate sensor assemblies that may have been required to provide these functions can be eliminated.

In redundant applications, strapdown systems offer further cost advantages through the application of strapdown skewed sensor redundancy.

## **STRAPDOWN SYSTEM CONCERNS**

- **MORE DIFFICULT SENSOR PERFORMANCE REQUIREMENTS**
  - **GYROS – HIGH ROTATION RATES**
  - **ACCELEROMETERS – NON-CANCELLING BIAS ERROR EFFECTS**
- **SENSOR CALIBRATION MORE DIFFICULT – NO BUILT-IN ONBOARD TEST PLATFORM**

## **STRAPDOWN SYSTEM CONCERNS**

Due to the strapdown mounting of the sensors in a strapdown system, they are exposed to the full aircraft angular rate environment. This places a significant demand on gyros which must achieve high accuracy while being exposed to angular rates that can be as high as 300 deg/sec (for military fighter aircraft). For both the strapdown gyros and accelerometers, the benefit of error cancellation (from sensor generated initial attitude and heading alignment errors) is lost because the sensor axes in flight will in general not be parallel to their preflight initial alignment orientation. For the case where the flight direction is opposite to the alignment direction, the initial alignment errors (which cancel gyro and accelerometer error effects in gimbale systems) will actually add to the errors in flight, thereby doubling their net impact on navigational error.

Because the gimbaled platform is eliminated in a strapdown system, the ability to use the platform as a self-contained test table is also eliminated. This makes it difficult (if not impossible) to separate earth rate and specific force acceleration inputs to the strapdown sensors from the sensor errors during a preflight self-calibration operation. The result is a more demanding requirement for long term stability from strapdown sensors (particularly the gyros) to eliminate the need for periodic system removals from the aircraft for calibration purposes.

## **STRAPDOWN SYSTEM STATE-OF-THE-ART**

- **TODAY'S GYRO AND ACCELEROMETER PERFORMANCE CAPABILITIES ARE COMPATIBLE WITH A BROAD RANGE OF STRAPDOWN APPLICATION REQUIREMENTS**
- **THE RING LASER GYRO (RLG) HAS PROVIDED THE ACCURACY REQUIRED FOR AIRCRAFT INERTIAL NAVIGATION QUALITY PERFORMANCE TO COMPENSATE FOR STRAPDOWN ROTATION ENVIRONMENT HANDICAPS**
- **THE RLG HAS PROVIDED HIGH RELIABILITY/LOW PRODUCTION COSTS TO DECREASE OVERALL LIFE CYCLE COSTS**
- **THE FIBER OPTIC GYRO (FOG) HAS RECENTLY PROVED CAPABLE OF PROVIDING AIRCRAFT INERTIAL NAVIGATION QUALITY PERFORMANCE**
- **EXCEPT FOR A FEW SPECIAL CASES, RLG (OR FOG) STRAPDOWN INERTIAL NAVIGATION TECHNOLOGY HAS MADE GIMBALED INERTIAL NAVIGATION SYSTEMS OBSOLETE**

## **STRAPDOWN SYSTEM STATE-OF-THE-ART**

Today's gyro and accelerometer capabilities meet the performance requirements for a broad range of strapdown applications. The particular instruments selected for a given application depend on tradeoffs involving accuracy, size, weight, power, cost, and reliability requirements.

Due to the advent of the ring laser gyro (RLG), the required high accuracy in aircraft inertial navigation quality systems can be provided in high body rate environments for costs comparable to gimbale platform gyros. Because the RLG has no rotating parts and a significant reduction in precision parts and assembly operations (compared to conventional momentum wheel gyros), RLG strapdown systems provide low production cost and high reliability, hence, reduced overall life cycle cost.

Recently, the fiber optic gyro (FOG) has also exhibited performance compatible with aircraft strapdown inertial navigation accuracy requirements.

The introduction of RLG strapdown technology since 1980 into aircraft quality inertial navigation (and recently the FOG as well) has, except for a few special cases, made gimbale inertial navigation systems obsolete.

**NOTES**

# **INERTIAL NAVIGATION POSITION/VELOCITY EQUATIONS**

## **TYPICAL INERTIAL NAVIGATION POSITION/VELOCITY EQUATIONS**

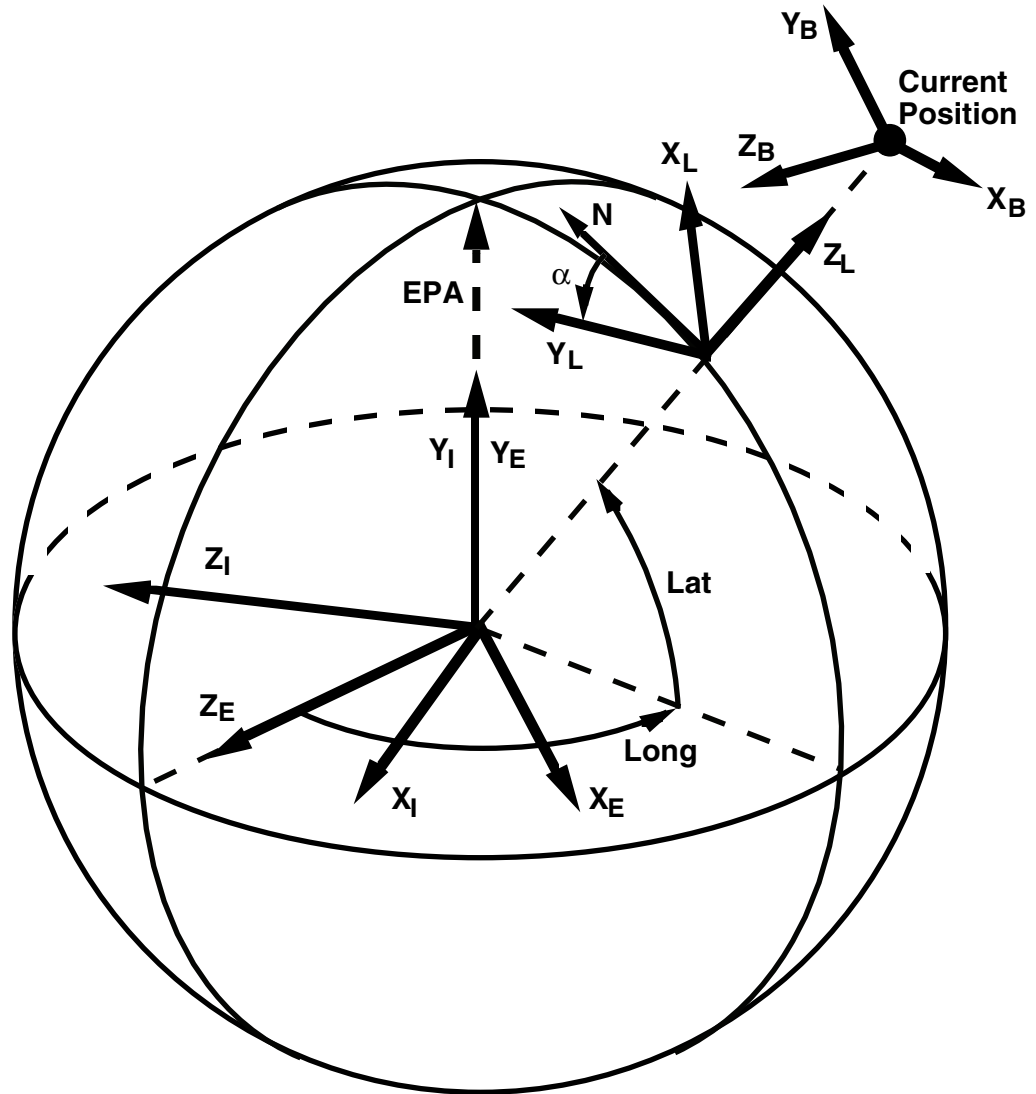
- **GEOGRAPHIC (OR LATITUDE/LONGITUDE) IMPLEMENTATION**
- **WANDER OR FREE AZIMUTH IMPLEMENTATION**

## TYPICAL INERTIAL NAVIGATION POSITION/VELOCITY EQUATIONS

To gain some insight into the details of the actual equations utilized to calculate position and velocity in inertial navigation, two representative equation types will be described: the geographic (or latitude/longitude) type, and the wander or free azimuth type. Both approaches calculate position/velocity parameters utilizing a locally level navigation coordinate frame. The methods differ in the azimuth (or heading) orientation of the navigation frame horizontal axes relative to North.

# COORDINATE FRAMES

- Lat = Latitude
- Long = Longitude
- $\alpha$  = Wander Angle
- EPA = Earth Polar Axis
- N = North
- B = Body (Sensor) Coordinates
- L = Local Level Navigation Coordinates
- E = Earth Fixed Coordinates
- I = Inertial (Non-rotating) Coordinates



## COORDINATE FRAMES

The principle coordinate frames used in this course are illustrated in the chart. The frames are shown with separated origins to aid in understanding. Mathematically, only the angular orientation between the frames is of importance for the analytical material presented in this course. All are orthogonal right-handed coordinate frames.

The earth frame (E) maintains a fixed angular orientation relative to the rotating earth. Using original inertial navigation coordinate axis assignments, the  $Y_E$  axis is parallel to the earth's rotation (polar) axis (EPA) and the  $Z_E$  and  $X_E$  axes are parallel to earth's equatorial plane. The  $Y_E - Z_E$  plane is parallel to the zero reference Prime Meridian (not indicated in the chart) that passes through Greenwich UK. A commonly defined non-rotating inertial (I) coordinate frame is also shown in the chart with the  $Y_I$  axis parallel to the EPA and with the  $Z_I$  and  $X_I$  axes parallel to earth's equatorial plane. The E Frame rotates around the I Frame at earth's inertial angular rotation rate. The I Frame is usually denoted as being earth centered, however as noted above, this has no bearing on analytical developments in this course.

The locally level (L) navigation frame has its  $Z_L$  axis upward and parallel to the "local vertical", a direction parallel to a line drawn from the current position that intersects perpendicularly to a plane tangent to the earth's surface directly below (or above) the current position location. The L Frame  $X_L$  and  $Y_L$  axes are parallel to the local tangent plan. The L Frame is used for velocity integration and as a reference for angular orientation of the strapdown sensor body (B) Frame. In general, depending on the L Frame type (e.g., geographic, free-azimuth, wander-azimuth), the  $Y_L$  axis may not lie along a northerly direction (N in the chart). The angle measured around  $Z_L$  between the  $Y_L$  axis and north is denoted as the wander angle.

The angular orientation of the  $Z_L$  axis relative to the E Frame defines the latitude and longitude of the current position location. Longitude is measured around  $Y_E$  from the  $Z_E$  axis to the local meridian containing  $Z_L$  and the EPA. Latitude is measured in the local meridian plane from earth's equatorial plane to  $Z_L$ .

The B Frame is parallel to the strapdown gyro and accelerometer input axes and is commonly oriented in an aircraft with  $X_B$  axis parallel to the aircraft longitudinal axis, the  $Y_B$  axis parallel to the right wing, and the  $Z_B$  axis parallel to the negative lift direction.

## TYPICAL L-FRAME CONFIGURATIONS

- **BY DEFINITION, LOCALLY LEVEL, Z-UP**
- **GEOGRAPHIC (OR LATITUDE/LONGITUDE) – Y NORTH, X EAST**
- **WANDER AZIMUTH – INERTIAL ROTATION RATE OF X, Y ABOUT Z EQUAL TO Z – COMPONENT OF EARTH RATE**
- **FREE AZIMUTH – INERTIAL ROTATION RATE OF X, Y ABOUT Z EQUAL TO ZERO**

## TYPICAL L-FRAME CONFIGURATIONS

For the discussion to follow, different locally level navigation coordinate frames (L-Frames) will be analyzed with regard to their suitability for inertial position/velocity calculations.

The classical L-Frame is the geographic (or latitude/longitude) type which has its horizontal axes directed along locally level North and East axes. The advantage of such a frame is that navigation data computed in its coordinates are in the normally desired North/East/vertical format for output.

Alternatively, wander or free azimuth locally level coordinate frames may be utilized. These frames do not attempt to constrain the horizontal axes to lie along specified earth geographic axes. Instead, the axes are allowed to assume some arbitrary form based on angular rotation rate considerations. In the azimuth wander case, the horizontal axes have zero rotation rate relative to the earth (or, equivalently, have a rotation rate about the vertical relative to inertial space equal to earth's rate). Such a frame has certain test advantages under static conditions (zero earth referenced velocity) because it is stationary in heading relative to the earth. As a result, system outputs (e.g., horizontal velocity) may be more easily interpreted during stationary tests.

The free azimuth navigation coordinate approach uses zero rotation rate relative to inertial space about the vertical. Such a coordinate frame under stationary earth conditions rotates about the vertical (relative to the earth) opposite to the vertical component of earth's rotation rate. This type of coordinate frame can be advantageous in gimballed systems (where the sensor platform is parallel to navigation axes) because it requires no torque generator input signal for the azimuth gyro. As a result, vertical gyro scale factor error effects are eliminated.

## GEOGRAPHIC IMPLEMENTATION POSITION RATE EQUATIONS

$$\rho_N = \frac{V_E}{R_0} \left[ 1 - \frac{h}{R_0} - e \sin^2 l \right]$$

$$\rho_E = -\frac{V_N}{R_0} \left[ 1 - \frac{h}{R_0} - e (1 - 3 \cos^2 l) \right]$$

$$\dot{l} = -\rho_E \quad l = \int_0^t \dot{l} dt + l_0$$

$$\dot{L} = \rho_N \sec l \quad L = \int_0^t \dot{L} dt + L_0$$

$$\dot{h} = V_Z + u_2 \quad h = \int_0^t \dot{h} dt + h_0$$

$V_N, V_E, V_Z$  = AIRCRAFT NORTH, EAST, VERTICAL VELOCITIES RELATIVE TO EARTH

$l, L, h$  = AIRCRAFT LATITUDE, LONGITUDE, AND ALTITUDE

$R_0$  = MEAN EARTH RADIUS AT EQUATOR

$e$  = EARTH OBLATENESS COEFFICIENT (ELLIPTICITY) EQUAL TO  $\frac{1}{298}$

$u_2$  = BAROMETRIC ALTITUDE DIVERGENCE CONTROL SIGNAL

$\rho_N, \rho_E$  = NORTH AND EAST COMPONENTS OF AIRCRAFT POSITION VECTOR ANGULAR RATE RELATIVE TO EARTH (TRANSPORT RATE)

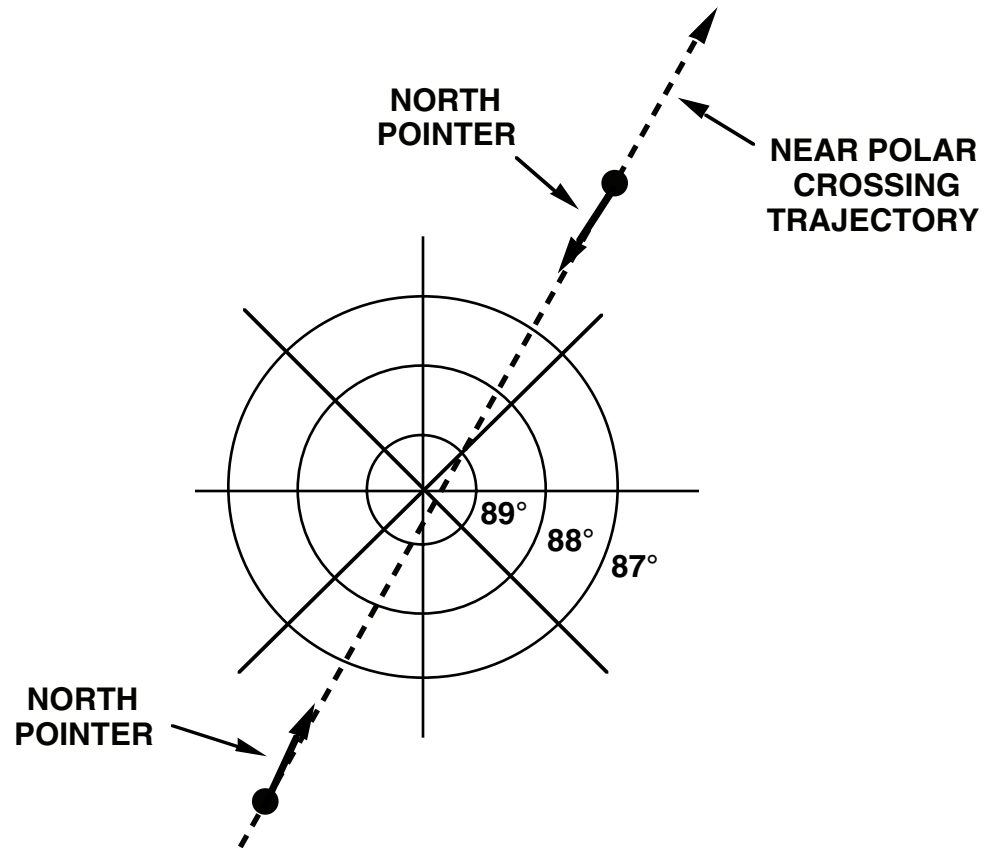
## GEOGRAPHIC IMPLEMENTATION POSITION RATE EQUATIONS

A typical geographic implementation of the inertial navigation position rate equations calculates latitude and longitude rate directly as functions of computed aircraft North and East velocity components. These signals are then continuously integrated to calculate current latitude and longitude.

As can be seen in the slide, the latitude and longitude rates are proportional to the North and East components of aircraft angular transport rate over the earth. The angular transport rate (rotation rate of the local vertical relative to the earth) is principally equal to aircraft North/East velocity components divided by earth's equatorial radius. Correction factors are included to account for earth's oblateness and aircraft altitude above the earth surface. The oblateness coefficient ( $e$ ) recognizes that the earth is not perfectly spherical, but an ellipsoid of revolution (approximately) about the earth polar axis. The altitude rate in the equations is equal to the calculated component of vertical velocity. A correction term ( $u_2$ ) is included in the vertical velocity rate equations derived from a barometric altitude signal input to the INS. The  $u_2$  signal is used to suppress vertical channel instabilities caused by sensor errors and approximations in the gravity calculation (as will be elaborated upon subsequently).

The principle advantage for the geographic position rate equations is their relative simplicity compared to other navigation computation approaches. This had advantages several years ago when flight computers had limited capabilities. The principle disadvantage in the geographic position rate equations is their singularity characteristics at earth polar regions (near  $\pm 90$  degrees latitude) where the secant latitude term in the longitude rate equation becomes excessively large. Due to this singularity, attempts to navigate across either pole would produce large permanent errors in longitude (the integral of longitude rate). As a result, use of direct geographic latitude/longitude position integration equations must be restricted to applications where polar operation will never be necessary.

# GEOGRAPHIC REFERENCE SINGULARITY NEAR POLE CROSSINGS



CIRCLES = CONSTANT LATITUDE (PARALLELS)

LINES = CONSTANT LONGITUDE (MERIDIANS)

EARTH POLAR AXIS = CENTER NORMAL TO PLANE OF DIAGRAM ( $90^{\circ}$  LATITUDE)

## **GEOGRAPHIC REFERENCE SINGULARITY NEAR POLE CROSSINGS**

The cause for the singularity in the geographic coordinate navigation equations is illustrated by a polar view of a near polar crossing. It should be obvious from the slide that as the crossing becomes nearer to the pole, the longitude rate increases excessively. Similarly, the heading direction rapidly slews through 180 degrees as the pole is passed, requiring a corresponding high rotation rate in the local level geographic frame axes (to remain oriented with Y-axis North). The most extreme situation occurs for a direct pole crossing which requires infinite longitude and North reference rotation rates.

# WANDER OR FREE AZIMUTH POSITION RATE EQUATIONS

$$\rho_x = -\frac{V_y}{R_o} \left[ 1 - \frac{h}{R_o} - e (1 - 3d_{22}^2 - d_{21}^2) \right] - \frac{V_x}{R_o} (2e d_{21} d_{22})$$

$$\rho_y = \frac{V_x}{R_o} \left[ 1 - \frac{h}{R_o} - e (1 - 3d_{21}^2 - d_{22}^2) \right] + \frac{V_y}{R_o} (2e d_{21} d_{22})$$

$$\rho_z = 0 \text{ FOR WANDER AZIMUTH OR } -W_e d_{23} \text{ FOR FREE AZIMUTH}$$

$$\begin{aligned} \dot{d}_{11} &= d_{12} \rho_z - d_{13} \rho_y & \dot{d}_{21} &= d_{22} \rho_z - d_{23} \rho_y & d_{ij} &= \int_0^t \dot{d}_{ij} dt + d_{ij0} \\ \dot{d}_{12} &= d_{13} \rho_x - d_{11} \rho_z & \dot{d}_{22} &= d_{23} \rho_x - d_{21} \rho_z & & \text{FOR } i = 1 \text{ to } 2 \\ \dot{d}_{13} &= d_{11} \rho_y - d_{12} \rho_x & \dot{d}_{23} &= d_{21} \rho_y - d_{22} \rho_x & & i = 1 \text{ to } 3 \end{aligned}$$

$$\dot{h} = V_z + u_2 \qquad h = \int_0^t \dot{h} dt + h_0$$

$$d_{33} = d_{11} d_{22} - d_{12} d_{21}$$

$$l = \text{TAN}^{-1} \frac{d_{23}}{(d_{21}^2 + d_{22}^2)^{1/2}} \qquad L = \text{TAN}^{-1} \frac{d_{13}}{d_{33}}$$

- $W_e$  = EARTH INERTIAL ROTATION RATE MAGNITUDE
- $\rho_x, \rho_y, \rho_z$  = L-FRAME X, Y, Z ANGULAR RATES RELATIVE TO EARTH (TRANSPORT RATES)
- $V_x, V_y, V_z$  = AIRCRAFT L-FRAME X, Y, Z VELOCITIES RELATIVE TO EARTH
- $d_{ij}$  = DIRECTION COSINE BETWEEN L-FRAME j-AXIS AND E-FRAME i-AXIS
- $h$  = ALTITUDE
- $l, L$  = LATITUDE AND LONGITUDE
- $R_o$  = EARTH MEAN EQUATORIAL RADIUS
- $e$  = EARTH OBLATENESS COEFFICIENT (ELLIPTICITY) EQUAL TO  $\frac{1}{298}$

## WANDER OR FREE AZIMUTH POSITION RATE EQUATIONS

In order to provide the ability to inertially calculate position over all portions of the globe, wander or free azimuth local level navigation coordinates have been extensively used. The position data with such approaches are calculated in terms of cosines of the angles between a unit vector along the vertical (the Z-axis of the L-Frame) and the earth equatorial/polar axes (E-Frame). The L-Frame Z-axis cosines in E-Frame axes represent the projections of the L-Frame Z-axis on the E-Frame coordinate axes. Clearly, a given set of L-Frame Z-axis projections on the E-Frame, completely defines the orientation of the local vertical in the E-Frame, hence, the position location relative to the earth.

The slide illustrates how rates of change of the cosines of the angles between the L-Frame and E-Frame (or direction cosines) are calculated using the wander or free azimuth approach. The direction cosine rates are proportional to the angular rate components of the L-Frame relative to the earth as determined from calculated L-Frame horizontal velocity components ( $V_x$ ,  $V_y$ ). The direction cosines rates are integrated in the system computer to continuously evaluate the desired direction cosine position data. Note that to calculate the three components of the L-Frame Z-axis in E-Frame coordinates ( $d_{13}$ ,  $d_{23}$ , and  $d_{33}$ ), only  $d_{13}$  and  $d_{23}$  need be explicitly evaluated in the integration process. The  $d_{33}$  component is calculated as  $(d_{11} d_{22} - d_{21} d_{12})$  from the other integrated direction cosine components. The latter relationship expresses the fact that a unit vector along the L-Frame Z-axis (represented in the E-Frame by the  $d_{i3}$  direction cosines) equals the cross-product of unit vectors along the L-Frame X and Y axes (the  $d_{i1}$  and  $d_{i2}$  direction cosines).

Once the calculated direction cosines are known, the aircraft latitude and longitude are easily calculated by trigonometric inversion.

## WANDER OR FREE AZIMUTH POSITION RATE EQUATIONS (CONTINUED)

Note in the slide that the direction cosine rates are proportional to transport and earth rate components that are always finite and well defined. The proportionality factors are the direction cosine elements themselves which by definition never exceed unity in magnitude. Hence, the cosine rates are also finite, well behaved, and easily integrated without singularity effects for all earth locations. The penalty is a more complex set of computations compared to the direct geographic latitude/longitude integration approach.

Although not readily apparent from the slide, the longitude computation (by trigonometric inversion) is undefined at the poles because both the numerator and denominator of the arc tangent function go to zero. This is merely an expression of the fact that longitude at the poles is truly undefined. For the wander or free azimuth approach to navigation, this only results in an inability to calculate longitude output data at the poles. No permanent navigation error is incurred at pole crossings (because the dij's remain intact), and after the polar region is left, accurate longitude output calculation ensues.

**NOTES**

# GRAVITY, CENTRIPETAL, SPECIFIC FORCE, AND CORIOLIS ACCELERATIONS

- ACCELERATION ELEMENTS THAT PRODUCE VELOCITY CHANGE RELATIVE TO EARTH
  - SPECIFIC FORCE — SENSED BY ACCELEROMETERS
  - GRAVITY — FUNCTION OF EARTH LOCATION AND ALTITUDE
  - CENTRIPETAL — APPARENT ACCELERATION IN ROTATING FRAMES DUE TO ANGULAR RATES OF POSITION VECTOR
  - CORIOLIS — APPARENT ACCELERATION IN ROTATING FRAMES DUE TO VELOCITY VECTOR ROTATION

$$\left(\frac{d\mathbf{V}}{dt}\right)_L = \mathbf{A} + \mathbf{G} - \mathbf{W} \times (\mathbf{W} \times \mathbf{R}) - (\mathbf{W} + \mathbf{w}) \times \mathbf{V}$$

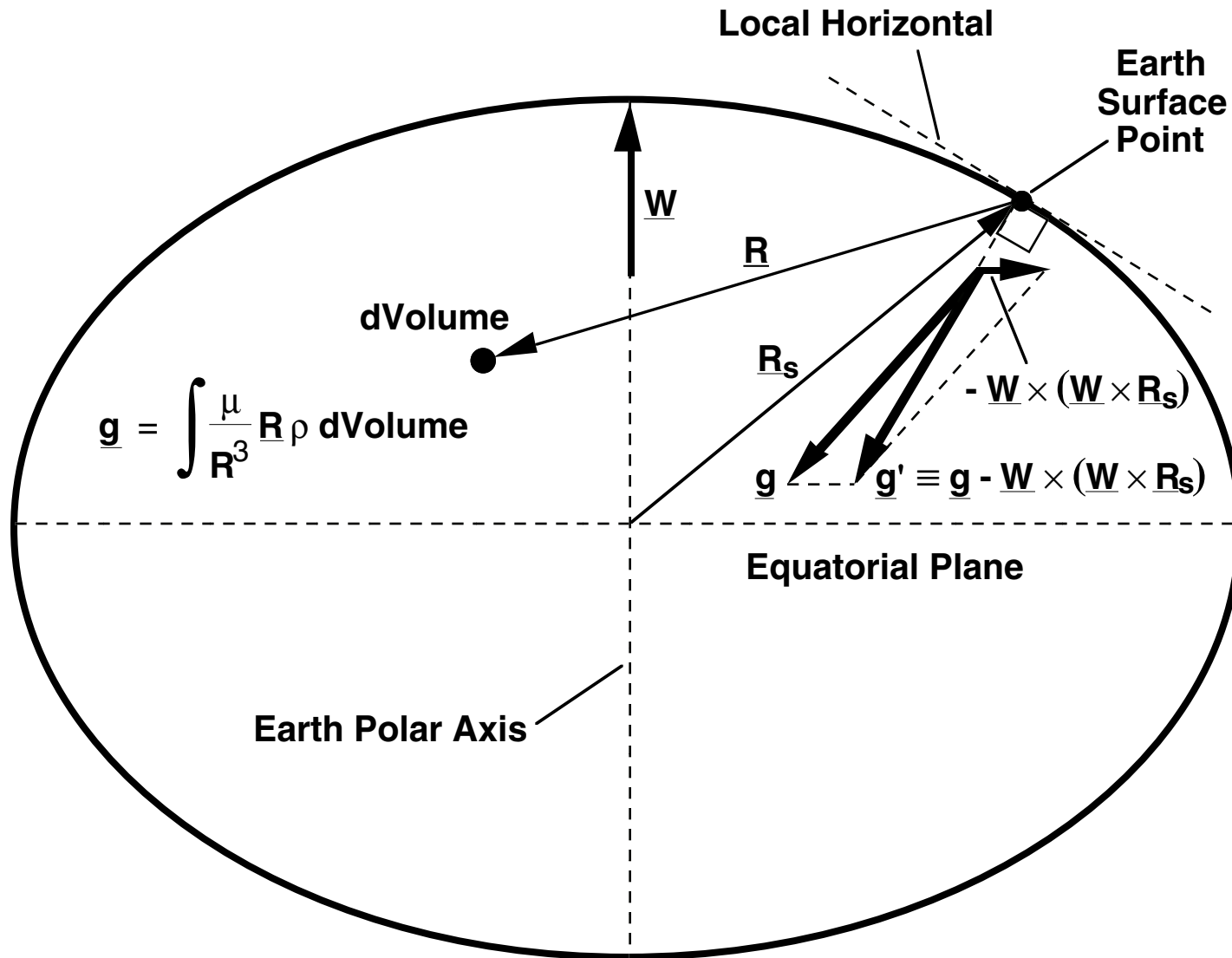

  
 SPECIFIC FORCE    GRAVITY    CENTRIPETAL    CORIOLIS

- $\underline{\mathbf{V}}$  = AIRCRAFT VELOCITY RELATIVE TO EARTH
- $\underline{\mathbf{W}}$  = EARTH ANGULAR RATE RELATIVE TO INERTIAL SPACE
- $\underline{\mathbf{w}}$  = L-FRAME ANGULAR RATE RELATIVE TO INERTIAL SPACE (EARTH RATE PLUS AIRCRAFT TRANSPORT RATE)
- $\underline{\mathbf{R}}$  = AIRCRAFT POSITION VECTOR RELATIVE TO EARTH CENTER
- $( )_L$  = DERIVATIVE RELATIVE TO L-FRAME AXES

## **GRAVITY, CENTRIPETAL, SPECIFIC FORCE, AND CORIOLIS ACCELERATIONS**

The components of aircraft earth referenced velocity in the L-Frame are calculated by integrating the L-Frame components of aircraft velocity change (acceleration) relative to the earth. The acceleration components are calculated as the sum of inertial specific force acceleration (sensed by accelerometers), gravity (calculated based on position location and altitude), plus centripetal and Coriolis corrections that account for the fact that the L-Frame is not inertial, but rotating. The Coriolis effect accounts for accelerations due to velocity vector rotation, and the centripetal effect accounts for position vector rotation (about earth center).

# GRAVITY ON EARTH'S SURFACE



## GRAVITY ON EARTH'S SURFACE

The chart depicts two definitions for gravity components at an earth surface location; gravity generated by mass attraction of the earth mass elements  $\underline{g}$ , and  $\underline{g}'$  defined as  $\underline{g}$  plus the earth rate generated centripetal acceleration term  $-\underline{W} \times (\underline{W} \times \underline{R}_S)$  (as shown on the previous chart in the velocity rate equation). On the chart,  $\underline{W}$  is earth's angular rotation rate,  $\underline{R}_S$  is the distance vector from earth's center to the surface point,  $\underline{R}$  is the distance from the surface point to a general earth mass differential volume ( $dV$ ),  $\rho$  is the density of the earth mass differential volume, and  $\mu$  is the universal gravitational constant. Mass attraction gravity  $\underline{g}$  is shown to equal the integral over earth's volume of differential gravity contributions from each differential volume based on the classical inverse square law for gravitational attraction.

The oblateness of earth's shape is exaggerated in the chart to illustrate the difference between  $\underline{g}$  and  $\underline{g}'$ . Mass attraction gravity  $\underline{g}$  is angled toward the equator at a slightly steeper angle than the position vector  $\underline{R}_S$ . This is because the average of earth mass elements to the right of earth's polar axis are closer to the surface point than the average of the mass elements to the left, thereby dipping  $\underline{g}$  down from  $\underline{R}_S$ . For a spherical earth,  $\underline{g}$  would be parallel to  $\underline{R}_S$ . The  $\underline{g}'$  vector has an even steeper angle to the equator than  $\underline{g}$  because of the  $-\underline{W} \times (\underline{W} \times \underline{R}_S)$  term (which is directed away from the polar axis). More significantly, however, is that  $\underline{g}'$  is perpendicular to the local horizontal at the earth surface point for which it is evaluated.

When stationary at the earth surface location, the velocity is zero as is its rate of change. The previous chart shows that under this condition the specific force equals the negative of  $\underline{g}'$ . A pendulum aligns itself with the negative of the specific force acting on its pivot, hence at the surface point, a pendulum (e.g., a plumb-bob) would thereby become aligned with  $\underline{g}'$ . For this reason,  $\underline{g}'$  is sometimes referred to as "plumb-bob gravity". But why is plumb-bob gravity (created from the sum of mass attraction gravity and earth's centripetal rotation effect) perpendicular to the local earth surface (within approximately 5 arc seconds)? Scientists point to this fact as evidence that below its crust, the earth is a molten mass whose elliptical shape is caused by earth's rotation. Without rotation, earth's gravity would shape the surface into a sphere (for a uniform density earth). Earth's rotation produces centripetal acceleration perpendicular to its rotation axis that pulls the surface shape into an ellipsoid of revolution. The earth surface action that produces this effect is horizontal specific force. The steady state ellipsoidal shape of the earth corresponds to zero horizontal specific force on the surface for earth's mass density and angular rate. And this is the reason that a plumb-bob aligns itself with the local vertical. Because it aligns itself along the negative of local upward specific force which has no local horizontal component due to earth's rotation.

## TRUE VERSUS PLUMB-BOB GRAVITY

TRUE GRAVITY =  $\underline{G}$

PLUMB-BOB GRAVITY =  $\underline{G} - \underline{W} \times (\underline{W} \times \underline{R}) = \underline{G}'$

- BOTH FUNCTIONS OF EARTH LOCATION AND ALTITUDE
- PLUMB-BOB GRAVITY IS ALMOST EXACTLY ALIGNED WITH GEODETIC VERTICAL
  - HORIZONTAL COMPONENTS CAN BE APPROXIMATED BY ZERO  
(NOTE: A MORE ACCURATE APPROXIMATION USES A SMALL LINEAR FUNCTION OF ALTITUDE FOR THE NORTH COMPONENT)
  - CONVENIENT TO USE IN LOCAL LEVEL NAVIGATION FRAME EQUATIONS

$$\left(\frac{dV}{dt}\right)_L = \underline{A} + \underline{G}' - (\underline{W} + \underline{w}) \times \underline{V}$$

## **TRUE VERSUS PLUMB-BOB GRAVITY**

Plumb-bob gravity is defined as the sum of true gravity plus the centripetal acceleration correction term associated with the L-Frame velocity rate equation. As discussed on page 93B, the term "plumb-bob" gravity arises because the plumb-bob gravity vector lies along a plumb-bob line suspended from a stationary point (relative to the earth) at the INS location.

Two reasons make it beneficial to combine true gravity and centripetal acceleration into one general plumb-bob gravity calculation in the INS computer. First, both are functions of earth position only. Second, plumb-bob gravity has a negligibly small horizontal component for geodetic vertical navigation frame implementations. Hence, for geodetic vertical navigation frame implementations, the calculation of the X, Y components of plumb-bob gravity (defined in the horizontal plane for a geodetic vertical system) can be approximated by zero. The latter approximation is most accurate at the earth's surface. For a more accurate approximation above the earth's surface, the north component of plumb-bob gravity can be approximated as a small linear function of altitude.

# GEOGRAPHIC IMPLEMENTATION VELOCITY RATE EQUATIONS

$$W_N = W_e \cos l$$

$$W_Z = W_e \sin l$$

$$w_N = \rho_N + W_N$$

$$w_E = \rho_E$$

$$w_Z = \rho_N \tan l + W_Z$$

$$\dot{V}_N = A_N + K_{gN} h \sin l \cos l - (W_Z + w_Z) V_E + w_E V_Z \quad V_N = \int_0^t \dot{V}_N dt + V_{N0}$$

$$\dot{V}_E = A_E - (W_N + w_N) V_Z + (W_Z + w_Z) V_N \quad V_E = \int_0^t \dot{V}_E dt + V_{E0}$$

$$\dot{V}_Z = A_Z - g - w_E V_N + (W_N + w_N) V_E + u_1 \quad V_Z = \int_0^t \dot{V}_Z dt + V_{Z0}$$

- $W_e$  = EARTH INERTIAL ROTATION RATE MAGNITUDE
- $W_N, W_Z$  = NORTH AND VERTICAL EARTH RATE COMPONENTS
- $w_N, w_E, w_Z$  = NORTH, EAST, AND VERTICAL COMPONENTS OF L-FRAME INERTIAL ANGULAR RATE
- $A_N, A_E, A_Z$  = NORTH, EAST, AND VERTICAL SPECIFIC FORCE ACCELERATIONS
- $V_N, V_E, V_Z$  = NORTH, EAST, AND VERTICAL VELOCITIES RELATIVE TO EARTH
- $g$  = PLUMB-BOB GRAVITY MAGNITUDE (INCLUDING EARTH CENTRIPETAL ACCELERATION)
- $K_{gN}$  = NORTH PLUMB-BOB GRAVITY VARIATION WITH ALTITUDE =  $-1.63 \text{ E-8 SEC}^{-2}$
- $u_1$  = BAROMETRIC ALTITUDE DIVERGENCE CONTROL SIGNAL
- $l$  = LATITUDE
- $\rho_N, \rho_E$  = NORTH AND EAST COMPONENTS OF AIRCRAFT POSITION VECTOR ANGULAR RATE RELATIVE TO EARTH (TRANSPORT RATE)

## GEOGRAPHIC IMPLEMENTATION VELOCITY RATE EQUATIONS

The slide illustrates how the North, East, and vertical velocity rates are calculated in a local level geographic coordinate frame from specific force acceleration components, plumb-bob gravity (along Z only), and Coriolis accelerations. These equations would be integrated in the INS to continuously calculate the North, East, and vertical velocities.

As for the position rate equations, the velocity rate equations in the geographic frame are fairly simple, readily implemented in a flight computer, and provide direct North/East/vertical velocity component outputs. The equations blow up near the poles, however, due to the need to sustain high Z-axis coordinate frame rotation rates ( $w_Z$ ) to maintain North alignment (due to the tangent latitude effect in the  $w_Z$  equation). Passage across the poles, thereby, results in a permanent error in the calculated North/East velocities which is irrecoverable after the pole crossing is completed. Note, also, that  $w_Z$  (and  $w_N$ ,  $w_E$ ) are the angular rate command signals fed back to the attitude reference as local level "platform rates" to maintain a locally level North oriented reference. The fact that  $w_Z$  becomes infinite at the poles, therefore, also causes the attitude reference to be permanently destroyed for polar flights.

Note that the vertical velocity rate equation (like the altitude rate equation) contains a control signal ( $u_1$ ) to prevent vertical channel divergence (to be discussed subsequently).

## WANDER OR FREE AZIMUTH VELOCITY RATE EQUATIONS

$$W_x = W_e d_{21} \quad w_x = \rho_x + W_x$$

$$W_y = W_e d_{22} \quad w_y = \rho_y + W_y$$

$$W_z = W_e d_{23} \quad w_z = \rho_z + W_z$$

$$\dot{V}_x = A_x + K_{gN} d_{23} d_{21} h - (W_y + w_y) V_z + (W_z + w_z) V_y$$

$$\dot{V}_y = A_y + K_{gN} d_{23} d_{22} h - (W_z + w_z) V_x + (W_x + w_x) V_z$$

$$\dot{V}_z = A_z - g - (W_x + w_x) V_y + (W_y + w_y) V_x$$

$$V_x = \int_0^t \dot{V}_x dt + V_{x0}$$

$$V_y = \int_0^t \dot{V}_y dt + V_{y0}$$

$$V_z = \int_0^t \dot{V}_z dt + V_{z0}$$

$$\alpha = \tan^{-1} \frac{d_{21}}{d_{22}}$$

$$V_N = V_y \cos \alpha + V_x \sin \alpha$$

$$V_E = V_x \cos \alpha - V_y \sin \alpha$$

$A_x, A_y, A_z =$  L-FRAME SPECIFIC FORCE ACCELERATIONS

$g =$  LOCAL PLUMB-BOB GRAVITY MAGNITUDE

$W_x, W_y, W_z =$  L-FRAME EARTH RATE COMPONENTS

$\rho_x, \rho_y, \rho_z =$  L-FRAME COMPONENTS OF L-FRAME ANGULAR RATE RELATIVE TO THE EARTH

$w_x, w_y, w_z =$  L-FRAME COMPONENTS OF L-FRAME ANGULAR RATE RELATIVE TO NON-ROTATING SPACE

$V_x, V_y, V_z =$  L-FRAME COMPONENTS OF VEHICLE VELOCITY RELATIVE TO THE EARTH

$V_N, V_E =$  NORTH, EAST COMPONENTS OF VEHICLE VELOCITY RELATIVE TO THE EARTH

$\alpha =$  WANDER ANGLE - ANGLE BETWEEN L-FRAME Y-AXIS AND NORTH (POSITIVE FOR Y WEST OF NORTH)

## WANDER OR FREE AZIMUTH VELOCITY RATE EQUATIONS

The velocity rate equations in wander or free azimuth coordinates are well behaved for all earth locations. All terms in the equations are finite and well defined. The integral of the velocity rate equations provides velocity components along wander (or free) azimuth coordinate axes.

The disadvantage in the wander (or free) azimuth approach to velocity calculation is the additional computational requirement to transform the X, Y horizontal velocities into their equivalent North/East form. This is accomplished using the wander angle data calculated from the dij position matrix elements (the angle about the vertical between the L-Frame Y-axis and North).

It should be noted (although not readily apparent from the equations) that the wander angle computation is undefined at (or near) the poles because the numerator and denominator of the arc tangent function both go to zero. This is a manifestation of the inability to define North at the poles (e.g., when at the South pole, all directions are North). The only penalty is a temporary inability to calculate North/East velocities for output. Since the L-Frame velocities remain intact through pole crossings, the ability to output valid North/East velocity is restored after the pole traversal is completed.

# GRAVITY CALCULATION

$$\begin{aligned}
 & \mathbf{g} = \mathbf{G}_1 \left( 1 - 2 \frac{h}{R_o} + 2e \sin^2 l \right) + \frac{3}{2} \mathbf{J}_2 \mathbf{G}_1 \left( 1 - 3 \sin^2 l \right) \\
 & \quad - R_o W_e^2 \left( 1 - e \sin^2 l + \frac{h}{R_o} \right) \cos^2 l \\
 \text{ABOVE} & \\
 \text{EARTH} & \\
 \text{SURFACE} & \\
 & = \mathbf{G}_1 \left( 1 - 2 \frac{h}{R_o} + 2e d_{23}^2 \right) + \frac{3}{2} \mathbf{J}_2 \mathbf{G}_1 \left( 1 - 3 d_{23}^2 \right) \\
 & \quad - R_o W_e^2 \left( 1 - e d_{23}^2 + \frac{h}{R_o} \right) \left( 1 - d_{23}^2 \right)
 \end{aligned}$$

$$\text{BELOW EARTH SURFACE} \quad \mathbf{g} \approx \mathbf{g}_{\text{SURFACE}} \left( 1 + \frac{h}{R_o} \right)$$

- g** = LOCAL PLUMB-BOB GRAVITY MAGNITUDE
- e** = EARTH OBLATENESS COEFFICIENT (ELLIPTICITY) EQUAL TO  $\frac{1}{298}$
- h** = ALTITUDE
- R<sub>o</sub>** = MEAN EARTH RADIUS AT EQUATOR
- W<sub>e</sub>** = EARTH INERTIAL ROTATION RATE MAGNITUDE
- l** = LATITUDE
- d<sub>23</sub>** = DIRECTION COSINE BETWEEN L-FRAME Z-AXIS AND E-FRAME Y-AXIS
- G<sub>1</sub>** = MEAN GRAVITY MAGNITUDE AT EARTH'S SURFACE AT THE EQUATOR
- J<sub>2</sub>** = EMPIRICAL CONSTANT EQUAL TO 0.00108

## GRAVITY CALCULATION

The slide illustrates the typical method for calculating plumb-bob gravity for either a geographic, wander or free azimuth geodetic vertical navigation coordinate frame implementation. The equation accounts for gravity variations with altitude and latitude (due to the earth oblateness effect). The equation for gravity magnitude below the surface of the earth is based on the approximation of a spherical earth with constant density.

# VERTICAL CHANNEL STABILIZATION

$C_1, C_2, C_3$  = VERTICAL STABILIZATION CONTROL LOOP GAINS

$U_1, U_2$  = BAROMETRIC ALTITUDE DIVERGENCE CONTROL SIGNAL

$U_3$  = INTEGRAL CONTROL SIGNAL

$A_z$  = VERTICAL SPECIFIC FORCE ACCELERATION

$V_z$  = VERTICAL VELOCITY RELATIVE TO EARTH

$h$  = ALTITUDE

$R_0$  = EARTH MEAN EQUATORIAL RADIUS

$h_{\text{BARO}}$  = BAROMETRIC ALTITUDE (FROM AIR DATA SYSTEM)

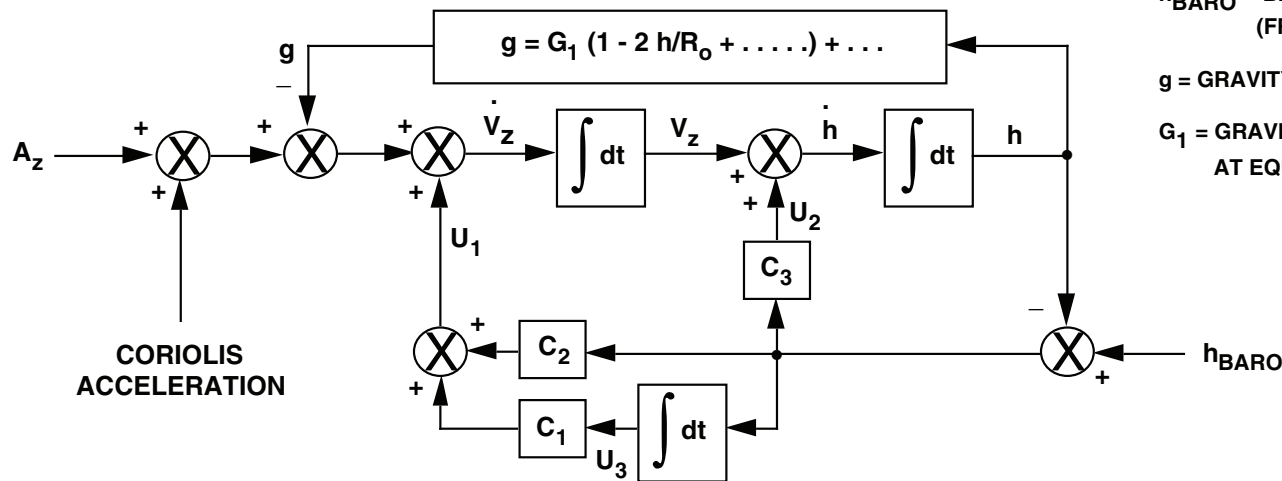
$g$  = GRAVITY MAGNITUDE

$G_1$  = GRAVITY MAGNITUDE AT EARTH SURFACE AT EQUATOR

$$\dot{U}_3 = h_{\text{BARO}} - h$$

$$U_1 = C_1 U_3 + C_2 (h_{\text{BARO}} - h)$$

$$U_2 = C_3 (h_{\text{BARO}} - h)$$



## VERTICAL CHANNEL STABILIZATION

The double integration of vertical acceleration to determine altitude rate and altitude in a long term inertial navigation system contains difficulties due to inertial instrument errors and inaccuracies in the gravity model used in the INS computer. The acceleration errors when doubly integrated, generate altitude errors. Because the calculation of gravity is a function of altitude, the altitude error produces a corresponding gravity error which modifies the calculated net vertical acceleration. This effect acts in a destabilizing manner to generate increasingly larger altitude errors (e.g., a positive acceleration error causes a positive altitude error. The positive altitude error generates a reduction in the computed downward gravity which further increases the positive altitude error).

For short term applications (a few minutes), the "vertical channel divergence" effect is generally small and tolerable. For long term cruise INS applications, the vertical error effect is intolerable and must be compensated. The typical compensation approach is through use of an externally input barometric altitude signal which is compared with the inertially calculated altitude. If both the INS and baro signals are free of error, the difference between the two is zero. If an error exists, the difference generates a feedback control signal into the altitude and altitude rate integrator. The result is an altitude and altitude rate that has the accurate wide bandwidth response characteristics of the INS, but has the stable long term accuracy of the baro signal.

The integral control signal ( $U_3$ ) in the slide is typically utilized to generate a bias that directly compensates vertical acceleration or gravity offset errors. Without the integral control, the vertical loop dynamics would produce a steady state altitude hang-off error to compensate for the acceleration errors.

NOTES

# **INERTIAL NAVIGATION SYSTEM INITIALIZATION**

## **BASIC INITIALIZATION REQUIREMENTS**

- **VELOCITY**
- **POSITION**
- **ATTITUDE (LEVELING)**
- **HEADING DETERMINATION**

## **BASIC INITIALIZATION REQUIREMENTS**

Inertial navigation systems integrate inertial sensor data to calculate velocity, position, attitude, and heading. An important part of INS operations is the initialization mode in which the INS integrators are initialized. This mode is typically denoted as the "alignment mode" whereas the basic operating condition where the integrations are actually being performed is denoted as the "navigation mode".

During the alignment mode, INS initialization operations consist of initializing the velocity and position integrators, initializing the accelerometer reference attitude relative to the horizontal (or leveling), and determining the heading of the system accelerometers relative to true North.

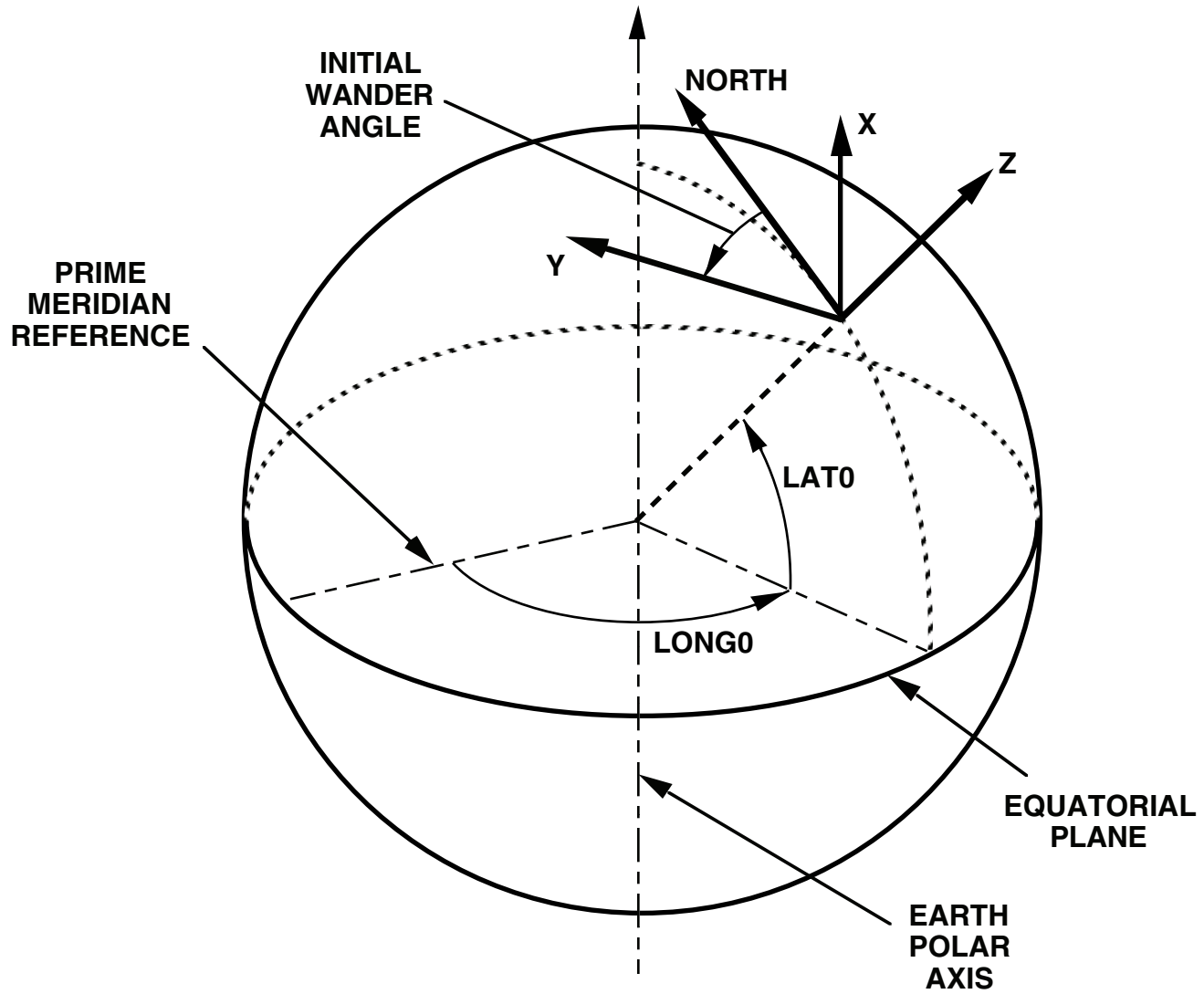
## **INITIALIZATION OF VELOCITY PARAMETERS**

- **INITIALIZED AT ZERO FOR STATIONARY GROUND ALIGNMENT**
- **INITIALIZED AT MOVING BASE VELOCITY FOR MOVING BASE ALIGNMENTS**
  - **SHIPBOARD ALIGNMENT**
  - **IN-AIR ALIGNMENT**
  - **REQUIRES EXTERNAL VELOCITY REFERENCE**

## **INITIALIZATION OF VELOCITY PARAMETERS**

For an INS initialized at a stationary location on the earth (such as in a stationary airplane on the ground prior to takeoff), the velocity integrators are simply initialized at zero. If the INS is to be initialized while in motion (such as in a Navy aircraft on a moving aircraft carrier deck, or in an airborne aircraft), an external velocity reference is needed as an input for INS initialization. For an at-sea carrier aircraft alignment, for example, the ship's INS is used as the aircraft INS reference.

# POSITION/HEADING INITIALIZATION SCHEMATIC



## **POSITION/HEADING INITIALIZATION SCHEMATIC**

The initialization of position parameters typically entails an input to the system by the INS operator of the initial latitude and longitude (relative to the Greenwich Prime Meridian). For the wander (or free) azimuth local level navigation position integration schemes, the initial latitude/longitude position data must then be converted into the initial position direction cosine form relating local level (L) and earth reference axes. The initial wander angle which defines the initial heading of the L-Frame Y-axis relative to North must also be included as an inherent part of the position direction cosine integrator initialization since the L-Frame axis orientations are defined, in part, by the wander angle.

# INITIALIZATION OF POSITION PARAMETERS

- **GEOGRAPHIC IMPLEMENTATION**
  - **INITIAL LATITUDE, LONGITUDE SET AT OPERATOR INPUT TO SYSTEM**
  
- **AZIMUTH WANDER OR FREE AZIMUTH IMPLEMENTATION**
  - **INITIAL LATITUDE ( $l_0$ ), LONGITUDE ( $L_0$ ) AND WANDER ANGLE ( $\alpha_0$ ) USED TO INITIALIZE POSITION DIRECTION COSINE MATRIX (L RELATIVE TO E FRAME)**
    - $d11_0 = \cos L_0 \cos \alpha_0 - \sin L_0 \sin l_0 \sin \alpha_0$
    - $d12_0 = -\cos L_0 \sin \alpha_0 - \sin L_0 \sin l_0 \cos \alpha_0$
    - $d13_0 = \sin L_0 \cos l_0$
    - $d21_0 = \cos l_0 \sin \alpha_0$
    - $d22_0 = \cos l_0 \cos \alpha_0$
    - $d23_0 = \sin l_0$
  
  - **INITIAL WANDER ANGLE ESTABLISHED BY INITIAL HEADING DETERMINATION OPERATIONS**

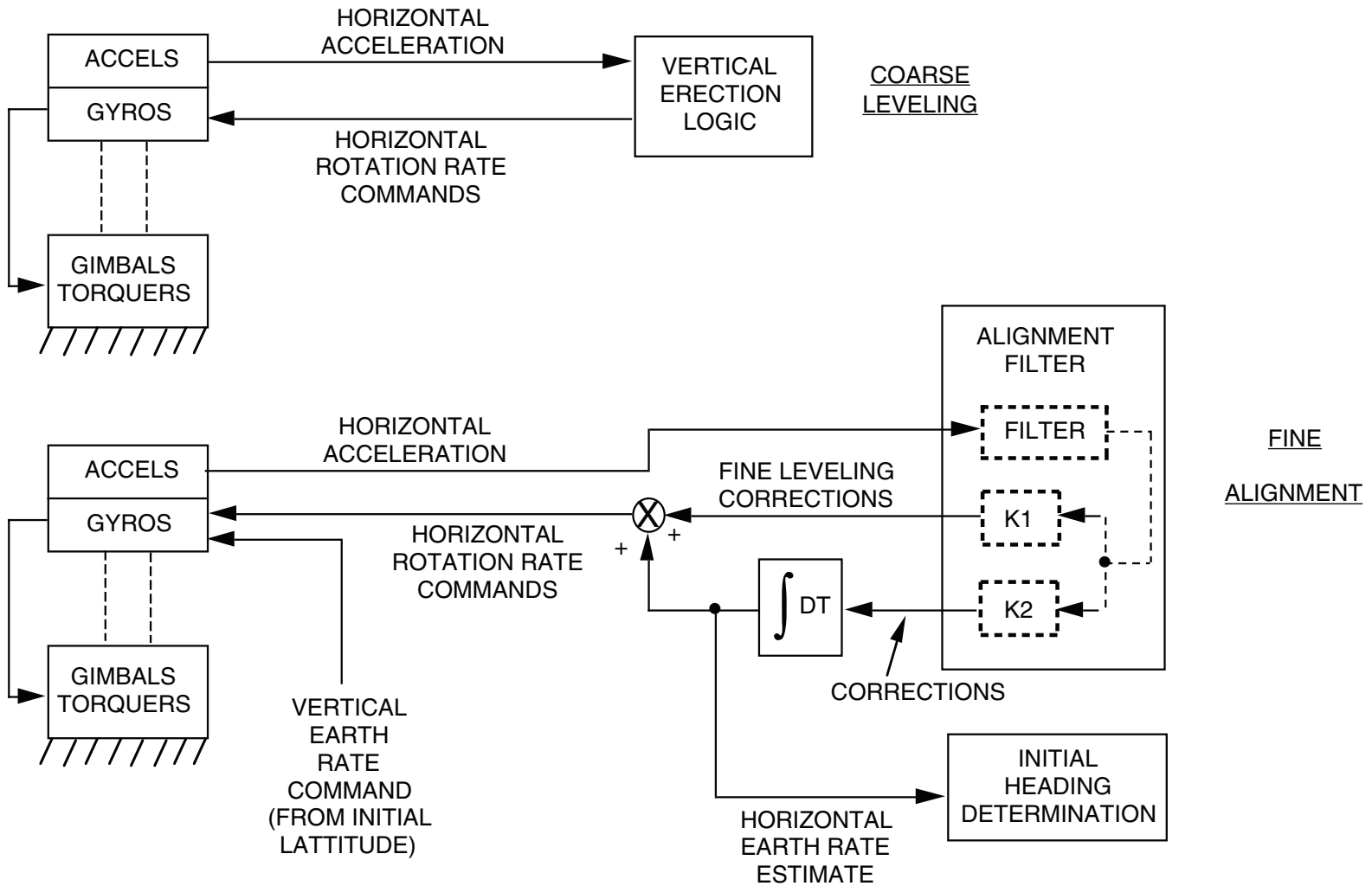
## INITIALIZATION OF POSITION PARAMETERS

For a geographic local level implementation, the position initialization process simply sets the latitude and longitude integrators equal to the system latitude/longitude inputs (by the operator).

For the azimuth wander or free azimuth implementation, the initial position direction cosines are set equal to the indicated functions of initial latitude, longitude and wander angle.

The sines and cosines of the wander angle data used for d matrix initialization are calculated as part of heading determination operations.

# TYPICAL GIMBALED SYSTEM LEVELING AND INITIAL HEADING DETERMINATION



## **TYPICAL GIMBALED SYSTEM LEVELING AND INITIAL HEADING DETERMINATION**

In a gimbaled inertial navigation system, the leveling initialization function generally entails a physical self-leveling of the platform stable element. The heading determination function is performed simultaneously with the leveling operations to determine the heading of the stable element relative to North.

The leveling operations in an INS are generally performed in two sequential phases: coarse and fine alignment. The purpose for the coarse alignment is to rapidly bring the platform to an approximately level attitude so that linear equations can be validly used for the ensuing fine alignment submodule. During fine alignment, the platform is brought to a fine level, and heading is simultaneously determined.

The coarse leveling operation rapidly rotates the platform to near level by using the "level" accelerometer outputs as gyro torque generator rate input commands so that the accelerometers are rotated to a null condition. Near null accelerometer outputs signifies a near level platform. The vertical erection logic connecting the gyro torque generators to the accelerometer signals typically consists of a simple linear amplifier with a gain set to effect a reasonably rapid coarse leveling (say within 30 seconds).

Fine alignment operations continue the leveling through a more sophisticated feedback arrangement between the gyros and accelerometers. The accelerometer signals are filtered to attenuate noise due to vehicle motion during alignment (caused by aircraft crew motion, fuel and stores loading, or wind buffeting), and then operated upon by gains which create the gyro torque generator input signals. The fine alignment gains are optimal functions of alignment time that are generally large during the early phases of fine alignment, and then diminish as the platform leveling errors reduce so that noise effects in the leveling loop become further and further attenuated. The method for calculating the optimum gains is generally handled through a Kalman filter formulation, the details of which will be discussed later in this course.

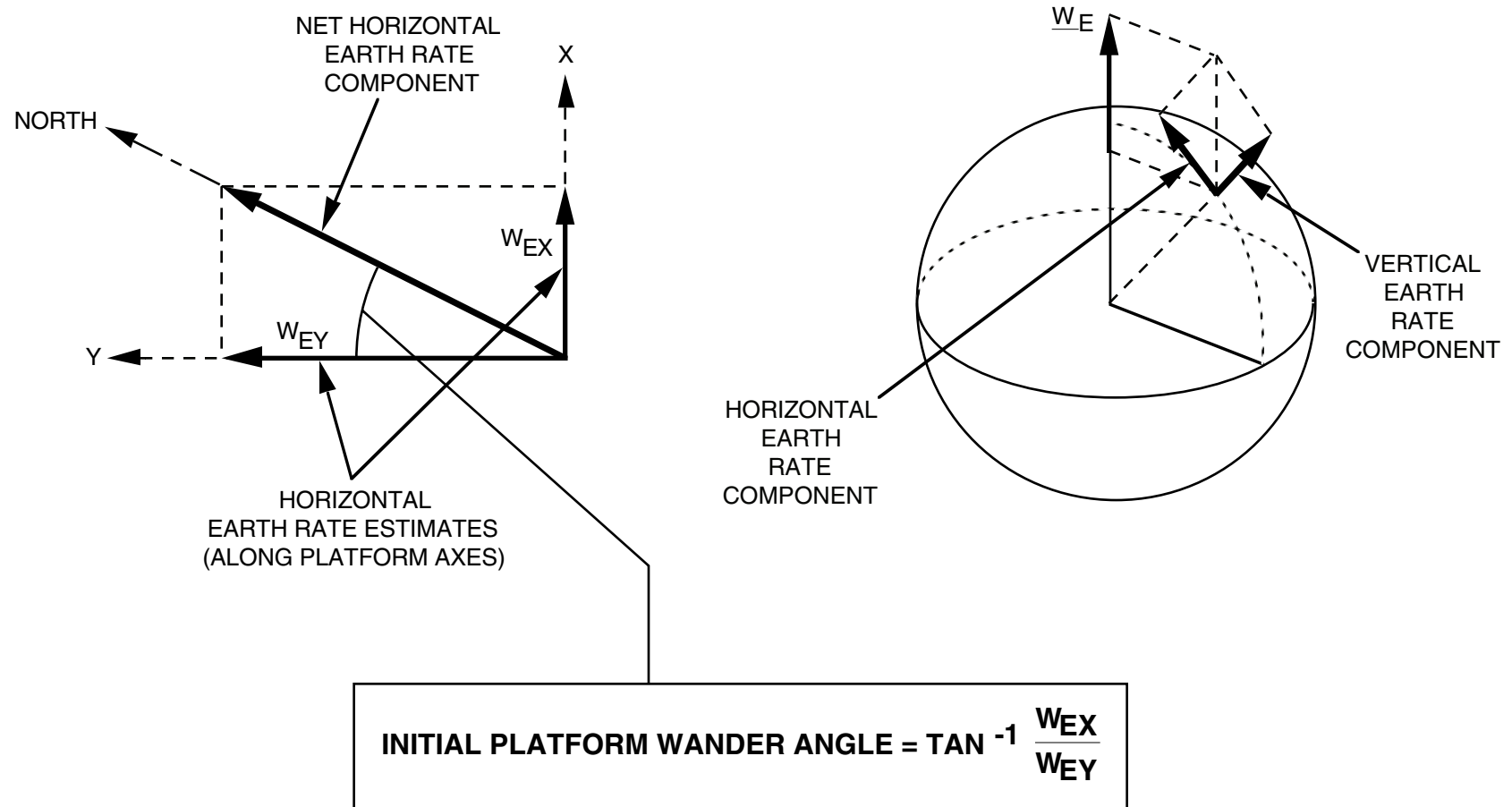
## TYPICAL GIMBALED SYSTEM LEVELING AND INITIAL HEADING DETERMINATION (CONTINUED)

An integral control function is also incorporated in the fine alignment leveling loop (the  $K_2$  integrator) to estimate the horizontal earth rate components as part of the fine alignment submode. Without the integral controller, horizontal earth rate (which continually rotates the local vertical) would tend to drag the platform gyro reference level off null due to the gyro control loop's attempt to maintain platform null relative to nonrotating inertial space (i.e., the gyros measure rotation relative to inertial space, not relative to the rotating earth. As a result, the gyro control loop introduces a natural restraint against rotations at earth rate commanded by the accelerometer leveling loops to maintain platform level). As the leveling gain ( $K_1$ ) diminishes, the hang-off error would increase. Use of the  $K_2$  loop allows the hang-off error to drive up the integral controller so that the hang-off error is eliminated. Under this condition, the integral control signal becomes proportional to the horizontal gyro input earth rate. In this manner, a steady command rate becomes applied to the gyro torque generator that balances earth's rotation rate of the local horizontal. The integral signal output thereby becomes a measure of the horizontal earth rate component along the platform gyro input axis. The earth rate signals calculated in this manner from each alignment loop axis (there are two leveling axes, each orthogonal to one another and along the platform sensor input axes) are used to determine platform initial heading (as will be described in the next slide).

It should also be noted that during fine alignment (depending on the navigation coordinate scheme utilized), the vertical sensing gyro torque generator is driven with an "open-loop" command component corresponding to the value for the L-Frame vertical rotation rate. The value for this signal during alignment is a function only of initial latitude (a system input). For example, for a wander azimuth mechanization, the vertical rotation rate would be set equal to the vertical component of earth rate.

NOTES

# INITIAL PLATFORM HEADING DETERMINATION



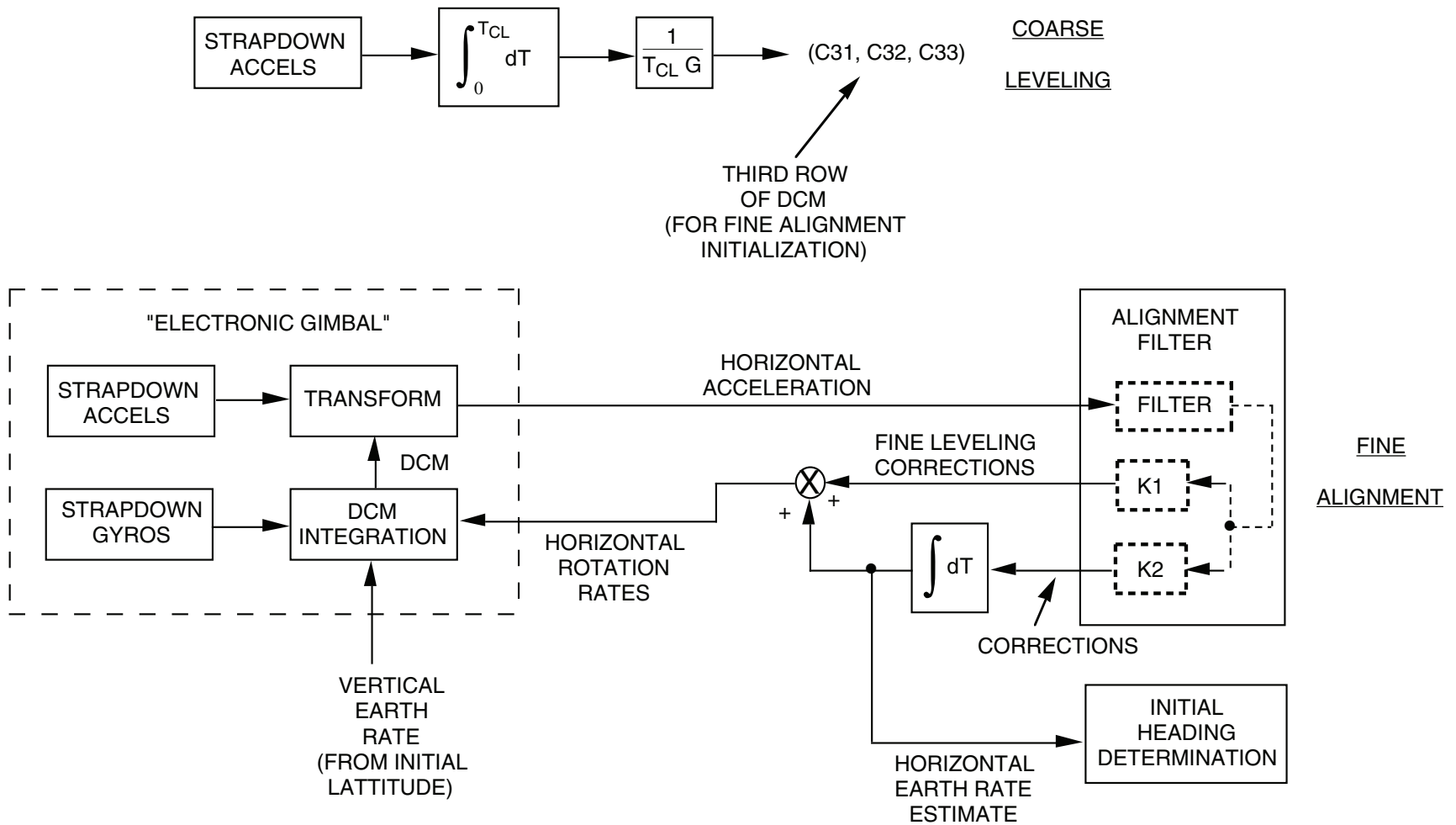
## INITIAL PLATFORM HEADING DETERMINATION

The slide indicates the manner in which the initial heading of the platform (or wander angle) is determined from the fine alignment loop horizontal earth rate estimates. The heading determination equation is based on the fact that the horizontal earth rate vector points North. Measuring the platform X, Y components of the horizontal earth rate, therefore, provide a measure of a North pointing vector. The relative ratio between the X, Y earth rate components measures the tangent of the angle between the platform sensor axes and North (i.e., the wander angle which is used to initialize the position direction cosine elements in the wander or free azimuth system). Note, that with this concept, the physical platform axes become the navigation coordinates for the system. The gyro torque generator input rates from the navigation computer during the navigation mode continue to rotate the platform as prescribed for the particular local level navigation coordinate frame to be mechanized (e.g., free azimuth). The accelerometer output from the platform with such an approach can be directly integrated to calculate navigation frame velocity components.

One further point should be noted regarding initial heading determination. An option exists for physically rotating the platform heading during alignment to bring the platform heading into a prescribed orientation relative to North. For a North seeking approach, the platform X-axis would be rotated to North by commanding the vertical gyro torque generator. From the slide, the North seeking function can be implemented by commanding the Z-gyro torque generator using the X-axis earth rate estimate. This will cause the platform X-axis to rotate East, thereby nulling  $W_{EX}$  and bringing the wander angle to zero (i.e., Y-North). Such a continuous North slaving heading alignment approach was one of the original methods used to initialize the heading in an INS and has been denoted as "gyrocompassing".

For a geographic local level coordinate frame physical mechanization using the platform, the initial North seeking operation becomes an inherent part of alignment operations. For wander or free azimuth systems, North seeking is not necessary, and wander azimuth measurement and initialization in the position direction cosines is all that is required.

# STRAPDOWN SYSTEM INITIAL ALIGNMENT



## STRAPDOWN SYSTEM INITIAL ALIGNMENT

The "electronic gimbal" concept makes the initial alignment operations for a strapdown system in the fine alignment mode virtually identical to that of the gimbale system. The fundamental difference with the strapdown system, of course, is that the actual alignment operation consists of a rotation of direction cosine elements residing in computer memory; no actual physical platform rotations are involved.

The fine alignment leveling operation in the strapdown system consists of a rotation of the direction cosine matrix (DCM) relating aircraft sensor axes to locally level navigation axes. The rotation rate signal for this operation is identical to the gimbale platform gyro torque generator input rate signal. In the strapdown system, the indication of level is that the horizontal components of the transformed body accelerations (using the DCM) be nulled. Thus, leveling is achieved when the DCM is analytically rotated such that the transformed body acceleration has zero X, Y components.

The heading determination function for the strapdown system is also directly equivalent to the gimbale system. The integral controller is used to generate horizontal direction cosine rotation rate signals in X, Y "platform" axes that cancel the effects of body mounted gyro sensed earth rate output components on the DCM integration process. In this manner, the integral controller X, Y output signals become equal to the horizontal earth rates in the local level frame defined by the DCM direction cosine elements. Gyrocompassing or North seeking is also possible with the strapdown approach by commanding the body axis direction cosine rates about the analytic vertical using the X-axis earth rate estimate signal.

A distinction between the strapdown and gimbale system initial alignment operations is the manner in which coarse alignment (or leveling) can be achieved. In the gimbale system, the rate at which coarse leveling completes is dictated by platform gyro maximum torque generator rate limits (e.g., a few degrees per minute). In the case of the strapdown mechanization, no physical rotation actually takes place, hence, no equivalent limit exists. The slide shows one particularly simple and rapid method for performing a strapdown coarse leveling function. The method is based on the fact that the strapdown accelerometers measure components of vertical specific force acceleration, hence, their components are proportional to the DCM cosines between body axes and the local vertical Z-axis (the proportionality factor is local gravity magnitude). The slide shows how this factor can be utilized to initialize the C3j row of the DCM which achieves a coarse level. The method is to average the body acceleration outputs for a short time period (TCL) by integration (typically TCL is half a second), then dividing the result by the product of gravity magnitude with the averaging time. The result is the C3J DCM row.

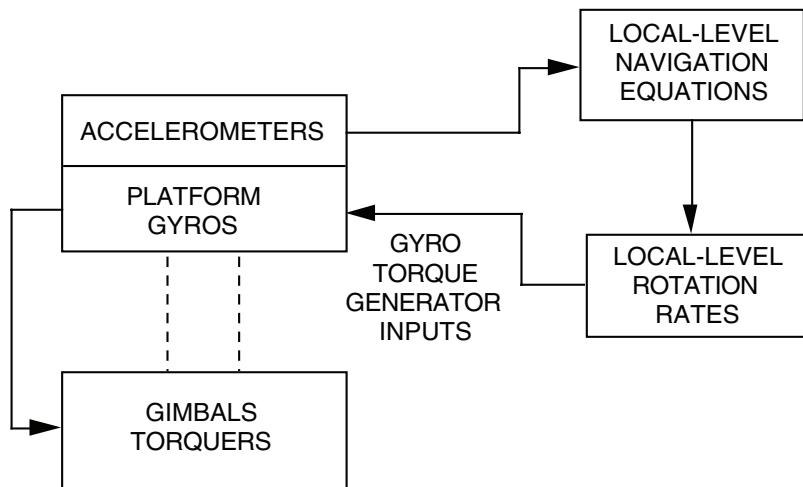
Initialization of the C1J and C2J rows must also be accomplished as part of coarse leveling, however, this is somewhat arbitrary, and primarily dictated by natural DCM constraints (e.g., the dot products between the C1J, C2J and C3J rows should be zero because each represents the components of a unit vector along orthogonal L-Frame axes, and the dot product of orthogonal vectors are zero).

**NOTES**

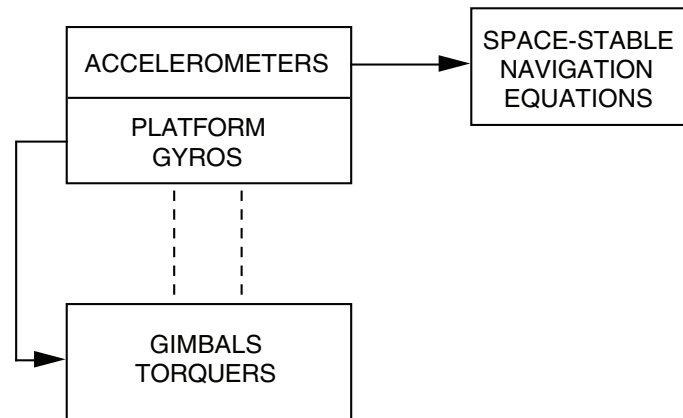
# **GIMBALED PLATFORM REFERENCE STABILIZATION**

# LOCAL LEVEL AND SPACE STABLE IMPLEMENTATION CONCEPTS

## LOCAL-LEVEL PLATFORM



## SPACE STABLE PLATFORM



## **LOCAL LEVEL AND SPACE STABLE IMPLEMENTATION CONCEPTS**

Thus far, the gimbale implementation concept discussed has utilized a gimbale platform mechanized through the gyro torque generator command loop to remain locally level. We should also note that an alternative mechanization available today in gimbale systems utilizes a space-stable approach whereby the orientation of the platform remains constant relative to nonrotating inertial space. Such an approach is realized by eliminating the gyro torque generator command loop in the INS mechanization.

The navigation equations utilized with the space stable approach differ from those for the locally level platform in that they must account for the orientation of the platform relative to the local horizontal, which now rotates due to earth rotation and aircraft transport rate over the earth.

# LOCAL LEVEL PLATFORM IMPLEMENTATION TRADEOFFS

- **GEOGRAPHIC**
  - DIRECT NORTH/EAST ACCELERATION/HEADING OUTPUTS
  - SUITABLE FOR SYSTEMS WITH LIMITED COMPUTER CAPACITY (OLD TECHNOLOGY)
  - SINGULARITIES NEAR POLES (GYRO TORQUE GENERATOR RATE LIMITS)
- **WANDER AZIMUTH**
  - FINITE GYRO TORQUE GENERATOR RATES AT ALL GLOBAL POSITIONS
  - STATIONARY PLATFORM HEADING AT FIXED POSITIONS ON EARTH (CAN SIMPLIFY TESTING)
- **FREE AZIMUTH**
  - FINITE GYRO TORQUE GENERATOR RATES AT ALL GLOBAL POSITIONS
  - ELIMINATES AZIMUTH GYRO TORQUE GENERATOR ERROR
  - PLATFORM HEADING ROTATES AT VERTICAL EARTH RATE FOR FIXED POSITIONS ON EARTH (CAN COMPLICATE TESTING)
- **DRIVEN AZIMUTH**
  - MECHANIZATION – LIKE FREE OR WANDER AZIMUTH EXCEPT PLATFORM HEADING IS DRIVEN AT CONSTANT FAIRLY HIGH RATE (e.g., 1 REV PER MINUTE)
  - CANCELLATION OF LEVEL GYRO AND ACCELEROMETER “STATIONARY” ERRORS
  - AMPLIFICATION OF AZIMUTH GYRO TORQUE GENERATOR ERROR IF ROTATION ACCOMPLISHED BY GYRO TORQUE GENERATOR INPUT
  - MORE COMPLICATED PLATFORM ASSEMBLY IF ROTATION ACCOMPLISHED BY TURN-TABLE MOUNTING OF LEVEL AXIS INSTRUMENTS

## LOCAL LEVEL PLATFORM IMPLEMENTATION TRADEOFFS

If a locally level gimballed platform mechanization is selected, several alternatives are available for the method used for azimuth control. Commonly used methods rotate the platform heading to maintain the sensor axes at a prescribed orientation or orientation rate about the vertical. Depending on the method selected, several advantage and disadvantage exists.

In the geographic implementation approach, the sensor axes are maintained level and aligned with locally North, East, and vertical axes. The advantage of this approach is that the accelerometer outputs (and platform heading data) are directly available to the navigation computer in geographic coordinates. Implementation of geographic locally level navigation equations in the computer is thereby facilitated. The disadvantage is that singularities exist for navigation near the poles, requiring excessively high azimuth rates to maintain North alignment. Due to the finite torque generator maximum rate limitations on the platform gyros, navigation near the poles becomes impossible. The geographic level implementation concept was utilized in the past to reduce the computational burden in old technology navigation computers. In modern day computers, the minor computational savings has negligible value compared to the handicap of poor performance near polar regions. As a result, the geographic level mechanization approach is largely obsolete today.

For the wander azimuth gimballed platform implementation approach, the platform is rotated about the vertical at the vertical component of earth's rate. As a result, vertical gyro torque generator command rates remain finite at all earth locations, providing a global capability void of gyro torque generator maximum rate limitations. When stationary, the platform heading remains constant relative to the earth which can facilitate interpreting platform sensor test data. A disadvantage is the need to command heading gyro rotation rates, hence, introduce heading gyro torque generator errors into the platform heading. Navigational position/velocity errors are, thereby, generated.

## LOCAL LEVEL PLATFORM IMPLEMENTATION TRADEOFFS (CONTINUED)

In the free azimuth gimbaled platform mechanization concept, the azimuth gyro torque generator input rate is zero, thereby eliminating the associated Z-gyro torque generator rate error. As with the wander azimuth approach, the technique has no gyro torque generator command rate singularities for all earth locations, providing a global navigation capability. Under stationary conditions, the platform rotates at minus vertical earth's rate relative to the earth which can complicate interpreting sensor error effects during test.

The driven azimuth gimbaled platform mechanization approach is similar to the free or wander azimuth locally level concept except that the platform is rotated at a fairly high constant rate about the vertical (e.g., one revolution per minute). The resulting rotation of the level sensor input axes (gyros and accelerometers) causes their error effects to rotate in the navigation calculation, thereby, canceling in the navigation integration operations. As a result, level gyro and accelerometer bias (and accelerometer misalignment) accuracy requirements can be reduced.

If the driven azimuth is achieved through azimuth gyro torque generator command, azimuth gyro torque generator scale factor error effects are amplified and become more critical to system navigation accuracy. An alternative approach splits the stable element into two parts so that the level axes can be rotated mechanically in azimuth relative to the azimuth gyro using a geared-down synchronous motor and small turn-table. This approach eliminates the azimuth gyro torque generator accuracy requirement but complicates the platform mechanical design (and cost).

**NOTES**

## LOCAL LEVEL VERSUS SPACE STABLE PLATFORM TRADEOFFS

	LOCAL LEVEL	SPACE STABLE
<b>ADVANTAGES</b>	<ul style="list-style-type: none"> <li>• REDUCES G-SENSITIVE SENSOR ERRORS</li> <li>• REDUCES ACCELEROMETER SCALE FACTOR ERRORS</li> <li>• LONG TERM BOUNDING OF SOME GYRO BIAS ERRORS</li> </ul>	<ul style="list-style-type: none"> <li>• NO GYRO TORQUE GENERATOR ERRORS</li> <li>• NO GYRO MISALIGNMENT CROSS-COUPLING ERRORS</li> </ul>
<b>DISADVANTAGES</b>	<ul style="list-style-type: none"> <li>• GYRO TORQUE GENERATOR ERRORS</li> <li>• GYRO MISALIGNMENT CROSS-COUPLING ERRORS</li> </ul>	<ul style="list-style-type: none"> <li>• G-SENSITIVE SENSOR ERRORS</li> <li>• ACCELEROMETER SCALE FACTOR ERRORS</li> <li>• UNBOUNDED GYRO BIAS ERRORS</li> </ul>
<b>WHEN USED</b>	<ul style="list-style-type: none"> <li>• WHEN GYROS WITH ACCURATE TORQUE GENERATORS USED</li> </ul>	<ul style="list-style-type: none"> <li>• WHEN GYROS WITHOUT ACCURATE TORQUE GENERATORS USED (ESGs)</li> </ul>

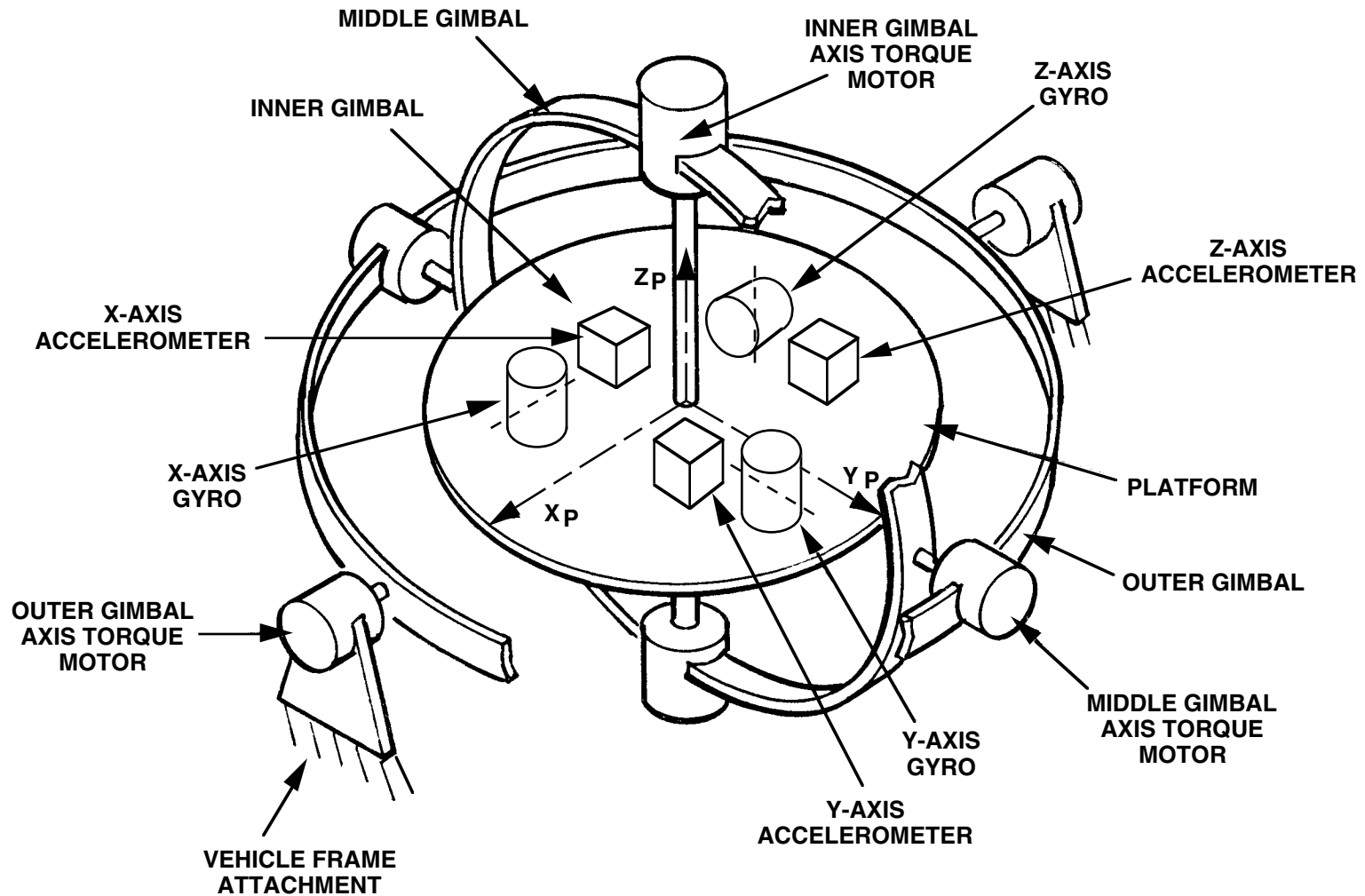
## LOCAL LEVEL VERSUS SPACE STABLE PLATFORM TRADEOFFS

The advantages of the locally level platform mechanization (compared to the space stable) are many, which explains its popularity in most contemporary gimballed INS implementations: sensor G-sensitive errors are minimized through orientation such that G-insensitive axes are vertical (to the extent possible), accelerometer scale factor errors are minimized because the critical sensors used to sense horizontal motion are horizontal, hence are not exposed to the dominant long term vertical specific force acceleration, and some of the long term gyro bias error effects are bounded due to platform input axis rotation relative to inertial space, hence, gyro error rotation (and integration cancellation). On the other hand, the locally level concept does contain the disadvantages of requiring platform gyro torque generator commands (hence, introduction of gyro torque generator errors on navigational performance), and the introduction of gyro misalignment errors which generate platform gyro torque generator command rotation rate errors due to mechanical cross-coupling of platform rotation rates into the gyro sensitive axes. These disadvantages are fairly minor compared to the benefits.

The space stable gimballed platform mechanization eliminates the gyro torque generator and misalignment error mechanisms, but excites G-sensitive sensor errors due to the continuing platform orientation change relative to the local vertical (from earth rate and aircraft transport rate) which causes the specific force vector direction on the platform to continually rotate relative to sensor axes. As a result of the nonstationary platform attitude relative to vertical, space stable platform accelerometer scale factor errors become a major error source, and gyro G-sensitivities are excited. Finally, because the gyros in a space stable system remain fixed relative to inertial space, their input axes remain fixed, hence, their error effects continually integrate into navigation error (i.e., no error bounding is present due to gyro error vector rotation).

In general, the disadvantages of the space stable gimballed mechanization largely overshadow the advantages. The space stable approach is only utilized, therefore, when it is not possible to mechanize a locally level configuration. Such is the case when using high accuracy electrostatic gyros (ESGs) which do not contain precision torque generators. The extremely high accuracy of the ESG makes its additional error in the space stable environment negligible compared to conventional momentum wheel gyro error effects in locally level or space stable implementations.

# THREE-GIMBAL PLATFORM SCHEMATIC



### THREE GIMBAL PLATFORM SCHEMATIC

The platform in a gimballed inertial navigation system is used for two purposes: to provide a measure of the components of the specific force acceleration vector in a known coordinate frame, and to provide a measure of vehicle attitude/heading relative to a known coordinate frame. The gimballed platform consists of an inertial instrument assembly (stable member or platform) and a surrounding gimbal structure.

The instrument assembly contains three single axis gyros (or two two-axis gyros), and three accelerometers. The gyros are mounted so that their input axes are mutually orthogonal. They thereby sense three orthogonal components of the platform rotational rate vector. The accelerometers are also mounted on the platform so that their sensitive axes are mutually orthogonal. Thus, the accelerometers sense three orthogonal components of the platform's nongravitational (specific force) acceleration vector. The gyro axis frame is aligned with the platform axis frame. The accelerometer axis frame in the slide is also parallel to the platform axis frame. This latter point is not a requirement, however, and we find some ballistic missile configurations where it is more accurate to align the accelerometer frame at a nonparallel attitude relative to the platform frame.

The gimbal structure consists of a set of gimbal rings interconnected through pivot bearings. Electrical torquers are mounted around each pivot so that one gimbal ring may be rotated relative to another by commanding the torquer with a voltage. The inner gimbal pivot is connected to the instrument assembly. The outer pivot is connected rigidly to the vehicle frame. One or two resolvers are also mounted around each pivot to provide a measure of the gimbal pivot angle.

It is the function of the gimbal assembly to hold the platform inertially stable. This is accomplished by commanding the gimbal torquers in such a manner that the platform is always oriented in a prescribed angular attitude (or is rotated at a prescribed angular rate). The manner in which the gimbal torquers are operated to perform their function satisfactorily is determined by the platform gyros. The gyro outputs represent three orthogonal components of the attitude deviation of the platform from the desired orientation. The gyro error signals are used to drive the gimbal torquers so that the platform is controlled to a nominal gyro null condition.

With the sensor platform stabilized through the gimbal torquer mechanization, the gimbal pivot angles can be used as a measure of vehicle attitude relative to the platform reference. The platform resolvers provide electronic measures of the gimbal attitude. Their outputs can therefore be used as measurements of vehicle attitude relative to the platform.

### THREE GIMBAL PLATFORM SCHEMATIC (CONTINUED)

Since the platform is controlled to a stationary attitude (relative to a command reference) by the gimbal torquers, it is assured that the platform accelerometers will always read components of acceleration along a known coordinate frame direction. Thus, the platform accelerometer outputs provide the desired inertial acceleration information to the INS computer by virtue of the platform gyro mechanization.

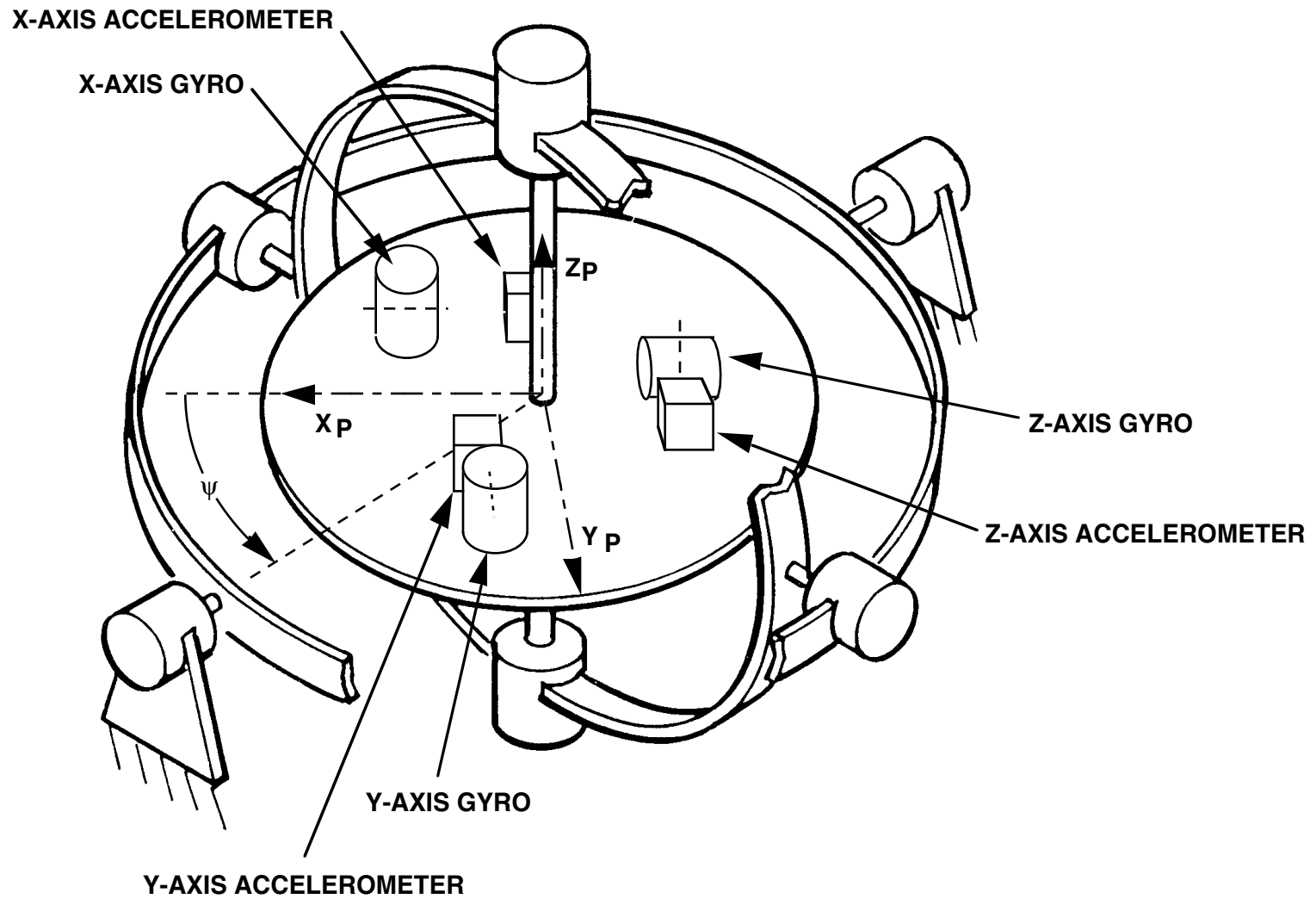
We have thus far tentatively overlooked specifying the number of gimbals necessary to provide the necessary freedom for maintaining the platform stable. Since there are three platform angular attitude errors (gyro signals) that must be held at null by the platform torquers, it would seem that three torquers mechanized properly could provide the necessary control. This is, in fact, the case for many special applications. The platform shown in the slide is of such a "three gimbal" type. For general INS applications, however, "practical" limitations typically require that an extra gimbal be used (these limitations will be discussed subsequently). Such "four gimbal platforms" are used where an unlimited attitude maneuvering capability is required.

The three gimbal platform pictured in the slide is the simplest of the platform concepts. It contains two gimbal rings (outer and middle gimbals), an instrument assembly (inner gimbal), and three gimbal pivots or axes. The three torquers on the gimbal pivots are used to hold the platform gyro signals nulled.

As discussed previously, the platform is held level by slaving the gimbal torquers to the platform gyros. The question that remains is which torquer should be slaved to which gyro? If the vehicle attitude is such that the gimbal orientation is as depicted in the slide, the answer is obvious. Clearly, in this orientation, the X-axis gyro measures platform attitude deviations about an axis along the outer gimbal axis. By rotating the outer gimbal about an axis along the outer gimbal axis, then, this gyro error can be nulled. This can be accomplished by slaving the outer gimbal torquer to the X-axis gyro. In a similar manner it can be reasoned that the Z and Y axis gyros can be nulled respectively by slaving the inner and middle gimbal torquers to these gyros. Remember, now, that this apparently simple solution was based upon the gimbals being in the indicated attitude. In practice, the gimbal attitude might be different. For example, consider the attitude shown in the next slide.

**NOTES**

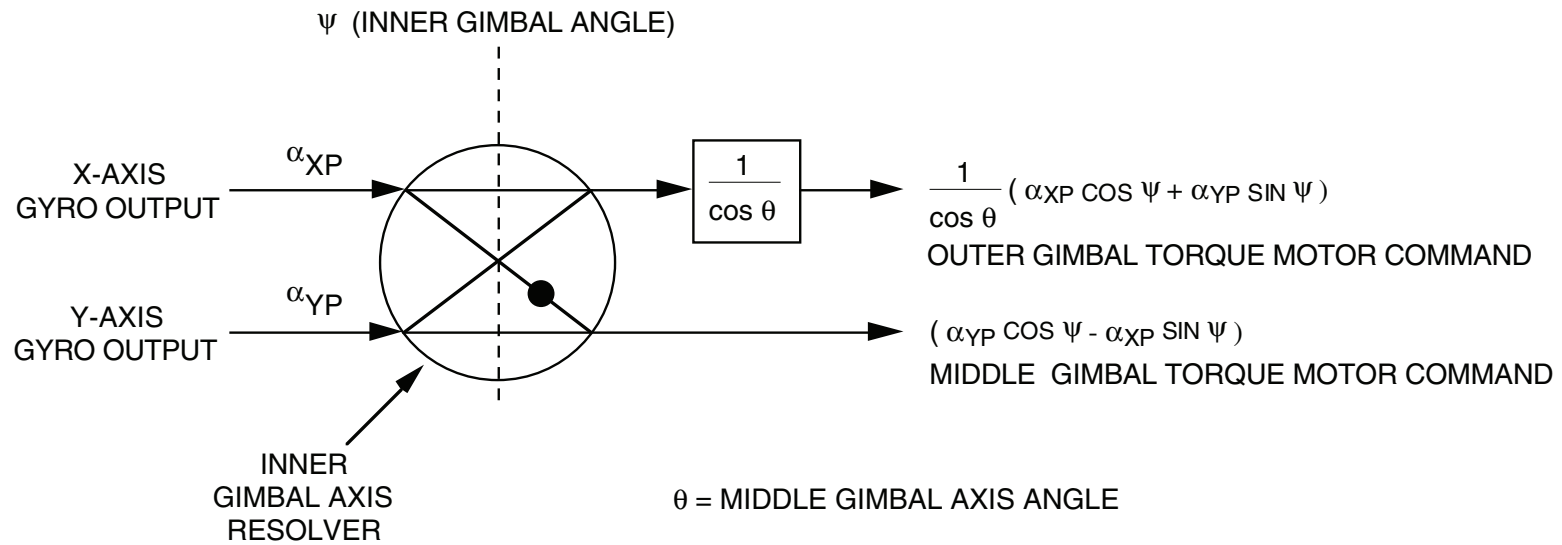
# THREE-GIMBAL PLATFORM AT NON-ZERO HEADING



### THREE GIMBAL PLATFORM AT NON-ZERO HEADING

In this slide, the vehicle is now oriented so that the Y and X-axis gyros are no longer aligned with the middle and outer gimbal axes as before. Instead, there is an angular deviation between these two axis sets equal to  $\psi$  about the inner gimbal axis. For this configuration, the Z-axis gyro error can still be nulled as before by using it to drive the inner gimbal torquer. Unlike the previous case, however, it is now not altogether clear whether to use the middle or outer gimbal torquers to null the Y-axis or X-axis gyro signals. The problem can be resolved by noting that the overall requirement for the gimbal torquer mechanization is to null three components of a platform attitude error vector. The gyro outputs represent the components of this vector along platform coordinate axes. In order to null this attitude error vector, the platform must be rotated negatively about an axis along the error vector direction; i.e., along the vector sum of the gyro outputs. Thus, the rate vector imposed on the platform by the gimbal torquers should lie along the error vector direction. The command signals to the torquers then should be such that their vector sum lies along this direction. This can be accomplished by commanding the torquers with signals proportional to the components of the error vector along the torquer axes.

# GYRO/PLATFORM TORQUE MOTOR COMMAND TRANSFORMATION

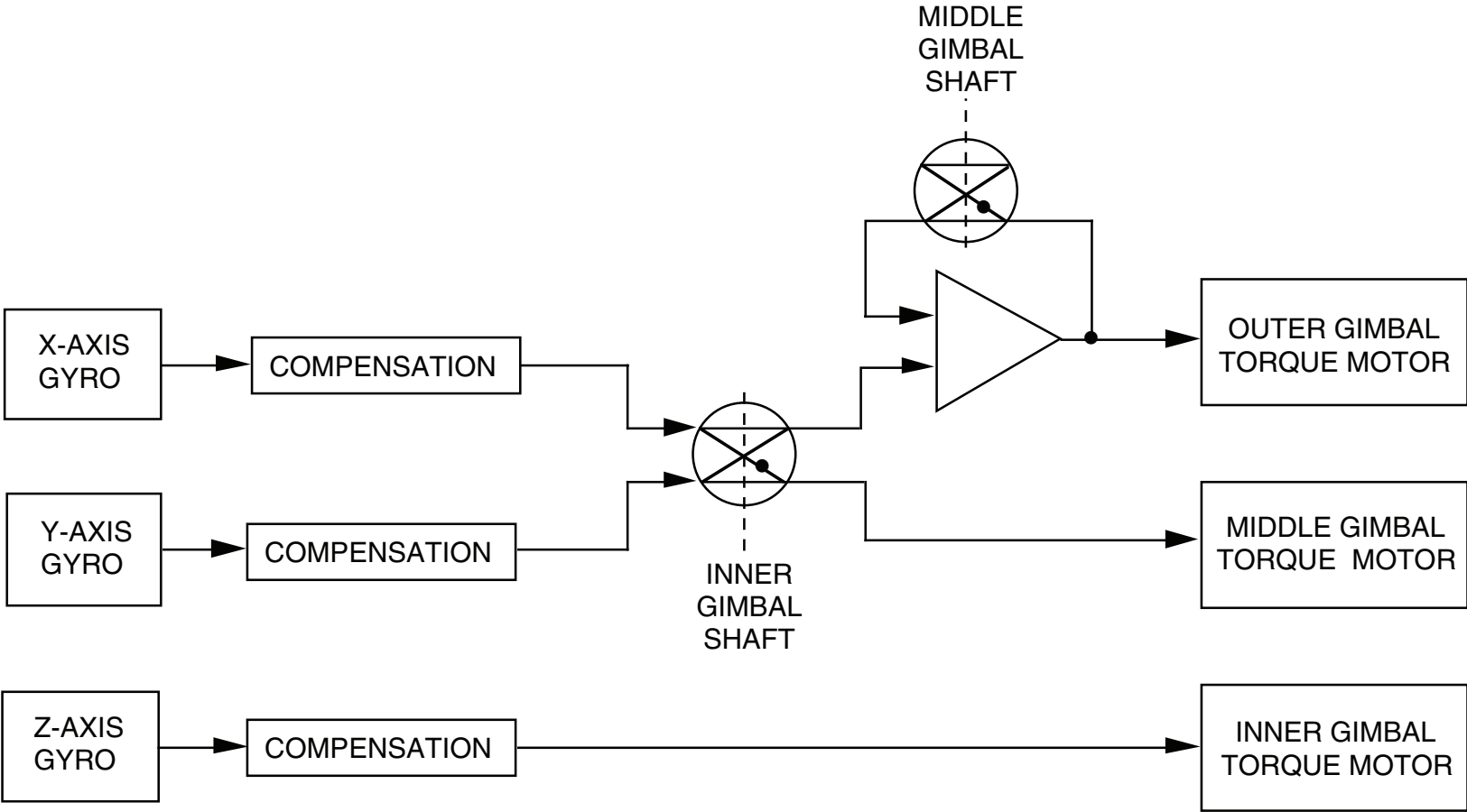


## **GYRO/PLATFORM TORQUE MOTOR COMMAND TRANSFORMATION**

The slide illustrates how the platform attitude error vector represented by the X and Y axis gyro output signals can be transformed to their equivalent form along the outer and middle gimbal axes. The transformed signals are then used as command signals to the gimbal torque motors which then rotate the platform to null the gyro errors.

The gyro error vector transformation operation is performed by mechanizing the inner gimbal angle resolver to perform the transformation from gyro to middle gimbal axes. The  $(1/\cos \theta)$  amplification factor on the outer gimbal torque motor command signal is needed to compensate for geometric attenuation of outer gimbal torque motor actuated rotations on platform axes (due to the middle gimbal being at a nonorthogonal orientation relative to the platform X, Y gyro input axis plane; i.e., non-zero  $\theta$ ).

# TYPICAL THREE GIMBAL PLATFORM TORQUE/MOTOR MECHANIZATION

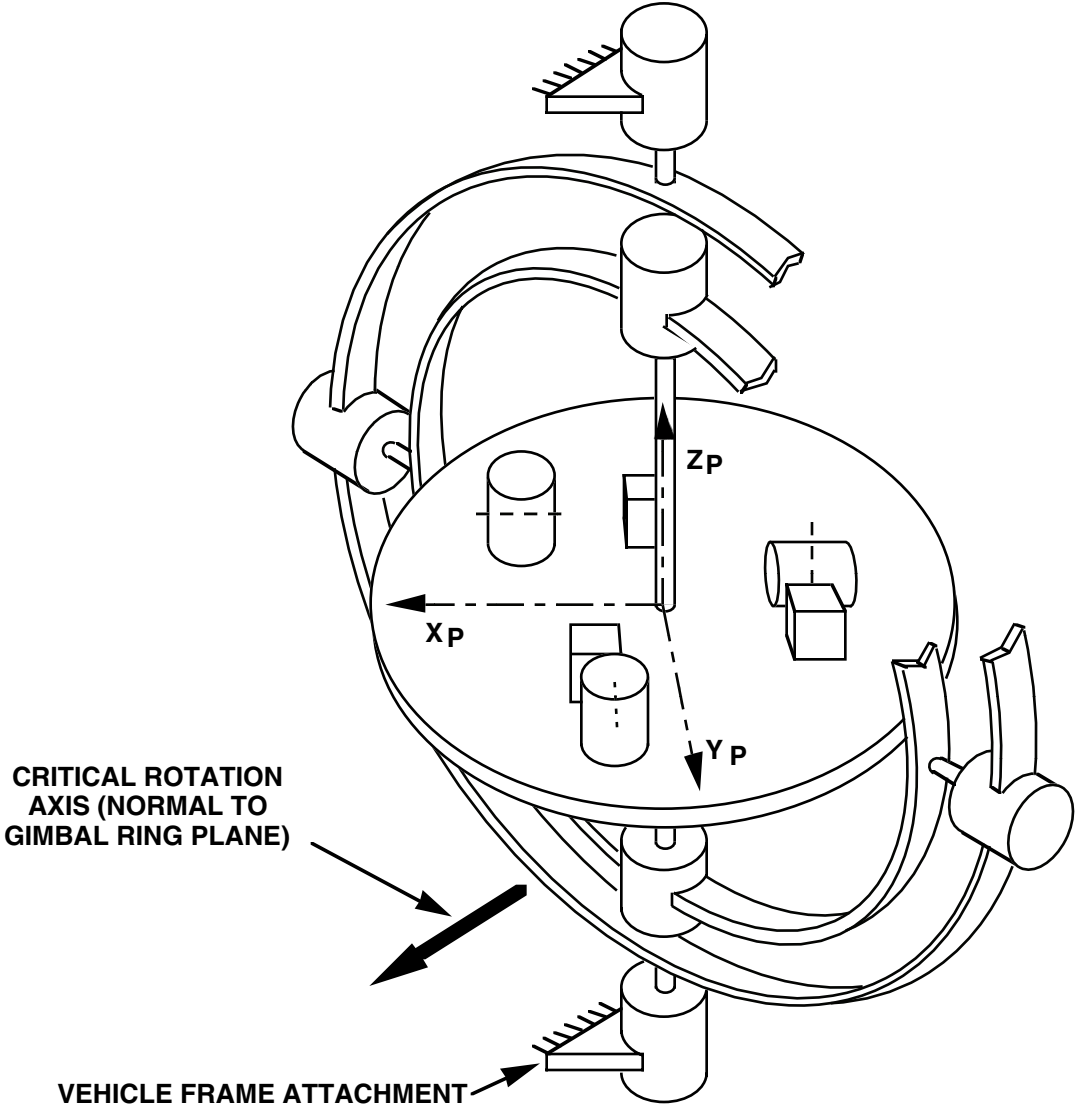


## TYPICAL THREE GIMBAL PLATFORM TORQUE MOTOR MECHANIZATION

The slide illustrates the mechanization of the gimbal torque motor drive signals for each axis in a three gimballed platform. The transformation operation described in the previous slide is shown connecting the X, Y gyro outputs to the outer and middle gimbal torque motors. The middle gimbal shaft resolver feedback around the outer middle gimbal torque motor amplifier mechanizes the  $(1/\cos \theta)$  scale factor described on the previous slide. The Z-axis gyro signal interfaces directly with the inner gimbal torque motor since rotations generated by this motor directly produce platform rotations about the Z-axis for arbitrary platform gimbal geometries.

The compensation networks shown are typically used to attenuate gyro cross-talk (created by gyro spin-motor induced vibrations in the case of tuned-rotor gyros for example), or increase torque loop gain in the low-frequency region to effect a higher static stiffness in the overall servo loop. The latter technique is typically accomplished using lag/lead analog electronic networks.

# THREE-GIMBAL PLATFORM AT "GIMBAL-LOCK" ATTITUDE



### THREE GIMBAL PLATFORM AT "GIMBAL-LOCK" ATTITUDE

The three gimbal platform concept has one fundamental limitation that prevents its usage in all applications. This limitation is a direct result of the fact the only three gimbal axes exist for platform rotations. The reasoning used to justify the use of only three axes in the gimbal structure was that three degrees of freedom were needed to null the three components of platform attitude error sensed by the gyros. Stated differently, three nonparallel axes were needed for torque generation so that a total platform rate could be created along any arbitrary platform error vector direction. This reasoning is valid in general. There is, however, one vehicle attitude where the reasoning breaks down due to the orientation assumed by the gimbals. Such a situation is depicted in the slide.

In the slide, the middle gimbal angle is equal to ninety degrees instead of the zero degree attitude in a previous slide. In this gimbal orientation, one significant factor stands out; the inner gimbal axis is now aligned with the outer gimbal axis. Thus, only two independent axes exist instead of the previous three for torque motor rotating of the platform. In view of this fact, consider how the torque motors should be commanded in order to rotate the platform about the axis marked "critical rotation axis". Clearly, no torquer axis exists along this direction, thus, a platform attitude error component along this critical direction cannot be nulled. In order to have the capability for stabilizing the platform then, some means must be used to insure that a platform error component never exists along this critical axis. This can only be accomplished by rotating the gimbal ring assembly with the outer and inner gimbal axis torquers until no platform attitude error component remains along the critical axis. The torque motor mechanization in the previous slide would indeed attempt to do just this. Notice, however, that in doing this, it may be necessary for the outer and inner gimbal torquers to drive the gimbal ring assembly through a very large angle to null only a small platform angle error having a component along the critical axis. We are thus faced with a situation where a large gimbal angle change must be generated to compensate for a small platform attitude error.

If the platform attitude error source is changing with time (as it would be for a maneuvering vehicle), it therefore also follows from the above reasoning that a large gimbal rate must be effected under this gimbal angle condition in order to counteract the gyro error rate, hence, prevent the platform from tipping. In order to accelerate the gimbal structure to these large rates, an extremely large outer gimbal torque capability would be required. In a practical design of course, this is impossible to achieve. A realistic torquer would not be capable of supplying the necessary torque and the platform could not be prevented from tipping excessively. This situation is known as "gimbal lock". Excess tipping of the platform produces large gyro deviations from null. Present day platform gyros have only a small output axis angular freedom limited by "stops". The excess tipping of the platform would force the gyros against their stops, platform attitude information would thereby be destroyed, and the inertial reference would be lost. The gimbal lock situation must therefore be prevented from occurring.

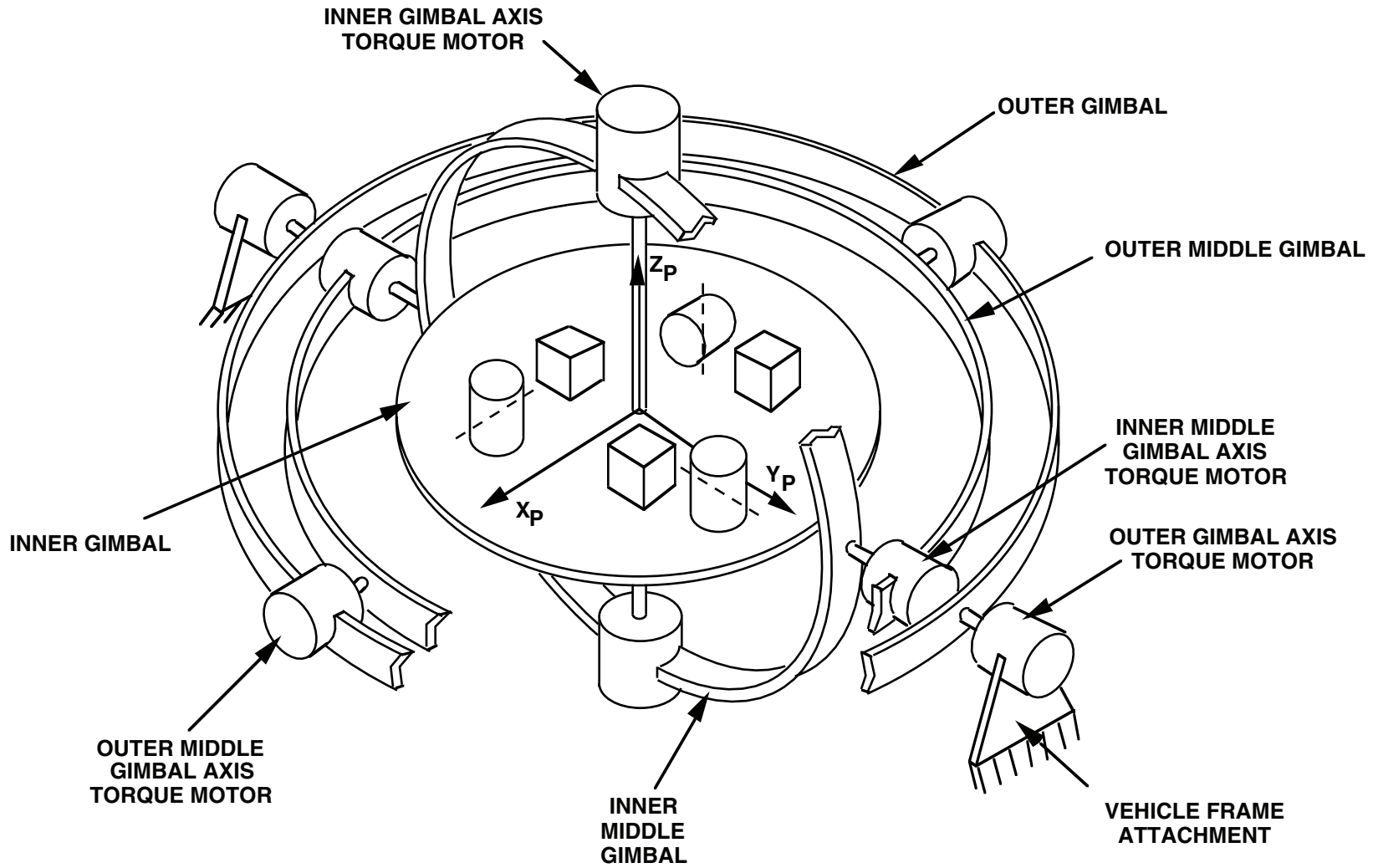
### THREE GIMBAL PLATFORM AT GIMBAL-LOCK ATTITUDE (CONTINUED)

Gimbal lock in a three-gimbal platform can be prevented by constraining the vehicle attitude freedom such that the middle gimbal angle is never allowed to approach the ninety degree condition illustrated in the slide. This, then, is the factor that limits the range of applicability for the three gimbal platform for all applications. The three gimbal concept can only be used if the vehicle attitude constraint requirement is acceptable from an overall mission standpoint.

It finally remains to determine just how closely the middle gimbal attitude can approach the ninety degree condition before gimbal lock occurs. The answer to this question is primarily dependent on three factors; the mass of the gimbal structure, the expected attitude rates of the vehicle, and the capability of the gimbal torquers. If the first two factors are large while the last is small, it can be expected that gimbal lock will occur considerably before the ninety degree middle gimbal condition is reached. In some applications, gimbal lock can actually occur for middle gimbal angles as small as twenty five degrees. At first sight this might appear unusually small. Since the platform torquers have the capability for holding gyro null at zero degree middle gimbal angle, it might appear that they could also hold gyro null for a forty five degree condition. The error in this assumption can be appreciated by observing the middle gimbal orientation in a previous slide for zero middle gimbal angle. Consider what is required from the torquers under this condition to hold the platform stable while the vehicle is rotating arbitrarily. Clearly, the torquers must only work against the friction in the gimbal pivots. The torquers need not accelerate the gimbals since this is accomplished naturally by the vehicle motion through the lateral bearing forces on the pivots. Thus, for a zero middle gimbal angle, no torque is needed to accelerate the gimbals. For a nonzero middle gimbal angle, however, this is no longer true, and the torquers must supply some of the gimbal acceleration torque. Thus, the nonzero middle gimbal attitude condition demands a gimbal acceleration capability from the torquers that is not required at the zero angle condition. Nonzero gimbal angle torquer capabilities therefore should not necessarily be expected to approximate the zero angle capability. It should not be surprising then that a gimbal lock condition might occur for nonzero middle gimbal angles that are still relatively far from the worst case ninety degree lock-up condition illustrated in the slide.

**NOTES**

# FOUR GIMBAL PLATFORM SCHEMATIC

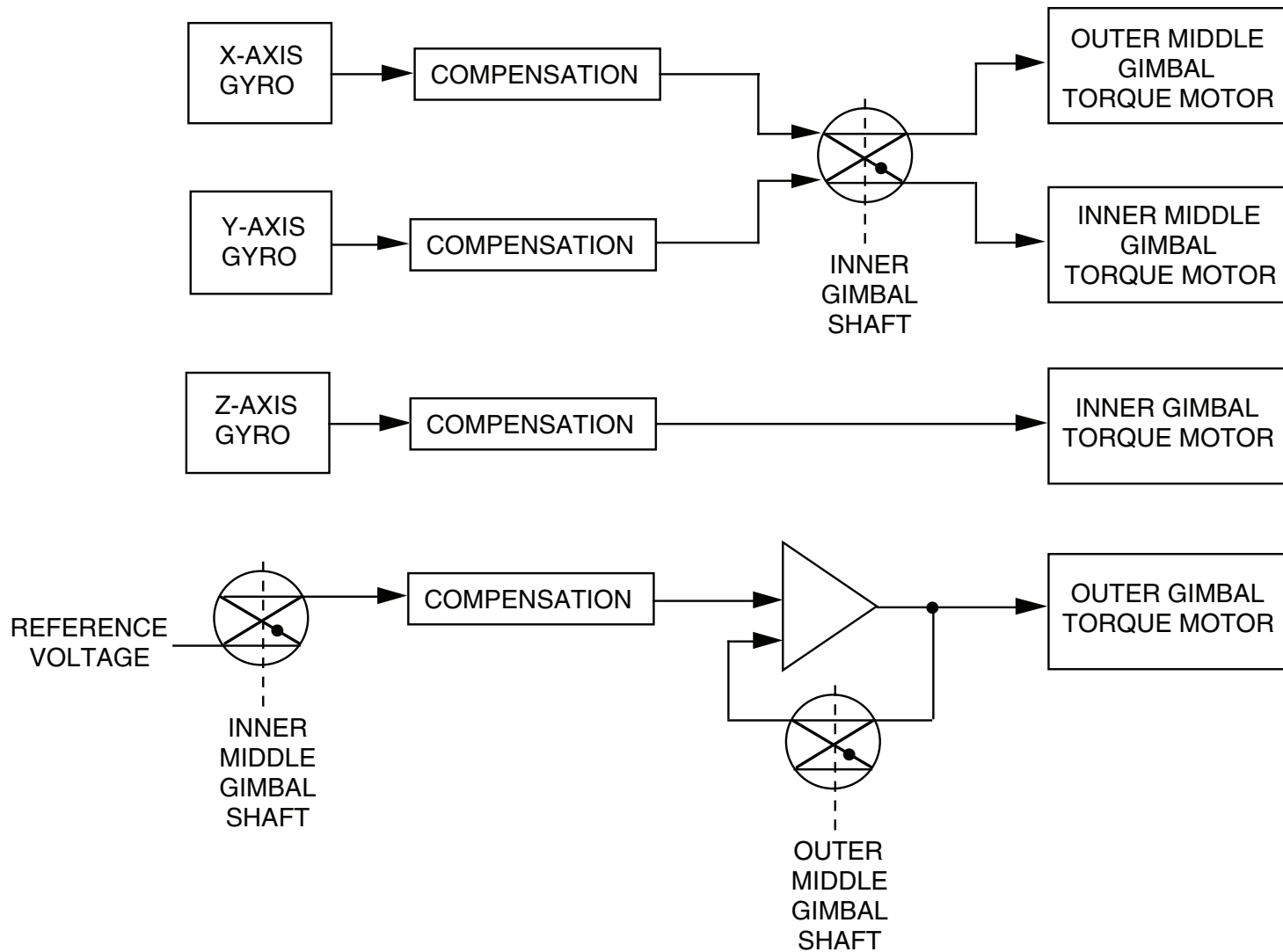


## FOUR GIMBAL PLATFORM SCHEMATIC

An alternative to restricting vehicle maneuver freedom as a means for avoiding three gimbal platform gimbal-lock is to add an outer gimbal ring to the three gimbal platform and control this gimbal such that the inner middle gimbal angle remains at zero (i.e., far from gimbal-lock). This mechanization is known as a four gimbal platform and is illustrated in the slide.

In the slide, the three gimbal platform discussed previously is mounted to another outer gimbal ring instead of the vehicle. The outer gimbal ring is mounted to the vehicle through a torquer pivot axis. The outer gimbal torquer is slaved to the inner middle gimbal shaft resolver so that it will drive in servo fashion to maintain the resolver output at null. In this manner, the inner middle gimbal angle (measured by the resolver) is maintained at zero, hence, far from the gimbal-lock condition for the inner three gimbal platform.

# FOUR GIMBAL PLATFORM TORQUE MOTOR MECHANIZATION



## FOUR GIMBAL PLATFORM TORQUE MOTOR MECHANIZATION

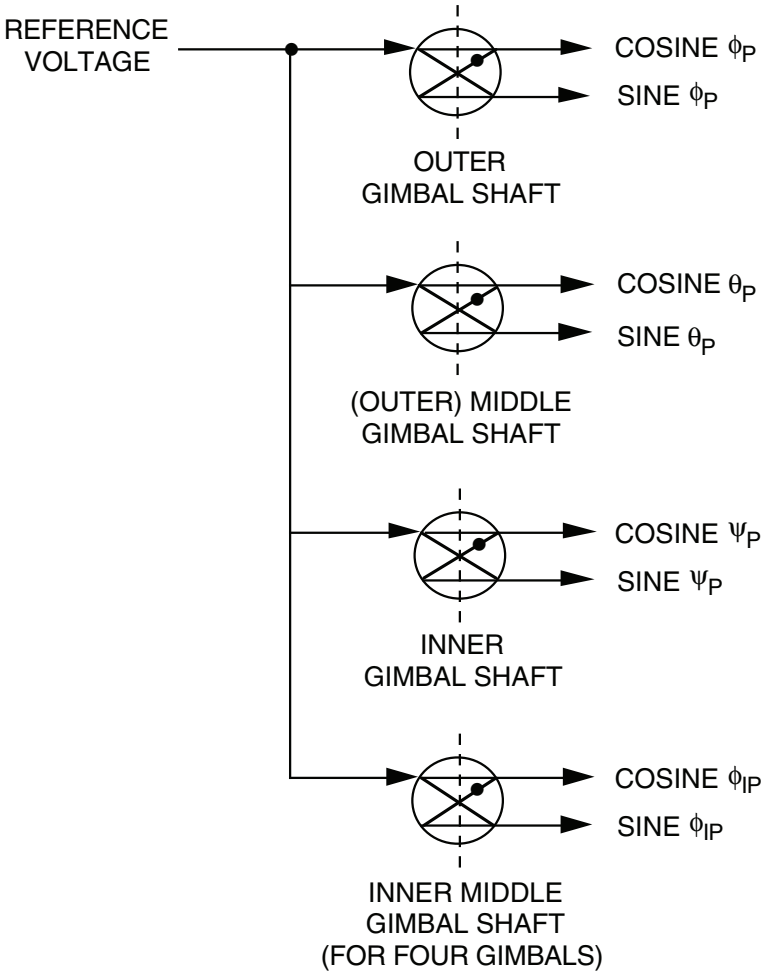
The slide illustrates how the platform torque motors are mechanized for the four gimbal platform. Note that the inner three gimbal torquers are slaved to the platform gyro outputs as with a conventional three gimbal platform. Also note that the  $1/\cos\theta_1$  gain adjustment is not needed for the outer middle gimbal torquer (as with the three gimbal platform) because the inner middle gimbal angle ( $\theta_1$ ) is maintained at null by virtue of the outer redundant gimbal torque motor servo.

Note that the outer gimbal torque motor control loop contains a  $1/\cos\theta_O$  amplification factor, where  $\theta_O$  is the outer middle gimbal angle. This is needed to compensate for the geometrical distortion of the outer gimbal torque motor axis relative to the inner middle gimbal (which would otherwise attenuate the percentage of inner middle gimbal angle correction developed from the outer gimbal torque motor drive). The need for the amplification factor provides a clue to maneuver angle problems that still remain for the four gimbal platform. When the outer middle gimbal shaft approaches ninety degrees, the  $1/\cos\theta_O$  term becomes infinite, indicating that the ability to control inner middle gimbal angles by outer gimbal rotation is lost (i.e., the infinite amplification requirement is a reflection of the fact that no component of outer gimbal drive exists along the inner middle gimbal). As a result, under the  $\theta_O$  near ninety degree condition, the inner middle gimbal angle will no longer be constrained at zero.

Depending on the particular outer gimbal torquer control logic mechanized, the inner middle gimbal angle will depart by varying degrees from zero as the  $\theta_O = 90$  deg condition is approached. Simultaneously, the platform gimbals are generally driven at fairly violent high rates in attempting to maintain gyro and inner middle gimbal angle null. From a practical standpoint, the result is an inability to dwell at the  $\theta_O = 90$  deg condition without risking platform reference loss (due to gyros hitting stops, or torque motors overheating). This limits operation of the four gimbal platform to conditions where the near  $\theta_O = 90$  deg condition can be traversed, but not dwelled at.

For aircraft using four gimbal platforms, the platform is typically mounted such that the outer gimbal axis is along the roll axis, the platform is level, and the outer middle gimbal angle represents pitch. In view of the latter restriction, the ability to dwell at 90 degree pitch up (or down) conditions cannot be practically achieved without risking platform reference loss. This is not a serious restriction since such a flight attitude in an aircraft is unusual. It could be encountered in high performance military aircraft during shake-down flights or when performing the classical Immelmann maneuver (pull-up climb "over the top" followed by roll-out to wings level).

# GIMBAL PLATFORM ATTITUDE/HEADING READOUT



$\psi_{TRUE} = \psi_P - \text{WANDER ANGLE (FROM NAV COMPUTER)}$

## **GIMBAL PLATFORM ATTITUDE/HEADING READOUT**

One of the functions provided by the attitude/heading reference in an inertial navigation system is to provide measures of aircraft roll, pitch, and heading to other aircraft systems. By virtue of the high accuracy of an INS, this data is extremely accurate compared to alternative sources of the same information (e.g., conventional vertical and heading gyroscopes).

For an INS using a locally level gimbaled platform, the attitude/heading data is directly measurable from the platform gimbal angles. The platform readout resolvers are excited to generate the desired outputs in the form of sines and cosines of aircraft roll angle ( $\phi_p$ ), pitch angle ( $\theta_p$ ), and heading relative to level platform axes ( $\psi_p$  or platform heading). True heading is obtained from the platform heading by adding the wander angle correction supplied by the INS navigation computer.

Note, that for a four gimbal platform, the inner middle gimbal angle is effectively nulled by virtue of the outer gimbal servo. As such, this gimbal angle may be assumed zero, and Euler angle output data may be derived from the inner, outer middle, and outer gimbal shaft resolvers (which define heading, pitch, and roll of the aircraft). To account for inner middle gimbal deviations from null, the inner middle gimbal data may also be provided as an output function to other aircraft systems (as shown in the slide).

**NOTES**

# **STRAPDOWN REFERENCE OPERATIONS**

# STRAPDOWN FUNCTIONS

- **BASIC ANALYTICAL EQUATIONS**
- **COMPUTER ITERATIVE ALGORITHMS**

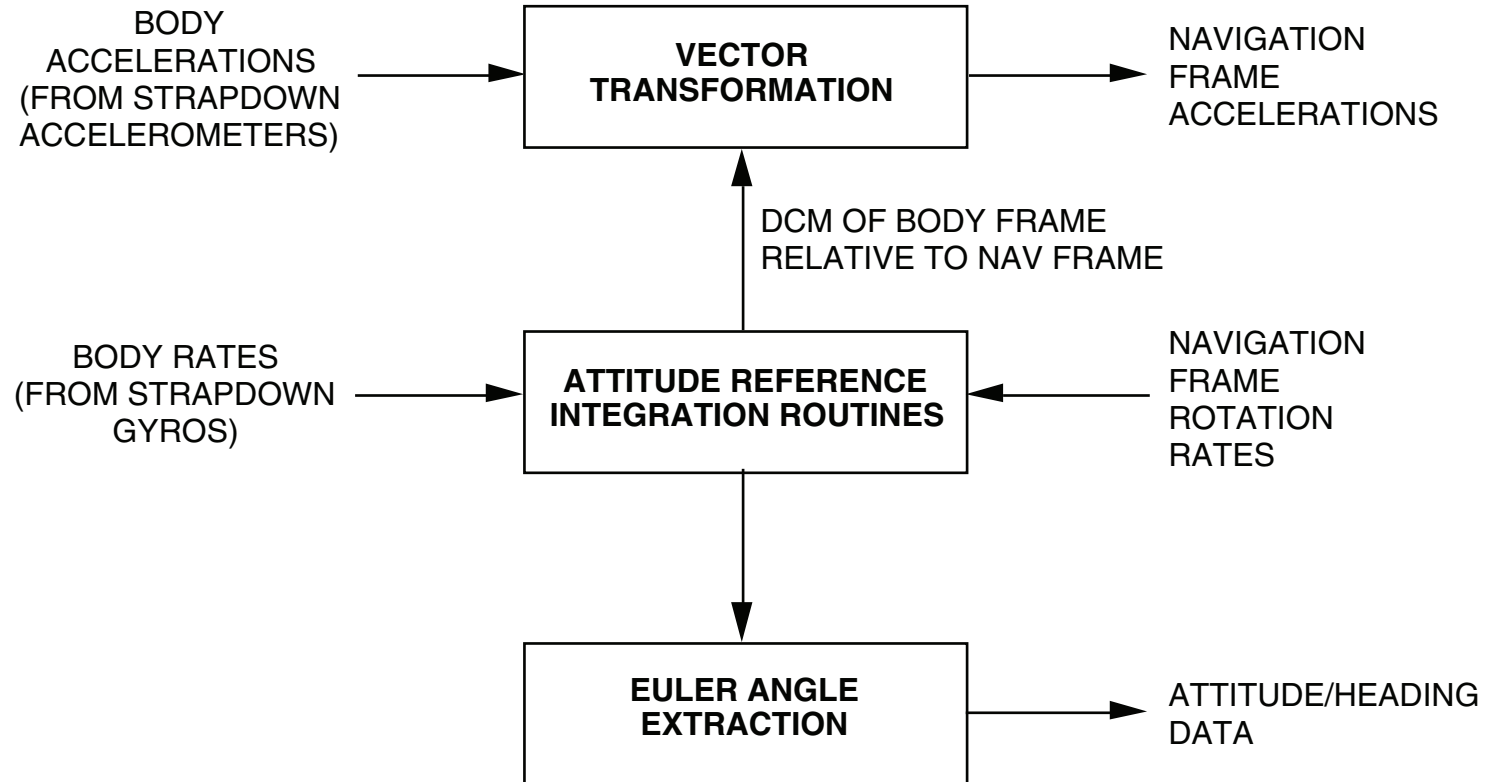
## STRAPDOWN FUNCTIONS

The operations used for the referencing function in a strapdown INS have a basic analytical form, and a computer algorithm form. The analytical form is based on continuous differential equations implying a continuous integration process. These equations are most easily understood, and are described first in the ensuing discussion. The computer algorithm form of the strapdown equations is somewhat more sophisticated, accounting for the finite computation rate of the digital computer used in the strapdown INS, and the form of the data provided by the strapdown sensors to the computer. The computer algorithms are described following the presentation of the classical continuous analytic equation forms.

A detailed discussion on strapdown computation algorithms is provided in the reproduced paper contained in the Strapdown Inertial Navigation Lecture Notes handout:

- NATO AGARD Lecture Series 133 paper: STRAPDOWN SYSTEM ALGORITHMS by Paul G. Savage.

# STRAPDOWN REFERENCE OPERATIONS



## **STRAPDOWN REFERENCE OPERATIONS**

There are three basic functions that can be classified as strapdown reference operations: the basic attitude reference integration routines that calculate body attitude relative to navigation reference coordinates based on strapdown gyro and navigation frame rotation rates, the vector transformation operation that converts strapdown accelerometer sensed specific force acceleration from body to navigation reference coordinates, and the Euler angle extraction function which converts the calculated attitude data to roll, pitch, and heading angle outputs. In combination, these computational elements provide the equivalent interface to the INS navigation computer and system output as the gimbale platform in a gimbale INS.

## ACCELERATION TRANSFORMATION

$$AXL = C11 \times AXB + C12 \times AYB + C13 \times AZB$$

$$AYL = C21 \times AXB + C22 \times AYB + C23 \times AZB$$

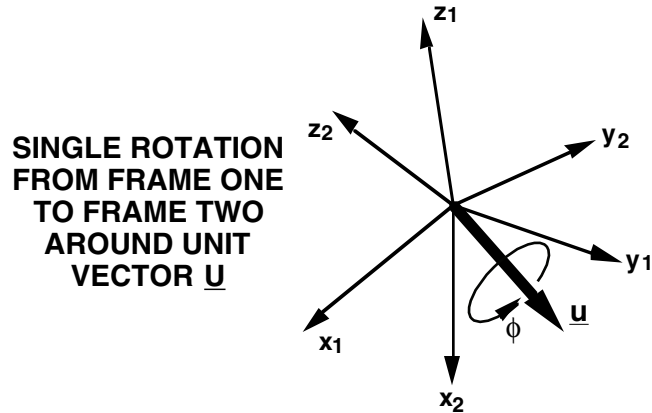
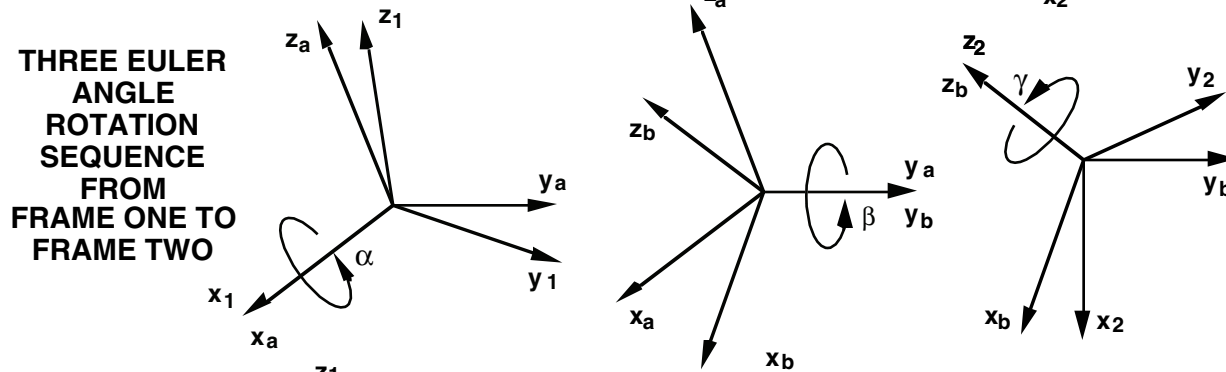
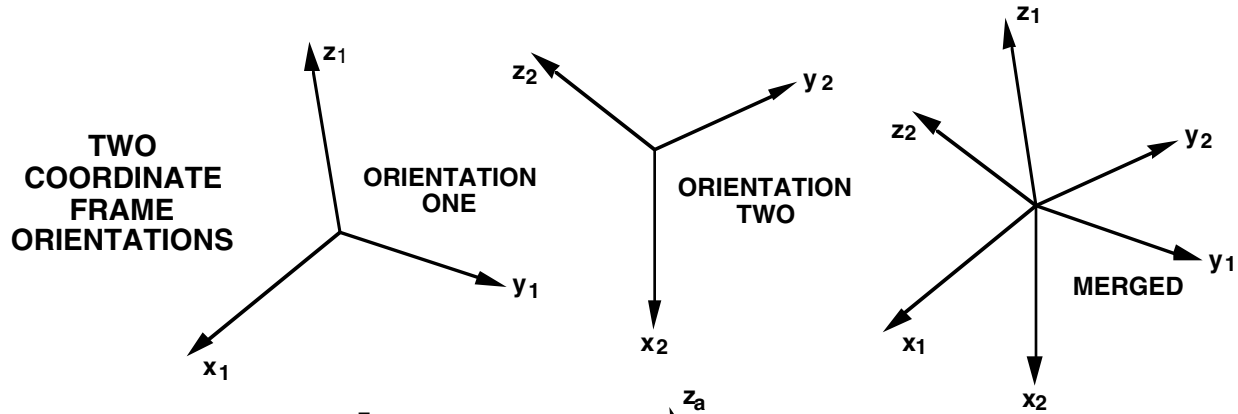
$$AZL = C31 \times AXB + C32 \times AYB + C33 \times AZB$$

$$\underline{A}^L = C_B^L \underline{A}^B$$

## ACCELERATION TRANSFORMATION

The classical analytical form of the acceleration transformation operation in a strapdown INS using locally level navigation reference coordinates is a matrix multiplication of the strapdown body frame specific force acceleration vector ( $\underline{A}^B$ ) with the direction cosine matrix relating body to local level navigation coordinates ( $C_B^L$ ). The components of  $\underline{A}^B$  represent the vector components sensed by the strapdown X, Y, Z body axis accelerometers.

# ATTITUDE ORIENTATION CONCEPTS



**ROTATION VECTOR**

$$\underline{\phi} = \phi \underline{u} = \begin{bmatrix} l \phi \\ m \phi \\ n \phi \end{bmatrix}$$

$$\underline{u} = \begin{bmatrix} l \\ m \\ n \end{bmatrix}$$

**ATTITUDE QUATERNION**

$$q = \underline{u} \sin \frac{\phi}{2} + \cos \frac{\phi}{2} = \begin{bmatrix} l \sin \frac{\phi}{2} \\ m \sin \frac{\phi}{2} \\ n \sin \frac{\phi}{2} \\ \cos \frac{\phi}{2} \end{bmatrix}$$

## ATTITUDE ORIENTATION CONCEPTS

The angular orientation between two coordinate frames (e.g., Frame 1 and Frame 2 in the chart) has been described by several alternative but equivalent methods. For relative angular measurements between two coordinate frames, the frames can be considered merged to a common origin. The chart on page 10 described a direction cosine matrix method whereby the attitude orientation between two merged frames is represented by the nine cosines of the angles between the frame axes. This chart illustrates three alternative coordinate frame relative angular orientation measurements; Euler angle rotations, the rotation vector, and the attitude quaternion.

The Euler angle method consists of a series of coordinate frame angular rotations that will rotate one coordinate frame (Frame 1) from its current orientation into the orientation of another coordinate frame (Frame 2). Each rotation is about one of the coordinate axes of the previously rotated coordinate frame. In the chart, the first Euler angle rotation  $\alpha$  is about the x axis of Frame 1 generating intermediate Frame a. A second Euler angle rotation  $\beta$  is about the y axis of Frame a generating intermediate Frame b. A third Euler angle rotation  $\gamma$  is about Frame b axis z resulting in a final coordinate frame orientation parallel to Frame 2 axes. The Euler angle sequence  $\alpha, \beta, \gamma$  in the rotation order x, y, z defines the orientation of Frame 2 relative to Frame 1.

The rotation vector concept is based on a theorem of Euler that a coordinate frame can be rotated from its current angular orientation to another specified orientation by a rotation  $\phi$  about a single unit vector  $\underline{u}$ . The angular orientation of  $\underline{u}$  relative to Frame 1 and the magnitude of  $\phi$  depend on the orientation of the rotated Frame 1 (i.e., Frame 2) relative to the Frame 1 orientation. The rotation vector  $\underline{\phi}$  is defined as the product of the scalar  $\phi$  with the vector  $\underline{u}$ . The rotation vector  $\underline{\phi}$  defines the orientation of Frame 2 relative to Frame 1 as a rotation of Frame 1 around  $\underline{\phi}$  through a rotation angle equal to the magnitude of  $\underline{\phi}$ . Note that in rotating Frame 1 to Frame 2 around  $\underline{\phi}$ , the angles between the rotating Frame 1 axes and  $\underline{\phi}$  do not change. Consequently, the components (projections) of  $\underline{\phi}$  on Frame 1 and Frame 2 are the same. This is a unique characteristic of the rotation vector and is the basis for an important characteristic of its formal analytical definition, i.e., the vector that has the same components in Frame 1 and Frame 2.

The attitude quaternion  $q$  is defined mathematically in the chart as a function of  $\phi$  and  $\underline{u}$ . Its properties are discussed in the Strapdown Inertial Navigation Lecture Notes handout. It is easily verified from the chart that the sum of the squares of the elements of  $q$  equal unity. This is the basis for the quaternion normalization algorithm on page 216.

The attitude orientation concepts described above are analytically equivalent; the defining parameters (e.g., Euler angles, direction cosines) for any one can be analytically described as a function of the defining parameters in any other.

## TYPICAL ATTITUDE DETERMINATION APPROACHES

- **EULER ANGLES**
  - **CALCULATES PARAMETERS EQUAL TO THREE-GIMBAL PLATFORM GIMBAL ANGLES**
  - **THREE PARAMETERS**
  
- **DIRECTION COSINES**
  - **CALCULATES BODY-TO-NAV FRAME DIRECTION COSINE MATRIX DIRECTLY**
  - **NINE PARAMETERS**
  
- **QUATERNION**
  - **FOUR PARAMETERS**
  - **THREE PARAMETERS EQUAL COMPONENTS OF A UNIT VECTOR ALONG “EULER AXIS” BETWEEN BODY AND NAV FRAME TIMES THE SINE OF ONE HALF THE ANGLE BETWEEN THE TWO FRAMES AROUND THE EULER AXIS**
  - **FOURTH PARAMETER EQUALS COSINE OF ONE HALF THE ANGLE BETWEEN THE TWO FRAMES AROUND THE EULER AXIS**

## TYPICAL ATTITUDE DETERMINATION APPROACHES

Several options are available for calculating the basic attitude data in a strapdown INS. The three classical methods typically considered during tradeoff analyses are based on Euler angles, direction cosines, or the quaternion as the basic attitude reference parameters.

The Euler angle approach is a direct analog of the gimballed platform. Three attitude parameters are computed, each equal to the roll, pitch, and heading angles that would be generated between the gimbals of a three gimbal gyro stabilized INS platform (i.e., the angles measured by the gimbal shaft resolvers).

In the direction cosine approach, the calculated attitude parameters represent the cosines of the angles between body and reference axes. Nine direction cosines exist.

In the quaternion approach, four parameters are calculated as the basic attitude reference data. The quaternion parameters are based on the "Euler axis" and angle that defines a body orientation relative to a reference attitude. The Euler axis is the single axis around which the body can be rotated from the reference coordinates into its current attitude. The Euler angle is the angle about the Euler axis that will rotate the body from reference to current body axes. It can be demonstrated that such an axis and angle exists for any arbitrary body attitude and completely defines the body attitude relative to reference coordinates.

The quaternion is a set of four parameters, three represent the components of a vector, the fourth is a scalar quantity. The quaternion vector equals a unit vector along the Euler axis scaled by the sine of half the Euler axis rotation angle that will rotate the body from reference to body axes. The scalar quantity equals the cosine of half the Euler axis rotation angle.

## NOMENCLATURE

$\phi, \theta, \psi_p$	= ROLL, PITCH, YAW EULER ANGLES RELATING BODY TO LOCAL LEVEL AXES
$\psi$	= TRUE HEADING (RELATIVE TO NORTH)
BODY AXES	= X-FORWARD, Y-RIGHT WING, Z-NORMALLY DOWN
LOCAL LEVEL AXES	= Z-DOWN, X,Y HORIZONTAL
$C_{IJ}$	= COSINE OF ANGLE BETWEEN J BODY AXIS AND I LOCAL LEVEL AXIS
$\underline{W}_{IB}^B$	= ANGULAR VELOCITY OF BODY FRAME RELATIVE TO INERTIAL SPACE AS PROJECTED ON BODY AXES
$\underline{W}_{IL}^L$	= ANGULAR VELOCITY OF LOCAL LEVEL FRAME RELATIVE TO INERTIAL SPACE AS PROJECTED ON LOCAL LEVEL AXES
$q_B^L$	= QUATERNION RELATING BODY TO LOCAL LEVEL AXES
a, b, c	= EULER AXIS VECTOR COMPONENTS OF $q_B^L$ QUATERNION
d	= FOURTH (SCALAR) COMPONENT OF $q_B^L$ QUATERNION

## **NOMENCLATURE**

In the ensuing discussion on attitude reference equations, the nomenclature in the slide will be utilized.

## EULER ANGLE EQUATIONS

$$\dot{\phi} = \text{WXB} + \text{TAN } \theta \text{ SIN } \phi \text{ WYB} + \text{TAN } \theta \text{ COS } \phi \text{ WZB} \\ - \text{SEC } \theta \text{ COS } \psi_p \text{ WXL} - \text{SEC } \theta \text{ SIN } \psi_p \text{ WYL}$$

$$\phi = \int_0^t \dot{\phi} dt + \phi_o$$

$$\dot{\theta} = \text{COS } \phi \text{ WYB} - \text{SIN } \phi \text{ WZB} + \text{SIN } \psi \text{ WXL} - \text{COS } \psi \text{ WYL}$$

$$\theta = \int_0^t \dot{\theta} dt + \theta_o$$

$$\dot{\psi}_p = \text{SEC } \theta \text{ SIN } \phi \text{ WYB} + \text{SEC } \theta \text{ COS } \phi \text{ WZB} \\ - \text{TAN } \theta \text{ COS } \psi_p \text{ WXL} - \text{TAN } \theta \text{ SIN } \psi_p \text{ WYL} - \text{WZL}$$

$$\psi_p = \int_0^t \dot{\psi}_p dt + \psi_{po}$$

$$\text{SIN } \phi = \phi - \frac{1}{6} \phi^3 + \frac{1}{120} \phi^5 - \dots$$

$$\text{COS } \phi = 1 - \frac{1}{2} \phi^2 + \frac{1}{24} \phi^4 - \dots$$

$$\text{SIN } \theta = \dots$$

$$\text{COS } \theta = \dots$$

$$\text{SIN } \psi_p = \dots$$

$$\text{COS } \psi_p = \dots$$

$$\text{SEC } \theta = \frac{1}{\text{COS } \theta}$$

$$\text{TAN } \theta = \frac{\text{SIN } \theta}{\text{COS } \theta}$$

## EULER ANGLE EQUATIONS

The Euler angle rate equations consist of three differential equations for the roll, pitch, and heading Euler angles in terms of gyro sensed body rates ( $B$ ), local level reference angular rates ( $L$ ), and trigonometric functions of Euler angles. The trigonometric functions must be evaluated in the INS computer based on Taylor series expansion formulas. The Euler rate equations must be integrated continuously to maintain knowledge of the  $\phi$ ,  $\theta$ , and  $\psi_p$  Euler angles during INS operation.

Note that both the roll ( $\phi$ ) and heading ( $\psi_p$ ) rate equations contain secant and tangent  $\theta$  coefficients multiplying the angular rate terms. At pitch angles approaching ninety degrees, these functions become infinite, calling for infinitely high Euler rates. This is an analytical representation of the mechanical "gimbal-lock" condition that limits the operation of three gimbal platforms to low pitch angle ( $\theta$ ) conditions (i.e., well away from ninety degrees). For the strapdown computer, the comparable problem would be an excessively high word length and iteration rate requirement to generate the high rate signals accurately, and accurately integrate them near the ninety degree pitch condition.

## EULER ANGLE EQUATIONS (CONTINUED)

$$C11 = \cos \theta \cos \psi_p$$

$$C12 = -\cos \phi \sin \psi_p + \sin \phi \sin \theta \cos \psi_p$$

$$C13 = \sin \phi \sin \psi_p + \cos \phi \sin \theta \cos \psi_p$$

$$C21 = \cos \theta \sin \psi_p$$

$$C22 = \cos \phi \cos \psi_p + \sin \phi \sin \theta \sin \psi_p$$

$$C23 = -\sin \phi \cos \psi_p + \cos \phi \sin \theta \sin \psi_p$$

$$C31 = -\sin \theta$$

$$C32 = \sin \phi \cos \theta$$

$$C33 = \cos \phi \cos \theta$$

$$\psi = \psi_p - \text{WANDER ANGLE}$$

## **EULER ANGLE EQUATIONS (CONTINUED)**

The Euler angle parameters are not in the direction cosine form needed for the strapdown acceleration transformation operation. Consequently, an additional set of computations is needed to calculate the direction cosine elements from the computed Euler angles. This computation involves the sum of products of sines and cosines of the Euler angles.

Note that the Euler angle extraction function is absent for the Euler angle approach because the calculated attitude parameters are identically equal to the desired Euler angle signals. The wander angle must be subtracted from platform heading to calculate the true heading Euler angle.

## DIRECTION COSINE EQUATIONS

$$\dot{C}_B^L = C_B^L (\underline{W}_{IB}^B \times) - (\underline{W}_{IL}^L \times) C_B^L$$

$$\dot{C}_{11} = C_{12} W_{ZB} - C_{13} W_{YB} + C_{21} W_{ZL} - C_{31} W_{YL}$$

$$\dot{C}_{12} = C_{13} W_{XB} - C_{11} W_{ZB} + C_{22} W_{ZL} - C_{32} W_{YL}$$

$$\dot{C}_{13} = C_{11} W_{YB} - C_{12} W_{XB} + C_{23} W_{ZL} - C_{33} W_{YL}$$

$$\dot{C}_{21} = C_{22} W_{ZB} - C_{23} W_{YB} + C_{31} W_{XL} - C_{11} W_{ZL}$$

$$\dot{C}_{22} = C_{23} W_{XB} - C_{21} W_{ZB} + C_{32} W_{XL} - C_{12} W_{ZL}$$

$$\dot{C}_{23} = C_{21} W_{YB} - C_{22} W_{XB} + C_{33} W_{XL} - C_{13} W_{ZL}$$

$$C_{IJ} = \int_0^t \dot{C}_{IJ} dt + C_{IJ0} \quad \text{FOR } \begin{matrix} I = 1 \text{ TO } 2 \\ J = 1 \text{ TO } 3 \end{matrix}$$

## **DIRECTION COSINE EQUATIONS**

The direction cosine rate equations are coupled linear functions of gyro sensed body rate, local level frame rates, and the calculated direction cosine elements. The direction cosine elements are calculated in a strapdown system by continuously integrating the cosine rate equations. Note that the third set of direction cosines (the C3J's) are not computed by the integration process. This is because they can be calculated from the first two sets using the fact that the third row of cosines equals the cross-product of the first two rows. This is simply a statement that the cross-product of unit vectors along L-Frame X and Y Axes (as represented by the C1J and C2J projections in body axes) equals a unit vector along the Z L-Frame axis (or the C3J body axis components).

It should also be noted that the coefficients that multiply the angular rates in the cosine rate equations are equal to the direction cosines which are well behaved, never exceeding unity in magnitude. Hence, the cosine rates are also well behaved and can be integrated without singularities for any aircraft orientation, even for the 90 degree pitch up condition that caused problems with the Euler angle (and three-gimbaled platform) attitude reference approach.

## DIRECTION COSINE EQUATIONS (CONTINUED)

$$C31 = C12 C23 - C13 C22$$

$$C32 = C13 C21 - C11 C23$$

$$C33 = C11 C22 - C12 C21$$

$$\phi = \text{TAN}^{-1} \frac{C32}{C33}$$

$$\theta = \text{TAN}^{-1} \frac{-C31}{(1 - C31^2)^{1/2}}$$

$$\psi_p = \text{TAN}^{-1} \frac{C21}{C11}$$

$$\psi = \psi_p - \text{WANDER ANGLE}$$

## DIRECTION COSINE EQUATIONS (CONTINUED)

The slide shows how the third row of direction cosines is calculated through a cross-product operation on the first two row cosines.

In order to provide the Euler angle output function, an additional computation is required when using direction cosines (as shown) to calculate the equivalent roll, pitch, and yaw (heading) Euler angle output signals. Although not readily apparent from the Euler angle extraction equations, the  $\phi$  and  $\psi_p$  Euler angles are ill-defined at the  $\theta$  equal  $\pm 90$  degree condition (the numerator and denominator of the associated arc tangent arguments go to zero). This is merely a statement of the fact that at ninety degree pitch, the roll and heading axes are colinear, hence, roll and heading are not separable. To circumvent the problem, an alternate algorithm can be used based on the direct sum of the two angles. Note, however, that this singularity is a temporary condition that affects only the Euler angle output and not the basic direction cosine attitude data elements. This contrasts with the direct Euler angle approach in which the basic attitude data (the Euler angles) are destroyed and irrecoverable if the  $\theta$  equal to  $\pm 90$  degree condition is approached.

It should also be noted that with the direction cosine approach, the direction cosine elements needed for acceleration transformation operations are directly available as a natural part of the attitude computation. No separate calculations are required.

## QUATERNION EQUATIONS

$$\dot{q}_B^L = \frac{1}{2} q_B^L w_{IB}^B - \frac{1}{2} w_{IL}^L q_B^L$$

$$\dot{a} = \frac{1}{2} (d \text{ WXB} - c \text{ WYB} + b \text{ WZB} - d \text{ WXL} - c \text{ WYL} + b \text{ WZL})$$

$$\dot{b} = \frac{1}{2} (c \text{ WXB} + d \text{ WYB} - a \text{ WZB} + c \text{ WXL} - d \text{ WYL} - a \text{ WZL})$$

$$\dot{c} = \frac{1}{2} (-b \text{ WXB} + a \text{ WYB} + d \text{ WZB} - b \text{ WXL} + a \text{ WYL} - d \text{ WZL})$$

$$\dot{d} = \frac{1}{2} (-a \text{ WXB} - b \text{ WYB} - c \text{ WZB} + a \text{ WXL} + b \text{ WYL} + c \text{ WZL})$$

$$a = \int_0^t \dot{a} \, dt + a_0$$

$$c = \int_0^t \dot{c} \, dt + c_0$$

$$b = \int_0^t \dot{b} \, dt + a_0$$

$$d = \int_0^t \dot{d} \, dt + d_0$$

## QUATERNION EQUATIONS

The quaternion rate equations consist of a set of four linear functions of input gyro body rate components, local level navigation frame rate components, and the quaternion elements themselves (a, b, c, d).

Because the quaternion elements represent components of the sine and cosine of half the Euler angle, each element never exceeds unity in magnitude. The coefficients that multiply the angular rates in the quaternion rate equations, therefore, never exceed one half in magnitude (note the 0.5 overall scale factor). As a result, the rate equations are well behaved, free of singularities for all vehicle attitudes.

The more concise quaternion rate equation shown in the box on the slide is a quaternion algebra expression whose meaning is defined in the Strapdown System Algorithms paper provided in the Lecture Notes handout document. The quaternion algebra equation is directly analogous to the matrix algebra equation given on a previous chart for the direction cosine rate equations.

## QUATERNION EQUATIONS (CONTINUED)

$$C11 = d^2 + a^2 - b^2 - c^2$$

$$C12 = 2(ab - cd)$$

$$C13 = 2(ac + bd)$$

$$C21 = 2(ab + cd)$$

$$C22 = d^2 + b^2 - c^2 - a^2$$

$$C23 = 2(bc - ad)$$

$$C31 = 2(ac - bd)$$

$$C32 = 2(bc + ad)$$

$$C33 = d^2 + c^2 - a^2 - b^2$$

$$\phi = \text{TAN}^{-1} \frac{C32}{C33}$$

$$\theta = \text{TAN}^{-1} \frac{-C31}{(1 - C31^2)^{1/2}}$$

$$\psi_p = \text{TAN}^{-1} \frac{C21}{C11}$$

$$\psi = \psi_p - \text{WANDER ANGLE}$$

## QUATERNION EQUATIONS (CONTINUED)

The quaternion elements are continuously evaluated in the strapdown INS by integrating the quaternion rate equations in the INS computer. The quaternion computation may appear simpler compared to either the Euler angle or direction cosine rate integration approaches. It is basically unusable, however, in its direct form for other INS functions. Hence, additional computations are needed when using the quaternion (as shown in the slide) to calculate the direction cosines for acceleration transformation and for Euler angle extraction.

It should be noted as indicated in the Strapdown System Algorithms paper provided in the Lecture Notes handout document, that the quaternion can be used directly to transform acceleration from body to navigation coordinates. The associated computations are somewhat more than is required to transform acceleration using direction cosines. However, if Euler angle extraction is also a requirement, the associated five direction cosine elements indicated in the slide for this operation (C11, C21, C31, C32, and C33) must still be calculated from the quaternion.

# COMPARISON BETWEEN ATTITUDE REFERENCE APPROACHES

- **EULER ANGLES**
  - 3 PARAMETERS
  - RATE EQUATION FORM CUMBERSOME (CONTAIN TRIG FUNCTIONS)
  - SINGULARITY AT 90 DEGREE PITCH
  - NEED CONVERSION TO DIRECTION COSINES FOR ACCELERATION TRANSFORMATION
  
- **QUATERNION**
  - 4 PARAMETERS
  - RATE EQUATION FORM SIMILAR TO DIRECTION COSINES
  - NO SINGULARITIES
  - NEED CONVERSION TO DIRECTION COSINES FOR ACCELERATION TRANSFORMATION AND EULER ANGLES FOR ATTITUDE OUTPUTS
  
- **DIRECTION COSINES**
  - 9 PARAMETERS
  - NO SINGULARITIES
  - USE DIRECTLY IN ACCELERATION TRANSFORMATION EQUATIONS
  - NEED CONVERSION TO EULER ANGLES FOR ATTITUDE OUTPUTS

## COMPARISONS BETWEEN ATTITUDE REFERENCE APPROACHES

A comparison between the attitude reference approaches discussed, generally reveals that Euler angles are not practical for strapdown INS use. Although only three parameters are required, their computation is complicated compared to the direction cosine or quaternion methods by the need to perform complex trigonometric operations as a part of the Euler angle updating process. Additionally, the direction cosines must still be calculated from the Euler angles for acceleration transformation operations. An advantage with the Euler angle approach is that an Euler angle extraction algorithm is not needed since the Euler angles themselves are in the proper form for Euler angle output. The principle disadvantage in using Euler angles is their inaccuracy near  $\pm 90$  degree pitch angles due to analytical singularities.

The quaternion requires only four parameters to define attitude, has relatively simple rate equations for integration, and has no singularities for all vehicle attitudes. Additional computations are required to calculate direction cosines for acceleration transformation, and for Euler angle extraction. In early strapdown systems, digital integration algorithms based on quaternions were believed to be more accurate than the comparable direction cosine approach under certain types of vehicle motion. Modern day algorithms (to be discussed subsequently) show no performance advantage (or disadvantage) for the quaternion.

Direction cosines require nine parameters to define attitude, have relatively simple rate equations for integration, and have no singularities for all vehicle attitudes. The calculated direction cosine parameters are in the exact form needed for acceleration transformation operations, hence, no additional calculations are needed for this function. Additional computations are required for Euler angle extraction from the calculated direction cosines.

# ACCELERATION TRANSFORMATION DIGITAL COMPUTER ALGORITHM

- **CONSTRAINTS**

- TRANSFORMED ACCELERATION MUST BE INTEGRATED ACCURATELY TO OBTAIN NAVIGATION FRAME VELOCITIES
- ACCELERATION DATA FROM ACCELEROMETERS AVAILABLE AS INTEGRATED ACCELERATION INCREMENTS (TO PRESERVE ACCURACY)
- COMPUTER ITERATION RATE MUST BE CONSTRAINED DUE TO THROUGHPUT LIMITATIONS

- **OVER A COMPUTER CYCLE:**

$$\begin{aligned} \underline{\Delta V}_m^L &= \int_{t_m}^{t_{m+1}} C_B^L \underline{A}^B dt = \int_{t_m}^{t_{m+1}} C_{B(m)}^L C_B^{B(m)} \underline{dV}^B \\ &= C_{B(m)}^L \int_{t_m}^{t_{m+1}} C_B^{B(m)} \underline{dV}^B \end{aligned}$$

$C_{B(m)}^L$  = VALUE OF  $C_B^L$  AT START OF COMPUTER CYCLE

$C_B^{B(m)}$  = DIRECTION COSINE MATRIX RELATING CURRENT B-FRAME ATTITUDE WITH B-FRAME ATTITUDE AT START OF COMPUTER CYCLE

$\underline{\Delta V}_m^L$  = CHANGE IN AIRCRAFT L-FRAME VELOCITY OVER COMPUTER CYCLE DUE TO SPECIFIC FORCE ACCELERATION

$\underline{dV}^B$  = INCREMENTAL CHANGE IN B-FRAME INTEGRATED SPECIFIC FORCE ACCELERATION (I.E. – ACCELEROMETER PULSE OUTPUT)

## ACCELERATION TRANSFORMATION DIGITAL COMPUTER ALGORITHM

The computer algorithm for performing the acceleration transformation operation is based on an integral form of the classical instantaneous equation form. The algorithm is structured so that its output represents the integral of the L-Frame specific force acceleration over a computer iteration cycle. As such, the algorithm output represents the L-Frame velocity change over the computer cycle due to integrated specific force acceleration. The velocity integration algorithm in the computer, then, can update the L-Frame velocity components by summing the calculate L-Frame specific force velocity increments with the previous velocity components. Gravity and Coriolis corrections are also added on a regular basis for the total velocity update as part of the velocity integration algorithm.

In structuring the transformation algorithm, it is important that it maintains accuracy as a function of computer cycle time period. The object is to make the algorithm accurate enough that it does not require high computer iteration rates to preserve accuracy. The computer cycle rate can thereby be dictated by other considerations (e.g., INS output rate) without sacrificing algorithm accuracy. In general, algorithms requiring high iteration rates to preserve accuracy should be avoided if possible to avoid computer throughput problems.

The algorithm shown in the slide is based on the integral of the acceleration transformation equation to obtain the integrated specific force acceleration over a computer cycle (or change in L-Frame velocity). The algorithm is based on the product of the  $C_B^L$  transformation matrix at the end of the previous iteration cycle, times the integral (over the computer cycle) of a small-angle transformation matrix product with an incremental velocity output vector from the strapdown accelerometers. The small angle matrix represents the direction cosines between the body attitude at the start of the computer cycle and the current body attitude within the computer cycle. The body velocity increment vector represents the output of typical strapdown precision body mounted accelerometers which are in the form of digital logic pulses. The occurrence of an output pulse from a given accelerometer is a digital indication that a specified fixed increment of integrated specific force acceleration has been received by the accelerometer. The  $d\underline{V}^B$  vector components (X, Y, and Z) represent the pulse outputs from the three strapdown accelerometers.

An expression for the small angle direction cosine matrix within the integral on the slide is developed in the following two slides.

## SMALL ANGLE DIRECTION COSINE MATRIX

$$\mathbf{C} \approx \begin{bmatrix} 1 & -\epsilon_Z & \epsilon_Y \\ \epsilon_Z & 1 & -\epsilon_X \\ -\epsilon_Y & \epsilon_X & 1 \end{bmatrix} = \mathbf{I} + (\underline{\epsilon} \times)$$

$$\underline{\epsilon} = \begin{bmatrix} \epsilon_X \\ \epsilon_Y \\ \epsilon_Z \end{bmatrix} = \text{SMALL ANGLE ROTATION VECTOR}$$

## SMALL ANGLE DIRECTION COSINE MATRIX

The small angle transformation matrix in the previous slide can be expressed in terms of a small angle vector through the approximation shown that is valid for small angle cosine matrices in general. The slide shows that a small rotation matrix can be approximated as the sum of the unity matrix plus the skew symmetric matrix (or cross-product operator) form of a small angle vector. Hence, the small angle matrix can be characterized by three parameters, equal to the components of the small angle error vector.

## DEVELOPMENT OF ACCELERATION TRANSFORMATION ALGORITHM

$$C_B^{B(m)} \approx I + (\underline{\alpha}^B \times)$$

$$\underline{\alpha}^B = \int_{t_m}^t \underline{w}_{IB}^B dt = \int_{t_m}^t d\underline{\alpha}^B$$

$$\int_{t_m}^{t_{m+1}} C_B^{B(m)} d\underline{V}^B = \int_{t_m}^{t_{m+1}} [d\underline{V}^B + (\underline{\alpha}^B \times) d\underline{V}^B]$$

$$= \underline{u}_m^B + \boxed{\int_{t_m}^{t_{m+1}} (\underline{\alpha}^B \times d\underline{V}^B)} \quad \text{SCULLING COMPENSATION}$$

$$\boxed{\Delta \underline{V}_m^L = C_{B(m)}^L \left[ \underline{u}_m^B + \int_{t_m}^{t_{m+1}} (\underline{\alpha}^B \times d\underline{V}^B) \right]}$$

$\underline{u}_m^B$  = INTEGRATED B-FRAME SPECIFIC FORCE ACCELERATION OVER COMPUTER CYCLE  
(ACCELEROMETER PULSE COUNT)

$\underline{\alpha}^B$  = INTEGRATED B-FRAME INERTIAL ANGULAR RATE (GYRO SIGNALS) SINCE START OF  
COMPUTER CYCLE

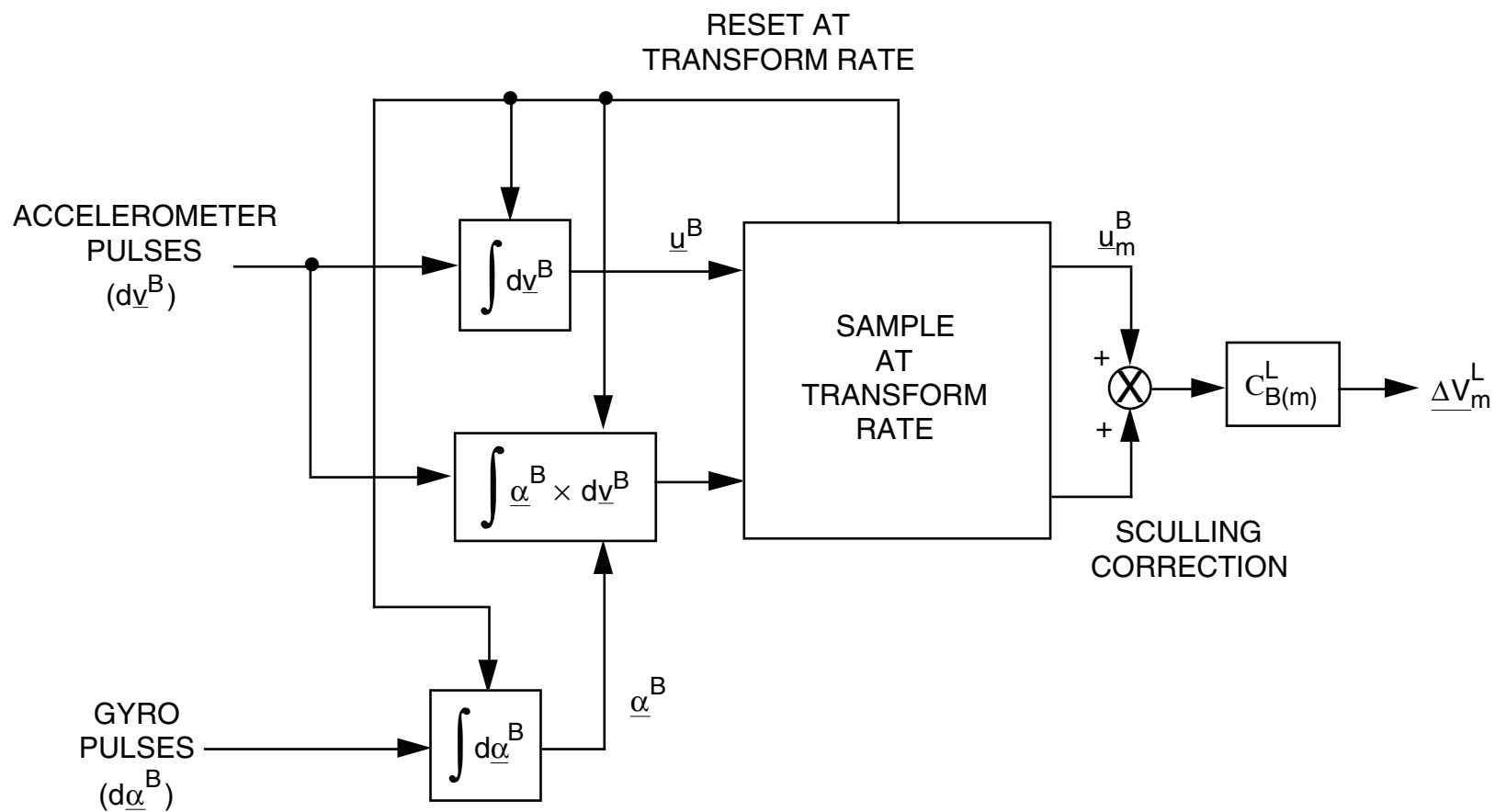
$d\underline{\alpha}^B$  = INCREMENTAL CHANGE IN B-FRAME INTEGRATED ANGULAR RATE VECTOR  
(I.E. – GYRO PULSE OUTPUT)

## DEVELOPMENT OF ACCELERATION TRANSFORMATION ALGORITHM

For the small angle transformation matrix in the acceleration transformation algorithm (i.e.,  $C_B^{B(m)}$ ), it can be shown that the associated small angle vector can be approximated by the integral of the strapdown gyro body rate components since the start of the computer cycle. This small angle vector is shown as the sum (or integral) of a strapdown gyro incremental pulse output vector. As for the strapdown accelerometer, strapdown rate gyros actually output pulses, each indicating that the particular gyro has rotated through a known fixed increment of integrated rate about the gyro input axis. The  $d\alpha^B$  vector components (X, Y, and Z) represent the pulse outputs from the three strapdown rate gyros.

The development in the slide shows that the change in L-Frame velocity calculated from the algorithm over a computer cycle equals the  $C_B^L$  matrix at the start of the computer interval, times the body accelerometer pulse count over the computer cycle plus a correction factor (known as sculling compensation). The sculling compensation is a correction to the accelerometer count vector equal to the integral (over the computer cycle) of the cross-product of the cumulative body gyro pulse count with the instantaneous body accelerometer pulse output.

# TYPICAL ACCELERATION TRANSFORMATION IMPLEMENTATION



## TYPICAL ACCELERATION TRANSFORMATION IMPLEMENTATION

The slide illustrates the acceleration transformation algorithm operations in block diagram form. The transform rate noted in the slide is the computer cycle rate discussed in the explanation of the previous slide. The block diagram suggests that the integral functions are actually performed at a rate higher than the basic computer cycle (or transformation) rate.

The accelerometer and gyro pulse integral functions are typically mechanized as up-down counter functions in the computer input/output section. The sculling computation could be implemented with special purpose high speed digital electronics as an Input/Output function, as a higher speed software algorithm in the main processor (i.e., at higher cycle rate than the main transformation algorithm), or through a simplified approximate software algorithm at the basic computer cycle rate.

## APPROXIMATE FORM OF SCULLING COMPENSATION

- FOR CONSTANT ANGULAR RATE AND LINEAR ACCELERATION OVER COMPUTER INTERVAL:

$$\int_{t_m}^{t_{m+1}} (\underline{\alpha}^B \times d\underline{V}^B) = \frac{1}{2} (\underline{\alpha}_m^B \times \underline{u}_m^B)$$

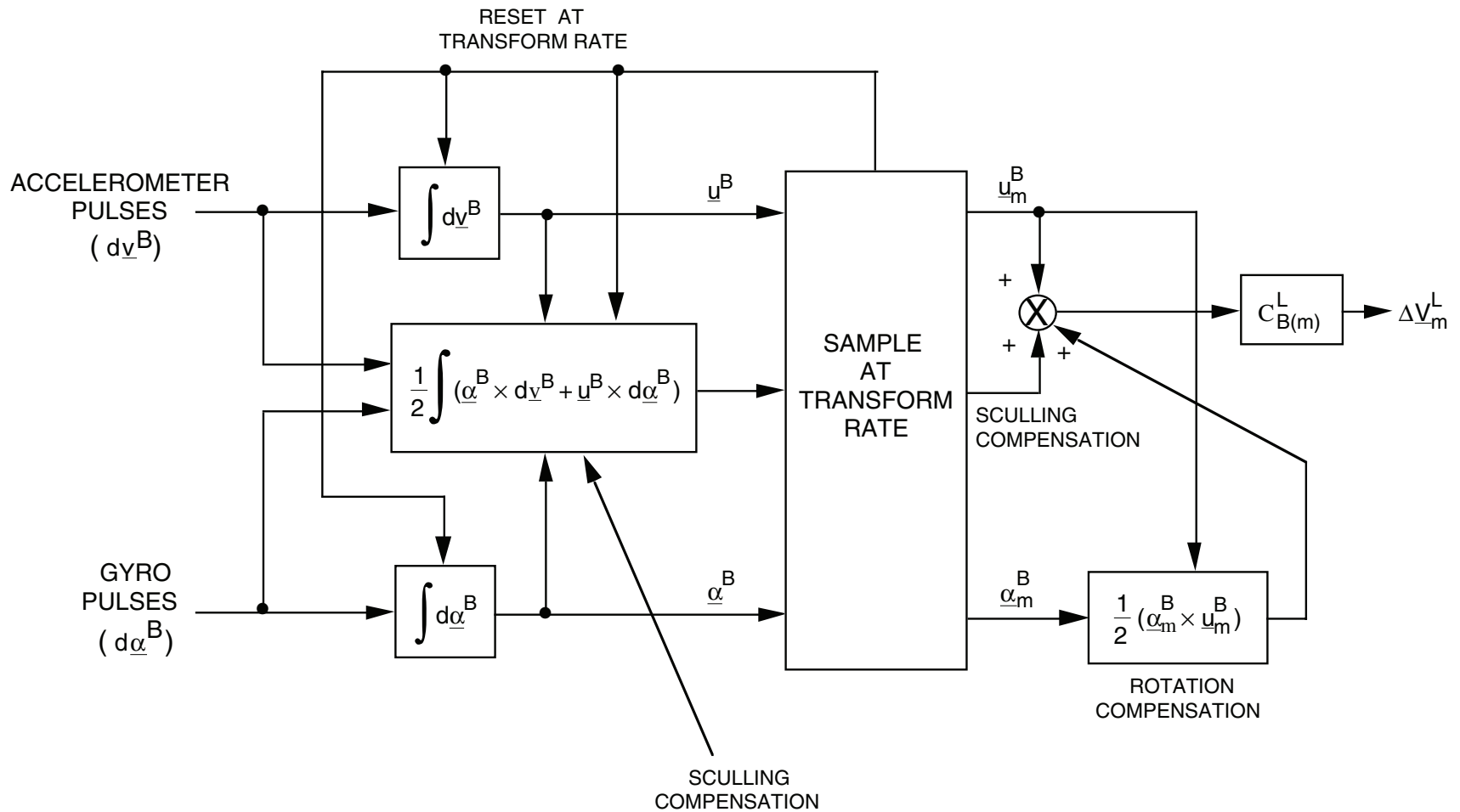
$\underline{\alpha}_m^B$  = INTEGRATED B-FRAME INERTIAL ANGULAR RATE OVER COMPUTER CYCLE (GYRO PULSE COUNT)

$\underline{u}_m^B$  = INTEGRATED B-FRAME SPECIFIC FORCE ACCELERATION OVER COMPUTER CYCLE (ACCELEROMETER PULSE COUNT)

## **APPROXIMATE FORM OF SCULLING COMPENSATION**

For constant body angular rates and linear accelerations over the computer cycle, the sculling compensation equals one half the cross-product of the gyro pulse count vector with the accelerometer pulse count vector (pulses accumulated over the computer cycle). The indicated simplified algorithm based on this approximation can be implemented at the basic computer cycle rate (i.e., without the need for a high speed sculling computation). The accuracy in the approximation depends on the frequency content of the angular rate and acceleration signals output from the strapdown sensors compared to the basic computer cycle frequency.

# ALTERNATE ACCELERATION TRANSFORMATION IMPLEMENTATION



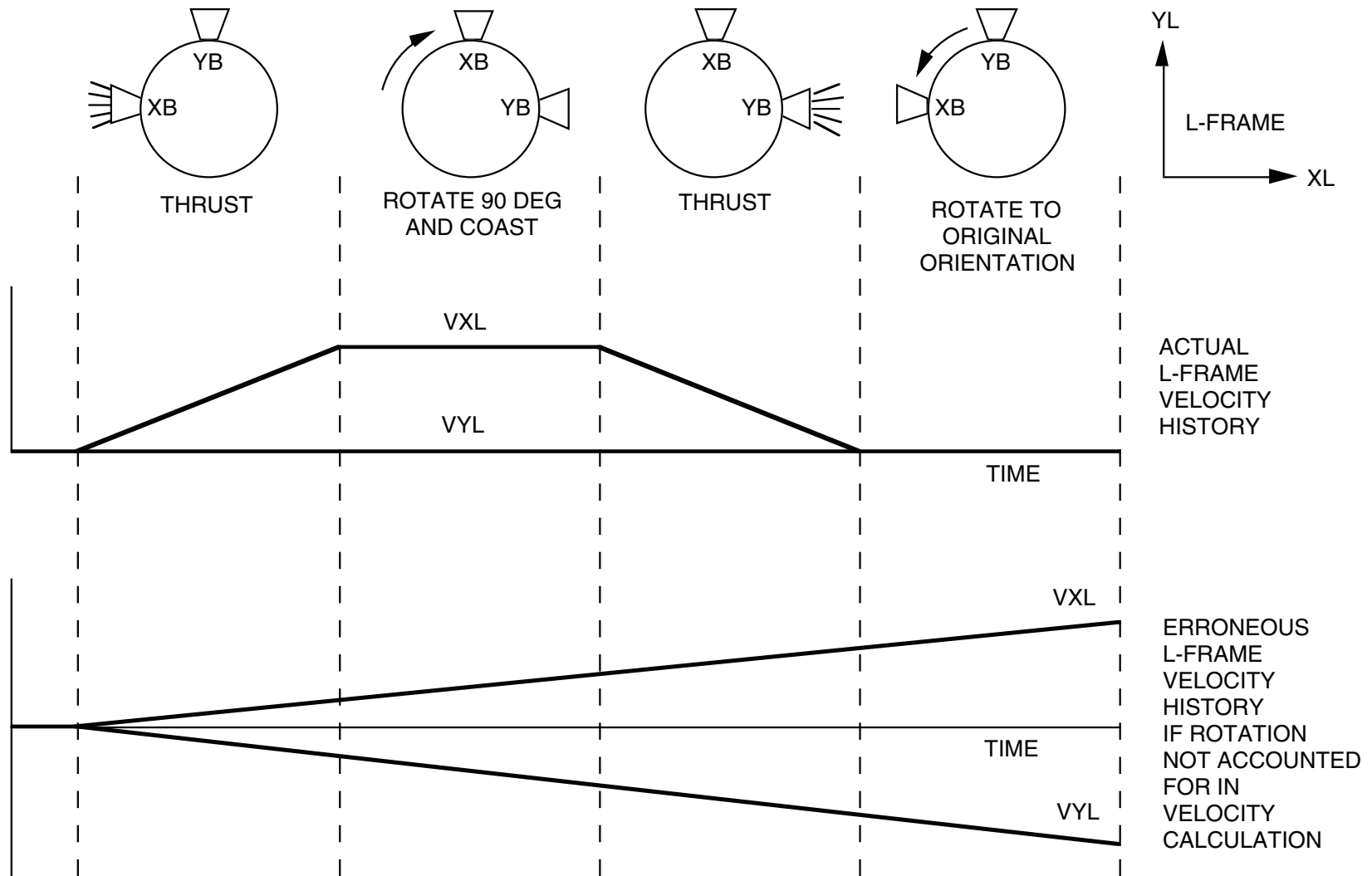
## ALTERNATE ACCELERATION TRANSFORMATION IMPLEMENTATION

The slide depicts an alternate acceleration transformation implementation based on the alternate transformation algorithm developed in the Strapdown System Algorithms paper provided in the back of the Lecture Notes handout document. Note that compared to the previously shown “Typical Acceleration Transformation Implementation” slide, this chart shows an expanded form of the sculling term (labeled “Sculling Compensation”) and the addition of a “Rotation Compensation” term executed at the transformation frequency.

Note that the rotation compensation term is identically equal to the approximate form of sculling compensation described previously based on constant angular rate and linear acceleration over the transformation cycle period. It can be verified analytically that under constant angular rate and linear acceleration, the alternate form sculling compensation term on this chart is identically zero. Therefore, the alternate sculling term measures only the dynamic rotation/acceleration effects over the transformation cycle and not the composite of constant and dynamic effects as measured by the previously shown sculling compensation term. If dynamic rotation/acceleration effects are negligible, the alternate sculling term can be deleted from the transformation operation while retaining the rotation compensation term. If dynamic rotation/acceleration effects are significant, the complete algorithm with the sculling term is implemented as shown in the slide.

The advantages of the alternate acceleration transformation approach are twofold: 1) A more accurate high speed digital sculling transformation algorithm can be structured for the alternate sculling compensation form and 2) A higher order algorithm can be constructed for the rotation compensation term that is more accurate than the first order form shown in the slide under high maneuver rate/acceleration conditions. The second advantage is a benefit because it can be achieved for minimum throughput penalty as it is implemented at the transformation frequency and not at the higher speed sculling compensation frequency. Introduction of a higher order algorithm using the previously described transformation/sculling approach could only be achieved at the high speed sculling computation frequency which defeats the fundamental purpose of separating the sculling portion from the basic transformation operation (i.e., The sculling portion is designed to entail a minimum amount of operations to minimize the high speed throughput requirement). Note that the high frequency dynamic effects intended to be measured by the sculling algorithm are generally always small in amplitude, hence, adequately handled by the first order form shown in this slide. From a throughput standpoint, it is instructive to note that the alternate sculling compensation term can be implemented digitally with little additional computational load compared to the previously defined sculling term (See page 564 compared with page 558).

# SCULLING ERROR DEMONSTRATION



## SCULLING ERROR DEMONSTRATION

The sculling compensation term in the strapdown INS accounts for combined linear and angular dynamic motion during the computer update cycle. An example of how neglected sculling effects can cause navigational errors is illustrated in the slide.

The slide illustrates a satellite undergoing a maneuver consisting of an acceleration forward (using the XB thruster) followed by an equal acceleration backward (using the YB thruster). The satellite is rotated to the proper attitude between thrustings so that the thrust is directed along the forward and backward directions. At the end of the maneuver, the satellite orientation is as it was originally, and the X, Y velocities in L-Frame coordinates are what they were before the maneuver was initiated (i.e., zero).

If the total maneuver was performed within the computer cycle of a strapdown system, and only gyro and accelerometer pulse count data was recorded over the computer interval, the system would think that no angular maneuver took place (i.e., the integrated angular rate over the maneuver is zero), and that the vehicle accelerated along XB and YB of the satellite in its orientation at the start of the maneuver. The computer would interpret this as a change in XL and YL velocities equal, respectively, to the XB integrated acceleration and the negative of the YB integrated acceleration. Furthermore, since the XB, YB acceleration counts would have been measured once at the end of the maneuver, the computer would have no knowledge of the time sequence of the XB, YB thrustings. Consequently, it would assume that the XB, YB accelerations occurred uniformly throughout the computer interval (or maneuver period). The result is that the computer would assume a net change in XL and YL velocity generated uniformly over the computer cycle. This is obviously an erroneous result and illustrates the importance of accounting for angular deviations during the computer interval if they are significant.

It should be noted that the sculling compensation algorithm shown previously is based on the assumption that the vehicle will not rotate through large angles between computer update cycles. The extreme maneuver illustrated in this slide could not be handled by this simplified algorithm. The effect could only be corrected by increasing the basic computer cycle rate so that the large attitude motion of the maneuver is measured by the main attitude algorithm and the acceleration data is transformed using this data at the rate needed to accurately account for the dynamic motion.

# SCULLING CORRECTION MAGNITUDE

## BODY ANGLE INCREMENTS

$$d\underline{\alpha}^B = 2 \pi f \begin{bmatrix} \theta_0 \cos 2 \pi f t \\ 0 \\ 0 \end{bmatrix} dt$$

## BODY VELOCITY INCREMENTS

$$d\underline{v}^B = \begin{bmatrix} 0 \\ A \sin (2 \pi f t + \phi) \\ 0 \end{bmatrix} dt$$

- f** = SCULLING MOTION FREQUENCY  
 **$\theta_0$**  = SCULLING MOTION ANGLE AMPLITUDE (NOTE: SCULLING MOTION ANGLE  $\theta = \theta_0 \sin 2 \pi f t$ )  
**A** = SCULLING MOTION ACCELERATION AMPLITUDE  
 **$\phi$**  = ACCELERATION PHASE ANGLE (RELATIVE TO ANGLE MOTION)

$$\text{SCULLING CORRECTION} = \int_{t_m}^{t_{m+1}} (\underline{\alpha}^B \times d\underline{v}^B) = \frac{1}{2} (\underline{\alpha}_m^B \times \underline{u}_m^B) + \delta \underline{v}$$

CONSTANT ANGULAR RATE AND  
LINEAR ACCELERATION APPROXIMATION

$$\delta \underline{v} = \begin{bmatrix} 0 \\ 0 \\ \frac{1}{2} \theta_0 A \cos \phi \left( 1 - \frac{\sin 2 \pi f T_m}{2 \pi f T_m} \right) T_m \end{bmatrix}$$

$$\delta \dot{V}_{ZAVG} = \frac{1}{2} \theta_0 A \cos \phi \left( 1 - \frac{\sin 2 \pi f T_m}{2 \pi f T_m} \right)$$

$T_m$  = TIME INTERVAL FROM  $t_m$  TO  $t_{m+1}$

## SCULLING CORRECTION MAGNITUDE

The slide defines the magnitude of the sculling compensation term in terms of an average acceleration over the computer cycle time that one would obtain under sinusoidal angular rotation and linear acceleration motion in the X and Y axes respectively. The equation shows that the sculling compensation is equal to the simplified approximation term (based on constant angular rate and acceleration over the sample period) plus a residual term  $\delta V$  along the Z axis which is a function of the product of the sculling frequency  $f$  and the computer cycle period  $T_m$  (Note that this is equivalent to the ratio of the sculling frequency  $f$  to the computer sample frequency which equals the reciprocal of  $T_m$ ). It is also instructive to recognize that  $\delta V$  is identically the term labeled “Sculling Compensation” in the “Alternate Acceleration Transformation Implementation” chart shown previously. The current slide depicts the average acceleration produced by  $\delta V$  over the sample period as equal to  $\delta V$  divided by the sample period  $T_m$  (the result is labeled  $\delta V Z_{AVG}$ ).

Note that the  $\delta V Z_{AVG}$  term (in L-Frame coordinates) is constant, even though it was generated by cyclic body motion. This is an important point because constant accelerations in navigation coordinates have a much more pronounced impact on navigation velocity/position computations than would cyclic accelerations in navigation coordinates, which would be averaged out in the L-Frame velocity/position integration process.

The  $\delta V Z_{AVG}$  term is proportional to the cosine of the phase angle between the sinusoidal acceleration in one axis and the sinusoidal angle oscillation in the other. Hence,  $\delta V Z_{AVG}$  is maximum when the acceleration and angle oscillations are in phase, and zero when they are ninety degrees out of phase. The amplitude of the  $\delta V Z_{AVG}$  term is proportional to half the product of the angular and linear acceleration amplitudes. The bracketed term in the  $\delta V Z_{AVG}$  expression equals unity for high sculling frequencies compared to the computer cycle frequency (i.e., when the  $f T_m$  product is greater than unity). For low sculling frequencies (a small  $f T_m$  product), the bracketed term equals zero. This latter condition implies that the sculling frequency is small enough that the angular rate and acceleration over the computer sample period can be considered constant, hence, the constant angular rate/acceleration approximation term in the slide accurately represents the dominant computational effect.

The  $\delta V Z_{AVG}$  equation in the slide is useful for determining the magnitude of this term that one can expect under anticipated vibration amplitudes and frequencies. If the magnitude is significant relative to tolerable acceleration errors, the sculling compensation algorithm must be mechanized in its high speed form to properly account for the effect in the navigation computation. If the  $\delta V Z_{AVG}$  magnitude is small relative to tolerable errors, the high speed sculling computation can be replaced by the simpler algorithm based on the constant angular rate/acceleration approximation, which is calculated only once each computer cycle.

## INTEGRATED INCREMENTAL FORM OF DIRECTION COSINE RATE EQUATIONS

CONTINUOUS

$$\dot{C}_B^L = C_B^L (\underline{W}_{IB}^B \times) - (\underline{W}_{IL}^L \times) C_B^L$$

HIGH SPEED COMPUTER  
UPDATE CYCLE (m) FOR  
BODY MOTION RELATIVE  
TO INERTIAL SPACE

$$C_{B(m+1)}^{L(n)} = C_{B(m)}^{L(n)} C_{B(m+1)}^{B(m)}$$

LOW SPEED COMPUTER  
UPDATE CYCLE (n) FOR  
LOCAL LEVEL MOTION  
RELATIVE TO INERTIAL  
SPACE

$$C_{B(m)}^{L(n+1)} = C_{L(n)}^{L(n+1)} C_{B(m)}^{L(n)}$$

$B(m)$  = BODY FRAME ORIENTATION AT START OF  $m^{\text{TH}}$  HIGH SPEED  
COMPUTATION CYCLE

$L(n)$  = LOCAL LEVEL FRAME ORIENTATION AT START OF  $n^{\text{TH}}$  LOW SPEED  
COMPUTATION CYCLE

## INTEGRATED INCREMENTAL FORM OF DIRECTION COSINE RATE EQUATIONS

The computational algorithm utilized to update the  $C_B^L$  body attitude direction cosine matrix (relative to local level coordinates) in a strapdown INS digital computer is based on an incremental form of the continuous direction cosine rate equation. The incremental form is actually two algorithms, one iterated at high speed to account for high body rotation rates, and a lower speed algorithm to account for low speed local level rotation rates.

The body rotation updating algorithm updates the  $C_B^L$  matrix as the product of  $C_B^L$  with a body rotation direction cosine matrix

$C_{B(m+1)}^{B(m)}$  representing the rotation of the body from its attitude at the beginning of a high speed update interval B(m) to its attitude at the end of the interval B(m+1). The  $C_B^L$  matrix is updated at each high speed m<sup>th</sup> computer cycle using a  $C_{B(m+1)}^{B(m)}$  matrix derived from strapdown gyro data accumulated over each m interval.

The local level rotation updating algorithm updates the  $C_B^L$  matrix as the product of  $C_B^L$  with a local level rotation direction cosine matrix  $C_{L(n)}^{L(n+1)}$  representing the rotation of the local level coordinate frame from its attitude at the beginning of a low speed update interval L(n) to its attitude at the end of the interval L(n+1). The  $C_B^L$  matrix is updated at each n<sup>th</sup> low speed computer cycle using the  $C_{L(n)}^{L(n+1)}$  matrix derived from local level rotation data accumulated from the navigation equations over each n interval.

The two speed attitude updating algorithm structure depicted in the chart has been used as a method of reducing computer throughput. With the continuing rapid increase in modern day microprocessor computational speed capabilities, the throughput savings offered by such a multirate algorithm approach is becoming more difficult to justify when traded-off against the attendant increase in complexity of the overall software development/verification process. The two speed algorithm structure presented in the chart and supporting slides to follow can be converted to single speed format by simply running the body rate and local level rate updating sections sequentially at the same iteration rate.

## LOCAL LEVEL FRAME UPDATE MATRIX

### CONTINUOUS

$$\dot{C}_B^L = - (\underline{W}_{IL}^L \times) C_B^L$$

### INCREMENTAL

$$C_{B(m)}^{L(n+1)} = C_{L(n)}^{L(n+1)} C_{B(m)}^{L(n)}$$

**INCREMENTAL ALGORITHM – ASSUMING LOCAL LEVEL FRAME RATES RELATIVE TO INERTIAL SPACE ARE SMALL (ORDER OF A FEW EARTH RATES IN MAGNITUDE):**

$$\begin{aligned} C_{B(m)}^{L(n+1)} &= C_{B(m)}^{L(n)} - (\underline{W}_{IL(AVG)}^L \times) T_n C_{B(m)}^{L(n)} \\ &= \left[ I - (\underline{W}_{IL(AVG)}^L \times) T_n \right] C_{B(m)}^{L(n)} \end{aligned}$$

$$\text{I.E.: } C_{L(n)}^{L(n+1)} = I - (\underline{W}_{IL(AVG)}^L \times) T_n$$

$\underline{W}_{IL(AVG)}^L$  = AVERAGE VALUE OF  $\underline{W}_{IL}^L$  OVER TIME INTERVAL BETWEEN  $n^{\text{TH}}$  AND  $(n+1)^{\text{TH}}$  COMPUTER ITERATION CYCLES

$T_n$  = TIME INTERVAL BETWEEN  $n^{\text{TH}}$  AND  $(n+1)^{\text{TH}}$  COMPUTER ITERATION CYCLES

## LOCAL LEVEL FRAME UPDATE MATRIX

The  $C_{L(n)}^{L(n+1)}$  updating matrix is derived as a simple first order integration approximation to the local level rate portion of the  $C_B^L$  rate equation. This simplified approach is valid because the angular movement of the local level is small over a typical local level update cycle (e.g., 0.1 sec), hence, second order effects are negligible. The first order approximation sets  $C_{L(n)}^{L(n+1)}$  equal to the unity matrix minus the skew symmetric form of the average local level angular rate vector times the computer low speed update cycle time.

## FIRST ORDER BODY AXIS MOTION DIRECTION COSINE UPDATING ALGORITHMS

### CONTINUOUS

$$\dot{C}_B^L = C_B^L (\underline{W}_{IB}^B \times)$$

### INCREMENTAL

$$C_{B(m+1)}^{L(n)} = C_{B(m)}^{L(n)} C_{B(m+1)}^{B(m)}$$

### EXAMPLE OF FIRST ORDER ALGORITHM

$$C_{B(m+1)}^{L(n)} = C_{B(m)}^{L(n)} + C_{B(m)}^{L(n)} (\underline{\alpha}_m \times) = C_{B(m)}^{L(n)} [I + (\underline{\alpha}_m \times)] \quad \text{I.E.: } C_{B(m+1)}^{B(m)} = I + (\underline{\alpha}_m \times)$$

$$\underline{\alpha}_m = \int_m^{m+1} \underline{W}_{IB}^B dt = \text{INTEGRATED GYRO BODY AXIS RATES OVER UPDATE INTERVAL}$$

## FIRST ORDER BODY AXIS MOTION DIRECTION COSINE UPDATING ALGORITHMS

The slide illustrates how a first order direction cosine updating algorithm might be structured for the body axis motion based on the body rate portion of the  $C_B^L$  continuous rate equation. This simplified algorithm sets the updating matrix  $C_{B(m+1)}^{B(m)}$  equal to the sum of the unity matrix plus the cross-product matrix form of the strapdown gyro pulse count vector (cumulative counts over the update period). The next slide illustrates the errors one can generate using such an oversimplified approach.

## EXAMPLE OF FIRST ORDER ALGORITHM ERRORS

### ROTATION SEQUENCE

$$\underline{\alpha}_m = (0, 0, + E)^T$$

$$\underline{\alpha}_{m+1} = (0, 0, - E)^T$$

### FIRST ORDER UPDATE ALGORITHM

$$C_{m+1} = C_m + C_m (\underline{\alpha}_m \times)$$

### UPDATE OF C11 AND C12 FOR $\alpha_m$

$$C11(m+1) = C11m + C12m E$$

$$C12(m+1) = C12m - C11m E$$

### UPDATE OF C11 AND C12 FOR $\alpha_{m+1}$

$$\begin{aligned} C11(m+2) &= C11(m+1) - C12(m+1) E \\ &= C11m + C12m E - (C12m - C11m E) E \\ &= C11m + C11m E^2 \end{aligned}$$

$$C12(m+2) = C12m + C12m E^2$$

### CORRECT SOLUTION AFTER ROTATION SEQUENCE

$$C11(m+2) = C11m$$

$$C12(m+2) = C12m$$

## EXAMPLE OF FIRST ORDER ALGORITHM ERRORS

To illustrate the magnitude of error that one can experience using a simple first order algorithm for body axis motion direction cosine updating, a simple rotation sequence has been analyzed consisting of a positive Z-axis rotation through angle  $E$  followed by a negative Z-axis rotation through the same angle.

Using the simplified first order updating algorithm of the previous slide, the C11 and C12 direction cosine elements are shown being updated for each rotation segment. The result after the maneuver is that both the C11 and C12 terms equal their original value (obviously, the correct solution) plus residual terms of the order  $E^2$ . This  $E^2$  error effect is characteristic of first order algorithms, and can only be constrained to be small by assuring that  $E$  is small. The  $E$  value can only be constrained in a general application by using an extremely high computer speed (e.g., 20 KHz) so that the cumulative gyro counts sampled each cycle will be small under high rotation rates. Such approaches were explored when strapdown navigation was in its infancy using special purpose digital differential analyzers (DDAs) mechanized to rapidly execute the first order algorithms. Various first order algorithms were investigated during this period that contained certain preferred characteristics approximating the character of the true solution (for example, one popular algorithm updated cosine elements sequentially depending on the sign of the angle data. This approach had the interesting property of being "reversible" in that the solution following a cyclic maneuver such as described previously would return the cosines to their original value without the  $E^2$  error).

Today's computer technology permits higher order algorithms to be mechanized for performing the body attitude updating function. These algorithms are accurate under high vehicle rates (large gyro count samples) using moderate update frequencies (e.g., 50 Hz). Additionally, use of the general purpose computer for the attitude updating function makes it possible to also improve the basic sensor accuracy through the use of more sophisticated compensation algorithms than could have been programmed into original technology DDA strapdown attitude computers.

## HIGHER ORDER BODY FRAME UPDATE MATRIX

$$C_{B(m+1)}^{B(m)} = I + \frac{\text{SIN } \phi}{\phi} (\underline{\phi} \times) + \frac{(1 - \text{COS } \phi)}{\phi^2} (\underline{\phi} \times) (\underline{\phi} \times)$$

$$= I + f_1 \begin{bmatrix} 0 & -\phi_z & \phi_y \\ \phi_z & 0 & -\phi_x \\ -\phi_y & \phi_x & 0 \end{bmatrix} + f_2 \begin{bmatrix} -(\phi_z^2 + \phi_y^2) & \phi_x \phi_y & \phi_x \phi_z \\ \phi_x \phi_y & -(\phi_z^2 + \phi_x^2) & \phi_y \phi_z \\ \phi_x \phi_z & \phi_y \phi_z & -(\phi_y^2 + \phi_x^2) \end{bmatrix}$$

$$f_1 = 1 - \frac{\phi^2}{3!} + \frac{\phi^4}{5!} - \dots \text{ POWERS OF } \phi^2$$

$$f_2 = \frac{1}{2!} - \frac{\phi^2}{4!} + \frac{\phi^4}{6!} - \dots \text{ POWERS OF } \phi^2$$

$$\phi^2 = \phi_x^2 + \phi_y^2 + \phi_z^2$$

$\phi_x, \phi_y, \phi_z =$  INTEGRAL FUNCTIONS OF BODY FRAME ANGULAR RATE RELATIVE TO INERTIAL SPACE OVER TIME INTERVAL BETWEEN  $m^{\text{TH}}$  AND  $(m+1)^{\text{TH}}$  COMPUTER CYCLE (DETERMINED FROM BODY FRAME GYRO SIGNALS)

## HIGHER ORDER BODY FRAME UPDATE MATRIX

Modern day strapdown body rate updating algorithms are based on higher order forms such as the classical algorithm illustrated in the slide. This algorithm exactly represents the body motion from  $B(m)$  to  $B(m+1)$  without error, except for minor errors associated with truncating the  $f_1$  and  $f_2$  functions at some reasonable level. The "order" of the algorithm used is dependent on the truncation point in the  $f_1$  and  $f_2$  series. A fifth order algorithm, for example retains terms of order  $\phi^4$  in  $f_1$  and  $\phi^2$  in  $f_2$  so that the  $C_{B(m+1)}^{B(m)}$  matrix has terms of up to and including  $\phi^5$ . The order of the algorithm needed for a given application is generally dictated by scale factor accuracy considerations at maximum vehicle rotation rates for which the  $\underline{\phi}$  components are at a maximum.

The  $\underline{\phi}$  vector in this algorithm has direction along the Euler axis of rotation about which the body can be rotated from its  $B(m)$  to its  $B(m+1)$  attitude. The magnitude of  $\underline{\phi}$  equals the Euler axis rotation angle that will rotate  $B(m)$  into  $B(m+1)$ . The components of  $\underline{\phi}$  are computed from the strapdown gyro outputs during the interval.

## COMPUTATION OF $\underline{\phi}$

- FOR A NONROTATING BODY RATE VECTOR:

$$\underline{\phi} = \int_{t_m}^{t_{m+1}} \underline{W}_{IB}^B dt = \int_{t_m}^{t_{m+1}} d\underline{\alpha}^B = \text{GYRO PULSE COUNT VECTOR FROM } t_m \text{ TO } t_{m+1}$$

- FOR GENERAL MOTION:

$$\dot{\underline{\phi}} = \underline{W}_{IB}^B + \underbrace{\frac{1}{2} \underline{\phi} \times \underline{W}_{IB}^B + \frac{1}{\phi^2} \left( 1 - \frac{\phi \sin \phi}{2(1 - \cos \phi)} \right) \underline{\phi} \times (\underline{\phi} \times \underline{W}_{IB}^B)}_{\text{"CONING CONTRIBUTION"}}$$

- APPROXIMATION FOR GENERAL MOTION:

$$\underline{\phi} = \left( \underline{\alpha}^B + \delta \underline{\phi} \right) \text{ SAMPLED AT } t_{m+1}$$

$$\underline{\alpha}^B = \int_{t_m}^t d\underline{\alpha}^B = \text{GYRO PULSE COUNT VECTOR FROM } t_m \text{ TO } t$$

$$\delta \underline{\phi} = \frac{1}{2} \int_{t_m}^t \underline{\alpha}^B \times d\underline{\alpha}^B = \text{"CONING CORRECTION"}$$

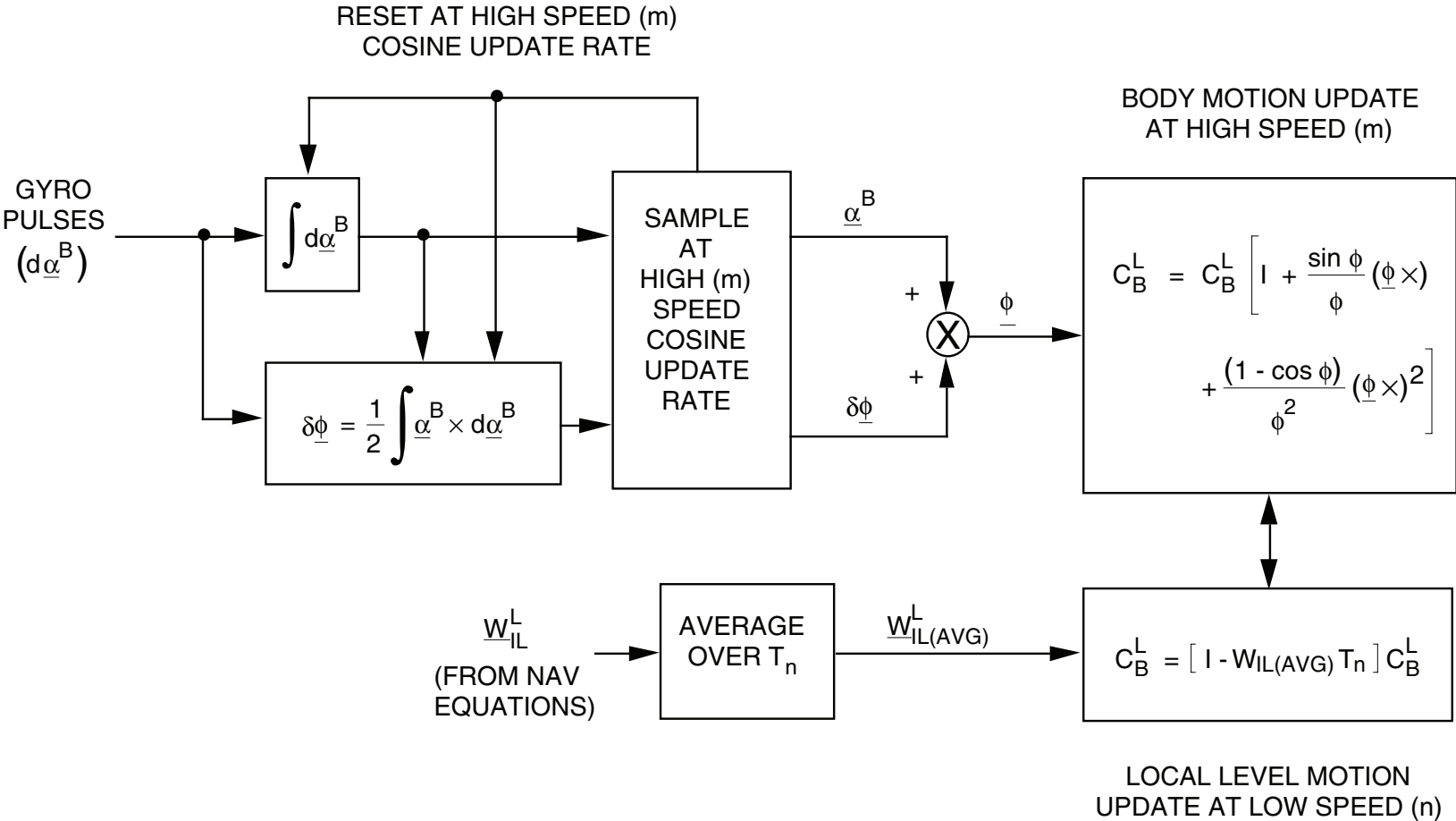
## COMPUTATION OF $\underline{\phi}$

If the body angular rate vector is nonrotating (i.e., the vehicle is rotating about an axis (not necessarily a cardinal body axis) that is fixed inertially over the  $C_B^L$  body rate update period), the  $\underline{\phi}$  vector is equal to the gyro pulse count vector over the sample period. This extremely simple relationship is indeed fortunate, because the dominant portion of typical vehicle angular rate profiles can be fairly accurately approximated by constant angular rotation axis segments between computer samples.

For general body motion, the  $\underline{\phi}$  vector equals the integral of a fairly complex  $\dot{\underline{\phi}}$  expression, the leading term of which is the strapdown gyro output rate vector. It is easily verified that the additional terms in the general  $\dot{\underline{\phi}}$  equation become zero if the direction of the  $\underline{w}_{IB}^B$  vector is constant. The additional terms to the  $\dot{\underline{\phi}}$  equation, therefore, represent the degree to which gyro rate vector rotation impacts the  $\dot{\underline{\phi}}$  calculation. This additional portion has been termed the "coning contribution" to the  $\dot{\underline{\phi}}$  calculation to indicate that it is excited by classical coning cyclic motion which generates a rotating angular rate vector (classical coning motion is characterized by cyclic angular rate motion along each of two orthogonal body axes where the cyclic rates are ninety degrees out of phase. Under such motion, the third body axis describes a cone in space, hence the term, "coning").

An excellent approximation to the general integrated  $\dot{\underline{\phi}}$  equation sets  $\underline{\phi}$  equal to the sum of the gyro count vector plus a correction term equal to one half the integral of the cross-product of the cumulative gyro count vector with the instantaneous gyro count vector. The  $\delta\underline{\phi}$  correction term is called the "coning correction" term and is an excellent approximation to the integral of the "coning contribution" term in the exact equation under typical aircraft angular rates, vibrations, and overall attitude algorithm body motion update rates (e.g., 50 Hz). The simple form of the "coning correction" term makes implementation relatively easy in a strapdown INS.

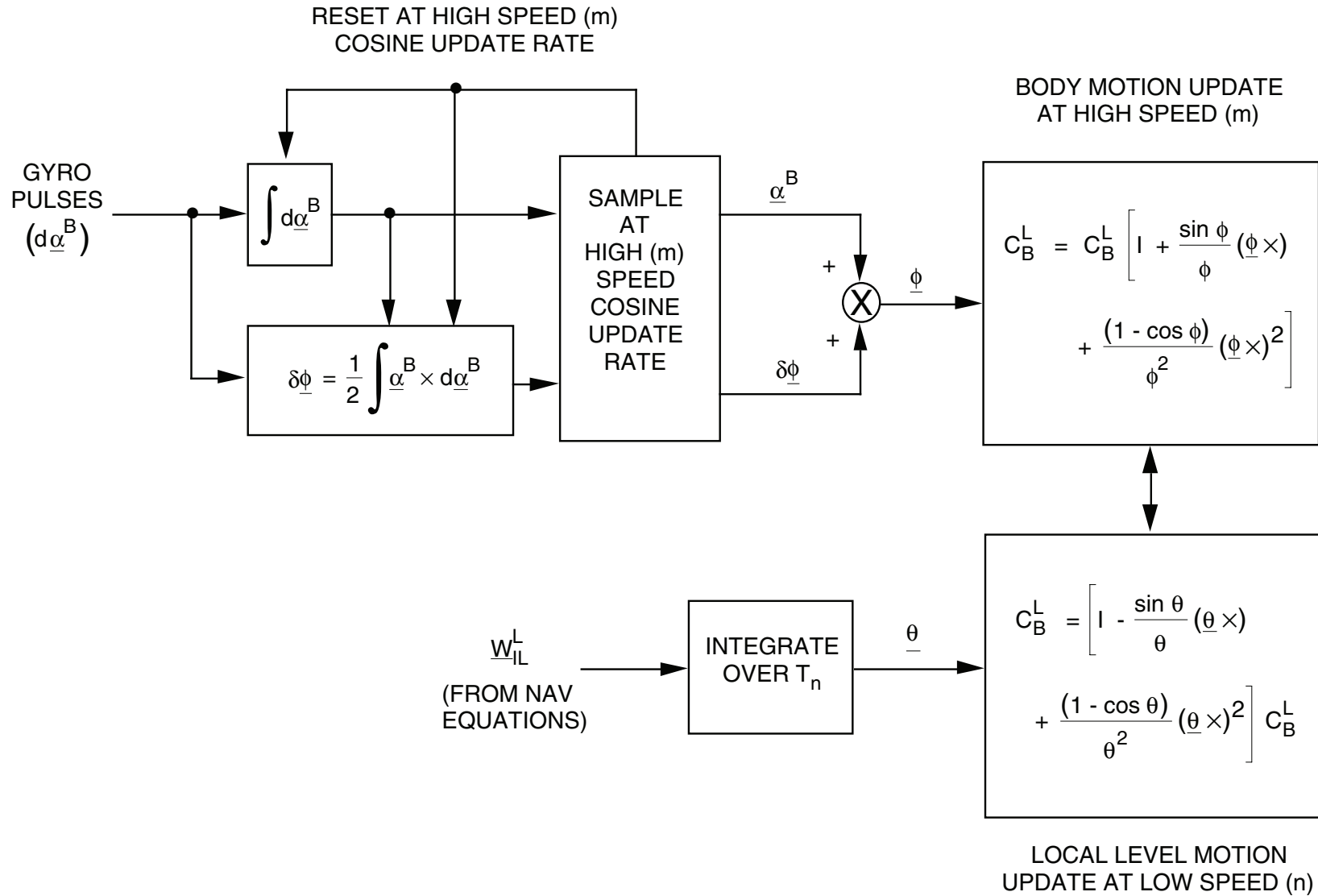
# TYPICAL DIRECTION COSINE UPDATE IMPLEMENTATION



## TYPICAL DIRECTION COSINE UPDATE IMPLEMENTATION

The slide illustrates in block diagram form the overall direction cosine updating operations typically performed in a strapdown INS, illustrating the division between high rate body motion updating ( $m$  cycle) and low speed local level reference updating ( $n$  cycle). The gyro pulse integral function would be typically performed with up/down counters as part of the computer input/output electronics. The  $\delta\phi$  coning correction integration computation could be mechanized using special purpose high speed digital electronics as part of the computer I/O, or as a special high speed software function (between  $m$  cycle updates) in the main system computer.

# ENHANCED DIRECTION COSINE UPDATE IMPLEMENTATION



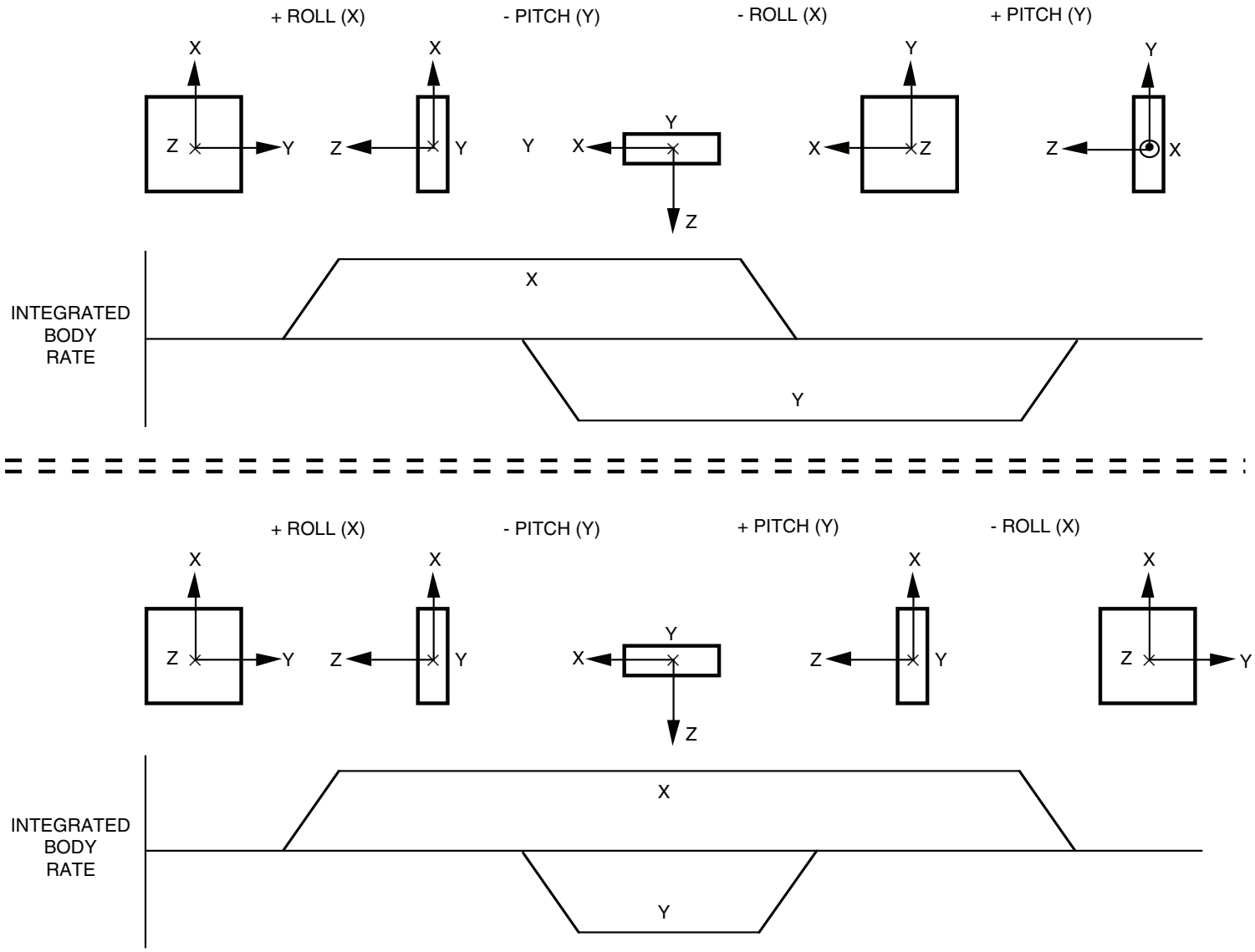
## ENHANCED DIRECTION COSINE UPDATE IMPLEMENTATION

The slide depicts an enhanced direction cosine update implementation based on the use of an exact algorithm for the local level updating process. The exact local level updating algorithm is similar in form to the body motion algorithm and can be derived through a procedure similar to the one used for the body motion algorithm in the Lecture Notes handout document.

Use of exact algorithms for both the body and local level portions of the attitude updating process assures that the basic characteristic of the direction cosine matrix remain intact: i.e., that the transpose equals the inverse (assuming that the direction cosine matrix was initialized with this characteristic and that adequate word length is utilized for the computational operations). The advantage is that the requirement for orthogonalization and normalization of the direction cosine matrix (to be discussed subsequently) is eliminated (provided that the direction cosine matrix was initialized to be orthogonal and normal, that the Taylor series expansion terms used contain a sufficient number of terms, and that adequate computational word length is provided for the attitude updating operations). The disadvantage is the added throughput for the exact local level updating algorithm which should be a minor penalty considering that this computation is performed in the low speed processing loop with a modern day high speed microprocessor.

It should be noted that the first order algorithm for the local level updating process (described in previous charts) is generally adequate to preserve the orthogonality/normality characteristics of the direction cosine matrix under typical navigation mode operating conditions. However, during initial fine alignment (and other Kalman filter operations), the local level updating algorithm is the routine used to provide attitude corrections to the direction cosine matrix. The first update cycle for these operations might require an attitude update on the order of 0.1 to 1.0 degrees which will generally add significant second order errors into the direction cosine matrix if a first order algorithm is utilized. The second order errors will be removed during subsequent iteration cycles of the attitude updating algorithms, however, orthogonality/normalization errors introduced by the second order effects will remain. To eliminate the orthogonality/normalization errors, a higher order algorithm can be utilized for the local level updating operations (such as the exact algorithm shown in the slide) or an orthogonality/normalization correction operation will be required (to be discussed subsequently).

# CONING ERROR DEMONSTRATION



## CONING ERROR DEMONSTRATION

The slide illustrates the effect of coning motion and how it can be misinterpreted if not accurately measured. The slide illustrates two sequential maneuver profiles; the first consists of a positive roll followed by a negative pitch, a negative roll and a positive pitch; the second profile is composed of a positive roll followed by a negative pitch, a positive pitch, and a negative roll.

For both profiles, the integrated body axis rates (gyro pulse counts) over the maneuver period are zero, hence, if a simple gyro count over the maneuver period was the measurement for the attitude computation (i.e., without the coning correction calculation), the strapdown computer would conclude that no net motion had taken place.

For the bottom profile, the vehicle attitude after the maneuver is the same as before the maneuver, hence, comparable to what would be predicted by the gyro pulse count vector (i.e., no net angular motion). For the top profile, on the other hand, the pulse count vector is also zero, but the orientation after the maneuver is significantly different from before the maneuver.

From the above discussion it can be concluded that the gyro pulse count vector alone is not a valid representation of vehicle angular motion under situations where erratic angular motion takes place during the pulse count period. If such erratic motion is expected, the coning compensation calculation must be mechanized to account for these added dynamic motion effects.

## CONING CORRECTION MAGNITUDE

**BODY ANGLE INCREMENTS**

$$d\underline{\alpha}^B = 2\pi f \begin{bmatrix} \theta_x \cos 2\pi f t \\ \theta_y \cos(2\pi f t - \phi) \\ 0 \end{bmatrix} dt$$

- f** = CONING MOTION FREQUENCY  
 **$\theta_x$**  = CONING MOTION ANGLE AMPLITUDE ABOUT X-AXIS  
 **$\theta_y$**  = CONING MOTION ANGLE AMPLITUDE ABOUT Y-AXIS  
 **$\phi$**  = PHASE ANGLE BETWEEN Y AND X-AXIS MOTION

**CONING CORRECTION**

$$\delta\underline{\phi} = \frac{1}{2} \int_{t_m}^{t_{m+1}} \underline{\alpha}^B \times d\underline{\alpha}^B = \begin{bmatrix} 0 \\ 0 \\ \pi f \theta_x \theta_y \sin \phi \left( 1 - \frac{\sin 2\pi f T_m}{2\pi f T_m} \right) T_m \end{bmatrix}$$

$$\delta\dot{\phi}_{zAVG} = \pi f \theta_x \theta_y \sin \phi \left( 1 - \frac{\sin 2\pi f T_m}{2\pi f T_m} \right)$$

**$T_m$  = TIME INTERVAL FROM  $t_m$  TO  $t_{m+1}$**

## CONING CORRECTION MAGNITUDE

The magnitude of the coning correction term can be easily evaluated for simple cyclic motion about each of the X and Y body axes. The chart shows the coning correction to be about the Z-axis and equal to a constant, even though the body axis rates were cyclic. This illustrates the importance in accounting for coning in the design of the strapdown attitude algorithm. Neglecting the presence of a large constant coning drift in the attitude equations would cause a large drifting attitude error build up, producing a large velocity/position error in the navigation equations through the acceleration transformation process.

Note that the compensation term is proportional to the sine of the phase angle between the X and Y axis cyclic angular motion. The coning compensation is maximized for a ninety degree phase angle and is zero when the cyclic motions are in phase. This is the opposite of the comparable sculling phasing effect.

Note that the coning compensation is proportional to the area swept out by a unit Z body axis vector under the cyclic motion ( $\pi \theta_x \theta_y$ ) times the cyclic motion frequency  $f$ . This product is equivalent to the time rate at which the area is swept.

Finally, note that the coning compensation is also proportional to the term in brackets which is identical to a similar term for the sculling situation studied previously. This term is unity for coning frequencies comparable or higher than the computer body motion attitude update frequency ( $f T_m$  greater than unity), and is zero for low coning compared to computer frequencies. This is a reflection of the fact that low coning frequency (compared to computer iteration rate) is adequately handled using the gyro pulse count vector alone for  $\phi$  in the attitude algorithm, while for high coning frequency (compared to the computer iteration rate), the computer rate is not fast enough to account for the higher frequency coning motion using gyro counts alone.

The coning correction result in this slide is useful for assessing whether it is necessary to mechanize the coning term in the attitude equations for the coning amplitudes and frequencies expected in the particular application (due to vibration for example).

## **CONING NOMENCLATURE**

- **CONING – ANGULAR RATE CONDITION CHARACTERIZED BY ROTATIONS OF THE ANGULAR VELOCITY VECTOR**
- **TRUE CONING – ACTUAL CONING MOTION**
- **PSEUDO-CONING**
  - **CYCLIC SENSOR OUTPUT ERRORS THAT APPEAR TO BE CONING MOTION**
  - **CAUSED FOR EXAMPLE BY PHASE LAG IN X-CHANNEL THAT DIFFERS FROM Y-CHANNEL UNDER X-Y ROCKING MOTION**
- **CONING ERROR – COMPUTATIONAL ERRORS CAUSED BY:**
  - **CORRECT PROCESSING OF PSEUDO-CONING SENSOR SIGNALS**
  - **INCORRECT PROCESSING OF TRUE CONING SIGNALS**

## **CONING NOMENCLATURE**

Some of the terminology used to describe coning motion in strapdown applications is illustrated in the slide. Similar terminology has been used to describe sculling motion.

## QUATERNION INCREMENTAL UPDATING

CONTINUOUS

$$\dot{q}_B^L = \frac{1}{2} q_B^L \underline{W}_{IB}^B - \frac{1}{2} \underline{W}_{IL}^L q_B^L$$

HIGH SPEED COMPUTER  
UPDATE CYCLE (m) FOR  
BODY MOTION RELATIVE  
TO INERTIAL SPACE

$$q_{B(m+1)}^{L(n)} = q_{B(m)}^{L(n)} h_{B(m+1)}^{B(m)}$$

LOW SPEED COMPUTER  
UPDATE CYCLE (n) FOR  
LOCAL LEVEL MOTION  
RELATIVE TO INERTIAL  
SPACE

$$q_{B(m)}^{L(n+1)} = r_{L(n)}^{L(n+1)} q_{B(m)}^{L(n)}$$

$h_{B(m+1)}^{B(m)}$  = QUATERNION BETWEEN BODY FRAME AT START AND END OF m<sup>TH</sup> HIGH SPEED COMPUTATION CYCLE

$r_{L(n)}^{L(n+1)}$  = QUATERNION BETWEEN LOCAL LEVEL FRAME AT START AND END OF n<sup>TH</sup> LOW SPEED COMPUTATION CYCLE

## QUATERNION INCREMENTAL UPDATING

As for the direction cosine computer updating algorithm, the quaternion updating algorithm is divided into a low speed update algorithm (for local level coordinate frame rotation), and a high speed update algorithm (for body motion). The main quaternion is updated by a quaternion product operation with small angle rotation quaternions that account for the body and local level movement over each computer sampling interval.

It should be noted that the quaternion products shown follow special quaternion product rules which differ from normal matrix product operations. Also, the W vectors shown in the slide are actually quaternions with the fourth element (the scalar element) equal to zero. The Strapdown Lecture Notes describe quaternion algebra in detail.

## QUATERNION UPDATE OPERATORS

$$h_{B(m+1)}^{B(m)} = \begin{bmatrix} f_3 \phi_X \\ f_3 \phi_Y \\ f_3 \phi_Z \\ f_4 \end{bmatrix} \begin{bmatrix} \phi_X \\ \phi_Y \\ \phi_Z \end{bmatrix} = \underline{\phi}$$

$$(0.5 \phi)^2 = 0.25 (\phi_X^2 + \phi_Y^2 + \phi_Z^2)$$

$$f_3 = \frac{\sin 0.5 \phi}{\phi} = 0.5 \left[ 1 - \frac{(0.5 \phi)^2}{3!} + \frac{(0.5 \phi)^4}{5!} - \dots \text{POWERS OF } (0.5 \phi)^2 \right]$$

$$f_4 = \cos 0.5 \phi = 1 - \frac{(0.5 \phi)^2}{2!} + \frac{(0.5 \phi)^4}{4!} - \dots \text{POWERS OF } (0.5 \phi)^2$$

$$r_{L(n)}^{L(n+1)} = \begin{bmatrix} -f_5 \theta_X \\ -f_5 \theta_Y \\ -f_5 \theta_Z \\ f_6 \end{bmatrix} \approx \begin{bmatrix} -0.5 \theta_X \\ -0.5 \theta_Y \\ -0.5 \theta_Z \\ 1 \end{bmatrix} \begin{bmatrix} \theta_X \\ \theta_Y \\ \theta_Z \end{bmatrix} = \underline{\theta} = \underline{W}_{IL(AVG)}^L T_n$$

$$(0.5 \theta)^2 = 0.25 (\theta_X^2 + \theta_Y^2 + \theta_Z^2)$$

$$f_5 = \frac{\sin 0.5 \theta}{\theta} = 0.5 \left[ 1 - \frac{(0.5 \theta)^2}{3!} + \frac{(0.5 \theta)^4}{5!} - \dots \text{POWERS OF } (0.5 \theta)^2 \right]$$

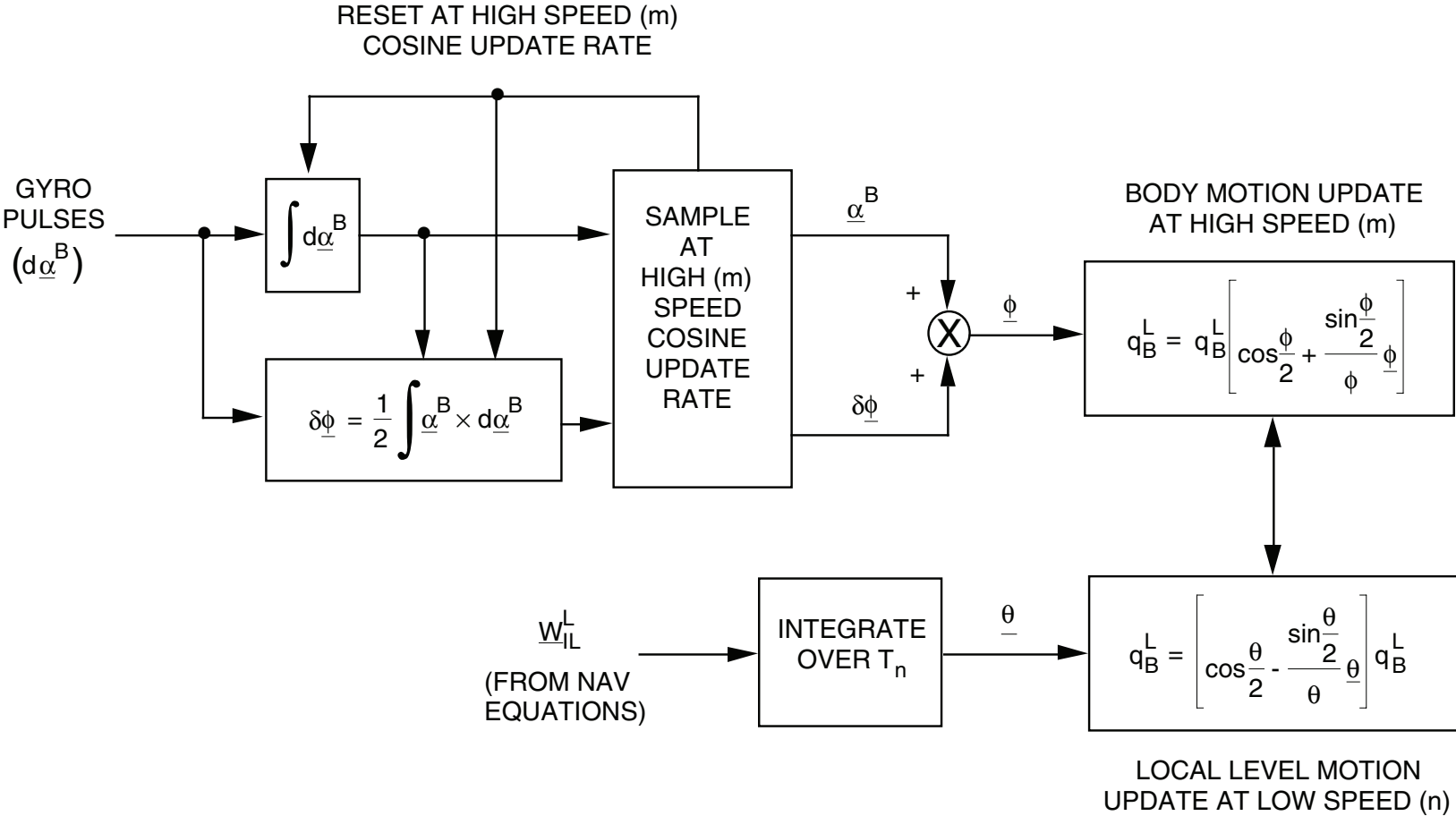
$$f_6 = \cos 0.5 \theta = 1 - \frac{(0.5 \theta)^2}{2!} + \frac{(0.5 \theta)^4}{4!} - \dots \text{POWERS OF } (0.5 \theta)^2$$

## QUATERNION UPDATE OPERATORS

The slide illustrates the equations used for the quaternion body and local level motion update operators. As can be seen, they parallel the forms for the direction cosine update operators. The  $\underline{\phi}$  and  $\underline{\theta}$  vectors in these equations are identical to the  $\underline{\phi}$ ,  $\underline{\theta}$  vectors for direction cosine updating and are calculated using the identically same set of equations.

The  $h_{B(m+1)}^{B(m)}$  body update quaternion expression is exact, except for  $f_3, f_4$  series truncation errors which are minimized by carrying sufficient terms to handle the worst case maximum body rate motion (when the  $\underline{\phi}$  components are maximum). The  $r_{L(n)}^{L(n+1)}$  local level updating quaternion is exact, except for  $f_5, f_6$  series truncation errors which are minimized to handle the worst case attitude corrections applied during initial alignment or Kalman reset operations. A first order approximation for  $r_{L(n)}^{L(n+1)}$  is also shown (similar to the first order local level update algorithm shown in a previous chart for the direction cosine matrix). These accuracy factors are identical to those for direction cosine updating, hence, no particular accuracy advantage should be obtained for direction cosines or quaternions using the described algorithms.

# QUATERNION UPDATE IMPLEMENTATION



## QUATERNION UPDATE IMPLEMENTATION

The chart depicts strapdown attitude updating operations using an attitude quaternion to represent B Frame angular orientation.

This chart is identical to the enhanced direction cosine updating chart on page 205A, but with the direction cosine equations replaced by the quaternion equivalents shown on pages 212 and 214.

# ORTHOGONALITY AND NORMALIZATION CORRECTIONS

- **DIRECTION COSINE ORTHOGONALIZATION**

$$\epsilon_{12} = C_{11} C_{21} + C_{12} C_{22} + C_{13} C_{23}$$

$$C_{1J} = C_{1J} - \frac{1}{2} \epsilon_{12} C_{2J} \quad (J = 1 \text{ TO } 3)$$

$$C_{2J} = C_{2J} - \frac{1}{2} \epsilon_{12} C_{1J} \quad (J = 1 \text{ TO } 3)$$

- **DIRECTION COSINE NORMALIZATION**

$$\epsilon_{11} = C_{11}^2 + C_{12}^2 + C_{13}^2 - 1$$

$$C_{1J} = C_{1J} - \frac{1}{2} \epsilon_{11} C_{1J} \quad (J = 1 \text{ TO } 3)$$

$$\epsilon_{22} = C_{21}^2 + C_{22}^2 + C_{23}^2 - 1$$

$$C_{2J} = C_{2J} - \frac{1}{2} \epsilon_{22} C_{2J} \quad (J = 1 \text{ TO } 3)$$

- **QUATERNION NORMALIZATION**

$$\epsilon_q = a^2 + b^2 + c^2 + d^2 - 1$$

$$q = q - \frac{1}{2} \epsilon_q q \quad (\text{FOR } a, b, c, \text{ AND } d)$$

## ORTHOGONALITY AND NORMALIZATION CORRECTIONS

Due to finite computer register lengths and minor algorithm errors, the computation of the direction cosine matrix or quaternion in a strapdown system may have a small degree of error build up. If the computer software is properly designed and computer word length is sufficient, these errors should be negligible compared to basic sensor error effects. However as a safeguard, most strapdown attitude algorithms contain some degree of built-in suppression for computational and algorithm error.

In the case of direction cosines, orthogonality and normality corrections can be applied periodically to the cosine matrix elements to assure that the correct normalization and orthogonality conditions for the matrix are preserved. The normality condition for a direction cosine matrix is that the sum of the squares of the elements in any row (or column) should be unity. This is a statement of the fact that a direction cosine row (or column) represents the components of a unit vector (along one axis, B or L, projected into the other B or L coordinate frame). The sum of the squares of unit vector components must be unity. The orthogonality condition for direction cosines states that the dot product between any two rows (treated as vectors) or columns (treated as vectors) should be zero. The orthogonality condition reflects the fact that the rows (or columns) of a DCM represent unit vectors along orthogonal reference frame axes (B or L). The dot product between orthogonal vectors is zero. Both the orthogonality and normality conditions for the direction cosine matrix rows and columns is equivalent to the statement that the inverse of a direction cosine matrix equals its transpose.

The slide shows how the errors in the normalization and orthogonality conditions are calculated for the first two rows of the DCM ( the  $\epsilon_{11}$ ,  $\epsilon_{22}$ , and  $\epsilon_{12}$  quantities) and used to update the DCM elements to achieve orthogonality and normality if an error exists. These operations (if needed) would typically be performed at a low rate (e.g., 1 Hz) so that negligible impact on computer throughput results.

The quaternion elements (through their definition) should be such that the sum of the squares should also be unity. This normalization condition can be tested periodically by  $\epsilon_q$  and used to correct the quaternion elements to achieve normality. Note, that an orthogonality operation associated with quaternions is not needed (i.e., is meaningless).

In performing a tradeoff study comparing direction cosine versus quaternion algorithms, orthogonality and normality computations should be included if planned to be used. Generally, these computations only affect computer memory requirements; throughput penalties are negligible due to the generally low iteration rates required.

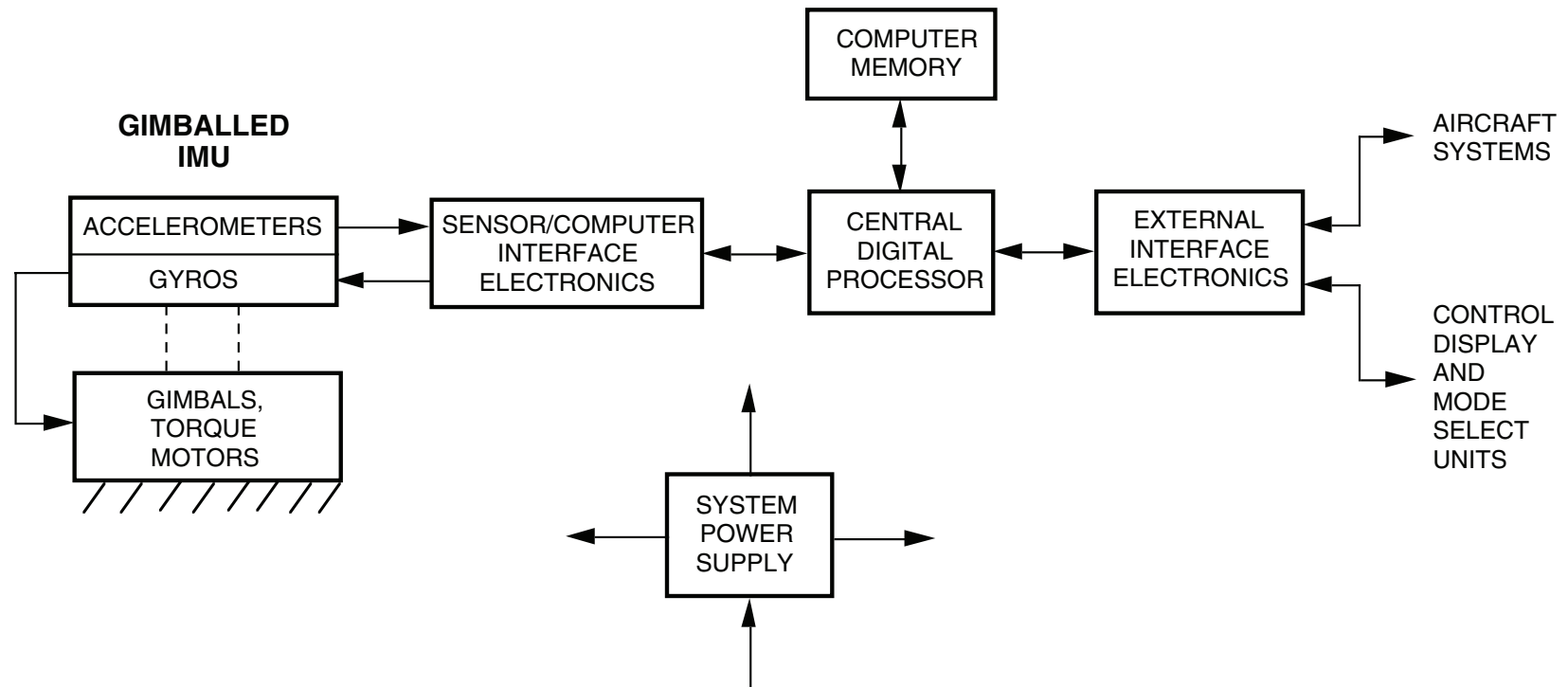
Note that if the exact algorithms described in previous charts are used for direction cosine or quaternion attitude updating

## **ORTHOGONALITY AND NORMALIZATION CORRECTIONS (CONTINUED)**

operations, orthogonalization and normalization should not be required (assuming that the attitude parameters were properly initialized to be normal (and for the direction cosine matrix, orthogonal), that the Taylor series expansion terms used in the exact algorithms contain a sufficient number of terms, and that adequate computational word length is provided for the attitude updating operations.

# **INERTIAL SENSORS**

# TYPICAL GIMBALED INS HARDWARE ELEMENTS



## TYPICAL GIMBALED INS HARDWARE ELEMENTS

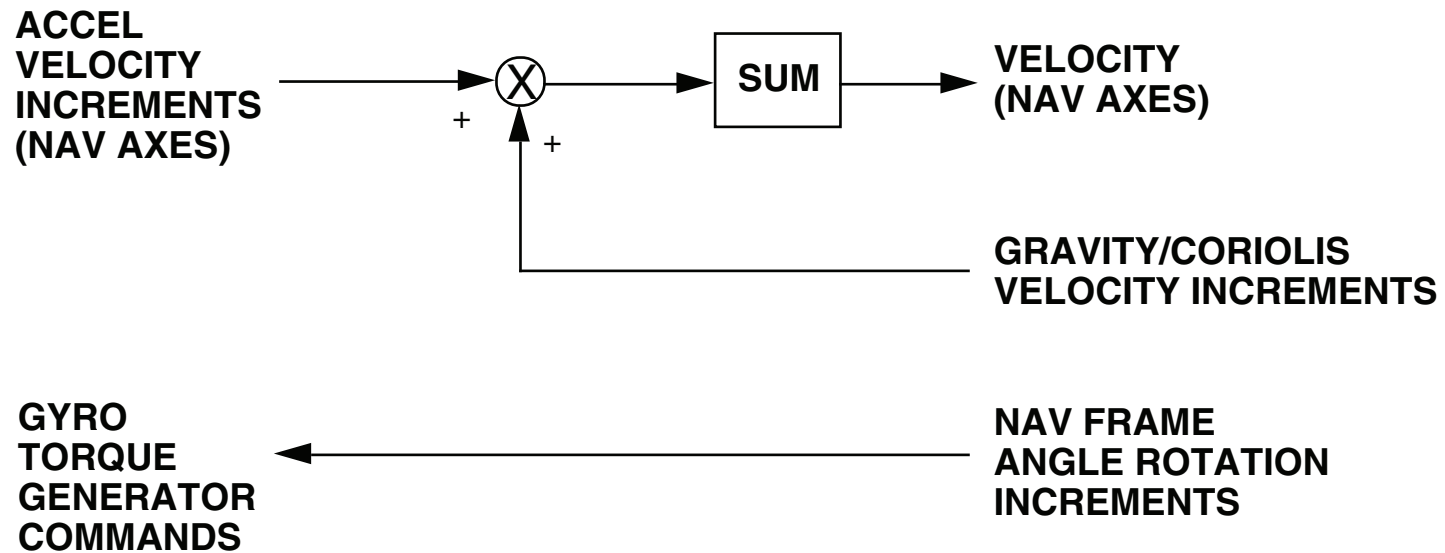
The slide depicts the interface between the major hardware elements in a gimbaled INS. The platform sensors interface with the INS computer through sensor/computer interface electronics. The accelerometer outputs are input to the computer and gyro torque generators are commanded by the computer through the interface electronics. The platform gimbal torque motors are controlled by the platform gyro outputs.

The gyro output/gimbal torque motor interface is of the analog type based on a gyro output nulling mechanization. As such, accuracy requirements in this electrical interface are generally not stringent.

The interface between the sensors and the INS computer require an analog-to-digital conversion for the accelerometers (which are inherently analog devices) and a digital-to-analog conversion for the gyros. The INS accuracy hinges on the accuracy of the sensor/computer interface (and the inherent sensor accuracy itself), hence, the sensor/computer interface electronics are fairly sophisticated.

The power supply indicated in the chart must be non-interruptible to assure that computer integration operations are not disrupted from the start of initial alignment until navigation termination. In the case of aircraft systems, this generally requires that a battery backup be included to assure continuous power to the inertial navigation system electronic assemblies in the presence of aircraft input power transients or temporary outages (e.g., after the aircraft engines are started, power is switched from the aircraft auxiliary power unit (APU) to the aircraft primary power generator, generally introducing a momentary power outage period of several milliseconds).

# GIMBALED SYSTEM COMPUTER SOFTWARE SENSOR DATA OPERATIONS



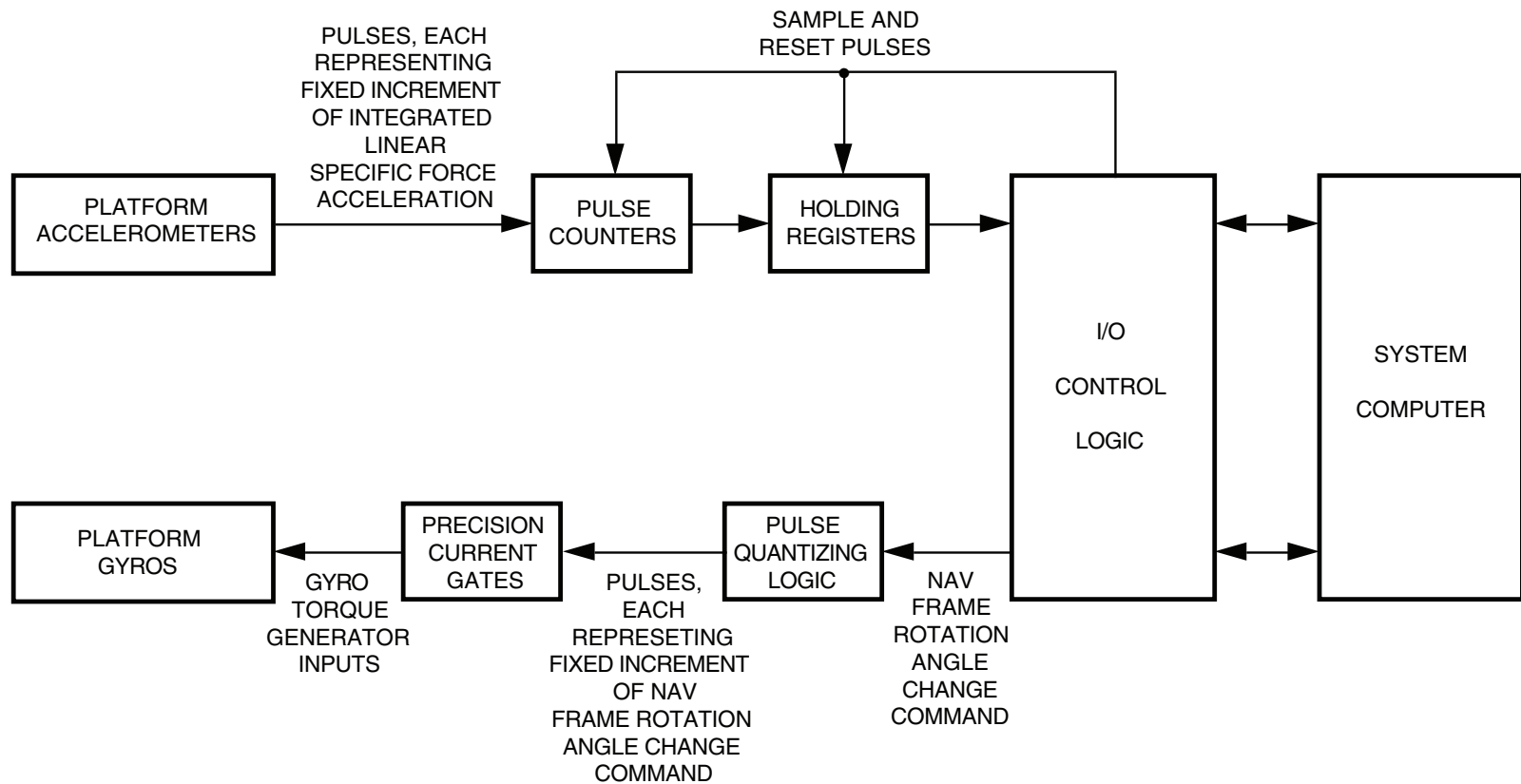
## **GIMBALED SYSTEM COMPUTER SOFTWARE SENSOR DATA OPERATIONS**

In order to properly define the sensor interface electronics in a gimbaled INS, it is important to understand how the sensor signals (in and out) are used in the basic INS concept.

The accelerometer signals are integrated in the system computer to calculate INS velocity, a digital integration summing operation. To assure that the acceleration integral function is performed flawlessly, the accelerometer electronics are designed to deliver integrated increments of acceleration to the computer (i.e., integrals of acceleration over the computer sample period). The computer samples the increments and sums them in the process of updating velocity. The gravity and Coriolis corrections are applied on a similar basis, but through software operations only.

The torque generator input signals to the gyro are designed such that the integrated torque generator input command equals the integral of the navigation coordinate frame rotation rate. Through the continuous gimbal servo loop gyro output nulling, this assures that the platform attitude (the integral of the rate) accurately replicates the desired navigation frame attitude. To achieve the integral interface with the gyro, the rotation rate commands to the gyro are calculated in the form of navigation frame rotation increments, representing the integrated navigation frame angular rate over the computer cycle period. The rotation increments are applied to the gyro torque generators through suitable electronics such that the integrated current into the torque generator exactly equals the sum of the angle rotation increments.

# TYPICAL GIMBALED SYSTEM SENSOR/COMPUTER INTERFACE



## TYPICAL GIMBALED SYSTEM SENSOR/COMPUTER INTERFACE

Based on the general design considerations noted in the previous slide, this slide illustrates a typical interface between the platform sensors and the INS computer in a gimbaled inertial navigation system.

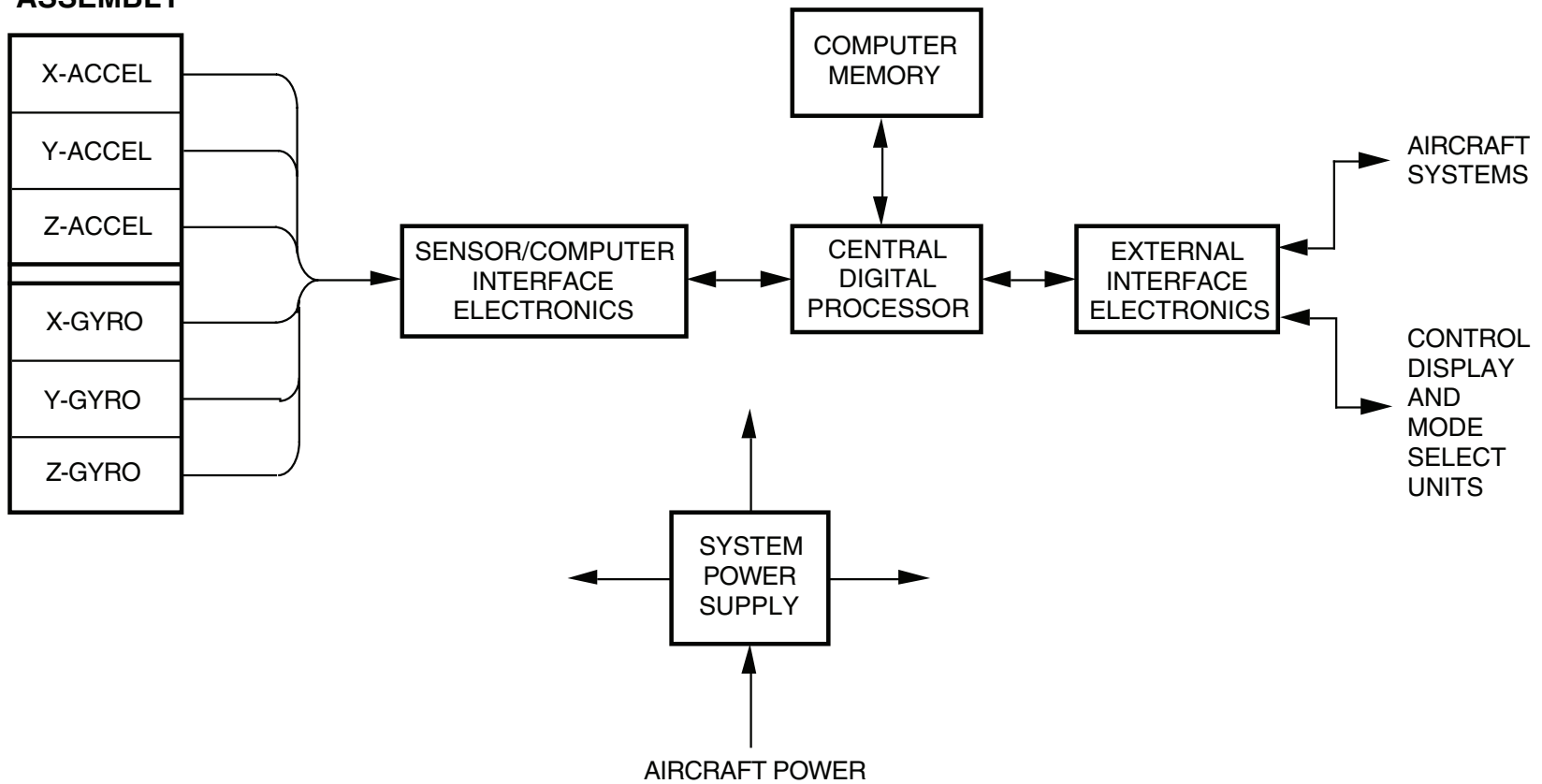
The accelerometers are mechanized with appropriate electronics to provide an incremental integrating function. Their outputs are in the form of pulses, each indicating that a prescribed fixed increment of integrated linear specific force acceleration has been received by the instrument along its input axis. The accelerometer pulses are counted in up/down counters (one for each accelerometer). At each computer sample time, all up/down counter contents are transferred simultaneously to holding registers, and the counters reset to begin the pulse count for the next sample interval. The holding register contents are then sequentially transferred into the system computer through the Input/Output (I/O) control logic.

The navigation frame rotation angle change data from the system computer is output at the local level frame reference update rate. These signals are in the form of digital words designed such that their sum equals the integral of the local level rates generated in the INS computer. The navigation frame angle increments are processed by pulse quantizing logic which generates pulse frequency outputs (e.g., 10 KHz maximum) such that the frequencies on the average are proportional to the rotation angle inputs, but more importantly, the sum of the pulses always balance the sum of the navigation frame rotation angle commands.

The gyro command pulses are then used to drive precision current gates which transfer a known fixed increment of current-time product into the gyro torque generator, one for each pulse. The result is that the integral of the precision gyro torque generator input signals identically equals the sum of the pulses, hence, through the previous rationale, equals the integrated local level rates calculated in the INS computer.

# TYPICAL STRAPDOWN INS HARDWARE ELEMENTS

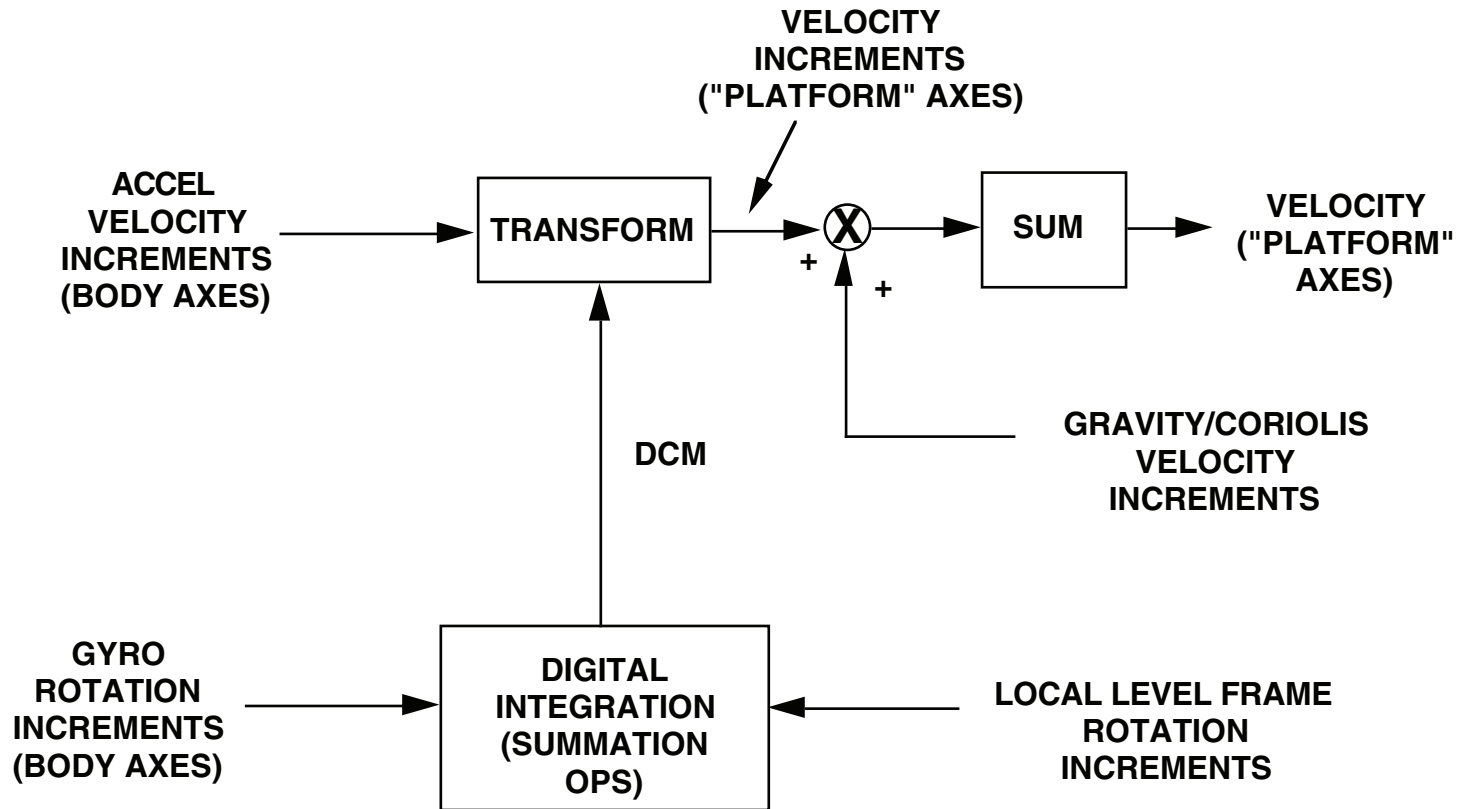
## STRAPDOWN INERTIAL SENSOR ASSEMBLY



## **TYPICAL STRAPDOWN INS HARDWARE ELEMENTS**

In a strapdown INS, the gimbal assembly is absent, and the strapdown sensor outputs are brought into the INS computer through sensor/computer interface electronics. No feedback torquing signals are fed back to the gyros (as in the gimbaled system).

# STRAPDOWN COMPUTER SOFTWARE SENSOR DATA OPERATIONS

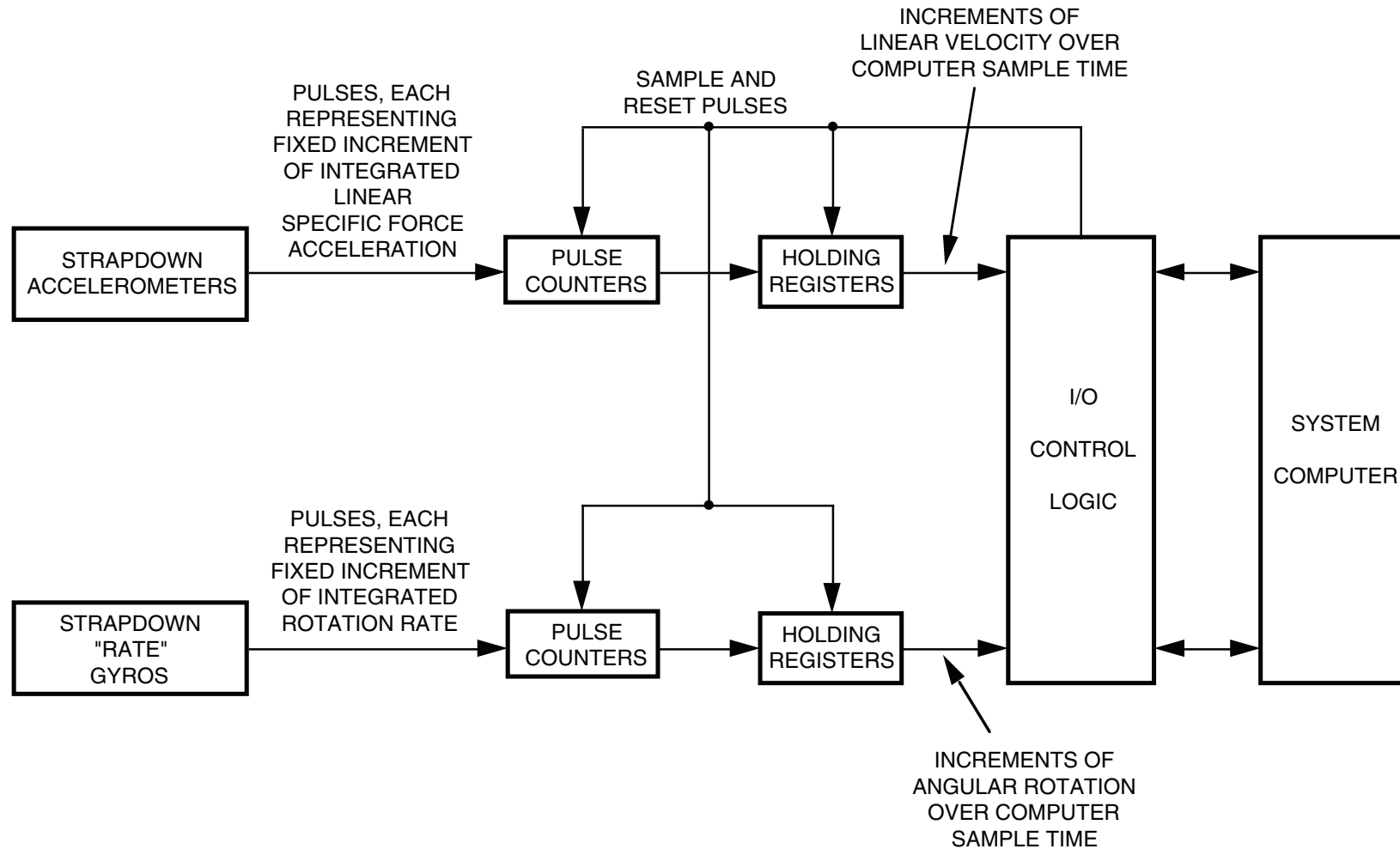


## **STRAPDOWN COMPUTER SOFTWARE SENSOR DATA OPERATIONS**

The computer operations in a strapdown system integrate the gyro and accelerometer data to calculate INS attitude and velocity.

The digital integration is a sequence of summation operations based on sensor data inputs. To assure that the integration operation is exact, the strapdown sensors are designed to provide preintegrated data to the INS computer in the form of integrals of sensor input over the computer sample period. These signals represent body axis rotation angle increments (for the gyros) and specific force velocity increments (in the case of the accelerometers). Note that the accelerometer outputs for the strapdown system are identical to the gimbaled system.

# TYPICAL STRAPDOWN SENSOR/COMPUTER INTERFACE



## **TYPICAL STRAPDOWN SENSOR/COMPUTER INTERFACE**

The slide illustrates a typical interface between the strapdown sensors and the INS computer. This interface (for both the gyros and accelerometers) is identical to the comparable interface between the accelerometers and computer in a gimbaled INS (shown previously). The strapdown coning and sculling computations, if included as a special purpose electronics function, would also be mechanized between the pulse counters and I/O control logic (not shown in the slide).

## **SENSORS DISCUSSED**

- **SINGLE-DEGREE-OF-FREEDOM FLOATED RATE-INTEGRATING GYRO**
- **TUNED ROTOR GYRO**
- **ELECTROSTATIC GYRO**
- **RING LASER GYRO**
- **PENDULOUS ELECTRICALLY SERVOED ACCELEROMETER**
- **GYRO ACCELEROMETER MECHANICALLY SERVOED**
- **FIBER-OPTIC GYRO**
- **VIBRATING BEAM ACCELEROMETER**
- **QUARTZ RATE SENSOR**
- **MICRO MACHINED SILICON INERTIAL SENSORS**
- **TORQUE-TO-BALANCE SENSOR ELECTRONICS**

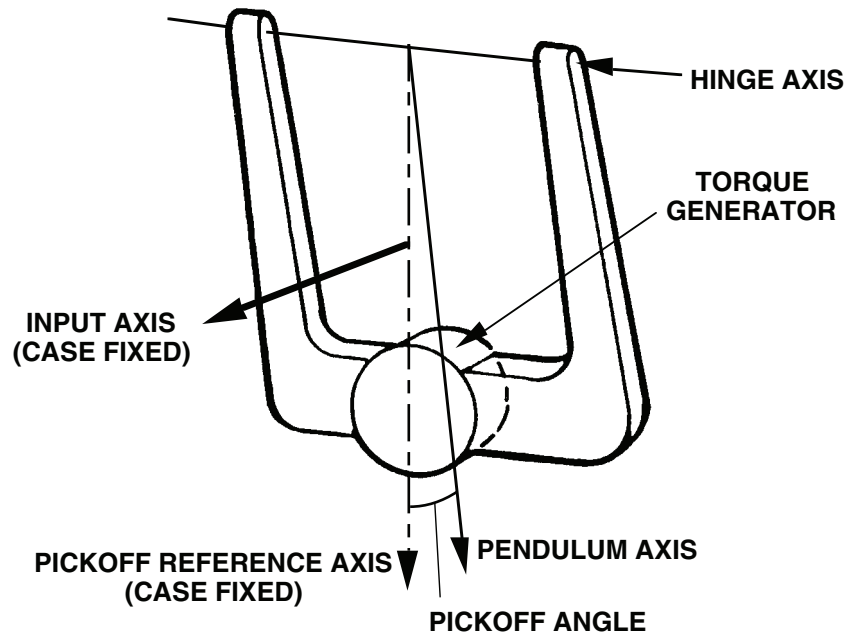
## **SENSORS DISCUSSED**

The discussion to follow on inertial sensors describes gyro and accelerometer types that have been utilized in gimballed and/or strapdown inertial navigation systems. Included in the sensor discussion is a description of the torque-to-balance sensor electronics utilized with several of the instruments (pendulous accelerometer, strapdown floated rate integrating gyro, tuned rotor gyro).

A more detailed discussion on inertial sensors is provided in two reproduced papers contained in the Strapdown Inertial Navigation Lecture Notes handout:

- NATO AGARD Lecture Series 95 paper: STRAPDOWN SENSORS by Paul G. Savage.
- NATO AGARD Lecture Series 133 paper: ADVANCES IN STRAPDOWN SENSORS by Paul G. Savage.

## ELECTRICALLY SERVOED PENDULOUS ACCELEROMETER CONCEPT



- INERTIAL REACTION TORQUE ABOUT HINGE AXIS EQUALS (PENDULUM MASS)  $\times$  (INPUT AXIS ACCELERATION)  $\times$  (MOMENT ARM TO PENDULUM CG)
- ELECTRICAL RESTRAINING TORQUE IS SUPPLIED BY TORQUE GENERATOR DRIVEN BY PICKOFF AMPLIFIER TO KEEP PICKOFF ANGLE SERVOED TO NULL (PENDULUM ALIGNED WITH CASE AXES)
- TORQUE CURRENT BECOMES PROPORTIONAL TO INPUT AXIS ACCELERATION

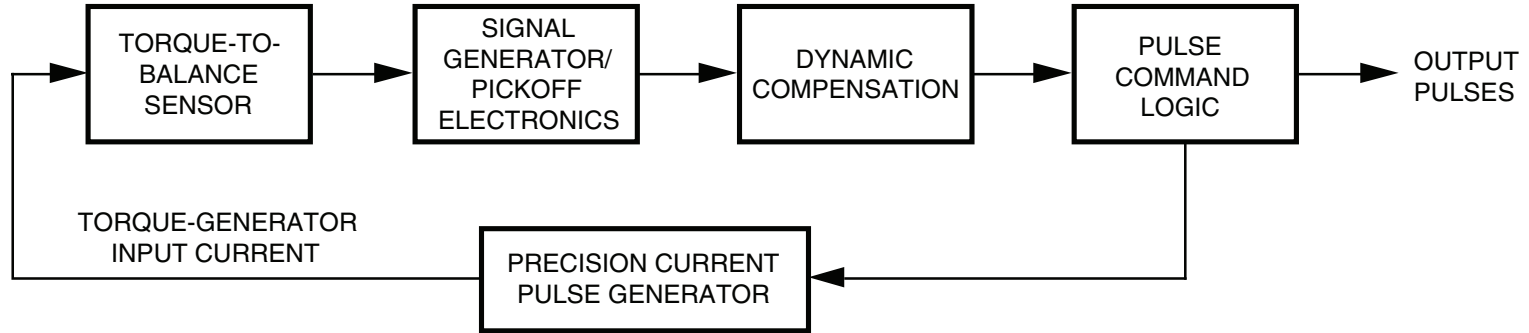
## **ELECTRICALLY SERVOED PENDULOUS ACCELEROMETER CONCEPT**

The electrically servoed pendulous accelerometer consists of a delicately flexure-hinged pendulum assembly, an electrical pickoff assembly that senses angular movement of the pendulum relative to the case from a nominally null position, and an electrical torque generator that enables the pendulum to be torqued relative to the case about the pendulum axis proportional to torquer electrical current inputs. The torque generator consists of a pendulum mounted torquer coil assembly and a case mounted permanent magnet. Application of current to the torquer coil generates a torque on the pendulum through the interaction of the coil electric field with the case fixed magnet field. The torquer current is generated through suitable capture loop electronics driven by the pickoff signal.

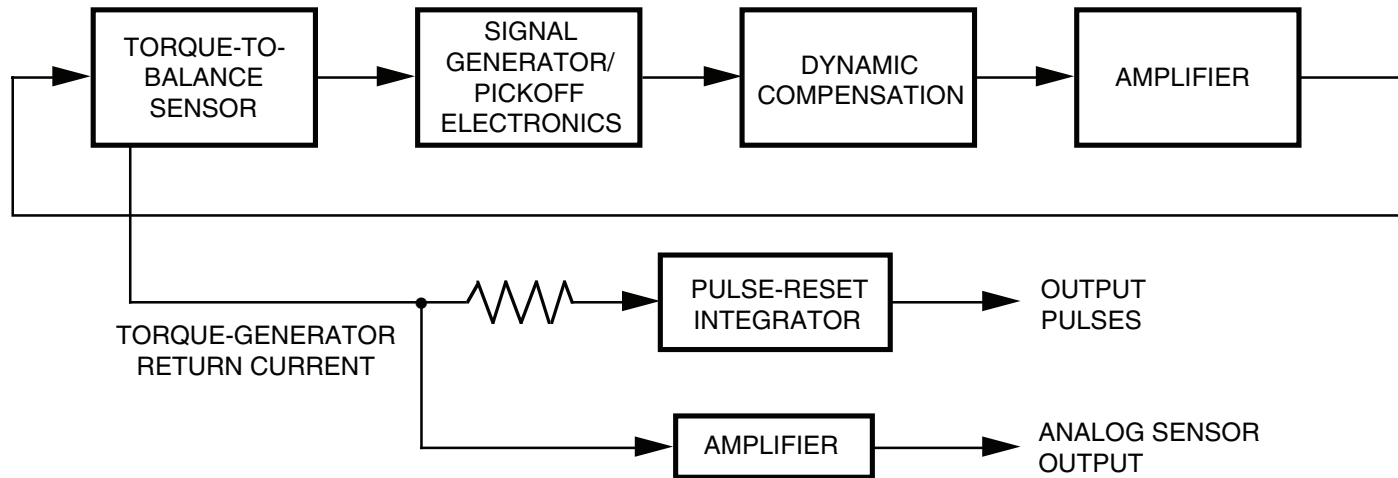
Under input acceleration (along the input axis, normal to the plane of the pendulum), an inertial reaction torque is generated about the pendulum hinge axis equal to the effective pendulum mass times the mass moment arm to the hinge axis times the input specific force acceleration. The pendulum is restrained to null under this acceleration through the servo action of the electrical torque generator driven by the pickoff output signal. In this manner, the torquer current (which generates the restraining torque in the torque generator) becomes proportional to input axis acceleration. The torquer current is the direct output signal from the accelerometer.

# TORQUE-REBALANCE-LOOP CONCEPTS

## DIGITAL REBALANCE



## ANALOG REBALANCE



## TORQUE-REBALANCE-LOOP CONCEPTS

Two basic methods can be used to mechanize the capture loop utilized with the pendulous accelerometer and other torque to balance instruments: digital rebalance or analog rebalance.

In the digital rebalance approach, the feedback signal to the sensor torque generator is in the form of precision fixed current-time pulses. The pulse frequency is established by electronics driven by the sensor pickoff to maintain pickoff null. Dynamic compensation may be included in these electronics to filter sensor pickoff demodulator noise or provide lag/lead shaping that stiffens the dynamic response characteristics in the low frequency region. By virtue of the loop maintaining the pickoff at null, each rebalance pulse counteracts a known fixed increment of integrated sensor input (acceleration or rate, depending on whether the instrument is an accelerometer or gyro). The occurrence of a pulse, therefore, is a digital indication that the sensor input has integrated a fixed pulse worth of input. The loop output is the same pulse data used to trigger the gates that generate the precision current-time pulse into the sensor torque generator.

In the analog rebalance approach, an analog current is generated from the pickoff output and used as the torque generator input. In this manner, the instantaneous torque generator current becomes proportional to the sensor input. To generate the incremental pulse output needed for input to the strapdown computer, an analog integrator is needed with a pulse-reset loop to rebalance the integrator each time it integrates a fixed quantum of torque generator return current. The pulse-rebalance on the analog integrator is mechanized in feedback fashion in much the same way as the digital sensor rebalance loop, developing a precision rebalance pulse train into the integrator. By virtue of the precision pulse feedback, each pulse represents a known fixed increment of integrated current from the torque generator, hence, also represents a known fixed increment of integrated sensor input. The pulses used to command the precision pulse generator gates in the integrator reset loop are output to the system computer as the sensor quantized pulse signal.

The principle advantages of the digital torque-rebalance approach is that the effect of electronic bias errors is minimized. If the gating logic accurately prevents leakage currents from entering the torque generator, the electronics error is governed by the ability to accurately generate the precision pulse. The disadvantage in the digital rebalance approach is that an analog sensor signal is not generated as a natural part of the rebalance operation (a useful output for other vehicle systems), and that high currents (depending on the sensor torque generator scale factor) may be needed to maintain pickoff null under maximum sensor input conditions. The latter problem has impact on the electronics design rebalance configuration and fineness of pulse size achievable. Another disadvantage is that the rebalance electronics tend to be uniquely matched to the particular sensor torque generator interface, making it difficult to develop a general rebalance circuit that is common to several sensor types (as when multiple sensor sourcing is used, for example). A disadvantage for pulse rebalance in precision dynamic applications is that the accelerometer pendulum

## TORQUE-REBALANCE-LOOP CONCEPTS (CONTINUED)

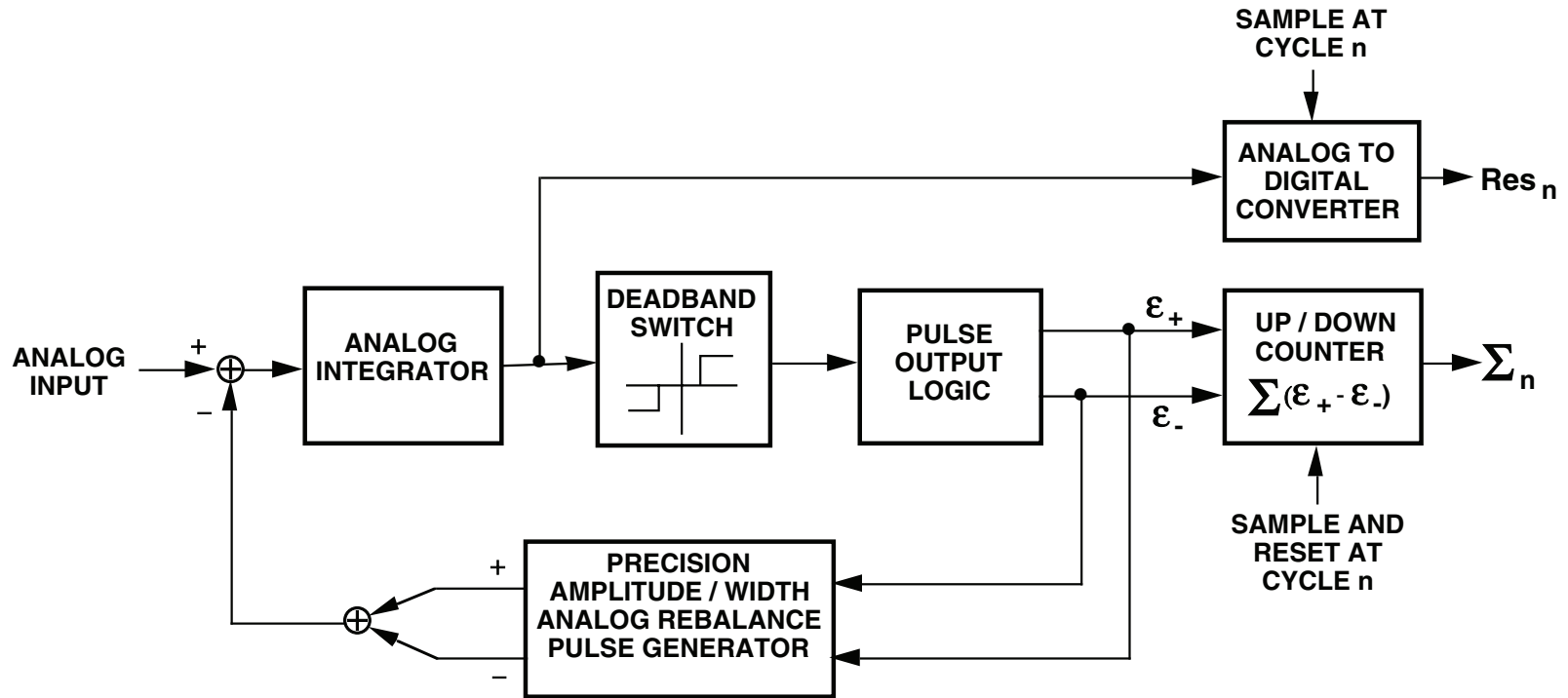
can only be controlled to null within the deadband of the pulse rebalance logic (typically one pulse wide). As a result, the accelerometer will have a small cross-coupling into the pendulum axis (by the pickoff off-null angle) which will erroneously couple a small component of the pendulum axis acceleration into the accelerometer input.

The disadvantage of the analog torque rebalance approach is the bias error associated with the outboard pulse-reset integrator which generates the equivalent of a sensor bias on the pulse output signal. Advances in operational amplifiers in recent years have significantly reduced this problem area. The advantages for analog rebalance are that the sensor torque generator analog return signal is available as an analog output, and that the pulse-reset integrator can generally be designed to interface with several sensor types. Additionally, because the pulse rebalance for the outboard integration does not have to control dynamic sensor inputs, scaling techniques can be used to assure that pulse reset current levels are optimized for compatibility with high speed low leakage pulse gating switches.

In many applications, the pulse size for the pulse rebalance approach or from the pulse reset integrator for the analog rebalance approach is too coarse for accurate usage in an inertial navigation system under all operating conditions. A classic example is during initial alignment operations. If either of the "horizontal" accelerometers is nearly horizontal under this condition a large accelerometer pulse weight could cause the pulse output frequency to be very low, thereby introducing transients in the earth rate estimation loop. To reduce the effective pulse size, many inertial navigation systems sample the residuals from the accelerometers into the system computer at the same instant that the pulse count sample is made. For pulse rebalanced accelerometers, the residuals would be the pickoff signals; for analog rebalanced accelerometers, the residuals would be the output from the integrators in the pulse reset integrators. The difference between the current and past residual samples are then used as corrections to the pulse count samples, thereby effectively eliminating the pulse quantization error effect (within the accuracy of the residual sampling process).

**NOTES**

# PULSE RESET INTEGRATOR



$$\Delta V_n = K_{Scale} \sum_n + Res_n - Res_{n-1}$$

## PULSE RESET INTEGRATOR

The chart illustrates a commonly used configuration for a pulse reset integrator (identified in the previous chart) for converting an analog input signal into output digital pulses, the occurrence of each pulse (plus or minus) indicating that the integral of the input has accumulated a net change equal to the pulse weight. The analog integrator could be an electronic device (as in the previous chart) or it could be an inertial component (e.g., a pendulous accelerometer). In the latter case, the chart configuration would be representative of the digital rebalance approach in the previous chart (as opposed to analog rebalance on the previous chart for which the electronic pulse reset integrator is used to generate the output digital pulses).

The basic principle used in the chart is that the sum of the signed output pulses is forced, through precision digital feedback, to equal the integral of the input signal. Thus we see that the output pulse logic signals ( $\epsilon_+$  and  $\epsilon_-$ ) are used to command the generation of precision amplitude / time-width electrical pulses with sign corresponding to the sign of the logic pulses. The precision pulses are then fed back and subtracted from the analog input to the integrator. Electronic deadband switch and pulse output logic blocks generate the  $\epsilon_+$ ,  $\epsilon_-$  signals to maintain the analog integrator output near zero (within the switch deadband). This assures that the sum of the signed output pulses balances the integral of the analog input within the width of the deadband (typically set to correspond to two pulses across the full deadband width). Simultaneously, the signed logic pulses are summed in an up-down counter for input to the strapdown navigation computer at specified sample times (at an  $n$  cycle rate corresponding to the highest computation rate in the computer that uses this input). At the instant after sampling, the counter is reset to zero so that the sampled counts  $\Sigma_n$  represents the pulse accumulation from sample cycle  $n-1$  to  $n$ . A computation algorithm in the computer then (in effect) sums successive scaled counter samples to regenerate the integral of the analog signal within the computer (e.g., to calculate velocity, the integral of acceleration).

The previous logic provides a simple and accurate method for digitally reconstructing the analog integral within the computer, but is limited in accuracy by the finite pulse size (the signed pulse sum can only balance the analog integral within a pulse). To reduce this quantization error effect, the residual signal on the analog integrator ( $Res$ ) can also be sampled at the  $n$  cycle rate and brought into the computer through an analog-to-digital converter. By adding the change in  $Res$  (from the  $n-1$  to the current  $n$  cycle measurement) to the sampled  $\Sigma_n$ , a more accurate digital integral increment  $\Delta v_n$  is obtained. A residual quantization type error will still remain on  $\Delta v_n$  due primarily to the scale factor error on the analog integrator in the chart. For a 5% scale factor error, the remaining quantization would be on the order of 2.5% of the full-width deadband (e.g., 2.5% of a pulse when the full width deadband equals two pulses).

The deadband switch pulse logic approach is but one of several methods for achieving pulse rebalance. Other methods are described in Section 4.1 of the Strapdown Sensor paper in the Strapdown Inertial Navigation Lecture Notes handout.

## **ELECTRICALLY SERVOED PENDULOUS ACCELEROMETER PROBLEM AREAS**

- **HIGH ACCURACY STRAPDOWN PERFORMANCE NOT READILY ACHIEVABLE IN A LOW COST INSTRUMENT**
- **LIMITED SCALE FACTOR ACCURACY IN SKEWED REDUNDANT APPLICATIONS**

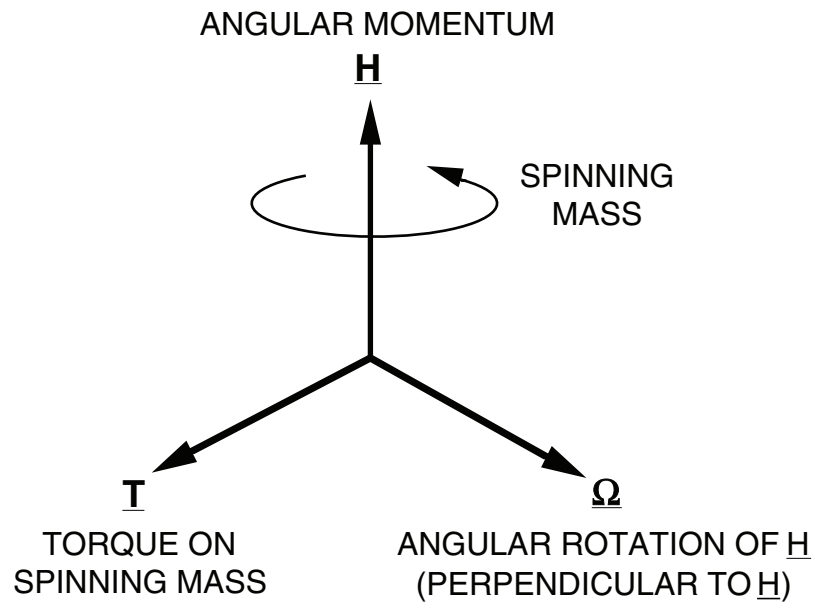
## **ELECTRICALLY SERVOED PENDULOUS ACCELEROMETER PROBLEM AREAS**

The electrically servoed pendulous accelerometer has found widespread successful usage in gimbale INS applications, and is the principle accelerometer mechanization concept utilized today in such applications.

For strapdown INS applications, accelerometer accuracy requirements increase compared to those for a comparable accuracy gimbale INS. One of the most demanding requirements for strapdown systems utilizing ring laser gyros (RLGs) is the requirement to achieve specified accuracy levels without using heaters for temperature control (i.e., heaterless). A heaterless instrument generally requires that the instrument temperature be measured continuously and used through an appropriate algorithm in the navigation computer to correct the temperature sensitive effects exhibited by the instrument. In the case of a heaterless accelerometer packaged as an individual assembly, a temperature sensor is typically included within the accelerometer package. Heater control of the entire gyro/accelerometer instrument cluster has been traditionally used in gimbale systems as a means of stabilizing performance variations with temperature. Because RLGs operate without heaters, use of heaters for the accelerometers would impose thermal gradients across the RLGs, thereby creating RLG thermal gradient sensitive bias shifts. In order to eliminate the thermal gradient induced bias shift, the requirement was created for the accelerometer to also operate without heaters. Fortunately, only modest design changes in the electrically servoed pendulous accelerometer have enabled the instrument to meet strapdown INS performance requirements, including accurate heaterless operation. However, the complexity of the strapdown electrically servoed pendulous accelerometer including the pulse quantizing electronics has not been amenable to continuing strapdown inertial system cost reduction goals.

Now that strapdown gyro accuracies have improved significantly, the accelerometer has emerged as a significant source of error in the higher accuracy strapdown INS error budget. In advanced skewed redundant strapdown systems the impact of accelerometer error on system performance is further compounded by the addition of a large horizontal bias created from accelerometer scale factor error (due to the effect of sustaining 1-g vertical input acceleration having significant components along the input axes of skewed accelerometers used to analytically generate horizontal acceleration measurements for navigation). It can be argued that the scale factor accuracy of contemporary high performance strapdown accelerometers, although acceptable with traditional vehicle axis orthogonal sensor geometries, is unacceptable today in a skewed redundant system.

# MOMENTUM WHEEL GYRO PRINCIPLE OF OPERATION



$$\underline{T} = \underline{\Omega} \times \underline{H} + \frac{d\underline{H}}{dt}$$

RESIDUAL TERM POTENTIALLY  
NEEDING COMPENSATION

- 
- T IS ELECTRICALLY GENERATED TORQUE APPLIED TO SPINNING MASS
  - Ω IS COMPONENT OF CASE ANGULAR RATE PERPENDICULAR TO H (SPIN AXIS) AND T (TORQUE GENERATOR INPUT AXIS)

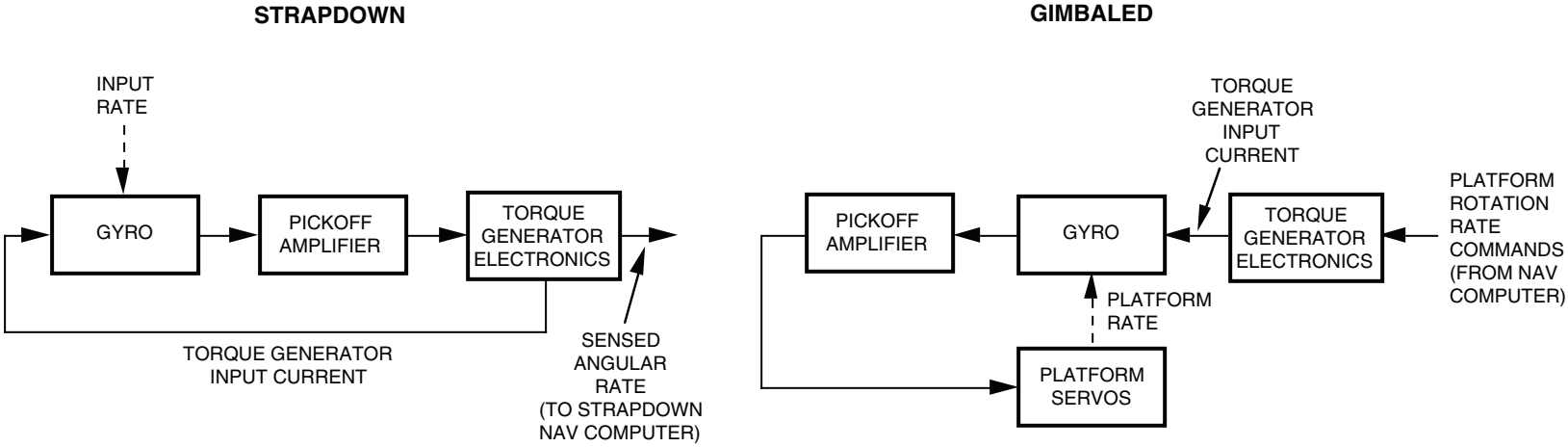
## **MOMENTUM WHEEL GYRO PRINCIPLE OF OPERATION**

The conventional momentum wheel gyroscope operates on the principle that the torque on a spinning mass causes it to precess at an angular rate proportional to the applied torque, with the proportionality factor equal to the spinning mass angular momentum.

The precessional rate is perpendicular to the torque and angular momentum vector.

In a conventional momentum wheel gyroscope, the torque on the spinning mass is applied intentionally by electrical input through a torque generator. In this manner, the gyro precessional rate can be controlled to fit the particular application for which it is used.

# STRAPDOWN AND GIMBALED MOMENTUM WHEEL GYROS UTILIZING ELECTRICAL TORQUE GENERATORS

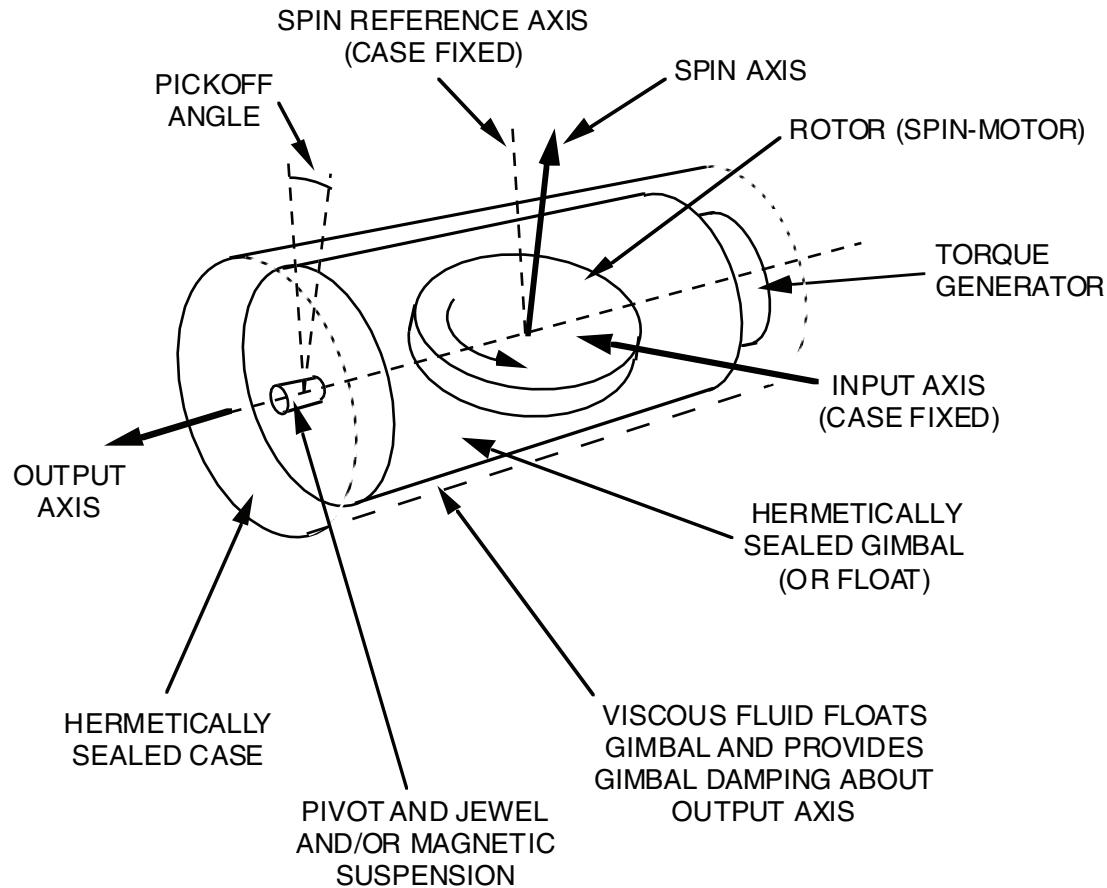


## **STRAPDOWN AND GIMBALED MOMENTUM WHEEL GYROS UTILIZING ELECTRICAL TORQUE GENERATORS**

In a strapdown application, the conventional gyro momentum wheel torque is controlled by the gyro pickoff signal which senses angular deviations between the gyro momentum wheel assembly and the gyro case. By controlling the pickoff to null in this manner, the gyro wheel is controlled to precess at the case angular rate (or at the input rate to the gyro). In this manner, the gyro angular momentum vector follows the gyro case motion, and the torque generator input signal creating this effect (which is proportional to the precessional rate) becomes also proportional to gyro input rate. The torque generator input signal, therefore, is also used to generate the strapdown rate signal input to the strapdown INS computer.

In the gimbaled INS, the gyro torque generator input rate is created by the INS computer to precess the gyro momentum wheel assembly at a rotation rate specified by the computer. The platform servos drive the platform so that the gyro pickoff signals remain at null. Since the gyro pickoff signal measures the angle between the gyro momentum wheel assembly and the gyro case, the gimbal servos force the gyro case (hence platform) to track the precessing gyro momentum wheel. In this manner, the INS platform is stabilized and controlled to follow the INS computer rotation rate commands.

# SINGLE-DEGREE-OF-FREEDOM FLOATED RATE-INTEGRATING GYRO CONCEPT



- SINGLE AXIS SENSOR
- PICKOFF SENSES ANGLE BETWEEN ROTOR SPIN AXIS AND GYRO CASE
- ELECTRICAL TORQUE GENERATOR APPLIES TORQUE TO FLOAT ABOUT OUTPUT AXIS
- PICKOFF SIGNAL PROPORTIONAL TO INTEGRAL OF DIFFERENCE BETWEEN INPUT RATE AND TORQUE GENERATOR RATE

## **SINGLE-DEGREE-OF-FREEDOM FLOATED RATE-INTEGRATING GYRO CONCEPT**

The floated rate-integrating gyro is the gyro with the longest production history and is the original high-accuracy gimbale platform gyro. The device consists of a cylindrical hermetically sealed momentum-wheel/spinmotor assembly (float) contained in a cylindrical hermetically sealed case. The float is interfaced to the case by a precision suspension assembly that is laterally rigid (normal to the cylinder case) but allows "frictionless" angular movement of the float relative to the case about the cylinder axis. The cavity between the case and float is filled with a fluid that serves the dual purpose of suspending the float at neutral buoyancy, and providing viscous damping to resist relative float-case angular motion about the suspension axis (output axis).

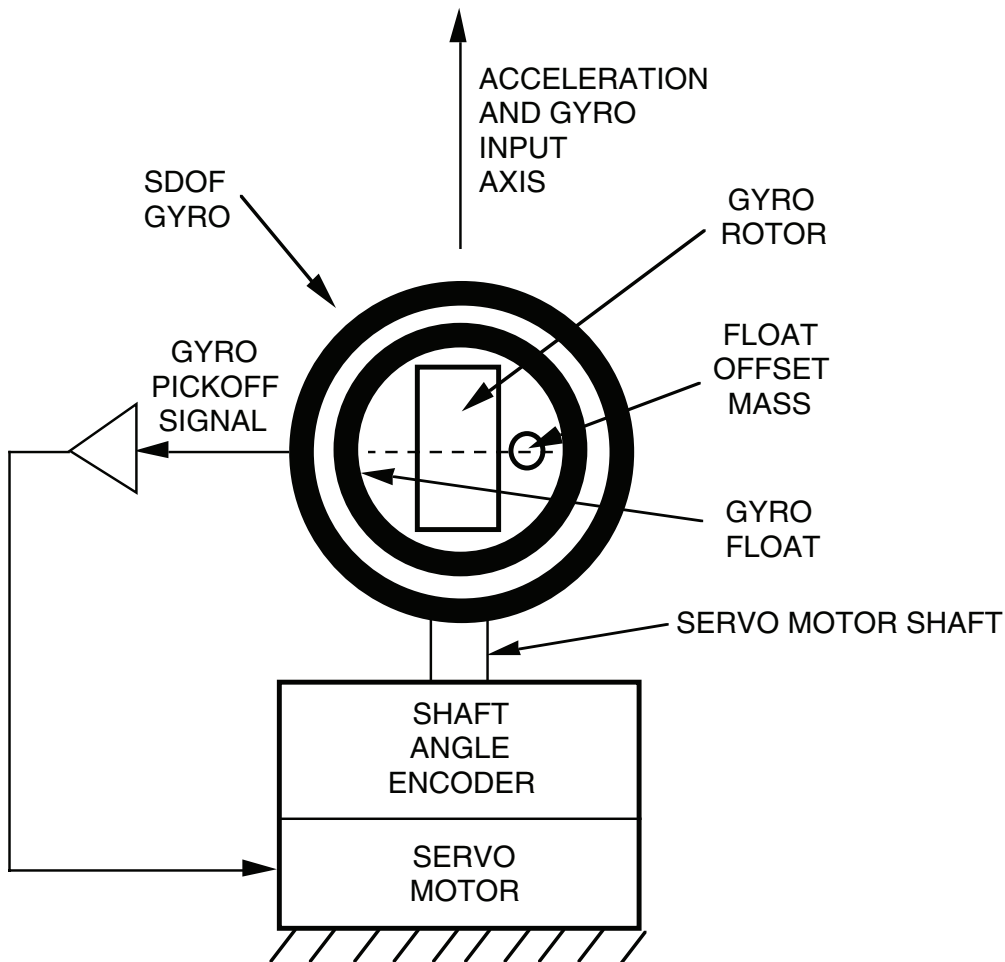
A ball-bearing or gas-bearing synchronous-hysteresis spinmotor is utilized in the float to maintain constant rotor spinspace, hence constant float angular momentum. An electrical pickoff assembly provides an electrical output signal from the gyro proportional to the angular displacement of the float relative to the case. An electrical torque generator (typically a torquer coil on the float and a permanent magnet on the case) provides the capability for applying known torques to the float about the suspension axis proportional to an applied electrical input current. Delicate flex leads are used to transmit electrical signals and power between the case and float.

Under applied angular rates about the input axis, the gyro float develops a precessional rate about the output axis (rotation rate of the angle sensed by the pick-off). The pick-off angle rate generates viscous torque on the float about the output axis (due to the damping fluid) which sums with the electrically applied torque-generator torque to precess the float about the input axis at the gyro input rate. The pick-off angle rate thereby becomes proportional to the difference between the input rate and the torque generator precessional rate; hence, the pickoff angle becomes proportional to the integral of the difference between the input and torque-generator rates (thus, the name rate-integrating gyro).

To operate the gyro in a gimbale application, the pickoff signal is used to drive the gimbal servo motor torquing loops, and the gyro torquer is controlled by the INS computer rotation rate commands. In this manner, the pickoff is maintained at null, and the platform rate (the input rate to the gyro) is forced to balance the computer command rate (in the integral sense).

To operate the gyro in a strapdown mode, the pickoff angle is electrically servoed to null by the torque generator which is driven by the pickoff output signal. The time integral of the difference between the input and torque-generator precessional rates is thereby maintained at zero, and the integral of the torque-generator electrical current provides the required measure of the integral of input rate for the strapdown INS computer.

## GYRO ACCELEROMETER MECHANICALLY SERVOED



- ACCELERATION GENERATES GYRO OUTPUT AXIS TORQUE DUE TO OFFSET MASS
- PICKOFF SIGNAL SENSES FLOAT DISPLACEMENT DUE TO ACCELERATION TORQUE
- SERVO MOTOR GENERATES ROTATION INPUT AXIS RATE TO GYRO TO KEEP PICKOFF NULLED
- SERVO MOTOR SHAFT ANGLE RATE BECOMES PROPORTIONAL TO ACCELERATION
- SHAFT ANGLE ENCODER OUTPUTS MOTOR SHAFT ANGLE CHANGE DATA

## **GYRO ACCELEROMETER MECHANICALLY SERVOED**

One of the most precise gimballed platform accelerometers in use today (in terms of scale factor accuracy) utilizes the single-degree-of-freedom floated rate integrating gyro as an inherent part of its mechanization. The concept is to include an intentional mass imbalance in the gyro float along the spin-axis relative to the center of buoyancy (“float offset mass” in the slide typically achieved by attaching a metal ring on the spin motor shaft), and to mount the gyro to a servo motor driven turn-table with the servo motor axis along the gyro input axis. The servo motor is controlled by the gyro pickoff output to maintain pickoff null.

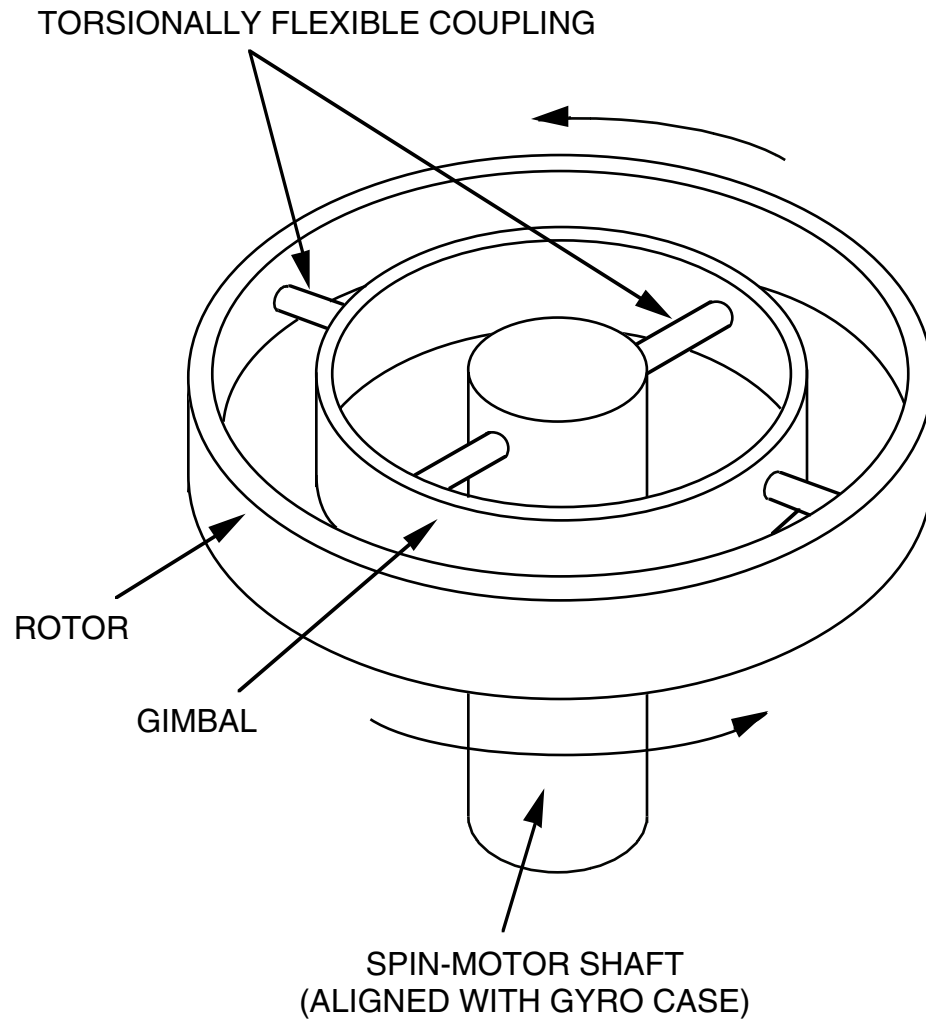
Under accelerations along the input axis, the offset mass generates a torque about the gyro output axis which produces a pickoff output. The servo motor develops a gyro rotation rate such that the mechanically generated gyroscopic momentum wheel precessional torque balances the acceleration torque. As a result, the servo motor angular rate becomes proportional to the input acceleration (in the integral sense), and the servo motor shaft angle equals the integrated acceleration. A shaft angle encoder is typically utilized as part of this device to digitally output fixed increments of shaft angle rotation, hence, fixed increments of integrated acceleration.

Because the gyro accelerometer does not depend on precision electrical rebalance principles to generate its output signal, its scale factor accuracy is not dependent on the electronic scale factor accuracy limitations present in the electrically servoed accelerometer (whose scale factor accuracy is determined by the stability of the electrical pulse generator and electromagnetic torque generator).

A disadvantage for the gyro accelerometer in strapdown applications is the fact that the gyro also senses rotation rates, which must be removed in the system computer based on independent system gyro measurements. Another disadvantage is its complexity and cost.

Due to its extremely good scale factor accuracy, the gyro accelerometer is used in high accuracy ballistic missile applications where large velocity changes must be precisely measured.

# TUNED ROTOR GYRO CONCEPT

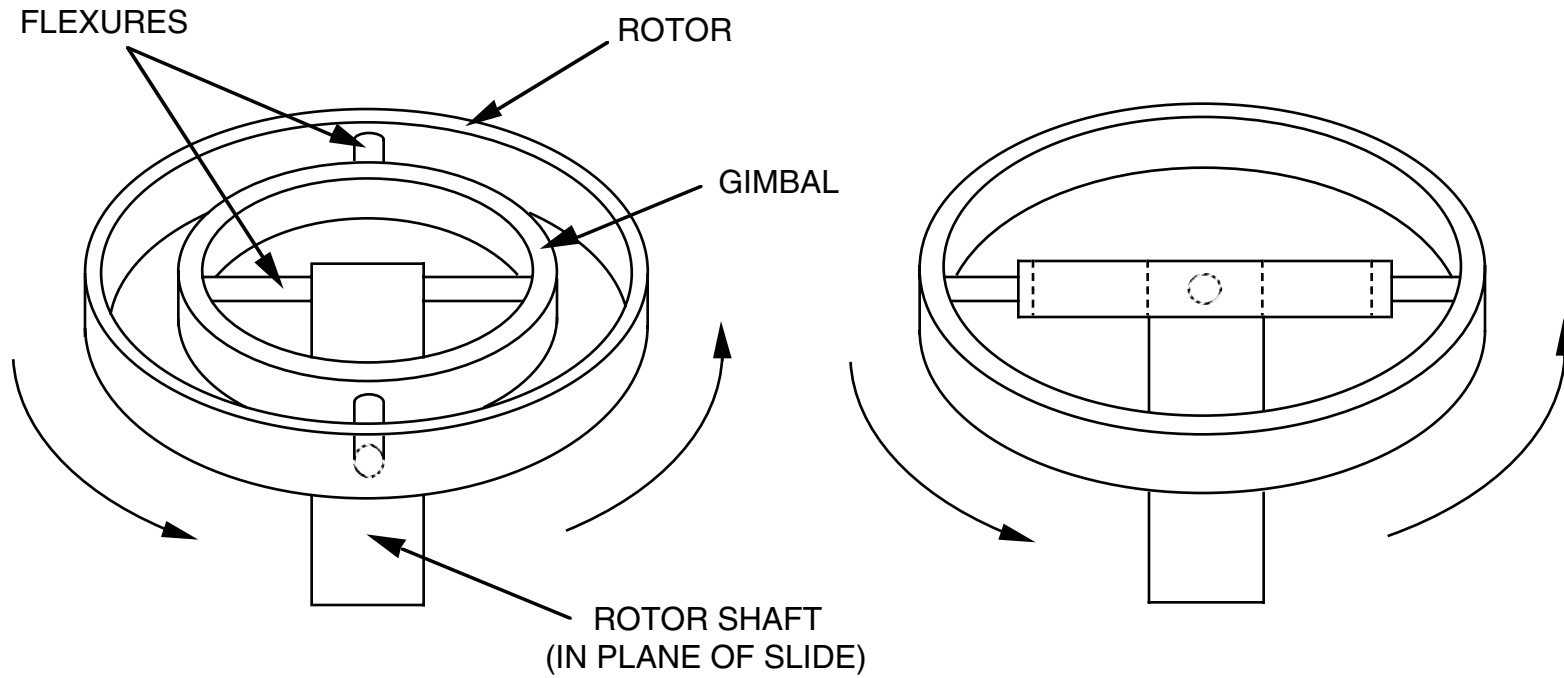


- TWO AXIS SENSOR
- DUAL PICKOFFS SENSE ANGLES BETWEEN GYRO ROTOR SPIN AXIS AND GYRO CASE
- DUAL ELECTRICAL TORQUE GENERATORS APPLY TORQUE TO ROTOR PERPENDICULAR TO SPIN AXIS

## **TUNED ROTOR GYRO CONCEPT**

The tuned rotor gyro consists of a momentum wheel (rotor) connected by a flexible gimbal to a case-fixed synchronous-hysteresis ball-bearing spinmotor drive shaft. The gimbal is attached to the motor and rotor through members that are torsionally flexible but laterally rigid. A two-axis pickoff is included that measures the angular deviation of the rotor (in two axes) relative to the case (to which the motor is attached). Also included is a two-axis permanent magnet torque generator assembly that allows the rotor to be torqued relative to the case on current command. The torquer magnets are attached to the rotor, and the torquer coils are attached to the gyro case.

## ROTOR ASSEMBLY DYNAMICS



- GIMBAL VIBRATES BETWEEN PLANE NORMAL TO ROTOR SHAFT AND ROTOR PLANE AT TWICE SPIN FREQUENCY (FOR OFF-NULL PICKOFF)
- DYNAMIC REACTION OF SPINNING GIMBAL ON ROTOR ACTS AS AN INVERSE SPRING TO CANCEL SPRING EFFECT OF FLEXURES (TUNING)
- COMPENSATES FLEXURE SUSPENSION BIAS ERRORS CAUSED BY OFF-NULL PICKOFF OPERATION AND PICKOFF NULL MOVEMENT

## ROTOR ASSEMBLY DYNAMICS

The key design feature of the tuned rotor gyro is the means by which it contains the reference momentum (spinning mass) within the case without introducing spurious torques in the process. Spurious momentum wheel torques in spinning mass gyros produce unwanted (and unknown) precessional rates that cannot be distinguished from the effect of real input rates to the gyro. As a result, such torques constitute the source of gyro bias errors and must be minimized to achieve a high performance instrument design.

For the tuned-rotor, the method of containing the momentum without introducing error torques is linked to the dynamic effect of the flexible gimbal attachment between the rotor and the motor. Geometrical reasoning reveals that when the rotor is spinning at an angle that deviates from the motor-shaft direction, the gimbal is driven into a cyclic oscillation in and out of the rotor plane at twice the rotor frequency. Dynamic analysis shows that the reaction torque on the rotor to sustain this motion has a systematic component along the angular-deviation vector that is proportional to the angular displacement, but which acts as a spring with a negative spring constant. The flexible pivot between the rotor and the gimbal, on the other hand, provides a similar spring torque on the rotor, but of opposite sign. Hence, to free the rotor from systematic torques associated with the angular displacement, it is only necessary to set the gimbal pivot springs such that their effect cancels the inverse spring effect of the gimbal. The result (tuning) is a rotor suspension that is insensitive to angular movement of the case.

The tuned-rotor gyro was originally developed as a two-axis platform gyro. In such applications, the gyro pickoff controls the platform gimbal torque motors (in two axes) to maintain gyro null, hence, force the platform to maintain alignment with the gyro angular momentum vector. Platform rotation rates are generated by torquing the gyro (in two-axes) at the desired platform rotation rates based on INS computer command. Note that two tuned-rotor gyros provide the necessary three-axis output (plus a redundant output channel) for gimballed platform stabilization.

Use of the tuned-rotor gyro in a strapdown mode parallels the technique used for the floated rate-integrating gyro. Exceptions are that damping must be provided electrically in the torque rebalance loop (as there is no fluid to provide damping), and the gyro must be captured in two axes simultaneously. The latter effect couples the two caging loops together due to the gyroscopic cross-axis reaction of the rotor to applied torques.

## **CONVENTIONAL MOMENTUM WHEEL GYRO ADVANTAGES**

- **LONG PRODUCTION HISTORY**
- **CAPABILITIES AND LIMITATIONS WELL UNDERSTOOD, PARTICULARLY IN GIMBALED APPLICATIONS**

## **CONVENTIONAL MOMENTUM WHEEL GYRO ADVANTAGES**

The principle advantages for conventional momentum wheel gyro (floated rate-integrating and tuned-rotor) in INS applications is that they have a long production history, have design maturity, and that their capabilities and limitations are well understood. This is particularly true in gimbaled INS applications where such instruments are the principle gyro type currently utilized.

# **BASIC LIMITATIONS OF CONVENTIONAL MOMENTUM WHEEL GYROS**

- **BANDWIDTH LIMITED (STRAPDOWN)**
- **VIBRATION RECTIFICATION ERRORS**
  - **ANISOINERTIA (STRAPDOWN)**
  - **SPIN-MOTOR DYNAMIC LAG (STRAPDOWN)**
  - **TORQUE-LOOP DYNAMIC HANG-OFF (STRAPDOWN)**
  - **ANISOELASTICITY**
- **G-SENSITIVITY**
- **TORQUE-LOOP SCALE FACTOR ERROR (STRAPDOWN)**
- **SPIN-MOTOR RELIABILITY**
- **MISALIGNMENT ERROR MECHANISMS (STRAPDOWN)**
  - **PICKOFF NULL MOVEMENT**
  - **TORQUE-LOOP DYNAMIC HANG-OFF**
  - **SPIN-MOTOR BEARING AND GIMBAL-PIVOT COMPLIANCE (SDOF RIG)**
- **QUESTIONABLE LONG TERM STABILITY (STRAPDOWN CALIBRATION REQUIREMENTS)**
- **LIMITED EXPERIENCE IN HIGH ACCURACY STRAPDOWN APPLICATIONS**

## BASIC LIMITATIONS OF CONVENTIONAL MOMENTUM WHEEL GYROS

On the other hand, conventional momentum wheel gyros contain several disadvantages, particularly in strapdown applications.

Because of their operation through an electrical torque-rebalance loop, conventional torque-rebalance momentum wheel gyros are bandwidth limited. Consequently, they can only measure aircraft angular rates with frequency content up to the bandwidth limit (e.g., 80 Hz). High frequency angular rates (due to vibration for example), if substantial in amplitude, could generate coning motion which would go undetected with these gyros.

Several vibration rectification error effects exist with conventional momentum wheel gyros that produce error torques on the rotor, hence, a false precessional rate (or bias). The anisoinertia effect is caused by additional spinning proof mass angular momentum introduced in the gyro due to the angular rate of the gyro case itself (Note: The spin motor angular rate is controlled relative to the case; the gyro angular momentum is based on angular rate relative to non-rotating inertial space). The additional momentum equals the product of the case angular rate with the gyro rotor assembly inertia. The additional torque needed to precess this momentum equals the momentum times the case rotational rate in the other axis. Hence, the net anisoinertia effect is proportional to the product of the gyro input and output axis rates. Angular vibrations which produce in-phase oscillations of these inputs, thereby generate systematic gyro bias error.

An additional effect in strapdown applications similar to anisoinertia is the effect of spin-motor servo dynamic lag. Under angular accelerations about the gyro spin axis, the rotor spin-motor servo adjusts the rotor speed relative to the gyro case. Due to the finite bandwidth of the spin-motor drive, a rotor speed error develops which causes a change in the gyro momentum. The scale factor of the gyro is, therefore, changed. If an input rate is applied under this condition, an uncertainty in the precessional torque develops equal to the product of the input rate with the momentum error. Since the momentum error is proportional to the rate along the spin-axis (modified by the spin-motor dynamics), the net error effect is proportional to the product of rates about the input and spin axes, with the dynamic phase angle between the two determining maximum gyro error sensitivity.

Torque-loop dynamic error refers to the finite bandwidth of conventional gyros in strapdown applications, hence, the inability to hold a precise pickoff null under dynamic input rate conditions. The result is a pickoff error which is a misalignment of the rotor spin axis relative to the case input axis. As a result, the gyro senses a component of rate from the non-input axis proportional to the hang-off angle, thereby generating an erroneous output. The output error becomes proportional to the product of input and output rates including a bandwidth phase angle factor.

Anisoelasticity refers to the mechanical compliance of the gyro rotor assembly under applied G-loading. Ideally, the gyro should have equal compliance along all axes such that an acceleration causes the rotor CG to deflect (due to mechanical bending of the

## **BASIC LIMITATIONS OF CONVENTIONAL MOMENTUM WHEEL GYROS (CONTINUED)**

structure) along the acceleration vector. If the gyro has unequal compliance along the cardinal axes, an acceleration vector between cardinal axes will produce a CG movement off the line of action of the acceleration. As a result, an inertial reaction is developed about the rotor center of suspension equal to the rotor mass times the CG lateral offset times the input acceleration. Since the CG offset is proportional to the input acceleration, the net torque error is proportional to the product of acceleration components. Anisolelasticity can be a significant error source in both gimbale and strapdown applications.

For the floated rate-integrating gyro, another potentially serious error mechanism in strapdown applications is the effect of suspension axis bearing loads under angular rates about the output axis. Such loads are the inevitable result of output axis rates producing gyroscopic reaction torque needed for rotor precession. The sensitivity to input axis rates under this condition may be questionable.

The error mechanisms discussed above are proportional to the products of rotation rate or acceleration components. Consequently, these effects can rectify under cyclic angular rate or linear acceleration motion (i.e., under vibration), generating serious systematic (constant) output errors.

G-sensitivity is an error source which exists in all momentum wheel instruments. Some G-sensitive effects have been described in the previous discussion. The dominant G-sensitivity error is mass unbalance caused by manufacturing tolerances. Mass unbalance produces a fictitious torque on the gyro rotor under acceleration proportional to the acceleration input. Such effects are present in both gimbale and strapdown momentum wheel gyros.

Gyro torquer input scale factor errors generate gyro errors proportional to input rate for momentum wheel torqued instruments. In strapdown applications, this can be a particularly serious error mechanism in maneuvering environments.

Conventional momentum wheel gyros contain spin-motors with associated mechanical wear-out mechanisms. Overall system reliability is thereby impacted.

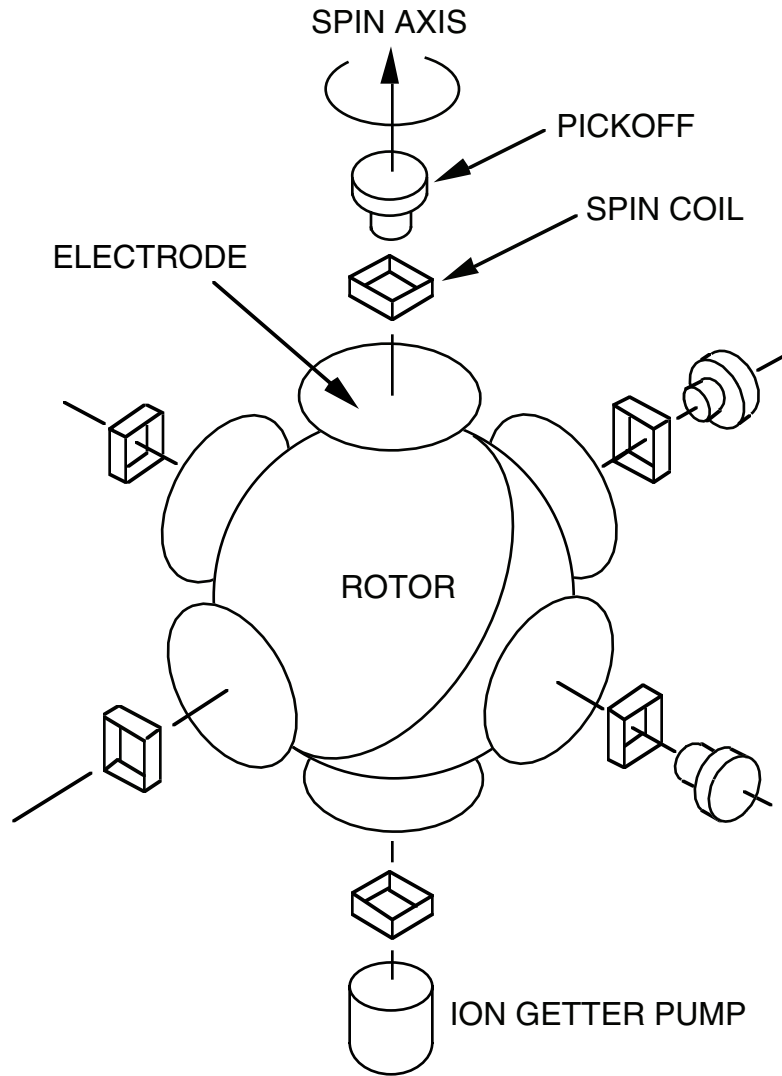
In strapdown applications, conventional momentum wheel gyros have several misalignment (cross-coupling) error mechanisms which produce misalignment errors that impact overall system performance under aircraft maneuvers. These include torque-loop dynamic hang-off error (discussed previously), mechanical (or electrical) movement of the pickoff null which causes the gyro torque-loop to capture the rotor at a misaligned attitude relative to the case, and in the case of the floated rate-integrating-gyro, spin-motor bearing and gimbal-pivot compliance which produce misalignment of the rotor relative to the case.

## **BASIC LIMITATIONS OF CONVENTIONAL MOMENTUM WHEEL GYROS (CONTINUED)**

For strapdown applications, conventional strapdown gyros have questionable long-term stability. Since it is difficult (if not impossible) to calibrate a strapdown INS in a vehicle without removing the system to a test area (where a rotation table is available), it is questionable whether conventional momentum wheel gyros can be utilized successfully in high accuracy strapdown INS applications.

Finally, in spite of the wealth of experience in high accuracy gimbaled INS and low performance strapdown missile guidance applications, there is only a limited amount of experience in the application of conventional momentum wheel gyros to high accuracy strapdown INS usage. Hence, a significant element of risk still exists for these well-developed instruments in strapdown high accuracy applications.

# ELECTROSTATIC GYRO CONCEPT



- SPINNING ROTOR IS ELECTROSTATICALLY SUSPENDED IN EVACUATED CAVITY BY ELECTRODES FIXED TO GYRO CASE
- ROTOR INITIALLY SPUN-UP BY SPIN COILS
- PICKOFFS SENSE TOTAL ATTITUDE OF CASE RELATIVE TO ROTOR SPIN AXIS
- TWO-AXIS ATTITUDE OUTPUT
- NO PRECISION ELECTRICAL TORQUE GENERATOR

## **ELECTROSTATIC GYRO CONCEPT**

The electrostatic gyro (ESG) is a momentum wheel gyro in which a spherical rotor is suspended in a vacuum (within the gyro case) by an electrostatic field generated by case-fixed electrodes. Hence, there is no physical contact with the rotor assembly. Pickoffs on the case sense the orientation of the case relative to the rotor. The gyro has a two-axis output, and contains no precision electrical torque generator. The rotor is initially spun-up by spin-coils in the case that generate a rotating electrostatic field across the rotor. Once spinning, sustained spin-motor drive is generally not needed.

Some mechanizations of the electrostatic-gyro pickoff have used optical detectors that sense scribe marks etched on the rotor (as in the slide). For, such an approach, the rotor is a hollow shell, 1 to 2 inches in diameter. Alternatively, a small solid rotor (typically 1 centimeter in diameter) can be used with a radially offset mass. The resulting modulation in the suspension field (due to the mass unbalance) is used as a measure of relative case/rotor orientation. Each of these approaches is being used for gimbale application.

The electrostatic gyro can be used only as an attitude gyro (there is no precision torque generator for the device), hence, in strapdown applications where large angular motion is common, the accuracy of the pickoff (which must sense total attitude) is a key performance parameter. In this respect, the gyro differs from the rate integrating and tuned rotor instruments that are operated with the pickoff angle held at null for strapdown applications.

In gimbale applications, the ESG pickoffs drive the platform servo motors, hence, are maintained at null. Because the ESGs have no precision torque generators, ESG platforms are generally operated in the space stable mode.

## **ESG ADVANTAGES**

- **HIGHLY STABLE ERROR CHARACTERISTICS**
- **NO INHERENT DYNAMIC ERRORS**  
**(e.g., BANDWIDTH, ANISOINERTIA)**
- **NO TORQUE GENERATOR SCALE FACTOR ERRORS**
- **NO SPIN-MOTOR BEARING WEAR-OUT (HIGH-RELIABILITY)**

## **ESG ADVANTAGES**

For a specified case orientation relative to the rotor (as in gimbale applications), ESG errors can be remarkably stable, hence, predictable and compensatable.

Due to the open-loop (no torque) operation of the device, there are no inherent dynamic errors such as produced by anisoinertia and bandwidth limits in the torqued gyro concepts. For similar reasons, there is no torquer error with ESGs.

One of the principle advantages of the ESG compared to the other spinning-mass instruments is the elimination of mechanical friction producing mechanisms (i.e., spinmotor bearings) and associated reliability problems.

## **BASIC LIMITATIONS OF ESG**

- **NO RATE SIGNAL OUTPUT (STRAPDOWN)**
- **G-SENSITIVITY**
- **BIAS SENSITIVITY TO ROTOR/CASE ORIENTATION (STRAPDOWN)**
- **PICKOFF ANGLE MISALIGNMENT ERROR (STRAPDOWN WIDE DYNAMIC RANGE REQUIREMENT)**
- **SPIN-MOTOR RUN-UP REACTION TIME LIMIT**
- **SUSPENSION VOLTAGE KEY ELEMENT IN GYRO RELIABILITY CHAIN**

## BASIC LIMITATIONS OF ESG

In a strapdown application, the ESG is operated as an attitude gyro, hence, has no natural body rate output. In this respect, the ESG lacks a capability present in the other strapdown gyros discussed.

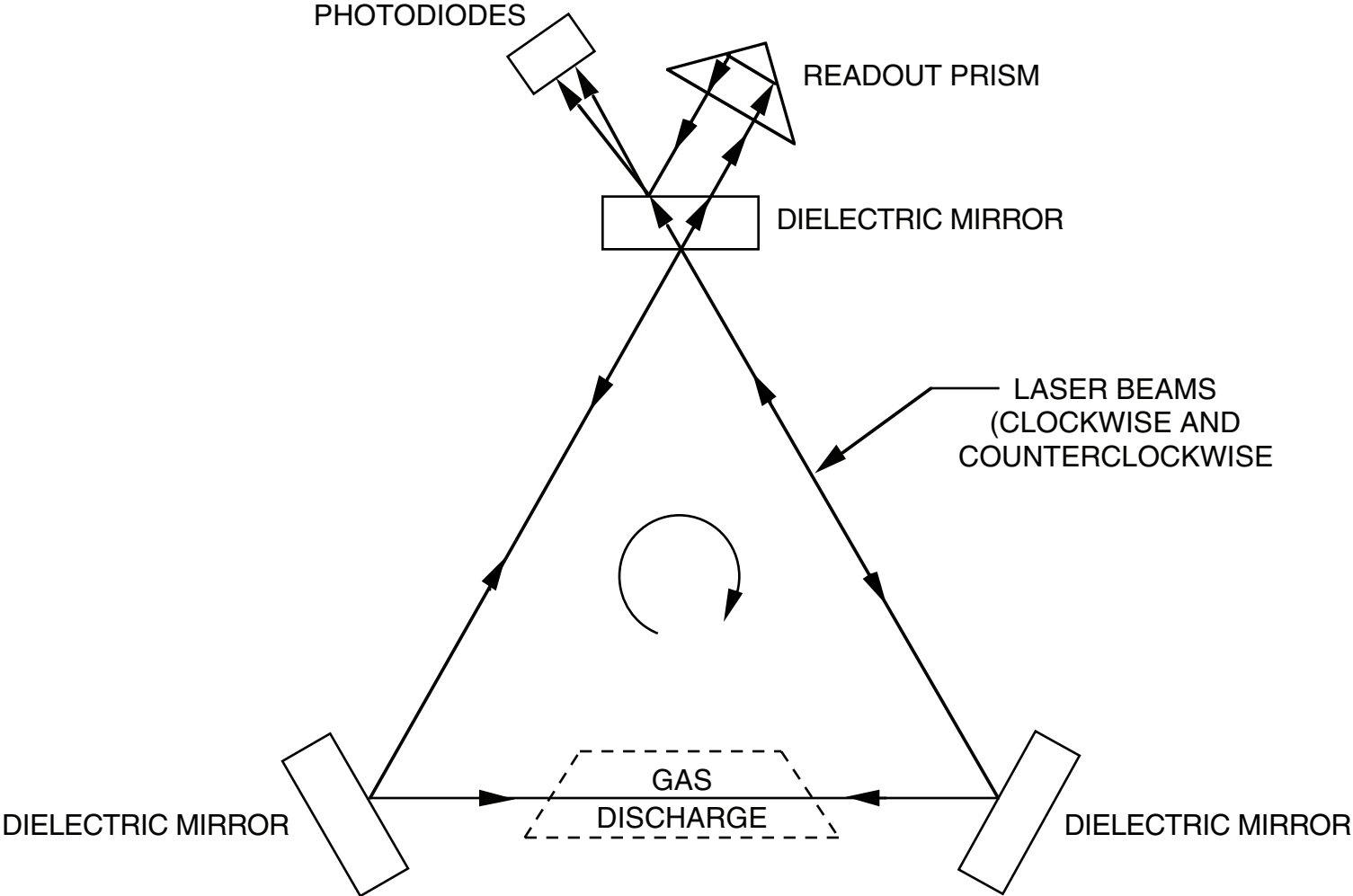
The ESG has G-sensitivity (mass unbalance bias error effects) due to rotor compliance, gyro manufacturing tolerances, and thermal expansion effects. Moreover, the G-sensitive errors (as well as G-insensitive errors) vary with rotor/case orientation. To overcome this latter difficulty, a turntable assembly has been incorporated in some strapdown applications, on which the inertial sensors are mounted. The turntable is rotated at a known rate relative to the system chassis, typically about the user vehicle yaw axis. This results in an averaging of the case-correlated bias-error effects such that the overall navigation system accuracy is improved. The penalty is the added cost and complexity of the turntable assembly.

For strapdown applications, the ESG pickoff angle measurement becomes a major part of the device performance in the system. The required wide angle readout capability for the device makes it difficult to simultaneously achieve high readout accuracy. Pickoff angle readout error creates misalignment error effects in the strapdown acceleration transformation operation.

Due to sensitivity of ESG performance to rotor heating, spin-motor run-up times for the ESG are generally slower than for most gyros (to reduce heating the rotor through spin-coil field eddy current effects). Additionally, the free suspension of the ESG rotor creates a potential reliability problem (rotor destruction) if the suspension voltage is inadvertently removed prior to gyro despin. It should be noted that some conventional gyros also require a despin operation before the gyro may be physically rotated, due to potential damage created by rotor suspension gyroscopic bearing loads under rapid rotations.

Due to difficulties in achieving a cost competitive strapdown ESG system design configuration, ESG manufacturers today have largely abandoned strapdown ESG applications, and have directed the technology exclusively toward very high accuracy gimballed systems.

# LASER GYRO OPERATING ELEMENTS



## LASER GYRO OPERATING ELEMENTS

Unlike gyros that utilize rotating mass for angular-measurement reference, the laser gyro operating principle is based on the relativistic properties of light. The slide depicts the basic operating elements in a laser gyro; a closed optical cavity containing two beams of correlated (single-frequency) light. The beams travel continuously between the reflecting surfaces of the cavity in a closed optical path; one beam travels in the clockwise direction, the other in the counter clockwise direction, each occupying the same physical space in the cavity. The light beams are generated from the lasing action of a helium-neon gas discharge within the optical cavity. The reflecting surfaces are dielectric mirrors designed to selectively reflect the frequency associated with the particular helium-neon transition being used.

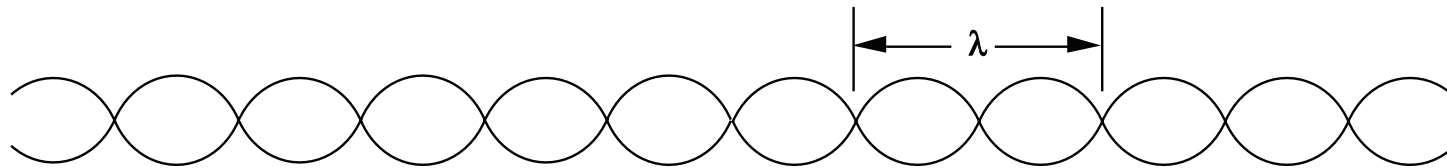
# WAVES



TRAVELING WAVE A AT FREQUENCY  $F$  →



← TRAVELING WAVE B AT FREQUENCY  $F$



$A + B =$  STANDING WAVE

**WHAT HAPPENS TO THE STANDING WAVE IF  
A AND B ARE AT DIFFERENT FREQUENCIES ?**

**WHAT WILL BE THE A AND B STANDING WAVE COMPONENT  
FREQUENCIES IF WE MEASURE THEM WHILE TRANSLATING  
TO THE RIGHT OR LEFT ?**

## WAVES

Consider two equal amplitude traveling waves A and B of the same frequency  $F$  and wavelength  $\lambda$ , but traveling in opposite directions. If the two waves are superimposed on one another (added together) they will form a stationary standing wave with nodes of minimum amplitude and anti-nodes of maximum amplitude. The distance between nodes (or anti-nodes) would be half the wavelength of the individual traveling waves.

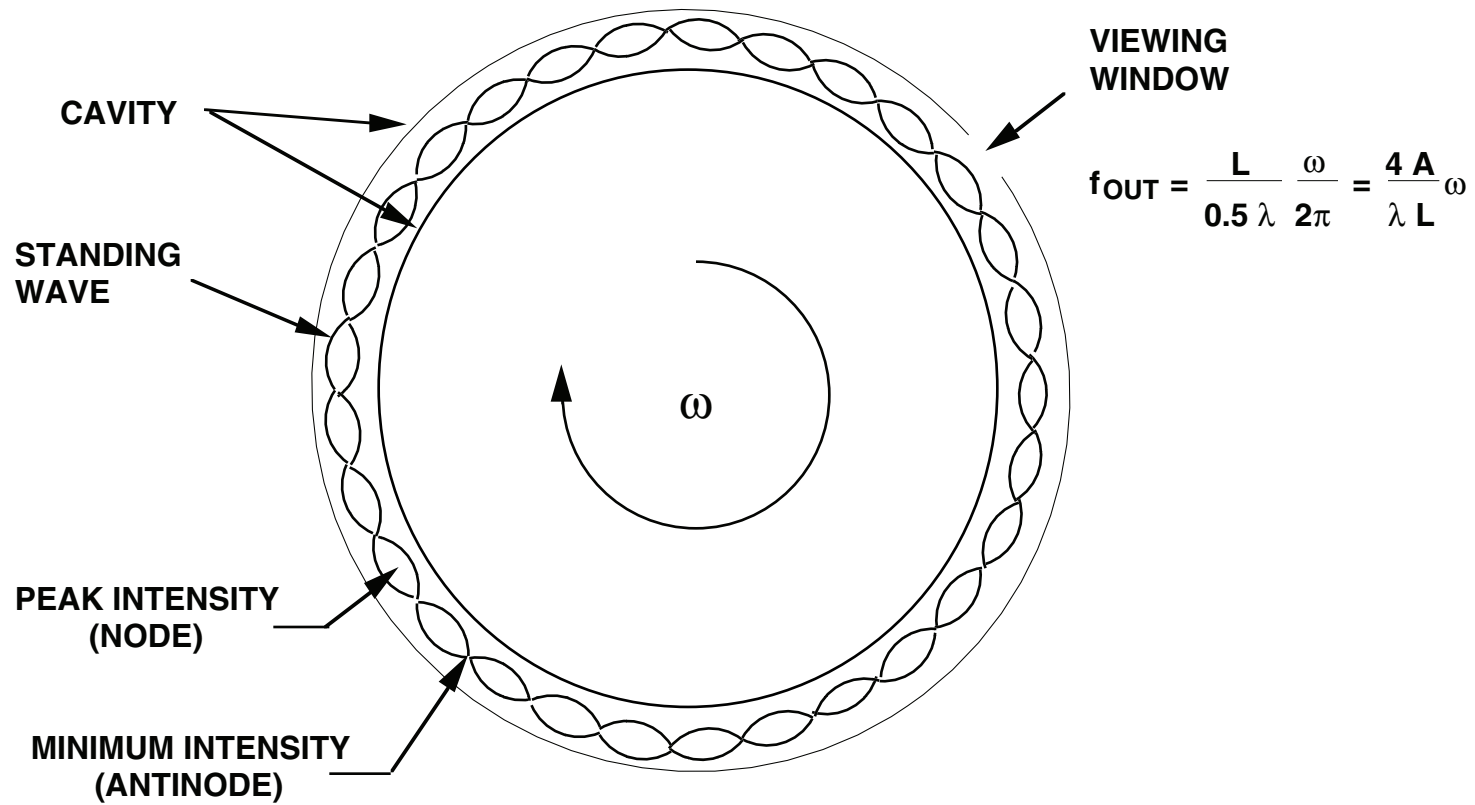
What would happen to the standing wave if the frequency of wave A is decreased relative to the frequency of wave B? The standing wave will then no longer be stationary, but would traverse to the left at a rate proportional to the frequency difference between waves A and B. The opposite would be true for the opposite frequency shift.

Returning to the original setup in which the A and B wave frequencies are originally the same (and the standing wave is fixed), what if we then move at a velocity to the right along the standing wave. What would we then measure for the A and B wave individual frequencies? The measured wave A frequency would be decreased and the B wave frequency increased by the same amount. The frequency shift would be proportional to the velocity change along the standing wave.

The two effects noted above are actually the same, a velocity change relative to the standing wave will produce an apparent shift in traveling wave frequencies in exactly the same way as a shift in traveling wave frequencies will produce apparent movement of the standing wave. This is because velocity relative to the standing wave is relative; it is produced by movement of the observer relative to a stationary standing wave or by motion of the standing wave relative to a stationary observer.

As described in the previous chart, a ring laser gyro creates superimposed clockwise and counterclockwise circularly traveling light waves within the gyro. The above general discussion of oppositely directed waves is useful for explaining the operation of a laser gyro.

# LASER GYRO STANDING WAVE OPERATING PRINCIPLE



## LASER GYRO STANDING WAVE OPERATING PRINCIPLE

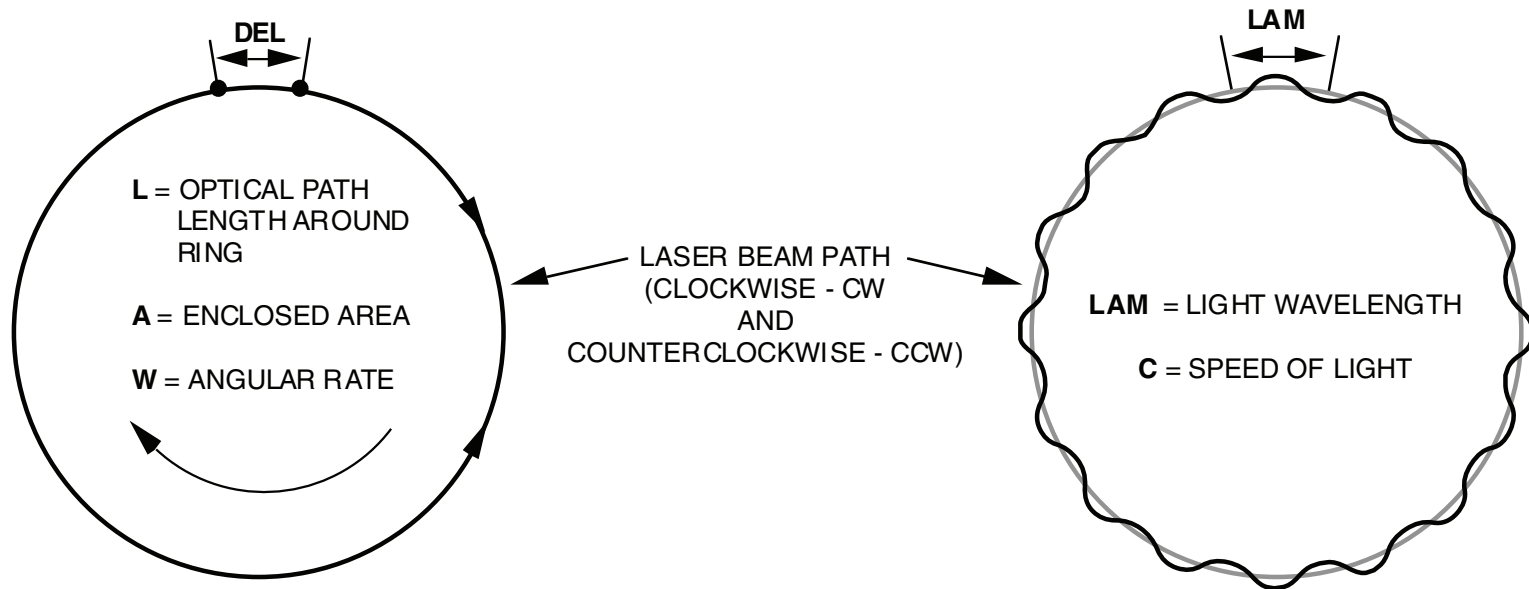
The chart explains the operation of the ring laser gyro based on the standing wave principles discussion for the previous chart. As discussed on page 267, a laser gyro generates superimposed clockwise and counter-clockwise laser beams. For a well-designed and manufactured gyro, the light beams are independent from one another and have the same frequency relative to non-rotating inertial space. As a result, the optical superposition of the two beams sets up a continuous standing wave of ring laser light along the gyro beam path (as in all lasers; linear and ring type). The length of each element of the standing wave (between antinodes) is one half the wave length ( $\lambda$ ) of the clockwise and counterclockwise light beams.

The fundamental principle of operation of the laser gyro is that the standing wave remains fixed relative to non-rotating space. As such, if the standing wave is viewed from the cavity as it rotates (through the “viewing window”), the nodes (optical peak intensity points) and antinodes (minimum optical intensity points) will pass by the viewing window. The frequency of passage of the nodes (or antinodes) by the window is the ring laser gyro output frequency  $f_{OUT}$ . The output frequency equals the optical path length (L) divided by the half wavelength, multiplied by the angular rate in cycles per second ( $\omega / 2 \pi$  where  $\omega$  is the angular rate in radians per second). Mathematical manipulation converts this equation to the classical laser gyro output frequency formula ( $4 A / \lambda L$ )  $\omega$  where A is the area enclosed by the laser beam.

From this explanation of the gyro operation it should be apparent that the laser gyro is an angular-rate-integrating instrument. The basic output signal represents the angular movement of the cavity relative to the fixed standing wave. The angular change signal is extracted as fixed incremental angle changes, one for each movement of the cavity past one maximum/minimum standing wave element, the exact form of the output needed for a strapdown inertial navigation system. The fine resolution of the laser gyro is due to the smallness of the laser wavelength (0.63 microns or 0.315 microns between standing wave nodes), hence, the large number of standing wave elements around the cavity. It should be obvious that larger gyros have finer resolution (angle between standing wave elements) because of the greater number of standing wave elements at the same node spacing around the cavity).

The laser gyro output is generated by allowing a small percentage of the laser radiation to escape through one of the mirrors (see page 266). A prism is typically used to reflect one of the beams such that it crosses the other in almost the same direction at a small angle (wedge angle). Due to the finite width of the beams, the effect of the wedge angle is to generate an optical fringe pattern in the readout zone. The fringe pattern represents a magnified image of the standing wave within the gyro. Digital integrated-rate-increment pulses are generated from the laser gyro by two photodiodes mounted in the fringe area (see page 266) and spaced 90 degrees apart (in fringe space). As the fringes pass by the diodes, sinusoidal output signals are generated, with each cycle of a sine wave corresponding to the movement of one fringe over the diodes. By observing which diode output is leading the other (by 90 degrees), the direction of rotation is determined. Simple digital-pulse triggering and direction logic operating on the photodiode outputs convert the sinusoidal signals to digital pulses for strapdown system computer input.

# LASER GYRO FREQUENCY SHIFT OPERATING PRINCIPLE



$$DEL = \frac{2A}{C} W$$

OPTICAL PATHLENGTH  
CHANGE CAUSED BY  
ANGULAR ROTATION

$$FCW = \frac{C}{LAM} - \frac{C DEL}{LAM L}$$

$$FCCW = \frac{C}{LAM} + \frac{C DEL}{LAM L}$$

BEAM FREQUENCY  
TO SUSTAIN INTEGRAL  
NUMBER OF  
WAVELENGTHS  
AROUND OPTICAL  
PATH

---


$$FCCW - FCW = \frac{2 C DEL}{LAM L} = \boxed{\text{BEAM FREQUENCY DIFFERENCE (OUTPUT SIGNAL)} = \frac{4 A}{LAM L} W}$$

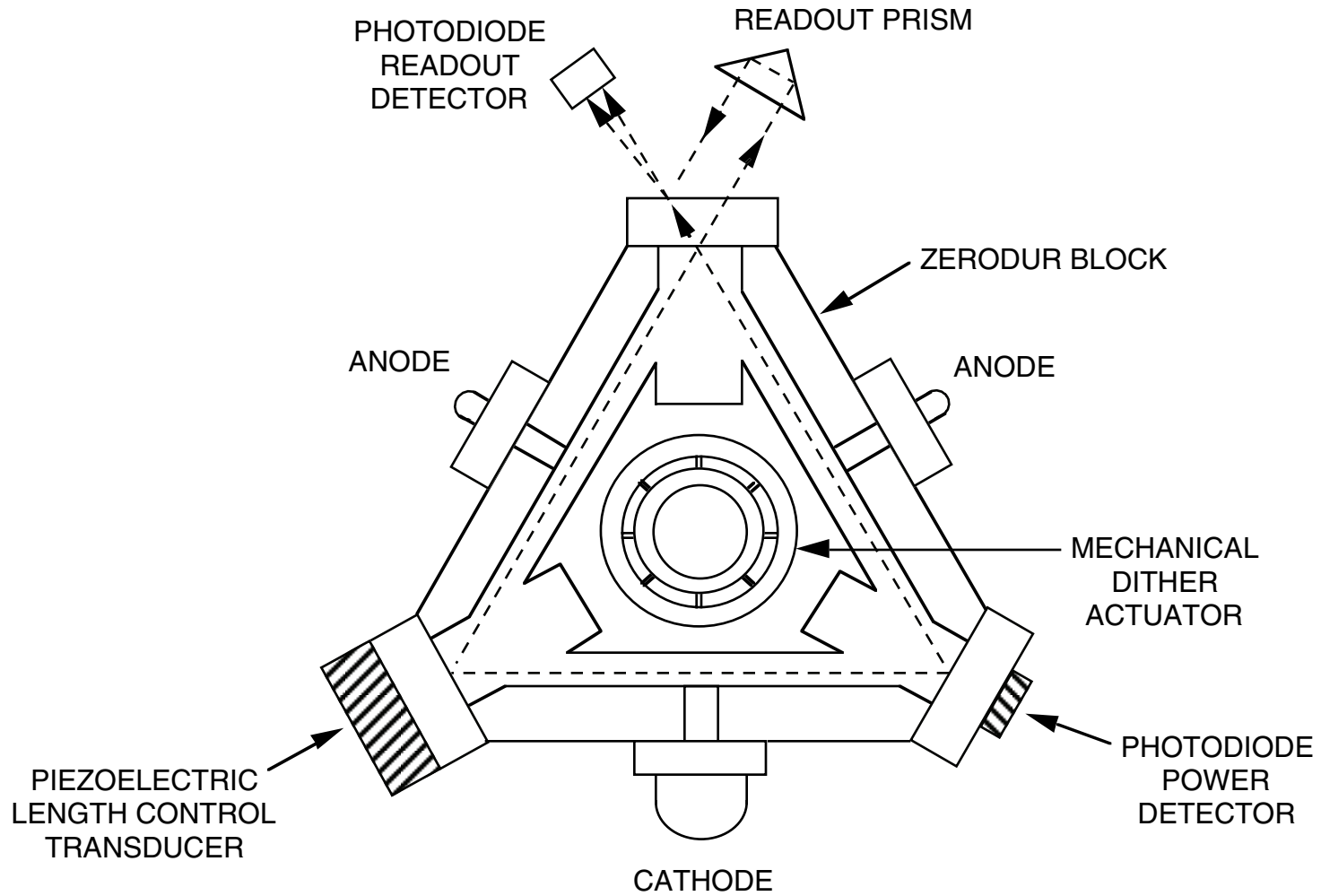
## LASER GYRO FREQUENCY SHIFT OPERATING PRINCIPLE

This chart explains the operation of the laser gyro based on the page 267A - 267B discussion of frequency shift observed for movement relative to oppositely directed waves that have the same frequency under zero movement.

The chart illustrates two beams of oppositely directed light traversing a closed optical path (contained within a cavity). Consider the effect of cavity rotation to an observer rotating with the cavity. Relative to the observer, it takes longer for a wave of light to traverse the distance around the optical path in the direction of rotation than in the direction opposite to the rotation. Due to the constancy of the speed of light, this effect is interpreted by the observer as a lengthening of the net optical path in the direction of rotation, and a shortening of the path length in the opposite direction. The optical path length change is directly proportional to the area enclosed by the laser and the angular rate of the cavity, and inversely proportional to the speed of light. Note: The differential path length shift effect is also the basis for the fiber optic gyro (FOG) concept described on pages 292 - 292A).

Because a fixed integral number of light waves must exist around the path at any instant of time (the beam in a laser is coherent, continuous, and for the ring laser, closes on itself), the path-length shift must also be accompanied by a frequency shift in the opposite sense. The frequency difference between the two beams thereby becomes a measure of rotation-rate. The slide shows that the frequency difference is directly proportional to the area enclosed by the laser beam and the input angular rotation rate, and inversely proportional to the laser wavelength and the perimeter (length) around the optical cavity (the same formula as on page 267C). The frequency shift is the identical effect noted on pages 267A-267B for movement past a standing wave, in this case the standing wave within the laser gyro created by superposition of the clockwise and counter clockwise traveling light beams. Note: The frequency shift effect is not generated in a fiber optic gyro (pages 292 - 292A) because the light source in a FOG for both clockwise and counter-clockwise beams originate from the same source outside the circular light path.

# REPRESENTATIVE LASER GYRO BLOCK ASSEMBLY



## REPRESENTATIVE LASER GYRO BLOCK ASSEMBLY

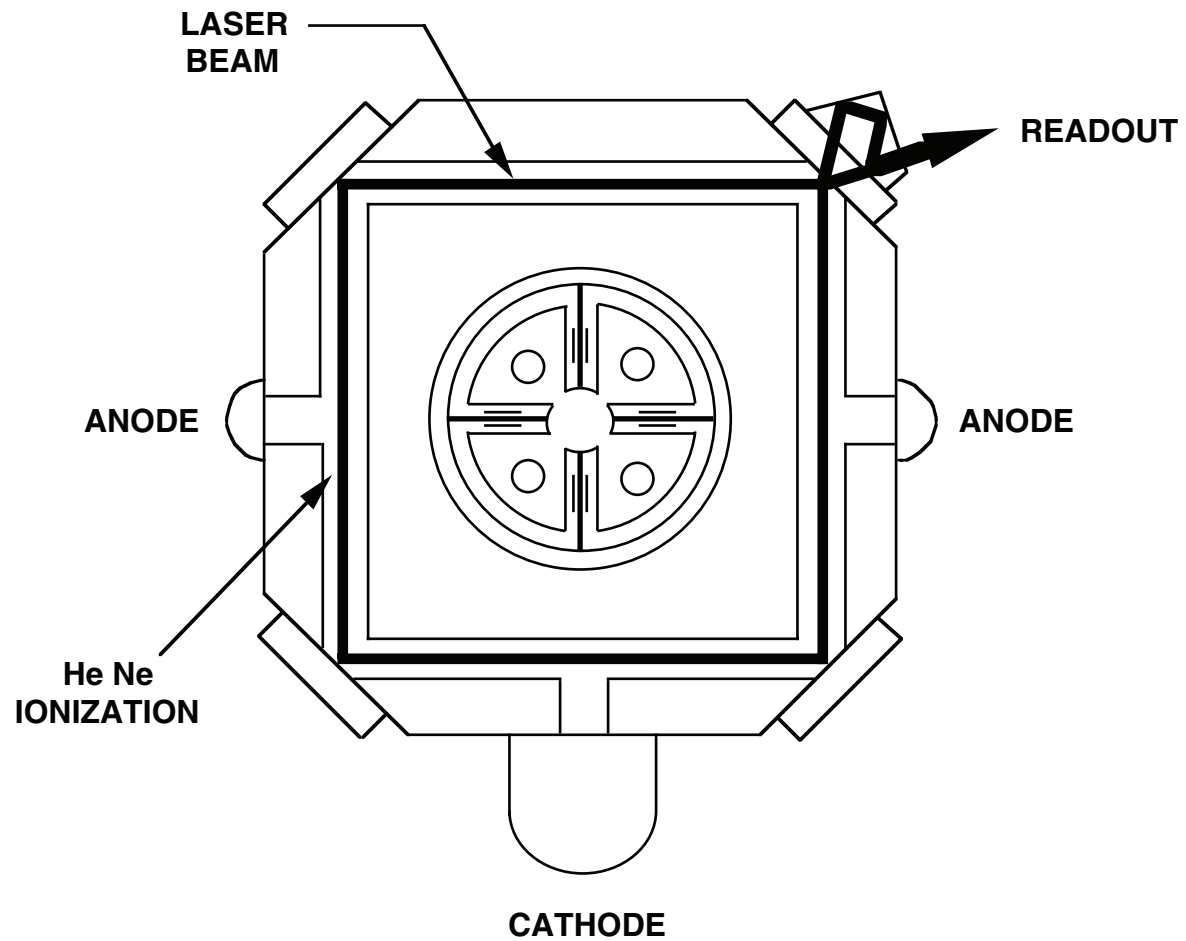
The accuracy of the laser gyro depends on the manner in which the laser beams are affected by the influences of the lasing cavity. A key requirement in this regard is that the average of the path lengths around the lasing cavity for the clockwise and counterclockwise beams be constant and equal to the value for peak average lasing power.

To achieve a high degree of path-length stability, the laser gyro optical cavity is typically constructed of Zerodur, a ceramic glass material which has an extremely low coefficient of thermal expansion. The slide illustrates a typical laser gyro mechanization concept. A Zerodur structure is used to contain the helium-neon gas, with the lasing mirrors and electrodes forming the seals. High voltage applied across the electrodes (one cathode and two anodes) ionizes the helium-neon gas mixture, thereby providing the required laser pumping action.

A piezoelectric transducer mounted on one of the mirror substrates is typically used to actively control the average path length of the cavity (Note: Many ring laser gyro designs utilize two piezoelectric crystals to maintain beam location symmetry in the cavity relative to the gyro axis of symmetry. Beam symmetry around the axis of symmetry provides improved accuracy). The control signal for the piezoelectric transducer is proportional to the deviation from the peak average power in the laser beams; hence, the control loop is designed to maintain a path length that produces peak average lasing power. The laser beam power is detected by a photodiode mounted on one of the laser mirrors that senses a small percentage of the radiation from the clockwise and counter clockwise beams. To enable measurement of the laser beam power variation from the power peak, a high frequency modulation signal (e.g. 1 KHz) is injected into the path length control loop to create a high frequency small amplitude oscillation of the beam path. Use of a phase sensitive demodulator on the photodiode output tuned to the injected modulation signal frequency provides the required signal for the path length control loop proportional to the deviation of the average lasing power from the power peak.

The mechanical dither actuator in the slide is a mechanical rotary spring that suspends the laser block from a centerpost attached to the gyro case. Piezoelectric transducers on the springs provide the drive mechanism that allows the block to be mechanically vibrated in angle about its input axis relative to the gyro case. The mechanical dither operation is used to compensate for the effect of lock-in, an error mechanism in laser gyros that must be circumvented if accurate INS quality performance is to be attained. The lock-in effect is described in a subsequent slide.

# SQUARE LASER GYRO CONFIGURATION



## **SQUARE LASER GYRO CONFIGURATION**

The slide illustrates the configuration of a four-sided ring laser gyro containing four mirrors to enclose the laser ring (as contrasted with the three-sided three-mirror configuration depicted in the previous chart). The essential tradeoffs involved with regard to the triangular versus the square geometry are discussed subsequently under Laser Gyro Design Tradeoffs And Performance Characteristics. From a functional standpoint both the triangular and square configurations are equivalent.

## **LASER GYRO ADVANTAGES**

- **IDEALLY SUITED FOR STRAPDOWN APPLICATIONS**
- **INFINITE BANDWIDTH**
- **NO VIBRATION RECTIFICATION ERROR**
- **NO G-SENSITIVITY**
- **LOW SCALE FACTOR ERROR**
- **HIGH RELIABILITY - NO FRICTION PRODUCING MECHANICAL PARTS**
- **RAPID REACTION TIME**
- **HIGH ALIGNMENT ACCURACY**
- **OUTSTANDING LONG TERM STABILITY - ELIMINATES CALIBRATION REQUIREMENTS**
- **LOW COST**
- **LONG PRODUCTION HISTORY**

## LASER GYRO ADVANTAGES

The laser gyro is ideally suited for strapdown applications because of its natural digital pulse output and advantages compared to other strapdown gyro configurations.

The laser gyro has no bandwidth limitation (such as with conventional torque-rebalanced momentum wheel gyros). The vibration rectification and G-sensitive bias errors present in conventional gyros are absent in laser gyros. Because it has no friction producing mechanical parts (such as the spin-motor in a conventional gyro) the laser gyro has high reliability. Because there is no spin-motor to run up, and because of the stable performance characteristics of the device, the laser gyro has an extremely rapid reaction time; operational performance is achievable after the laser ignites.

Because of the direct mechanical linkage between the laser plane (sensing element) and the gyro mount, the laser gyro has excellent alignment stability. The scale factor accuracy of the device is also highly stable, with full linear performance achievable over the complete operating range of the highest performance military aircraft. The high alignment and scale factor accuracy of the laser gyro are key reasons why it is capable of accurate operation in a strapdown dynamic aircraft maneuvering environment.

The bias accuracy of the laser gyro is highly stable, another important requirement for strapdown applications where it is not convenient (or cost effective) to require scheduled removals of systems for the purpose of calibration.

Because of the simplicity of its construction, the laser gyro is relatively low cost in production. Low production cost coupled with high field usage reliability have provided unique life-cycle cost benefits for strapdown systems using the device.

Finally, the ring laser gyro now has a long production and field usage history in both commercial and military environments which reduces user risk in new applications.

## **LASER GYRO LIMITATIONS**

- **DIGITAL OUTPUT UNIQUE TO STRAPDOWN APPLICATIONS**
- **SIZE AND WEIGHT (ORIGINAL TECHNOLOGY)**
  - **NOT A PROBLEM FOR NEWER LASER GYRO TECHNOLOGY**

## LASER GYRO LIMITATIONS

The natural digital quantized output of the laser gyro that make it ideal for strapdown applications, make it difficult to be used in gimbaled applications where the gimbal servoes must operate on low noise continuous analog gyro output signals.

Probably the most significant technical limitation associated with laser gyros has been their relatively large size and weight compared with comparable performance mature gimbaled platform conventional gyros. For example, a typical path length for a triangular laser gyro for high performance strapdown INS usage is 4.2 inches on each side of the laser beam. As a result, the size of contemporary high performance strapdown systems utilizing laser gyros has been no smaller than contemporary gimbaled systems (even though no gimbaled platform is needed with the strapdown approach), and the strapdown system weight has typically been 30% heavier than the comparable gimbaled INS. Recent advances in laser gyro technology, however, now make it possible to achieve 1.0 nmph medium accuracy inertial navigation performance with gyros half this size. The net result has been a reduction of system weight to be equal to the comparable gimbaled system weight.

## **CONCLUSIONS**

- **SEVERAL INERTIAL SENSOR TYPES AVAILABLE TODAY FOR INERTIAL SYSTEM APPLICATIONS**
  - **CHOICE IS TRADEOFF OF PERFORMANCE REQUIREMENTS VERSUS COST, RELIABILITY, MAINTAINABILITY, POWER, WEIGHT, SIZE**
- **KEY TRADEOFF AREA – POTENTIAL ADVANTAGES PROJECTED FOR NEW INERTIAL SENSOR TECHNOLOGIES VERSUS KNOWN CAPABILITIES AND LIMITATIONS OF ESTABLISHED PRODUCTION TECHNOLOGY**

## CONCLUSIONS

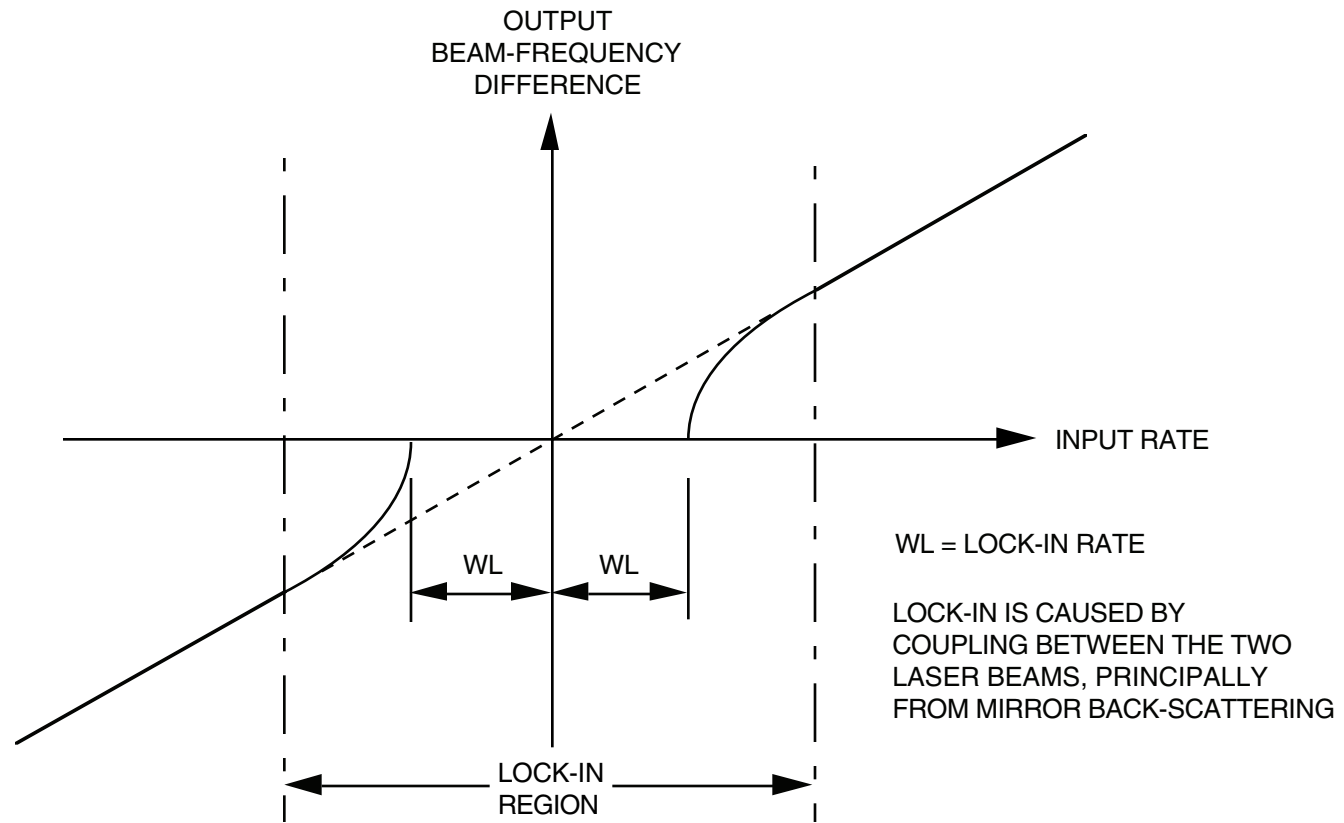
Several inertial sensors are available today for inertial system usage, each with advantages and limitations, depending on the area of application. The ultimate selection of a sensor to meet particular requirements can only be made after performing a careful tradeoff evaluation that assesses reliability, maintainability, cost, size, weight, and power factors as well as accuracy. One of the principle tradeoffs in the selection of an inertial sensor is the potential advantages projected for newer technology instruments just entering production versus the known capabilities and limitations of established production-inertial technology.

**LASER GYRO DESIGN TRADEOFFS  
AND PERFORMANCE CHARACTERISTICS**

## **LASER GYRO DESIGN TRADEOFFS AND PERFORMANCE CHARACTERISTICS**

Because of the current interest in this new uniquely strapdown instrument, the following discussion has been prepared to describe the general design tradeoffs and performance characteristics of laser gyros. Similar discussions regarding the other available sensors are contained in the Strapdown Inertial Navigation Lecture Notes in the reproduced AGARD papers on Strapdown Sensors and Advances In Strapdown Sensors.

# LASER GYRO LOCK-IN



## LASER GYRO LOCK-IN

The phenomenon of lock-in has historically been a most prominent error source in the laser gyro and the most difficult to handle. The means for compensating lock-in has been the principle factor determining the configuration and performance of laser gyros from different manufacturers.

The phenomenon of laser gyro lock-in arises because of imperfections in the lasing cavity, principally the mirrors, that produce backscattering from one laser beam into the other. The resulting coupling action tends to pull the frequencies of the two beams together at low rates producing a scale-factor error. For rates below a threshold known as the lock-in rate, the two beams lock together at the same frequency producing no output. The slide illustrates the effect of lock-in on the output of the laser gyro as a function of steady input rate.

The magnitude of the lock-in effect depends primarily on the quality of the mirrors. In general, lock-in rates on the order of 0.01 to 0.1 degrees-per-second are achievable with today's laser gyro technology (with 0.63 micron laser wavelength). Compared with 0.01 degree-per-hour navigation requirements, this is a serious error source that must be overcome.

A straight-forward and effective approach for overcoming lock-in, is mechanically dithering the laser block at high frequency through a stiff dither flexure suspension built into the gyro assembly. The dither rate amplitude and acceleration are designed so that the dwell time in the lock-in zone is short such that lock-in will never develop. The result is a gyro that has continuous resolution over the complete rate range. The residual effect of lock-in is a negligible scale factor nonlinearity due to the averaging of the gyro input rate across the lock-in region, and a small random error in the gyro output (random rate noise) that is introduced each time the block passes through lock-in (at twice the dither frequency).

By mounting the readout reflector prism and photodiodes on the gyro case (see previous slide entitled "Representative Laser Gyro Block Assembly"), a simple mechanism can be provided to remove the dither signal from the gyro output. The effect is most easily understood by reference to the standing wave concept for laser gyro operation. Recall from a previous chart (Laser Gyro Standing Wave Operating Principle) that the photodiode readout assembly (or optical "viewing window") measures the angular rate that the window moves relative to the laser gyro standing wave. Since the standing wave is rotationally fixed relative to inertial space, the optical readout therefore measures the rate of rotation of the optical readout assembly mount relative to inertial space. By mounting the optical readout assembly on the gyro case, the readout measures the angular rotation of the gyro case and not the gyro block which contains the additional dither motion. The result is an output signal that accurately measures the rotation of the gyro case, free from the dither oscillation. Alternatively, the readout-prism can be mounted with the readout-diodes directly on the gyro block, with a digital notch filter used to eliminate the unwanted dither motion from the gyro output. The penalty is the elimination of real angular motion within the notch filter bandpass.

## **COMMONLY USED LOCK-IN COMPENSATION TECHNIQUES**

- **MECHANICAL DITHER**
  - **NO DELETERIOUS BIAS EFFECTS (INDIVIDUAL GYRO)**
  - **HIGH AMPLITUDES – HIGH SCALE FACTOR ACCURACY**
  - **SIZE/WEIGHT PENALTY**
- **MAGNETIC MIRROR BIAS**
  - **AMPLITUDE LIMITED – SCALE FACTOR NONLINEARITIES**
  - **HIGH LOSSES WITH ORIGINAL FERROUS COATING TECHNOLOGY**
    - > **COMPATIBLE WITH EARLY TECHNOLOGY 1.15 MICRON LASER GYROS (TOLERANT OF HIGH GAIN)**
  - **FERROUS REPLACED BY GARNET COATING FOR REDUCED LOSS**
    - > **COMPATIBLE WITH CURRENT HIGHER ACCURACY 0.63 MICRON LASER GYROS (GAIN LIMITED)**
- **FARADAY CELL BIAS**
  - **HIGH AMPLITUDES**
  - **HIGH BIAS UNCERTAINTIES**
- **DIFFERENTIAL LASER GYRO (DILAG) OR MULTIOSCILLATOR**
  - **HIGH AMPLITUDES WITH FARADAY CELL**
  - **THEORETICALLY ELIMINATES FARADAY CELL ERRORS**
  - **ADDED LOSSES/BIAS ERRORS FROM POLARIZING CRYSTAL**
  - **POLARIZING CRYSTAL REPLACED BY CLEAR-PATH OUT-OF-PLANE BEAM/MIRROR GEOMETRY**

## COMMONLY USED LOCK-IN COMPENSATION TECHNIQUES

Methods that have been used to overcome laser gyro lock-in include mechanical dither, magnetic mirror bias, Faraday cell bias, and the differential laser gyro or multioscillator approach. The mechanical dither approach was the first successful method for overcoming lock-in for high accuracy applications. It introduces no deleterious bias error effects (on an individual gyro basis), and high frequency/high amplitude dither motion is readily attainable, producing high scale factor accuracy and low random noise (due to short dwell times in the lock-in region). One disadvantage in the mechanical dither approach is the size/weight penalty associated with the dither drive assembly, particular for sensor assemblies using single dither assemblies for each gyro (Note: One supplier of mechanically dithered laser gyro sensor assemblies has utilized a single Zerodur structure for all three gyros coupled with a single dither motor assembly mounted skewed to the gyro input axes to impart dither motion into all three orthogonal gyro axes).

Another approach for overcoming lock-in has been the magnetic-mirror concept (based on the magneto-optic Kerr effect) in which a magnetically sensitive inner coating (e.g., ferromagnetic metal) is applied to one of the laser mirrors. By applying a magnetic field to the mirror transverse to the laser beam, a differential phase shift is introduced between the reflected clockwise and counterclockwise beams which appears as a differential path-length change around the cavity. The result is a bias imposed on the gyro output that is controllable by the applied magnetic field.

The original alternative to mechanical dither was the use of a Faraday cell within the laser cavity. A Faraday cell contains a magnetically active optical material whose index-of-refraction to circularly-polarized light can be altered by an applied magnetic field. Since laser gyros operate with plane-polarized laser beams, quarter wave plates must be included in the Faraday-cell to circularly polarize the light entering, and plane-polarize the light leaving the cell. By applying a magnetic field across the Faraday cell, a differential index-of-refraction shift is created between the clockwise and counterclockwise laser beams, producing a differential change in the optical path length between the two beams. A frequency difference or bias is thereby generated between the two beams with amplitude and phase determined by the amplitude and phase of the applied magnetic field.

An advantage for the Faraday-cell or magnetic-mirror concepts is the ability to develop lock-in bias compensation electrically without a mechanical dither flexure requirement for each gyro. As a result, size/weight reductions are potentially achievable through multi-gyro integration in a single Zerodur structure. Another advantage arises because of the ability to generate a square-wave dithered electrical bias that has a low frequency and a rapid traversal rate through lock-in (i.e., short dwell time in the lock-in zone for each traversal, and few traversals per unit of time). Thus, lower random noise is theoretically generated from this potential error source (as contrasted with mechanically dithered units where, due to the inertial/spring physical characteristics of

## COMMONLY USED LOCK-IN COMPENSATION TECHNIQUES (CONTINUED)

the gyro block/dither assembly, high traversal rates through lock-in to reduce random error each dither cycle tend to be accompanied by high dither frequencies, hence many random errors per unit time.

The principle difficulty with the Faraday-cell has been the introduction of thermally and acceleration-sensitive bias errors into the gyro through unpredictable birefringent and anisotropic effects in the Faraday cell. Literature on the error mechanisms associated with magnetic mirrors indicate that original ferromagnetic metal coated mirrors designed for a large lock-in biasing capability also introduce large losses into the lasing cavity due to their accompanying low reflectivity. The loss effect is diluted as bias amplitude capability is reduced. Since high gain (and an accompanying degradation in gyro performance stability) is generally required to overcome added cavity losses, this suggests that a tradeoff exists in the design of ferromagnetic mirrors between increased gyro scale factor nonlinearities (for low-bias-amplitude mirrors, hence less effective lock-in compensation) versus decreased gyro stability (for high-bias-amplitude mirrors). It also suggests that ferromagnetic-mirror technology may be difficult to apply in current technology 0.63-micron lasers, a higher accuracy gyro configuration compared to the 1.15-micron wavelength original technology units, but with lower available gain to overcome cavity losses. In general, ferromagnetic metal coated mirror technology has only been applied to the less accurate older technology 1.15 micron wavelength laser-gyros. The most recent work on laser gyro magnetic mirror technology concentrated on the development of a garnet mirror in which the dielectric layer coatings on the laser mirror are made with a transparent garnet film that produces a differential phase shift between the clockwise and counterclockwise laser beams on application of a magnetic field. The result was that the loss effect (associated with the ferromagnetic mirror technology) was significantly reduced so that higher bias levels could be achieved with 0.63 micron lasers. A temperature sensitive bias remained, however, which was attempted to be minimized by doping the Garnet coating.

Another approach for overcoming lock-in has been the multioscillator or differential laser gyro (DILAG) concept. This method also incorporates a Faraday bias cell, but in a manner that tends to cancel the effects of bias shaft generated by the intrusion of the cell into the laser cavity. A polarizing crystal has been used within the cavity to create two pairs of counter-rotating beams, each pair circularly and oppositely polarized from the other. Hence, two laser gyros are created in the same cavity, each being separable through use of a polaroid filter on the output. The effect of the opposite polarization between the two laser sets is to make each respond in the opposite sense to the applied Faraday bias. Hence, one gyro output becomes biased in the opposite direction from the other. Summing the two signals doubles the sensed rate signal and theoretically cancels the Faraday bias from the output, including the deleterious effects of bias uncertainties. As a result, high amplitudes of Faraday bias can be used, providing adequate capability for compensating lock-in. The DILAG is typically operated with a large constant Faraday bias to assure that the instrument will never enter the lock-in region under any operating rate condition. One of the principle advantages of the DILAG is that traversals through the lock-in region are not utilized to overcome lock-in (as with mechanical dither), hence, the random walk error associated with dithering through lock-in is eliminated.

## COMMONLY USED LOCK-IN COMPENSATION TECHNIQUES (CONTINUED)

The accuracy of the DILAG approach hinges on the degree to which error effects in the gyro pairs are equal and opposite. Two sources of noncancelling bias error in the DILAG have been anisotropic and birefringent effects in the polarizing crystal and Faraday cell. Because of the polarizing crystal and Faraday cell in the laser cavity, higher losses are also present which must be compensated by higher gain. Further accuracy degradation can thereby result. Advances in multioscillator design techniques have replaced the quartz crystal circular polarization generator with an out-of-plane beam path geometry that rotates the laser beam by optical reflection at the mirrors (thereby mimicking the rotational effect of the quartz crystal). The result is elimination of birefringence and loss effects originally created by the presence of the quartz crystal in the beam path. Later work on the multioscillator has addressed the development of improved methods to provide Faraday biasing of the gyro that have smaller and more predictable error characteristics than were achieved with original multioscillator design configurations.

As of the date of this printing, both the mechanical dither and multioscillator approaches for overcoming lock-in have been the only methods to enter high volume production.

# SOURCES OF LASER GYRO ERROR

- **BIAS**
  - **LANGMUIR FLOW (CURRENT BALANCE, THERMAL SYMMETRY, GAIN)**
  - **FORWARD SCATTERING (MIRROR QUALITY)**
  - **BIREFRINGENCE AND ANISOTROPIC EFFECTS OF ADDITIONAL ELEMENTS IN BEAM PATH (LOCK-IN BIASING ELEMENTS)**
  - **MAGNETIC MIRROR THERMALLY SENSITIVE BIAS ERROR**
  - **PLC MIRROR TILT (THERMALLY DRIVEN)**
  - **MECHANICAL/THERMAL STRESS AT MECHANICALLY DITHERED LASER BLOCK/MOUNT INTERFACE**
  
- **SCALE FACTOR ERROR**
  - **GAIN VARIATION (CURRENT MAGNITUDE, SUB-WAVELENGTH PATHLENGTH VARIATION)**
  - **MULTIPLE PATHLENGTH VARIATIONS**
  - **RESIDUAL LOCK-IN COMPENSATION ERROR**
  
- **WIDE BAND RATE OUTPUT NOISE (RANDOM WALK)**
  - **MECHANICAL DITHER LOCK-IN COMPENSATION ERROR**
    - **LOWER FOR LOWER LOCK-IN (MIRROR QUALITY-BACKSCATTERING, BEAM/CAVITY GEOMETRY STABILITY)**
  - **RANDOM PHOTON ADDITION THROUGH GAIN MEDIUM**

## SOURCES OF LASER GYRO ERROR

Laser gyro bias is the steady output error under zero input rate conditions. A principle cause for bias in the laser gyro is circulating flow phenomena (e.g., Langmuir flow) in the lasing cavity that produce differential optical path-length variations between the clockwise and counterclockwise laser beams. Langmuir flow is produced by current unbalance and thermal asymmetry across the ionization paths in the gyro. The lasing gain amplifies the flow bias. Variations in current balance, thermal symmetry, or gain can produce bias instabilities (i.e., uncompensatable errors). Circuitry is utilized in the gyro to maintain a constant current balance between the gyro ionization paths.

Forward-scattering effects caused by laser beam interactions with imperfect mirror surfaces produce differential phase shifts between the counter-rotating laser beams, hence, gyro bias. Another cause for laser gyro bias is birefringence and anisotropic effects on the laser beam produced by spurious elements in the beam path (e.g., lock-in biasing elements). Magnetic mirrors are known to produce thermally sensitive bias errors. If the path-length-control (PLC) mirror transducer is not designed properly, mirror tilt can be generated as the PLC is actuated to correct for gyro block thermal expansion, thereby creating temperature sensitive bias. One of the sources of bias instability in high accuracy mechanically dithered laser gyros is mechanical stress at the physical junction between the laser gyro block and the block mount. The block mount is typically made of Invar, a metal alloy with a low coefficient of thermal expansion selected to match the thermal expansion properties of the gyro block material (e.g., Zerodur). The gyro block is typically attached to the mount by a clamping or cementing operation. Under temperature variations, the difference between the gyro block and mount thermal expansion coefficients, although small, is still significant enough to set up stress patterns in the gyro block that can alter the position of the laser beam in the gyro cavity. This can produce a change in the gyro bias as a function of temperature. Depending on the manner in which the gyro block is attached to the mount, this error characteristic can be repeatable (hence, compensatable, based on temperature measurements), or unstable with temperature cycling and aging.

Laser gyro scale factor error is caused principally by laser beam gain/loss variations in the cavity produced, for example, by current magnitude variations or errors in optimally controlling the path-length to the peak-power condition. Since the gyro scale factor is inversely proportional to path length, a variation in the total number of wavelengths of light around the cavity impacts gyro scale factor accuracy. Finally, the method for compensating lock-in can also affect laser gyro scale factor linearity accuracy, depending on the average operation of the compensation technique on the nonlinear input/output lock-in curve (see previous slide). For dither compensated lock-in techniques with high dither amplitudes and rapid traversals through the lock-in region, the deleterious impact of the nonlinear lock-in region on gyro performance is minimized, and good scale factor linearity is obtained.

Random walk in laser gyros is modeled as a white noise gyro output error. The term “random walk” derives from the output characteristics of the integral of the gyro white noise output which wanders randomly in attitude increasing on a root-mean square basis proportional to the square root of integration time. For mechanically dithered laser gyros, random walk is primarily caused by a random-angle error introduced into the gyro output each time the gyro input rate is cycled through the lock-in zone (twice each dither cycle). For mechanically dithered gyros with low lock-in (e.g., using high quality low-backscattering mirrors and good beam/cavity geometry stability) random walk is reduced. The random addition of photons to the laser beam through the Helium-Neon gain is a fundamental source of random walk in the laser gyro for both the mechanically dithered and multioscillator versions.

## LASER GYRO DESIGN TRADEOFFS

### 1.15 MICRON HELIUM NEON TRANSITION SIMPLER TO BUILD

- HIGHER GAIN – TOLERATES HIGHER LOSSES
- NEED HIGHER GAIN FOR READOUT PHOTODIODE (SILICON HAS LOWER GAIN FOR 1.15 MICRON WAVELENGTHS)
- LOW SENSITIVITY OF MIRROR TRANSMISSIBILITY WITH MANUFACTURING TOLERANCES

### • 0.63 MICRON HELIUM NEON TRANSITION PROVIDES HIGHER ACCURACY

- LOWER LOCK-IN (FACTOR OF FOUR)
- LOWER GAIN, HENCE, LOWER BIAS ERROR (LOWER LANGMUIR FLOW) AND LOWER SCALE FACTOR ERROR
- HIGH PHOTODIODE READOUT GAIN (SILICON)
- ALL RLGs TODAY UTILIZE THE 0.63 MICRON WAVELENGTH

### • GYRO SIZE

- LOCK-IN AND BIAS ERROR DECREASE WITH LINEAR DIMENSION APPROXIMATELY TO THE 2.5 POWER ( $L^{2.5}$ )
- SCALE FACTOR ERROR DECREASES LINEARLY WITH INCREASING L
- OUTPUT PULSE SIZE (ARC SEC PER PULSE) DECREASES LINEARLY WITH INCREASING L – 12.6 INCH PERIMETER 0.63 GYRO HAS 2 ARC SEC PULSE

## LASER GYRO DESIGN TRADEOFFS

The design of a laser gyro involves several tradeoff factors, two of the most notable of which are the Helium-neon transition used (i.e., operating wavelength), and the gyro physical size.

Laser gyros have been designed for operation with 0.63-micron (visible red) or 1.15-micron (infrared) laser wavelengths. In general, the tradeoff between the two wavelength configurations has been higher accuracy but a more sophisticated design and manufacturing technology for the visible lasers, versus lower performance but simpler design and manufacturing methods for the infrared units.

From a performance standpoint, laser gyro lock-in bias and scale-factor errors are generally lower for the 0.63-micron instruments. Lock-in is proportional to the operating wavelength squared, hence, other factors being equal, is a factor-of-four smaller for the 0.63 micron gyro. Laser gyro readout detectors (typically silicon) have a higher amplitude response to the 0.63-micron compared to the 1.15-micron wavelength, hence higher gains are generally required in 1.15-micron lasers for adequate output signal strength. Because laser gyro scale-factor error increases with laser gain, decreased scale-factor accuracy results. Langmuir flow also increases with increasing gyro gain, thus lower gyro bias stability is generally characteristic of 1.15-micron laser-gyro configurations.

Laser gain increases with increasing wavelengths, hence higher gains are typically achievable with 1.15 micron units and cavity losses are more easily overcome (or conversely, cavity loss design and manufacturing requirements can be relaxed). For the 0.63-micron laser gyro, cavity design and manufacturing processes must be carefully controlled to assure that losses are stable and less than the available gain. From a mirror technology standpoint, the 1.15-micron laser dielectric mirror is typically simpler to design and manufacture, due to the lower sensitivity of its transmissibility characteristic with material parameter variations. The 0.63-micron mirror technology on the other hand can have significant transmissibility variations with parameter changes. Consequently 0.63-micron mirror materials must be more stable to maintain constant gain/loss characteristics in the laser cavity for repeatable gyro performance. Current technology laser gyros utilize the 0.63 micron wavelength, hence, the original 1.15 micron technology is now essentially obsolete.

General scaling laws for laser gyros vary, depending upon gyro configuration and analytical error theory assumptions. Experience with mechanically dithered units has been that lock-in and bias uncertainty vary inversely between the square and cube of the gyro path length, and scale-factor uncertainty varies inversely as the path length. Thus, laser gyro performance is heavily influenced by gyro size, with the larger units being the most accurate.

# TRIANGULAR VERSUS SQUARE RING LASER GYROS

## PRO-TRIANGLE

- **MINIMUM NUMBER OF MIRRORS FOR CLOSED-PATH**
  - LOWEST COST
  - SMALLEST NUMBER OF SCATTERERS - LOWER LOCK-IN
- **SIMPLEST MIRROR ALIGNMENT FOR LASER BEAM CLOSURE**
  - SELF-ALIGNING IN-PLANE
  - SINGLE MIRROR ADJUSTMENT OUT-OF-PLANE
  - LOW COST
- **PLANAR GEOMETRY**
  - REDUCED MAGNETIC SENSITIVITY
- **MINOR PERFORMANCE PENALTY DUE TO NON-OPTIMUM AREA/PERIMETER RATIO**
  - WILL BE OVERCOME WITH TECHNOLOGY ADVANCES
- **SIZE PENALTY TO ACHIEVE GIVEN LEVEL OF PERFORMANCE NEGLIGIBLE IF ELECTRODES/ PACKAGING INCLUDED IN TRADEOFF**
- **MACHINING OF TRIANGLES WELL UNDERSTOOD AND NO PROBLEM WITH PROPER TOOLING**

## PRO-SQUARE

- **ADDITIONAL MIRROR MINOR COST PENALTY AS TECHNOLOGY ADVANCES**
- **REDUNDANT MIRROR AVAILABLE FOR OPTIMUM LASER BEAM ALIGNMENT**
  - FLEXIBILITY IN ALIGNMENT FOR BEAM CLOSURE
  - ABILITY TO ALSO OPTIMIZE PERFORMANCE FOR GIVEN MIRROR SET DURING DEVICE ASSEMBLY ALIGNMENT
- **ALIGNMENT TOLERANCES READILY CONTROLLED TO ACHIEVE PLANAR GEOMETRY**
  - MAGNETIC SENSITIVITY NOT A PROBLEM
- **SMALLER LASER/MIRROR ANGLE-OF-INCIDENCE**
  - REDUCED BACKSCATTERING PER MIRROR
  - NET REDUCTION IN OVERALL GYRO SCATTERING
  - \* LOWER LOCK-IN
- **HIGHER AREA-TO-PERIMETER RATIO**
  - HIGHER ACCURACY FOR A GIVEN SIZE
- **SIMPLER TOOLING & MACHINING FOR SQUARE GEOMETRIES**
  - LOWER COST

## TRIANGULAR VERSUS SQUARE RING LASER GYROS

The chart summarizes the rationale espoused by ring laser gyro design organizations utilizing triangular or square gyro configurations to justify their particular geometry selection.

Proponents of the triangular geometry point to the three-mirror configuration as having the minimum mirror count to form an enclosed laser ring. As a result mirror costs per gyro are minimized, and lock-in is reduced due to the minimum number of scatterers (the mirrors) in the laser beam path. From a manufacturing standpoint, the proponents of the triangle point out that alignment of the mirrors on the gyro block is simplified (hence, cost reduced) because the triangle geometry is self-aligning in the lasing plane (through use of one curved mirror) and alignment out of the lasing plane is readily achieved by out-of-plane position adjustment of the curved mirror during device assembly.

A source of magnetic bias sensitivity in the laser gyro is the Faraday effect of the gain medium operating on residual circular polarization components in the laser beam. A generator of circular polarization is an out-of-plane beam geometry (such as intentionally utilized in the multioscillator to create circular polarization). Triangular laser gyro proponents point to the triangular gyro geometry as being inherently planar, hence, less likely to generate magnetically sensitive bias.

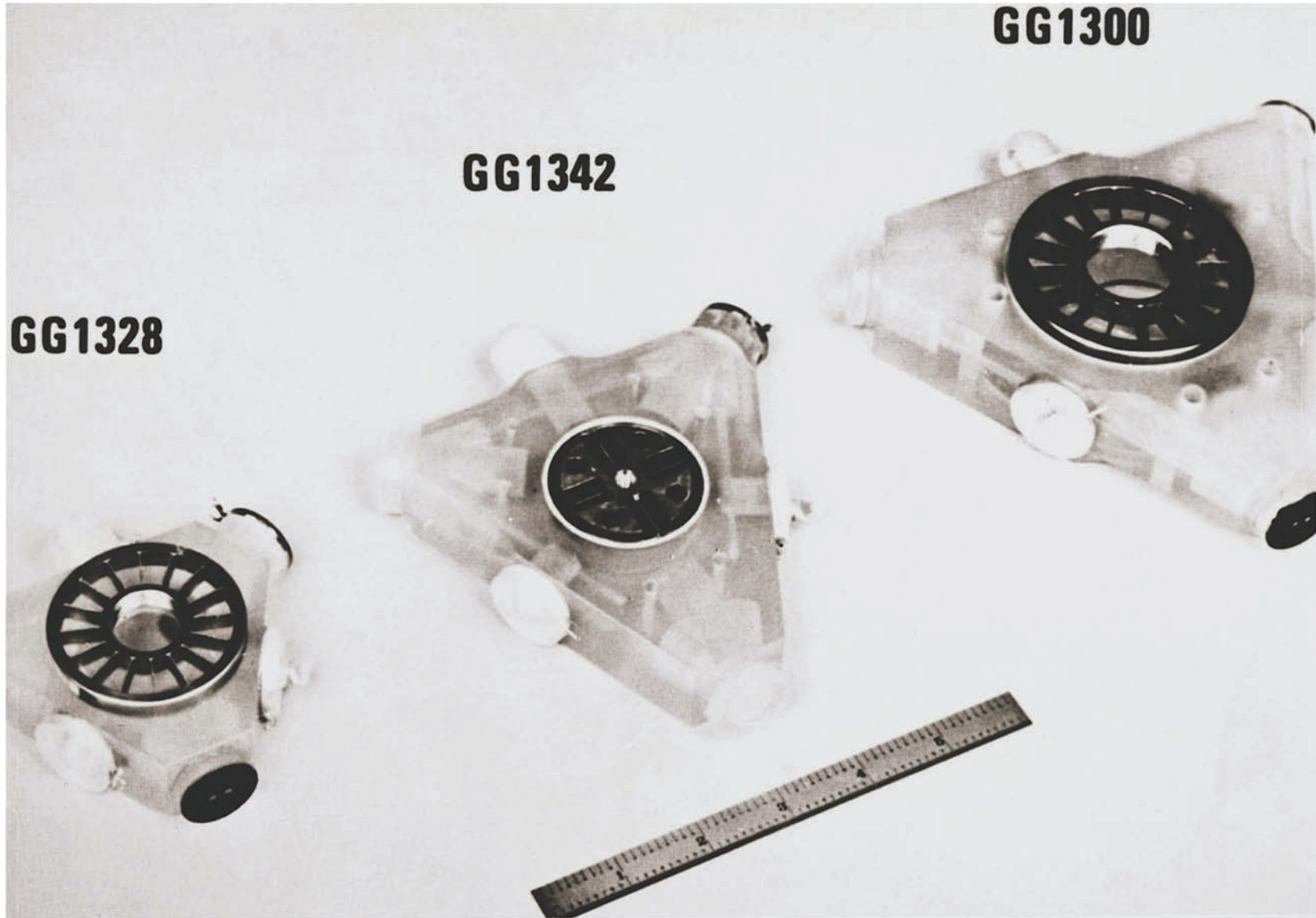
Proponents of the square laser gyro discard the additional mirror cost as a negligible penalty when technology advances are taken into account. The additional alignment requirement for the fourth mirror in a square is identified as a benefit by square gyro proponents due to the added flexibility it affords to adjust beam/cavity positioning, and thereby optimize performance. Square laser gyro enthusiasts maintain that required mirror alignment tolerances are readily achievable. Furthermore, that mirror alignment accuracies achieved are well within requirements for control of residual out-of-plane geometry effects so that associated magnetic bias sensitivities are negligible.

Another performance advantage identified for the square is its higher area-to-perimeter ratio compared to a triangle of the same size, which directly increases accuracy. Additionally, proponents of the square point to the lower angle of incidence at the laser beam/mirror interface which reduces back scattering per mirror. The net result is a combined mirror reduction in back scattering which more than compensates for the additional mirror scattering, hence, reduces overall gyro lock-in. Finally, from a manufacturing standpoint, square laser gyro enthusiasts claim simpler tooling and machining for square compared to triangular devices, hence, reduced production costs.

Triangular laser gyro proponents acknowledge a performance penalty due to the less favorable area-to-perimeter ratio and beam-incidence geometry. However, they believe that these advantages are minor and largely overcome by technology advances. Additionally, triangle proponents argue that when the gyro electrodes (size and geometry) are taken into account, no real size advantage exists for the square gyro configuration. From a machining standpoint, triangle proponents claim no advantage exists for any particular geometry once tooling is complete and experience has been attained.

At this stage in the laser gyro development cycle, it is not clear whether one geometry is superior to another as a general rule.

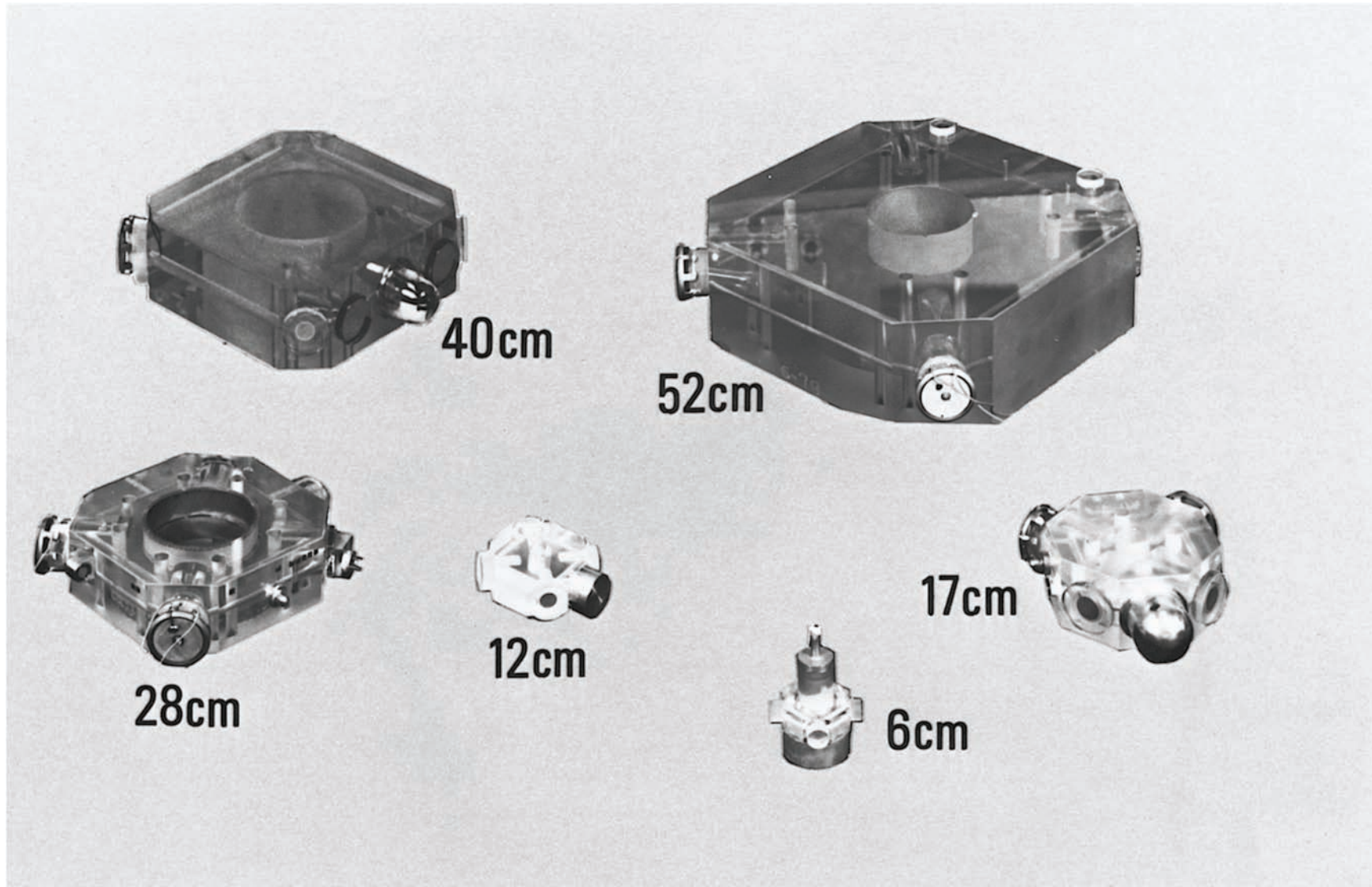
# HONEYWELL RLG BLOCK ASSEMBLIES



## **HONEYWELL RLG BLOCK ASSEMBLIES**

The slide is a photograph of the triangular laser gyro design configurations developed at Honeywell. The GG1300 (5.7 inches per side) was the original unit to demonstrate 1 nmph (nautical-miles-per-hour) navigation accuracy in 1975 (corresponding to 0.01 deg/hr gyro accuracy). The GG1342 gyro (4.2 inches per side) was the first production unit Honeywell developed for medium accuracy 1 nmph aircraft inertial navigation applications. Current GG1342 production configurations have random walk performance ranging from 0.002 to 0.0004 deg/rt-hr, compatible with medium to medium-high accuracy inertial navigation requirements. The Honeywell GG1328 laser gyro (2.8 inches per side) was developed for applications where performance in the 0.03 to 0.1 deg per hr category was required. All units shown in the photograph utilize plane polarized light, employ mechanical dither for lock-in compensation, and all utilize the 0.63 micron Helium Neon lasing wavelength.

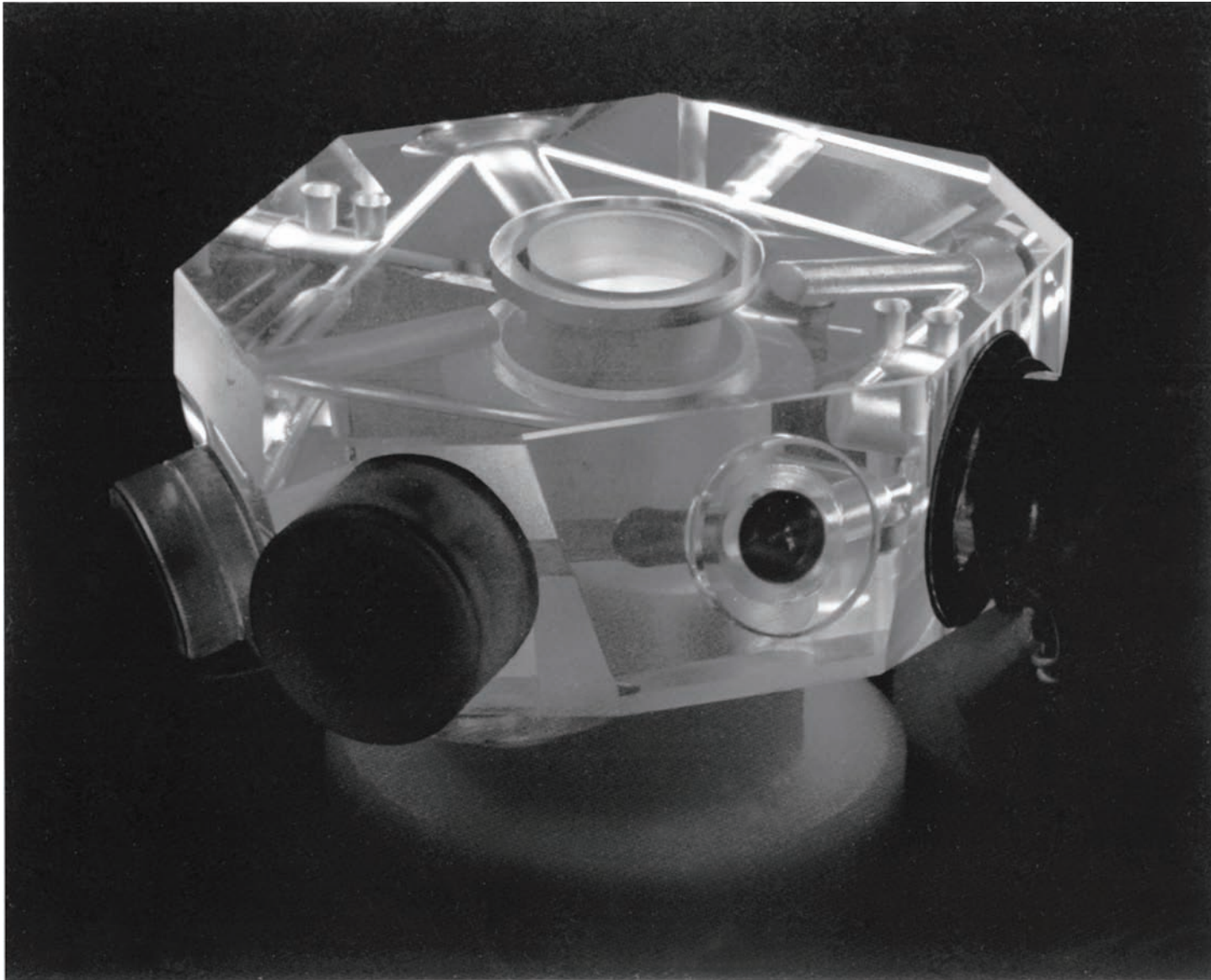
# THE LITTON RING LASER GYRO FAMILY



## **THE LITTON RING LASER GYRO FAMILY**

The slide illustrates the square laser gyro configurations developed at Litton, a major proponent of the square geometry. The 28 cm path length unit was developed for medium to medium-high accuracy inertial navigation (0.002 to 0.0004 deg/rt-hr random walk) and integrated flight control applications. The 17 cm unit provides medium accuracy (0.002 deg/rt-hr random walk) as a result of recent design improvements. The 40 cm unit has been designed for higher accuracy strategic missile applications, while the 52 cm unit has been developed for the highest accuracy aircraft and shipboard inertial navigation applications. The 12 and 6 cm path length units respectively have been designed for lesser accuracy applications (0.3 and 10.0 deg/hr respectively) where size/performance tradeoffs favor the smaller geometry. All units shown in the photograph utilize a plane polarized 0.63 micron Helium Neon lasing wavelength and incorporate mechanical input rate (e.g., dither) for lock-in compensation.

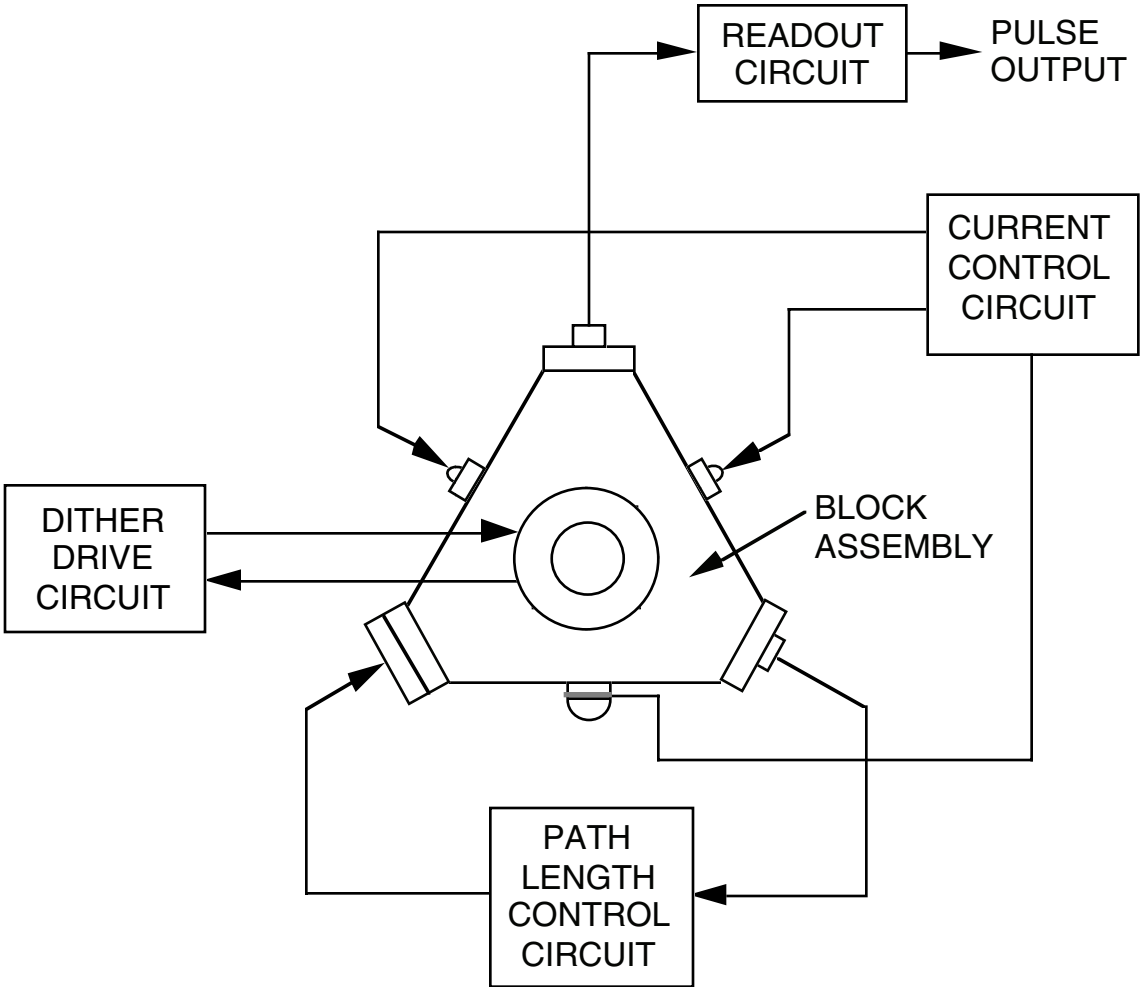
# LITTON MULTIOSCILLATOR RING LASER GYRO



## LITTON MULTIOSCILLATOR RING LASER GYRO

The photograph is of the Litton ZLG (“Zero-Lock Gyro”), the first multioscillator ring laser gyro to enter large scale production. The ZLG has an 18 cm perimeter, utilizes the 0.63 micron wavelength with an out-of plane beam geometry to create the multioscillator right and left circularly polarized laser beams, and is Faraday biased at a constant rate that is significantly higher than the maximum input rate expected in its intended high performance aircraft application area to continuously maintain the effective input rate well outside the lock-in zone. According to Litton, long term bias stability of the ZLG is 0.003 deg/hr one sigma with a random walk error of 0.001 deg/rt-hr, significantly lower than the comparable mechanically dithered RLG random walk due to the elimination of mechanical dither for lock-in compensation.

# REPRESENTATIVE LASER GYRO ELECTRONIC ASSEMBLIES

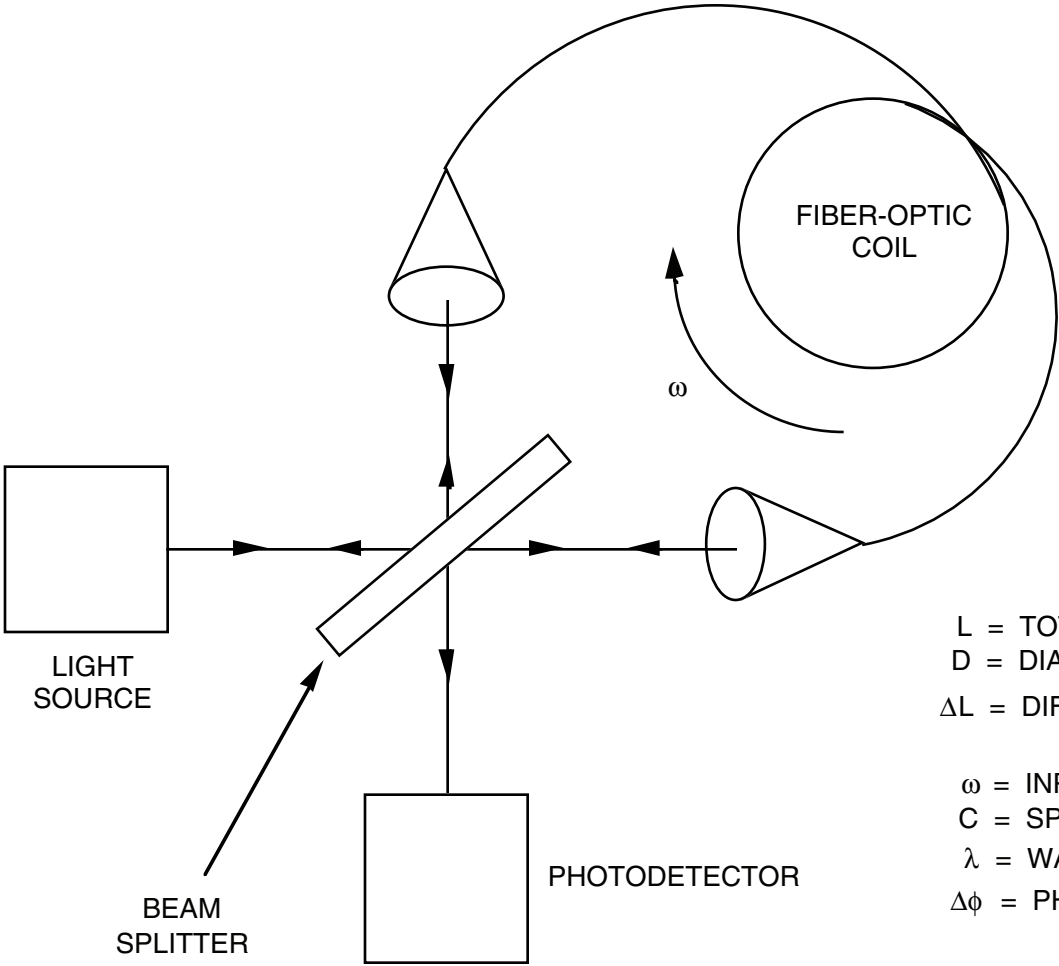


## **REPRESENTATIVE LASER GYRO ELECTRONIC ASSEMBLIES**

The slide illustrates the principle electronic assemblies typically used to operate a mechanically dithered laser gyro. The dither drive circuit compensates for lock-in by maintaining the gyro in a continuous angularly vibrating condition about its input axis. The path length control circuit controls the gyro to a constant average optical path length corresponding to the peak average laser beam power to maintain stationary gyro performance parameters (using a piezoelectric driver on one of the mirrors to maintain the average power in the laser beam at peak). The current control circuit maintains a constant current magnitude and balance between the ionization paths, thereby, reducing the likelihood of Langmuir flow variations and associated bias changes. Finally, the readout circuit converts the sinusoidal outputs from the photodiodes to logic pulses for the strapdown INS computer.

For a multioscillator ring laser gyro, the dither drive assembly and circuit in the diagram would be replaced by the multioscillator Faraday biasing assembly and electronics, and the physical block configuration would be modified to reflect the multioscillator block geometry and mirror count. In other respects, the diagram would generally remain the same, however, the functions implemented in each block would be configured for compatibility with four beam (right and left circularly polarized, clockwise and counterclockwise) multioscillator operations.

# BASIC FIBER-OPTIC ROTATION RATE SENSOR CONCEPT



$$\Delta L = \frac{L D}{C} \omega$$

$$\Delta \phi = 2 \pi \frac{\Delta L}{\lambda} = 2 \pi \frac{L D}{C \lambda} \omega$$

- L = TOTAL FIBER LENGTH
- D = DIAMETER OF COIL (ASSUMED CIRCULAR)
- $\Delta L$  = DIFFERENCE BETWEEN CW AND CCW OPTICAL PATH LENGTHS
- $\omega$  = INPUT ANGULAR RATE
- C = SPEED OF LIGHT
- $\lambda$  = WAVELENGTH OF LIGHT SOURCE
- $\Delta \phi$  = PHASE SHIFT DEVELOPED BETWEEN CW AND CCW BEAMS

## BASIC FIBER-OPTIC ROTATION RATE SENSOR CONCEPT

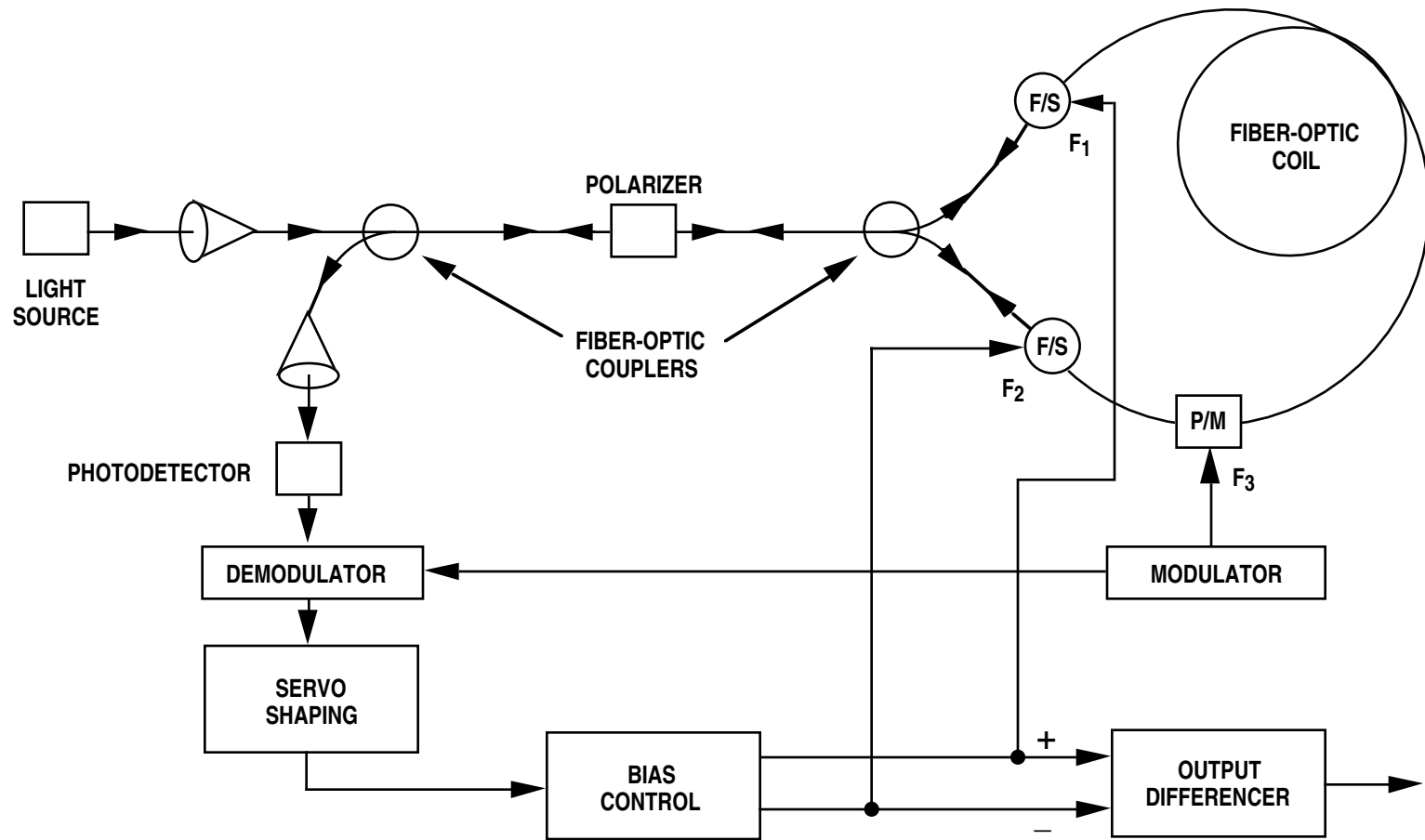
One of the newer rate sensor technologies that has emerged over the past few years is the fiber-optic rotation rate sensor. The concept for the device is illustrated in the slide. Light generated from a suitable light source at a specified design frequency is transmitted through a fiber-optic coil. The light beam is first split by a beam-splitter so that half the radiation traverses the coil in the clockwise (CW) direction, and half in the counterclockwise (CCW) direction. The emerging light from both ends of the coil are then recombined at the beam splitter, and transmitted onto a photodetector. The photodetector output power is proportional to the average intensity of the recombined light.

Under rotation of the device about an axis normal to the plane of the fiber-optic coil, the effective optical path length is changed for the CW compared to the CCW beams in a manner similar to the ring laser gyro. In the direction of rotation a photon of light has to traverse the length of the coil plus the distance that the coil has been rotated during the traversal period, hence, the path length increases proportional to the applied angular rate. In the direction opposite to the rotation, the light traverses the length of the coil, minus the distance that the coil has been rotated during the traversal period. The resulting difference between the CCW and CW optical path lengths produces a phase shift in the light beams emerging from the coil that is proportional to the input angular rate. This contrasts with the ring laser gyro resonator for which the phase angle change is proportional to the integral of the input rate. Hence, the basic fiber-optic rotation sensor is a “rate gyro” while the laser gyro is a “rate integrating gyro” (Note: The fiber optic rate sensor phase angle change is actually proportional to the integrated rate over the time period that the light beam traversed the fiber coil length to reach the photodetector. The full rate integral can in principle be calculated by summing measured phase angle changes sampled at sequential fiber coil length light transit time intervals). The difference between a laser and fiber-optic gyro from a frequency standpoint are that for the laser gyro the CW and CCW beam frequencies are shifted from each other proportional to the input rotation rate (due to the self-resonance of the laser within the optical cavity), while for the fiber-optic gyro the frequencies for the CW and CCW beams remain equal under rotation rates because the light source is outside the “optical cavity”.

The photodetector in the slide is used to sense the phase shift  $\Delta\phi$  between the CW and CCW beams. The amplitude of the combined beams at the photodiode equals the sum of the individual beam amplitudes, including the phase shift factor. The result is a combined beam intensity which is maximum for  $\Delta\phi = 0$  and minimum (zero) for  $\Delta\phi = \pi$  (i.e., varies as  $\cos^2(\Delta\phi/2)$ ). The photodetector output is proportional to the light intensity, hence, also varies approximately as  $\cos^2(\Delta\phi/2)$ .

In order to achieve high sensitivity (high scale factor), the length L of the fiber coil is large. For an L value of 400 meters, a coil diameter D of 0.1 meters and a light source wavelength  $\lambda$  of 0.82 microns, the formula in the slide shows that a phase shift  $\Delta\phi$  of one radian is produced at 1 rad/sec input rate  $\omega$ .

# IMPROVED FIBER-OPTIC ROTATION RATE SENSOR CONFIGURATION



## IMPROVED FIBER-OPTIC ROTATION RATE SENSOR CONFIGURATION

As depicted in the previous slide, the fiber-optic rotation rate sensor has fundamental error mechanisms that make it impractical to implement. Among these are large scale factor errors associated with photodetector scale factor uncertainties, light source intensity variations, and light amplitude losses in the fiber; loss of rate sensitivity around zero input rate due to the  $\cos^2(\Delta\phi/2)$  output characteristic of the photodetector; phase angle variations due to mechanical movement between the beam splitter and fiber that produce changes in path length between the CW and CCW beams; and polarization state differences between the CW and CCW beams that produce phase shifts due to nonreciprocal birefringence and anisotropic effects in the fiber material that are aggravated by environmental exposure. To overcome these fundamental problems, recent fiber-optic rotation sensor configurations have adopted refined interface and control elements such as those depicted in this slide.

In this slide, the discrete component beam-splitter in the previous slide is replaced by fiber-optic couplers which consist of integrated fiber-optic junctions that split entering beams 50% to the left and 50% to the right. A polarizer is included to suppress unwanted polarization states in the light. The fiber itself is specifically manufactured to preserve a single polarization state (“polarization preserving fiber”). In this manner, nonreciprocal fiber-beam interactions are suppressed.

A light source (typically a super-luminescent diode such as Gallium Arsenide) transmits narrow frequency bandwidth light into the fiber that splits into CW and CCW components at the coupler junction. Original fiber-optic sensors used laser light. One of the major technological break-throughs for the fiber-optic sensor was replacement of the coherent laser light with a broader spectrum source (such as the Gallium Arsenide diode). The result was a significant reduction in nonreciprocal beam/fiber interaction error mechanisms due to the shorter correlation distance for the broader spectrum light.

Frequency shifters (F/S) at the end of the fiber coil are used to generate a controlled phase shift between the CW and CCW light beams illuminating the photodetector (i.e., the equivalent of a controlled input angular rate bias). The basic method for generating the phase shift at the photodiode readout is to design each F/S device to impart a controlled frequency shift to both the CW and CCW light passing through it. Because each F/S device is at one end of the fiber coil, the shifted frequency for the light beam traveling the shorter distance (directly from the F/S device to the photodiode) will have a different phase shift at the photodiode than will the beam traveling the longer distance (back through the fiber coil to the photodiode), thereby creating the desired phase difference between the CW and CCW beams for each F/S device at the photodiode. Two F/S devices are typically utilized as shown in the slide, one at each end of the coil, to allow each to operate from a large bias frequency offset point (a requirement for proper operation of the F/S devices currently in use). For a symmetrical dual F/S biasing approach, a phase shift between the CW and CCW beams at the photodiode is then generated by operating one F/S device at  $F_1$ , the fixed bias frequency offset plus half the desired bias frequency, while operating the other F/S device at  $F_2$ , the frequency offset minus half the desired bias frequency.

## IMPROVED FIBER-OPTIC ROTATION RATE SENSOR CONFIGURATION (CONTINUED)

The composite effect from both F/S devices operating together is to cancel the bias offset frequency while creating the desired net bias frequency. In the chart, the  $F_1$  and  $F_2$  control frequencies are generated in servo fashion by the “Bias Control” element to maintain the photodetector output at peak power (i.e., zero net phase angle). Under input angular rate, the resulting close-loop servo action creates a net frequency difference between the F/S devices proportional to the input angular rate (which in turn generates an equivalent phase shift at the readout detector to null the phase shift created by input rotation). It can be demonstrated that the frequency difference  $\Delta f$  generated to achieve a net zero readout phase angle is given by:

$$\Delta f = \frac{4 A}{\lambda L} \omega$$

where  $l$  is the length and  $A$  is the area enclosed by a single coil of the fiber. The latter frequency difference is identical to the frequency shift generated within the laser gyro resonator which is measured for output from the fringe movement across the gyro readout photodiodes. In the fiber optic gyro, the frequency difference generated for output is obtained from the F/S servo loop as shown in the chart by subtracting the  $F_1$  and  $F_2$  control frequencies.

Acoustic-optic Bragg cells and more recently, active electro-optic crystals, have been utilized for F/S devices in fiber-optic rate sensors. A Bragg cell is typically implemented as a piezoelectric crystal that imparts an acoustical vibration transverse to the light beam at its input drive frequency (typically 40-80 MHz). The result is a bending of the light (by the “Bragg angle”) with an accompanying frequency shift in the light passing through the cell equal to the Bragg cell drive frequency. To function properly, each Bragg cell must be biased at a large offset frequency (e.g., 20 MHz). Lithium niobate is a commonly utilized active electro-optic crystal material for the F/S function which changes the optical index of refraction to transmitted light proportional to an applied electric field across light passing through the crystal. This results in a phase shift in both the CW and CCW light entering and leaving the crystal proportional to the applied electrical field strength. Titanium strips diffused on the surface of the lithium niobate crystal act as wave guides for the light passing through the crystal by alteration of the light refractive index. To create a frequency shift in the light guided through the lithium niobate, a ramping electric field is applied, thereby creating a ramping phase shift (i.e., the equivalent of a frequency shift). The ramp input is reset for every  $2 \pi$  radians of phase change (in sawtooth fashion) in what is known as a “serrodyne” frequency shifting approach. To allow rapid changes in the applied ramp slope (i.e., the applied bias), the serrodyne ramp input to each lithium niobate F/S device must complete the  $2 \pi$  phase change rapidly so that

## IMPROVED FIBER-OPTIC ROTATION RATE SENSOR CONFIGURATION (CONTINUED)

a new ramp at the new desired bias rate can be quickly applied. This is achieved in practice by operating each F/S device from a high fixed bias point (i.e., at a high gyrodynamic frequency), but using two F/S devices in “push-pull” fashion (as in the slide) to create the desired net bias change (large or small over the desired control bias spectrum from maximum minus to maximum plus).

The slide also includes a phase modulator (P/M) driven at frequency  $F_3$  at one end of the fiber, which imparts an oscillating path length change to the CW and CCW beams passing through. The P/M device is typically implemented using a lithium niobate active electro-optical crystal or as a piezoelectric actuated “stretcher” which physically changes the length of the fiber by introducing stresses in the fiber proportional to applied voltage, thereby inducing an equivalent phase shift in the light beams. Because the P/M driver is at one end of the coil, the light beam passing out of the coil delivers the phase shift effect first to the photodetector. The beam traveling in the opposite direction has to traverse a longer length of fiber to the photodetector, hence, delivers its phase shift, by an equal amount, later. The delay creates an alternating phase bias at the photodiode mixed beam output, generating an oscillation of the output about the peak power point. By comparing the positive half cycle output decrease with the negative cycle decrease, a linear signal can be generated proportional to the average deviation of the input light phase angle difference from zero. The linear signal is generated in the phase sensitive demodulator shown in the slide driven by  $F_3$ .

The result is a signal out of the demodulator that is linearly proportional to the  $\Delta\phi$  phase deviation from zero, thereby eliminating the  $\cos^2(\Delta\phi/2)$  sensitivity problem around  $\Delta\phi = 0$  that exists without the P/M device.

The basic advantages for this slide compared to the previous slide implementation approach are the elimination of the discrete light/beam-splitter/fiber junctions, thereby reducing phase shift errors caused by mechanical movement; elimination of the photodetector zero-phase angle sensitivity problem through use of the P/M device; and, through the F/S closed-loop servo operation that maintains the phase angle signal at null, elimination of scale factor errors associated with light source intensity, optical intensity losses in the fiber and beam-splitters, and photodetector scale factor uncertainties.

The basic motivation behind the development of the fiber-optic rate sensor was to design a low cost alternative to the ring laser gyro that was inherently void of lock-in problems. The resonant characteristic of the laser gyro which regenerates its light source by stimulated emission, is the transfer mechanism that couples the CW and CCW beams together from back-scatter, producing lock-in. For the fiber-optic rate sensor, the light source is external to the sensing ring, hence, does not amplify the effects of back-scatter. As a result, the lock-in phenomenon associated with the laser gyro is absent in the fiber-optic sensor. The rationale

## IMPROVED FIBER-OPTIC ROTATION RATE SENSOR CONFIGURATION (CONTINUED)

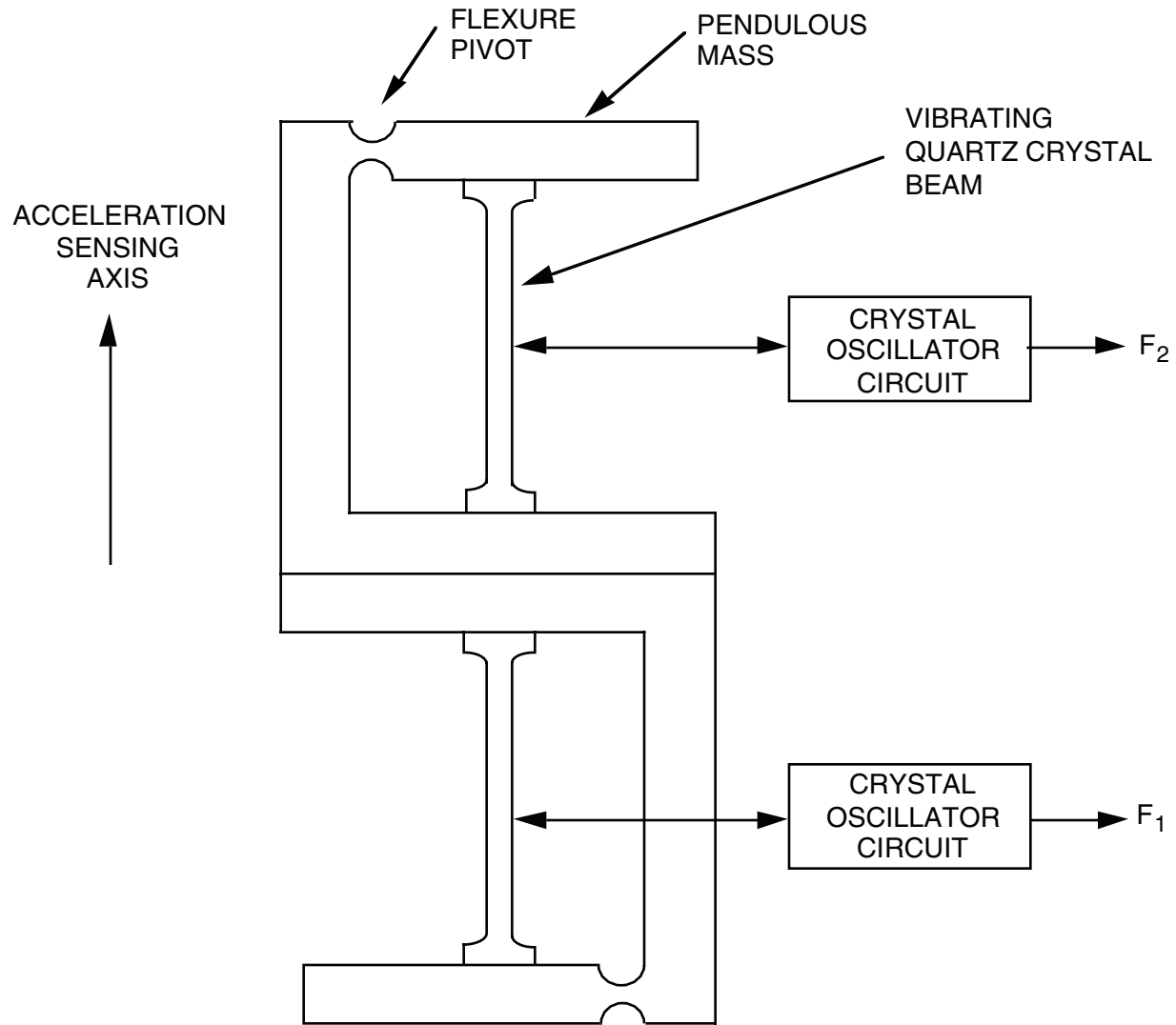
behind the projected low cost of the fiber-optic sensor is that use of fiber-optics and integrated-optics technologies should reduce labor hours associated with device manufacture. It also assumed continuing reductions in the cost of high quality optical fiber which has since been occurring.

From a performance standpoint, the fiber-optic rotation sensor was originally not expected to compete with the high performance laser gyro for accuracy. Original production configurations had accuracies compatible with tactical missile and AHRS applications. Some of the technical issues that have been addressed to achieve design goals in the fiber-optic gyro include the reliability of the fiber junction splices; scale factor errors due to photodiode output frequency variations with temperature; bias errors associated with photodiode output frequency side-bands creating phase offsets at the photodetector; bias errors created from large required F/S device drive frequency offsets coupled with variations in the CW and CCW F/S biased coil lengths due to off-nominal variations between the F/S distances to the fiber-optic coupler (see current slide); different polarization states in the light beam that created variations in optical path length between polarization components due to fiber imperfections; and increasing complexity of the sensor configuration (including the requirement for special elliptical cross-section plane-polarization-preserving fiber) to resolve problem areas. A problem area for the fiber-optic rotation rate sensor has been a larger than desired size (1.5 to 4 inches in diameter) for the fiber-optic ring to avoid introducing beam interactions with the fiber walls under tight fiber turns.

Much has been accomplished since 1976 when the fiber-optic rotation sensor concept was originally conceived. To a large degree, these accomplishments are summarized by the evolution of the concept from its original form (in the previous slide) to its more refined practical form (in the current slide). Design refinements introduced in some later fiber optic gyro configurations have increased their accuracy to be comparable to high accuracy ring laser gyros. Unfortunately, the performance improvements have been accomplished at the sacrifice of increasing cost so that cost advantages originally projected for fiber optic compared to ring laser gyros has largely been eliminated.

NOTES

# VIBRATING BEAM ACCELEROMETER CONCEPT



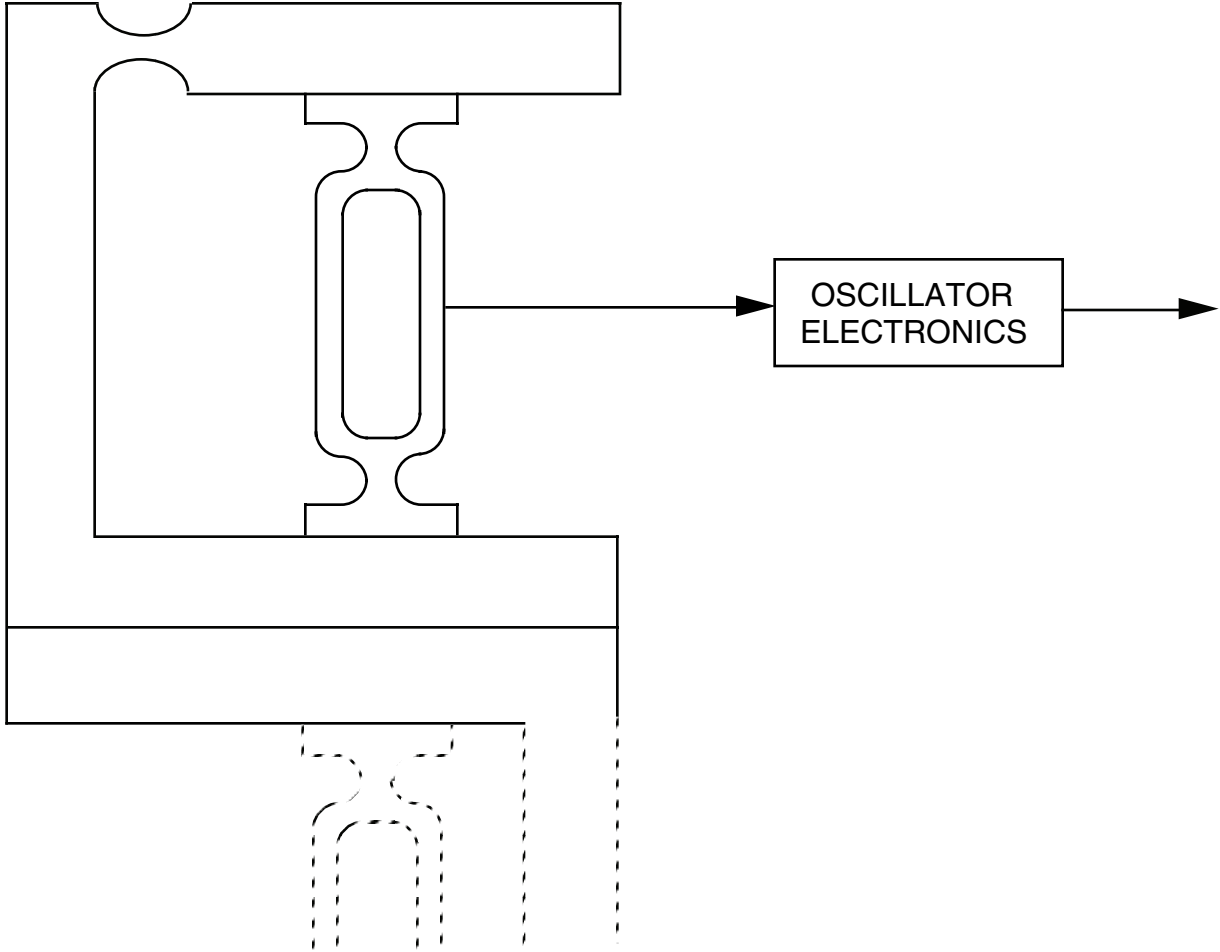
## VIBRATING BEAM ACCELEROMETER CONCEPT

Much of the cost for conventional pendulous electrically-servoed accelerometers is associated with the torque-generator and electronics needed to close-the-loop on the instrument and generate precision pulse outputs representing quantized increments of integrated input acceleration. The vibrating beam accelerometer depicted in the slide replaces the torque-rebalance mechanism with an open-loop direct-digital-output transducer based on quartz-crystal oscillator technology. Two quartz-crystal beams are mounted symmetrically back-to-back so that each axially supports a proof mass pendulum. Each beam is vibrated at its resonant frequency by an electronics loop in a manner similar to the method used to sustain amplitude in quartz-crystal oscillator clock references. In the absence of acceleration along the acceleration sensing axis, both beams are selected to nominally resonate at the same frequency. Under applied acceleration, one beam is placed in compression and the other in tension by the inertial reaction of the pendulous proof masses. This produces an increase in frequency for the beam in tension, and a decrease in frequency for the beam in compression. The frequency difference ( $F_2 - F_1$  in the slide) is a direct digital output proportional to the input acceleration.

An area to be addressed in the design of the vibrating beam accelerometer is the output resolution. Typical implementations are based on using crystals with a 40 KHz center frequency (zero input acceleration) with 10% variation over the design acceleration range. Hence, the inherent maximum frequency output of the device (beam frequency difference) under this resolution is generally too coarse (by at least an order of magnitude under certain conditions). In order to enhance the basic resolution, design techniques that can be considered include using time measurement between frequency difference pulses as the output or use of digital phase-lock loop external circuitry to generate higher frequency waveforms whose integral tracks the frequency difference output signal.

The symmetrical arrangement of the beams in the slide produces a cancellation of several error effects that would exist for one beam mounted individually. Error effects that are nominally canceled include nominal beam frequency variations with temperature and aging, asymmetrical scale factor nonlinearities, anisoinertia errors, and vibropendulous errors that are common between the individual beam assemblies. Error mechanisms in the vibrating beam accelerometer arise from unpredictable variations between the two beam assemblies that are temperature or vibration sensitive and which vary over time. Matching of the two beams is an important consideration in design and production to reduce sensor errors. One of the more important error mechanisms that must be dealt with in the design of the unit is the potential problem of mechanical coupling between the beam assemblies that pull the frequencies together under low input acceleration (an effect similar to lock-in for laser gyros). The result is a detection threshold for the unit that is a function of the strength of the mechanical coupling. The key to the design of an accurate vibrating beam accelerometer lies in the ability to isolate one crystal beam from the other.

# DUAL-BEAM CRYSTAL OSCILLATOR CONCEPT

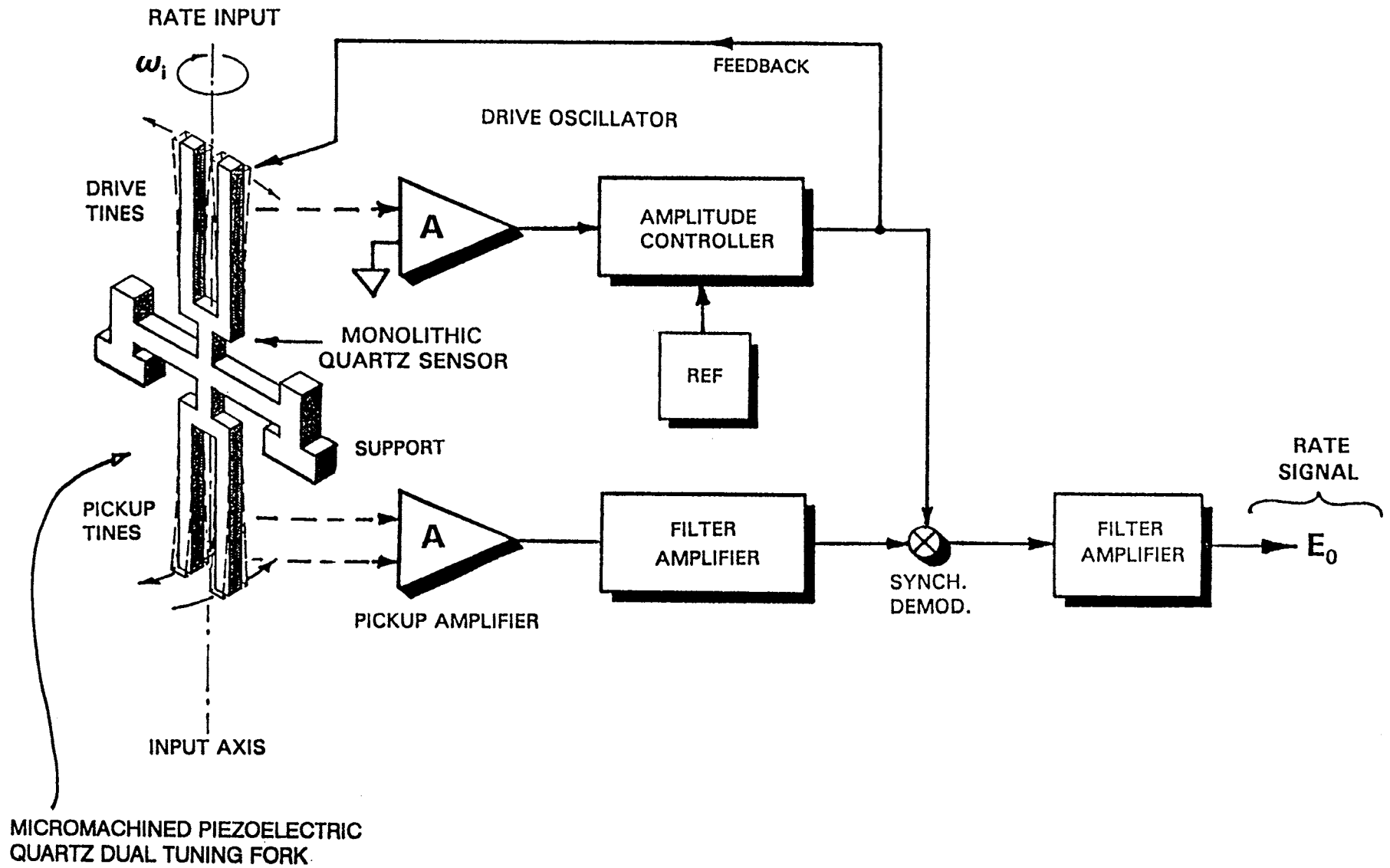


## **DUAL-BEAM CRYSTAL OSCILLATOR CONCEPT**

Dynamic coupling between the independent beams of the vibrating beam accelerometer can be minimized by reducing mechanical losses in the resonant mode of each vibrating beam assembly (i.e., high Q). One approach being used to achieve mechanical isolation between the two crystal beam assemblies is through application of a dual-beam construction for each crystal assembly as illustrated in the slide; each beam assembly is composed of an integral dual beam arrangement in which the beam elements vibrate in opposition (180 degrees out of phase). The resulting counter-vibration allows each beam movement to be counter-acted mechanically by the other such that the net vibration transmitted into the mount is reduced (i.e., similar to the tines of a tuning fork). The result is a reduction in the mechanical coupling mechanisms between the independent crystal beam assemblies. A penalty is the added need to manufacture dual beam assemblies where each tine matches the characteristics of the other.

The vibrating beam accelerometer has been developed as a lower cost alternative to the conventional pendulous electrically-servoed accelerometer through elimination of the torque-generator and associated torque-to-balance and pulse quantizer readout electronics. Versions of the device have been built that meet strapdown system accuracy requirements for applications from the lower to upper end of the performance spectrum. The ultimate success of the vibrating beam accelerometer will depend on whether its accuracy capabilities compare with those for mature technology pendulous accelerometers at a competitive price.

# QUARTZ RATE SENSOR

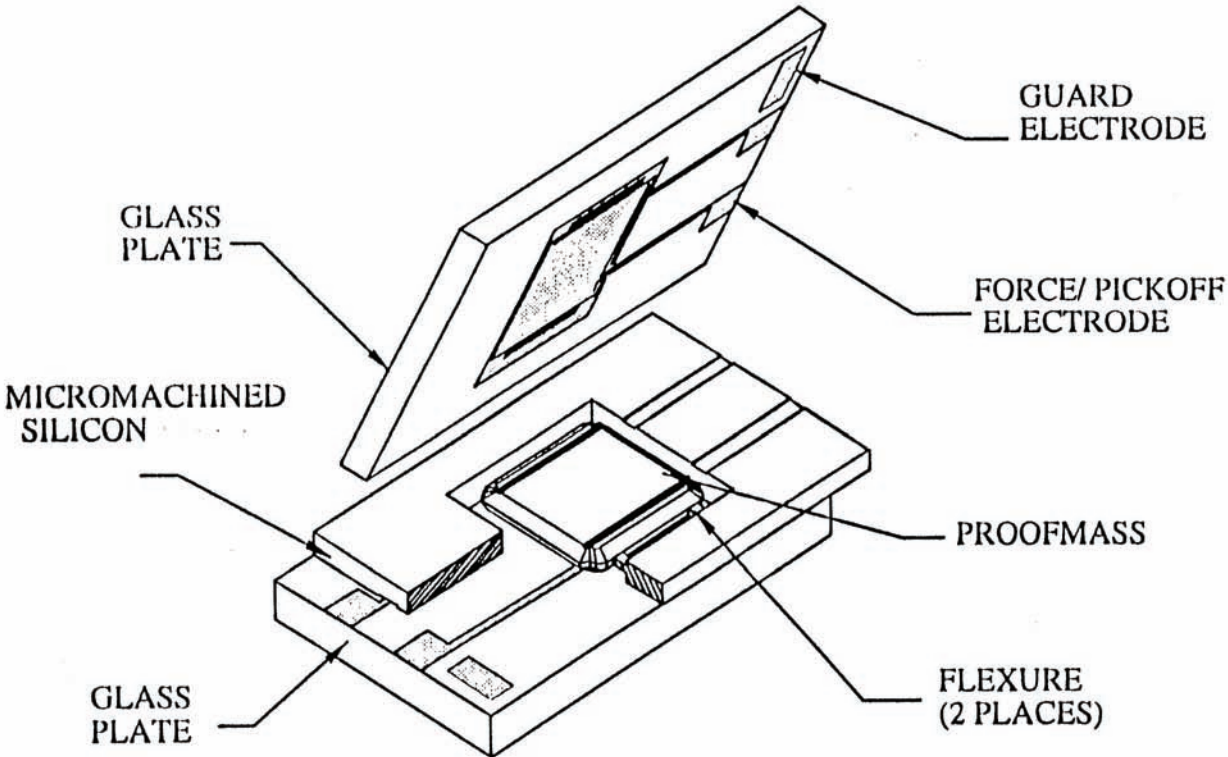


## QUARTZ RATE SENSOR

The Quartz Rate Sensor (QRS) uses crystal quartz in a tuning fork configuration to sense angular rate. The Systron Donner QRS concept is depicted in the slide in which a crystal quartz tuning fork is driven at its natural frequency by appropriate drive electronics interfaced to the crystal. The piezoelectric characteristic of crystal quartz converts the drive electronics output to a mechanical flexure of the fork crystal; the dynamic flexure of the crystal creates a proportional voltage sensed by the drive electronics input, thereby closing the drive loop and creating a sustained oscillation in the quartz tuning fork drive tines. The resulting in-plane linear oscillation of the drive tines creates an oscillating in-plane linear momentum of the tines that produces an oscillating reaction force to angular rate about the tuning fork axis through the resulting Coriolis acceleration effect (i.e., rotation of a linear velocity vector requires an applied acceleration normal to the velocity vector and applied angular rate). The oscillating Coriolis reaction force is equal but opposite for each tine (because the linear momentum of each is opposite the other) which produces an out of plane differential oscillation of the drive tines at the drive frequency proportional to the applied angular rate. The drive fork out-of-plane oscillation is mechanically transmitted to a second crystal quartz tuning fork (pickup fork) which is physically connected to the drive fork, thereby creating an out-of plane differential oscillation of the pickup fork tines at the drive fork frequency proportional to the applied angular rate. A pickup amplifier senses the resulting differential voltage generated in the pickup fork tines which is demodulated at the drive fork oscillation frequency to obtain a DC output proportional to the applied angular rate.

Performance characteristics of the QRS are consistent with some tactical missile requirements. Because of its low cost in mass production (each fork assembly is acid etched as a single unit on a substrate of several units) the unit has great attraction for high volume markets where high performance is not required and very low cost is mandatory (e.g., the automotive market). Because of its simple one piece construction, the QRS is rugged and reliable which fits the requirements of several lower performance applications. The accuracy of the QRS is dependent on the design of the fork assembly mounting, dynamic coupling between its natural internal resonance modes, and its internal mass balance, with a combined effect to attenuate the transmission of externally applied linear vibrations and shock to the QRS pickup fork differential out-of-plane oscillation output. Because crystal quartz has sharply defined resonance modes (i.e., high Q) there is natural attenuation of residual input vibration effects outside the resonance mode passbands. The mechanical modulation of the input rate at the drive fork frequency and associated demodulation of the pickup fork response further attenuates residual error effects outside the modulation/demodulation passband. On the other hand, because of the modulation/demodulation angular rate transmission characteristic, the QRS cannot sense angular rate components with frequency content approaching the fork drive frequency. In addition the QRS is an angular rate sensor (not an integrating angular rate sensor) with an analog output (requiring sampling and conversion to digital format for strapdown system usage). Increased bias uncertainty results with some accuracy loss under high frequency angular vibrations. Continuing QRS development work has been directed at increasing accuracy for the higher performance application areas.

# MICROMACHINED SILICON ACCELEROMETER



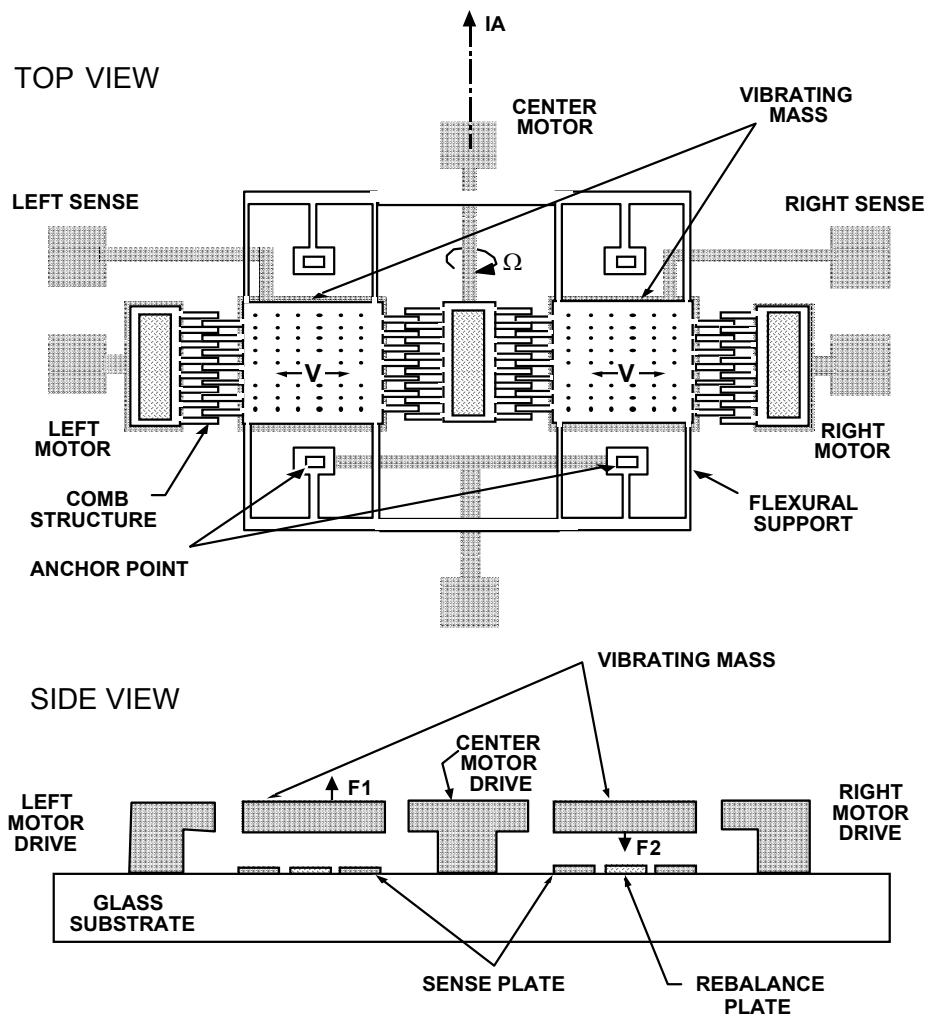
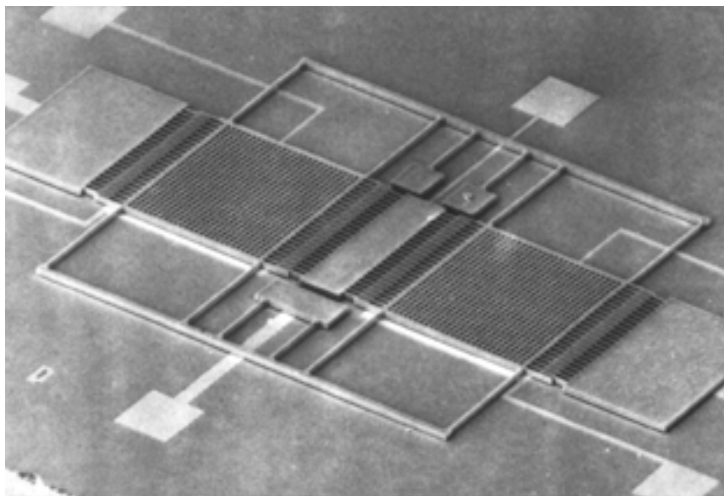
## MICRO MACHINED SILICON ACCELEROMETER

The slide is a drawing of the Endevco micro machined silicon accelerometer, one of the newer inertial sensing technologies to emerge in recent years. The accelerometer is of the electrically rebalanced pendulous type in which the pendulum is micro machined into a crystalline silicon wafer. The pendulum is formed by through-cut micro machining the silicon along three edges of a square, with the pendulum hinge formed on the fourth side by a partial through-cut and necking-down process. Glass plates are bonded on each side of the silicon wafer to constrain pendulum motion, and to also support electrostatic-forcer/capacitive-pickoff electrodes for pendulum rebalance (to the pickoff null position). Manufacturing processes for the device use the same methods applied to silicon integrated circuits (ICs), hence, are projected to result in low cost for mass production. In practice, 80 or more pendulum assemblies can be produced on a single silicon wafer, with the pendulums cut from the wafer using an IC saw. Bias accuracy is in the 1 milli-g category.

The Endevco electrical rebalance approach is but one method of generating silicon accelerometer output. Both Allied Signal and Kearfott have similar silicon pendulous accelerometer designs based on a vibrating beam pickoff in which the vibrating beam is micro machined into the silicon wafer to support the pendulum. IEC/L-3 Communications and Kearfott also have designs that in each silicon wafer, incorporate two accelerometers with parallel input axes, and in which the silicon is micro machined to also enable an applied differential linear vibration of the accelerometers perpendicular to their input axes. Under angular rate perpendicular to the applied vibration and accelerometer input axes, the accelerometers develop outputs at the applied vibration frequency with amplitude proportional to the input angular rate (due to Coriolis coupling of applied vibration velocity with input angular rate). By differencing the accelerometer outputs and demodulating/filtering the resulting AC signal, an angular rate output is obtained. Summing the accelerometer outputs (with filtering to remove residual vibration induced effects) generates an acceleration output. Thus, the combined unit acts as a multi-sensor, providing one axis of sensed acceleration and angular rate. Angular rate bias accuracy for the silicon multi-sensor is forecasted to be in the 1 - 10 degree per hour category.

Due to small size, rugged construction and forecasted low cost, one of the principal application areas for silicon micro machined inertial sensor technology is in guided artillery shells.

# MICROMACHINED SILICON COMB DRIVE TUNING FORK GYRO



## MICROMACHINED SILICON COMB DRIVE TUNING FORK GYRO

The slide depicts a micromachined silicon gyro configuration designed at the Charles Stark Draper Laboratory. A version of the unit is in production at Honeywell Minneapolis. The gyro consists of a silicon structure mounted to a glass substrate with deposited metallization for sensor interfacing. The silicon structure is micromachined to contain two masses suspended by a sequence of beams anchored to the substrate in an arrangement characterized as a double ended tuning fork. By applying oscillatory voltages to the outer motor drives, the two masses are electrostatically forced through a comb structure into a lateral in-plane velocity oscillation  $V$ . The comb structure provides added surface area to magnify the electrostatic driving force. Each motor drive control loop is a self-drive oscillator using proof mass position feedback to sustain constant proof mass motion amplitude. The linear proof mass motion creates oscillating in-plane linear momentum that rotates under applied input axis angular rate  $\Omega$ . Rotation of the oscillating linear momentum vectors generates oscillating reaction forces ( $F_1$  and  $F_2$ ) through the Coriolis effect (i.e., rotating a linear momentum vector requires applied force perpendicular to the momentum and rotation rate vectors). The oscillating Coriolis reaction forces are equal but opposite for each mass (because the linear momentum of each is opposite the other) which produces out of plane differential oscillations of the masses with amplitude directly proportional to applied angular rate and inversely proportional to the silicon suspension stiffness. The out-of-plane oscillation is measured by capacitor plate pickoffs under each of the two masses, generating an oscillatory electrical signal proportional to applied angular rate. The oscillatory angular rate signal is then demodulated for output using a reference voltage generated in the motor drive control loop. For improved accuracy, electrostatic oscillatory closed loop control can be employed to maintain the masses at null, thereby reducing the effect of pickoff scale factor and silicon structure stiffness uncertainty as error sources. The closed loop control voltage amplitude would then be used as the measured angular rate signal.

The Draper/Honeywell silicon gyro design is but one of several silicon MEMS (Micromachined ElectroMechanical System) devices under development for angular rate sensing. Other design groups include BAE Systems, Analog Systems and Northrop Grumman. The fundamental principal of operation for each of these gyro configurations is the same, angular rate is sensed through Coriolis generated reaction force on driven vibrating mass. The configurations differ in their physical structure and mechanism for creating the vibration and for sensing the Coriolis reaction. Motivation for their development is projected low cost through mass production; hundreds of gyros can be manufactured on a single silicon wafer using manufacturing techniques similar to those applied to silicon microcircuit production. Small size and ruggedness provide added advantages; initial applications are for angular rate sensing in automotive and guided munition applications. Performance goals are in the 1 deg/hr bias accuracy category with 10 - 50 deg/hr performance achieved as of 2005.

**NOTES**

**SYSTEM MECHANICAL,  
THERMAL,  
PACKAGING DESIGN  
CONSIDERATIONS**

# **INS THERMAL/MECHANICAL DESIGN CONSIDERATIONS**

- **THERMAL**
  - **ELECTRONIC COMPONENT MAXIMUM TEMPERATURE LIMITS**
  - **SENSOR ERRORS (THERMAL CONTROLS IF NECESSARY)**
  - **SENSOR ALIGNMENT STABILITY (STRAPDOWN)**
  - **SIZE/WEIGHT**
  - **COOLING PHILOSOPHY**
  - **THERMAL DRIVERS**
    - **SYSTEM SELF-HEATING/TURN-ON TRANSIENTS**
    - **ENVIRONMENT TEMPERATURE (SYSTEM/VEHICLE INSTALLATION, COOLING AIR CHARACTERISTICS, ALTITUDE, EARTH LOCATION, SEASON)**
    - **SENSOR THERMAL CONTROLS IF NECESSARY**
  
- **STRUCTURAL**
  - **STRUCTURAL DESIGN DRIVERS**
    - **ACCELERATION**
    - **VIBRATION**
    - **SHOCK**
  - **STRUCTURAL RESONANCES (SENSOR ERRORS, STRUCTURAL RELIABILITY)**
  - **SIZE/WEIGHT**
  - **THERMAL CONDUCTIVITY**
  - **SENSOR ASSEMBLY MECHANICAL DISTORTION**
  - **MECHANICALLY DITHERED LASER GYRO CROSS-COUPLING**

## INS THERMAL/MECHANICAL DESIGN CONSIDERATIONS

The packaging design of an inertial navigation system involves the packaging of the sensors, gimbals (if present), and system electronics in a physical configuration that is compatible with the installation constraints of the user. In general, the packaging arrangement is driven by thermal and structural design considerations, which inevitably set competing requirements.

The thermal design of a system must primarily assure that component part temperatures do not exceed prescribed limits for nominal reliable operation. For an INS, this requirement is compounded by the need to maintain a quasi-static thermal environment for the inertial sensors to assure high accuracy. All inertial sensors to various degrees, experience performance variations under the presence of thermal gradients across the sensors and as a function of the temperature of the sensors. For some sensors (e.g., laser gyros and some pendulous accelerometers) most of these performance variations are predictable based on temperature measurements, hence, are correctable by software compensation in the INS computer based on temperature measurements. For such sensors, it is important that the INS thermal design assure a uniform slowly changing thermal environment at the sensor to minimize the performance variations needing compensation, thereby, reducing the effect of compensation modeling errors. In the case of laser gyros, this is a fairly straight-forward task because, compared to other available sensors, laser gyros have generally small performance variations with temperature, with thermal error modeling techniques that are fairly accurate.

In the case of sensors experiencing large performance variations with temperature, it is generally required that the sensor temperature be actively controlled by heating to assure operation at a known temperature condition where performance has been optimized. Generally, this requires continuously operating the instrument at a temperature above the highest ambient temperature expected in the application. Because INS sensors are typically mounted to a common sensor mount in close proximity to one another, thermal control requirements for one sensor generally require the entire sensor assembly to be temperature controlled, including the electronic elements mounted with the sensors on the sensor mount. Further, the active temperature control design must be designed so that it does not introduce thermal gradients across the sensors that degrade performance. The initial turn-on warm-up period for systems requiring active sensor thermal control is generally critical from a performance standpoint, and usually requires a warm-up period for the sensors to reach a reasonable thermal equilibrium where performance has stabilized. The result is a reaction time penalty from turn-on until the time the sensor outputs can be used for normal system functions (e.g., self-alignment).

For strapdown systems, alignment uncertainties between the sensors must be minimized to preserve system accuracy in dynamic maneuvering environments. The alignment accuracy requirement also drives the thermal design to minimize sensor mount thermal gradients that would produce mechanical distortions between the sensors. Additionally, sensor and mount materials matching must be considered to avoid bi-metal distortion effects at uniform temperatures which could distort the sensor-to-sensor alignment (and could also produce errors in some sensors due to internal mechanical stresses).

## **INS THERMAL/MECHANICAL DESIGN CONSIDERATIONS (CONTINUED)**

The thermal design of an INS is impacted by the size and weight allowable for the system. Massive structure tends to stabilize thermal variation effects. On the other hand, if thermal controls are needed, a massive system causes a penalty due to generally longer warm-up requirements and higher heater power (not to mention the added weight disadvantage). Most electronic flight systems require some form of cooling to maintain reasonable component part temperatures. For an inertial navigation system, the cooling subsystem must also be designed to avoid thermal dynamic effects at the sensors so that performance is not deteriorated.

The basic thermal drivers to the system (heat input and output) that affect the thermal design are system self-heating due to system electronics (another potential source of turn-on transient errors for the sensors), system external environment temperature (a function of the particular system installation in the user vehicle, system cooling air characteristics, and external vehicle temperatures which vary with altitude, earth location, and season of the year, etc.), and sensor thermal controls (heaters) if needed.

The structural design of the system must assure that the package has the structural integrity to avoid mechanical damage under expected dynamic inputs to the system. These include vibration, sustained acceleration, and shock loads. The vibration requirement is generally the critical structural design requirement. The system must be designed so that vibration induced structural resonances will not physically damage the basic system structure or delicate electrical part interfaces (e.g., connectors, or circuit board/electrical part interfaces). For an INS, the vibration design must also account for potential vibration induced sensor error effects.

The structural design has a direct impact on the system size/weight. Conversely, system size/weight requirements can influence the degree to which structural design goals can be achieved in the anticipated user environment.

The structural design has a direct bearing on the thermal design since the structural elements in the system are the vehicle by which heat is transferred. The structural design must be such that system generated heat is conducted to the cooling system without thermal dynamic effects at the sensors, and without high temperature buildup on localized electronic assemblies.

The structural design must be such that the sensor assembly remains mechanically intact under thermal and acceleration loads. In the case of a strapdown system, the structural design must provide adequate stiffness to maintain sensor-to-sensor alignment

## INS THERMAL/MECHANICAL DESIGN CONSIDERATIONS (CONTINUED)

accuracy under high accelerations, and must provide compliance between the sensor assembly and system chassis to assure that differential temperatures between the sensor assembly and chassis will not produce mechanical stresses between the two assemblies that could distort the relative sensor alignment. In the case of gimballed systems, the chassis/platform interface must also allow compliance to prevent stress buildup in the gimbal motor/bearings.

Finally, for systems utilizing individually mechanically dithered ring laser gyros, the mechanical design of the sensor assembly, its interface with the system chassis, and the individual gyro mechanical design must minimize angular cross-coupling between gyro axes. The mechanical dithering of each laser gyro block creates a back reaction torque into the sensor assembly which generally produces three axis angular vibratory motion at dither frequency. If mechanical cross-coupling exists between gyro axes (e.g., elastomeric isolator imbalance or product of inertia dynamic coupling) the angular vibratory motion at one gyro's dither frequency can cross-couple into another axis which, if out-of phase, will generate coning motion at dither frequency (recall that coning motion is characterized by out of phase angular vibrations around two orthogonal axes which produces a constant attitude rate about the third axis). Simultaneously, false outputs can also be generated from the same back reaction torque response due to gyro and sensor assembly mechanical design deficiencies (e.g., bending effects), thereby also creating potential pseudo-coning at dither frequency. A conflict is thereby created for the strapdown attitude integration algorithm design which on one hand, must accurately calculate the correct attitude solution under real coning motion at dither frequency while on the other hand, must suppress pseudo-coning inputs, also at dither frequency. The problem is complicated by the fact that the dither coupling effects can be amplified by the tendency of two gyro dither loop frequencies to lock together at a common dither frequency if the individual gyro dither frequencies are near one another and mechanical coupling exists between the gyro axes.

## **PACKAGING PHILOSOPHY**

- **ISOLATE SENSORS FROM EXTERNAL/INTERNAL THERMAL ENVIRONMENTS**
  - SLOW THERMAL RATES
  - LOW THERMAL GRADIENTS
  - MINIMIZES SENSOR THERMAL RATE/GRADIENT SENSITIVE ERRORS
  - MINIMIZES SENSOR ASSEMBLY MISALIGNMENT THERMAL DISTORTION (STRAPDOWN)
  - THERMAL CONTROLS IF NECESSARY
  
- **PROVIDE THERMALLY SYMMETRIC SENSOR ASSEMBLY/CHASSIS/EXTERNAL INTERFACES**
  - SENSOR ASSEMBLY THERMAL CONTROLS
  - RESPONSE TO EXTERNAL AMBIENT CHANGES
  - RESPONSE TO TURN-ON THERMAL TRANSIENTS
  
- **PROVIDE MECHANICAL COMPLIANCE FOR UNEQUAL THERMAL EXPANSION OF SENSOR ASSEMBLY AND CHASSIS**
  - MECHANICAL ISOLATORS
  - MINIMIZE SENSOR ASSEMBLY MECHANICAL DISTORTION (STRAPDOWN)
  - MINIMIZE TORQUE MOTOR BEARING LOADS (GIMBALED)

## PACKAGING PHILOSOPHY

Based on the thermal/structural design considerations in the previous slide, the packaging philosophy utilized with typical inertial navigation systems has been to isolate the sensors from thermal dynamic environments (both externally and internally generated) to the greatest extent possible. The sensor assembly design approach has been to assure slowly changing temperatures at the sensors and low thermal gradients across the sensors. This design approach minimizes exciting sensor thermal rate and gradient sensitive errors making it straightforward to compensate residual errors if necessary by temperature measurement and software. Additionally (in the case of strapdown systems) this approach minimizes sensor-to-sensor alignment distortion produced by thermal gradients. If necessary (due to high sensor thermal sensitivity), the sensor assembly thermal design can be achieved using active thermal controls.

Packaging arrangements for inertial systems have been designed so that sensor assembly interfaces with the system chassis and external world are also thermally symmetric to the greatest extent possible. Thermal symmetry in this context refers to thermal conduction and convection path symmetry being such that heat flow in and out of the sensor assembly does not produce thermal gradients or rapid temperature changes at the sensors. If active sensor assembly thermal controls (e.g., heaters) are required, they should be designed with such symmetry considerations in mind, particularly with regard to initial warm-up effects. Similarly, the sensor assembly interface should be designed for symmetry under system electronics warm-up heating, external ambient temperature changes, and cooling system temperature changes (and initial transients).

The sensor assembly/chassis mechanical interface should provide compliance for unequal thermal expansion of the sensor assembly and chassis. Due to the thermal isolation philosophy for the sensor assembly, this becomes an important requirement, because it can be assured that the chassis and sensor assembly will be at significantly different temperatures under particular user conditions. The method for achieving mechanical compliance is through the use of mechanical isolators between the sensor assembly and chassis. Use of mechanical isolators minimizes sensor-to-sensor input axis distortion for strapdown systems, and minimizes torque motor bearing loads for gimbaled systems, caused by mechanical stresses between the sensor assembly and chassis under temperature differential conditions that produce unequal thermal expansion between the two assemblies.

## **PACKAGING PHILOSOPHY (CONTINUED)**

- **ATTENUATE EXTERNAL VIBRATION TRANSMISSION TO SENSORS**
  - **ACCELEROMETER DYNAMIC RANGE**
  - **ACCELERATION SENSITIVE ERRORS**
  - **MECHANICAL ISOLATORS**
  - **DAMPING TO AVOID LARGE RESONANCES**
  - **SWAY SPACE**
  - **CG MOUNT**
- **PROVIDE ACCURATE ALIGNMENT BETWEEN SENSOR ASSEMBLY AND CHASSIS – ATTITUDE/HEADING REFERENCE ACCURACY**
- **MOUNT INSTRUMENTS NEAR ONE ANOTHER TO MINIMIZE CASTING INSTABILITY MISALIGNMENTS**
- **DESIGN FOR MECHANICALLY DITHERED LASER GYRO SENSOR ASSEMBLY TO MINIMIZE CONING AND PSEUDO CONING AT DITHER FREQUENCY**
  - **STIFF SENSOR ASSEMBLY AND GYRO INTERNAL STRUCTURE TO MINIMIZE MECHANICAL RESONANCES AT DITHER FREQUENCY**
  - **SYMMETRICAL SENSOR ASSEMBLY AND MECHANICAL ISOLATOR MOUNTING TO MINIMIZE DITHER COUPLING BETWEEN AXES AND VIBRATION INDUCED HIGH FREQUENCY CONING**
- **MOUNT ACCELS NEAR SENSOR ASSEMBLY CG – MINIMIZES MECHANICALLY DITHERED LASER GYRO REACTION TORQUE VIBRATION PICKUP**

## PACKAGING PHILOSOPHY (CONTINUED)

The packaging philosophy should attenuate external vibration transmission to the inertial sensors if performance sensitivities to vibration exist. This requirement is particularly evident for the accelerometers which must be designed to measure all acceleration inputs. Under system input vibration conditions, the acceleration input range requirements can be substantial if provisions are not included in the system design for vibration attenuation at the accelerometer, particularly if system mechanical resonances amplify the vibration. If the sensor accuracy is impacted by vibration due to acceleration error sensitivity (e.g., conventional spinning wheel gyros, or gimbal platform resonances), the requirement to attenuate vibrations into the sensor assembly is increased. The mechanical isolation system used for thermal expansion compliance between the sensor assembly and chassis is the identically same element used to provide sensor assembly vibration isolation in the INS.

The isolation design must include damping to prevent large resonances of the sensor assembly at its natural frequency on the isolators. The damping and stiffness of the isolators must be high enough that sway space (between the sensor assembly and chassis) is adequate to contain the sensor assembly motion under expected dynamic inputs to the system. The isolator interface must also be of the "CG mount" type such that linear accelerations generate reaction forces from the isolators into the sensor assembly that act through the sensor assembly center of mass. This assures that linear accelerations will not produce rotations of the sensor assembly which could produce dynamic sensor errors, and coning/sculling effects in the case of strapdown systems which might require higher bandwidth sensors and computational software algorithms for accurate analytical reference updating, or in the case of gimbale systems, "stable" element angular vibrations that may be difficult, if not impossible, to control to null by the gimbal torque motor servo loop.

The mechanical isolator selection must be tempered by the ability to also maintain a reasonably accurate mechanical alignment between the sensor assembly and chassis. This capability assures that the system Euler angle attitude/heading readout data faithfully represents the attitude of the aircraft/chassis mount and not only the sensor assembly attitude. Note, that the alignment of the sensor assembly relative to the aircraft does not impact system navigational (position/velocity) accuracy; only the accuracy by which aircraft attitude/heading data is derived from the INS (i.e., the INS calculates the position and velocity of itself in a defined earth referenced coordinate frame. As long as the INS is physically located in the aircraft, INS position is equivalent to aircraft position, within the moment arm from the INS to the aircraft position reference point such as the CG). Isolator design to maintain good sensor assembly/chassis alignment generally conflicts with the design requirement for sensor assembly isolation. In general, good alignment stability favors the stiffer isolators that are less compliant.

For strapdown sensor assembly design, it is generally preferred to mount the sensors near one another to minimize sensor mount

## **PACKAGING PHILOSOPHY (CONTINUED)**

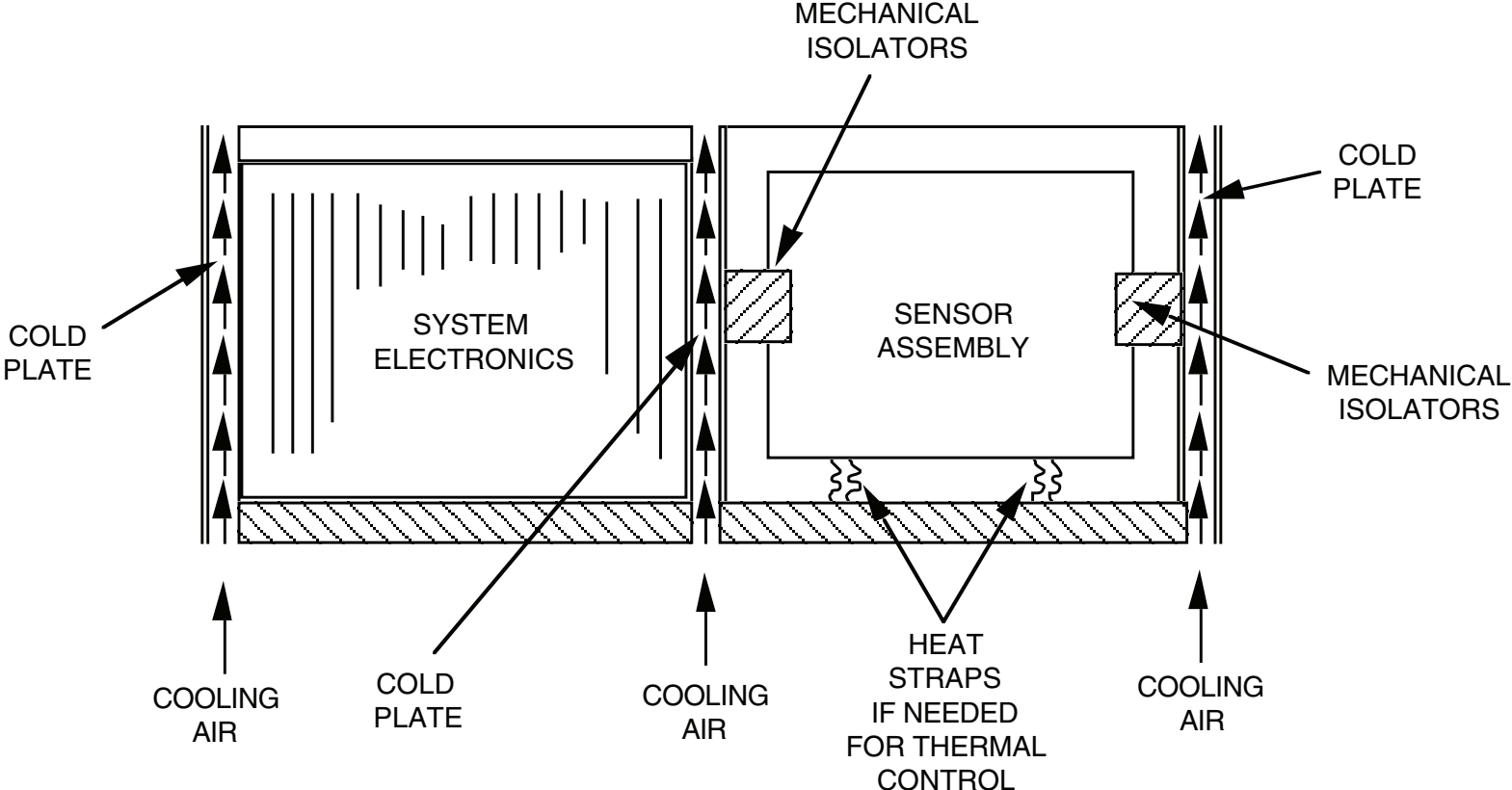
bending between sensors, hence sensor misalignments under dynamic maneuvers (or under thermal gradients across the mount). Close sensor proximity tends to also reduce thermal gradient effects.

For mechanically dithered laser gyro sensor assemblies, the sensor assembly/chassis mechanical design must minimize the coupling of mechanical dither from one axis to the other (creating coning at dither frequency) while also minimizing the creation of pseudo-coning effects at dither frequency. Additionally, high frequency sensor assembly coning motion created by external vibrations operating through the sensor assembly mechanical isolator mountings must also be minimized. This generally translates into a requirement for a mass symmetrical sensor assembly, a stiff sensor assembly structure (i.e., bending mode natural frequencies being well above the dither frequency) with a symmetrical mechanical isolator mounting within the chassis, and a stiff chassis structure. The gyro internal mechanical design must also be mechanically stiff around the cross-axes and the readout mechanism must be void of dither induced resonance effects. In order to minimize the dynamic tendency of mechanically dithered gyros with dither frequencies near one another to lock together at a common dither frequency, thereby creating a worst case dither coning environment, suppliers of mechanically dithered laser gyro systems have had to resort to establishing a design requirement for the dither frequencies between gyro axes to be separated by a specified tolerance.

For strapdown systems utilizing mechanically dithered ring laser gyros, it is also preferred to mount the accelerometers near the sensor assembly center-of-mass to minimize vibration pick-up from the mechanical reaction generated from the gyro dither motors.

**NOTES**

# TYPICAL STRAPDOWN INS AIRCRAFT CHASSIS PACKAGING ARRANGEMENT



## TYPICAL STRAPDOWN INS AIRCRAFT CHASSIS PACKAGING ARRANGEMENT

The slide illustrates a typical packaging arrangement for a strapdown INS. A similar arrangement is utilized for gimbalede systems.

The INS is packaged as a single unit containing all sensing, computing, and associated power generation/distribution functions. The device chassis is divided into two sections; one housing the system electronics, the other housing the sensor assembly. The chassis electronics compartment contains interface electronics and connectors for the electrical subassemblies (typically printed circuit boards), and cold plates to conduct system generated heat out of the chassis. The cold plates are typically metal channels formed as part of the chassis structure through which vehicle supplied cooling air is blown or drawn. The electronic assemblies are adequately heat-sunk to the chassis so that self-generated heat is conducted to the cold plates without producing local hot spots in electrical circuit assemblies.

The sensor assembly contains the gyros and accelerometers mounted to a rigid metal mount. A minimum of electronics is mounted on the sensor assembly to prevent thermal gradient build-up due to self-heating. The sensor assembly is attached to the chassis by elastomeric (rubberized) isolators that form a CG mount for the sensor assembly. The elastomers serve the threefold purpose of vibration isolating the sensor assembly (to minimize vibration induced sensor errors), thermally isolating the sensor assembly to minimize temperature gradient induced sensor errors, and providing compliance between the sensor assembly and chassis for unequal temperature expansion of the two assemblies. Compliance is important for strapdown systems to minimize thermally induced sensor assembly bending (hence, sensor misalignment) and, for mechanically dithered laser gyros, to minimize dither reaction torque induced dynamic cross-coupling between sensor axes that could cause coning and pseudo coning effects at dither frequency (Note: Compliance is also important for gimbalede systems to minimize binding of the gimbal bearings caused by thermally induced stress). It should be noted that the symmetrical orientation of the isolators shown in the chart is an idealized arrangement to minimize dynamic cross-coupling and thermal gradient effects. In practice, the right cold plate wall of the chassis is generally not stiff enough to support the sensor assembly and a more practical mounting arrangement must be utilized (e.g., high/low diagonal mount for mechanically dithered ring laser gyro sensor assemblies as depicted in photos to follow).

Cold plates are located around the sensor assembly to maintain a uniform thermal environment, thereby minimizing thermal gradient build-up. The sensor assembly is thermally isolated from the chassis walls by an air gap (and the elastomeric mount interface which generally has low thermal conductivity). Sensor assemblies that generate significant amounts of self-heating (from sensor heater operation for example) may utilize copper heat straps between the sensor assembly and chassis to conduct heat out of the sensor assembly and, therefore, avoid overheating under operation at high external ambient or high cooling air temperatures. For strapdown systems utilizing ring laser gyros, little power is dissipated on the sensor assembly, and copper straps are not required.

## **REPRESENTATIVE INS CONFIGURATIONS**

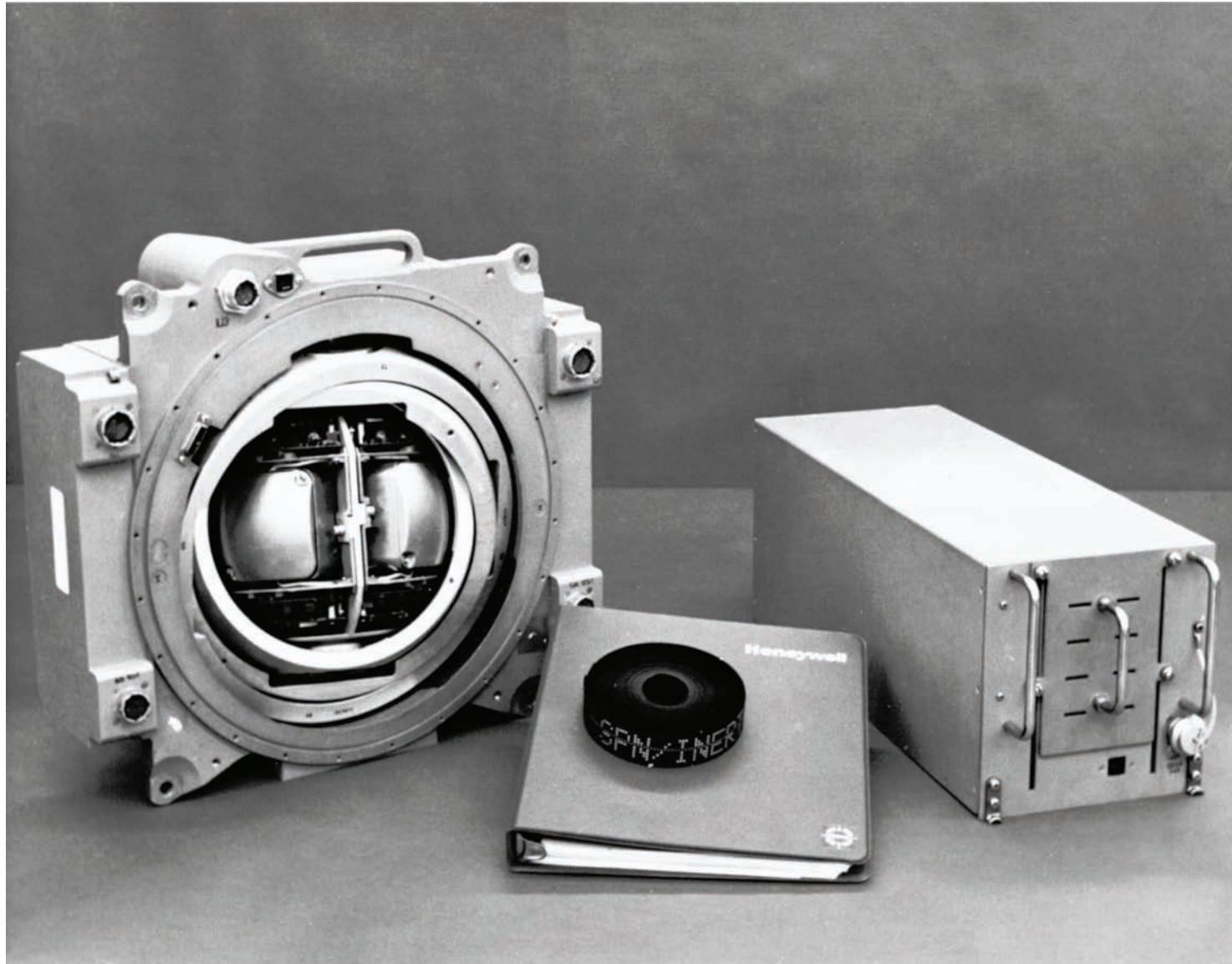
- **AIRCRAFT GIMBALED ESG INS**
- **AIRCRAFT GIMBALED TRG INS**
- **HONEYWELL RLG STRAPDOWN INS EVOLUTIONARY DEVELOPMENT CYCLE – ADVANCED DEVELOPMENT TO PRODUCTION**
- **LITTON RLG STRAPDOWN INS CONFIGURATIONS**
- **KEARFOTT RLG STRAPDOWN CONFIGURATIONS**
- **ADVANCED SKEWED REDUNDANT INS – IISA, BOEING 777 IRS**

## REPRESENTATIVE INS CONFIGURATIONS

To illustrate the packaging configurations being employed in modern day inertial navigation systems, the following photographs will be reviewed for an aircraft gimbaled ESG and TRG INS, and a series of ring laser gyro strapdown systems. Photographs shown were provided through the courtesy of Honeywell, Litton, and Kearfott, industry leaders in the development and production of inertial navigation systems. In the case of the Honeywell strapdown systems, photographs shown have been selected to illustrate a typical evolutionary packaging design development cycle to gain insight into the difference between engineering developmental hardware and production hardware configurations.

Final packaging discussions center on advanced strapdown inertial systems based on the concept of skewed strapdown sensor redundancy. As we shall see, the practicalities of the real world introduce several significant design goals that must be achieved during the engineering development cycle when applying skewed sensor redundancy in actual applications. The design approach promoted by the Navy with their IISA (Integrated Inertial Sensor Assembly) skewed redundancy concept is illustrated by several slides depicting the Litton IISA developmental configuration. A photograph is provided of the Honeywell skewed redundant hexad inertial reference system used on the Boeing 777 commercial airplane, the first skewed redundant system to enter large scale production.

# HONEYWELL GEANS GIMBALED ESG PLATFORM

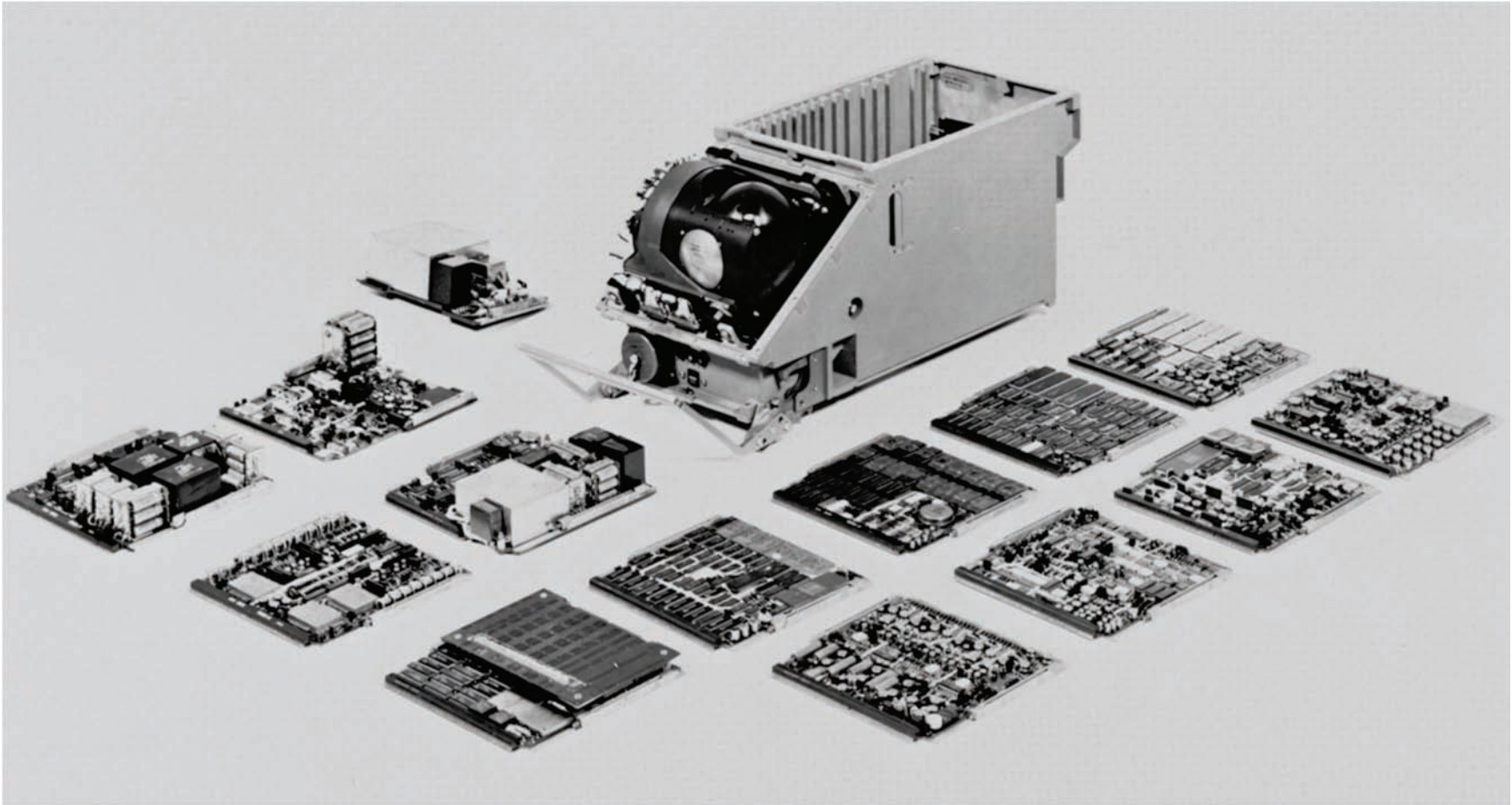


## **HONEYWELL GEANS GIMBALED PLATFORM**

The Honeywell Gimbaled ESG Aircraft Navigation System (GEANS) is a gimbaled INS developed for high accuracy Air Force strategic aircraft application. The platform in the system (shown in the slide) incorporates two electrostatic gyros (ESGs) and three electrically servoed pulse rebalanced pendulous accelerometers. Accuracy is in the 0.1 nautical-mile-per hour range, making this the most accurate large scale production aircraft INS.

The gimbal rings for the platform are visible in the slide, illustrating the light weight rigid shell gimbal design that typifies the construction used in airborne gimbaled IMUs.

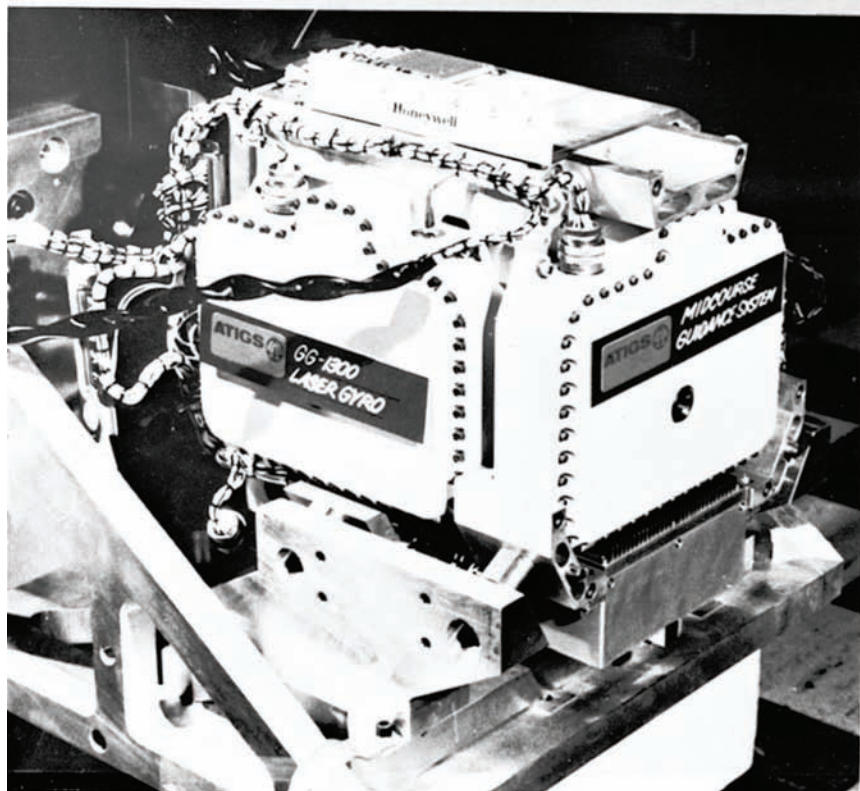
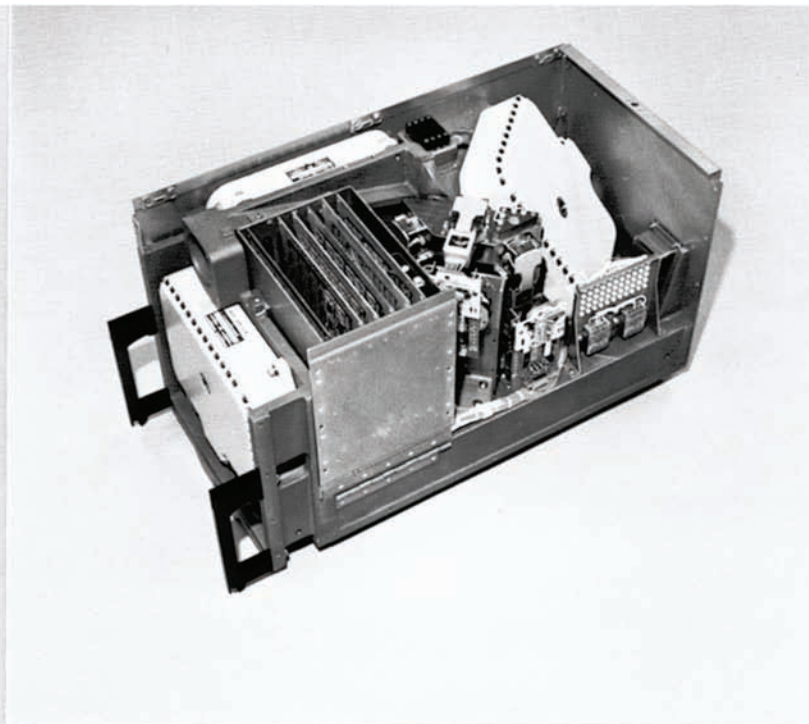
## LITTON LN-39 GIMBALED INU



## **LITTON LN-39 GIMBALED INU**

The slide is of the Litton LN-39 Inertial Navigation Unit (INU) developed for the Air Force as a first generation standard navigation unit in accordance with specification ASD/ENAC 77-1. The LN-39 contains a four gimbal sensor assembly with dry tuned rotor G-1200 gyros and provides 0.8 nmph navigation accuracy. The photo shows the sensor assembly installed in the sensor assembly compartment and the complement of electrical assemblies comprising the LN-39. Overall weight of the LN-39 INU is 38 pounds.

# HONEYWELL LASER GYRO SYSTEMS



↑  
LINS

←  
ATIGS

## HONEYWELL LASER GYRO SYSTEMS

The slide shows the Honeywell engineering prototype hardware that demonstrated the feasibility of laser gyro strapdown technology for aircraft inertial navigation in 1974-1975.

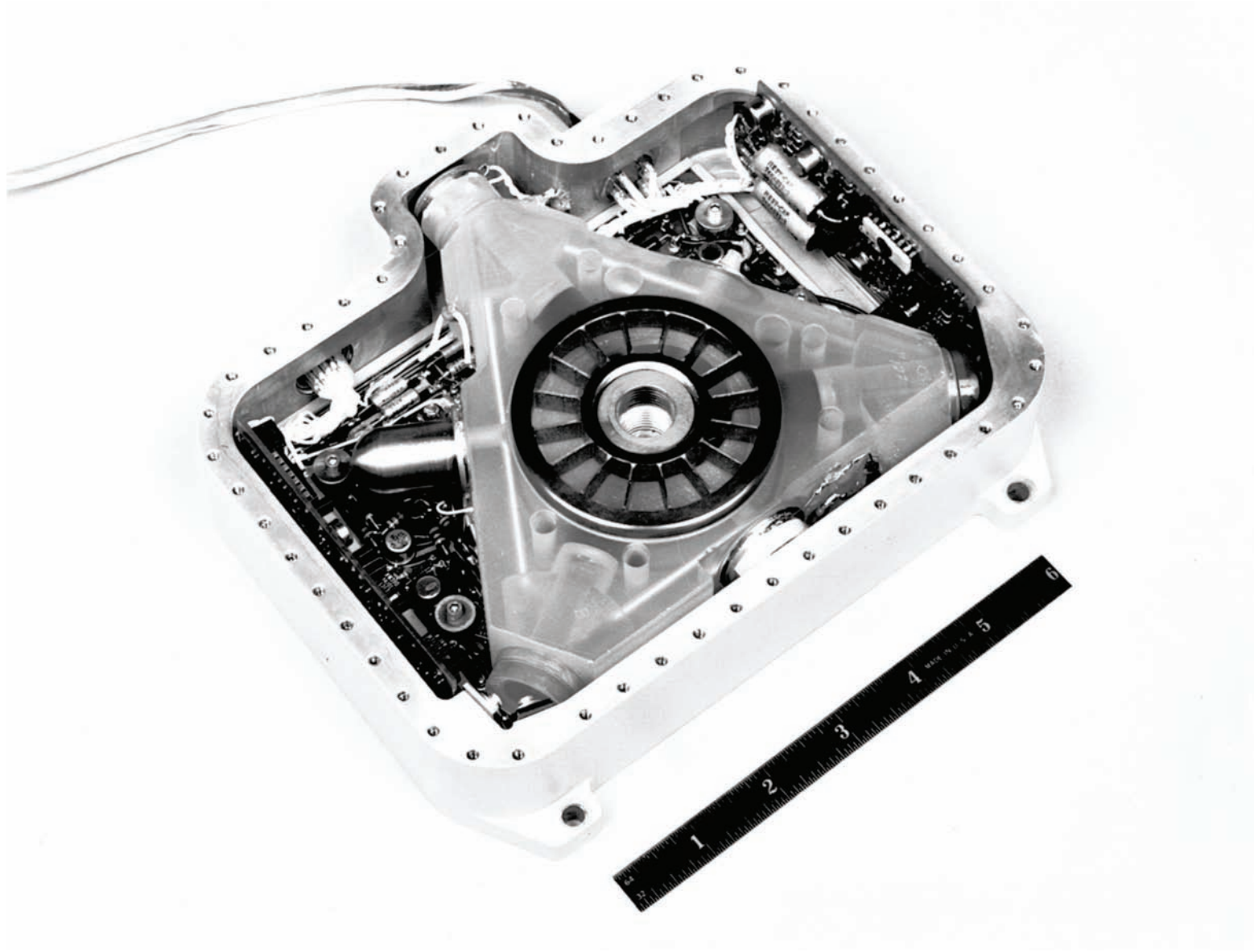
The ATIGS (Advanced Tactical Inertial Guidance System) was developed under sponsorship by Naval Weapons Center, China Lake for midcourse guidance tactical missile applications. The ATIGS-X0 system (shown in the figure) contained three orthogonal GG1300 laser gyros and three analog rebalanced pendulous accelerometers with follow-up pulse quantizers (pulse-reset-integrators). The sensors were mounted to the outside of a casting which also internally housed the system computer. Elastomeric mounts were used to mount the entire system (weighing approximately 55 pounds) to the test vehicle.

Performance of the ATIGS-X0 system during captive flight tests on an A-7 aircraft in 1974-1975 was in the 3 nautical-mile-per-hour category, two to three times better than specifications required. The high accuracy of the ATIGS flight test results demonstrated the feasibility of the laser gyro for strapdown inertial navigation in higher performance aircraft applications.

The LINS-0 (Laser INS) was a laser gyro strapdown INS engineering unit designed in the 1974 time frame to demonstrate the accuracy capabilities of laser gyro technology in military aircraft. The LINS-0 sensor assembly shown in the figure contained three orthogonal GG1300 laser gyros, three orthogonal analog rebalanced accelerometers with follow-up pulse quantizers, plus one skewed GG1300 laser gyro for skewed redundancy experiments. The device computer was a separate assembly. Elastomeric isolators connected the entire sensor assembly (a 75 pound device) plus the sensor assembly mount (a 25 pound device) to the test aircraft.

Flight tests of the LINS-0 during 1975 in a C-141 aircraft at Holloman AFB Central Inertial Guidance Test Facility under Joint Service (Navy, Air Force, Army) sponsorship marked a landmark in the development of strapdown inertial navigation technology. Accuracy of the system was well under the classical 1 nautical-mile-per-hour requirement for military INS equipment for the series of 12 flight tests flown, half of which were out of Alaska where high latitude alignments were required (a more difficult requirement for the heading determination function due to the smallness of the horizontal earth rate measured for North referencing). System reliability and dependability was flawless; no failures occurred, no recalibrations were required, and all test data was valid for the duration of the four month test period.

# HONEYWELL GG1300 LASER GYRO



## **GG1300 LASER GYRO**

The Honeywell GG1300 laser gyro used in both the ATIGS-X0 and LINS-0 systems was the first laser gyro with the ability to meet 1 nautical-mile-per-hour aircraft strapdown INS accuracy requirements with high reliability. The device operated with a 0.63 micron wavelength, was 5.7 inches in length on each leg of its lasing triangle (16.1 inches perimeter), had a 1.5 arc sec pulse size, and utilized mechanical dither for lock-in compensation. The spoke-like structure in the center of the gyro is the mechanical dither spring.

# HONEYWELL H700-3 RLG TRIAD

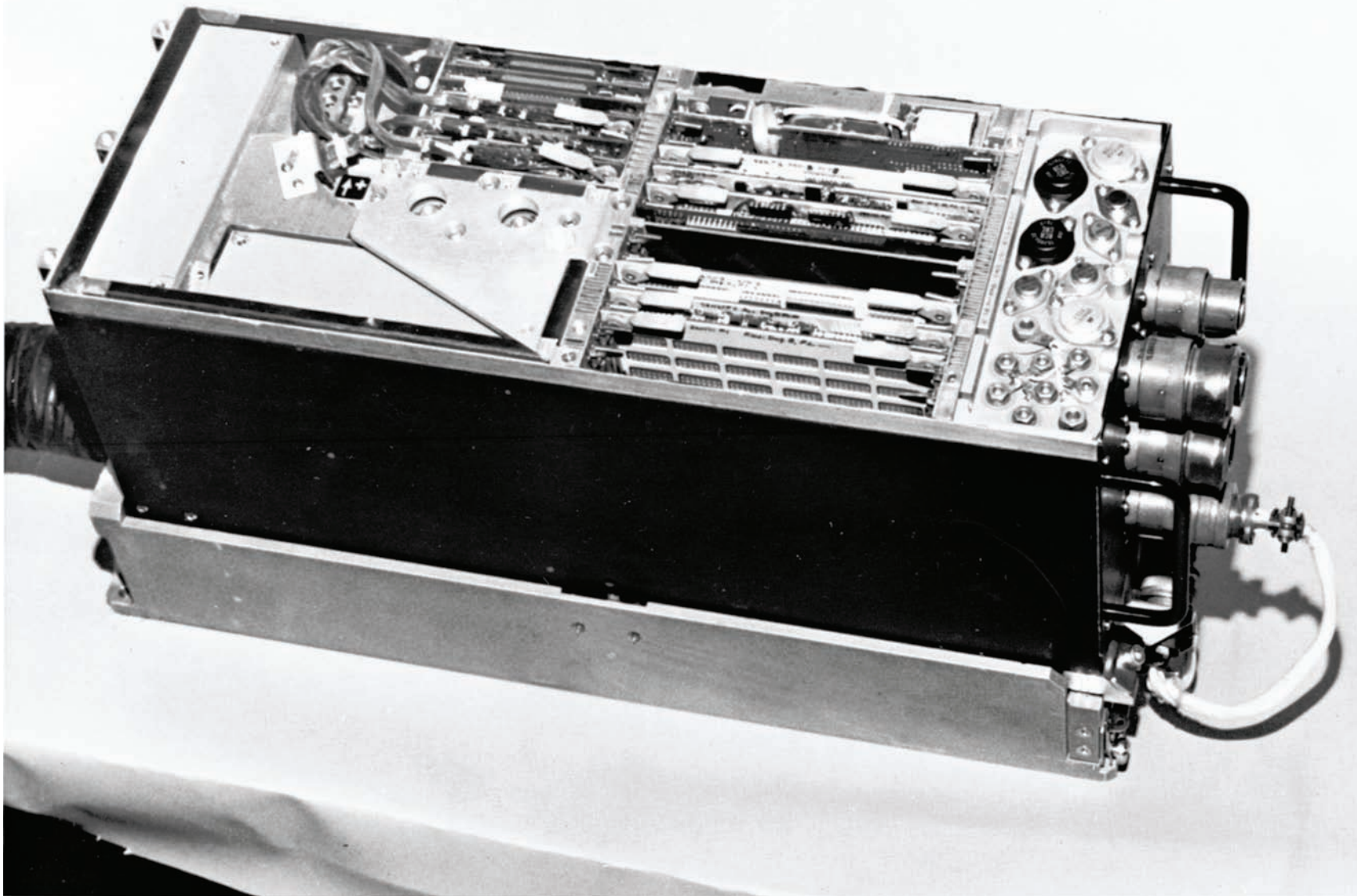


### **HONEYWELL H700-3 RLG TRIAD**

The H700-3 is a Honeywell production tactical missile strapdown laser gyro inertial guidance system. The sensor assembly for the system shown in the figure contains three GG1328 laser gyros and three analog rebalanced pendulous accelerometers with follow-up pulse quantizers. The GG1328 laser gyro operates with a 0.63-micron wavelength, is 2.8 inches on each side of its lasing triangle, has a 3.2 arc sec pulse size, and incorporates mechanical dither for lock-in compensation. Each gyro is mounted to the sensor assembly uncovered, and the entire sensor assembly is covered and hermetically sealed (not shown) to prevent laser gyro electrical input power high voltage corona discharge at altitude.

The complete system consists of a cylindrical computer assembly and a sensor assembly, both of which attach to the large central mounting ring structure shown in the photo. The sensor assembly attaches to the mounting ring through elastomeric isolators. The orthogonal sensor assembly is symmetrically skewed relative to the mounting ring so that the sensor input axes form a symmetrical cone around the device cylindrical axis.

# RING LASER GYRO NAVIGATION UNIT

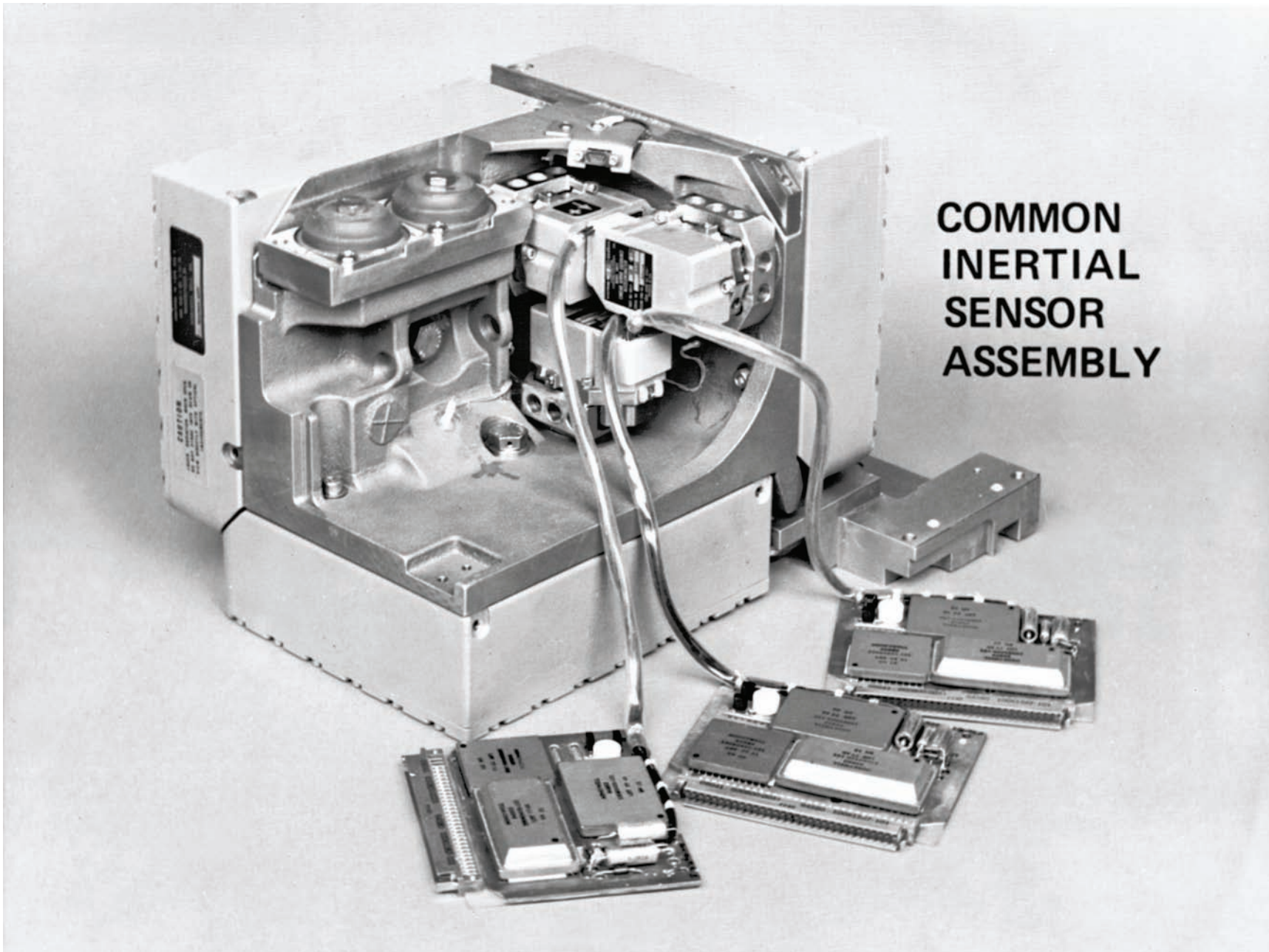


## **RING LASER GYRO NAVIGATION UNIT**

The Ring Laser Gyro Navigator (RLGN) was an Advanced Development Model strapdown INS developed by Honeywell under contract to Naval Air Development Center as a direct result of the successful LINS-0 Holloman flight test program. The RLGN was developed to assess the reliability, maintainability, and performance characteristics of representative RLG strapdown system technology in typical military aircraft environments. The GG1342 laser gyro developed for the system under contract to Naval Weapons Center, China Lake, is a 0.63-micron mechanically dithered unit with performance capabilities equal to those of its larger GG1300 predecessor. The GG1342 size is 4.2 inches per triangle leg with a 2 arc sec pulse size. This smaller size gyro was developed to enable system packaging designs that are compatible with modern small size aircraft INS form factor specifications.

The RLGN shown in the photo is a 7.6 inch by 7.6 inch by 19.6 inch system containing all sensing, computer, and power conversion functions. The system weight is approximately 58 pounds (excluding the test mount which contains the system back-up battery, also shown in the photo). This marked a considerable improvement in size and weight over the original LINS-0 configuration whose sensor assembly alone weighed 75 pounds, and which contained separate computer and power supply units.

Flight test results for the RLGN during an extensive test program (from 1978-1980) in A-7, P-3C, and C-141 aircraft were under 1 NMPH. Reliability was outstanding, having experienced only one minor electrical part failure in 3600 device operating hours since system delivery. Of particular importance was the 2.5 fps velocity accuracy capability demonstrated for the system which marked a more than two-fold improvement compared to original LINS-0 velocity accuracy test results.



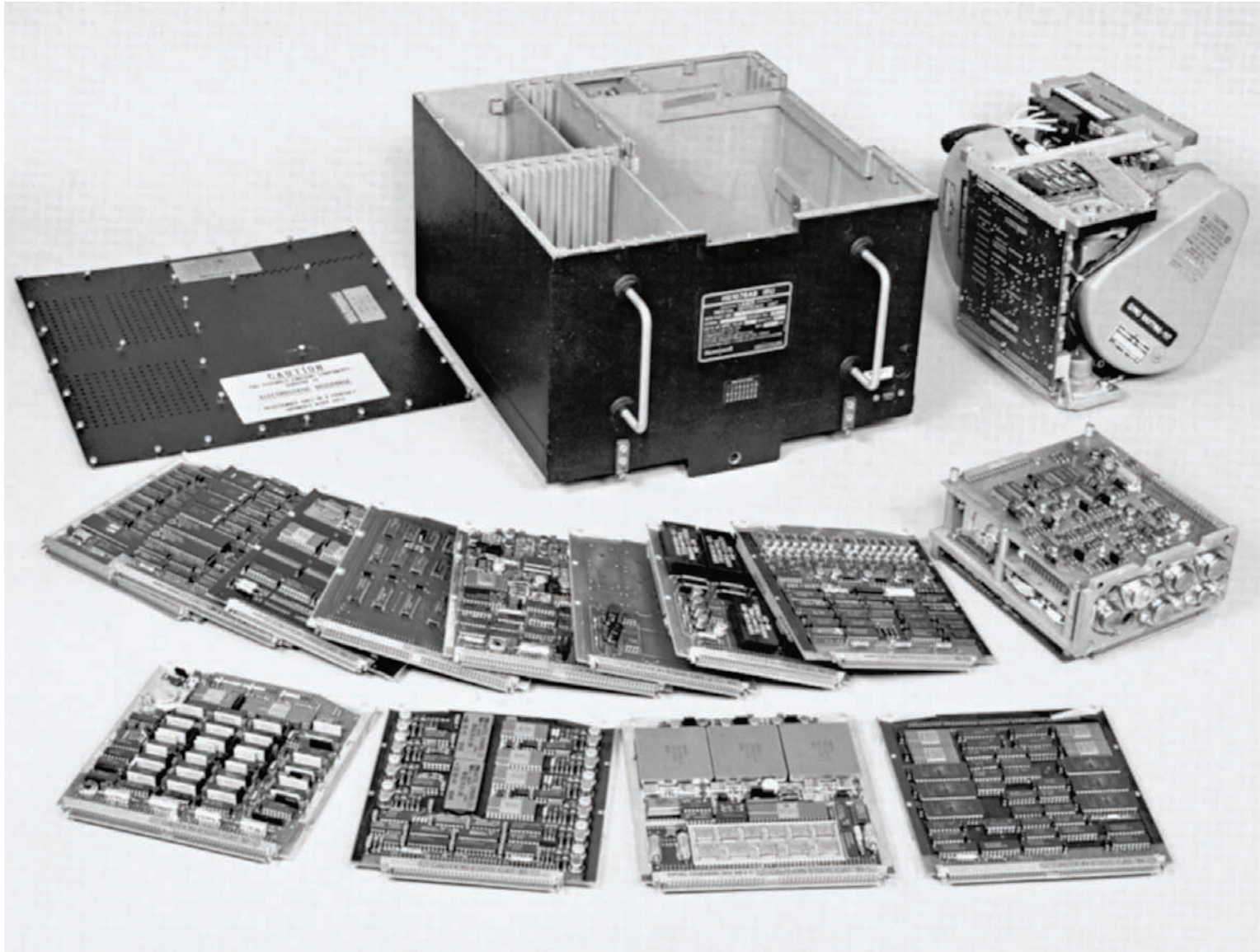
**COMMON  
INERTIAL  
SENSOR  
ASSEMBLY**

## **COMMON INERTIAL SENSOR ASSEMBLY**

The sensor assembly for the RLGN was a small aluminum casting to which were mounted the three orthogonal GG1342 laser gyros and three pendulous analog rebalanced accelerometers with follow-up pulse quantizers. The pulse-quantizer assemblies are shown hardwired to the accelerometers by pig-tails such that the assemblies could then be mounted and heat sunk to the main chassis (to minimize heat dissipation on the sensor assembly). The sensor assembly mounted to the chassis through elastomeric isolators.

This same sensor assembly design configuration was used in several other Honeywell strapdown system configurations during the 1977-1979 time frame.

# HONEYWELL RING LASER GYRO STRAPDOWN IRS



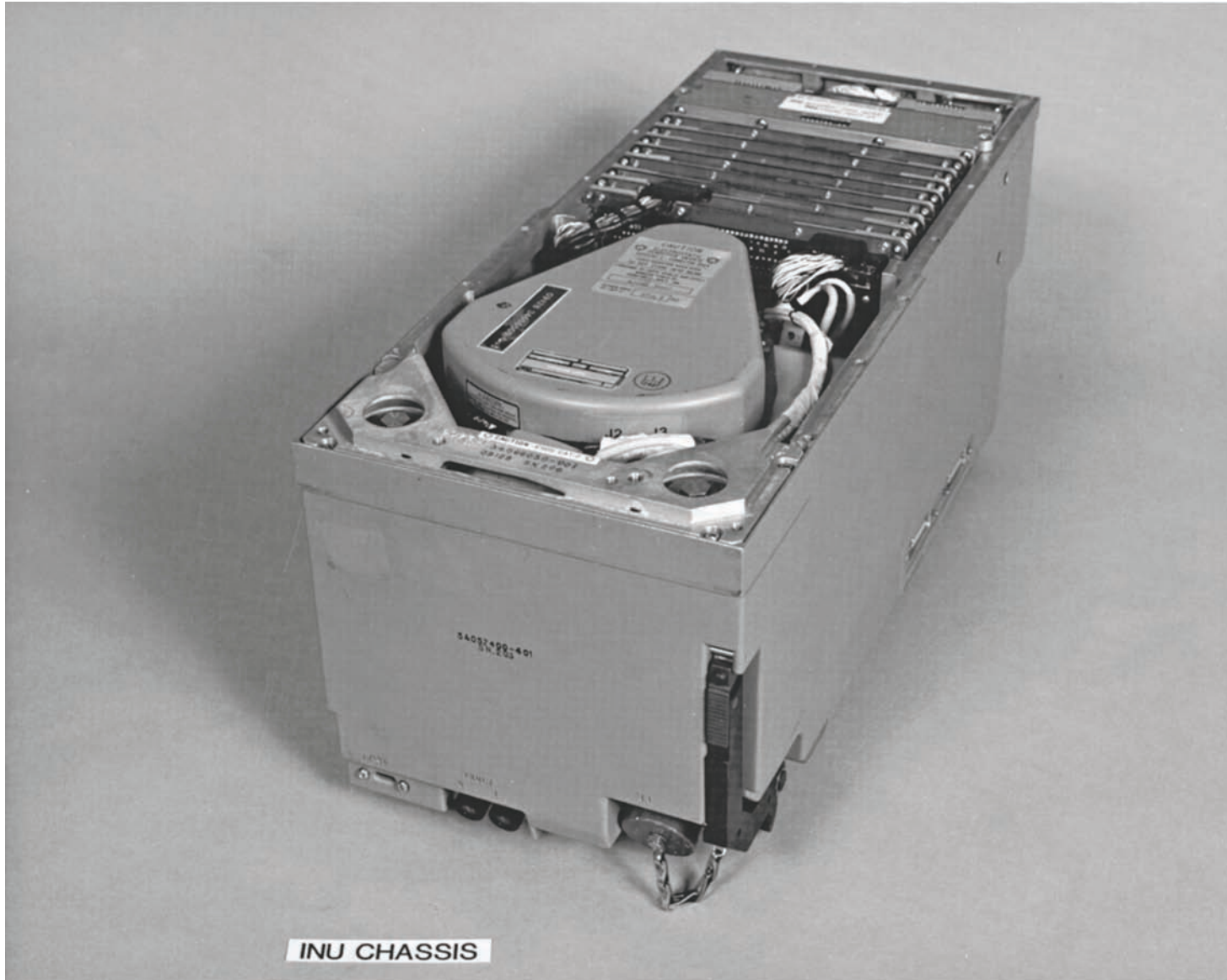
## **HONEYWELL RING LASER GYRO STRAPDOWN IRS**

The laser IRS (Inertial Reference System) shown in the photo is the first aircraft laser gyro strapdown inertial navigation system to enter production. The device was developed by Honeywell under contract to Boeing for use in the 757/767 series commercial aircraft. The unit provides position, velocity, attitude, heading, body acceleration, and body rate outputs to the aircraft flight management and flight control systems. A triple redundant installation is contained in each 757/767 aircraft because of the system usage as the primary flight control reference. System accuracy is better than 1 nmph CEP.

The design of the system is similar to the RLGN shown previously. The chassis form factor was modified for compatibility with the ARINC 704 characteristic drawn up as a standard interface specification for the IRS. The unit employs three orthogonal GG1342 laser gyros and three analog rebalanced pendulous accelerometers with follow-up pulse quantizers. The sensors mount to an aluminum casting which attaches to the chassis through elastomeric isolators (in a manner similar to the RLGN).

To achieve reduced weight and low cost goals, the device electronics were redesigned using large scale integrated circuits. The device contains all sensor, computer, and power conditioning electronics, is 12.7 inches by 12.8 inches by 7.6 inches high, and weighs 43.5 pounds, a significant improvement over the RLGN 58 pound weight.

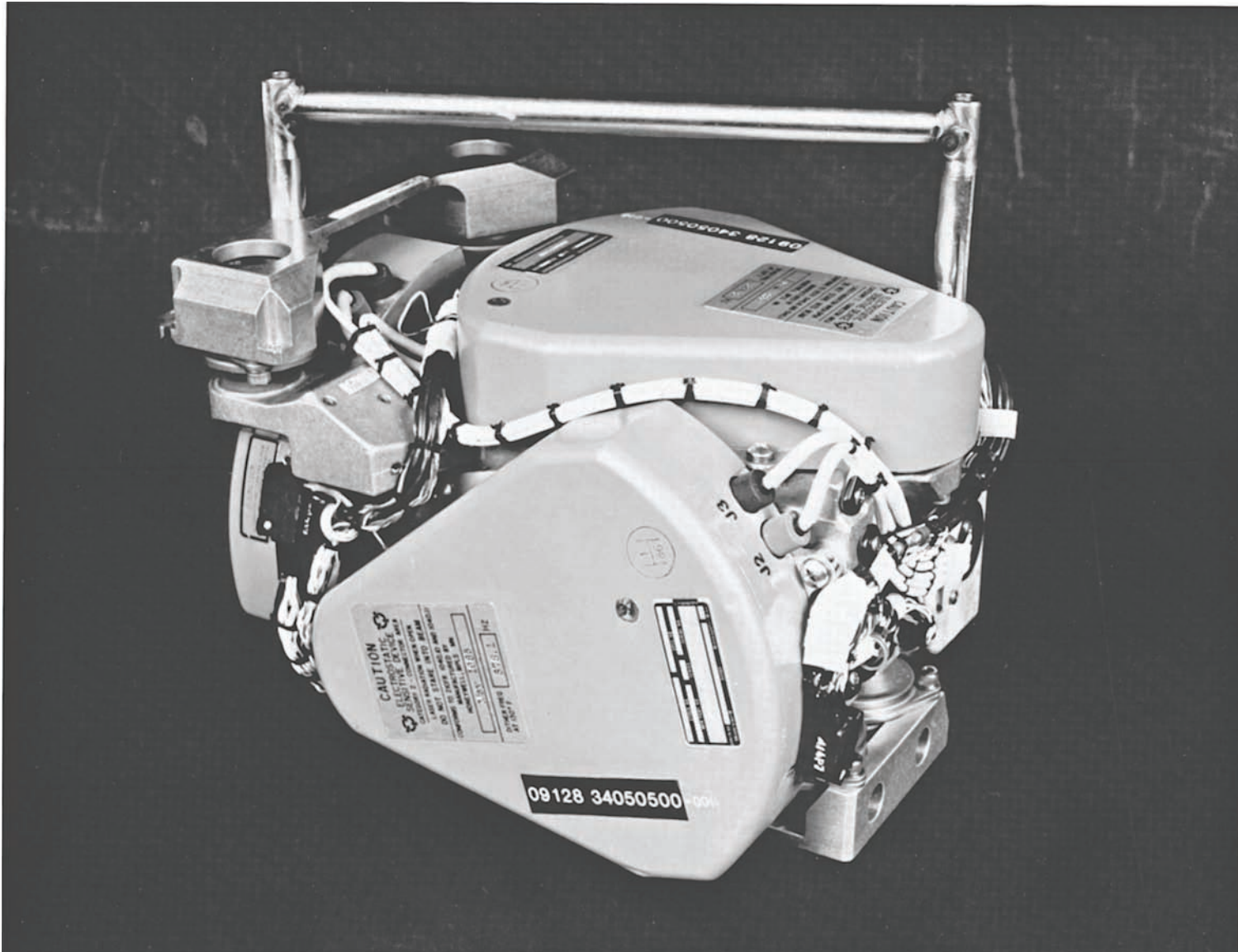
# HONEYWELL H423 LASER INERTIAL NAVIGATION SYSTEM



## **HONEYWELL H-423 LASER INERTIAL NAVIGATION SYSTEM**

The photo is of the Honeywell H-423 laser gyro inertial navigation system developed for better than 0.8 nmph accuracy military aircraft production applications. The sensor assembly for the device (shown separately in the next figure) incorporates three mechanically dithered GG1342 ring laser gyros and three pendulous accelerometers. The sensor assembly is elastomerically mounted within the system chassis.

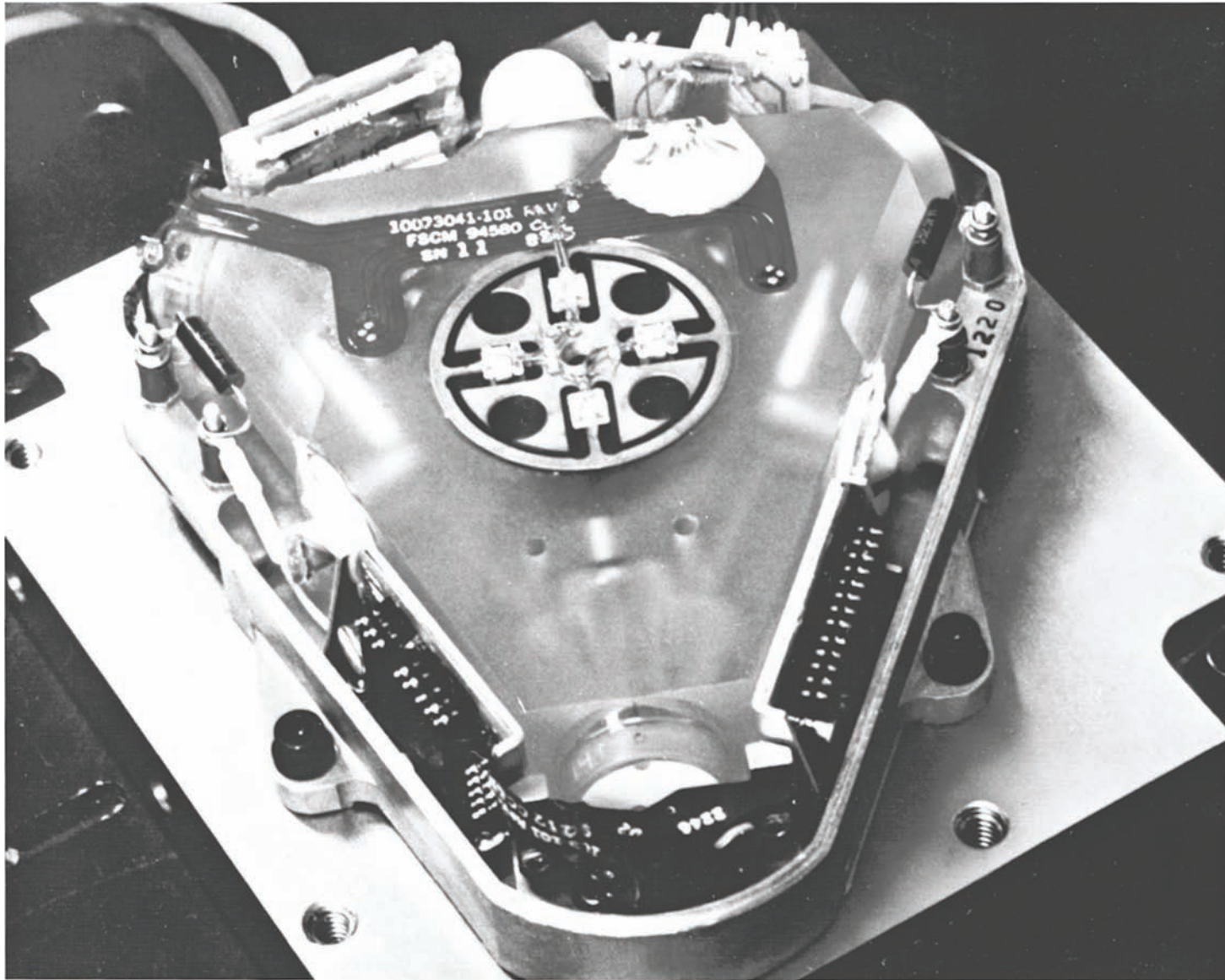
# HONEYWELL H-423 SENSOR ASSEMBLY



## **HONEYWELL H-423 SENSOR ASSEMBLY**

The slide shows the sensor assembly used in the Honeywell H-423 strapdown RLG inertial navigation system.

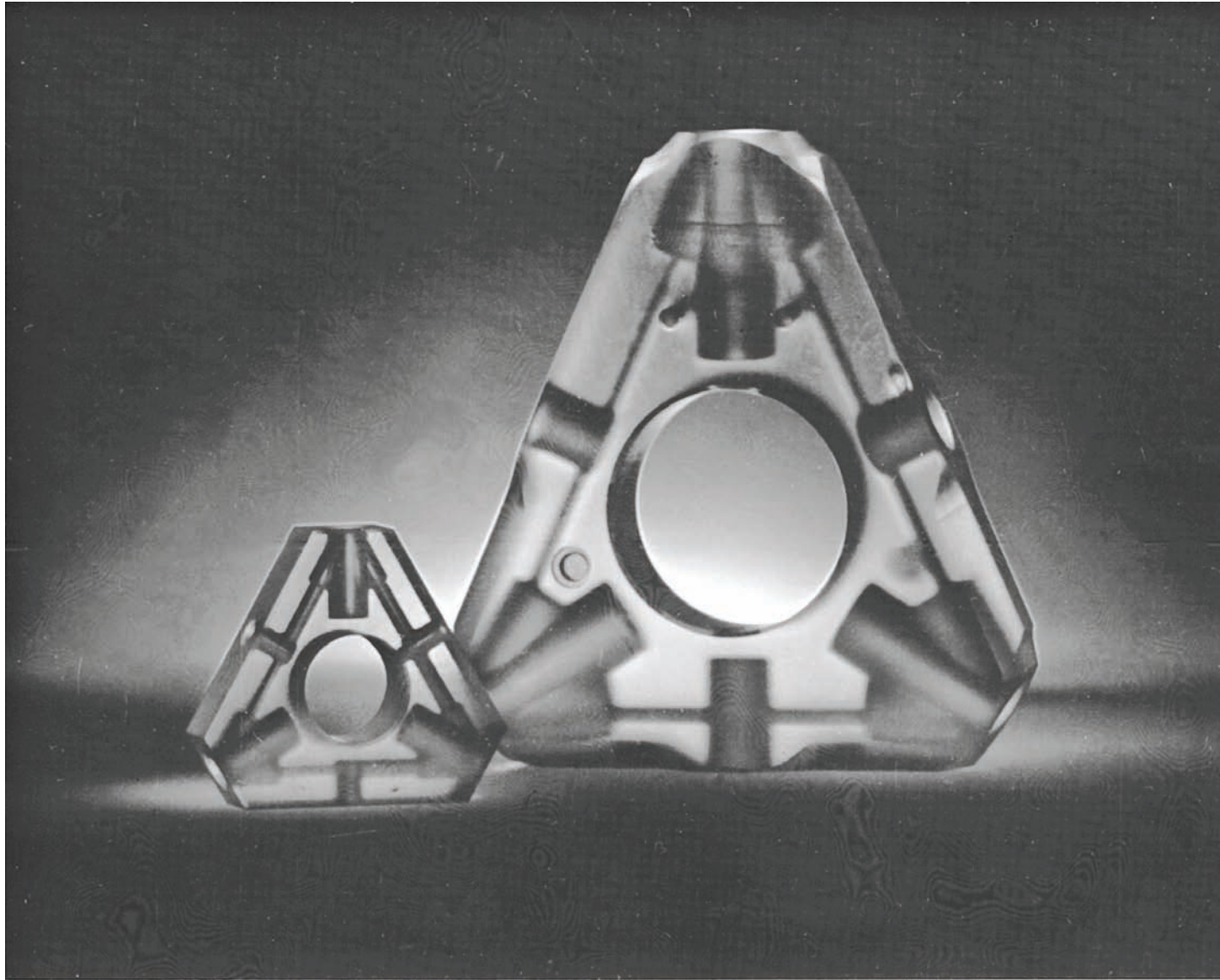
# HONEYWELL GG1342 RING LASER GYRO PACKAGING



## **HONEYWELL GG1342 RING LASER GYRO PACKAGING**

The slide illustrates the internal packaging concept utilized with the production version of the Honeywell GG1342 triangular ring laser gyro, the device incorporated in the military and commercial production systems illustrated on the previous slides. In contrast with the developmental GG1300 configuration shown previously, the GG1342 utilizes a more compact symmetrical case design with non-performance critical electronics mounted externally from the gyro in another compartment of the system chassis. Minimizing the percentage of electronics housed in the laser gyro case reduces the potential for thermally induced performance variations, and enhances maintainability through the ability to correct "outboard" electronic failures without a gyro removal/tear-down/retest. Performance capabilities of the GG1342 are compatible with medium to medium-high inertial navigation applications (e.g., 0.002 to 0.004 deg/rt-hr random walk).

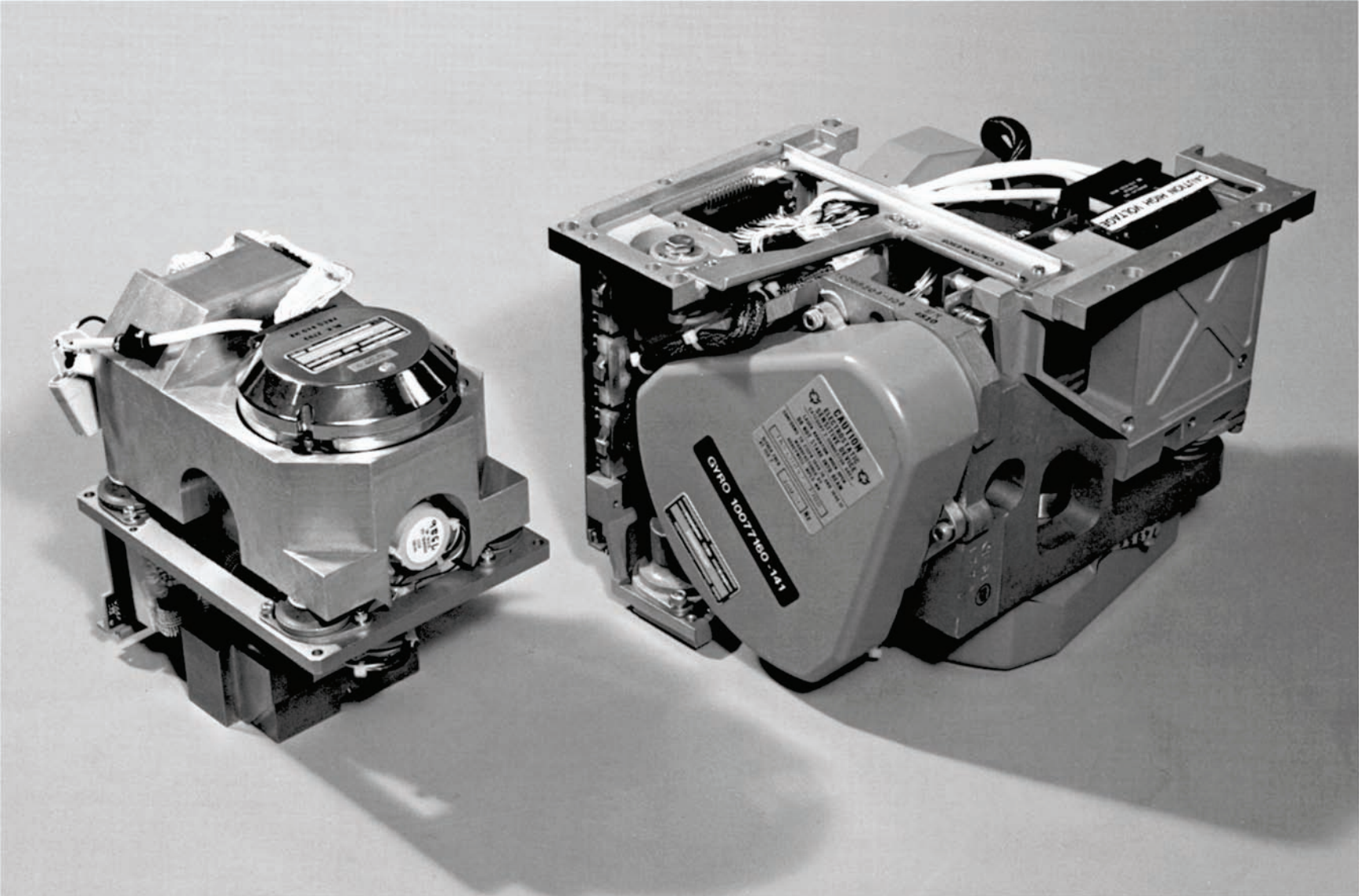
# HONEYWELL GG1320 RING LASER GYRO BLOCK



## **HONEYWELL GG1320 RING LASER GYRO BLOCK**

The slide shows the GG1320 Honeywell production ring laser gyro block assembly compared with that of the Honeywell GG1342 ring laser gyro. The GG1320 is two inches on each side (6 inches perimeter) compared to the GG1342 4.2 inches per side. Experience gained with the GG1342 have made it possible to design the GG1320 to achieve performance compatible with 1.0 nmph CEP medium accuracy inertial navigation requirements (e.g., 0.003 to 0.005 deg/rt-hr random walk).

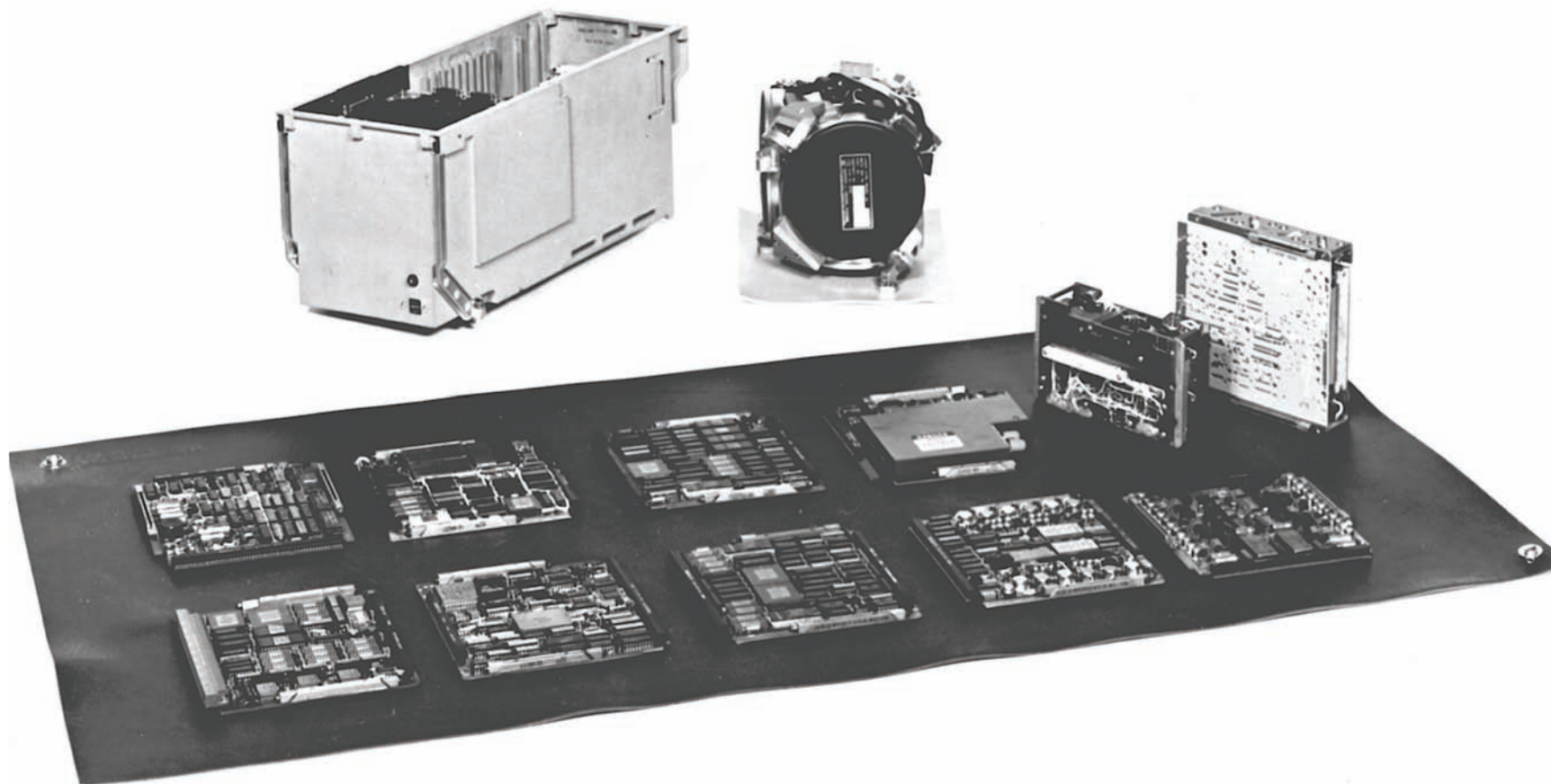
# HONEYWELL GG1320 COMMERCIAL INS SENSOR ASSEMBLY



## **HONEYWELL GG1320 COMMERCIAL INS SENSOR ASSEMBLY**

The slide shows the size advantage afforded by the new Honeywell commercial sensor assembly using the GG1320 ring laser gyro compared to the GG1342 sensor assembly utilized in the original commercial Honeywell IRS.

# LITTON STRAPDOWN RLG INU



## **LITTON STRAPDOWN RLG INU**

The photograph is of the LN-93 strapdown RLG INU (Inertial Navigation Unit) developed by Litton for better than 0.8 nautical-mile-per-hour CEP military applications. The photo shows the open chassis, the sensor assembly, and associated electronic assemblies.

The sensor assembly houses three LG9028 28 cm path length square mechanically dithered ring laser gyros and three pendulous electrically servoed A-4 accelerometers on an elastomerically isolated sensor casting. The sensor assembly and gyro packaging is representative of the ruggedized configuration developed by Litton for operation in military environments.

# LN-93 CLUSTER



## **LN-93 CLUSTER**

The photo shows further detail of the sensor assembly utilized in the Litton LN-93 militarized RLG INU.

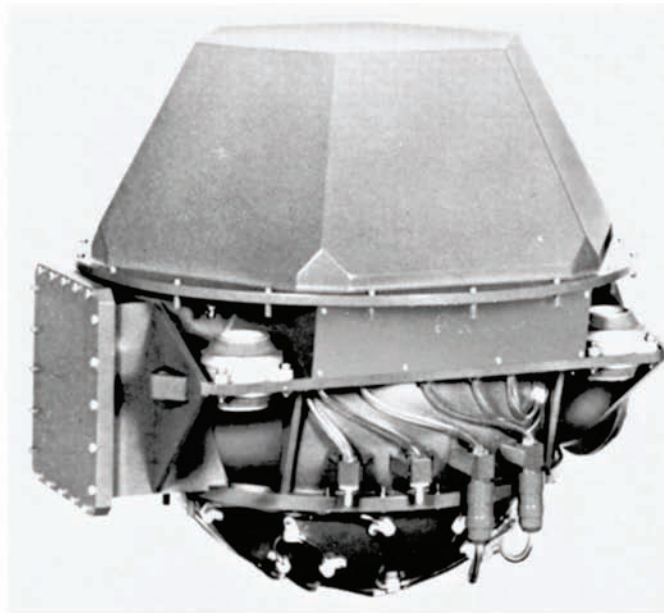
# LITTON LN-95 AINS IMU AND ASSOCIATED COMPONENTS



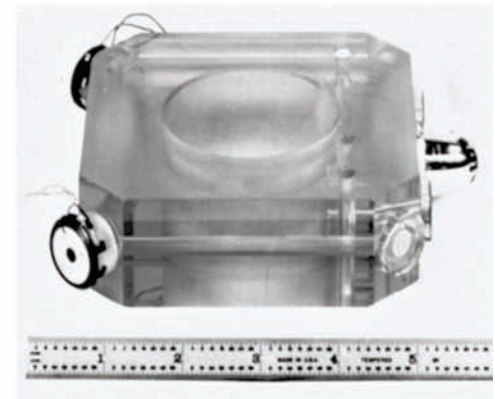
SFIR



BELL MOD XI



INERTIAL MEASUREMENT UNIT

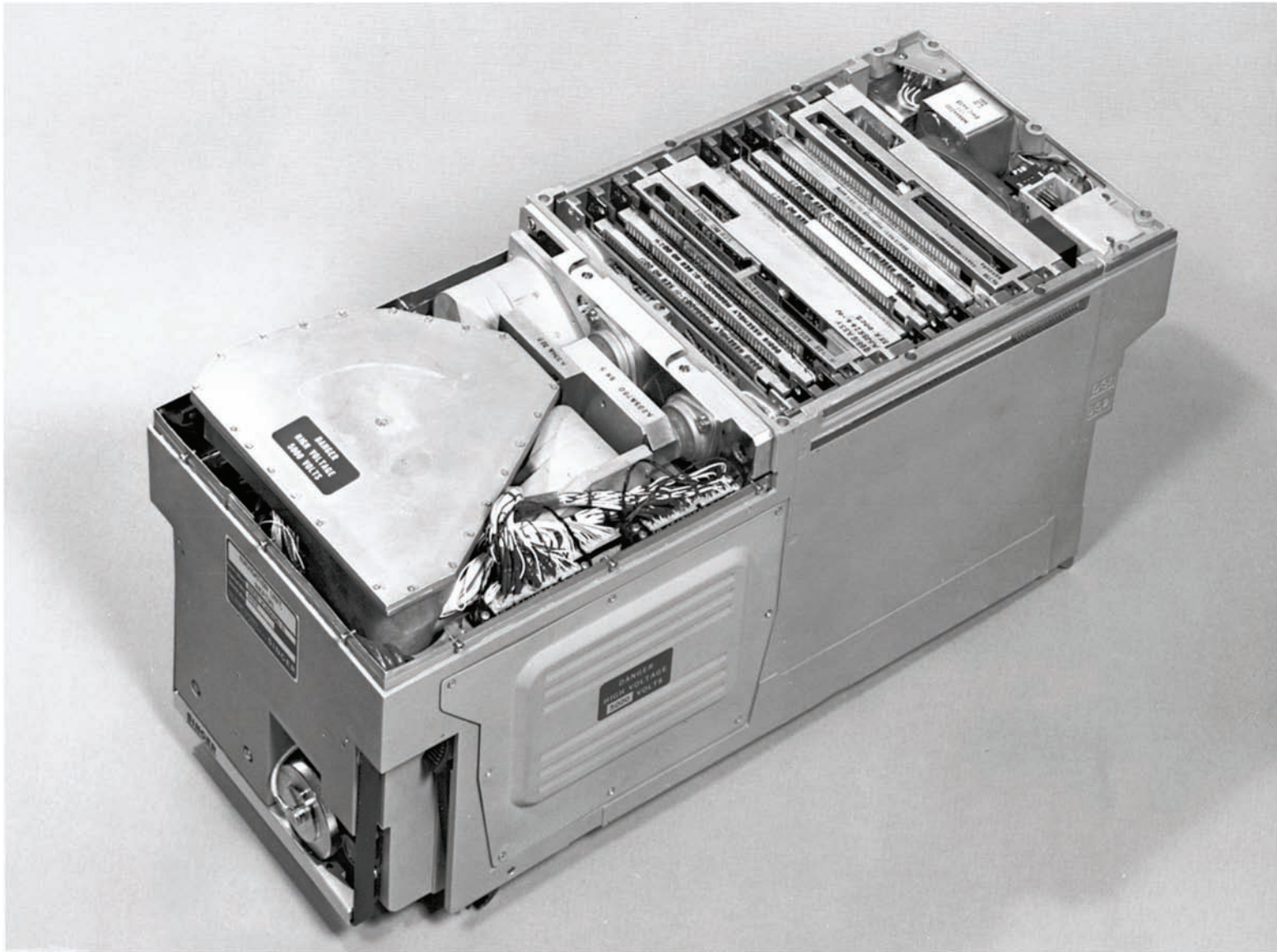


40-cm RLG

## **LITTON LN-95 AINS IMU AND ASSOCIATED COMPONENTS**

The slide shows the Litton LN-95 Alternate Inertial Navigation System (AINS) and some of the associated components contained in the unit. The system was developed as an advanced guidance system for an intercontinental ballistic missile. The LN-95 uses 40 cm ring laser gyros without mechanical dither by operating the gyros in a continuous three-axis angular rate environment to keep the gyros out of lock-in (rate bias). The angular rate is provided by a three-axis mechanical rotation assembly within the IMU. Using rate bias rather than mechanical dither eliminates the gyro random walk that would have been caused by mechanically dithering through lock-in.

# KEARFOTT RING LASER GYRO STRAPDOWN INU

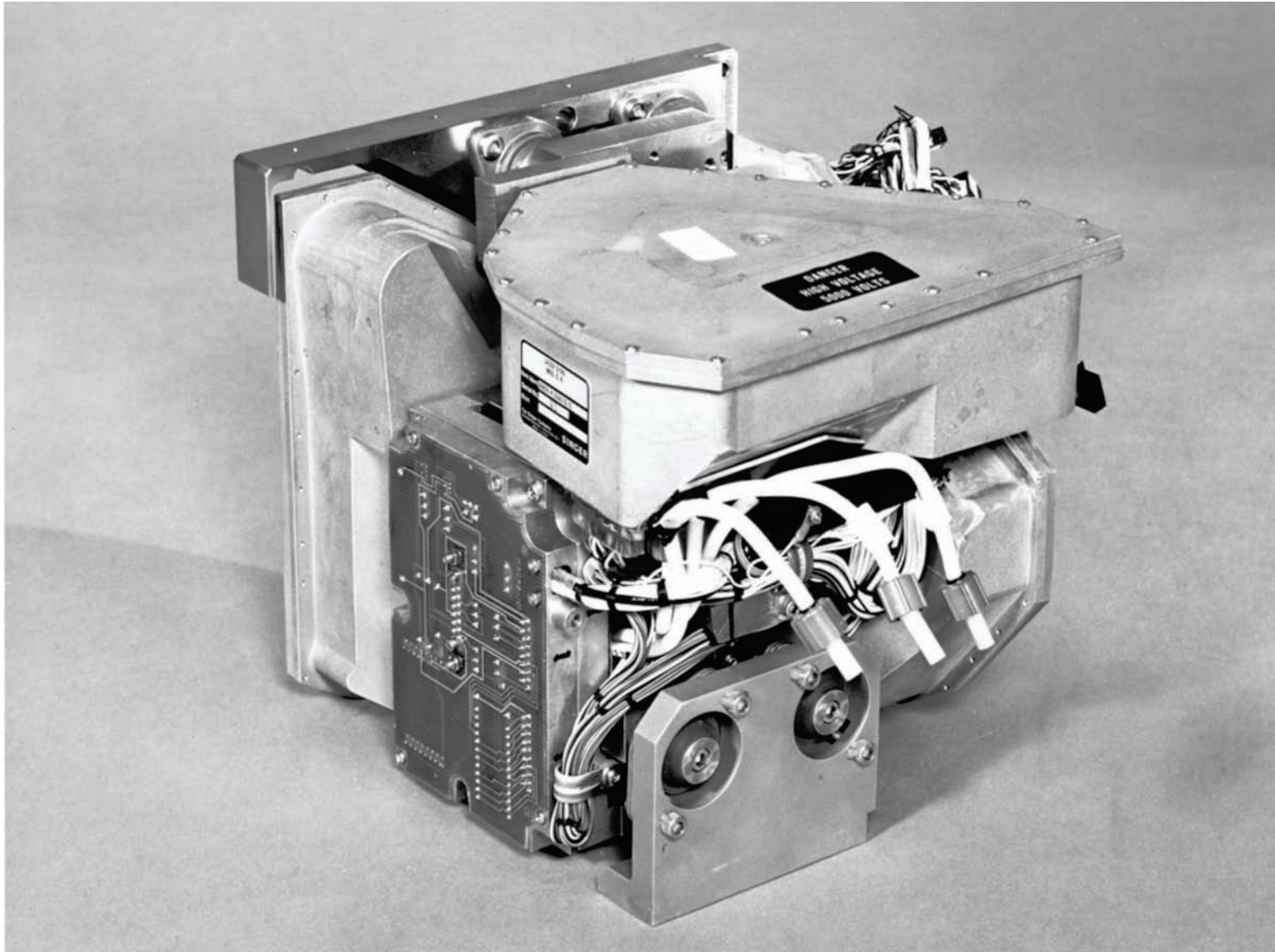


## **KEARFOTT RING LASER GYRO STRAPDOWN INU**

The photograph is of the Kearfott SKN-4030 ring laser gyro strapdown inertial navigation system developed for 0.8 nautical-mile-per-hour performance applications.

The INU contains a strapdown Inertial Measurement Unit (IMU) and system electronics to operate the IMU sensors, perform the strapdown inertial navigation computations, and provide external interface input/output functions. The IMU contains three mechanically dithered ring laser gyros and three pendulous electrically servoed accelerometers.

# KEARFOTT RLG INERTIAL SENSOR BLOCK

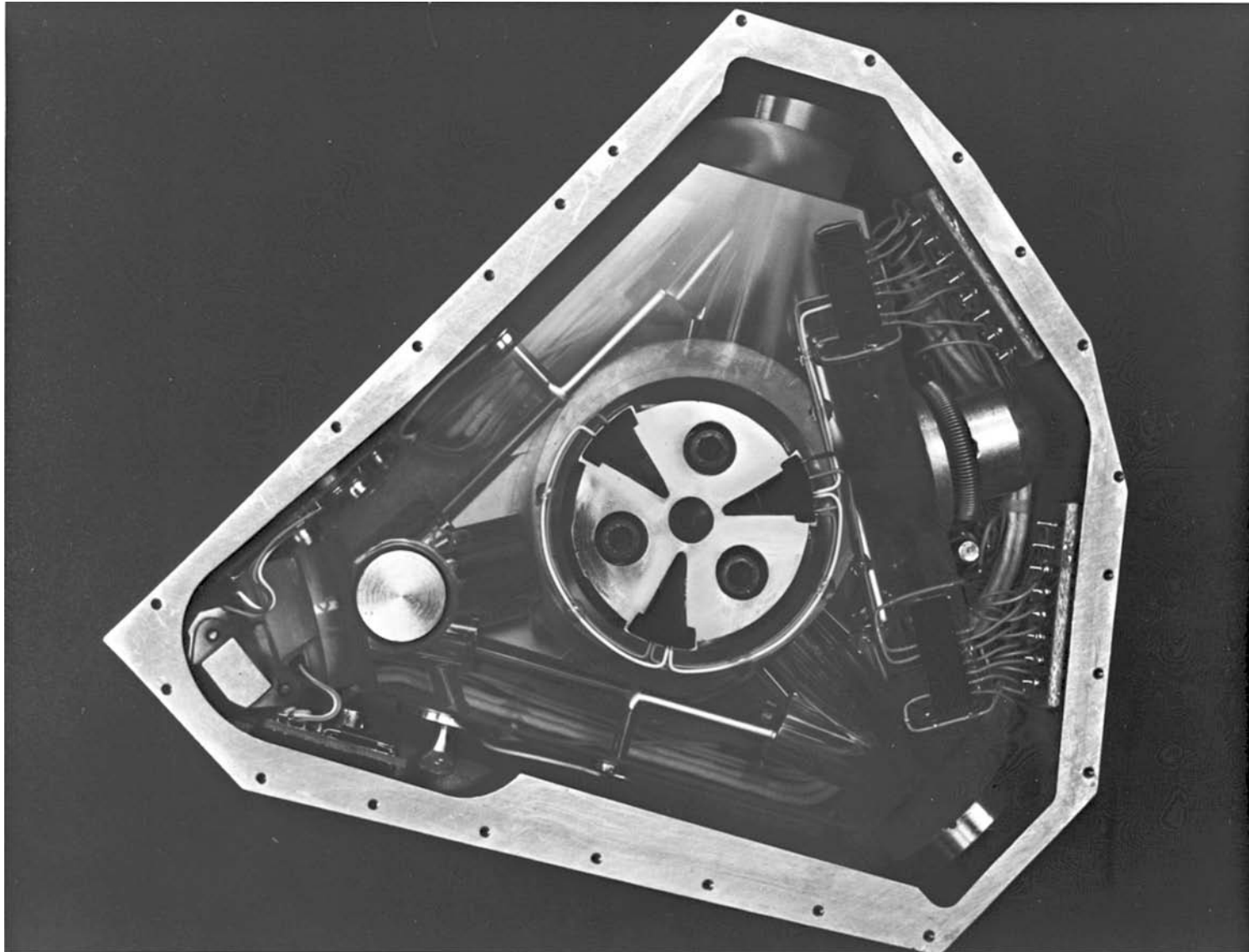


## **KEARFOTT RLG INERTIAL SENSOR BLOCK**

The ring laser gyros and accelerometers in the SKN-4030 are mounted to a common inertial sensor block which is suspended within the INU chassis by four elastomeric vibration isolators. The accelerometer triad is configured as a separate subassembly mounted to the inertial sensor block such that rotational inputs due to shock, vibration and dither reactions are minimized.

The compact design of the sensor block assembly minimizes the possibility of thermal gradients and mechanical distortion between sensor axes, each of which can deteriorate sensor performance.

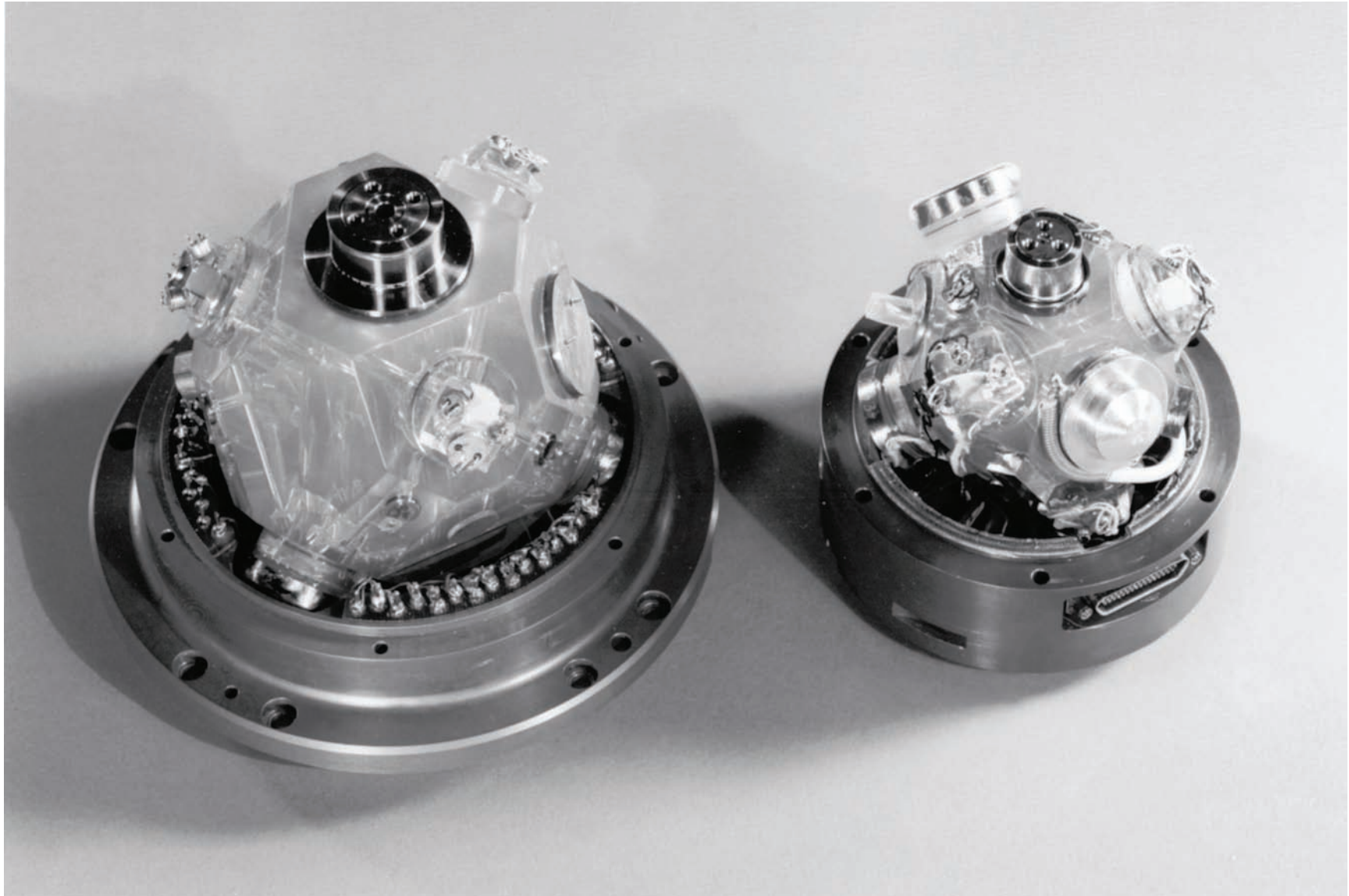
# KEARFOTT RING LASER GYRO PACKAGING



## **KEARFOTT RING LASER GYRO PACKAGING**

The Kearfott triangular ring laser gyro utilized in the SKN-4030 has a 32 cm path length, operates with a 0.63 micron laser wavelength, and incorporates mechanical dither for lock-in compensation. Symmetrical packaging of the unit and minimization of internally mounted electrical heat producing components reduces the likelihood of thermally generated sensor errors.

# KEARFOTT MONOLITHIC THREE-AXIS RLG SENSOR ASSEMBLIES

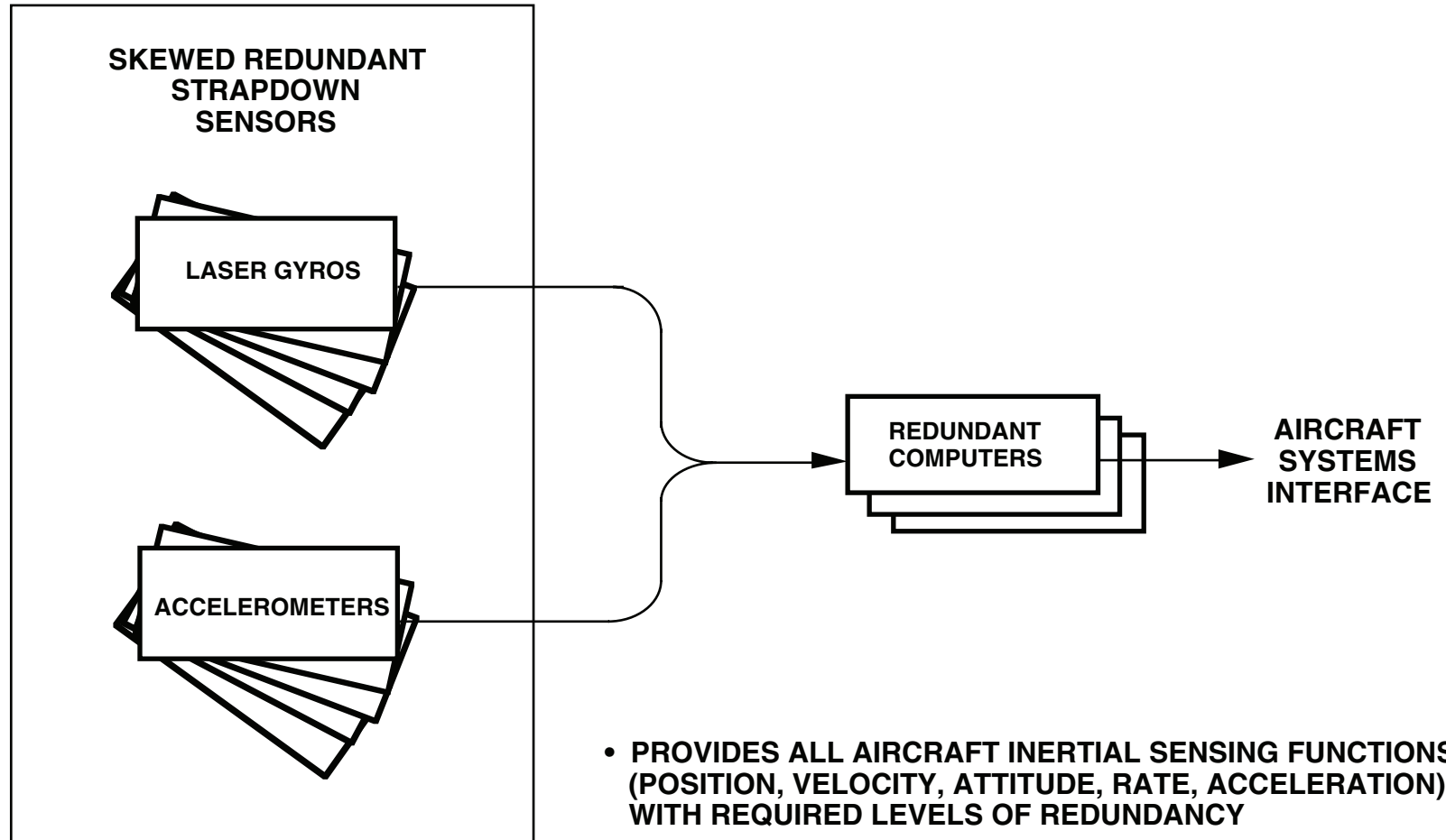


## KEARFOTT MONOLITHIC THREE-AXIS RLG SENSOR ASSEMBLIES

The photo is of the Kearfott T24 (left) and T16 (right) monolithic three-axis ring laser gyro (RLG) sensor assemblies. Each unit consists of a single Zerodur substrate housing three orthogonal four sided RLG resonators. In order to reduce production costs, only six mirrors are utilized for each three-axis assembly with each RLG sharing its mirrors with the other two orthogonal RLGs. The mirror substrates can be envisioned to lie on the six surfaces of a cube. Lock-in is compensated by mechanical dithering of the monolithic structure about a single axis that is symmetrically skewed relative to the orthogonal RLG input axes such that each RLG is provided with an equal component of the dither rate. The readout optics for the RLGs are mounted on the Zerodur structure (i.e., "block mounted readout). The accelerometer triad for the INS utilizing the monolith are mounted to the frame to which the monolith is affixed. Compensation for the angular movement between the accelerometer and gyro triads from the mechanical dither is provided in the INS computer based on electronic dither angle measurements at the inertial sensor sample frequency.

The lasing path perimeter for each RLG in the monolith is 24 cm for the T24 and 16 cm for the T16. A T10 unit has also been developed with a 10 cm perimeter, the overall T10 monolith diameter being approximately two thirds that of a golf ball. Accuracy of the RLGs in these units is advertised at better than aircraft INS 0.8 nautical mile per hour CEP requirements for the T24, 1 deg/hr for the T16 (i.e., AHRS or high performance tactical missile quality), and 2-3 deg/hr for the T10 (tactical missile grade).

## ADVANCED SKEWED REDUNDANT INS



## ADVANCED SKEWED REDUNDANT INS

The ultimate potential of the strapdown implementation rests on its forecasted ability to provide all inertial output functions required in advanced aircraft (i.e., rate, acceleration, attitude, heading, velocity, and position) with redundant operations achieved at lower cost through the use of skewed sensor geometries. The slide illustrates the skewed strapdown system hardware complement that would be needed, for example, to isolate and correct one single failure, and to detect the presence of any second failure. The hardware consists of a triple redundant computer installation plus a redundant pentad (five axes) of single-axis strapdown gyros and accelerometers. All sensors feed each computer. The redundancy level achievable with the pentad geometry is equivalent to what would normally be achievable with a triple redundant orthogonal three-axis sensor assembly installation (i.e., three gyros and accelerometers per axis, or nine gyro/accelerometer sets).

Packaging and software design for advanced skewed redundant strapdown systems introduces new requirements not generally addressed in the design of orthogonal sensor systems. These constraints stem from simultaneous desires to achieve required multiple system redundancy levels, redundant element physical separation, locate sensors at strategic bending mode locations in the aircraft, maintain accurate sensor-to-sensor alignment stability, and achieve a skew geometry that minimizes sensor errors.

Multiple redundancy requirements extend beyond the sensors. It impacts sensor electronics, power supplies, sensor/computer interface electronics, and the computers themselves. The overall skewed system design must provide redundancy in each of these areas as well as in the sensors. The design questions raised by the overall requirement are whether separate dedicated electronics are required for each sensor (including power supplies), how a redundant interface is best achieved between skewed sensors that must feed each redundant computer, and what the preferred computer redundancy management design concept is. Additionally, the basic design of effective skewed sensor failure detection logic must be achieved. This latter requirement may seem deceptively simple on a theoretical basis based on perfect continuous ideal sensor measurements. In a real strapdown system, however, the sensor data is quantized and contains errors, even when functioning normally. The skewed sensor redundancy logic must be designed to detect real failures on the one hand that will deteriorate system performance, but be insensitive to "normal" sensor errors and data forms that are acceptable at the system level. The logic design is complicated by failure detection time requirements on the one hand which are dictated by flight safety, and failure level detection capability on the other hand which generally require long averaging times to detect low level failures. Additionally, the failure detection logic design must be based on several output functions which generally have different failure detection accuracy/time requirements (e.g., body rate and acceleration for stability augmentation, attitude/heading for flight control, and position/velocity for navigation).

## ADVANCED SKEWED REDUNDANT INS (CONTINUED)

Physical separation is desired for redundant systems to assure that a single catastrophic event will not cause multiple system failures. Physical separation of skewed redundant sensors conflicts with the additional requirement to maintain accurate alignment between sensors. Generally, navigation grade strapdown sensor-to-sensor alignment accuracies can only be achieved with the sensors in close proximity to one another on a common mount. The accelerometer skewed redundancy computational process becomes further complicated by the separation requirement due to the need to incorporate large “size effect” corrections on the accelerometer signals so that the outputs are referenced to a common reference point for skewed voting comparisons (“size effect” refers to the added acceleration effect created on the output of an accelerometer by angular rotation and angular acceleration coupled with a lever arm separation of the accelerometer from the point where acceleration is to be measured). Angular rotation and angular vibration of the accelerometers is calculated from the gyro outputs. In the case of mechanically dithered laser gyro sensor assemblies, the angular vibration of the sensor assembly produced by gyro dither reaction torque creates real angular vibration inputs to the gyros, thereby adding complexity to the process of obtaining an accurate measure of accelerometer angular acceleration from gyro rate signals for size effect compensation.

For flight control applications, it is generally preferred (for optimum performance) to locate particular flight control sensors (e.g., the pitch gyros and the longitudinal accelerometers) on aircraft stations that minimize bending mode pick-up in the flight control stabilization loops. Implementing this requirement generally implies that the sensors be remotely located relative to one another, thereby creating another conflict with skewed sensor-to-sensor high accuracy alignment requirements.

To achieve satisfactory quality angular rate and linear acceleration signals for flight control, filtering may be required in the strapdown INS to attenuate sensor quantization noise, accelerometer size effect compensation noise, mechanically dithered ring laser gyro sensor assembly dither reaction response into the gyros and accelerometers, elastomerically isolated sensor assembly dynamic response relative to the airframe, and dynamic bending between separated sensor assemblies.

From a geometry configuration standpoint, skewed sensor orientations relative to sensor and aircraft axes must also minimize sensor error effects. One of the more serious error potentials in this regard is accelerometer scale factor error which can have a significant horizontal error component if oriented near forty five degrees out of the aircraft roll-pitch plane (due to the 0.707 g input under cruise conditions with a 70.7% reflection back to the horizontal, or a net horizontal error of 0.5 g times the scale factor error). Utilization of accelerometer orientations near this condition can produce large equivalent horizontal biases, hence

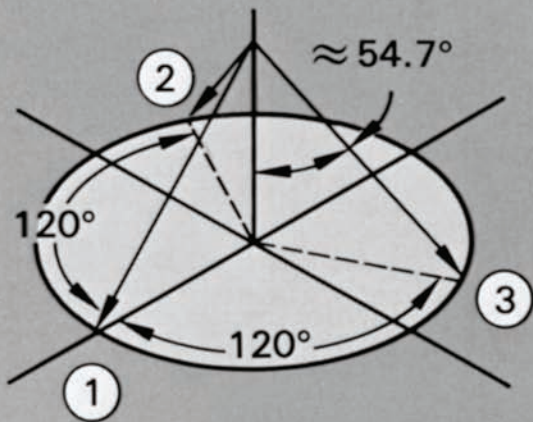
## **ADVANCED SKEWED REDUNDANT INS (CONTINUED)**

navigational velocity/position error build-up. If such orientations must be used, increased accelerometer scale factor accuracy requirements would be the outcome.

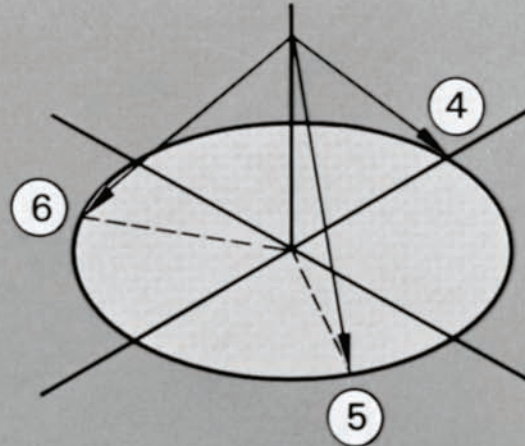
From an electrical standpoint, the redundancy requirement must also encompass the sensor electronics, the system computer assembly, the system power supplies (including the power supplies for the skewed redundant sensors), and the interface between the skewed redundant sensors and system computer(s). From an electrical packaging standpoint, the redundant sensor assemblies must be mounted and interfaced so that failures in one redundant assembly do not propagate to another.

The overall skewed redundant system design must achieve an acceptable level of compromise between the above conflicting design requirements so that an overall system concept evolves that is both cost effective and able to achieve performance and redundancy levels that are compatible with advanced aircraft user requirements.

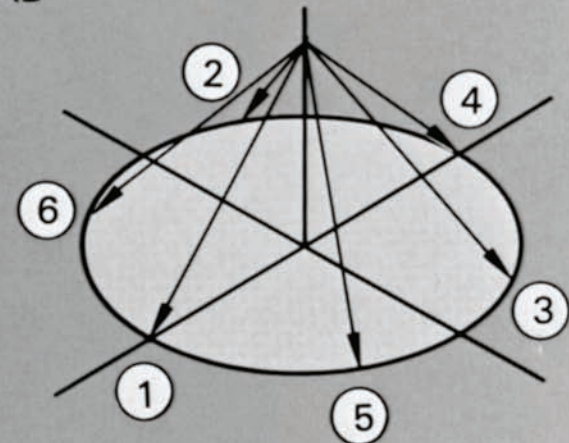
# IISA SENSOR AXIS CONFIGURATION



INA NO. 1 ORTHOGONAL TRIAD



INA NO. 2 TRIAD  
ORTHOGONAL TRIAD

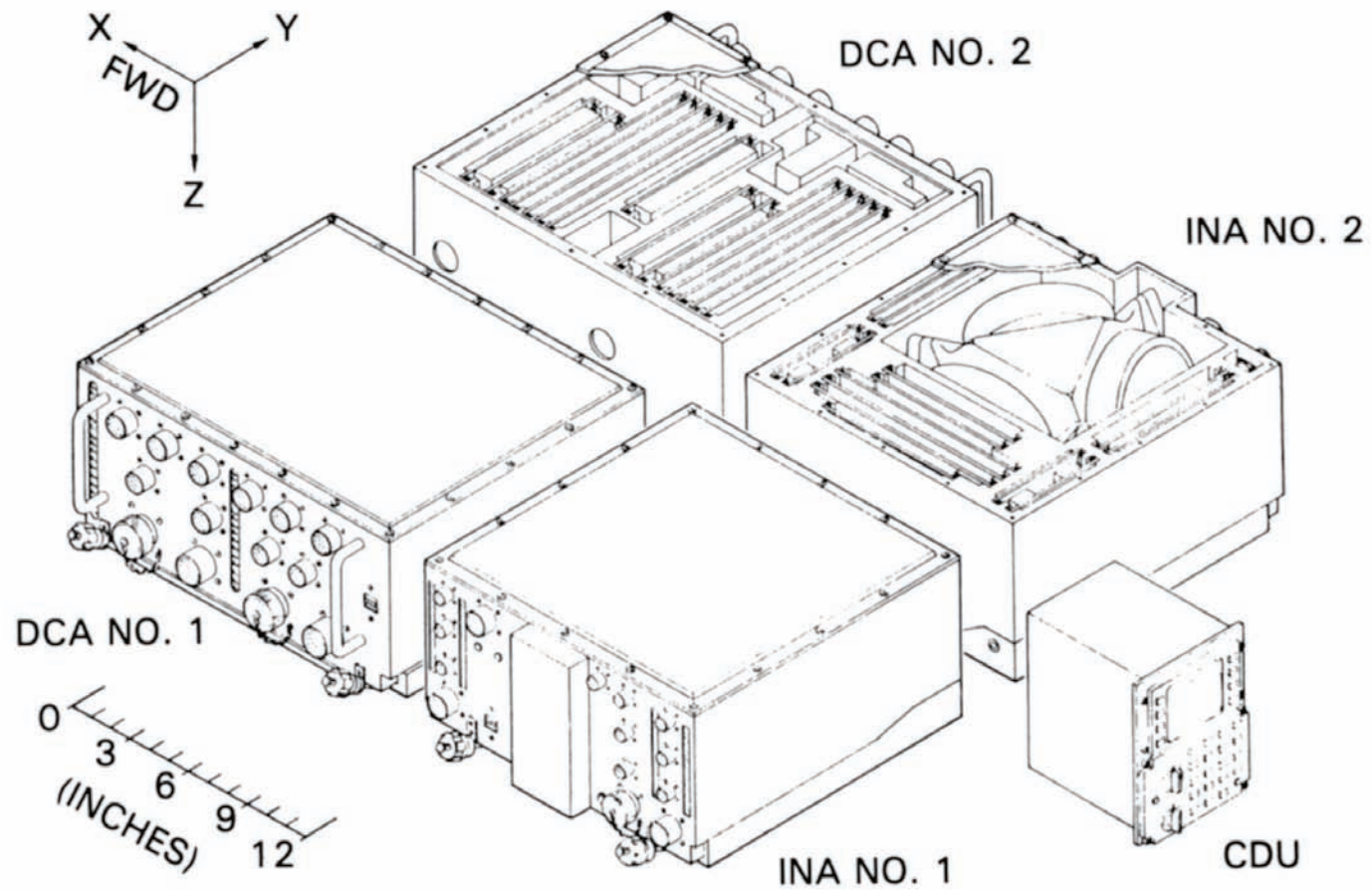


COMBINED TRIADS PROVIDE  
6 AXES EQUALLY SPACED  
ON 54.7° CONE

## **IISA SENSOR AXIS CONFIGURATION**

IISA (Integrated Inertial Sensor Assembly) is the Navy acronym for a skewed redundant hexad strapdown inertial navigation system designed for multipurpose application in high performance fighter/attack aircraft. The primary requirement placed on IISA is to provide Fail-Op/Fail-Op/Fail-Safe flight control rate and acceleration outputs in body axes. Navigational outputs must be dual redundant. IISA is implemented using Ring Laser Gyros (RLGs) with mechanical dither. Provisions must be included for dither and sensor assembly isolator resonance filtering in the redundancy management logic. The sensor separation requirement for IISA is that the sensors be divided into two sets of three gyros and accelerometers separated by 30 inches minimum for redundancy failure survivability. Each set of three comprises an orthogonal triad, with each triad mounted skewed to airframe axes and symmetric about the airframe yaw axis. Each triad (identified as an Inertial Navigation Assembly - INA) is identical. A six-axis skewed geometry between the dual-INA sensor axes is achieved by installing the INA's 180 degrees rotated from each other about the vehicle yaw axis. The slide illustrates the IISA sensor geometry. The next slide illustrates the installation configuration.

# LITTON INTEGRATED INERTIAL SENSOR ASSEMBLY (IISA)



## **LITTON INTEGRATED INERTIAL SENSOR ASSEMBLY (IISA)**

The Advanced Development Model (ADM) version of IISA was designed by Litton under contract with Naval Air Development Center for concept evaluation in the laboratory and in an F-15 fighter aircraft. The primary IISA performance characteristic evaluated in the flight test program was the flight control signal performance and associated redundancy management operations when interfaced with the F-15 flight control system. IISA navigational accuracy was also assessed to verify that performance met standard 1.0 nmph CEP medium accuracy INS requirements.

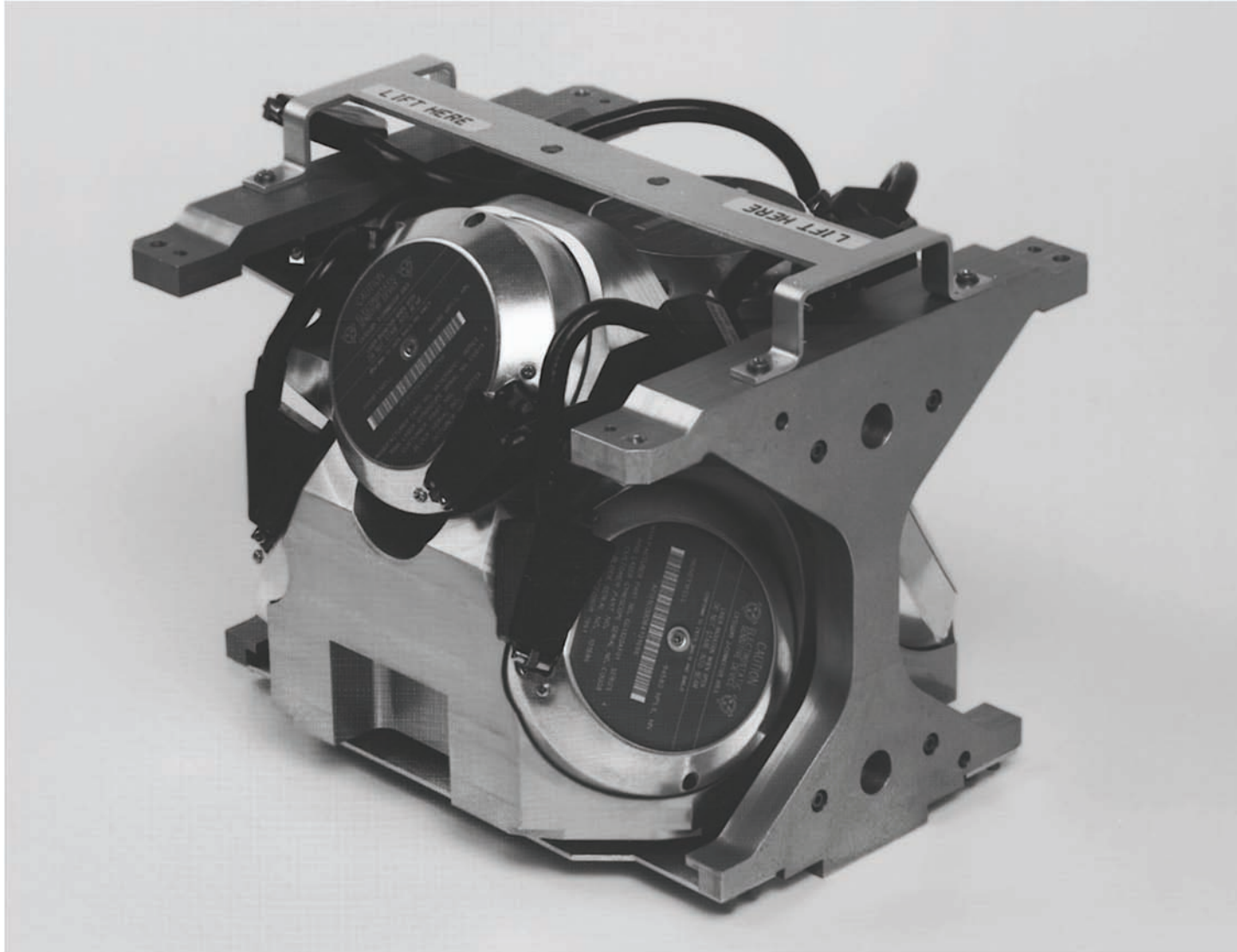
The Litton IISA-ADM configuration depicted in the slide consists of five assemblies: two identical Inertial Navigation Assemblies (INAs) containing the inertial sensors and navigation computer; two identical Digital Computer Assemblies (DCAs) each containing dual redundant flight control redundancy management and sensor selection logic computers; and a multi-function Control Display Unit (CDU) for displaying IISA data and providing the operator interface for initialization, mode selection, insertion of simulated failure data and execution of simulated failures.

Each INA contains two navigation processors that operate on the sensor triad data to generate an independent strapdown inertial navigation solution provided as an INA output. The dual INAs provide a dual redundant navigation capability. Each INA also provides three independent dedicated channels of flight control sensor data to two independent processors in each DCA. Each INA gyro and accelerometer channel (3 for each INA) contains a dedicated processor to generate the flight control sensor outputs. Each INA gyro and accelerometer flight control output signal channel is filtered in the dedicated processor to attenuate sensor quantization, RLG dither and sensor assembly isolator resonance effects. To eliminate common mode electrical failures between INA flight control output channels, each gyro/accelerometer axis channel (3 for each INA) is electrically isolated from other INA electrical assemblies by having dedicated sensor electronics, power supply, processor, interconnect wiring, and input/output connectors.

Redundancy management software in each DCA processor operates on the data from the six INA sensor channels for Failure Detection/Isolation (FDI) and sensor selection. Dual processor outputs from the two DCAs provide a Fail-Op/Fail-Op/Fail-Safe flight control output redundancy capability. Moment arm compensation is applied to the acceleration signals for parity equations and output sensor selection based on body axis angular rates/accelerations generated from gyro signals.

The DCA also contains simulations of typical failures for each sensor (e.g., to zero, hardover, to constant, to random, scale factor shift, bias shift, bias ramp) that can be set on CDU command to artificially corrupt the real sensor signal. This allows evaluation of IISA redundancy management performance under planned controlled failure sequences. Sensor failure plans for a given flight are input by type, magnitude, and sequence through the CDU. The CDU also provides the means to input moment arm data describing each INA location relative to the nominal aircraft center of gravity. The moment arm data is used by the DCA FDI and sensor select logic for accelerometer moment arm compensation.

# HONEYWELL SHEWED REDUNDANT HEXAD PRODUCTION SENSOR ASSEMBLY



## **HONEYWELL SKEWED REDUNDANT HEXAD PRODUCTION SENSOR ASSEMBLY**

The slide is a photograph of the Honeywell ring laser gyro skewed redundant hexad strapdown sensor assembly used on the Boeing 777 commercial airplane. This is the first skewed redundant strapdown sensor assembly to enter large scale production. The unit utilizes six Honeywell GG1320 ring laser gyros and six Allied Signal QA 2000 (Q Flex) accelerometers. The input axis geometry for the gyros and accelerometers places one axis along the aircraft yaw axis (i.e., approximately vertical during straight and level flight), with the remaining five axes positioned uniformly on the surface of a cone (at 72 degree intervals) for which the sixth (yaw) sensor axis is the cone axis. The angle between the cone surface sensor axes and the yaw sensor axis is 63.43 degrees, or 26.57 degrees from each cone sensor axis to the aircraft roll/pitch plane. This geometry also makes the angle between any two of the six sensor axes equal to 63.43 degrees (or  $180 - 63.43 = 116.57$  degrees, depending on input axis polarity).

Because all inertial sensors (6 gyros and accelerometers) are mounted to the same metal frame, precision alignment stability can be assured between sensor axes. This allows any grouping of 3 or more sensors to be used in generating flight control angular-rate/acceleration as well as inertial navigation outputs. The hexad (6) sensor axis geometry provides Fail-Op/Fail-Op/Fail-Safe redundancy for both the flight control and inertial navigation functions.

**NOTES**

**STRAPDOWN INERTIAL  
NAVIGATION SYSTEM  
ERROR CHARACTERISTICS**

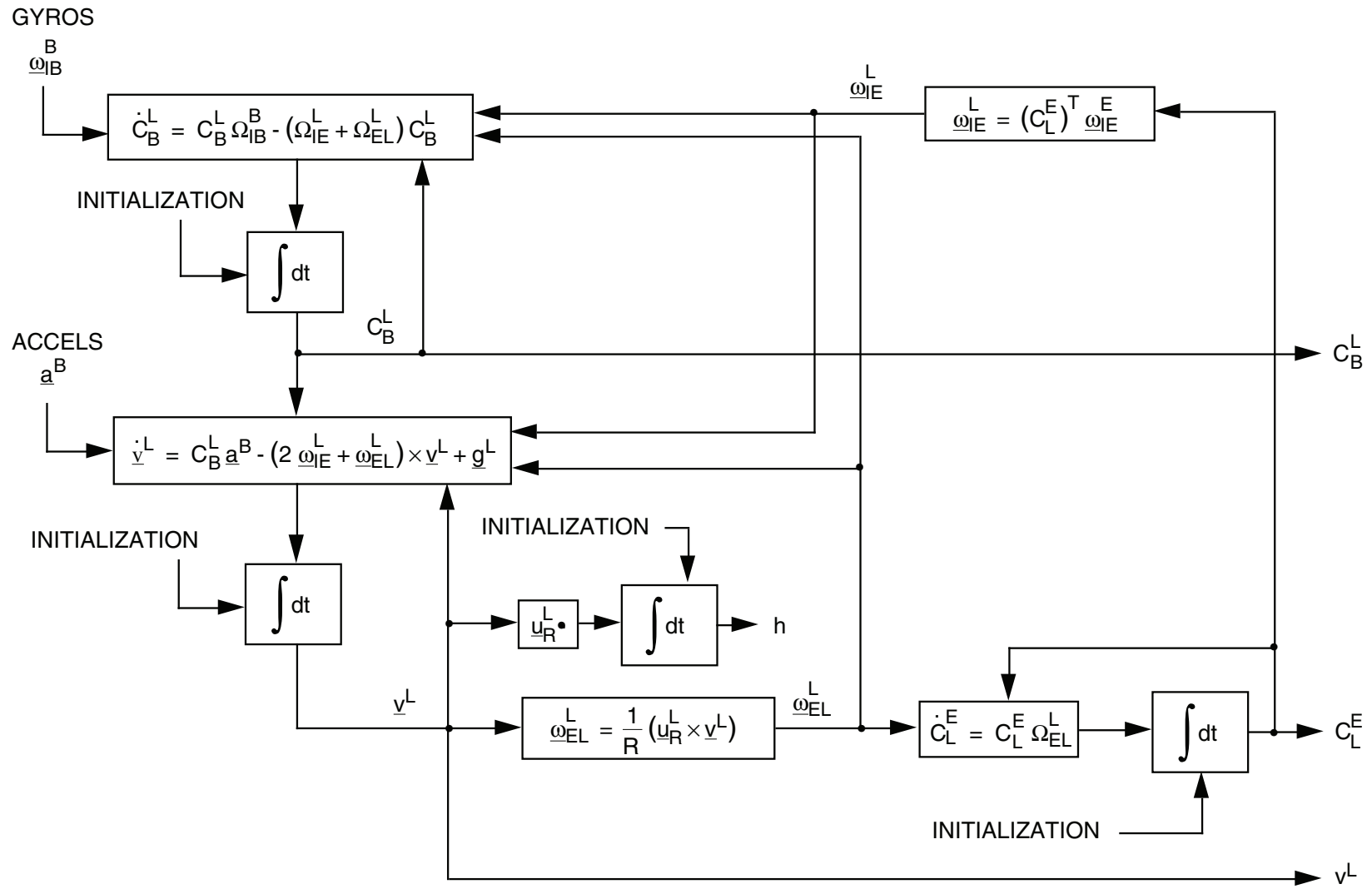
## NOMENCLATURE

<b>B</b>	=	<b>BODY OR SENSOR AXES</b>
<b>L</b>	=	<b>LOCAL LEVEL (NAVIGATION) AXES (Z-UP)</b>
<b>E</b>	=	<b>EARTH FIXED AXES (Y ALONG POLE)</b>
<b>I</b>	=	<b>INERTIAL (NONROTATING) AXES – Y ALONG EARTH POLAR AXIS</b>
$\underline{\omega}_{IE}^L$	=	<b>ANGULAR RATE OF EARTH RELATIVE TO INERTIAL SPACE PROJECTED ON L-FRAME AXES</b>
$\underline{\omega}_{EL}^L$	=	<b>ANGULAR RATE OF LOCAL LEVEL FRAME RELATIVE TO THE EARTH PROJECTED ON L-FRAME AXES</b>
$\underline{\omega}_{IB}^B$	=	<b>ANGULAR RATE OF B-FRAME RELATIVE TO INERTIAL SPACE PROJECTED ON B-FRAME AXES (SENSED BY STRAPDOWN GYROS)</b>
$\underline{\Omega}_{()}^{()}$	=	<b>SKEW SYMMETRIC FORM OF <math>\underline{\omega}_{()}^{()}</math> ANGULAR RATE VECTOR</b>
$\underline{a}^B$	=	<b>SPECIFIC FORCE ACCELERATION ALONG BODY AXES (SENSED BY STRAPDOWN ACCELEROMETERS)</b>
$\underline{v}^L$	=	<b>VELOCITY RELATIVE TO EARTH ALONG LOCAL LEVEL AXES</b>
$\underline{u}_R^L$	=	<b>UNIT VECTOR UPWARD ALONG LOCAL VERTICAL (ALONG L-FRAME Z-AXIS)</b>
$\underline{g}^L$	=	<b>LOCAL GRAVITY ALONG L-FRAME AXES</b>

## NOMENCLATURE

The slide defines the nomenclature used in the general vector discussion on strapdown inertial navigation system error characteristics.

# STRAPDOWN NAVIGATOR WANDER AZIMUTH COMPUTATION FLOW



## STRAPDOWN NAVIGATOR WANDER AZIMUTH COMPUTATION FLOW

The block diagram illustrates the basic computational flow (in analog continuous form) mechanized in a strapdown inertial navigation system computer based on wander azimuth coordinates (i.e., zero rotation rate of the navigation frame relative to the earth). The equations are approximate in that they are based on a spherical earth (i.e., the oblateness factor  $e$  is zero). For purposes of analyzing the effect of sensor errors on system performance, the spherical earth approximation has negligible impact.

The block diagram shows how the body-to-local level direction cosine matrix ( $C_B^L$ ) is computed through an integration process from sensed gyro data and calculated local level and earth rate components, with the result used to transform sensed accelerometer data from body to local level navigation coordinates. The transformed acceleration vector is corrected for gravity and Coriolis effects, and integrated to calculate vehicle velocity relative to the earth. The calculated velocity vector is then used to determine the angular rate of the system over the earth, which is then input to an integration algorithm that updates the position direction cosines relating local level navigation coordinates to earth coordinates ( $C_L^E$ ). The  $C_L^E$  matrix defines the vehicle position location relative to the earth. The  $C_L^E$  matrix is also used to calculate local level frame earth rate components which, with the calculated aircraft angular rate over the earth surface, are fed back into the body direction cosine integration equation.

Note that the vertical altitude calculation in the diagram is an open loop integration of vertical velocity into altitude ( $h$ ). For inertial navigation applications of more than fifteen minutes in duration, the vertical channel would typically also include altitude error feedback (into vertical velocity and altitude) using a suitable altitude reference (e.g., barometric altitude) to form the feedback error signal with inertially computed altitude, thereby bounding the altitude (and altitude rate) error. If a bounded vertical channel is utilized, the vertical channel is normally excluded from the analytical diagram because the resulting altitude (and altitude rate) error being bounded by the external altitude input, typically has small impact on the more critical horizontal velocity and position errors.

## SMALL ANGLE DIRECTION COSINE MATRIX ERRORS

$$\delta \mathbf{C} = \hat{\mathbf{C}} - \mathbf{C}$$

$$\hat{\mathbf{C}} = \mathbf{A} \mathbf{C} \quad \hat{\quad} = \text{COMPUTED } \mathbf{C} \text{ (I.E. - WITH ERROR)}$$

$$\mathbf{A} = \begin{bmatrix} 1 & -\alpha_z & \alpha_y \\ \alpha_z & 1 & -\alpha_x \\ -\alpha_y & \alpha_x & 1 \end{bmatrix} = \mathbf{I} + (\underline{\alpha} \times)$$

$$\underline{\alpha} = \begin{bmatrix} \alpha_x \\ \alpha_y \\ \alpha_z \end{bmatrix} = \text{SMALL ANGLE ERROR VECTOR ASSOCIATED WITH COMPUTED } \mathbf{C}$$

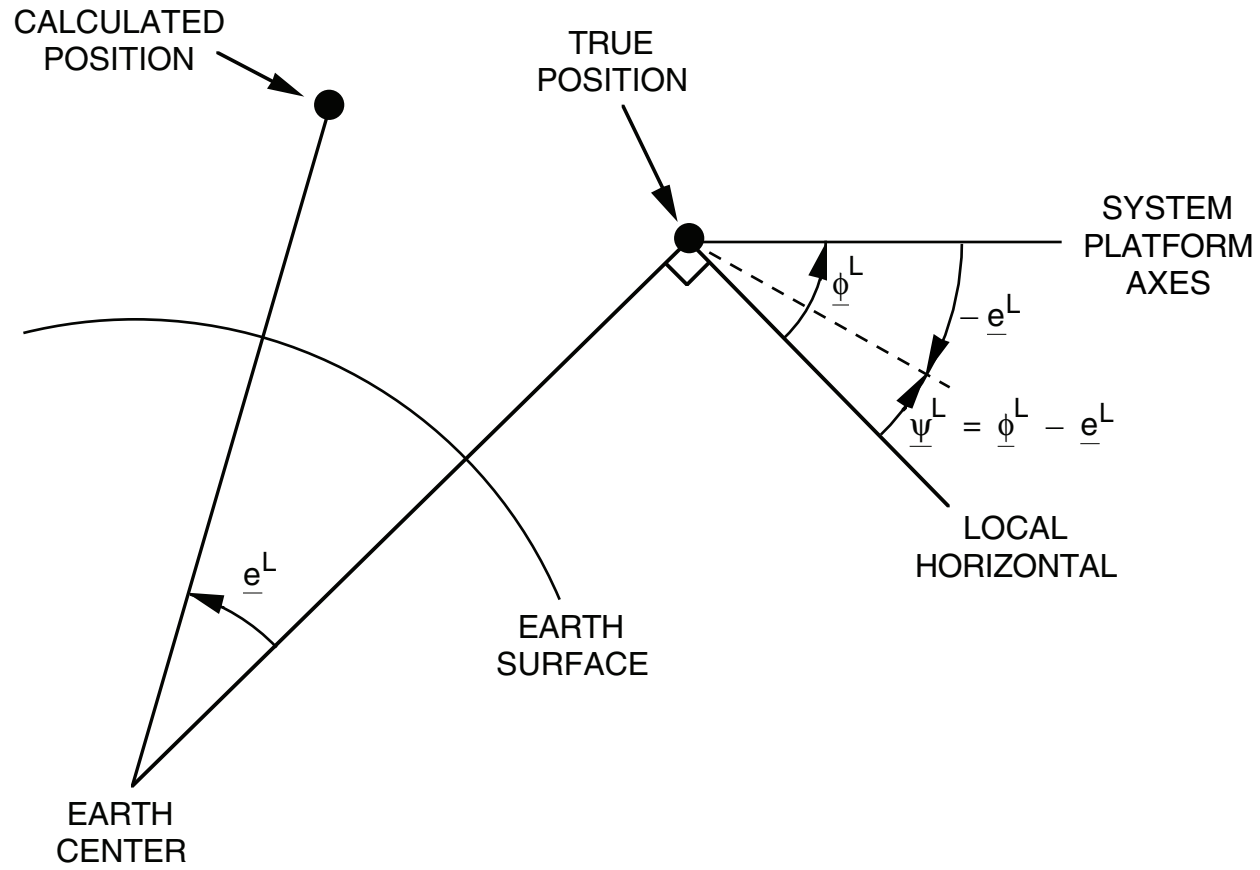
$$\delta \mathbf{C} = [\mathbf{I} + (\underline{\alpha} \times)] \mathbf{C} - \mathbf{C} = (\underline{\alpha} \times) \mathbf{C}$$

## SMALL ANGLE DIRECTION COSINE ERRORS

The errors in a direction cosine matrix can be approximated using a small angle vector representing the rotation angle about the X, Y, Z axes of one coordinate frame relative to another. For error analysis purposes, it is convenient to evaluate direction cosine errors in terms of such an error vector because it is defined in terms of only three independent components (as opposed to nine for the errors in each of the nine direction cosine elements).

The fact that only three independent parameters can be used to represent nine direction cosine errors reflects the orthogonality and normalization constraints existing between the nine direction cosine elements (i.e., the nine cosines are related through the constraints that each of their defining coordinate frame axes are orthogonal, and that direction cosines represent unit vector projections).

# ERROR ANGLES



## ERROR ANGLES

The direction cosine matrices typically implemented in a strapdown INS relate the body frame to the local level navigation axes ( $C_B^L$ ) and the local level to earth axes ( $C_L^E$ ). Errors in these matrices represent body axis attitude/platform heading errors in the case of  $C_B^L$ , and positioning/wander angle errors in the case of  $C_L^E$ .

Errors in the  $C_B^L$  matrix can be defined in terms of a small angle vector  $\underline{\phi}^L$  in level axes. Similarly, the  $C_L^E$  matrix error can be defined in terms of a small angle vector  $\underline{e}^L$  in level axes. The horizontal components of  $\underline{\phi}^L$  would represent stabilized platform tilt in a gimbaled INS, and the vertical component of  $\underline{\phi}^L$  represents equivalent gimbaled platform heading error. The horizontal components of  $\underline{e}^L$  represent the angular position error of the vehicle over the earth surface, and the vertical component of  $\underline{e}^L$  is related to the platform wander angle error.

Both  $\underline{\phi}^L$  and  $\underline{e}^L$  are illustrated in the slide. Also illustrated is another angle  $\underline{\psi}^L$  equal to the difference between  $\underline{\phi}^L$  and  $\underline{e}^L$ . The  $\underline{\psi}^L$  parameter will be useful later on when long term navigation system errors are analyzed. It represents the error in the transformation matrix relating body-to-earth coordinates (i.e., the product of the  $C_L^E$  and  $C_B^L$  matrices). The  $\underline{\psi}^L$  vector is a measure of the ability to accurately point a telescope at a star (assuming that earth's rate and position relative to the universe is known).

## ERROR DEFINITIONS

$$\hat{C}_B^L = [I - (\underline{\phi}^L \times)] C_B^L \Rightarrow \delta C_B^L = - (\underline{\phi}^L \times) C_B^L$$

$\underline{\phi}^L$  = “PLATFORM” ANGLE ERROR VECTOR (ANGLE VECTOR BETWEEN COMPUTED AND TRUE LOCAL LEVEL FRAME RELATIVE TO BODY AXES)

$$\hat{C}_L^E = C_L^E [I + (\underline{e}^L \times)] \Rightarrow \delta C_L^E = C_L^E (\underline{e}^L \times)$$

$\underline{e}^L$  = “POSITION” ANGLE ERROR VECTOR (ANGLE VECTOR BETWEEN COMPUTED AND TRUE LOCAL LEVEL FRAME RELATIVE TO EARTH AXES)

$$\delta \underline{v}^L = \hat{\underline{v}}^L - \underline{v}^L$$

$\underline{v}^L$  = COMPUTED VELOCITY ERROR

$$\delta \underline{R}^L = C_E^L (\hat{\underline{R}}^E - \underline{R}^E) = R (\underline{e}^L \times \underline{u}_R^L) + \underline{u}_R^L \delta h$$

$\underline{R}^L$  = COMPUTED POSITION ERROR

$$\delta \underline{w}_{IB}^B = \tilde{\underline{w}}_{IB}^B - \underline{w}_{IB}^B$$

$\delta h$  = ALTITUDE ERROR

$R$  = RADIAL DISTANCE FROM EARTH CENTER TO VEHICLE

$$\delta \underline{a}^B = \tilde{\underline{a}}^B - \underline{a}^B$$

$\delta \underline{w}_{IB}^B$  = STRAPDOWN GYRO ERROR VECTOR

$$\delta \underline{w}_{EL}^L = \hat{\underline{w}}_{EL}^L - \underline{w}_{EL}^L$$

$\delta \underline{a}^B$  = STRAPDOWN ACCELEROMETER ERROR VECTOR

$\delta \underline{w}_{EL}^L$  = COMPUTED TRANSPORT RATE ERROR

$$\delta \underline{w}_{IE}^L = \hat{\underline{w}}_{IE}^L - \underline{w}_{IE}^L$$

$\delta \underline{w}_{IE}^L$  = COMPUTED EARTH RATE ERROR

$\sim$  = MEASURED INS PARAMETERS CONTAINING ERRORS

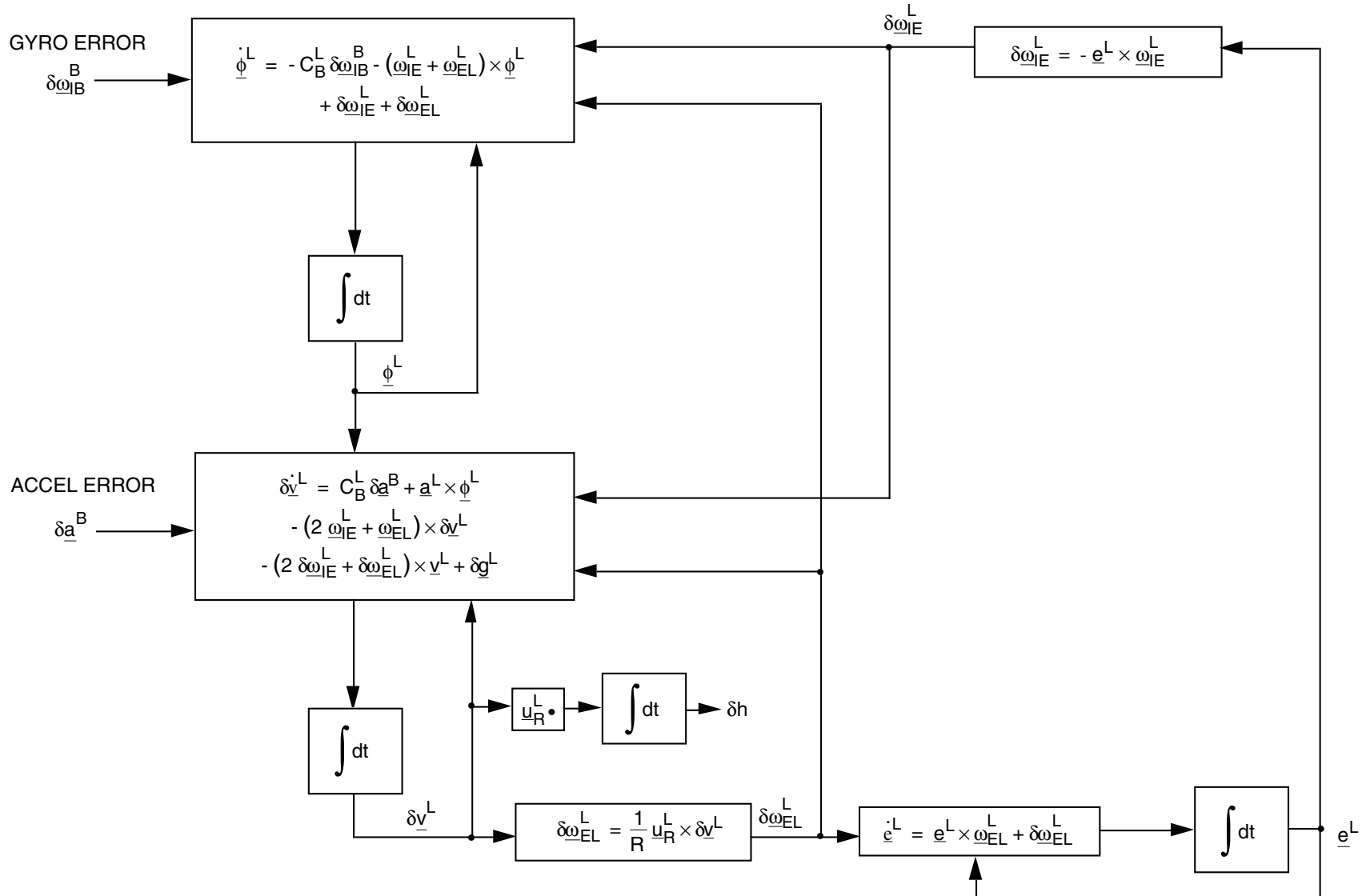
$\hat{\phantom{x}}$  = COMPUTED INS PARAMETERS CONTAINING ERRORS

## **ERROR DEFINITIONS**

System errors are defined in the slide as the differences between the navigation data calculated in a real system (containing errors) compared with the data that would have been calculated in a perfect (error free) system. The real system errors are generated by strapdown sensor errors (gyros and accelerometers) driving the strapdown inertial navigation equations. The result is a set of computed navigation parameters that differ from those in the ideal error free system.

Note that implicit in the above discussion is the assumption that system computational errors (e.g., computer software and round-off errors) are negligible. This should be readily achievable in well designed strapdown systems using modern day computers and thorough software validation techniques.

# STRAPDOWN NAVIGATOR ERROR DIAGRAM



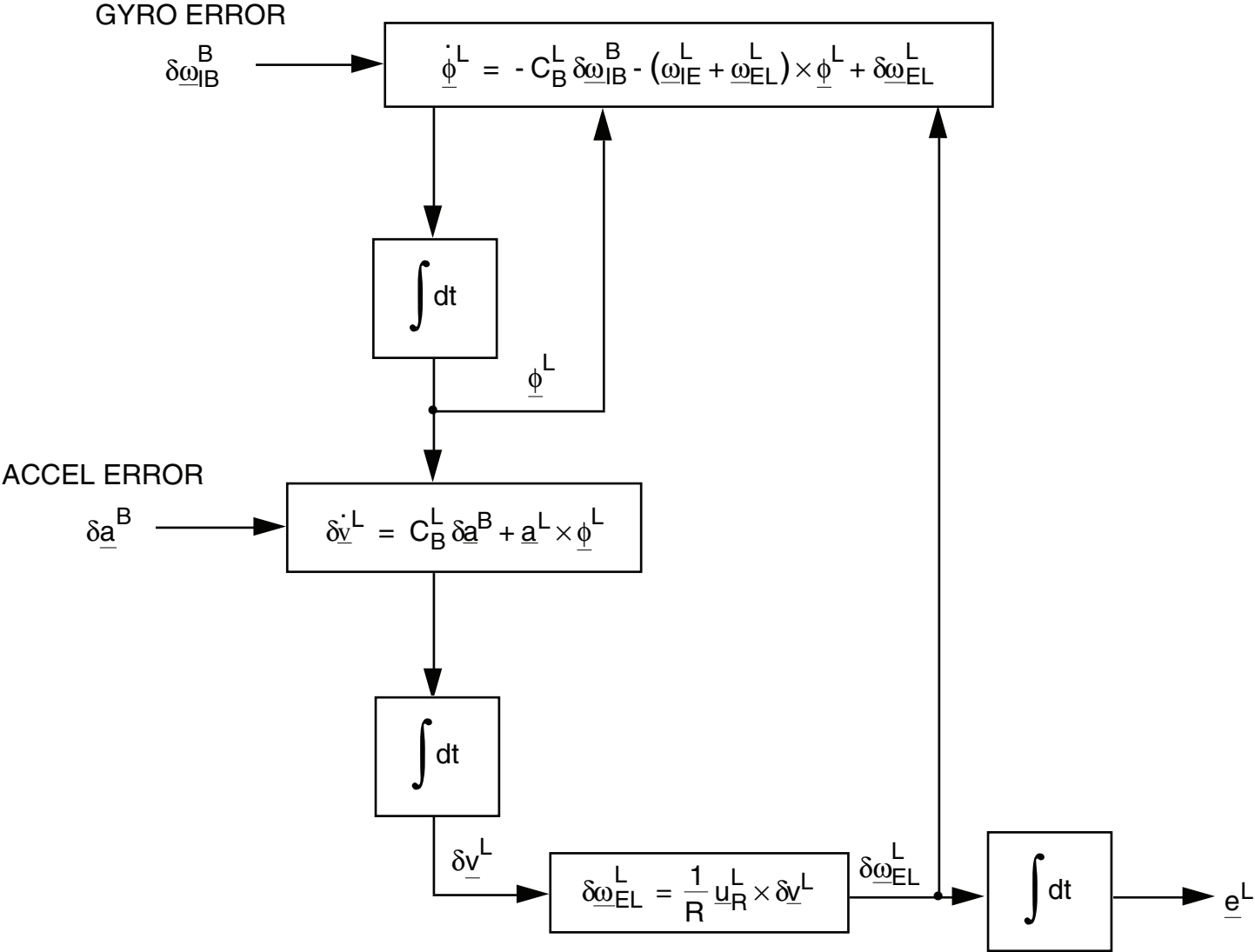
## STRAPDOWN NAVIGATOR ERROR DIAGRAM

A set of error propagation equations for a strapdown INS can be obtained by subtracting the strapdown navigation equations corresponding to the ideal system (without error) from the real system (with error). The form of the real and ideal equations are identical. They differ only in that the real set is calculated in a real computer using real sensor input data containing error. The strapdown equation forms used for this exercise are the set illustrated in block diagram form in an earlier slide entitled “Strapdown Navigator Wander Azimuth Computation Flow”.

After carrying out the latter operation, applying the error definitions given previously (including the small angle approximations for the direction cosine errors), and neglecting error products as second order, the error block diagram illustrated in the slide is obtained. The error diagram describes the position, velocity, and attitude/heading errors in a strapdown INS as a function of strapdown sensor errors (gyros and accelerometers). Note that the system errors are dynamic functions of sensor error (as reflected in the integrators present in the analytical error response loops). Also note that the inertial integration of vertical velocity error into altitude error is shown as a direct differential of the previously shown “Strapdown Navigator Wander Azimuth Computation Flow” chart (i.e., without vertical channel divergence control). If the vertical channel is bounded by a vertical position error feedback, this chart would be modified accordingly (including the altitude reference error); alternatively, the altitude error term can be eliminated from the diagram as an approximation that control of the vertical channel bounds the vertical position error to essentially zero.

A digital simulation of the error equations illustrated can be used to ascertain expected performance errors in a strapdown INS as a function of sensor errors, flight profile (i.e.,  $C_B^L$ ,  $\underline{a}^L$ ,  $\underline{v}^L$ , etc.), and time.

# SHORT TERM STRAPDOWN NAVIGATOR ERROR DIAGRAM

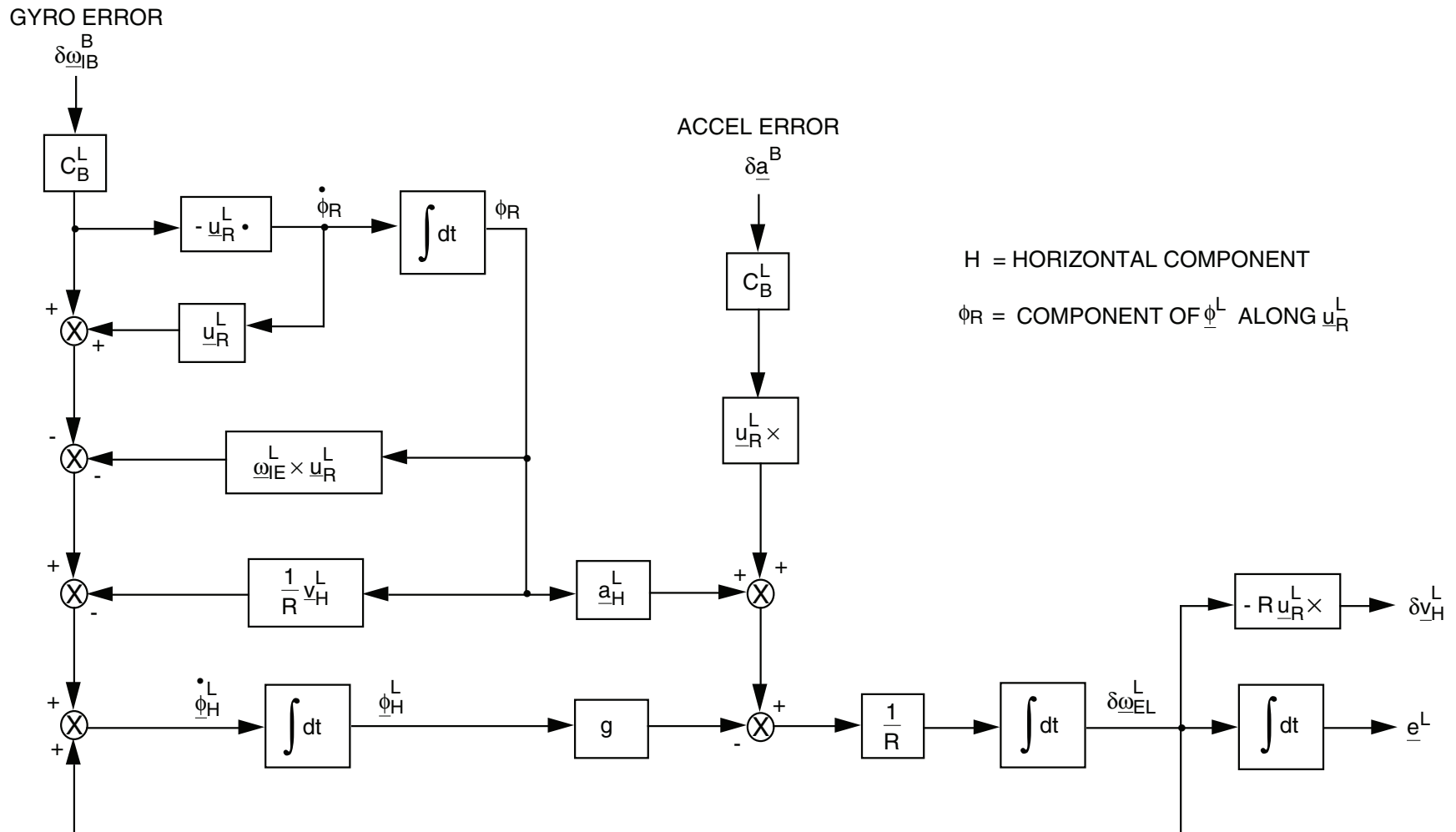


## SHORT TERM STRAPDOWN NAVIGATOR ERROR DIAGRAM

For short term application (e.g., one to two hours), the calculated earth rate error  $\delta\omega_{IE}^L$  (produced by  $e^L$  position error) generally has a minor impact on the overall system error characteristics. Consequently, a good approximation to system performance for short flight times can be obtained by neglecting the "earth loop" feedback. Such an approach is illustrated in the slide (compare with the previous slide). Additionally, the Coriolis error terms in the velocity error equation have been dropped in this as contrasted with the previous slide because of their relative smallness for error analysis purposes compared to other terms in the slide.

This chart implicitly assumes that an external altitude reference is used to bound the error growth in the vertical channel. Consequently, the altitude error calculation block is not shown with the understanding that the altitude control loop maintains the altitude error at a negligibly small value. For applications without vertical channel control, the altitude error calculation would be included as shown on the previous chart.

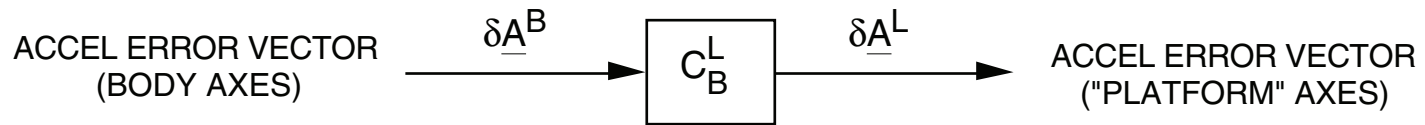
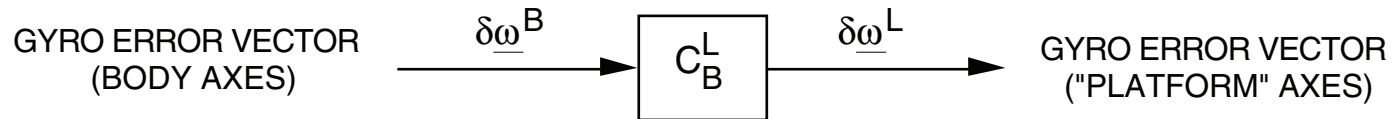
# SHORT TERM STRAPDOWN ERROR ANALYSIS DIAGRAM



## SHORT TERM STRAPDOWN ERROR ANALYSIS DIAGRAM

Mathematical manipulation of the previous short term navigator error diagram together with the simplifying assumptions of constant vertical velocity and  $\phi_R$  being generally much larger than  $\phi_H^L$  (as described in the Strapdown Inertial Navigation Lecture Notes handout) can be used to convert the previous diagram into the form illustrated in the slide. The form of this diagram is more conducive to direct analytical interpretation (as performed in the Lecture Notes). For the course, a single axis of this diagram (i.e., in scalar algebraic form) will be used for simplicity to describe the error behavior of strapdown inertial navigation systems.

## STRAPDOWN SENSOR ERRORS ACT AS VECTORS ALONG SENSOR (BODY) AXES



$$\delta \underline{\omega}^B = \begin{bmatrix} \delta \omega_{Bx} \\ \delta \omega_{By} \\ \delta \omega_{Bz} \end{bmatrix}$$

$$\delta \underline{A}^B = \begin{bmatrix} \delta A_{Bx} \\ \delta A_{By} \\ \delta A_{Bz} \end{bmatrix}$$

## STRAPDOWN SENSOR ERRORS ACT AS VECTORS ALONG SENSOR (BODY) AXES

A clear understanding of this important strapdown system characteristic will provide significant aid in the interpretation of strapdown error behavior patterns.

The previous slides showed that the navigation attitude, velocity, and position errors in a strapdown system ( $\underline{\phi}^L$ ,  $\underline{\delta v}^L$ ,  $\underline{e}^L$ ) are all driven by the sensor errors (in body axes) transformed into local navigation coordinate axes (through the  $C_B^L$  matrix). An error analysis for a gimbaled INS would result in the identically same navigation error equations driven by sensor errors in local level axes. Hence, the only difference between the strapdown and gimbaled system navigation error equations is the added sensor error transformation to navigation coordinates.

The  $C_B^L$  sensor error transformation operation in the strapdown error equations is simply a statement of the fact that navigation errors which are expressed in a locally level stabilized frame of reference are impacted differently for different orientations of the body mounted sensors relative to the level reference. For example, a positive X-accelerometer error in body axes will generate a positive X-velocity error in level axes if the X-body axis is parallel to the X-level axis. If the X-body axis is opposite to the X-level axis, a negative X-level axis velocity error will be generated. The  $C_B^L$  operation converts the body axis data so that its direction of operation in the L-frame is properly accounted for. In this sense, the  $C_B^L$  matrix can be thought of as an analytical rotation operator that rotates body axis data by the angle between the B and L frames to determine the L frame components.

In interpreting strapdown system performance it helps to visualize the direction of the body sensors (hence, their errors) relative to navigation axes. The body axis projections on the navigation axes determine the direction of navigation error propagation.

## SIMPLIFIED SENSOR ERROR MODELS

- **GYROS**

$$\Delta WX = \text{BIAS} + (\text{SCALE FACTOR ERROR}) WX + (\text{Y-MISALIGN}) WY \\ + (\text{Z-MISALIGN}) WZ + \text{RANDOM NOISE}$$

- **ACCELEROMETERS**

$$\Delta AX = \text{BIAS} + (\text{SCALE FACTOR ERROR}) AX + (\text{Y-MISALIGN}) AY \\ + (\text{Z-MISALIGN}) AZ + \text{RANDOM NOISE}$$

## **SIMPLIFIED SENSOR MODELS**

For the discussion to follow, the sensor errors will be assumed to have the error model characteristics illustrated in the slide. In actuality, the bias, scale factor, and misalignment errors may be composed of systematic (constant) components as well as acceleration and temperature sensitive elements, and time variations.

It is also important to realize that the "errors" we are dealing with represent the "uncertainties" in the sensor input/output characteristics. Predictable sensor error effects are compensated in the inertial navigation system by computer software, hence, have no net effect on system navigational accuracy.

**STRAPDOWN AND GIMBALED SYSTEM ERRORS  
ARE EQUIVALENT FOR SENSOR (BODY) AXES  
THAT ARE FIXED RELATIVE TO LOCAL LEVEL AXES**

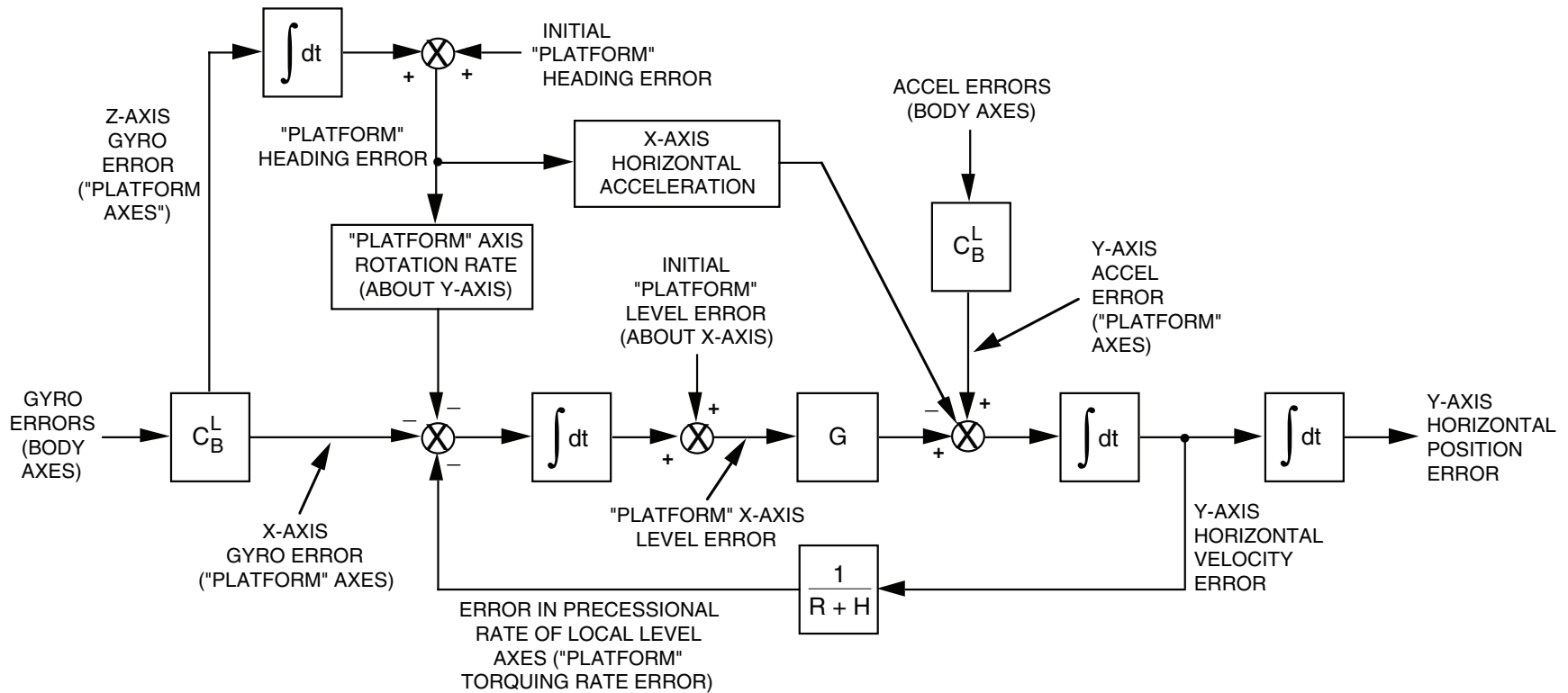
**I.E., FOR  $C_B^L = \text{CONSTANT}$**

**STRAPDOWN AND GIMBALED SYSTEM ERRORS ARE EQUIVALENT FOR SENSOR (BODY) AXES THAT ARE FIXED RELATIVE TO LOCAL LEVEL AXES**

For  $C_B^L$  equal to a constant, the body axes maintain their orientation relative to local level navigation axes. This condition is equivalent to the sensors being attached to the navigation axes, hence, is functionally equivalent to a gimbaled INS with a locally level stabilized platform aligned to navigation axes. Under such a condition, the strapdown system performance characteristics are comparable to those for the gimbaled system.

It is informative to first analyze the strapdown system from a constant  $C_B^L$  standpoint to gain an understanding of gimbaled and strapdown system error characteristics that are equivalent.

# SIMPLIFIED STRAPDOWN INS SHORT TERM ERROR CHARACTERISTICS



## SCHULER OSCILLATIONS

- TWO INTEGRATIONS IN A CLOSED LOOP
- LOOP GAIN EQUALS  $G / (R+H)$
- OSCILLATION FREQUENCY =  $\sqrt{G / (R+H)} \approx \sqrt{G / R} = \frac{2 \pi \text{ RADIANS}}{84 \text{ MINUTE PERIOD}}$

## SIMPLIFIED STRAPDOWN INS SHORT TERM ERROR CHARACTERISTICS

The slide illustrates one of the horizontal components of the vector error diagram shown previously entitled "Short Term Strapdown Error Analysis Diagram". The diagram in this slide will be utilized to examine the effect of sensor errors and navigation parameter initialization errors on short term system accuracy.

The gyro errors in body axes are shown being transformed into local level navigation axes, generating horizontal and vertical components (note that the navigation axes are referred to as "platform axes" to indicate the analogy with the coordinates of an equivalent gimbaled platform operated in the typical locally level mode parallel to navigation axes). The horizontal component of the gyro error is integrated to generate an attitude (or level) error. The level error corresponds to the physical tilt that would be generated in a real gimbaled platform, or the small level angle error associated with the direction cosine attitude data reference in a strapdown INS. The initial "platform" level error is shown as an offset bias on the level error integrator output.

The level error is shown multiplied by  $G$  in the figure, representing the horizontal acceleration error one would experience in a gimbaled system under a platform tilt in which the nominally horizontal platform accelerometers sense a component of the dominant vertical  $1\text{ G}$  specific force acceleration operating on the platform (for cruise applications where the average acceleration is vertical). In a strapdown system, the equivalent acceleration error effect is generated from the transformation of body acceleration data through the body direction cosine matrix containing the level error.

The tilt effect acceleration error is then summed with the transformed accelerometer instrument errors to generate the net acceleration error in "platform axes". This sum is integrated to generate the velocity error in the system (the effect of integrating erroneous accelerations in the system computer). The velocity error is then fed back to the level error integrator through a gain equal to the reciprocal of the radial distance from the center of the earth to the vehicle (earth's radius  $R$  plus altitude  $H$ ). The error feedback represents the platform gyro torquing rate error experienced in a gimbaled system under velocity error conditions (recall that the platform is maintained level by torquing the platform gyros at a rate equal to horizontal velocity divided by  $(R + H)$  as the vehicle translates over the spherical earth).

The velocity error feedback into the level error integrator forms a closed negative feedback loop in the INS containing two integrators (leveling and velocity errors) with a net loop gain of  $G/(R + H)$  or approximately  $G/R$ . It is easily verified that the natural response of such a loop is characterized by sinusoidal oscillations at a frequency equal to the square root of  $G/R$ . Numerically, the period of oscillations equal 84 minutes. Such characteristic oscillations of all inertial navigation system are known as Schuler oscillations because of their direct analogy to (and mechanization of) the classical Schuler pendulum concept

## **SIMPLIFIED STRAPDOWN INS SHORT TERM ERROR CHARACTERISTICS (CONTINUED)**

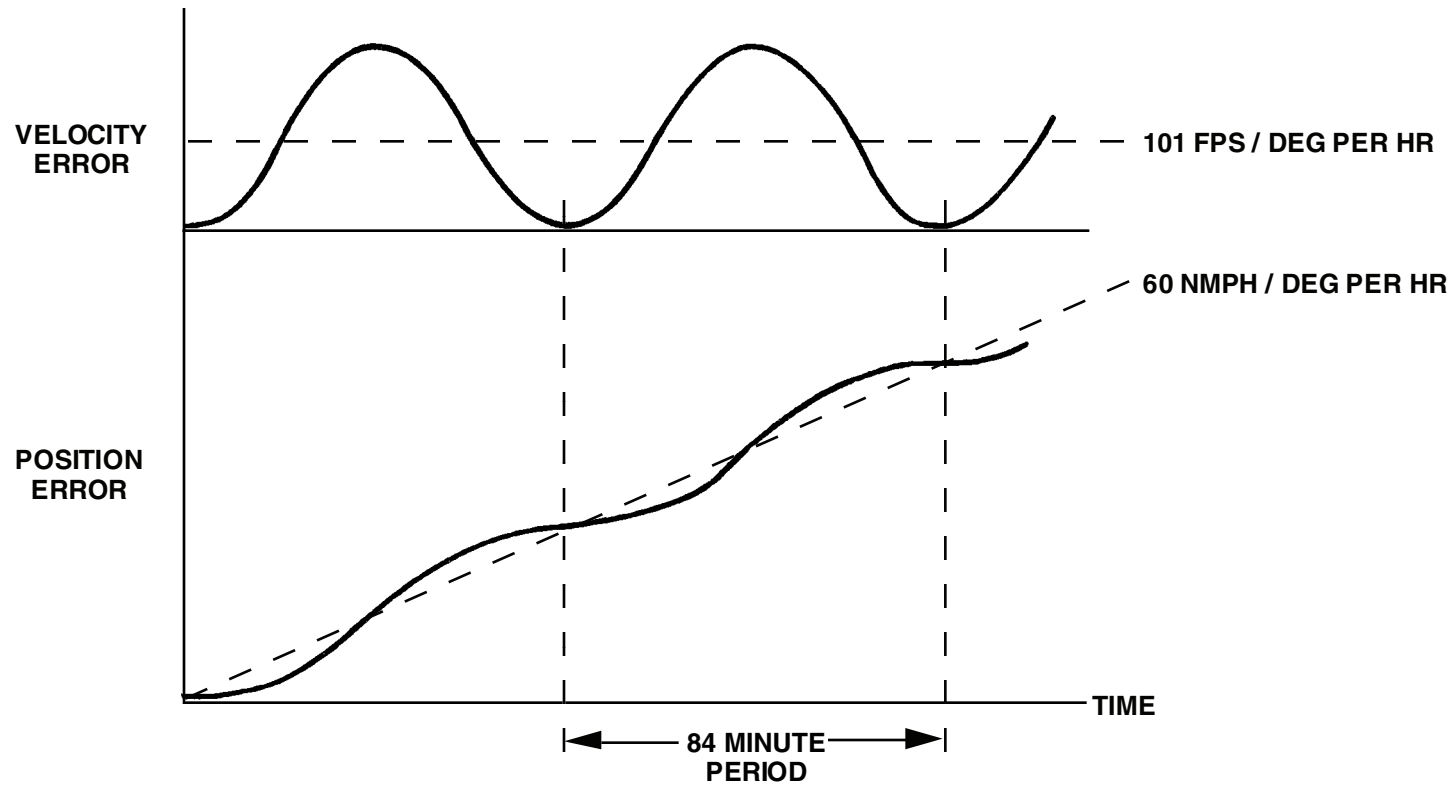
invented in the early part of this century by Dr. Maximilian Schuler. The Schuler pendulum is an ideal pendulum having a period of oscillation of 84 minutes. Dr. Schuler reasoned through dynamic analysis that such a pendulum would remain level under horizontal accelerations of the pendulum pivot. The reasoning was based on the principle that for the 84 minute pendulum, the inertial angular acceleration of the pendulum generated by horizontal pivot acceleration, is exactly equal to the angular acceleration of the vertical to the pivot as the pivot accelerates over the spherical earth. Hence, the pendulum rotation generated inertially is exactly balanced by the kinematic rotation of the earth referenced vertical due to pivot translation. This is exactly the concept used to mechanize the INS locally level gyro stabilized platform, hence, the INS platform also oscillates like a Schuler pendulum when disturbed (by errors).

Again, referring to the figure, the heading error in the platform axes (or strapdown direction cosines) is shown to have two input paths to the Schuler loop. One input causes horizontal acceleration errors into the platform under horizontally accelerating flight due to misinterpretation in the system computer of the heading direction of the accelerometer sensed accelerations; the other produces leveling errors in the platform due to misdirection of the platform axis rates from the system computer (commands to the gimbaled platform gyro torquers) for maintaining platform axes level. In the case of a strapdown system, the latter error is generated during the analytical rotation of the attitude data using the calculated navigation axis rotation rates. The platform heading error that produces the above effects is caused by "platform" heading initialization errors plus the integrated effect of "platform axis" vertical gyro errors.

Finally, the velocity errors in the slide are integrated to generate the system position errors. The position error represents the INS computer error generated in the position integration process using velocity data containing errors.

**NOTES**

# RESPONSE TO LEVEL PLATFORM AXIS CONSTANT GYRO ERROR



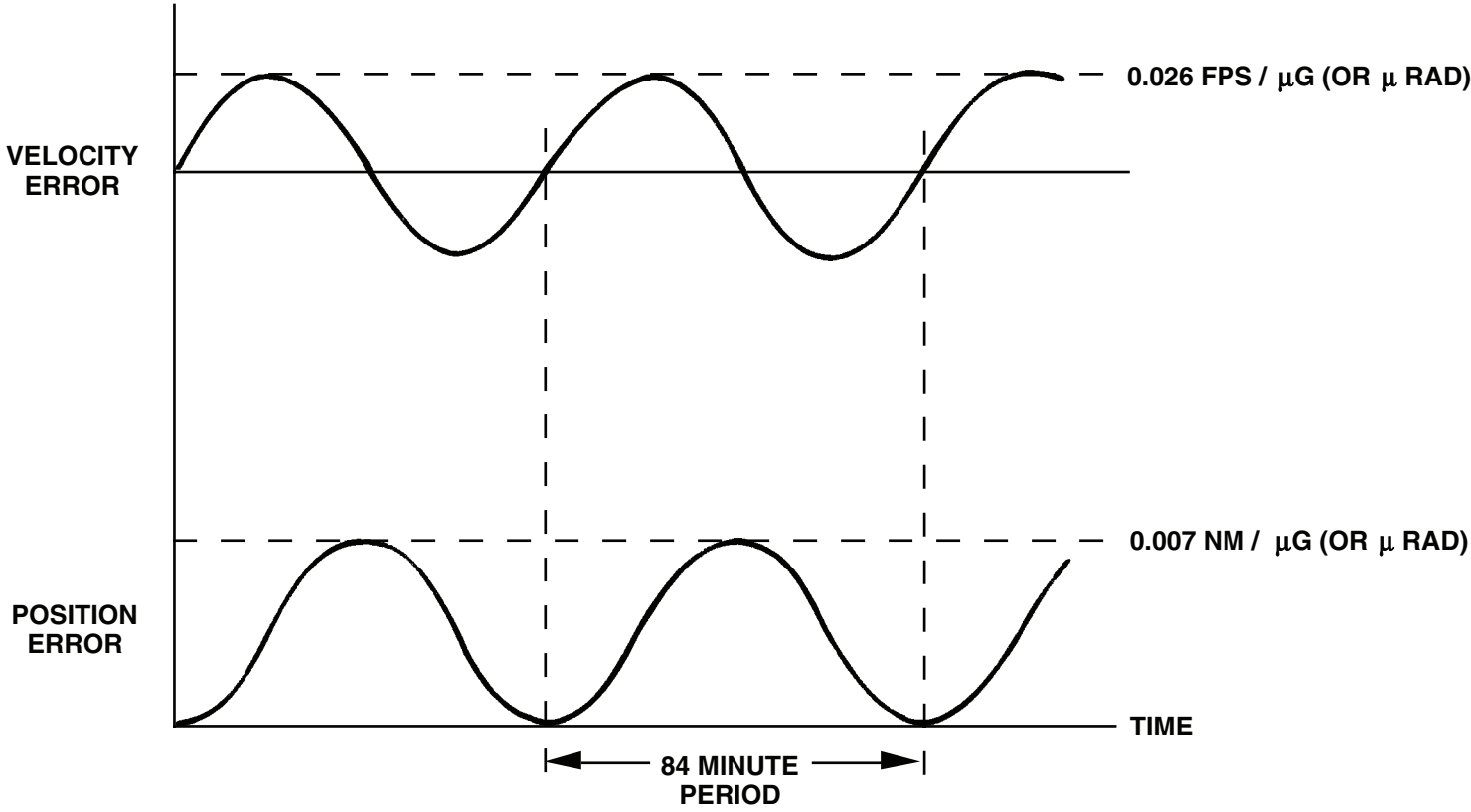
## RESPONSE TO LEVEL PLATFORM AXIS CONSTANT GYRO ERROR

The diagram in the previous slide is easily analyzed to determine system error response to constant horizontal (level) axis gyro errors (i.e., the horizontal component of the transformed strapdown gyro error being constant). This situation would arise for a constant body axis gyro error and a fixed orientation of the body axes (B) relative to local level navigation axes (L) which makes  $C_B^L$  constant. A constant gyro error in the level axis gyros on a gimbaled platform would produce similar results.

The error response as a function of navigation time shows an offset cosine wave at the Schuler frequency for the velocity error (42 minute peak), with an average offset of 101 fps per deg per hr gyro error. The corresponding position error is the integral of the velocity error curve, or a ramping error with an average slope of 60 nautical-miles-per-hour per deg-per-hour gyro error. Schuler oscillations are also seen on the position error response.

The unbounded ramp position error response of an INS to constant platform axis gyro error has traditionally been a principle (if not the most important) error source. This particular response characteristic is the reason that INS accuracy requirements are expressed in nautical-miles-per-hour average position drift. For an overall 1 nautical-mile-per-hour system, 0.01 degree per hour gyro bias errors are generally required (as can be seen from the indicated sensitivity, this would generate 0.6 nmph position error, leaving a margin for other system/sensor error effects).

# RESPONSE TO LEVEL PLATFORM AXIS CONSTANT ACCELEROMETER ERROR (OR INITIAL ATTITUDE TILT)



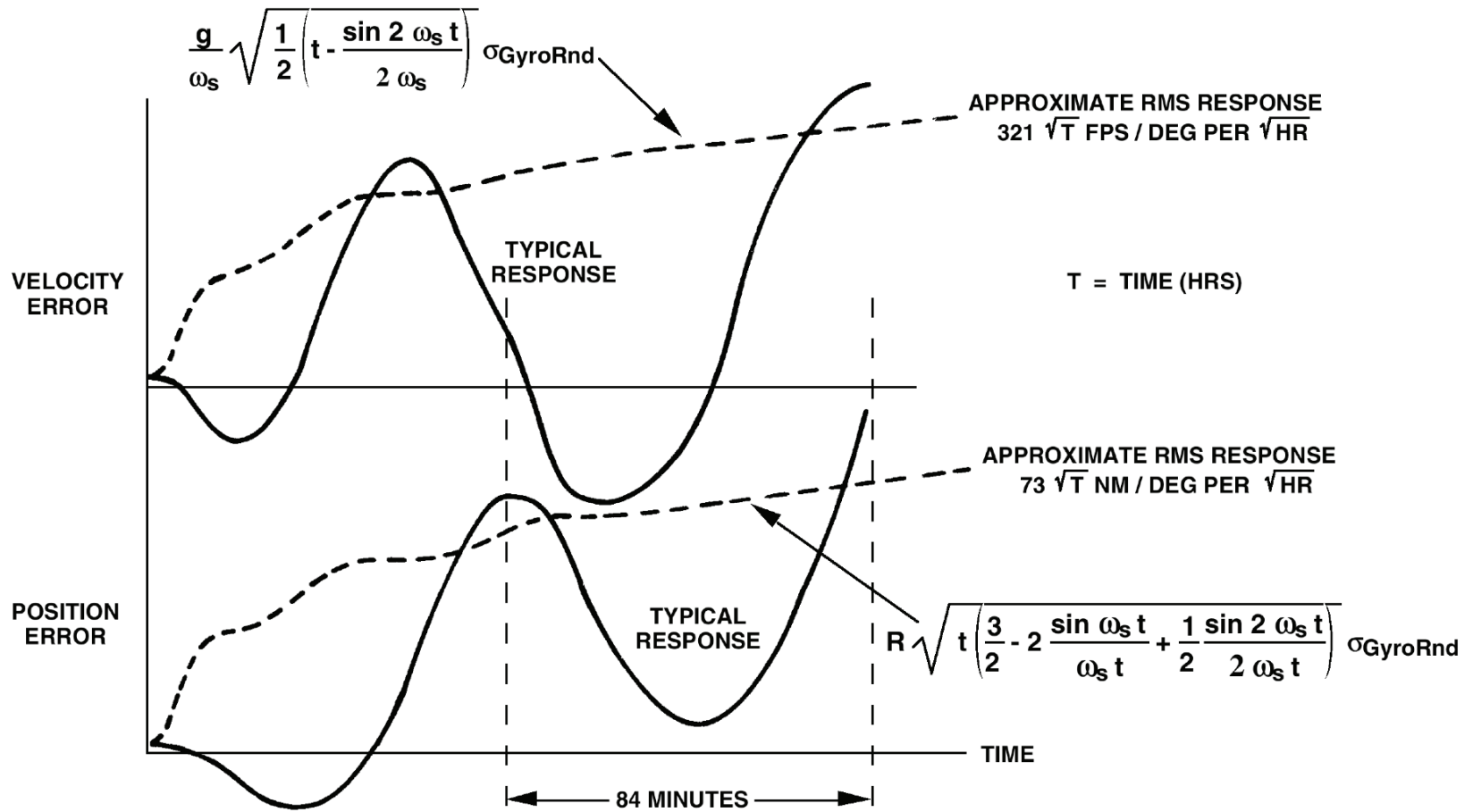
## **RESPONSE TO LEVEL PLATFORM AXIS CONSTANT ACCELEROMETER ERROR (OR INITIAL ATTITUDE TILT)**

As can be deduced analytically from the previous dynamic error diagram, constant horizontal acceleration errors produce a sinusoidal INS velocity error versus navigation time, with zero mean. The velocity error amplitude is 0.026 fps per micro-G accelerometer error. The corresponding position error is a bounded offset Schuler cosine wave at a peak amplitude of 0.007 nautical miles per micro-G.

Note from the error diagram, that initial platform tilts enter the Schuler error loop at exactly the same point as the acceleration errors. Hence, they produce comparable error forms as indicated in this slide (one micro-radian platform tilt produces the same effect as one micro-G accelerometer bias).

Accelerometer bias errors are of concern in inertial navigation systems principally due to their impact on velocity accuracy. For an INS with a 2.5 fps velocity accuracy requirement, 50 micro-G accelerometers are typically utilized. The error sensitivity shows that such accelerometers would generate 1.3 fps peak velocity error (when operated at a fixed orientation relative to navigation axes so that the navigation axis error is constant).

# RESPONSE TO LEVEL AXIS GYRO RANDOM NOISE



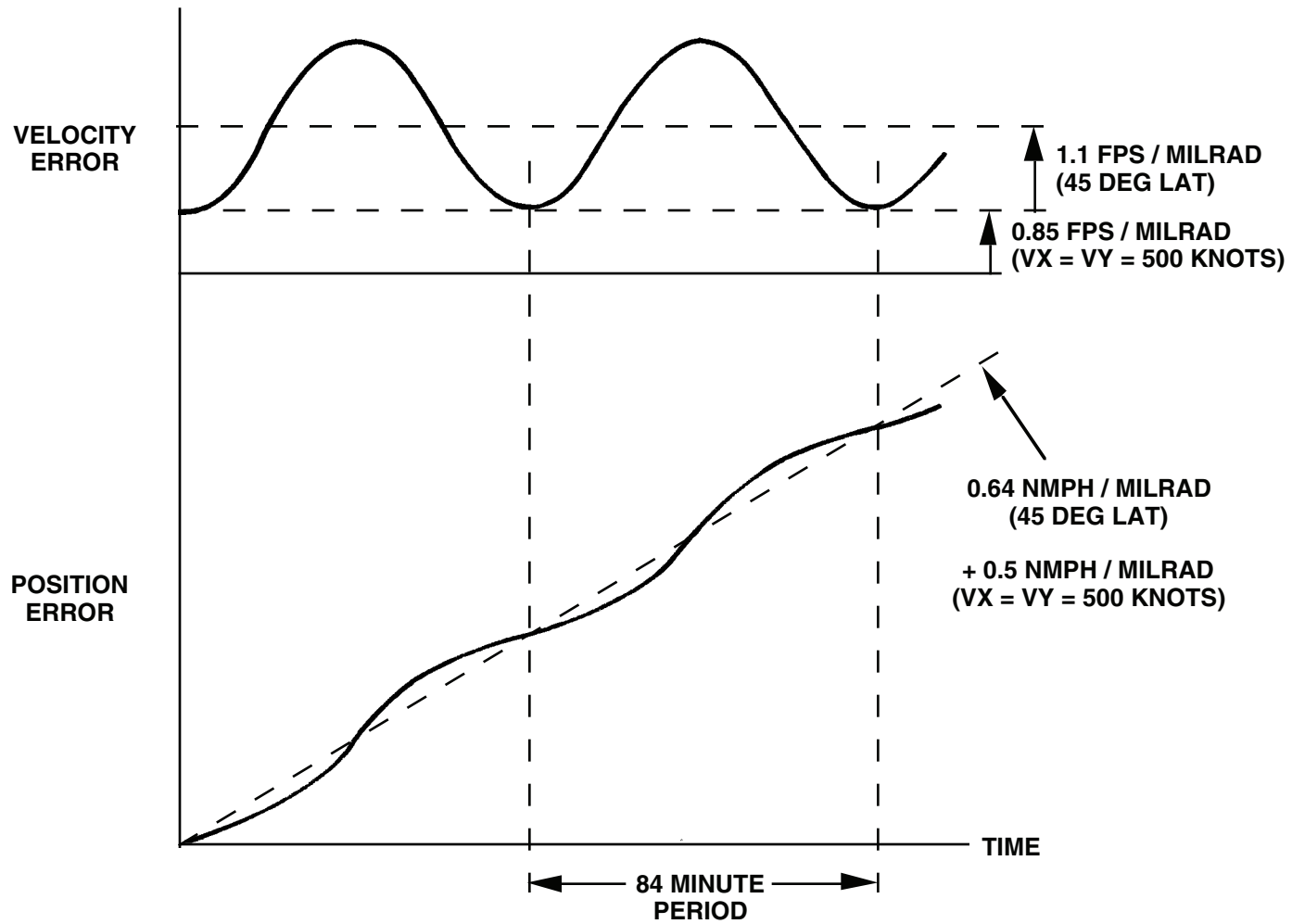
## RESPONSE TO LEVEL AXIS GYRO RANDOM NOISE

Gyro random noise inputs to the Schuler loop produce random Schuler oscillators. On an ensemble basis (several sets of navigation runs), the average error has a zero mean but an increasing standard deviation in both the velocity and position errors as a function of navigation time. The chart provides analytical expressions for the velocity/position errors in terms of earth's surface gravity magnitude  $g$  (32.2 ft/sec), the Schuler frequency  $\omega_s$  (1 cycle per 84 minutes = 0.00124 rad/sec), earth's radius  $R$  (2.09E7 ft), navigation time  $t$  (in seconds), and gyro random noise  $\sigma_{\text{GyroRNd}}$  (in radians per square-root-of-seconds).

The chart also shows approximate values for the velocity/position errors (based on the leading term under the analytical velocity/position expression square roots). The standard deviation of the velocity error increases proportional to the square root of the navigation time at 321 fps per square root of flight hour per deg per square root of hour gyro random noise. The standard deviation of the position error also increases with the square root of time at 73 nautical miles per square root of flight hour per degree per square root of hour gyro random noise. Rate gyro random noise is typically measured as the standard deviation of the ensemble of the integral of the gyro output noise error. For a white random noise, the standard deviation of this integral increases as the square root of the integration time. Hence, gyro white random noise is measured in terms of degrees standard deviation per square root of integration time.

For a typical high performance laser gyro random noise of 0.002 deg per square root of hour, the resulting velocity error is 0.64 fps per square root of flight hour and the position error would be 0.15 nautical miles per square root of flight hour.

# RESPONSE TO INITIAL HEADING ERROR



## RESPONSE TO INITIAL HEADING ERROR

The response of the Schuler loop to initial heading error is to generate an offset Schuler cosine wave in velocity and a ramp position error with superimposed Schuler oscillations. It should be noted that the response indicated in the chart is based on the assumption that the horizontal velocity is constant, and initially generated rapidly (i.e., mathematically instantaneously) at time zero from a starting zero velocity condition. This simulates an aircraft takeoff from a ground base followed by rapid acceleration to its constant cruise velocity.

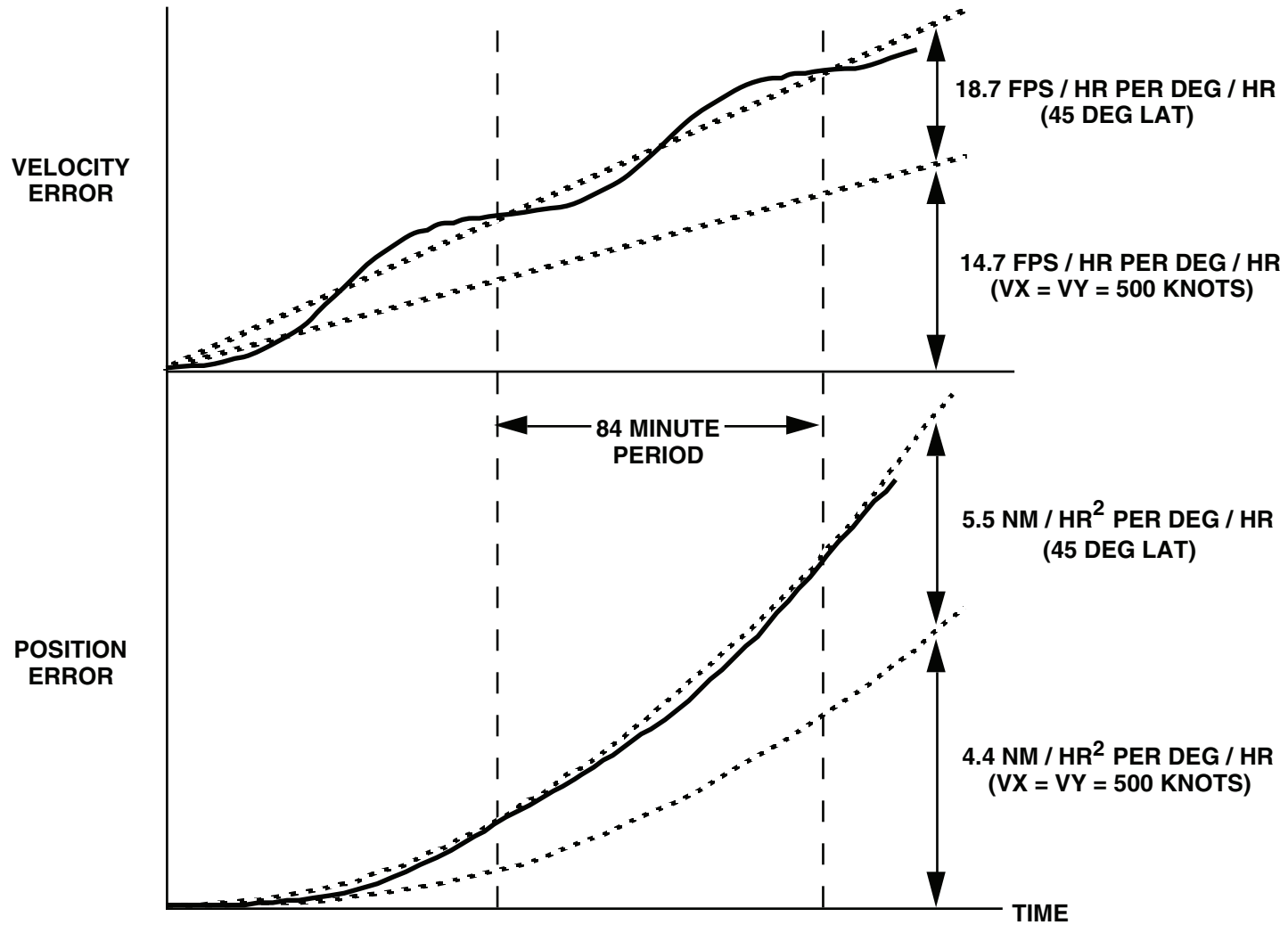
The heading error produces navigation error principally through a misdirecting (in azimuth) of platform rotation rates to maintain a level reference. The magnitude of the effect equals the nominal platform horizontal rotation rate times the heading error (see single axis Schuler loop analytical diagram). The nominal platform rotation rate is the sum of the horizontal earth rate plus the aircraft transport rate. As such, we would expect the heading error effect in the INS to be a function of aircraft velocity over the earth (i.e., transport rate) and latitude (which determines horizontal earth rate). The system sensitivities shown in the figure correspond to North position and velocity errors for a typical operating latitude of 45 degrees, with North and East cruise velocity components of 500 knots. The East channel error response would not contain the earth rate effect which produces the 1.1 fps and 0.64 nmph errors indicated in the North channel per milliradian of heading error.

Note, that for a 1 mil rad initial heading error (under zero velocity conditions) the positioning error is 0.64 nmph. This explains why at least 1 mil rad initial heading determination accuracy is typically required for 1 nmph inertial navigation systems.

**NOTES**

**NOTES**

# RESPONSE TO VERTICAL PLATFORM AXIS CONSTANT GYRO ERROR

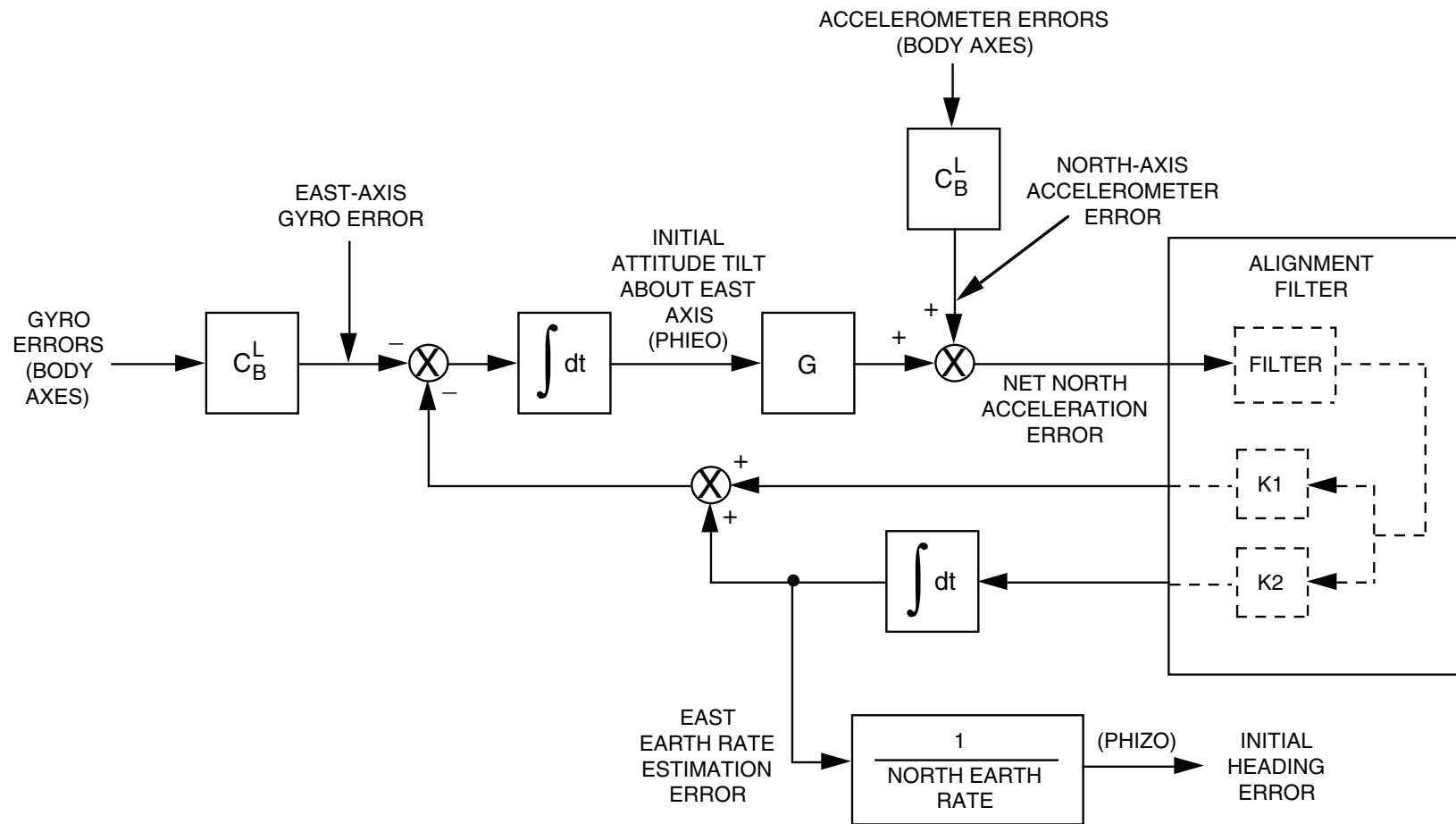


## RESPONSE TO VERTICAL PLATFORM AXIS CONSTANT GYRO ERROR

The slide illustrates the effect of constant vertical "platform" axis gyro error on navigational accuracy. The changing heading error caused by the vertical gyro error produces an error response that is comparable to the integral of the response characteristics shown previously for the constant heading error case. As for the constant heading case, the response characteristics here are functions of aircraft latitude and velocity. The curves presented illustrate the North channel response. East channel errors would not contain the earth rate effect (the term associated with the 45 deg latitude condition).

The curves show a ramp velocity error build-up and a parabolic position error build-up, each with Schuler oscillations. For a typical 0.01 deg per hour gyro error, the net North position error at 2 hours would equal  $9.9 \times 2^2 \times 0.01 = 0.4$  nautical miles, or 0.2 nautical miles average per hour flight time. This illustrates that for short flight times, the vertical gyro bias error effect is generally small compared to other error effects. For example, 0.01 deg per hour horizontal gyro bias error was shown to produce 0.64 nmph error. For long flight times, on the other hand, the effect of vertical gyro error becomes as significant as the horizontal gyro error effects.

# INITIAL ALIGNMENT LOOP ERROR CHARACTERISTICS



## INITIAL ALIGNMENT LOOP ERROR CHARACTERISTICS

Thus far, we have discussed sensor error propagation during navigation. Because the sensors in an inertial navigation system are also utilized during the system initial alignment, the sensor errors also impact initial alignment accuracy in attitude (leveling) and heading. These initial attitude/heading errors then propagate into position and velocity errors during the system navigation mode (as shown in previous slides).

The slide illustrates a dynamic error diagram for the initial alignment loops mechanized along "platform" horizontal axes in a typical strapdown inertial navigation system. This diagram is the error form of another diagram shown previously entitled "Strapdown System Initial Alignment".

Note, that for many strapdown system applications, the body attitude relative to the local level is constant during alignment (e.g., for a typical aircraft INS ground alignment). Consequently, results obtained based on a constant  $C_B^L$  assumption (which makes the sensor errors constant in level axes), is representative of many strapdown system operational situations.

Note also, that the single axis diagram represents the East error channel for a system where the "platform" heading is near North. As a result, the initial heading error satisfies the simple analytical expression indicated as a function of system estimated East earth rate error. For the general case of an arbitrary initial "platform" axis orientation, heading error equals the East component of the vector sum of the "platform" X and Y axis earth rate error components. The qualitative and numerical performance results obtained using the simplified model in the slide are identical to those for the general case.

The heading error equal to East earth rate error divided by North earth rate, is the error form of the initial heading determination equation given in a previous slide entitled: "Initial Platform Heading Determination". Geometrically, it should be obvious that the heading angle error resulting from small earth rate estimation errors is caused by an error in estimating the direction of the horizontal earth rate vector. The horizontal earth rate direction error (for small earth rate estimation errors) equals the earth rate error component perpendicular to the horizontal earth rate, divided by the horizontal earth rate magnitude. Since horizontal earth rate is North, the critical perpendicular earth rate error component is East. Hence, heading error equals East earth rate estimation error divided by North earth rate.

## INITIAL ALIGNMENT ERRORS CAUSED BY CONSTANT “PLATFORM” AXIS SENSOR ERRORS

$$\left. \begin{aligned} \text{PHIX}_0 &= - \frac{\text{Y-ACCEL ERROR (PLATFORM AXES)}}{G} \\ \text{PHIY}_0 &= + \frac{\text{X-ACCEL ERROR (PLATFORM AXES)}}{G} \end{aligned} \right\} \text{INITIAL LEVEL ERRORS}$$

$$\text{PHIZ}_0 = - \frac{\text{EAST GYRO ERROR}}{\text{NORTH EARTH RATE}} \quad \text{INITIAL HEADING ERROR}$$

## INITIAL ALIGNMENT ERRORS CAUSED BY CONSTANT "PLATFORM" AXIS SENSOR ERRORS

To analyze the impact of constant "platform axis" gyro and accelerometer errors on system alignment accuracy, we need only analyze the final steady state response of the indicated alignment loops in the previous slide. In the steady state, assuming the alignment loops are stable (through proper loop gain design), the integrator outputs will be stationary. Consequently, the integrator inputs will be zero. This latter condition can be used to easily relate tilt and heading errors in the diagram to the sensor errors that produce them.

The steady state condition that the input to the earth rate error integrator be zero in the previous alignment error loop diagram, sets the condition that the steady state attitude error (tilt) times  $G$  equals ( $\pm$ ) the horizontal accelerometer bias error. This relationship determines the equations shown in the slide for the initial X, Y level errors as functions of X and Y platform axis accelerometer error.

The condition that the input to the attitude tilt error integrator be zero in the steady state, sets the condition that the East-axis gyro error equal the negative of the earth rate estimation error. (Note that the K1 amplified output signal in the alignment loop error diagram slide is zero in the steady state because it is derived from the input to the earth rate estimation integrator. It has already been shown that this latter signal is zero in the steady state). The initial heading error equation shown in the slide is based on this latter relationship, divided by North earth rate as shown in the error loop diagram slide.

The heading error equation illustrates the sensitivity of initial heading error to alignment latitude. For high (or low) latitudes, the North earth rate is small (proportional to cosine latitude), hence, the heading error caused by East gyro bias is large. Because of this effect, self-alignments of an inertial navigation system at high latitudes generally result in large initial heading errors and subsequent navigation errors.

# INITIAL HEADING ERROR CAUSED BY ACCELEROMETER ERROR TRENDING DURING ALIGNMENT

$$\text{PHIZ}_0 = \frac{\text{NORTH ACCELEROMETER ERROR TRENDING}}{\text{G} \times \text{NORTH EARTH RATE}} \quad \text{INITIAL HEADING ERROR}$$

FOR 1 MICRO-G PER SECOND ACCELEROMETER ERROR TRENDING  
AT 45 DEGREES ALIGNMENT LATITUDE:

INITIAL HEADING ERROR = 19.4 MILLI-RAD'S

## **INITIAL HEADING ERROR CAUSED BY ACCELEROMETER ERROR TRENDING DURING ALIGNMENT**

One of the more subtle error sources in inertial navigation systems during alignment is the effect of small changes in the North accelerometer error (error trending) during the alignment process. From the previous Initial Alignment Loop Error Characteristics diagram it can be seen that the effect of a ramping North-axis accelerometer error has the same signature at the input to the Alignment Filter as the East-axis Gyro Error (except for the G scaling on the gyro error and a difference in phasing). We can conclude that the effect of North accelerometer error trending during alignment will also produce an initial heading error through the same formula as for the East gyro error given on the previous chart, modified by the G scaling and a change in sign.

The magnitude of the heading error produced by North accelerometer error trending during alignment can be substantial. At 45 degrees latitude, one micro-g per second of North accelerometer error trending will produce a 19.4 milliradian heading error. Accelerometer error trending can be produced by thermal transients created during the system turn-on/alignment period. To reduce accelerometer error trending during alignment, it is important for the system thermal design to minimize thermal transients around the accelerometers.

## HEADING ERROR DUE TO LASER GYRO RANDOM NOISE

$$\text{RMS HEADING ERROR} = \frac{\text{EAST GYRO RANDOM WALK (DEG/\sqrt{H})}}{\text{NORTH EARTH RATE} \times \sqrt{\text{ALIGN TIME}}}$$

FOR }  
45 DEGREE LATITUDE (NORTH EARTH RATE = 11 DEG/H)  
ALIGN TIME = 0.05 HOURS (3 MINUTES)  
RMS HEADING ERROR = 1 MIL RAD

EAST GYRO RANDOM WALK REQUIREMENT = 0.0024 (DEG/\sqrt{H})

- IMPACTS STRAPDOWN LASER GYRO SYSTEMS (RANDOM WALK IS A KEY RLG DESIGN PARAMETER)

## HEADING ERROR DUE TO LASER GYRO RANDOM NOISE

A significant source of navigation error in laser gyro strapdown inertial navigation systems is produced by initial heading error created by laser gyro random output noise (random walk on attitude) during alignment. From the previous Initial Alignment Loop Error Characteristics diagram, it can be shown that the closed loop alignment operations will modify the East Earth Rate Estimation Error so that its feedback integral into Initial Attitude Tilt tends to balance the integral of East gyro random walk noise into Initial Attitude Tilt. The resulting East Earth Rate Estimation Error component creates a heading error equal to the East component of the laser gyro random walk error coefficient (measured in degrees per square root of hour) divided by North earth rate, divided by the square root of the alignment time. Hence, the heading error is larger for short alignment times. This reflects the averaging of the alignment filtering process on heading determination accuracy. The longer the alignment time, the longer the filtering effect on the gyro noise, hence, the more accurate the heading determination.

For the case of an alignment at 45 degrees latitude for a three minute alignment time (fairly rapid for a typical INS) the slide shows that 0.0024 deg per square root of hour gyro random walk is required to meet a typical 1 mil rad heading error requirement. Allowing for other error source contributors, 0.002 deg per square root of hour is required. Such performance is close to the limit of the capability of today's production laser gyro technology.

For fast reaction time applications, the above discussion illustrates that laser gyro random walk is a key system design parameter.

# RANDOM WALK ANALYTICS

$\varepsilon_{\theta_i}$  =  $i^{\text{th}}$  RANDOM ANGLE INCREMENTAL ERROR

$\Delta\theta$  =  $\sum_i^n \varepsilon_{\theta_i}$  CUMULATIVE RANDOM ANGLE ERROR

$E(\Delta\theta^2)$  =  $\sigma_\theta^2$  EXPECTED VALUE OF  $\Delta\theta^2$  (I.E., VARIANCE)

$$\begin{aligned} E\left(\sum_i^n \varepsilon_{\theta_i} \sum_j^n \varepsilon_{\theta_j}\right) &= E\left(\varepsilon_{\theta_1}^2 + \varepsilon_{\theta_2}^2 + \varepsilon_{\theta_3}^2 + \cdots + 2\varepsilon_{\theta_1} \varepsilon_{\theta_2} + 2\varepsilon_{\theta_1} \varepsilon_{\theta_3} + \cdots\right) \\ &= \sum_i^n \varepsilon_{\theta_i}^2 = \sum_i^n \sigma_\varepsilon^2 = n \sigma_\varepsilon^2 = t f_\varepsilon \sigma_\varepsilon^2 \end{aligned}$$

$$\sigma_\theta = \sqrt{t} \sigma_\varepsilon \sqrt{f_\varepsilon} \quad \sigma_\varepsilon \sqrt{f_\varepsilon} = \text{RANDOM WALK COEFFICIENT}$$

## RANDOM WALK ANALYTICS

Random walk is a noise process defined analytically as the integral of white noise. A defining property of random walk is that the root-mean-square (rms) of its integral increases as the square root of the integration time. An important error output characteristic of a strapdown gyro is its random noise output which, when integrated into angular attitude, gives rise to a random walk error "on attitude". The chart shows analytically how the random walk square-root-of-integration-time error buildup occurs.

Consider the white noise error output contributions from the gyro to be a sequence  $i$  of small uncorrelated (random) zero-mean angle increments  $\epsilon_{\theta_i}$ . The digital integral of the gyro output is a summation operation. The integral (summation) of the  $\epsilon_{\theta_i}$ s gives a total random angle error of  $\Delta\theta$ . The "variance" about the zero mean is the expected (average) value of  $\Delta\theta$  squared and  $\sigma_{\theta}$  is the rms. Substituting the  $\Delta\theta$  definition into the variance equation (with a change in  $i$  index to  $j$  for one of the summations), expansion of terms, setting the expected value of  $\epsilon_{\theta_i} \epsilon_{\theta_j}$  products to zero for  $i \neq j$  (because the  $\epsilon_{\theta_i}$ s are uncorrelated), and defining the variance of each  $\epsilon_{\theta_i}$  as equal to the same value  $\sigma_{\epsilon}$  (a time stationary white noise process) shows that the  $\Delta\theta$  variance equals the number of samples in the summation  $n$  multiplied by  $\sigma_{\epsilon}$  squared. Setting  $n$  equal to the summation frequency  $f_{\epsilon}$  times the integration time  $t$  and taking the square root of the result yields a simple expression for  $\sigma_{\theta}$ .

Grouping of terms in the final result shows that  $\sigma_{\theta}$  equals a constant coefficient (the "random walk coefficient") multiplied by the square root of integration time. For an angular rate measuring gyro used in this example, the units of the random walk coefficient are degrees per square root of integration time (e.g., degrees per square root of hour or deg/rt-hr).



## CORRELATION BETWEEN INITIAL ATTITUDE ERRORS AND NAVIGATION ERRORS

Because tilt errors generated during the alignment process are caused by accelerometer bias, the effect of the initial tilt errors on system accuracy during navigation is correlated with the effect of accelerometer bias errors during navigation. The slide shows the North channel (for example) of a typical Schuler loop to illustrate the effect of this correlation. This discussion is equally valid for the East or any arbitrary platform horizontal axis channel.

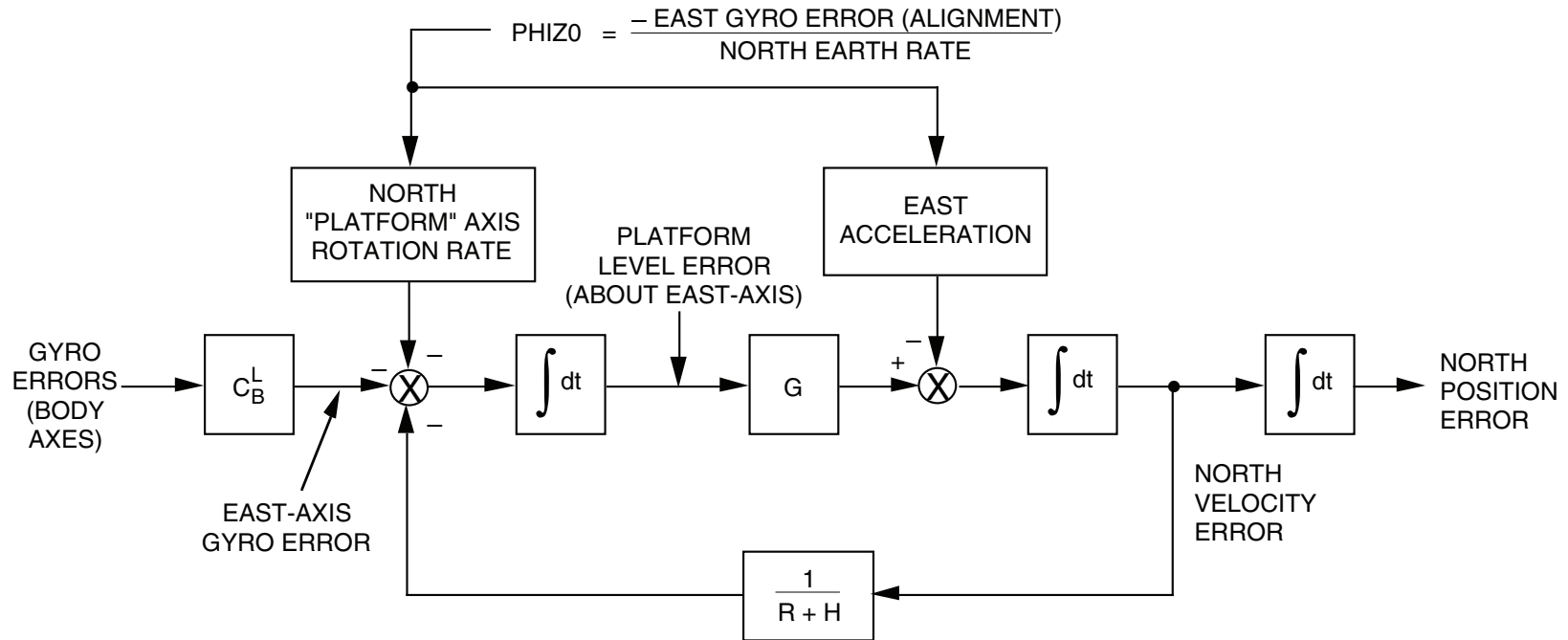
The initial tilt (PHIE0) is shown (as in a previous slide) equal to the negative of the North component of the "platform" axis acceleration error divided by G. The North component of accelerometer error during navigation is shown being generated as the transformation of the body axis acceleration error vector.

For the North acceleration error during alignment equal to the North acceleration error during navigation, the product of the platform level error with G in the diagram cancels the North acceleration error during navigation (observe the summing junction in the slide). This condition will occur if the body attitude during alignment as manifested in  $C_B^L$  equals the body attitude during navigation. For gimballed systems, the body and platform axes are equivalent (i.e., the sensor axes are the platform axes), hence,  $C_B^L$  during alignment and navigation will be equal (for short flight times; one to two hours). As a result, constant accelerometer errors in gimballed systems tend to be cancelled by the initial platform tilt effects, so that navigational accuracy becomes relatively insensitive to accelerometer error. Hence, long term accelerometer accuracy requirements in gimballed systems for cruise applications are not critical.

For strapdown systems, the sensor attitude during flight can be at any arbitrary attitude relative to the alignment attitude (depending on aircraft flight direction relative to alignment direction). If the flight direction is the same as the alignment direction, the initial attitude level errors cancel the fixed accelerometer bias errors during flight. On the other hand, if the flight direction is opposite to the alignment direction, the  $C_B^L$  matrix will reverse the platform axis acceleration error during flight so that it is opposite to its value during alignment. The net result is that the tilt effect will add to the accelerometer error during navigation, thereby effectively doubling the accelerometer bias error effect.

One of the most demanding tests for a strapdown system in the laboratory is a navigation run at a heading that is 180 degrees different from the alignment heading. Such a test doubles the navigation error from accelerometer bias effects. A static laboratory test for a strapdown system, on the other hand, in which the alignment and navigation headings are the same, produces accelerometer error/initial tilt cancellation, hence, generally superior system navigational accuracy.

# CORRELATION BETWEEN INITIAL HEADING ERROR AND NAVIGATION ERRORS



- FOR SAME ATTITUDE IN ALIGN AND NAV, EAST GYRO ERROR CANCELS AT ZERO VELOCITY
  - BENEFITS GIMBALED SYSTEMS
  
- ATTITUDE CHANGES IN STRAPDOWN SYSTEMS ALTER  $C_B^L$ 
  - UNCOUPLES GYRO ERROR CANCELLATION MECHANISM

## CORRELATION BETWEEN INITIAL HEADING ERROR AND NAVIGATION ERRORS

A correlation also exists between initial platform heading error and gyro bias during cruise because the heading error is produced (in part) by gyro bias during system alignment. The slide illustrates the effect on system accuracy of initial heading error (produced, as shown in a previous slide, by the East "platform axis" gyro error component during alignment) and gyro bias during navigation.

The North platform axis rotation rate in the slide equals North earth rate plus North transport rate. Therefore, for zero or low velocity conditions (i.e., zero transport rate) the product of the initial heading error with the North platform axis rotation rate equals the East gyro bias during alignment. For body axes during navigation parallel to body axes during alignment, the East gyro error during navigation is the same as during alignment, and the heading error effect cancels the East gyro error at the entry point into the Schuler loop (summing junction into the level error integration). This effect benefits gimbale systems in which the sensor heading during alignment and navigation is equivalent. Under non-zero velocity conditions, the East gyro bias is still cancelled by the earth rate component of the North "platform" axis rotation rate multiplying the heading error, however, the transport rate component of platform axis rotation rate generates an additional noncancelling error through its product with the initial heading error.

In the case of strapdown systems, the  $C_B^L$  matrix can produce a different East gyro bias component during navigation compared to alignment (depending on relative aircraft heading). For the same alignment and navigation heading, the initial heading error cancels the East gyro bias. For navigation opposite to the initial heading direction, the initial heading error doubles the effective East gyro bias through the earth rate coupling. For laboratory tests, a navigation run at a heading 180 degrees from the alignment heading, doubles the effective East gyro bias error component, generating a worst case North velocity/position navigation error. For the same navigation and alignment headings, the constant East gyro error is cancelled by the heading error, and no North navigation error results (except as produced by random gyro error effects).

It should be noted that in gimbale systems, North gyro bias error cancellation is also possible by calibration during alignment. Since the correct North earth rate magnitude is known (from initial latitude) it can be subtracted from the estimated North earth rate to calculate the platform axis North gyro bias error. The calculated North gyro bias error can then be used as a North axis platform rotation rate correction during navigation to compensate the North gyro error. For strapdown systems, this same technique can also be used to measure the North component of the composite strapdown gyro bias error vector. For laser gyro strapdown systems, the accuracy by which the North bias can be determined depends on the gyro random noise and alignment time. If an accurate enough estimate is achievable (compared to expected bias errors), the gyro bias error vector component measurement can be successfully used to compensate a portion of the gyro bias error vector during navigation. This would be achieved by applying a fixed vector correction to the strapdown gyro sensed angular rate vector in body axes. This fixed correction vector magnitude would be set equal to the North bias measured during alignment. The direction sense of the fixed body axis bias correction vector would point North if the body axes were oriented as they were during alignment.

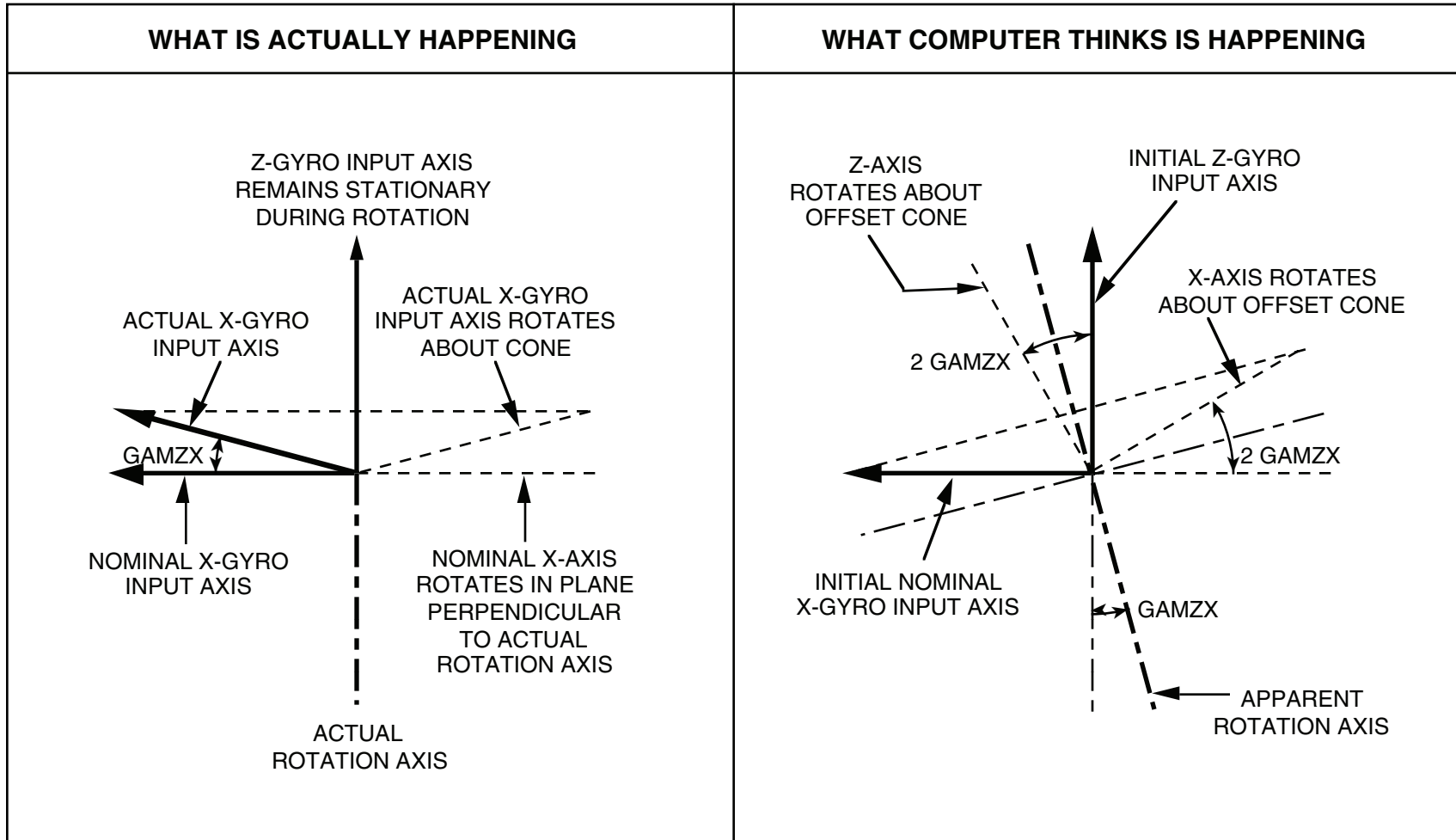
**STRAPDOWN SENSORS HAVE SEVERAL ERROR  
MECHANISMS THAT ARE EXCITED BY THE BODY  
MOUNTED ROTATION RATE ENVIRONMENT**

## **STRAPDOWN SENSORS HAVE SEVERAL ERROR MECHANISMS THAT ARE EXCITED BY THE BODY MOUNTED ROTATION RATE ENVIRONMENT**

Thus far, we have discussed strapdown sensor error effects under generally constant body attitude conditions. As we have seen, many strapdown system error effects under these conditions are directly comparable to that which would be obtained from a gimbaled system. An exception was the effect of differences in the body attitude during alignment and navigation that allowed propagation of accelerometer and gyro errors in strapdown systems into navigational error whereas the same errors in gimbaled systems tended to be suppressed by compensating tilts and heading error created during the initial alignment process.

Under general dynamic rotation environments during navigation, the strapdown system generates several additional error effects that are not present with gimbaled systems.

# EFFECT OF GYRO MISALIGNMENT ON SHORT TERM ATTITUDE ACCURACY (ROTATION ABOUT SINGLE SENSOR AXIS)



## **EFFECT OF GYRO MISALIGNMENT ON SHORT TERM ATTITUDE ACCURACY (ROTATION ABOUT SINGLE SENSOR AXIS)**

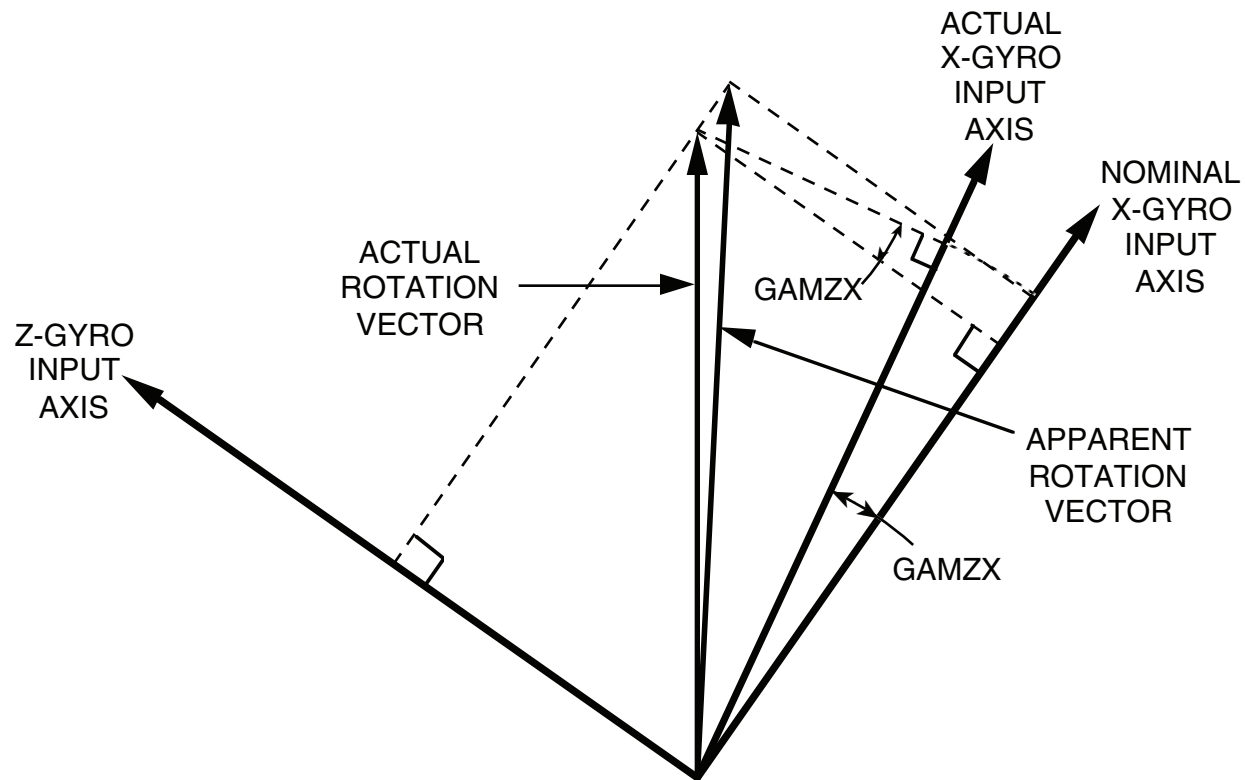
The slide graphically illustrates the effect of gyro misalignment on system attitude accuracy due to rotation about one of the cardinal sensor assembly axes (assuming an orthogonal sensor triad).

For a real rotation about the Z-axis, the nominal X-axis rotates in a plane about Z, and Z remains stationary. If the X-axis gyro is misaligned by GAMZX into Z, it rotates on the surface of the cone as indicated in the slide about Z. Due to the misalignment, the X-gyro outputs an erroneous signal proportional to the Z-axis rate during the maneuver.

Because the computer is unaware of the gyro misalignment, it interprets the output data from the gyros under this maneuver as if they were obtained from an orthogonal sensor set. Under the maneuver indicated, the Z and X gyros both provide outputs, the Z-gyro indicating the correct data, and the X-gyro erroneous data due to the misalignment coupling. The computer interprets the X, Z rates as if they were generated from orthogonal gyros, and calculates the attitude history shown in the slide. As can be seen, the attitude history calculated by the computer is about an offset rotation axis (by GAMZX) which rotates the X-axis (in the computer) out of the actual plane of X-axis rotation about an offset cone.

For a 180 degree rotation, the computed X-axis attitude has a maximum error (out of the actual rotation plane) of twice the gyro misalignment angle GAMZX. For a 360 degree rotation, the computed X-axis orientation returns to the correct initial attitude. Hence, repeated 360 degree rotations about a single sensor axis (e.g., snap rolls in an aircraft) generate cyclic attitude errors with no net cumulative error build-up.

## EFFECT OF GYRO MISALIGNMENT ON SHORT TERM ATTITUDE ACCURACY (SINGLE AXIS ROTATION ABOUT MULTIPLE SENSOR AXES)



- APPARENT ROTATION VECTOR IS TILTED AND DIFFERENT IN MAGNITUDE FROM ACTUAL ROTATION VECTOR
- MAGNITUDE EFFECT GENERATES NET ANGLE ERROR BUILD-UP UNDER CONTINUOUS ROTATIONS

## **EFFECT OF GYRO MISALIGNMENT ON SHORT TERM ATTITUDE ACCURACY (SINGLE AXIS ROTATION ABOUT MULTIPLE SENSOR AXES)**

For single axis rotations about an axis that is skewed relative to nominally orthogonal sensor axes, the gyro misalignments generate attitude reference errors that rectify during sustained rotations. The slide graphically illustrates this error mechanism during a rotation about an axis skewed between the nominally orthogonal X and Z gyro axes (as during a constant rate of turn holding pattern maneuver in an aircraft in a banked roll attitude condition).

The geometry in the slide shows the actual rotation vector and its projection on the nominal orthogonal sensor axes. It also shows the projection along the X-gyro axis which is at a misalignment  $GAMZX$  relative to the nominal orthogonal condition with Z. Because the computer receives the Z and X axis gyro signals and is not aware of the misalignment, it interprets the data as if it was obtained along orthogonal sensor axes. The slide shows how the X and Z sensed rates are interpreted as a vector in the computer based on this erroneous orthogonality assumption.

Note in the figure that the apparent rotation vector (to the computer) is tilted relative to the true rotation vector. Consequently, the computer interprets the rotation to be about an axis which is slightly tilted from the true rotation axis. In this respect, the error generated in the computer attitude data is comparable in character and magnitude to the error generated when the actual rotation is about one of the sensor axes.

Note, however, that the magnitude of the apparent rotation vector for this case is larger than the true rotation vector magnitude. This significant factor produces a scale factor error in the attitude computation such that an error is developed proportional to the total angle traversed during the maneuver. This is an unbounded error source that continues to grow for the duration of the rotation. Note also that the net angle error developed in the attitude data from this latter effect is about the actual rotation axis (to first order).

**EFFECT OF GYRO SCALE FACTOR ERRORS ON  
SHORT TERM ACCURACY (ROTATION ABOUT  
FIXED ROTATION AXIS)**

- **ATTITUDE ERROR BUILDUP EQUAL TO  
PRODUCT OF SCALE FACTOR ERROR AND  
NET ROTATION ANGLE**

## **EFFECT OF GYRO SCALE FACTOR ERRORS ON SHORT TERM ATTITUDE ACCURACY (ROTATION ABOUT FIXED ROTATION AXIS)**

Gyro scale factor errors in strapdown systems generate attitude errors during rotations about one axis (not necessarily along sensor axes) proportional to the product of the net rotation angle with the scale factor error. For a rotation about one of the sensor axes, the attitude error will be about that axis direction.

For strapdown applications where continuous turning may be expected (e.g., continuous rolling), it is important that gyro scale factor accuracy be precise. One of the significant advantages of the laser gyro in strapdown applications is its precise scale factor accuracy (e.g., 5 ppm).

## **EFFECT OF GYRO SCALE FACTOR AND MISALIGNMENT ERRORS ON SHORT TERM ATTITUDE ACCURACY (OSCILLATORY ROTATIONS ABOUT SINGLE AXIS)**

- **MISALIGNMENT ERROR EFFECTS**
  - **NO NET ATTITUDE ERROR BUILD-UP – POSITIVE CYCLE EFFECTS CANCEL  
NEGATIVE CYCLE ERRORS**
  
- **SCALE FACTOR ERROR EFFECTS**
  - **SYMMETRICAL ERRORS – NO NET ATTITUDE ERROR BUILD-UP: POSITIVE  
CYCLE EFFECTS CANCEL NEGATIVE CYCLE ERRORS**
  - **ASYMMETRICAL ERRORS – ATTITUDE ERRORS ACCUMULATE DUE TO  
RECTIFICATION EFFECT**

## **EFFECT OF GYRO SCALE FACTOR AND MISALIGNMENT ON SHORT TERM ATTITUDE ACCURACY (OSCILLATORY ROTATIONS ABOUT SINGLE AXIS)**

The previous slides can be used to deduce the effect of gyro misalignment on attitude accuracy for rotations about a fixed axis in which the rotation rate is cyclic so that there is no net build-up in actual rotation angle (e.g., such as an angular oscillation in an aircraft autopilot around a fixed axis). It should be apparent that no net attitude error should develop because the positive cycle error should be equal and opposite to the negative cycle error.

In the case of gyro scale factor errors under a similar cyclic rotation (about a single axis, but not necessarily along sensor axes), it is easily reasoned that a similar result applies; i.e., there is no net attitude error build-up because the positive cycle error cancels the negative cycle error.

If the gyro scale factor error has an asymmetrical component (i.e., difference between scale factor errors under positive and negative rates), a net attitude error build-up will develop under cyclic single axis rotations proportional to the scale factor asymmetry times the angular oscillation rate (i.e., the positive cycle error fails to cancel the negative cycle error by the amount of the asymmetry). For a 1 deg per sec oscillation amplitude (e.g., an aircraft autopilot response in gusty wind), a scale factor asymmetry of 1 ppm will produce a net attitude drift of 0.004 deg per hour. Such an error is significant for a strapdown INS designed for 1 nmph accuracy (where 0.01 deg per hr is the typical total allocation for constant gyro errors). This example illustrates why gyro scale factor asymmetry cannot be tolerated in high accuracy strapdown systems. Laser gyros are particularly accurate in this regard, having virtually no difference in their positive and negative scale factor error characteristics.

## **EFFECT OF GYRO SCALE FACTOR AND MISALIGNMENT ERRORS ON SHORT TERM ATTITUDE ACCURACY (SEQUENTIAL ROTATIONS)**

- **EXAMPLE**

**YAW (+90) → PITCH (+90) → ROLL (+90) → PITCH (-90)**

**NO NET ROTATION WITH ABOVE EULER ANGLE SEQUENCE**

- **SCALE FACTOR ERROR ON Z-GYRO LEAVES NET ERROR ABOUT VERTICAL (FROM YAW ROTATION)**
- **MISALIGNMENT OF PITCH OR ROLL GYROS WITH YAW AXIS LEAVES NET HORIZONTAL ATTITUDE ERROR**

**FOR COMPLEX MANEUVERS, GYRO MISALIGNMENT AND SCALE FACTOR ERROR EFFECTS ON ATTITUDE ACCURACY CAN ACCUMULATE**

**EFFECT OF GYRO SCALE FACTOR AND MISALIGNMENT ERRORS  
ON SHORT TERM ATTITUDE ACCURACY  
(SEQUENTIAL ROTATIONS)**

Attitude maneuvers consisting of sequential rotations about different sensor axes can rectify gyro scale factor errors in the strapdown attitude computation, even when the net maneuver returns the system to its original orientation. For example, consider the rotation sequence in the slide.

It is easily verified that the sensor attitude after the rotation sequence is as it was at the start of the sequence. However, note that the rotation about the Z-axis occurs at one time point in the maneuver and is positive. A Z-gyro scale factor error would generate a net attitude error at this time which would remain for the rest of the maneuver. Similarly, a misalignment of either the pitch or roll gyros into the Z (yaw) axis would also produce a net attitude error during the 90 degree yaw rotation, which would remain for the duration of the maneuver.

It can be concluded that for complex maneuvers (such as air-to-air combat), gyro misalignment and scale factor error effects on strapdown system attitude accuracy can accumulate.

## **EFFECT OF ACCELEROMETER MISALIGNMENT ERROR**

**FOR CRUISE INERTIAL NAVIGATION SYSTEMS:**

**DOMINANT EFFECT IS EQUIVALENT ACCELEROMETER BIAS DUE TO COUPLING OF YAW-AXIS ACCELERATION (1G) INTO ROLL, PITCH AXIS ACCELEROMETERS**

**IN GENERAL:**

**COUPLES CROSS-AXIS ACCELERATIONS INTO ACCELEROMETER INPUT AXES, THEREBY CREATING VELOCITY ERROR BUILD-UP**

## **EFFECT OF ACCELEROMETER MISALIGNMENT ERROR**

The dominant effect of accelerometer misalignment error under strapdown INS cruise conditions (e.g., in aircraft cruise applications) is a coupling of the predominant 1-G specific force acceleration from the yaw (Z) axis into the approximately level roll, pitch axis (X, Y) accelerometers due to the X, Y instrument misalignment (nonorthogonality) relative to the Z sensing axis. This appears as an average constant accelerometer output error, hence, acts as an accelerometer bias error during system operation.

For cruise applications, High G acceleration maneuvers will also produce velocity errors due to accelerometer misalignment. However, if the time duration for the maneuvers is significantly less than the average cruise time, the effect of the maneuvers on accelerometer misalignment induced errors will generally be negligible compared to the sustaining long term bias error effect during cruise.

For the general case, the effect of accelerometer misalignment is to couple the cross-axis specific force accelerations into the accelerometer input axes, thereby producing velocity error buildup. Each application should be investigated to determine the overall error effect for the expected acceleration profiles relative to the navigation reference frame and relative to the accelerometer input and cross-axis directions.

## **EFFECT OF MANEUVERS ON ACCELEROMETER SCALE FACTOR ERROR**

- **EXAMPLE**
  - **ACCELERATE (+X), THEN CHANGE HEADING (+90 DEG)**
  - **DECELERATE (-X) TO ORIGINAL SPEED, THEN CHANGE HEADING (+270 DEG)**
  - **NO NET CHANGE IN ATTITUDE, VELOCITY**
  - **NET VELOCITY ERROR ALONG-TRACK AND CROSS-TRACK FROM X-ACCELEROMETER SCALE FACTOR ERROR**

**ACCELEROMETER SCALE FACTOR ERROR EFFECTS CAN ACCUMULATE UNDER  
MANEUVERING FLIGHT CONDITIONS**

## **EFFECT OF MANEUVERS ON ACCELEROMETER SCALE FACTOR ERROR**

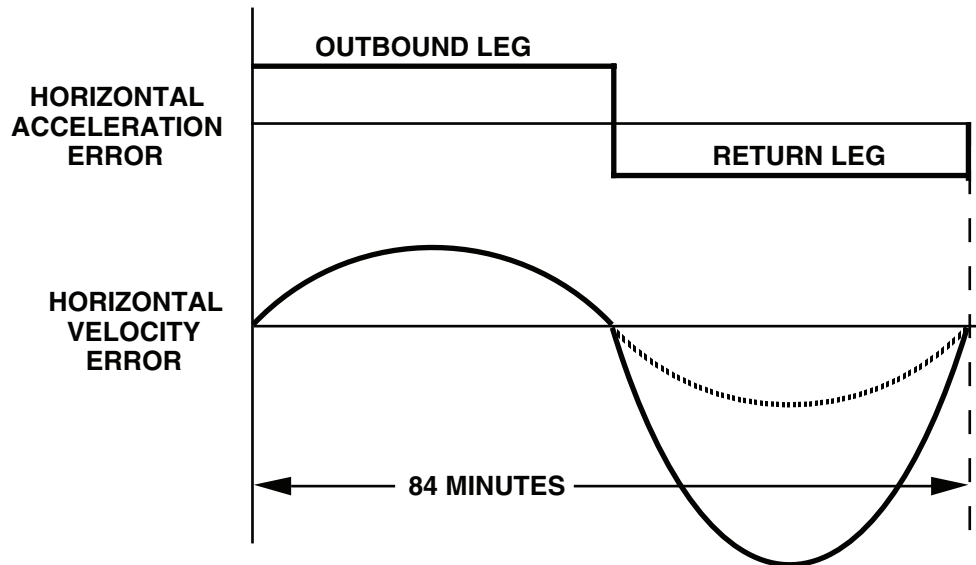
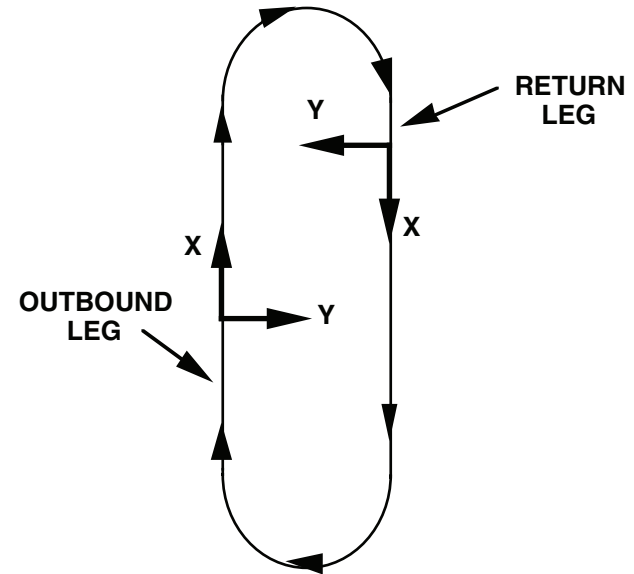
Consider the maneuver illustrated in the slide. The aircraft velocity and attitude (and approximately the position) is the same after as before the maneuver. Note that for the first leg of the maneuver, the velocity was increased along the aircraft X-axis. During the second leg (90 degrees in heading from the first leg) velocity was decreased to the original velocity.

For an X-axis accelerometer scale factor error in a strapdown system, a net velocity error would be generated during the first leg along the direction of the first leg. During the second leg the same X-axis accelerometer would generate an equal velocity error along aircraft axes but of the opposite sign to the error along the first leg (due to the negative acceleration). However, note that because the second leg is at ninety degrees in heading from the first, the second leg velocity error is along a navigation axis direction that is ninety degrees from the first leg velocity error. Thus, the same accelerometer error generates a net velocity error with an along and cross-track component (relative to the original velocity direction). Because the remainder of the maneuver generates no further X-axis acceleration, the net velocity error remains after maneuver completion.

The example illustrates that accelerometer errors in strapdown systems can accumulate under maneuvering flight conditions. This contrasts with gimbaled systems in which the platform mounted accelerometers maintain their orientation relative to navigation axes under aircraft maneuvers. Consequently, a maneuver that yields no net velocity change generates no net error from accelerometer scale factor error in gimbaled systems (i.e., the integral of the scale factor error effect is zero).

## EFFECT OF CLOSED-COURSE TRAJECTORIES ON FIXED GYRO/ACCELEROMETER ERRORS

- VERTICAL GYRO BIAS AND SCALE FACTOR ERRORS ACCUMULATE INTO HEADING ERROR (AND NORTH POSITION/VELOCITY ERROR)
- POSITION DRIFT CAUSED BY FIXED HORIZONTAL GYRO BIAS IS BOUNDED
- ALL FIXED HORIZONTAL SENSOR ERROR EFFECTS CANCEL FOR CLOSED TRAJECTORY TRAVERSAL PERIODS THAT ARE SMALL COMPARED TO THE SCHULER PERIOD (84 MINUTES)
- SCHULER OSCILLATION EFFECTS ACCUMULATE FOR TRAJECTORY TRAVERSAL PERIODS THAT ARE ODD MULTIPLES OF THE 84 MINUTE SCHULER PERIOD



## EFFECT OF CLOSED-COURSE TRAJECTORIES ON FIXED GYRO/ACCELEROMETER ERRORS

The fact that the sensors in a strapdown INS are fixed to aircraft axes can have a pronounced effect on performance when operated along closed-course trajectories. Under such trajectories, the horizontal sensor errors (the projections of the gyro and accelerometer sensor errors onto the horizontal plane) rotate with the flight path direction. For the horizontal errors that are constant in magnitude, the net effect of this error rotation is to bound the growth rate of the errors in the navigation equations.

The bounding effect of closed course trajectories on strapdown INS error build-up is simply a statement of the fact that the integral of a rotating error in navigation axes is oscillatory at the trajectory rotation frequency. From an analytical standpoint, the trajectory path rotation causes the  $C_B^L$  matrix to contain cyclic components such that transformed body axis gyro and accelerometer errors become cyclic in the horizontal plane. Referring to a previous slide "Simplified Strapdown INS Short Term Error Characteristics", the rotating errors are integrated in the Schuler loop into cyclic attitude, velocity, and position errors at the trajectory rotation rate frequency. The equivalent error bounding is not present with gimbale systems because the sensor axes do not turn with the aircraft.

Note, that the vertical axis error effects remain vertical with the same magnitude under a constant turning condition. Hence, vertical errors (such as caused by the vertical component of gyro bias error vector, gyro misalignment, or gyro scale factor error) will produce continually increasing heading errors (heading drift). These errors in turn propagate into North position and velocity errors as described in a previous slide for constant vertical gyro error effects.

Because of the Schuler oscillation dynamic response characteristic of all inertial systems, the response of the strapdown system horizontal errors can have dynamic resonance growth under closed-circuit trajectory conditions where the trajectory period equals the Schuler period. The slide illustrates the effect of such "Schuler pumping" on accelerometer errors. The slide shows the

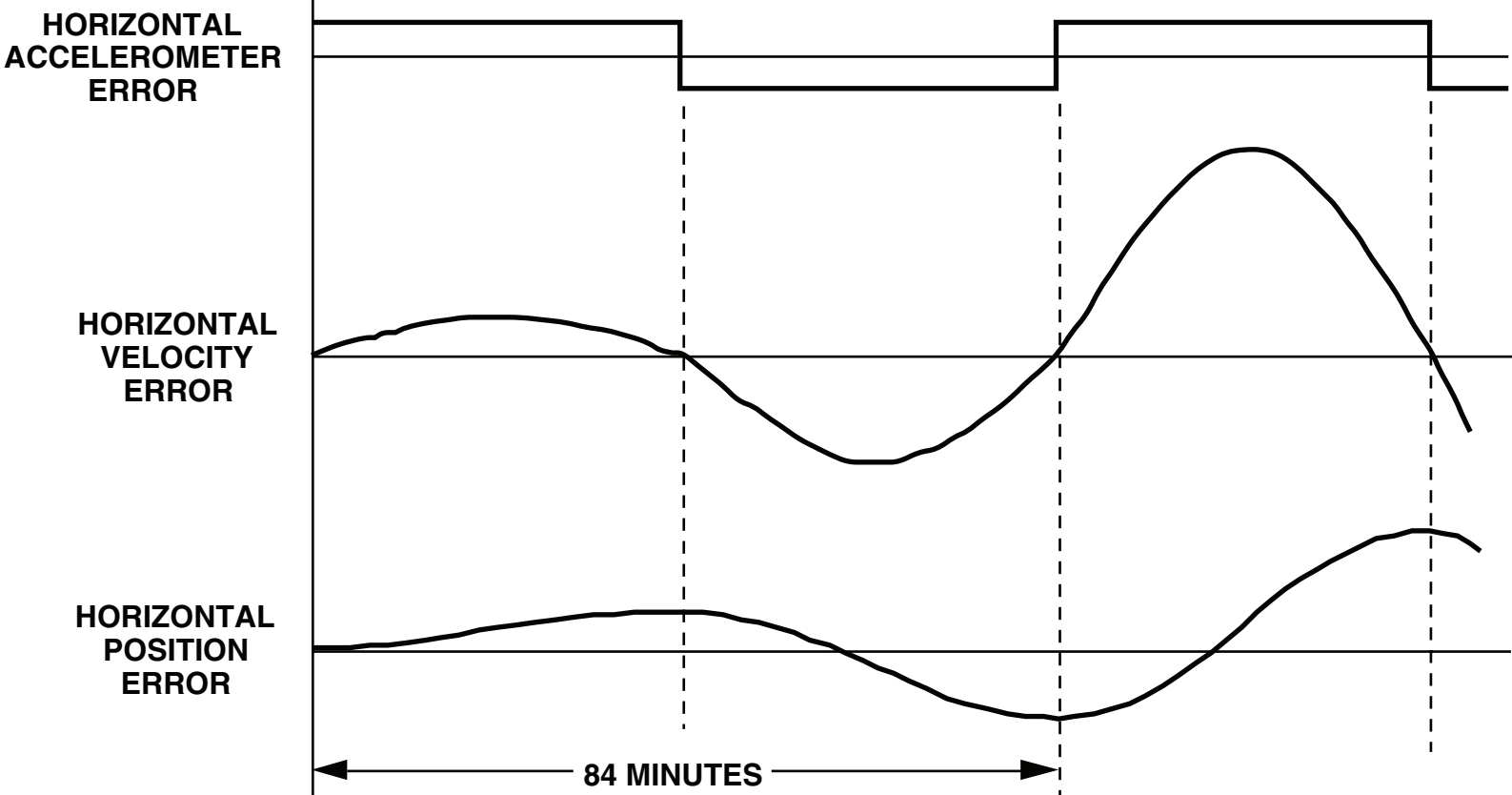
## **EFFECT OF CLOSED-COURSE TRAJECTORIES ON FIXED GYRO/ACCELEROMETER ERRORS (CONTINUED)**

characteristic Schuler sinusoidal velocity error response to accelerometer error on the outbound leg, and the continuation of this sinusoid (dotted) if the outbound leg was to continue. Because the accelerometer error reverses direction on the return leg, another Schuler oscillation is triggered in the opposite direction from the initial oscillation. The new oscillation is initiated at 42 minutes (half a Schuler period) from the first, hence, generates a velocity error that adds in magnitude to the reverse swing of the starting Schuler oscillation. As can be seen from the figure, the resulting velocity error for the second half of the Schuler cycle is three times what its magnitude would have been without the trajectory reversal.

The Schuler pumping effect is a worst case error amplification closed-course trajectory condition for strapdown systems that occurs for 84 minute period trajectories. The effect is not present for trajectory periods that are small compared to the 84 minute Schuler period (such as a typical constant rate of turn aircraft holding pattern).

**NOTES**

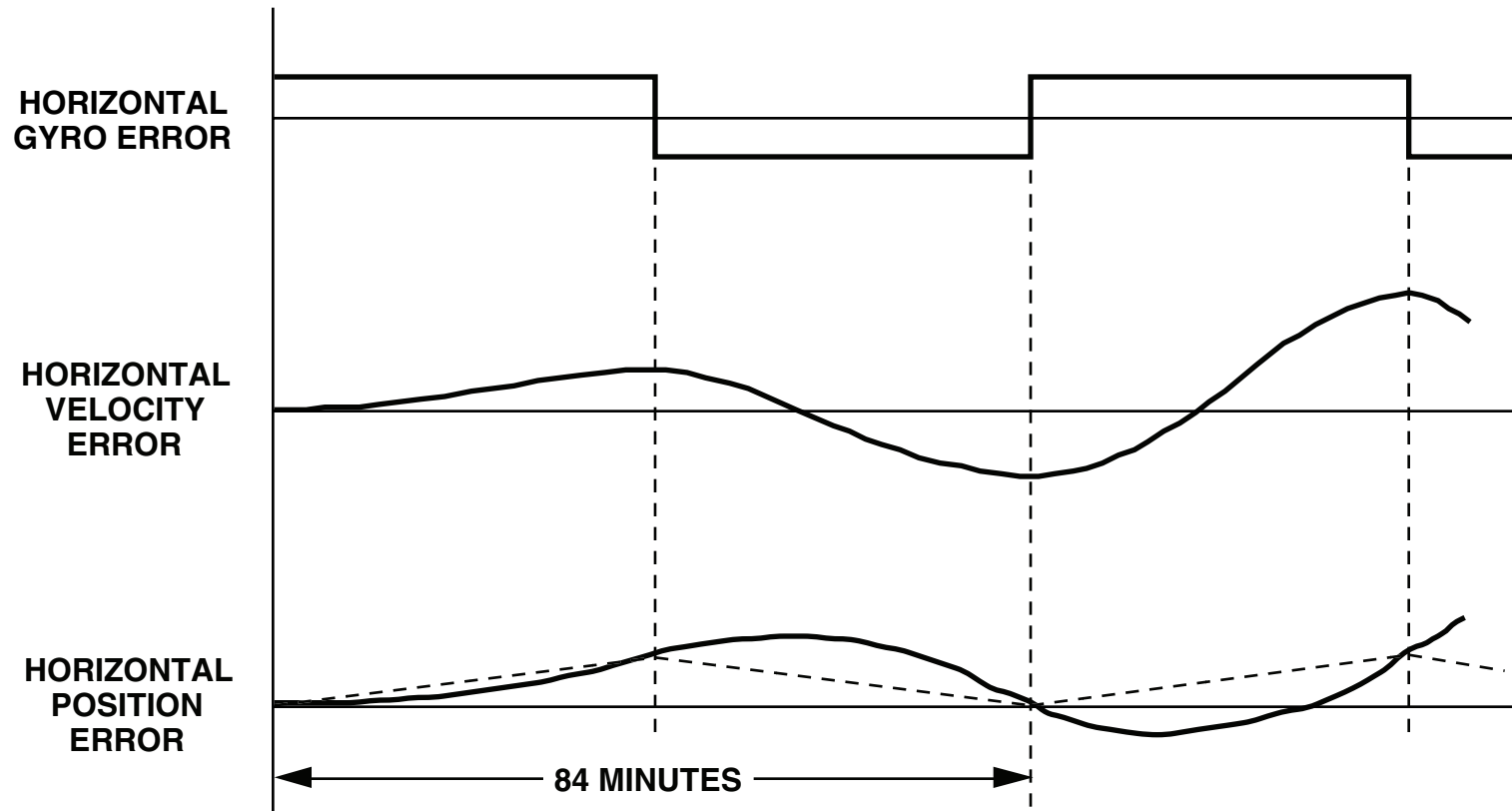
# STRAPDOWN ACCELEROMETER SCHULER PUMPING



## **STRAPDOWN ACCELEROMETER SCHULER PUMPING**

The slide illustrates the effect of continuous Schuler pumping of the accelerometer error in a strapdown INS on both velocity and position performance. Note the increasing unbounded cyclic error amplitude.

# STRAPDOWN GYRO SCHULER PUMPING



## **STRAPDOWN GYRO SCHULER PUMPING**

The slide illustrates the effect of horizontal gyro error Schuler pumping (through closed-course navigation) on strapdown INS horizontal velocity and position error. The slide shows that the average gyro error effect has no systematic offset in velocity or position growth as it would for a constant flight path heading. However, the 84 minute period of the gyro error in horizontal navigation axes excites the Schuler dynamics in the system so that both the position and velocity error are driven into cyclic oscillation at the Schuler frequency with a ramping amplitude.

The dotted lines for the position error indicate the average position error that would be generated from the gyro bias if the Schuler oscillations were somehow suppressed.

## COMPARISON BETWEEN STRAPDOWN AND GIMBALED SENSOR ONE SIGMA PERFORMANCE REQUIREMENTS (1 NM/H 1-2 HOUR INERTIAL NAVIGATOR)

PERFORMANCE PARAMETER	TYPICAL SYSTEM REQUIREMENTS	
	STRAPDOWN	GIMBALED
GYRO INPUT RANGE (DEG/SEC)	400	0.02
GYRO BIAS ACCURACY (DEG/HR)	0.007	0.01
GYRO TURN-ON TRANSIENT (DEG/HR)	0.005	0.005
GYRO SCALE FACTOR ACCURACY (PPM)	5	300
GYRO ALIGNMENT ACCURACY (ARC SEC)	3	60
GYRO RANDOM NOISE (DEG/ $\sqrt{\text{HR}}$ )	0.002*	NEGLIG
ACCELEROMETER INPUT RANGE (G)	15	15
ACCELEROMETER BIAS ACCURACY ( $\mu\text{G}$ )	40	150
ACCELEROMETER BIAS TRENDING IN ALIGNMENT ( $\mu\text{G/SEC}$ )	0.01	0.01
ACCELEROMETER SCALE FACTOR ACCURACY (PPM)	200	200
ACCELEROMETER ALIGNMENT ACCURACY (ARC SEC)	7	60

\* A PRINCIPAL ERROR SOURCE FOR LASER GYROS

## COMPARISON BETWEEN STRAPDOWN AND GIMBALED SENSOR ONE SIGMA PERFORMANCE REQUIREMENTS (1 NM/H 1-2 HOUR INERTIAL NAVIGATOR)

The slide illustrates typical error budgets for the sensors in a strapdown or gimbaled INS with 1 nautical mile per hour accuracy requirements. The largest differences between the two lie in the tighter requirements for the strapdown system in gyro scale factor accuracy, gyro misalignment accuracy, accelerometer bias accuracy, and accelerometer misalignment accuracy. The tighter gyro requirements stem from the body motion in the strapdown system that rotates the gyros through large angles (at high rate). The tighter accelerometer accuracy requirements stem from the inability of the strapdown system to provide the accelerometer error canceling mechanism present in the gimbaled system from initial platform tilt.

Note that the strapdown gyro bias accuracy requirements are also somewhat tighter than for the gimbaled system to reflect the inability to compensate gyro bias errors in the strapdown system through initial platform heading error cancellation of East gyro bias (a natural capability for gimbaled systems). Additionally, laser gyro strapdown systems cannot provide as accurate a calibration of the North component of gyro bias (measured during alignment) as gimbaled systems due to North bias estimation errors generated during alignment from laser gyro random noise.

It is interesting to note that the accelerometer bias trending requirement has generally limited the reaction time of gimbaled systems (time from turn-on to start of navigation) due to the need for a lengthy time prior to engaging the fine alignment mode to allow settling time for thermal turn-on transients around the accelerometers. In gimbaled systems, initial accelerometer turn-on transients are produced by heaters around the sensors (gyros and accelerometers) required to stabilize the thermally sensitive errors at a fixed temperature. The sensor heater requirement in gimbaled systems stems principally from the gyros which have the greater temperature sensitivity, however, to reduce thermal gradients from the gyro heaters, the accelerometers must also be heated. In the case of ring laser gyro strapdown inertial systems, the gyros do not require thermal control because the thermal error sensitivities are small and correctable by temperature measurement and software modeling compensation. To reduce thermal gradients around the gyros, however, the accelerometers must then be operated "heaterless" (i.e., compensated by thermal measurement modeling), a generally more difficult requirement than operating under temperature control.

Finally, it is important to note that the performance figures for the strapdown sensors generally have to be achieved over a longer period of time than for the gimbaled system where onboard recalibration is straightforward using the gimbal assembly as a rotation test platform. Recalibration of a strapdown system generally requires a time consuming removal of the system from the aircraft to a test location where proper test rotation tables are available. Strapdown sensor long term stability requirements are stringent to eliminate the need for scheduled system removals for recalibration purposes.

## TYPICAL STRAPDOWN SENSOR PERFORMANCE REQUIREMENTS

PERFORMANCE PARAMETER	TYPICAL REQUIREMENTS			
	0.1 NMPH INS	1.0 NMPH INS	AHRS	TACTICAL MISSILE MIDCOURSE GUIDANCE
GYRO BIAS ACCURACY (DEG/HR)	0.0007	0.007	1.0 (0.1)* TO 10	1 TO 30
GYRO TURN-ON TRANSIENT (DEG/HR)	0.0005	0.005	0.5 (0.05)* TO 5	2.5 TO 15
GYRO SCALE FACTOR ACCURACY (PPM)	1	5	200	1000
GYRO ALIGNMENT ACCURACY (ARC SEC)	0.7	3	200	300
GYRO RANDOM NOISE (DEG/ $\sqrt{\text{HR}}$ )**	0.0002	0.002	0.01	0.05
ACCELEROMETER BIAS ACCURACY ( $\mu\text{G}$ )	5	40	1000	1000
ACCELEROMETER BIAS TRENDING IN ALIGNMENT ( $\mu\text{G}/\text{SEC}$ )	0.002	0.01	NA (0.1)*	NA
ACCELEROMETER SCALE FACTOR ACCURACY (PPM)	40	200	1000	1000
ACCELEROMETER ALIGNMENT ACCURACY (ARC SEC)	1	7	200	300

\* FOR AHRS WITH EARTH RATE HEADING DETERMINATION REQUIREMENT. OTHER FIGURE SHOWN IS FOR AHRS WITH INERTIAL HEADING SLAVED TO MAGNETIC FLUX HEADING DETECTOR.

\*\* A CHARACTERISTIC PRINCIPALLY OF LASER GYROS.

## **TYPICAL STRAPDOWN SENSOR PERFORMANCE REQUIREMENTS**

The chart compares typical performance characteristics of four types of strapdown inertial navigation systems: a 0.1 nmph accuracy inertial navigation system (INS), a 1.0 nmph INS (such as depicted in the previous chart), a strapdown attitude/heading reference system (AHRS), and a tactical missile midcourse guidance system.

# **LONG TERM INS ERROR PROPAGATION**

## **LONG TERM INS ERROR PROPAGATION**

Thus far, the discussion of errors in strapdown systems has been limited to short term (1-2 hr) applications. For long duration (e.g., 8 to 10 hour) missions, "earth loop" system error characteristics come into play as discussed in the following slides.

## NEW ERROR VARIABLE DEFINITION

$$\widehat{\mathbf{C}}_B^E = \mathbf{C}_L^E [ \mathbf{I} - (\underline{\psi}^L \times) ] \mathbf{C}_B^L \quad \delta \mathbf{C}_B^E = - \mathbf{C}_L^E (\underline{\psi}^L \times) \mathbf{C}_B^L \quad \underline{\psi}^L = \underline{\phi}^L - \underline{e}^L$$

$\underline{\psi}$  = “TELESCOPE POINTING” ANGLE ERROR VECTOR (ANGLE VECTOR BETWEEN COMPUTED AND TRUE BODY FRAMES RELATIVE TO EARTH FRAME)

$\underline{\phi}_H^L$  = HORIZONTAL TILT (SMALL OFFSET PLUS SCHULER OSCILLATIONS)

$\underline{e}_H^L$  = ANGULAR POSITION ERROR (LONG TERM GROWTH PLUS SCHULER OSCILLATIONS)

$\underline{\psi}_H^L = \underline{\phi}_H^L - \underline{e}_H^L \approx$  - AVERAGE LONG TERM ANGULAR POSITION ERROR  
(I.E., WITHOUT SCHULER OSCILLATIONS)

$( )_H$  = HORIZONTAL COMPONENTS OF  $( )$

$\delta \mathbf{R}^L = \mathbf{R} (\mathbf{U}_R^L \times \underline{\psi}_H^L) = \mathbf{R} (\mathbf{U}_R^L \times \underline{\psi}^L) =$  AVERAGE LONG TERM LINEAR POSITION ERROR

$\dot{\underline{\psi}}^L = \underline{\psi}^L \times (\mathbf{W}_{IE}^L + \mathbf{W}_{EL}^L) - \mathbf{C}_B^L \delta \mathbf{W}_{IB}^B \quad \dot{\underline{\psi}}^I = - \delta \mathbf{W}_{IB}^I$
--

## NEW ERROR VARIABLE DEFINITION

In order to analyze the long term (greater than two hours) effects of sensor and initialization errors in strapdown inertial navigation systems, it is convenient to utilize the error angle vector  $\Psi$  defined as the small angle rotation vector associated with the  $C_B^E$  direction cosine matrix (the matrix that transforms vectors from body (B) to earth (E) coordinates axes). The superscript on the vectors in the slide indicates the coordinate frame in which its components are projected. Thus  $\Psi^L$  refers to  $\Psi$  as projected on L-Frame axes.

The slide defines the  $\Psi$  error in terms of the error in the  $C_B^E$  matrix. It can be shown analytically that the  $\Psi$  vector equals the difference between the  $C_B^L$  error angle vector  $\phi$  and the  $C_L^E$  error angle vector  $\underline{e}$ . A previous slide entitled "Error Angles" illustrated the geometrical relationship between  $\Psi$ ,  $\phi$ , and  $\underline{e}$  and pointed out that the  $\Psi$  quantity was a measure of the ability to direct a telescope at a distant star, hence the terminology "telescope pointing" angle for this angle error vector.

From the previous discussion on short term error propagation and Schuler dynamics, it can be shown that the horizontal  $\phi$  error portion (the "platform tilt" angle error) is characterized by cyclic Schuler oscillations plus a small offset. This behavior pattern can be deduced by analysis of the single axis Schuler loop dynamic analysis diagrams presented in earlier slides. The horizontal components of the  $\underline{e}$  vector represents the angular position error of the INS over the earth surface, hence, reflects long term error growth including Schuler oscillations. It can be shown that the Schuler oscillations in the horizontal tilt equal the Schuler oscillations in the angular position error. Therefore, the horizontal components of  $\Psi$  (the difference between the tilt and position angle error) represents the negative of the average position error growth (i.e., the position error with the Schuler oscillations removed). After two Schuler cycles, the magnitude of the average position error is typically much larger than the Schuler position error oscillations. This approximation forms the basis for using the horizontal components of  $\Psi$  as the measure of position angle error for long term error analysis. The corresponding linear horizontal position error  $\delta R$  is obtained from the cross-product of  $\Psi$  with the radial vector from earth center to the vehicle ( $R$  along the unit vector  $\underline{U}_R$  directed upward along the local vertical).

The  $\Psi$  variable is only a function of gyro error and can be calculated by integrating a simple vector differential equation in local level (L) coordinates. The equivalent form of the  $\Psi$  rate equation in inertial (I) coordinates is the even simpler relationship equating the rate of change of  $\Psi$  in I-Frame axes to the negative of the gyro error vector in I-Frame axes. This latter relationship can be used for simplified analysis of long term system position error propagation.

## LONG TERM ERROR PROPAGATION EQUATIONS

$$\dot{\underline{\psi}}^I = -\underline{\delta w}_{IB}^I$$

$$\underline{\delta w}_{IB}^I = C_{G_0}^I C_G^{G_0} C_B^G \underline{\delta w}_{IB}^B$$

$$\underline{\psi}^G = C_{G_0}^G C_I^{G_0} \underline{\psi}^I$$

$$\underline{\psi}_0^I = \underline{\psi}_0^E = C_{G_0}^E \underline{\psi}_0^{G_0}$$

**G = GEOGRAPHIC LOCAL LEVEL COORDINATES (Y-NORTH, X-EAST, Z-UP)**

**G<sub>0</sub> = GEOGRAPHIC COORDINATES AT START OF NAV**

**I, E = AXES COINCIDENT AT START OF NAV**

**$\underline{\psi}_0$  = INITIAL VALUE OF  $\underline{\psi}$  AT START OF NAV**

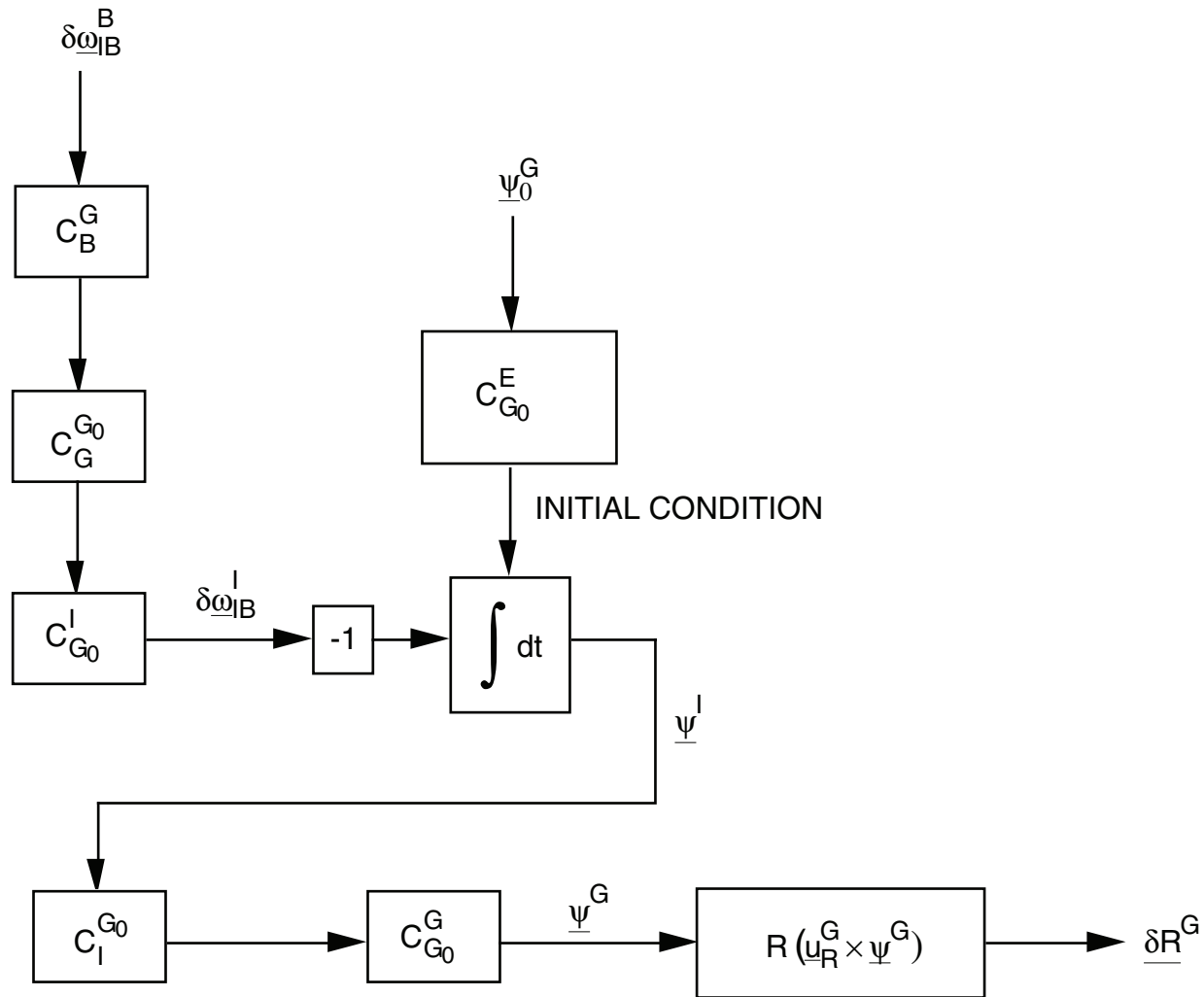
## LONG TERM ERROR PROPAGATION EQUATIONS

The basic I-frame rate equation for  $\underline{\Psi}$  shown on the previous slide is repeated here. The gyro rate error vector in inertial axes input to the  $\underline{\Psi}$  rate equation is obtained from a transformation operation on the body axis angular rate errors (i.e., gyro errors) from body-to-inertial coordinates. The transformation operation is performed as a series of transformations from body-to-geographic local level navigation coordinates, from local geographic-to-initial starting point geographic, and from initial geographic-to-inertial.

The  $\underline{\Psi}$  vector is calculated in I-Frame axes by integrating the indicated I-Frame rate equation. The  $\underline{\Psi}$  vector in local geographic coordinates is the desired output for position error determination (i.e., its cross product with the earth centered radius arm vector equals the North and East components of linear position error). The G-Frame components of  $\underline{\Psi}$  are obtained by transforming  $\underline{\Psi}^I$  from I-to-Go and then from Go-to-G.

The initial value of  $\underline{\Psi}^I$  is obtained by transforming the initial value for  $\underline{\Psi}$  (known in Go coordinates) from the Go to I coordinate frames.

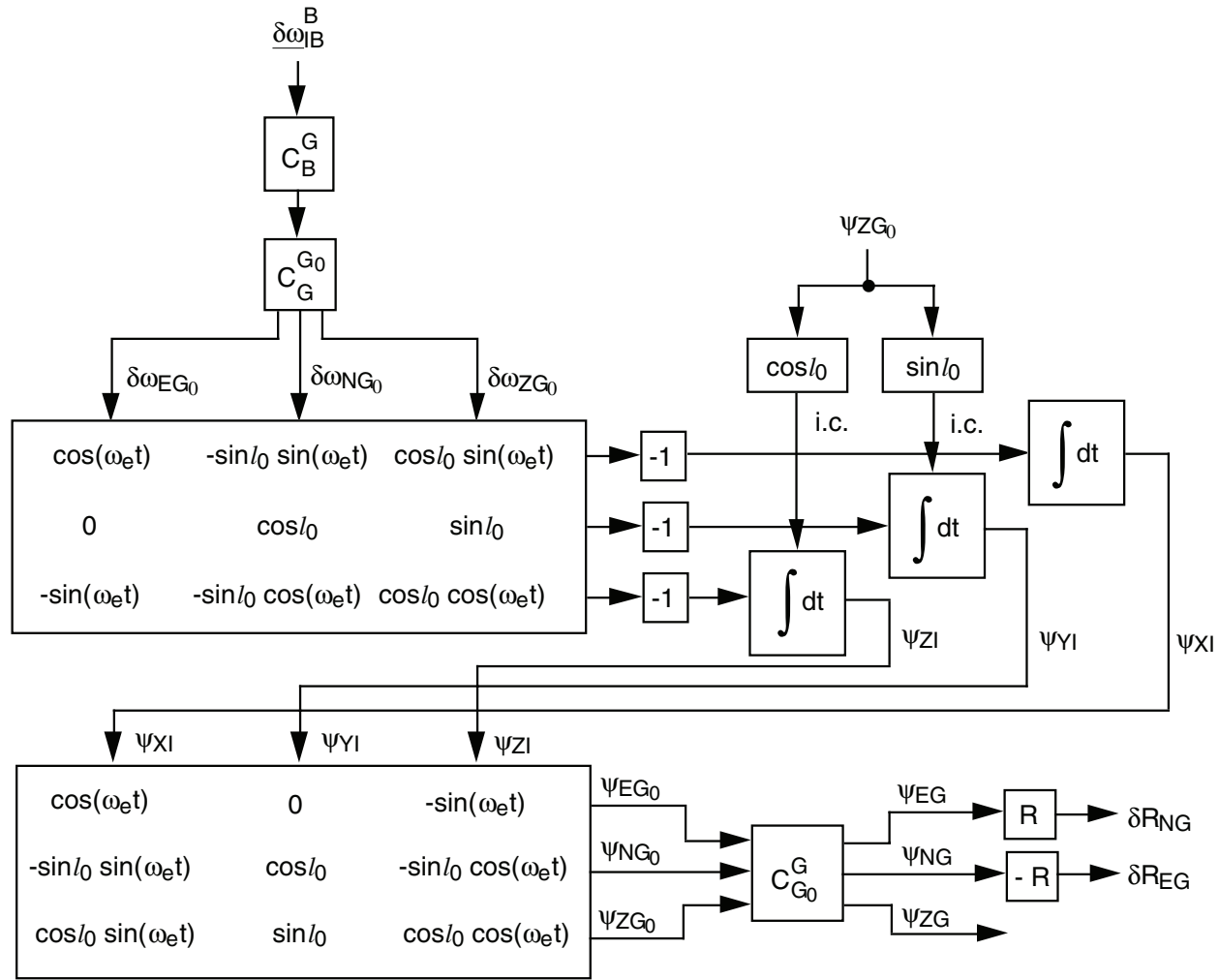
# LONG TERM ERROR PROPAGATION FLOW DIAGRAM



## LONG TERM ERROR PROPAGATION FLOW DIAGRAM

The slide illustrates the implementation of the previous slide equations in block diagram form. The block diagram flow shows the transmission of body axis rate errors (gyro errors) and initial errors in  $\Psi$  (in initial geographic coordinate axes) into horizontal INS position errors in local geographic coordinates. Note the cross-product operation of  $\Psi^G$  with the radius arm vector (discussed earlier) to convert position angle data into the equivalent linear position error  $\delta R^G$  (i.e., with North and East components measured in nautical miles).

# LONG TERM NAVIGATION ERROR MATRIX DIAGRAM



$\omega_e$  = EARTH RATE  
 $l_0$  = INITIAL LATITUDE  
 0 = INITIAL (AT  $t = 0$ ; START OF NAV)

N, E = NORTH, EAST  
 Z = UP

## LONG TERM NAVIGATION ERROR MATRIX DIAGRAM

This slide is a further expansion of the previous block diagram to illustrate the details of the scalar operations involved in the Go-to-I and I-to-Go transformations, the  $\underline{\Psi}$  rate integration, the Go-to-E transformation operation in the initialization function (noted as i.c. or "initial condition" in the slide), and the calculation of North/East position error components from the  $\underline{\Psi}^G$  output components. This diagram can be used directly to infer long term error behavior patterns in cruise inertial navigation systems.

For example, consider the case of a slowly moving vehicle where the G and Go frames are nearly coincident. Then the G-to-Go and Go-to-G transformation matrices are approximately unity. Furthermore, let's assume that the body attitude of the strapdown INS is fixed relative to local geographic axes so that the geographic frame components of fixed gyro bias errors are constant. Under these conditions, the North, East, and Z axis gyro components in the G frame (shown feeding the large Go-to-I matrix in the top of the diagram) are constant. Additionally, the transmission path from the large matrix at the bottom of the diagram to the position errors is constant, and direct. Under these simplified conditions, the following characteristic behavior patterns can be observed.

The long term effect of East gyro bias ( $\delta W_{EG0}$ ) is bounded and characterized by cyclic oscillations at earth's rate (i.e., 24 hour period). This can be observed by noting that the East gyro bias is multiplied by the sine and cosine of the earth rotation angle (earth rate times navigation time t) prior to integration in both the X and Z inertial  $\underline{\Psi}$  channels. The integral of sinusoidal functions are also sinusoidal at the same frequency (earth rate). The projection of the X, Z integrator outputs into horizontal position error (through the bottom matrix) is an algebraic function of earth rotation angle during navigation and of system latitude.

The North and Vertical (Z) gyro bias terms produce similar earth rate oscillation effects in the North/East position error channels. In addition, both the North and Vertical gyro biases produce an unbounded linear error build-up in the East position error channel. This latter effect can be observed by noting that the North and Vertical (Z) gyro biases are multiplied by constant sine and cosine latitude terms, and integrated in the Y Inertial-axis integrator. A constant integrator output ramp results for constant gyro bias. The ramping integrator output is then scaled by a cosine latitude constant (in the lower matrix) to form the East position error which then also appears as an unbounded ramp. The ramp behavior is not present in the North position error channel.

The figure illustrates that initial heading errors (as manifested in  $\psi_{ZG0}$ ) produce bounded oscillations at the earth rate frequency. Note, from a short term standpoint, that a sinusoid at earth frequency looks like a ramp. This is equivalent to the ramp position error response predicted in the previous short term analysis for initial heading errors. Similar equivalencies can be drawn

## LONG TERM NAVIGATOR ERROR MATRIX DIAGRAM (CONTINUED)

between the predicted short term position error ramp response to gyro bias effects and the ramp or earth rate frequency sinusoidal response predicted from the accompanying diagram based on long term analysis. Note also that the parabolic position response to vertical gyro bias predicted by short term analysis is actually a bounded one minus cosine earth angle effect based on the accompanying slide with a peak at 12 hours.

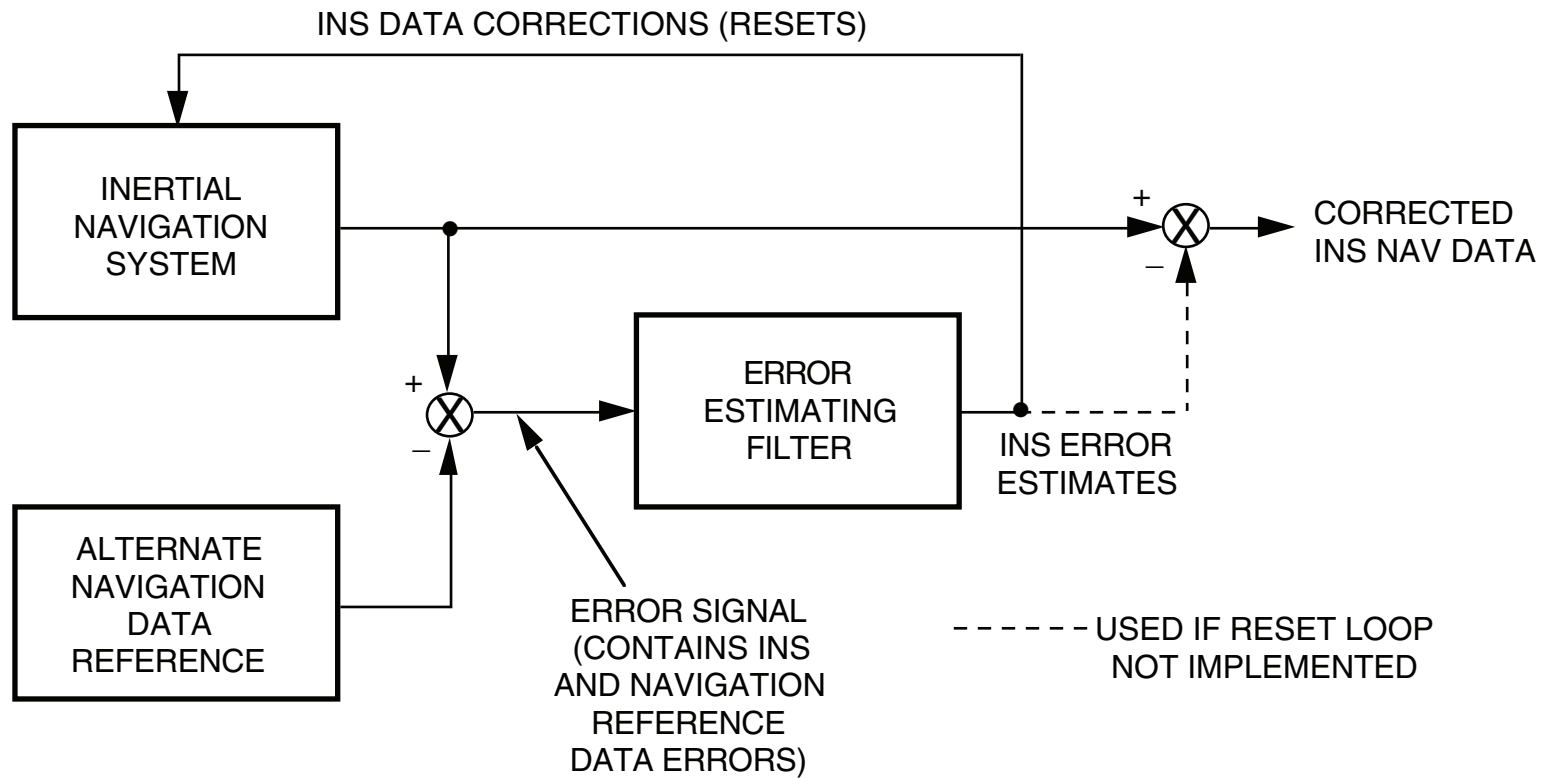
One important point should be noted from the above discussion. A significant portion of the error effects in inertial systems that appear to be unbounded on a short term basis, are actually bounded when long term earth loop effects are taken into consideration. This has the effect of attenuating the net position error growth for inertial systems under long term flights, lowering the average position error rate for these longer flight profiles compared to the average position error rates during shorter one to two hour flights. This factor can have an important bearing on flight test planning to evaluate INS performance and in the structuring of INS performance specifications based on mission duration.

**NOTES**

**NOTES**

# **AIDED INERTIAL SYSTEMS**

# BASIC INERTIAL AIDING CONCEPT



## **BASIC INERTIAL AIDING CONCEPT**

The slide illustrates the fundamental method for improving inertial navigation system accuracy through aiding with another source of navigation data on the aircraft.

The technique, known as inertial aiding, calculates a measure of INS error by comparing the INS output data with comparable information obtained from the alternate source of navigation data (identified as the "reference" in the slide). The calculated error signal would be zero if both the INS and reference were perfect. Imperfections in either the INS or reference generate an error signal composed of both INS and navigation reference errors.

The error signal is used as an input to an error estimating filter (such as a Kalman filter) which calculates estimates for the INS errors based on the error signal characteristics. The calculated INS error is then used to either correct the INS output data, or correct (reset) the INS errors within the INS itself. The result is a corrected INS navigation output with higher accuracy than would have been obtainable from the basic free inertial (unaided) INS.

## **USES FOR INERTIAL AIDING**

- **IMPROVED INS POSITIONING ACCURACY**
- **SUPPRESS INS SCHULER OSCILLATIONS**
- **IMPROVED NAVIGATION REFERENCE SIGNAL QUALITY (E.G., BANDWIDTH, LOW NOISE)**
- **IMPROVED NAVIGATION OUTPUT COVERAGE**
- **MOVING BASE ALIGNMENT**
- **GENERAL REDUNDANT NAVIGATION DATA BLENDING**

## USES FOR INERTIAL AIDING

Inertial aiding is used in general, to improve the overall accuracy capability of a stand alone INS. Depending on system requirements, accuracy enhancement can take on several forms. The most basic, is improved positioning accuracy. For military applications where high accuracy velocity data is required for weapon delivery, inertial aiding is used to suppress INS Schuler oscillations (which can produce substantial velocity errors even though net position error oscillations are tolerable).

From an overall navigation system accuracy standpoint, inertial aiding can be used to improve the overall signal quality of navigational information available. For example, a blended high accuracy navigation signal can be obtained that has the wide bandwidth, low noise characteristics of an INS, and the long term positioning accuracy stability of a radio navigation aid (for example) but without the noise and filter lags that might be present on the navigational position/velocity data derived directly from the radio data. Additionally, because the reference data may not have full time coverage (due to black-out periods over areas on the earth where data, such as VOR/DME, is not available), the INS provides the autonomous capability to provide continuous unaided coverage, when the aid is unavailable.

A classical use for inertial aiding is the implementation of the INS initial alignment function on a moving base. In this situation, the reference data provided from the aid is used for comparison with the INS to assess alignment accuracy. The error signal forms the basis for erecting the INS attitude and heading reference to alignment with earth reference axes (e.g., local level and North). The moving base alignment capability is required on Navy military aircraft where the INS is aligned on a moving carrier deck, or for alignments of the INS in air (due, for example, to inadequate time to align on the ground before takeoff, or due to a temporary loss of power in the air which causes a temporary INS shut-down).

Finally, the basic inertial aiding implementation concept provides a general mechanism for integrating redundant sources of navigation data in a moving vehicle. If designed properly, the aiding logic can also provide an implicit redundancy management function that isolates failed navigational outputs in the presence of subsystem failures by blending the data from all available operating navigation devices.

## **EXAMPLES OF AIDED INERTIAL SYSTEMS**

- **DOPPLER/INERTIAL**
- **STELLAR/INERTIAL**
- **RADIO/INERTIAL (E.G., LORAN, VOR/DME)**
- **GPS/INERTIAL**
- **SINS/INERTIAL AT-SEA ALIGNMENT**

## EXAMPLES OF AIDED INERTIAL SYSTEMS

Commonly used inertial aiding system configurations are listed in the slide.

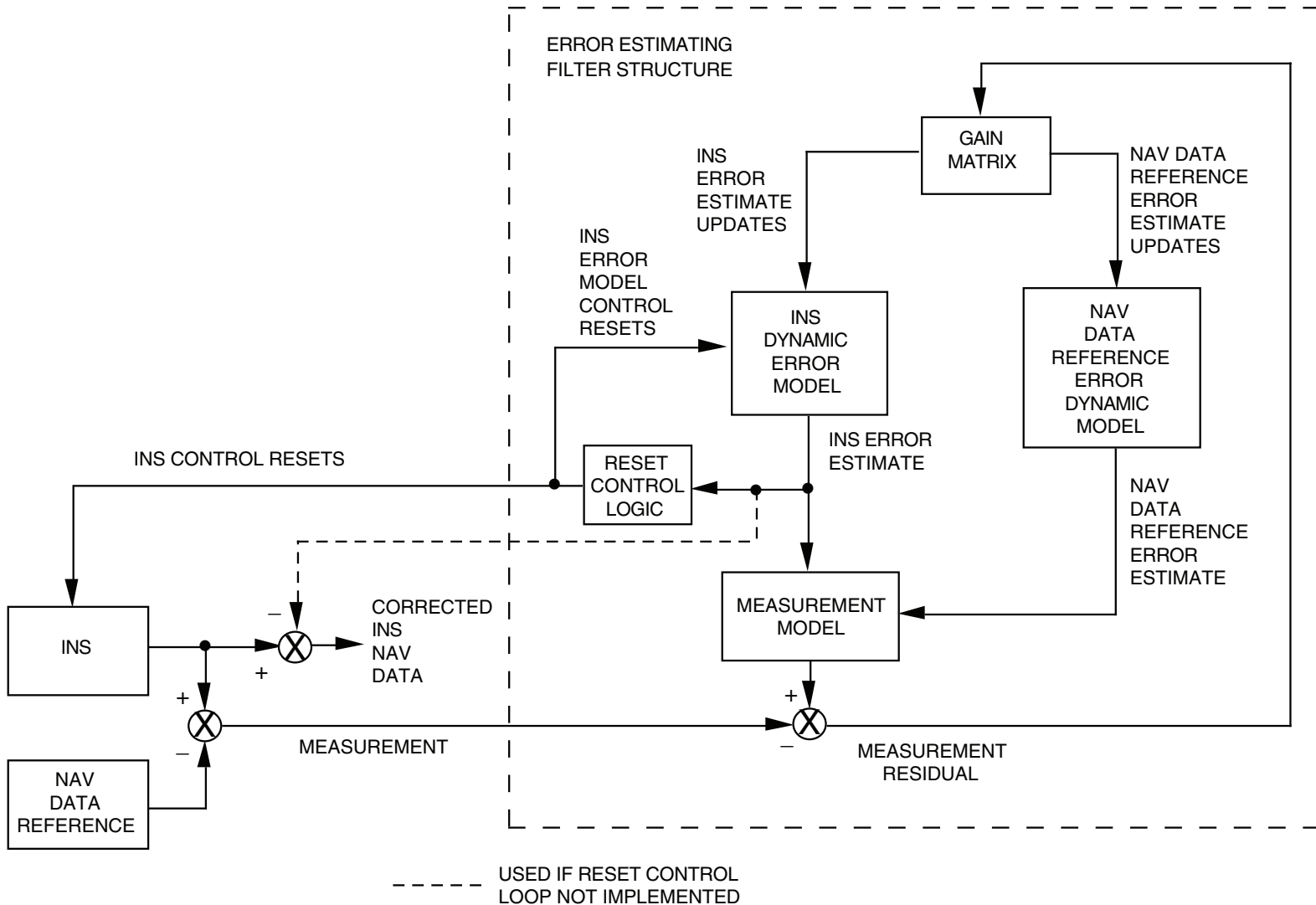
The Doppler/Inertial concept uses Doppler radar ground velocity data for the navigation reference, typically for in-air alignment and to suppress INS Schuler oscillations. The Stellar/Inertial concept uses a star tracker to obtain attitude updates to the INS based on the measured angle from the INS attitude reference to selected stars with known inertial position (via a star catalog). The stellar update compensates for inertial attitude drift caused by gyro error.

Several ground based radio navigation position references have been utilized (e.g., Loran, VOR/DME) for INS aiding based on measurements of electromagnetic signals emitted from ground based transmitters with known position coordinates. Range to the transmitters is generally calculated (with Loran or DME-Distance Measuring Equipment) based on the measurement of transit time from the ground transmitter(s) to the user receiver. Range measurements to several transmitters at favorable relative angular geometry are required to enable an accurate position fix. In the case of the VOR signal (VHF Omnidirectional Range) the bearing to the transmitter is also calculated from the angle data on the VOR transmission signal which is coded to the angular position of a rotating element in the VOR transmitting antenna. When used for INS aiding, the radio aid bounds the long term drift of the INS, and the INS provides wide bandwidth, low noise, continuous navigation output data that may be deficient in the radio aid alone.

GPS (Global Positioning System) is a satellite based navigation system developed by the US Air Force that provides high accuracy reference data (position and velocity) for both military and nonmilitary users equipped with GPS receivers. The GPS concept is based on measurement of receive time and frequency of user received electromagnetic signals emitted from GPS navigation satellites. Knowledge of the satellite ephemeris and signal transmission times (provided on the GPS data transmission) allows the receive time measurements to be translated into signal transit time from each satellite, range to each satellite, position relative to the satellites, and finally, position relative to the earth. Velocity is calculated from the change in position or from the Doppler frequency shift measured on each satellite transmission signal. Three satellites at sufficient angular geometry relative to the user receiver allow for an unambiguous position fix. A fourth satellite measurement is required to also calibrate the user receiver reference clock to the satellite clocks to enable accurate transit time measurements (user received time minus satellite transmission time). Use of GPS as an inertial aiding device will enable INS moving base alignments, provide bounding of INS error build-up, and also provide GPS receiver antenna pointing and frequency tuning based on computed range rate, hence, Doppler shift to each satellite. The latter technique allows more effective GPS operation in dynamic jamming environments.

A classical use of inertial aiding has been the alignment of an aircraft INS on a moving Navy aircraft carrier using the ship's INS (SINS) for reference position and velocity data. The position data is used to initialize the INS position information; the velocity (and attitude) data is used to effect aircraft INS tilt/heading alignment in the presence of dynamic carrier deck motion.

# INERTIAL AIDING USING ERROR MODEL FEEDBACK



## INERTIAL AIDING USING ERROR MODEL FEEDBACK

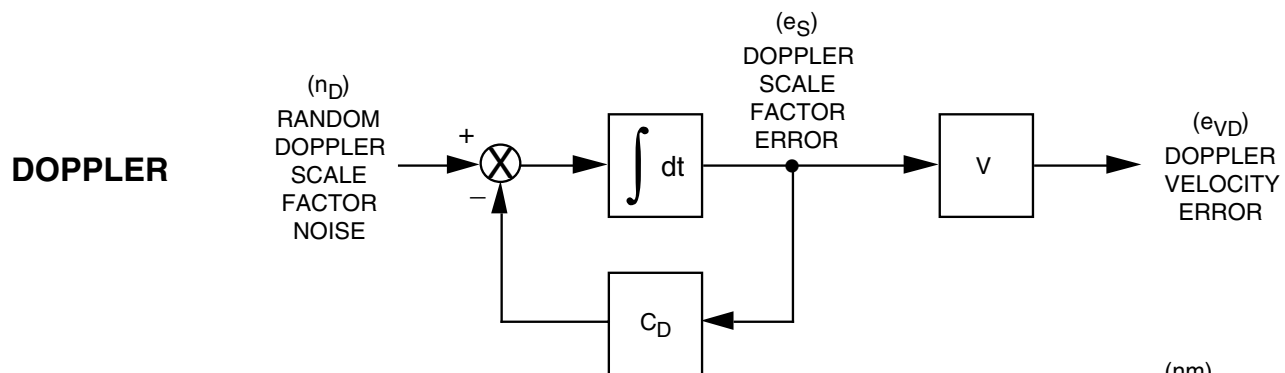
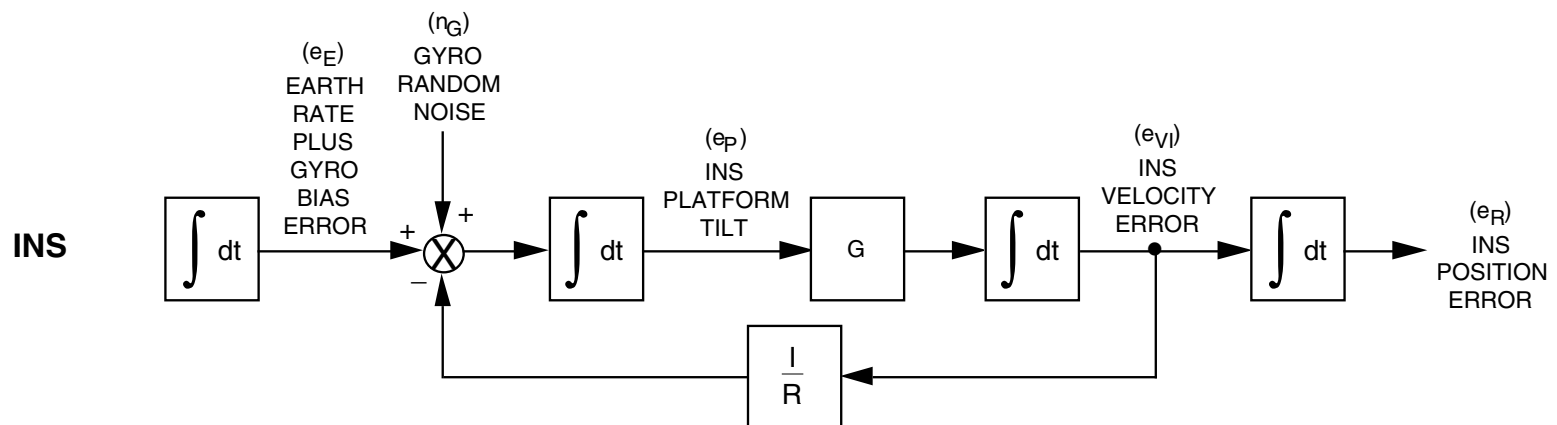
The slide illustrates a typical structure of an inertial aiding estimation filter based on error model feedback. This is the structure used to implement a classical Kalman filter in performing the aiding function.

As can be seen in the slide, the difference between the INS and Navigation Data Reference (called the "measurement") is the input to the filter. This signal is compared with a dynamic model of the measurement generated analytically within the digital computer implementing the filter. The Measurement Model is generated from dynamic error models of the INS and Navigation Data Reference whose dynamic characteristics simulate the error behavior patterns of these navigation data sources. The dynamic error models generate continuous estimates of estimated INS and Navigation Data Reference errors.

The INS and Navigation Data Reference error models are recursively updated in the filter based on the difference between the actual measurement and the measurement model. The difference, called the "measurement residual", is used through a set of appropriate gains to develop the error model updates. In this closed-loop manner the error models are updated until the measurement residual remains at a stationary low noise minimum. Under these conditions, the system error estimates being generated by the error models are accurate representations of the actual system errors. They, therefore, can be used as corrections to the basic INS data.

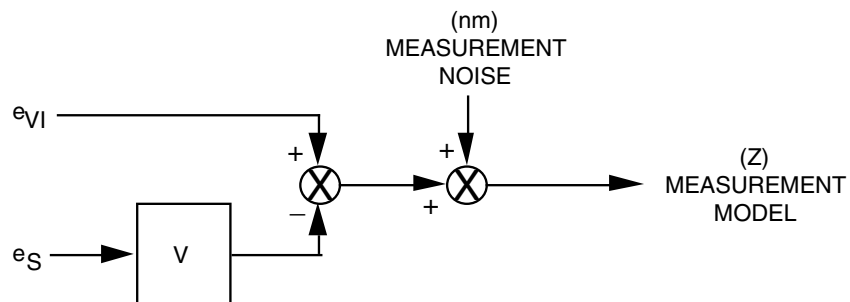
The INS output data correction operation can be accomplished by altering the INS output data directly (shown dotted). Alternatively, the error estimates can be used to reset the data in the INS so that the error is eliminated. Note, that if the actual INS error is reset in this manner, the INS dynamic error model must also be reset in the same manner to maintain a correct knowledge of the estimated error state in the actual INS. The use of the filter estimates to reset the INS data is known as the "control" function.

# EXAMPLE OF SIMPLIFIED ERROR MODELS



**MEASUREMENT**

$$\begin{aligned} \text{MEASUREMENT } Z &= \text{INS VELOCITY } (V_I) \\ &\quad - \text{DOPPLER VELOCITY } (V_D) \\ &= V + e_{vI} - (V + e_{vD}) \\ &= e_{vI} - e_{vD} = e_{vI} - V e_S \end{aligned}$$



## EXAMPLE OF SIMPLIFIED ERROR MODELS

An example of the form of the error models used in an error model feedback filter is illustrated in the slide. As can be seen, the error models are nothing more than a dynamically integrated set of linear differential equations that approximate the system error behavior.

The form of the INS error model is similar to the simplified forms we have used previously for error analysis purposes. A simplified error model is shown for a Doppler radar aid. Similarly, a simplified measurement model is shown.

The error models in the figure are shown with random noise input elements. For the error models used in the error model feedback filter (see previous slide), the noise terms are not included because they are random, unknown, hence, unpredictable (unmodelable). The noise terms are included in the model on this slide to set the stage for further developments, when we will consider the basis for selecting the feedback gains for the filter error estimate updating process. As we shall see, the gains are a function of the statistical properties of the noise propagated through the error model equations.

One further point should be noted. The "error estimate update" operation referred to in the previous slide is nothing more than updates to the error model integrators shown in this slide. The integrators are updated by adding the error estimate update signals calculated in the feedback gain path to the previous values for the integrators.

## SIMPLIFIED MODEL IN ERROR STATE VECTOR FORMAT

$$\underline{X} = (e_E, e_P, e_{V_I}, e_{R_I}, e_S)^T = \text{ERROR STATE VECTOR}$$

$$\dot{e}_E = 0$$

$$\dot{e}_P = e_E - \frac{1}{R} e_{V_I} + n_G$$

$$\vdots \quad \quad \quad \vdots \quad \quad \quad \vdots$$

$$\dot{\underline{X}} = \underline{A} \underline{X} + \underline{n} \quad \text{ERROR STATE DYNAMIC EQUATION}$$

$\underline{A}$  = ERROR STATE DYNAMIC MATRIX

$\underline{n}$  = PROCESS NOISE VECTOR

$$z_1 = e_{V_I} - V e_S + n_M$$

$$\vdots \quad \quad \quad \vdots \quad \quad \quad \vdots$$

$$\underline{Z} = \underline{H} \underline{X} + \underline{v} \quad \text{MEASUREMENT EQUATION}$$

$\underline{Z}$  = MEASUREMENT VECTOR

$\underline{H}$  = MEASUREMENT MATRIX

$\underline{v}$  = MEASUREMENT NOISE VECTOR

## SIMPLIFIED MODEL IN ERROR STATE VECTOR FORMAT

To simplify the mathematics associated with error model feedback filters, a more compact "state vector" notation is adopted. The slide illustrates how the particular error model illustrated in the previous slide can be formatted in "state vector" notation.

The "error state vector" ( $\underline{X}$ ) is defined as a column matrix formed by all the error elements (or error "states") in the total filter error model (i.e., the INS and Reference Data error states). The error state dynamic equation is a linear differential equation for the rate of change of the error state vector. The error state dynamic equation shown is an elegant concise form of the dynamic relations expressed on the previous slide for the Doppler and INS errors.

As seen in the slide, the error state dynamic equation equates the rate of change of the error state vector ( $\dot{\underline{X}}$ ) to the product of an "error state dynamic matrix" ( $A$ ) with  $\underline{X}$  plus a "process noise source vector" ( $\underline{n}$ ). The process noise vector is the vector collection of the noise terms feeding the error state states.

The measurement model of the previous slide can also be written in a more generalized form called the "measurement equation" as shown in this slide. The measurement equation equates a general measurement vector  $\underline{Z}$  to the product of a "measurement matrix"  $H$  with the error state vector  $\underline{X}$  plus a "measurement noise vector"  $\underline{v}$ . For the simplified model on the previous slide,  $\underline{Z}$  has only one component. In the more general case (e.g., where the horizontal errors in the direction orthogonal to those in the previous slide are also modeled),  $\underline{Z}$  would have more than one component.

# GENERALIZED ERROR STATE VECTOR FORM OF SIMPLIFIED MODEL

$$\underline{X} = (e_E, e_p, e_{VI}, e_R, e_S)^T = \text{ERROR STATE VECTOR}$$

$$A = \begin{bmatrix} 0 & 0 & 0 & 0 & 0 \\ 1 & 0 & -\frac{1}{R} & 0 & 0 \\ 0 & g & 0 & 0 & 0 \\ 0 & 0 & 1 & 0 & 0 \\ 0 & 0 & 0 & 0 & -C_D \end{bmatrix} = \text{ERROR STATE DYNAMIC MATRIX}$$

$$\underline{n} = (0, n_G, 0, 0, n_D)^T = \text{ERROR STATE UNCORRELATED PROCESS NOISE SOURCE VECTOR}$$

$$G_p = \text{IDENTITY (FOR EXAMPLE PROBLEM)} = \text{PROCESS NOISE DYNAMIC COUPLING MATRIX}$$

$$\dot{\underline{X}} = A \underline{X} + G_p \underline{n} = \text{ERROR STATE DYNAMIC EQUATION}$$

$$H = (0, 0, 1, 0, -V) = \text{MEASUREMENT MATRIX}$$

$$\underline{v} = (n_M) = \text{UNCORRELATED MEASUREMENT NOISE SOURCE VECTOR}$$

$$G_M = \text{IDENTITY (FOR EXAMPLE PROBLEM)} = \text{MEASUREMENT NOISE DYNAMIC COUPLING MATRIX}$$

$$\underline{Z} = H \underline{X} + G_M \underline{v} = \text{MEASUREMENT EQUATION}$$

## GENERALIZED ERROR STATE VECTOR FORM OF SIMPLIFIED MODEL

This chart further generalizes on the error state vector formulation in the previous chart to define vector equations that are suitable for a broad class of system applications.

In this chart  $\underline{n}$  is the "process noise source vector" defined to be uncorrelated (between vector components). It is coupled into the error state dynamic equation by a "process noise dynamic coupling matrix" ( $G_P$ ). Correlation between process noise source elements is handled through the  $G_P$  matrix. The error state dynamic matrix  $A$  and  $\underline{n}$  vector components are shown in this slide for the INS/Doppler error models of the previous slides. For the INS/Doppler sample problem, the  $G_P$  matrix is identity. In the more general case,  $G_P$  could have off-diagonal terms (if the same noise source feeds more than one error state). The general form shown for the error state dynamic equation can be used for any linear system error model.

In this chart  $\underline{v}$  is the "measurement noise source vector" defined to be uncorrelated (between vector components). It is coupled into the measurement equation by a "measurement noise dynamic coupling matrix" ( $G_M$ ). Correlation between measurement noise source elements is handled through the  $G_M$  matrix. The measurement matrix  $H$  and  $\underline{v}$  vector components are shown in this slide for the INS/Doppler error models of the previous slides. For the INS/Doppler sample problem, the  $G_M$  matrix is identity. In the more general case,  $G_M$  could have off-diagonal terms (if the same noise source feeds more than one measurement component). The general form shown for the measurement equation can be used for any linear system error model.

# DISCRETE ERROR PROPAGATION FORM

## CONTINUOUS FORM

$$\dot{\underline{X}} = \underline{A} \underline{X} + \underline{G}_p \underline{n}$$

$$\underline{Z} = \underline{H} \underline{X} + \underline{G}_M \underline{v}$$

## DISCRETE FORM

$$\underline{X}_n = \underline{F}_n \underline{X}_{n-1} + \underline{W}_n$$

$$\underline{Z}_n = \underline{H}_n \underline{X}_n + \underline{G}_{M_n} \underline{v}_n$$

$n$  = COMPUTER CYCLE FOR AIDING FILTER

$\underline{F}_n$  = ERROR STATE TRANSITION MATRIX (RELATED TO  $\underline{A}$ )

$\underline{W}_n$  = RANDOM VECTOR REPRESENTING INTEGRATED  
EFFECT OF  $\underline{G}_p \underline{n}$  OVER COMPUTER CYCLE

## DISCRETE ERROR PROPAGATION FORM

At this point it is important to recognize that the error model feedback filter will be implemented in a digital computer using a finite computation cycle rate. Hence, the implementation of continuous differential error model dynamic equations must be accomplished by the equivalent incremental discrete form of these equations.

The slide depicts the equivalent discrete form of the error state dynamic equation that defines the value of the error state vector  $\underline{X}$  for the  $n^{\text{th}}$  computer cycle as a function of  $\underline{X}$  at the past computer cycle time plus the integrated effect of the coupled process noise over the computer cycle. The discrete equation expressing this relationship equates  $\underline{X}_n$  (the value of  $\underline{X}$  at the  $n^{\text{th}}$  computer cycle) to the product of an error state transition matrix  $F_n$  with the past computer cycle value of  $\underline{X}$  plus a random vector  $\underline{W}$  representing the integrated effect of  $G_p \underline{n}$  over the computer cycle. The  $F_n$  matrix is directly related to  $A$ .

The discrete form of the error model propagation equation is the form actually implemented in the digital computer used for the error model filter mechanization. Note that a discrete measurement equation is also shown to indicate that measurements are made at each computer cycle.

## RELATIONSHIP BETWEEN DISCRETE AND CONTINUOUS PARAMETERS

$$F(t, t_{n-1}) = \int_{t_{n-1}}^t A F(\tau, t_{n-1}) d\tau$$

$$F(t_{n-1}, t_{n-1}) = I \quad \text{AT START OF COMPUTER CYCLE}$$

$$F_n = F(t_n, t_{n-1})$$

$$\underline{W}_n = \int_{t_{n-1}}^{t_n} F(t_n, \tau) G_p \underline{n} d\tau$$

$F(t_B, t_A)$  = ERROR STATE TRANSITION MATRIX THAT PROPAGATES  
ERROR STATE VECTOR FROM TIME  $t_A$  TO TIME  $t_B$

## RELATIONSHIP BETWEEN DISCRETE AND CONTINUOUS PARAMETERS

The slide depicts the analytical relationship between the continuous error model parameters and discrete error model parameters.

As can be seen, the error state transition matrix equals the integral over the computer cycle of the product of the error state dynamic matrix ( $A$ ) with the evolving error state transition matrix ( $F$ ), starting with the identity matrix as an initial condition. The discrete random error vector  $\underline{W}$  input to the discrete state vector error propagation equation each computer cycle equals the weighted integral (using  $F$  as the weighting factor) of the coupled process noise vector ( $G_p \underline{n}$ ) over the computer cycle.

## NOMENCLATURE

X, Z = ACTUAL SYSTEM ERRORS AND THE ACTUAL MEASUREMENT

\* \*  
X, Z = FILTER ESTIMATE FOR X, Z

\* \*  
X ( - ) = X IMMEDIATELY PRIOR TO ESTIMATE UPDATE (A PRIORI)

\* \*  
X ( + ) = X IMMEDIATELY AFTER ESTIMATE UPDATE (A POSTERIORI)

## NOMENCLATURE

We will now delve into the basic updating process equations used in the filter which determine updates to the filter estimate for  $\underline{X}$  based on the measurement residual. During the development to follow, the nomenclature shown in the slide will be adopted to distinguish between actual values for the error state vector  $\underline{X}$  and measurement  $\underline{Z}$ , the filter estimate for these quantities (designated with an asterisk superscript), values for  $\underline{X}$  immediately prior to applying an update (designated with a (-)), and values for  $\underline{X}$  immediately following an update (designated with a (+)).

## DISCRETE ERROR FORM INCLUDING CONTROL RESETS AND ERROR ESTIMATE UPDATES

### ACTUAL

$$\underline{X}_n = F_n (\underline{X}_{n-1} + \underline{U}_{n-1}) + \underline{W}_n$$

$$\underline{Z}_n = H_n \underline{X}_n + G_{M_n} \underline{v}_n$$

### FILTER

$$\overset{*}{\underline{X}}_n(-) = F_n (\overset{*}{\underline{X}}_{n-1}(+) + \underline{U}_{n-1})$$

$$\underline{Z}_n = H_n \overset{*}{\underline{X}}_n(-)$$

$$\overset{*}{\underline{X}}_n(+) = \overset{*}{\underline{X}}_n(-) + K_n (\underline{Z}_n - \overset{*}{\underline{Z}}_n)$$

U = CONTROL RESET VECTOR

$K_n$  = ERROR ESTIMATE UPDATE GAIN MATRIX

## DISCRETE ERROR FORM INCLUDING CONTROL RESETS AND ERROR ESTIMATE UPDATES

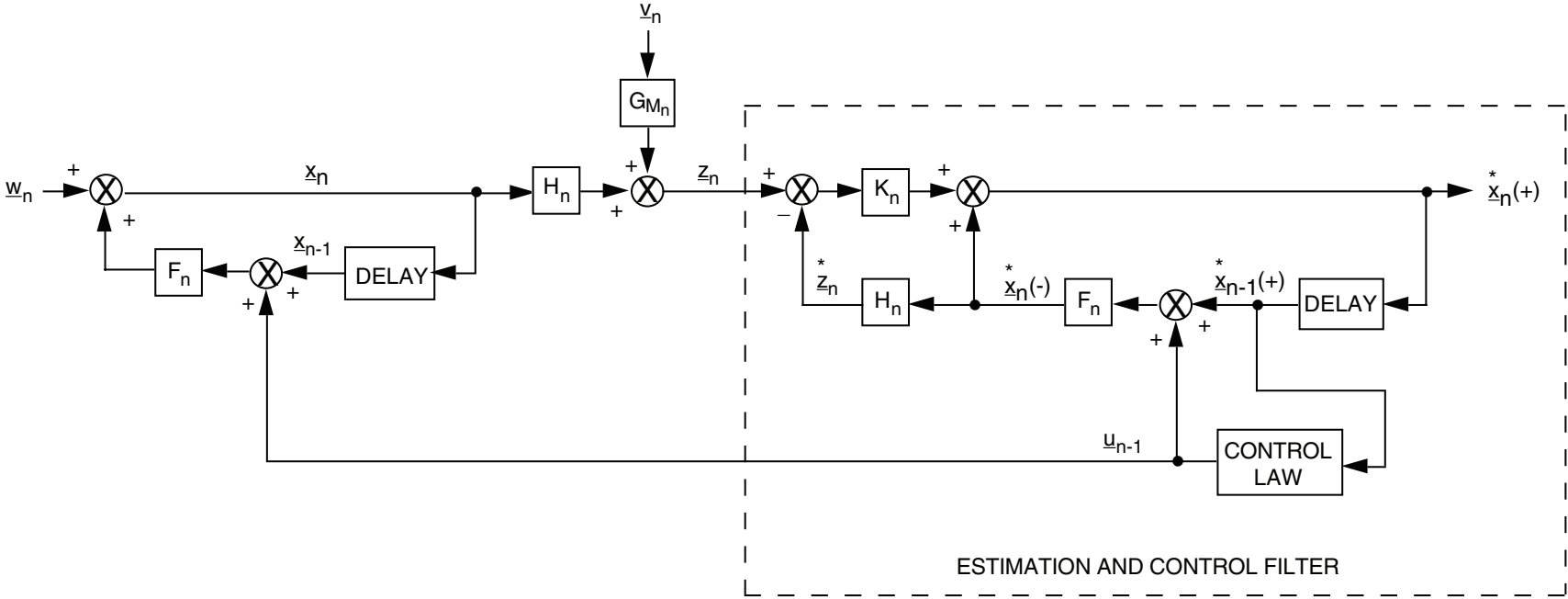
At this point we begin to distinguish between the error model mechanized in the filter and the actual error model.

The discrete form of the actual error model is shown at the top of the slide. This is identical to the forms shown previously except that a control vector  $\underline{U}_{n-1}$  has been added to the error state propagation equation. The  $\underline{U}_{n-1}$  vector represents the controls or updates applied to  $\underline{X}_{n-1}$  at the previous computer cycle from the filter (see previous slide entitled "Inertial Aiding Using Error Model Feedback"). The  $\underline{U}_{n-1}$  vector is calculated based on the filter estimate for  $\underline{X}$  as will be discussed in a subsequent slide.

The filter implements an equation to estimate the propagation of  $\underline{X}$  except that the  $\underline{W}$  random term is excluded because it is unknown. Additionally, the filter implements the  $K_n$  feedback update of the  $\underline{X}$  estimate for  $\underline{X}$  based on the error in the comparison between the actual and filter estimates for the measurement  $\underline{Z}$  (see previous slide entitled "Inertial Aiding Using Error Model Feedback"). The equation used to estimate the measurement  $\underline{Z}$  is identical in form to the actual measurement equation except that the measurement noise term is excluded because it is unknown.

The  $K_n$  matrix updating operation is the mechanism that corrects the filter  $\underline{X}$  estimate for the unpredictable effects of  $\underline{W}$  in the actual  $\underline{X}$  propagation, and for the error in the actual  $\underline{Z}$  measurement caused by  $G_M \underline{v}$  measurement noise. Additionally,  $K_n$  performs the initial filter transient function for generating an  $\underline{X}$  estimate that will track the effect of actual  $\underline{X}$  initial conditions. Since the filter has no way of knowing what to set for the correct initial value for  $\underline{X}$ , it assumes  $\underline{X}$  is initially zero. The  $K_n$  gain matrix must correct for this initialization error.

# GENERALIZED DISCRETE AIDING FILTER STRUCTURE



## GENERALIZED DISCRETE AIDING FILTER STRUCTURE

The diagram presents the equations of the previous slide in block form. The figure clearly illustrates the similarity between the filter model of the system errors, and the method for using the measurement residual (the difference between the real and estimated measurement  $\underline{Z}$ ) to correct the filter error state estimate (through the filter gain matrix  $K_n$ ).

## OPTIMAL GAIN DETERMINATION

- BASED ON MINIMIZING THE VARIANCE OF  $\hat{X}^*$  ERRORS AFTER EACH UPDATE
- COMPUTED FROM KNOWLEDGE OF  $\hat{X}^*$  ERROR STATISTICS AND MEASUREMENT ERROR STATISTICS
- KALMAN FILTER APPROACH

## OPTIMAL GAIN DETERMINATION

Thus far we have tentatively assumed that a gain matrix is available in the filter that will enable the filter to generate accurate estimates of the actual error state vector. In fact, a particular optimum gain matrix exists that can be calculated in the filter each computer cycle.

The optimal gain is defined as the gain matrix that at each filter cycle minimizes the variance of the error in each element of the estimated error state vector. This optimal gain matrix can be calculated from a knowledge of the error state vector process noise and measurement noise statistics. A filter structured with such an optimal gain matrix (based on the minimum error variance) is known as a Kalman filter.

## ESTIMATION ERROR COVARIANCE

$$\underline{\Delta X} = \underline{X}^{\Delta} - \underline{X}^* = \text{ERROR IN } \underline{X}^{\Delta} \text{ (ESTIMATION ERROR)}$$

$$P = E(\underline{\Delta X} \underline{\Delta X}^T) = \text{ESTIMATION ERROR COVARIANCE MATRIX}$$

$$E(\ ) = \text{EXPECTED VALUE OF BRACKETED QUANTITY}$$

FOR:  $\underline{X} = (X_1, X_2, X_3, \dots \dots)^T$

$$P = \begin{bmatrix} E(\Delta X_1^2) & E(\Delta X_1 \Delta X_2) & E(\Delta X_1 \Delta X_3) & \dots \dots \\ E(\Delta X_2 \Delta X_1) & E(\Delta X_2^2) & E(\Delta X_2 \Delta X_3) & \dots \dots \\ E(\Delta X_3 \Delta X_1) & E(\Delta X_3 \Delta X_2) & E(\Delta X_3^2) & \dots \dots \\ \vdots & \vdots & \vdots & \vdots \end{bmatrix}$$

## ESTIMATION ERROR COVARIANCE

The "estimation error" is defined to equal the difference between the filter estimated value for the error state vector and the actual value for the error state vector. The statistical parameters used to characterize the estimation error are the elements of the estimation error "covariance matrix". The slide defines the error covariance to equal the expected value of the product of the estimation error vector with its transpose. The optimal Kalman filter gain is based, in part, on the error covariance which must be calculated as an integral part of the optimal gain computation process.

Some of the characteristics of the covariance matrix ( $P$ ) are that it is symmetric (element in row  $i$ , column  $j$  equals element in row  $j$ , column  $i$ ), each diagonal element is positive, and the matrix is positive definite. The positive definite characteristic of  $P$  is mathematically defined as the requirement that the operator  $\underline{V}^T P \underline{V}$  be greater than zero for all real  $\underline{V}$  where  $\underline{V}$  is an arbitrary vector (Note: If the latter operator is less than zero for any  $\underline{V}$ , then  $P$  is said to be negative definite). The positive definite requirement embodies the positive diagonal element requirement as well as the requirement that  $P_{ij}^2$  be less than  $P_{ii} P_{jj}$  (where  $P_{ij}$  is the element of  $P$  in row  $i$ , column  $j$ ). As part of Kalman filter software background computations involved in the calculation of  $P$ , control algorithms are frequently utilized to preserve the positive definite characteristic of  $P$  in the presence of numerical roundoff which could drive  $P$  to be negative definite. Negative definite values for  $P$  can produce instabilities in the Kalman filter which utilizes  $P$  as a basic building block in the Kalman estimation process.

## ESTIMATION ERROR AND COVARIANCE PROPAGATION

$$\underline{X}_n^*(-) = F_n (\underline{X}_{n-1}^*(+) + \underline{U}_{n-1})$$

$$\underline{X}_n = F_n (\underline{X}_{n-1} + \underline{U}_{n-1}) + \underline{W}_n$$

$$\Delta \underline{X}_n(-) = F_n \Delta \underline{X}_{n-1}(+) - \underline{W}_n \quad \text{ESTIMATION ERROR PROPAGATION}$$

$$P_n(-) = F_n P_{n-1}(+) F_n^T + Q_n \quad \text{COVARIANCE PROPAGATION}$$

$$Q_n \stackrel{\Delta}{=} E(\underline{W}_n \underline{W}_n^T) = \text{INTEGRATED PROCESS NOISE MATRIX}$$

$$Q_n \approx \frac{1}{2} (Q_{0n} + F_n Q_{0n} F_n^T) T_{K_n} \quad \text{SECOND ORDER APPROXIMATION}$$

$$Q_{0n} = G_{P_n} Q_{PDN_n} G_{P_n}^T$$

$Q_{PDN}$  = UNCORRELATED (DIAGONAL) PROCESS NOISE DENSITY  
MATRIX ASSOCIATED WITH THE EXPECTED VALUE OF  $\underline{n} \underline{n}^T$

$T_K$  = KALMAN FILTER CYCLE TIME

## ESTIMATION ERROR AND COVARIANCE PROPAGATION

The estimation error covariance is calculated in the Kalman filter (for optimal gain determination) through an error propagation equation which represents the statistical form of the estimation error vector dynamic propagation.

The slide develops the discrete propagation equation for the estimation error (first boxed equation) as the difference between the discrete propagation equations for the filter estimated and actual error state vectors. The  $\underline{\Delta X}$  estimation error has been defined in the previous slide.

The discrete propagation equation for the  $\underline{\Delta X}$  covariance matrix  $P$  (second boxed equation) is the statistical equivalent of the estimation error propagation equation shown (for  $\underline{\Delta X}$ ). The  $Q$  "integrated process noise matrix" driving the  $P$  equation equals the covariance of the random error vector  $\underline{W}$  that drives the  $\underline{\Delta X}$  equation. The slide also shows a second order approximation for calculating  $Q$  from the uncorrelated process noise density matrix (the diagonal matrix associated with the expected value of  $\underline{n} \underline{n}^T$  whose elements equal the densities of each element of  $\underline{n}$ ).

The  $P$  covariance propagation equation in the slide is implemented in the Kalman filter as part of the process for maintaining knowledge of  $P$  so that it may be used for the optimal gain calculation.

## ESTIMATION ERROR AND COVARIANCE CORRECTIONS

$$\underline{X}_n^*(+) = \underline{X}_n^*(-) + K_n (\underline{Z}_n - \underline{Z}_n^*)$$

$$\underline{Z}_n = H_n \underline{X}_n + G_M \underline{v}_n$$

$$\underline{Z}_n^* = H_n \underline{X}_n^*(-)$$

$$\Delta \underline{X}_n = \underline{X}_n - \underline{X}_n^*$$

$$\Delta \underline{X}_n(+) = (I - K_n H_n) \Delta \underline{X}_n(-) + K_n G_M \underline{v}_n \quad \text{ESTIMATION ERROR CORRECTIONS (UPDATE)}$$

$$P_n(+) = (I - K_n H_n) P_n(-) (I - K_n H_n)^T + K_n R_n K_n^T \quad \text{COVARIANCE UPDATE}$$

$$R_n = G_{M_n} R_{0_n} G_{M_n}^T = \text{MEASUREMENT NOISE MATRIX}$$

$$R_{0_n} = E(\underline{v}_n \underline{v}_n^T) = \text{UNCORRELATED (DIAGONAL) MEASUREMENT NOISE SOURCE MATRIX}$$

## ESTIMATION ERROR AND COVARIANCE CORRECTIONS

In addition to the "open-loop" propagation of the error state covariance described in the previous slide, the covariance matrix is also modified as a result of the Kalman estimate updating process. This effect must be included in the calculation of the covariance matrix in the Kalman filter so that it reflects both the propagation and updates of the real world (and filter model) error state vector.

The slide develops the equation for the estimation error after the Kalman update ( $\underline{\Delta X}(+)$ ) (first boxed equation) as a function of the estimation error before the update ( $\underline{\Delta X}(-)$ ), the Kalman gain matrix  $\mathbf{K}$ , the measurement matrix  $\mathbf{H}$ , and the coupled measurement noise  $\mathbf{G}_M \underline{v}$ . This expression is obtained from the basic filter error state estimate update equation (repeated at the top

\*

of the page), by subtracting  $\underline{X}_n$  from both sides, substituting for the  $\underline{Z}_n$  and  $\underline{Z}_n$  measurements as given, and introducing the definition for  $\underline{\Delta X}_n$ . Note that because the error estimate update process only affects the filter states, the value for the real world error state vector  $\underline{X}$  is the same before and after the Kalman update (which occurs instantaneously).

The slide also shows (second boxed equation) the equivalent error covariance update form of the estimation error update equation. The covariance update equation is a function of the error covariance before the update, the Kalman gain matrix, the measurement matrix, and a "measurement noise matrix". The measurement noise matrix is calculated from an uncorrelated (diagonal) "measurement noise source matrix"  $\mathbf{R}_0$  (equal to the covariance of the measurement noise vector  $\underline{v}$ ) translated into the measurement matrix by the measurement noise dynamic coupling matrix  $\mathbf{G}_M$ . Each element of the  $\mathbf{R}_0$  matrix equals the variance of the corresponding element in  $\underline{v}$ .

The covariance update equation together with the covariance propagation equation must be implemented as an integral part of the Kalman filter to maintain a running knowledge of the estimation error covariance. The estimation error covariance is then used at each Kalman update cycle to calculate the optimal Kalman gain matrix for the filter update operation.

## KALMAN GAIN

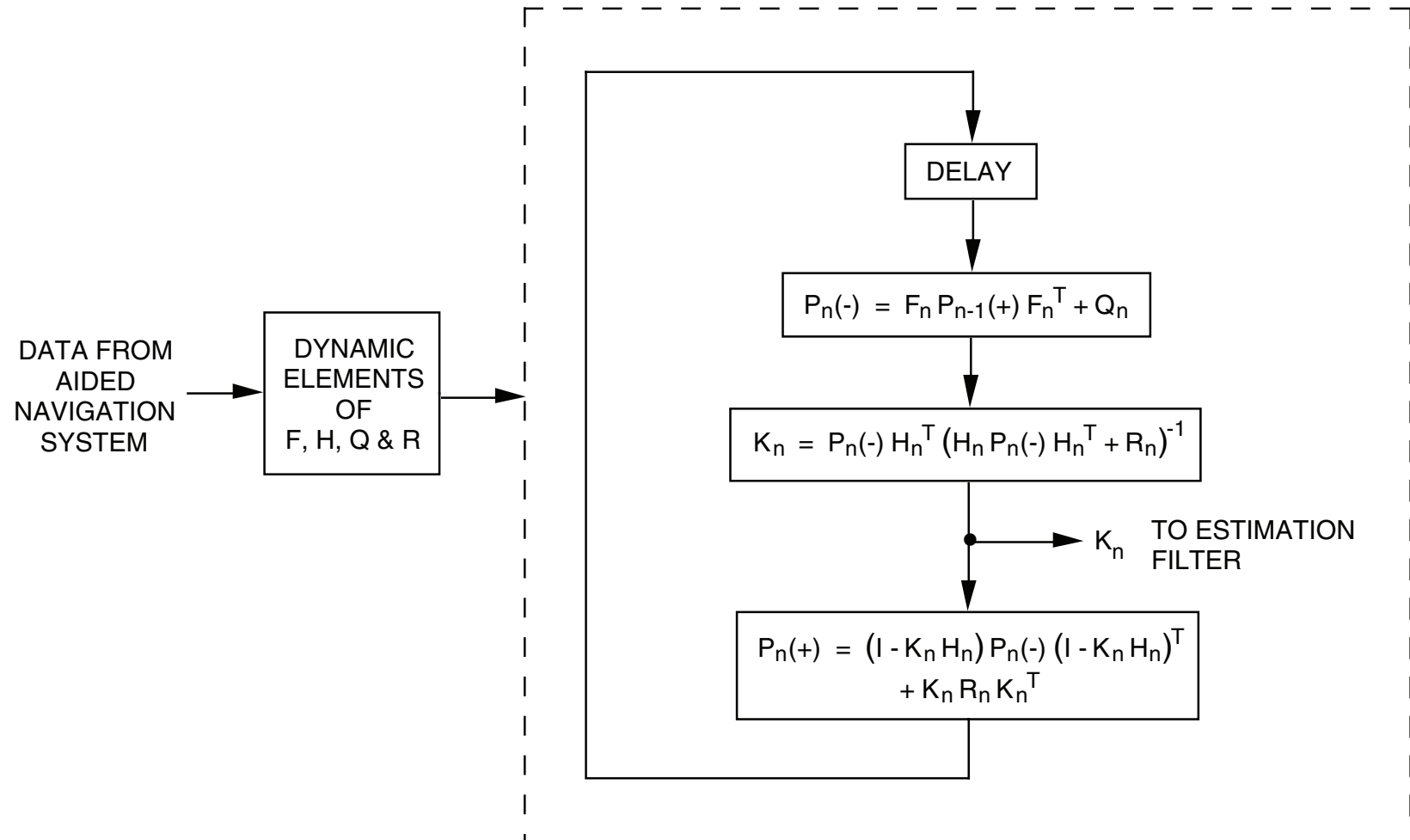
**KALMAN (OR OPTIMAL) GAIN IS GAIN THAT MINIMIZES  
DIAGONAL ELEMENTS OF P AFTER EACH UPDATE**

$$K_n = P_n(-) H_n^T [H_n P_n(-) H_n^T + R_n]^{-1}$$

## KALMAN GAIN

The Kalman gain equation is presented in the slide. As shown, the Kalman gain is the gain that minimizes the estimation error element variances (i.e., the diagonal elements of  $P$ ) after each filter update cycle. This gain matrix optimizes filter performance because it results in a minimum error at each time point in the filter estimate for the error state vector. Hence, use of the estimated error state vector to correct the actual system data provides an optimum correction (in a minimum variance sense).

# OPTIMAL GAIN DETERMINATION



## OPTIMAL GAIN DETERMINATION

The computation flow in the slide summarizes the operations required in the Kalman filter to compute the Kalman gain matrix.

Three steps are involved in each computer cycle: covariance propagation, gain calculation, and covariance update. The dynamic elements in the F, H, Q and R matrices are calculated as functions of the data provided in the aided navigation system computer.

The operations shown in the chart is an integration process for the covariance matrix which requires an initialization at the first computer cycle. The initial value used for P is based on an understanding of the expected variances of the actual error state vector at the start of filter operations (i.e., since  $\underline{X}$  equals zero at filter initiation,  $\Delta \underline{X}$  equals  $\underline{X}$ , hence, initial P equals the initial covariance in  $\underline{X}$ ).

## SIMPLIFIED COVARIANCE UPDATING BASED ON OPTIMAL GAIN

### GENERAL (JOSEPH'S) FORM

$$P_n(+)= (I - K_n H_n) P_n(-) (I - K_n H_n)^T + K_n R_n K_n^T$$

### OPTIMAL GAIN EQUATION

$$K_n = P_n(-) H_n^T [H_n P_n(-) H_n^T + R_n]^{-1}$$

### SIMPLIFIED FORM ASSUMING USE OF OPTIMAL GAIN

$$P_n(+)= (I - K_n H_n) P_n(-)$$

## SIMPLIFIED COVARIANCE UPDATING BASED ON OPTIMAL GAIN

The covariance updating equation shown previously was a general form that is valid for any filter gain matrix, not only the optimal gain. This form is known as the "Joseph's form".

If the optimal gain is to be used, the form of the covariance updating equation used in the filter can be simplified. The slide shows the "simplified form" based on use of the optimal gain. The simplified form is derived from the general Joseph's form by substitution of the optimal gain expression.

It is important to note that if the optimum gain matrix is not explicitly utilized, use of the simplified form (which is based on use of the optimal gain) could lead to covariance computation loop instabilities. An example of a commonly encountered situation where the gain matrix is not optimal is the "considered variable approach" where the gain matrix is calculated optimally, but then elements for selected states are set to zero to reflect uncertainties in the error model for these states. In this case, the zeroing of the selected element gains makes the gain matrix suboptimal, and the full Joseph's form must be utilized for covariance updating.

An important performance characteristic associated with the Joseph's form is that it has less of a tendency to produce numerical instabilities (due to computer roundoff error driving the covariance matrix toward negative definiteness) than the simplified form. For this reason, and to retain flexibility for possible design changes to a suboptimal gain matrix configuration during the development process, the Joseph's form for the covariance update is sometimes selected over the simplified form (assuming the additional computational burden for the Joseph's form is acceptable), even if the optimal gain matrix is initially intended to be utilized for the Kalman filter.

## IDEAL KALMAN FILTER CONTROL RESET FORMULATION

- IDEAL CONTROL RESET:  $\underline{U}_{n-1} = -\underline{X}_{n-1}^*$  APPLIED AT (n-1)

### SYSTEM

$$\begin{aligned}\underline{X}_n(-) &= F_n [\underline{X}_{n-1}(+) + \underline{U}_{n-1}] + \underline{W}_n \\ &= F_n [\underline{X}_{n-1}(+) - \underline{X}_{n-1}^*] + \underline{W}_n \\ &= -F_n \underline{\Delta X}_{n-1}(+) + \underline{W}_n = -\underline{\Delta X}_n(-)\end{aligned}$$

### FILTER

$$\begin{aligned}\underline{X}_n(-) &= F_n [\underline{X}_{n-1}^* + \underline{U}_{n-1}] \\ &= 0\end{aligned}$$

- IMPLIED COMPUTATIONS
  - MAKE MEASUREMENT AT (n-1)
  - COMPUTE KALMAN GAIN FOR (n-1)
    - > COMPUTE STATE TRANSITION BASED ON DATA TAKEN FROM (n-2) TO (n-1)
    - > UPDATE COVARIANCE USING COMPUTED STATE TRANSITION MATRIX
    - > CALCULATE KALMAN GAIN WITH COVARIANCE
  - UPDATE ERROR STATE ESTIMATE AT (n-1) USING MEASUREMENT AND KALMAN GAIN
  - CALCULATE AND APPLY CONTROL RESET AT (n-1) BASED ON UPDATED ERROR STATE ESTIMATE
- PROBLEM FOR REAL-TIME FILTERS
  - CANNOT MAKE CALCULATION INSTANTANEOUSLY AND CANNOT STOP TIME

## IDEAL KALMAN FILTER CONTROL RESET FORMULATION

Let us now discuss the process of applying control resets to the error state vector to correct the system errors based on the Kalman filter estimates for the error states. The slide illustrates an idealized reset ( $\underline{U}$ ) as equal to the negative of the estimate for  $\underline{X}$ . As can be seen in the slide, application of such a control reset will null the estimate for the error state vector in the Kalman filter. From an information theory standpoint, application of this control to the real system will correct its error within the uncertainty of the optimum estimation process (assuming it is based on a Kalman gain formulation).

The slide shows the effect of applying the control to the real world. As can be seen, the effect of the reset is to reduce the "real-world" error state to equal the error in the Kalman filter state vector estimate (compare the expression shown with the expression for  $\Delta\underline{X}$  on a previous slide entitled "Covariance and Estimation Error Propagation").

The control reset formulation shown is listed as "ideal" for two reasons. First, it may not be possible to apply controls to all error states, because some of them may represent phenomena outside of the INS that affect the measurement but cannot be physically controlled. The actual control vector in such a case would equal a control matrix  $L$  times the idealized  $\underline{U}$  control vector shown such that the  $L\underline{U}$  product equals the negative of the estimated errors in the INS (i.e.,  $L$  would consist of a unity matrix for the controllable INS states and zero for the noncontrollable states). The second reason the indicated reset concept is ideal entails the practicalities of actually performing the required operations within the confines of a real-time flight computer.

The basic assumption in the reset equation shown is that the reset will be applied at the  $(n-1)$  filter cycle time based on data measurements at  $(n-1)$  and a host of complex calculations. The slide illustrates the calculations required for computing the Kalman gain (at  $(n-1)$ ), updating the error state estimate (at  $(n-1)$ ), then calculating and applying the indicated controls at  $(n-1)$ . The point in the slide is that a finite time period is required in a real-time computer to perform this multiplicity of operations, hence, they cannot be performed instantaneously as implied by the idealized control equation shown.

## REAL-TIME KALMAN FILTER DELAYED CONTROL RESET FORMULATION

- CALCULATE CONTROL BASED ON IDEAL APPLICATION
- APPLY CONTROL ONE CYCLE LATER – ALLOWS ONE CYCLE TO COMPUTE CONTROL

$$\underline{U}_{n-1} = -\underline{\dot{X}}_{n-1}^*(+)$$

BUT APPLY AT n

### SYSTEM

$$\begin{aligned} \underline{X}_n(-) &= \underline{U}_{n-1} + F_n \underline{X}_{n-1}(+) + \underline{W}_n \\ &= F_n \underline{X}_{n-1}(+) - \underline{\dot{X}}_{n-1}^*(+) + \underline{W}_n \\ &= F_n \underline{X}_{n-1}(+) + F_n \left[ \underline{\dot{X}}_{n-1}^*(+) - \underline{\dot{X}}_{n-1}(+) \right] - \underline{\dot{X}}_{n-1}(+) + \underline{W}_n \\ &= (F_n - I) \underline{\dot{X}}_{n-1}(+) + F_n \left[ \underline{X}_{n-1}(+) - \underline{\dot{X}}_{n-1}(+) \right] + \underline{W}_n \\ &= (F_n - I) \underline{\dot{X}}_{n-1}(+) - F_n \underline{\Delta X}_{n-1}(+) + \underline{W}_n \\ &= (F_n - I) \underline{\dot{X}}_{n-1}(+) - \underline{\Delta X}_n(-) \end{aligned}$$

### FILTER

$$\begin{aligned} \underline{\dot{X}}_n^*(-) &= \underline{U}_{n-1} + F_n \underline{\dot{X}}_{n-1}^*(+) \\ &= F_n \underline{\dot{X}}_{n-1}^*(+) - \underline{\dot{X}}_{n-1}^*(+) \\ &= (F_n - I) \underline{\dot{X}}_{n-1}^*(+) \end{aligned}$$

## REAL-TIME KALMAN FILTER DELAYED CONTROL RESET FORMULATION

A commonly used method for accommodating the real-time computer computational time delay in the Kalman filter control reset process, is through use of "delayed control resets". With this formulation, the controls are applied one filter cycle late. This allows the time length of a complete filter cycle to perform the calculations listed on the previous slide in computing the control vector. The slide illustrates the impact of the delayed control reset on overall performance in the real-world and in the filter world.

If this slide is compared to the previous slide, it can be seen that the delayed reset leaves a residual error in the error state vector equal to the product of the error state at the previous update with an  $(F-I)$  matrix. Because the state transition matrix  $F$  is close to unity, the  $(F-I)$  matrix is generally small, and has little impact on overall closed-loop performance compared to what would be theoretically possible using the idealized resets.

## **SUBOPTIMAL KALMAN FILTERS**

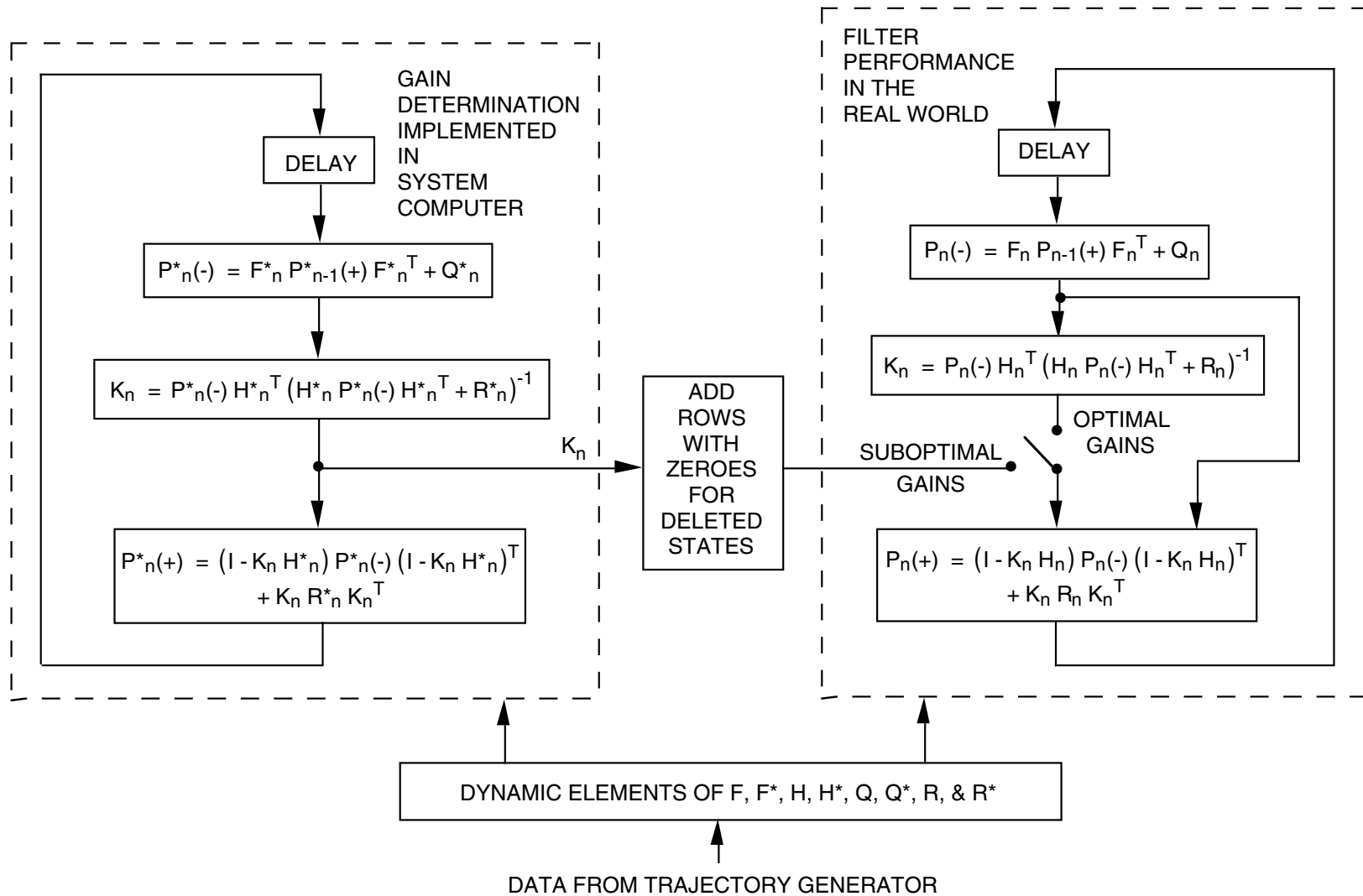
- **GAIN DETERMINATION BASED ON SIMPLIFIED ERROR STATE MODEL (e.g., REDUCED NUMBER STATES)**
  - **REDUCED PROGRAM MEMORY AND THROUGHPUT REQUIREMENTS**
  - **GAIN DETERMINATION STILL BASED ON OPTIMAL KALMAN EQUATION**
- **“SUBOPTIMAL” PERFORMANCE**
  - **DUE TO “SUBOPTIMAL GAIN”**
  - **CAUSED BY:**
    - > **COVARIANCE INITIALIZATION ERROR**
    - > **INCORRECT NOISE MATRIX VALUES**
    - > **NEGLECTED ERROR STATES**
    - > **ERRORS IN STATE TRANSITION AND MEASUREMENT MATRICES**

## SUBOPTIMAL KALMAN FILTERS

Thus far, we have assumed that the analytical forms for the Kalman filter error models are identical to those of the real-world. In fact, such a mechanization would be virtually impossible to implement in a real computer due to the enormity of the number of states that would have to be accounted for. To simplify the mechanization problem, the error model used by the filter is only an approximate (reduced) form of the real-world model that (hopefully) retains the significant performance characteristics. The Kalman filter equations, however, are still based on the optimal form discussed in the previous slides, but using the simplified approximate model. Such Kalman filters are denoted as "suboptimal" filters.

Because the suboptimal filter used in a real system uses a filter gain based on an approximate error model, the resulting suboptimal gain matrix will not provide the optimal performance achievable within an ideal perfect filter. The suboptimal gain can differ from the idealized optimal gain due to several factors as listed in the slide, some of which are produced by intentional approximations introduced in the actual filter, and some of which are produced by uncertainties in our basic understanding of the real world error model.

# COVARIANCE PERFORMANCE ANALYSIS OF SUBOPTIMAL KALMAN FILTER



## COVARIANCE PERFORMANCE ANALYSIS OF SUBOPTIMAL KALMAN FILTER

In the design of a Kalman filter, the impact of its "suboptimality" on overall system performance must be assessed to assure sufficient accuracy compared to the theoretically ideal optimal filter performance. A commonly used method for evaluating suboptimal filter performance is through a suboptimal covariance digital computer simulation. The slide illustrates the general arrangement of such a simulation.

The slide illustrates the gain calculation performed for the suboptimal filter in the system computer based on the use of suboptimal model parameters (marked with an asterisk). The performance of the system calculated suboptimal gain matrix in the real world is then evaluated by the real world covariance matrix (P) which is propagated and reset using the suboptimal gains. Alternatively, the theoretically ideal optimum performance of the filter can be calculated (as a "best obtainable" reference solution) by using the optimal Kalman gain matrix calculated from the real world covariance, measurement, and measurement noise matrices. Note that the form for the real world covariance propagation and reset equations is identical to the forms used in the system computer gain determination. The difference is in the values used for the matrix elements (F, Q, H, R and their effect on P which are marked with asterisks for the system filter and without asterisks for the real world), values used for the initial value of P, and the fact that the real world model typically includes error states not accounted for in the system filter (hence, the need to add rows with zero elements for the deleted states in the suboptimal gain matrix when applying it to the real world covariance reset equation).

An important element in the suboptimal covariance simulation program is a trajectory generator used to provide navigation parameters as a function of time that are used in the calculation of dynamic elements in the F, F\*, H, H\*, Q, Q\*, R and R\* matrices. The trajectory generator typically has an interface with the simulation operator that allows the creation of realistic trajectory profiles for the particular application being investigated.

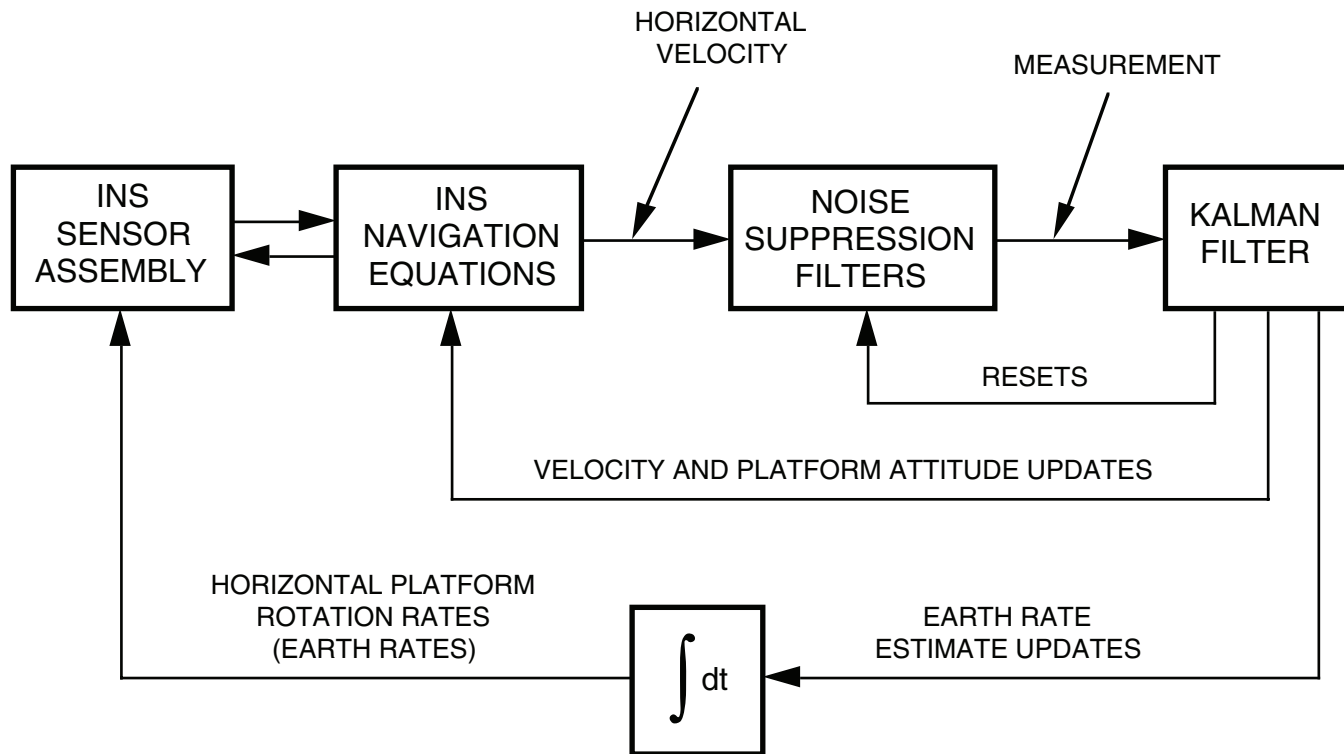
## **EXAMPLES OF KALMAN FILTER-AIDED INERTIAL SYSTEMS**

- **INS GROUND ALIGNMENT**
- **INS AT-SEA ALIGNMENT**

## **EXAMPLES OF KALMAN FILTER AIDED INERTIAL SYSTEMS**

To gain some insight into the form of Kalman filters typically used in aided inertial systems, Kalman filters structured for INS ground and at-sea alignment will be reviewed.

## INS GROUND ALIGNMENT FILTER LOOP



- **UPDATES BASED ON NULLING ESTIMATED ERRORS**

## INS GROUND ALIGNMENT FILTER LOOP

A Kalman filter can be utilized to perform the ground alignment function in an INS. The slide illustrates how the Kalman filter would be interfaced with the system navigation equations to perform this function.

The "measurement" for the Kalman filter is the filtered horizontal velocity from the INS. The noise suppression filter is incorporated to attenuate aircraft disturbance noise effects on the INS velocity (caused for example by fuel/stores loading, crew motion, or wind gusts) between Kalman filter measurement/update cycles. The noise filter would be mechanized digitally in the INS computer software (as a simple integrator for example) with an iteration rate that was higher than the basic filter cycle period. The purpose for the noise suppression filter is to relax the requirements for the Kalman filter so that it does not have to operate at a high iteration rate merely for the purpose of filtering input noise. Such "prefiltering" techniques are commonly used with real Kalman filters where computer throughput is at a premium and high speed iteration rates for the Kalman updating equations are intolerable. Note, however, that the prefilter dynamics may then have to be included in the Kalman filter error model.

The ground alignment loop shown in the figure is a nulling loop based on nulling the error states estimated by the Kalman filter through resets. Resets are computed and applied to the noise filter, the INS velocity, INS attitude, and the earth rate estimate used to rotate the local level coordinate frame erected in the INS. These operations are performed in each of the two horizontal navigation channels and are identical to the alignment functions described in a previous section on "Inertial Navigation System Initialization". The "Filter" function shown in the "Alignment Filter" blocks in the latter section encompasses the velocity integration (in the INS) and velocity filter functions shown in this slide.

## **INS GROUND ALIGNMENT KALMAN FILTER**

- **ENVIRONMENT**
  - **QUASI-STATIONARY**
  - **ACCELERATION DISTURBANCES – WIND GUSTS, CREW MOTION, FUEL/STORES LOADING**
- **INITIAL UNCERTAINTIES**
  - **LEVELING ERRORS – ORDER 1 DEG**
  - **HEADING ERROR – UP TO  $\pm 180$  DEG**
  - **VELOCITY ERRORS – CORRELATED WITH DISTURBANCES**
  - **POSITION ERRORS – NO UNCERTAINTY**
- **REFERENCE DATA – KNOWLEDGE THAT AIRCRAFT QUASI-STATIONARY**
- **MEASUREMENT – FILTERED HORIZONTAL SYSTEM VELOCITIES**

## INS GROUND ALIGNMENT KALMAN FILTER

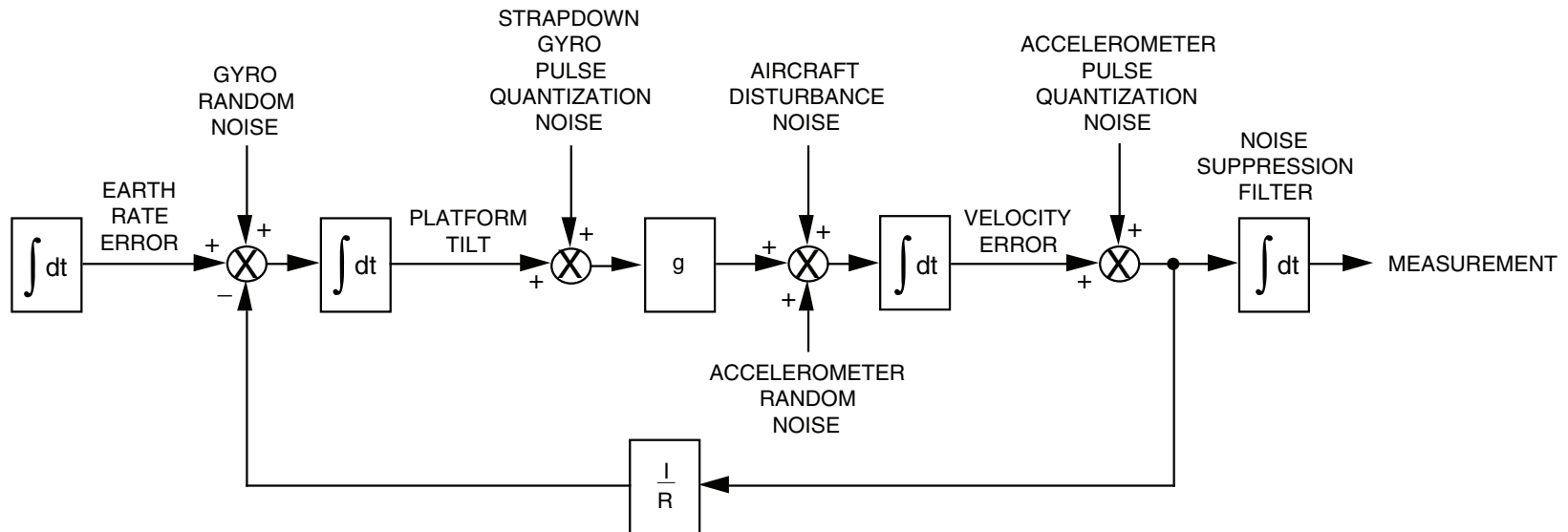
The INS ground alignment Kalman filter is designed for an environment in which the INS is quasi-stationary: i.e., it is stationary relative to the earth except for random acceleration effects on the aircraft due to wind gusts, crew motion, and fuel/stores loading.

The initial alignment function must correct for system errors at alignment initiation with uncertainties of typically  $\pm 1$  degree in attitude reference tilt relative to vertical (leveling error),  $\pm 180$  degrees in heading relative to North, and initial velocity uncertainties due to aircraft disturbances. The position error uncertainty is assumed to be zero based on a perfect latitude/longitude input by the operator at system start-up.

Measurement reference data for ground alignment is not measured directly, but is instead inferred from the knowledge that the aircraft is quasi-stationary. Hence, the output of the velocity filter should have an average zero output when the INS attitude, heading, and velocity data are correct.

The measurement for the Kalman alignment filter is the filtered horizontal system velocities (in each of two axes), the signals that should average zero when the filter converges the INS data to the correct values.

## INS GROUND ALIGNMENT ERROR MODEL



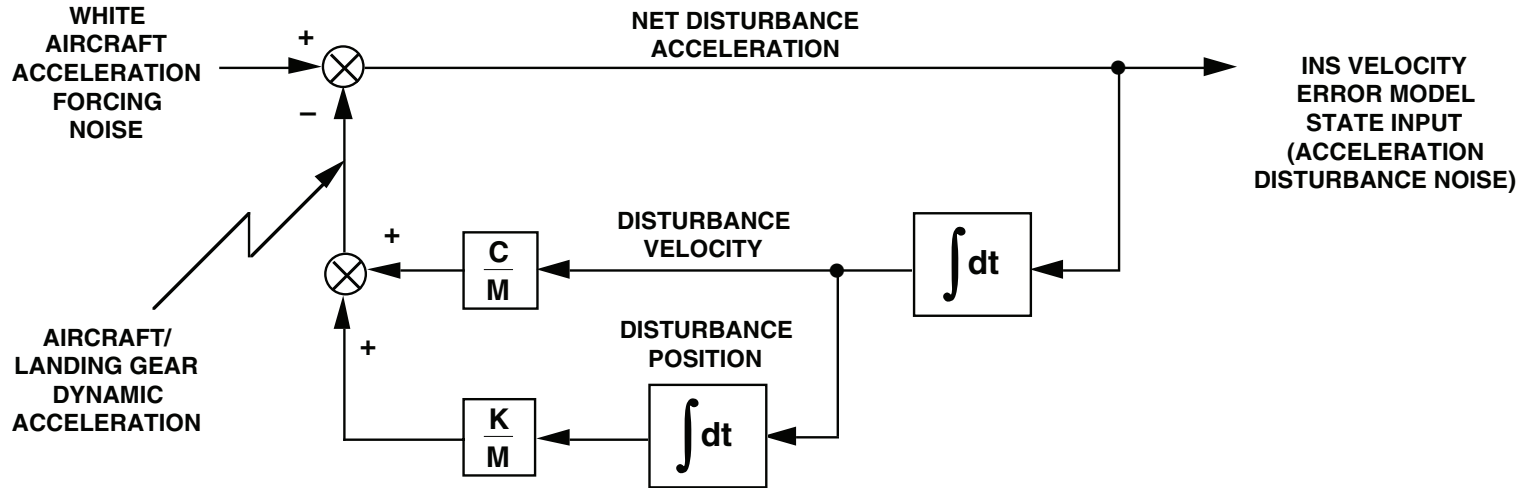
- BASIS FOR GAIN CALCULATION
- IDENTICAL FORM IN EACH HORIZONTAL CHANNEL

## **INS GROUND ALIGNMENT ERROR MODEL**

The slide illustrates a typical error model that would be used in a strapdown INS ground alignment Kalman filter. This model would form the basis for the optimal gain calculation. Note that the velocity prefilter used for the measurement is a simple integrator. The identical error model is used for each of the horizontal axes. This allows one set of single channel Kalman gains to be calculated and then used in each of the two horizontal alignment loop channels.

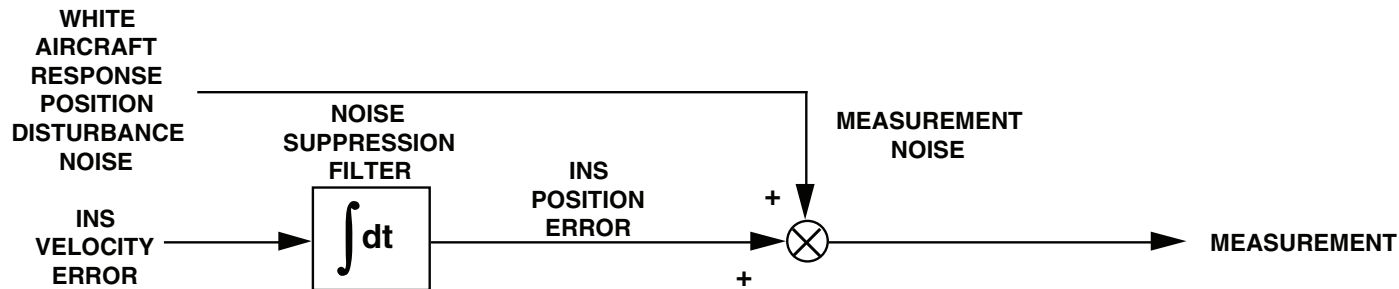
# AIRCRAFT DISTURBANCE NOISE ERROR MODEL

TYPICAL DYNAMIC MODEL OF AIRCRAFT RESPONSE TO WIND GUST, CREW MOTION, FUEL/STORES LOADING DISTURBANCES



NOTE: M = EQUIVALENT AIRCRAFT DYNAMIC MASS  
 C = AIRCRAFT/LANDING-GEAR DYNAMIC DAMPING CONSTANT  
 K = AIRCRAFT/LANDING-GEAR DYNAMIC SPRING CONSTANT

## APPROXIMATE AIRCRAFT DISTURBANCE MODEL AND INTERFACE WITH INS ERROR MODEL



## AIRCRAFT DISTURBANCE NOISE ERROR MODEL

The slide illustrates a typical dynamic model for the acceleration disturbance noise input to the velocity error integrator in the previous slide. The elements in the figure are intended to characterize the random motion of a stationary vehicle under disturbance input acceleration buffeting. The feedback elements in the diagram represent the dynamic acceleration response of the vehicle spring/damping characteristics to an assumed white acceleration noise forcing function. Such an error model approximates the behavior (for example) of a stationary aircraft under random forcing disturbances from wind gusts, crew motion, or fuel/stores loading. The feedback elements in this case would represent the spring/damping characteristics of the aircraft/landing gear dynamics. Note that the net acceleration sensed by an accelerometer in the vehicle (i.e., the input to the velocity error integrator in the previous slide) equals the sum of the disturbance acceleration input to the vehicle plus the spring/damping response accelerations of the vehicle to the disturbance.

If the dynamic model illustrated in the figure was utilized as shown for the acceleration disturbance noise in the previous chart, two additional states per axis would have to be included in the overall INS error model (representing the disturbance velocity and position feedbacks in this slide). If the total INS error model is to be used as the basis for a real-time Kalman filter configuration mechanized within the INS, this could impose computer throughput loading difficulties due to the additional states required, and the need to properly account for the associated disturbance response bandwidth characteristic (typically 0.5 to 1.0 Hz). As a result, the approximate disturbance model shown in the lower diagram is typically used in real-time Kalman filters to eliminate the need for the additional error states.

The approximate model shown in the lower diagram treats the disturbance noise as position measurement noise rather than acceleration process noise (indicated in the previous chart). Since the measurement is the second integral of acceleration (see previous chart), this is a valid equivalency. A simplifying assumption also implicitly incorporated in the lower diagram is that the Kalman filter measurement cycle time is long compared to the response time characteristic of the disturbance dynamics (in the upper diagram). Under these conditions, the position disturbance measurement noise is uncorrelated from measurement-to-measurement, and can therefore be validly approximated by white noise (i.e., without additional dynamic error states). This is the concept represented by the lower diagram in the chart.

One final note is worthy of mention with regard to the validity of using white measurement noise as the disturbance noise model. It could be argued that white acceleration noise (i.e., without feedback dynamics) could also have been used as process input noise to the velocity error integrator in the previous diagram to approximate the disturbance dynamics. The fallacy in this approximation is that the double integral of pure white noise generated at the position measurement for such an approach, would not be a bounded process (it would grow randomly in amplitude as a function of time). This is clearly in conflict with the reality of the situation which sustains a bounded random position disturbance (i.e., constant RMS noise amplitude). As such, the use of white position measurement noise to approximate the random input is the proper approximate method to model the disturbance noise.

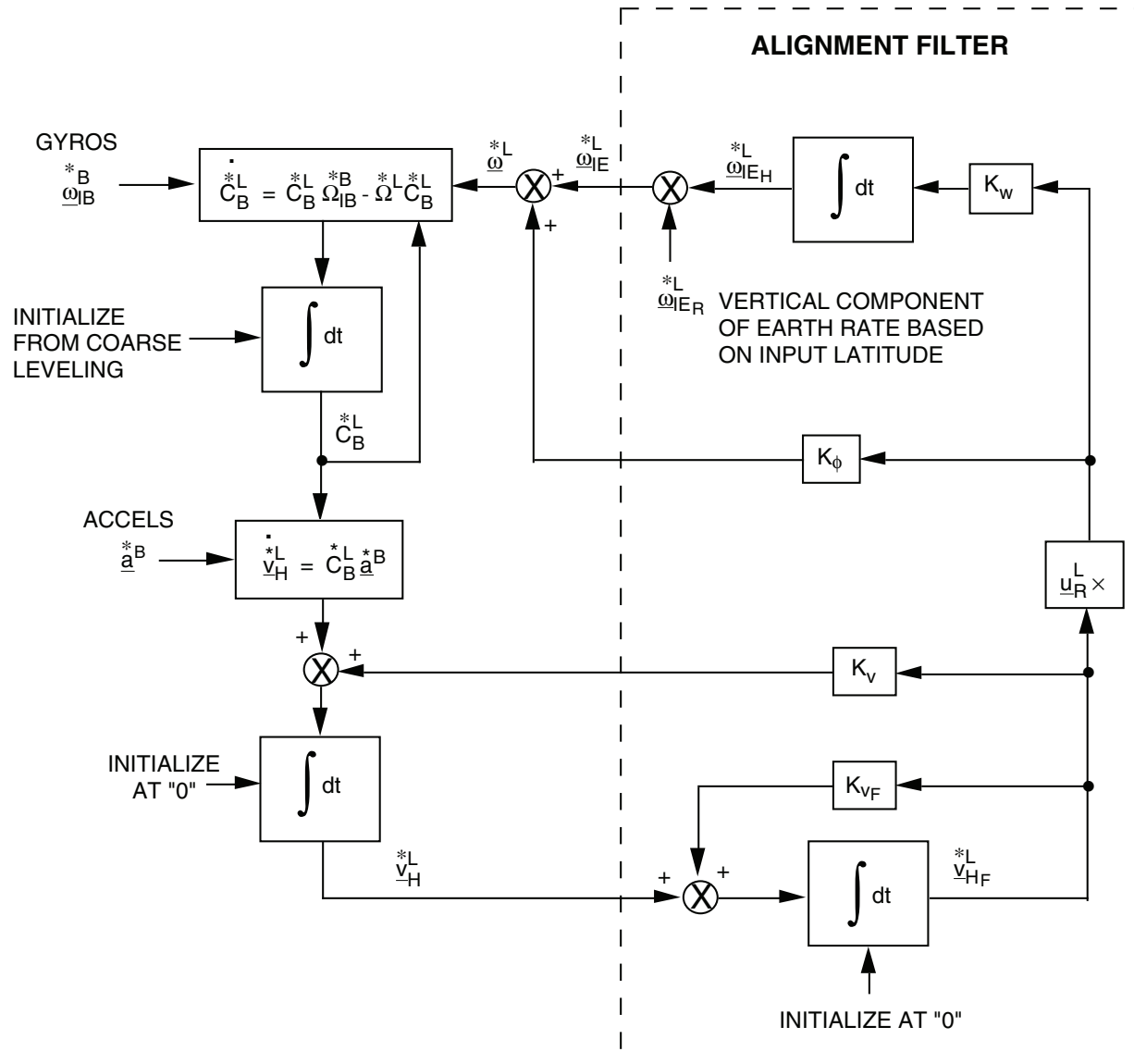
## **GROUND ALIGNMENT KALMAN FILTER (CONTINUED)**

- **ERROR STATES MODELED AND RESET**
  - **PLATFORM TILTS (2)**
  - **HORIZONTAL EARTH RATES (2) – HEADING**
  - **HORIZONTAL VELOCITIES (2)**
  - **FILTERED (INTEGRATED) HORIZONTAL VELOCITIES (2)**
  
- **PROCESS NOISE**
  - **GYRO AND ACCELEROMETER RANDOM NOISE**
  - **GYRO PULSE QUANTIZATION (IF STRAPDOWN)**
  - **ACCELEROMETER PULSE QUANTIZATION**
  
- **MEASUREMENT NOISE**
  - **AIRCRAFT RANDOM POSITION DISTURBANCE NOISE**

## **GROUND ALIGNMENT KALMAN FILTER (CONTINUED)**

The states modeled and reset in the ground alignment filter are those illustrated in the previous error model diagram (and summarized in this slide). The process noise vector components for the filter are similarly listed. The measurement noise for this Kalman filter is shown as the aircraft random position disturbance noise (based on the approximation for ground disturbance discussed in the previously shown "Aircraft Disturbance Noise Error Model" slide).

# GROUND ALIGNMENT LOOP ANALYTICAL DIAGRAM



## GROUND ALIGNMENT LOOP ANALYTICAL DIAGRAM

The slide illustrates the closed-loop computations for a strapdown INS ground alignment Kalman filter based on the error model formulation presented previously. The nomenclature in the diagram is the same as defined in a previous section on "Strapdown Inertial Navigation System Error Characteristics". One difference is that the asterisk (\*) is used to indicate (in this slide) parameters in the system computer that are in error from the true values for these variables.

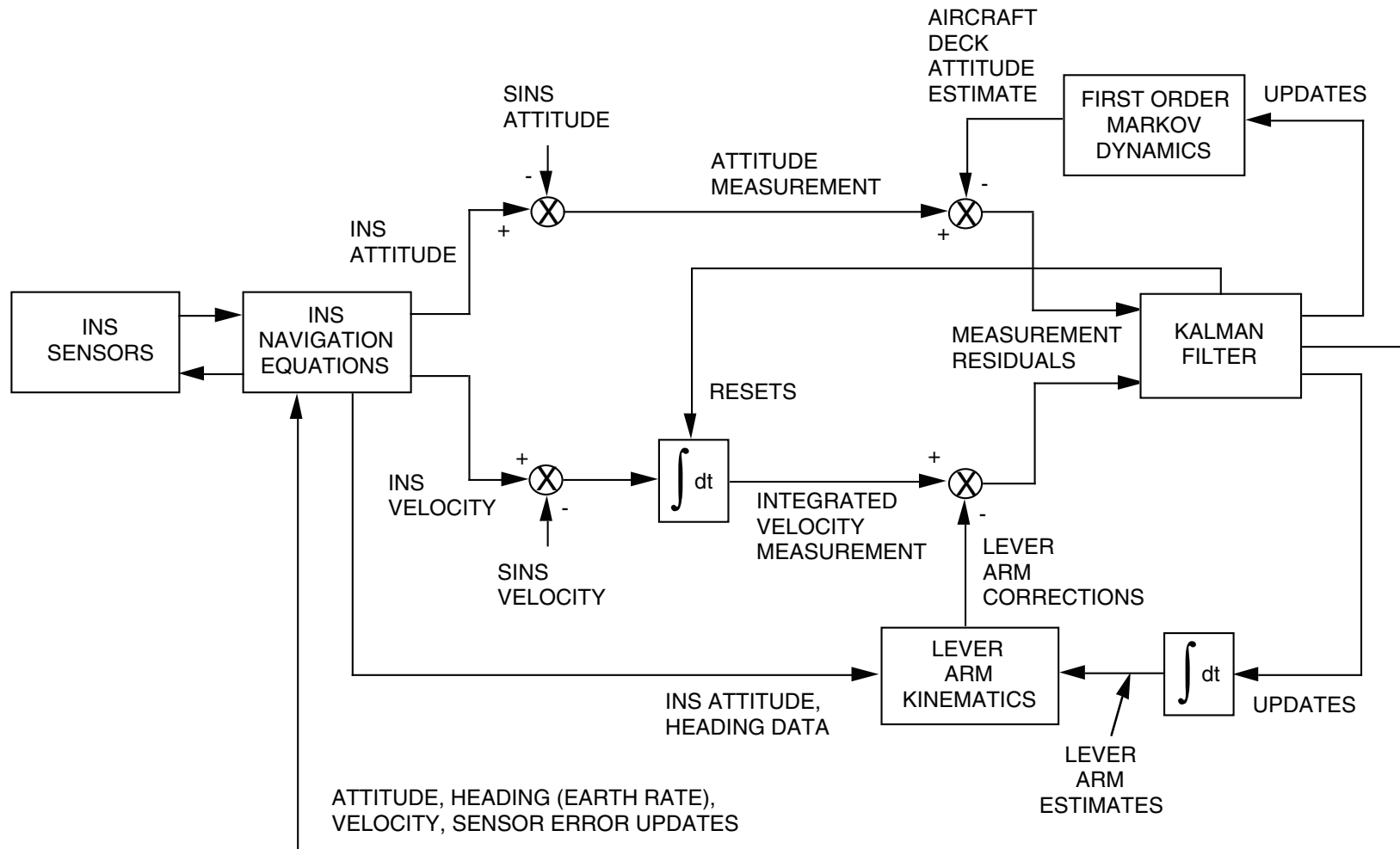
The four gains shown in the slide are the optimal Kalman gains that would be calculated using the previously described Kalman gain equations. The four gains are shown multiplying the integrated (i.e., filtered) horizontal velocity measurement to develop the reset controls for the attitude ( $K_\phi$ ), horizontal earth rate estimate ( $K_w$ ), horizontal velocity ( $K_v$ ), and filtered (integrated) horizontal velocity ( $K_{vf}$ ).

Note that the alignment Kalman filter structure in the slide lacks the dynamic model of the error states shown in previous slides on Kalman filter structure (e.g., the slide entitled "Inertial Aiding Using Error Model Feedback"). This is because the filter controls for this problem are designed to null the estimates of the error states. Consequently, the model for the error state estimates from cycle-to-cycle is zero. As such, error state estimate dynamics that propagate a null vector are superfluous, and are, therefore, not included in the filter. The slide entitled "Generalized Discrete Aiding Filter Structure" can be used to verify that the error estimate dynamic model has no impact on filter performance for the case where the control vector  $\underline{U}$  is used to null the error state estimate

(i.e., for  $\underline{U} = -\underline{\dot{X}}_{n-1}^*$ ). Note also that the form of the alignment filter in this analytical diagram is identical to the form presented previously on a qualitative basis in the section entitled "Inertial Navigation System Initialization". Hence, the  $K_1$ ,  $K_2$  alignment gains in the latter section are identical to the  $K_\phi$  and  $K_w$  gains of this diagram. The  $K_v$  and  $K_{vf}$  resets (and the velocity and filtered velocity calculations) are included in the latter section in the "Filter" function shown in the "Alignment Filter" block.

One final point should be noted regarding implementation of the control reset function  $\underline{U}$  described above. As indicated above, the error state vector estimate from cycle-to-cycle is zero, however, from a previous chart on "Kalman Filter Control Reset Formulation", this is only exactly true if the control reset is applied at the instant that the measurement is made (i.e., at  $n-1$ ). This allows zero time for calculation of the Kalman gain, if the gain matrix is calculated after the measurement is made. It is to be noted, however, from the "INS Ground Alignment Error Model" slide, that the state dynamic matrix for this situation is constant, independent of the computed navigation parameters. For this unique situation, the gains can be computed during the previous cycle so that they are ready to be applied at the instant the measurement is made. In this manner, an ideal "instantaneous" control reset can actually be implemented in real time, thereby making the assumption of a zero error state vector estimate, exactly correct.

# INS AT-SEA ALIGNMENT KALMAN FILTER LOOP



## INS AT-SEA ALIGNMENT KALMAN FILTER LOOP

The slide illustrates the operation of a Kalman filter used in the past for the initial alignment of an aircraft INS on a moving aircraft carrier. The reference data in this case is the ship's inertial navigation system (SINS) which provides both attitude and horizontal velocity data to the aircraft INS for use in establishing vertical and heading alignment. Study of the SINS at-sea alignment concept is instructive because in one configuration, it embodies several key elements incorporated in many inertial aiding techniques; integrated velocity measurement, lever arm effects, and attitude measurement.

The principle "measurement" for the at-sea alignment Kalman filter is the integrated difference between the SINS and INS North/East velocities. Because the aircraft containing the INS can be several hundred feet from the SINS, the measurement will be non-zero, even if the INS was perfectly aligned and navigating, due to lever arm effects of the INS relative to the SINS deck station under angular rotations of the ship deck (due to turning, pitching, and rolling). The measurement model in the Kalman filter accounts for the lever arm effect based on SINS attitude data inputs (to measure ship deck angular motion), and lever arms estimated by the Kalman filter. The measurement residual for Kalman filter input is formed from the measurement corrected for the estimated lever arm effect.

To aid in early heading error convergence, an attitude measurement can be employed in the at-sea alignment filter based on the difference between INS and SINS attitude data. The attitude data used are the direction cosines representing the components of a unit vector perpendicular to the ship deck plane as projected onto North/East local level axes. Under pitch/roll motion, these projections will be in error if the North/East heading reference is incorrect. Hence, a comparison between these cosines for the SINS and aircraft INS provides a measure of INS heading error to the Kalman filter (the SINS heading is assumed perfect).

## **INS AT-SEA ALIGNMENT KALMAN FILTER LOOP (CONTINUED)**

The measurement model in the Kalman filter used to offset the attitude measurement is based on a model for the off-nominal attitude the aircraft might have relative to the ship deck (due to stores/fuel loading configuration or crew motion, for example). The aircraft deck attitude error is dynamically modeled as a first order Markov process to account for dynamic correlation. The attitude measurement residual input to the Kalman filter is formed from the difference between the attitude measurement and aircraft deck attitude estimates (in each of the two horizontal axes).

INS attitude heading velocity, and sensor error updates are employed by the Kalman filter for the control reset function. Additionally, the SINS/INS velocity difference integrator which resides in the INS computer is also reset as part of Kalman filter control resets operations. The latter integrator serves the same function for the at-sea alignment as the velocity filter in the ground alignment; to filter high frequency disturbance velocity components caused principally by aircraft disturbances. This prefiltering allows the Kalman filter to operate with a longer cycle time and achieve high quality performance with a relatively small number of measurements per unit time.

**NOTES**

## **INS AT-SEA ALIGNMENT KALMAN FILTER**

- **ENVIRONMENT**
  - **DYNAMIC SHIP MOTION**
  - **QUASI-STATIONARY AIRCRAFT MOTION RELATIVE TO DECK**
- **REFERENCE DATA**
  - **SHIP'S INS (SINS) – POSITION, VELOCITY, ATTITUDE, HEADING OF SHIP**
- **MEASUREMENT**
  - **INTEGRATED DIFFERENCE BETWEEN AIRCRAFT INS AND SINS HORIZONTAL VELOCITIES**
  - **DIFFERENCE BETWEEN AIRCRAFT INS AND SINS ATTITUDE COSINES**
- **INITIAL UNCERTAINTIES**
  - **LEVELING ERRORS**
  - **HEADING ERROR – UP TO  $\pm 180$  DEG**
  - **VELOCITY – CAUSED BY SHIP DYNAMICS**
  - **POSITION – ASSUME NO UNCERTAINTY (INITIALIZE AT SINS POSITION)**
  - **LEVER ARMS BETWEEN AIRCRAFT INS AND SINS**
  - **AIRCRAFT DECK ATTITUDE**
  - **SENSOR ERRORS**

## INS AT-SEA ALIGNMENT KALMAN FILTER

The at-sea alignment Kalman filter must be designed to account for the quasi-stationary aircraft motion of the aircraft relative to the carrier deck (similar to the ground alignment filter) but must also account for the dynamics of the carrier deck due to ship's motion. This includes heading, roll, and pitch "rigid body" motion as well as bending effects.

Reference data for at-sea alignment is provided by the SINS in the form of ship's position (latitude, longitude), velocity (North, East), and attitude (roll, pitch, heading) of the SINS station in the ship. Aircraft deck location relative to the SINS is unknown and must be estimated by the filter as part of the alignment process. Two "measurements" are used for at-sea alignment: the integrated horizontal velocity difference between the aircraft INS and SINS (two components), and the difference between the INS and SINS attitude cosines (two components). The latter two measurements are used only during the initial phases of alignment to speed heading convergence.

Initial error state uncertainties for the at-sea alignment problem are aircraft INS leveling (typically  $\pm 1$  deg), heading (up to  $\pm 180$  deg), and velocity (caused by ship dynamics). The initial position is assumed to have zero uncertainty (i.e., the assumed perfect SINS position is close enough). Additional uncertainties are the lever arm distances from the aircraft INS to the SINS, the aircraft attitude relative to the ship deck, and certain INS sensor errors.

## **INS AT-SEA ALIGNMENT KALMAN FILTER (CONTINUED)**

- **ERROR STATES MODELED**
  - **PLATFORM TILTS (2)**
  - **HORIZONTAL EARTH RATES (2) – HEADING**
  - **HORIZONTAL VELOCITIES (2)**
  - **INTEGRATED INS/SINS VELOCITY DIFFERENCE (2)**
  - **LEVER ARMS (3)**
  - **AIRCRAFT DECK ATTITUDE (2)**
  - **SENSOR ERRORS (3 GIMBALED, 2 RLG STRAPDOWN)**
  
- **PROCESS NOISE**
  - **GYRO RANDOM NOISE**
  - **GYRO PULSE QUANTIZATION (IF STRAPDOWN)**
  - **AIRCRAFT INS AND SINS ACCELEROMETER PULSE QUANTIZATION**
  - **AIRCRAFT ATTITUDE DISTURBANCES**
  
- **MEASUREMENT NOISE**
  - **ATTITUDE MEASUREMENT:**
    - **SINS SYNCHRO NOISE AND SHIP ANGULAR FLEXURE**
  - **INTEGRATED VELOCITY DIFFERENCE MEASUREMENT:**
    - **AIRCRAFT RANDOM POSITION DISTURBANCE NOISE**
    - **AND SHIP TRANSLATIONAL FLEXURE**

## INS AT-SEA ALIGNMENT KALMAN FILTER (CONTINUED)

The at-sea alignment process is generally divided into "Coarse" and "Fine" alignment phases. During Coarse alignment, 13 states are typically modeled in the Kalman filter: INS platform tilts (2), horizontal earth rates representing heading error (2), the integrated INS/SINS velocity difference (2), lever arms (3), and aircraft deck attitudes (2). Both integrated velocity and attitude measurements are used during Coarse alignment. Coarse alignment completion (and Fine alignment initiation) is based on the heading uncertainty (from the covariance matrix) being less than a prescribed value (e.g., 2 degrees).

During Fine alignment, typical error states modeled are the platform tilts (2), heading error (2 if two earth rate components are used or 1 if based on small angle theory), horizontal velocities (2), integrated INS/SINS velocity difference (2), lever arms (3), and sensor errors (typically 3 gyro biases for gimballed systems or 2 equivalent horizontal accelerometer biases for strapdown systems). This results in typically 13 states for the Fine alignment mode. Only integrated velocity measurements are used during Fine alignment.

The process noise vector for the at-sea alignment problem is listed in the slide. Measurement noise associated with the SINS angle measurements is produced by synchro noise and ship angular bending. Measurement noise associated with the integrated velocity difference measurement is produced primarily by ship translational bending and aircraft random position disturbance noise relative to the ship deck (as discussed in a previous "Aircraft Disturbance Noise Error Model" slide). It should be noted that the attitude measurement noise also impacts the velocity measurement to a small degree due to errors in the process of calculating lever arm effects in the measurement model using SINS attitude data for deck attitude rotation measurements.

## **STRAPDOWN INS KALMAN FILTER SENSOR ERROR STATES**

- **GENERAL STRAPDOWN SENSOR ERRORS (24)**
  - **GYRO BIAS – X, Y, Z**
  - **GYRO ORTHOGONALITY ERROR – XY, YZ, ZX**
  - **GYRO SCALE FACTOR ERROR – X, Y, Z**
  - **ACCELEROMETER BIAS – X, Y, Z**
  - **ACCELEROMETER MISALIGNMENT RELATIVE TO MEAN GYRO AXES**
    - **XY, XZ, YX, YZ, ZX, ZY**
  - **ACCELEROMETER SCALE FACTOR ERROR – X, Y, Z**
  - **MEAN GYRO AXES MISALIGNMENT RELATIVE TO MOUNT – XY, YZ, ZX**
  
- **NUMBER OF STATES REQUIRED IN KALMAN FILTER DEPENDS ON:**
  - **SENSOR ACCURACY**
  - **MANEUVERS EXPECTED**
  - **SENSOR ERROR OBSERVABILITY**
  - **OVERALL SYSTEM ACCURACY REQUIRED AND ACCURACY OF REFERENCE DATA**

## STRAPDOWN INS KALMAN FILTER SENSOR ERROR STATES

In the design of a Kalman filter for a strapdown ring laser gyro INS, it is important to recognize that 24 error states can exist for the strapdown sensors, each potentially having a significant impact on system performance. The slide identifies each of these error states. Note that only three misalignment errors (orthogonality) have been identified for the strapdown gyros. Since relative sensor misalignments are the only parameters affecting navigational accuracy, the "mean gyro axes" can be arbitrarily defined as the sensor assembly navigation reference axes, with the accelerometer misalignments referenced to these. Misalignment of the mean gyro axes relative to the sensor assembly mount in the user vehicle affects the INS/vehicle attitude reporting accuracy which may be important if misalignments between different systems in the vehicle affect the measurement process (e.g., misalignments between a star tracker and the INS sensor assembly for a stellar aided inertial navigation system configuration). Note also that G-sensitive effects have been excluded for the gyro errors. If conventional strapdown momentum wheel gyros are utilized, G-sensitive error states may also have to be included to account for all sources of system navigation error.

A Kalman filter designed in a flight computer to account for all 24 error states indicated would impose a considerable burden on the system computer. For many applications, all of these error states need not be modeled.

The number of strapdown sensor error states required in the Kalman filter depends on several considerations. Sensor accuracy, of course, is one of the key factors. If certain sensor errors are known to be negligibly small for a particular application, they need not be included in the error model. "Small" relative to Kalman filter model requirements can mean that the error is small enough that its effect on even unaided INS performance is negligible. On the other hand, it can also mean that the Kalman filter measurements or operation time are insufficient to have the capability for estimating the error, hence, including it in the Kalman Filter provides no useful benefit. The latter is the situation for ring laser gyro bias error during INS alignment. The bias error is compatible with 1 nmph unaided INS accuracy (but not negligible). For a Kalman alignment filter, the ring laser gyro bias error generally cannot be easily distinguished from heading alignment error for the alignment periods involved because it has a similar effect on the velocity measurement (as alignment error). As such, including a gyro bias error provides little, if any, benefit in improved overall filter performance.

As has been discussed previously, aircraft maneuvers can have a pronounced impact on how strapdown sensor errors affect navigational accuracy. The maneuvers expected during Kalman Filter operation must be considered when deciding which sensor errors need be included.

Sensor observability is another factor which can be both a hindrance and an aid in Kalman filter design. If certain sensor error effects are not excited (i.e., do not impact the measurement) during Kalman filter operation, they are not "observable" hence, will not be estimatable by the filter. Obviously, such errors need not be modeled in the filter. On the other hand if one of the functions of the filter is to calibrate the sensor errors, such observability limitations will limit calibration capabilities. Calibration

## **STRAPDOWN INS KALMAN FILTER SENSOR ERROR STATES (CONTINUED)**

of currently nonobservable sensor errors may be important during a later portion of flight when flight profile conditions may suddenly make them have a significant impact on navigational performance. Another aspect of observability is that for certain maneuvers, certain sensor errors have a similar impact on navigational accuracy (e.g., the bias and misalignment error for horizontal accelerometers in a strapdown cruise INS produce similar velocity/position error characteristics during flat turns). Under such conditions, a combined error state can be defined that accounts for both effects as one. The filter, not being able to distinguish one effect from the other, will do a fine job estimating the combined state. Note, however, that under other conditions when the error states are excited differently and have different measurement signatures, the filter may become confused and yield poor performance.

Finally, the selection of the states actually modeled in the filter must depend on the overall aided system accuracy requirement, and the accuracy available from the reference data being used for INS data comparison. If only moderately accurate reference data is available, it doesn't make sense to construct an elaborate sensor error model in the INS whose states cannot be estimated properly due to poor measurement data quality.

**NOTES**

## **RLG INS STRAPDOWN KALMAN FILTER ERROR STATES FOR GROUND AND AT-SEA ALIGNMENT**

- **STATIC GROUND ALIGNMENT – NO SENSOR ERROR STATES**
- **INTERRUPTED GROUND ALIGNMENT – COMBINED ACCELEROMETER  
BIAS/MISALIGNMENT ERRORS (X/XZ, Y/YZ)**
- **AT-SEA SINS ALIGNMENT**
  - **COMBINED ACCELEROMETER BIAS/MISALIGNMENT ERRORS (X/XZ, Y/YZ)**
  - **POTENTIALLY COMBINED ACCELEROMETER SCALE FACTOR ERRORS  
(X/Z, Y/Z) IF LARGE SHIP PITCH/ROLL MOTION**
  - **HORIZONTAL SHIP DYNAMIC ACCELERATION CAN UNCOUPLE EAST  
GYRO BIAS FROM HEADING ERROR**
- **ASSUMPTIONS**
  - **GYRO SCALE FACTOR ERRORS SMALL**
  - **STRAPDOWN GYRO BIAS ERRORS SMALL  
(RLG LONG TERM STABILITY)**

## **RLG INS STRAPDOWN KALMAN FILTER ERROR STATES FOR GROUND AND AT-SEA ALIGNMENT**

For the ground and at-sea alignment filters discussed in the previous section, the slide describes the sensor error states required in the Kalman filter model assuming a ring laser gyro strapdown INS.

For the case of a static (quasi-stationary) ground alignment, sensor errors are indistinguishable from reference axis tilt and heading errors (review the "Strapdown Inertial Navigation System Error Characteristics" section for the discussion on correlations between accelerometer errors and platform tilts and the correlation between gyro bias and initial heading errors). Stated differently, the alignment mechanization is based on the assumption that the sensors are perfect measures of sensor assembly attitude relative to the vertical and North. Hence, the sensor data as manifested through the strapdown navigation equations, becomes the reference for the alignment process. As such, no sensor models are used in the static ground alignment filter.

For some applications, it is required that an alignment in progress be interrupted if the aircraft is moved and resumed when the aircraft stops. The resumed alignment must initiate from the condition achieved prior to aircraft movement. The method used to implement this function is through the cessation of measurements to the alignment Kalman filter during the period the aircraft is being moved. During this period, the navigation equations are processed (as they are during the actual alignment operations) so that the attitude, heading, and velocity reference data is held intact. The covariance matrix in the Kalman filter is also processed during the alignment "interrupt" period so that knowledge of the error covariance will be retained when alignment functions resume. Similarly, all Kalman filter error state estimates are also propagated through the interrupt period.

The key factor that distinguishes the interrupted from the static alignment case is the fact that the sensor axes may be moved in heading. This produces attitude tilts due to gyro misalignment errors, and horizontal acceleration changes due to the rotation of the body fixed accelerometer bias and misalignment errors. All of these effects, in combination, produce a ramping of the horizontal velocity which appears as if caused by an accelerometer bias. If not modeled in the Kalman filter, this would be interpreted as a changing platform tilt (since the start of alignment) which, from the simplified static model, can only be caused by earth rate error. Thus, the Kalman filter would update the tilts and earth rate estimates, the latter producing a significant heading estimation error. Including two accelerometer bias states along X, Y body axes (representing the combined effects of accelerometer bias/misalignment, and gyro misalignment) will allow the filter to attribute the change in horizontal acceleration during rotation to strapdown accelerometer bias (rather than earth rate), hence, avoid misestimating the earth rates. Note that in the slide, the gyro misalignment error effect is not shown as part of the combined accelerometer state because it is generally small and negligible in RLG strapdown systems.

## **RLG INS STRAPDOWN KALMAN FILTER ERROR STATES FOR GROUND AND AT-SEA ALIGNMENT (CONTINUED)**

In the case of an at-sea alignment, the ship (hence the aircraft) can rotate in heading during alignment operations. Because the rotations are generally about the vertical, the sensor error rotation effect can be approximated as two combined accelerometer bias error states (X and Y). Additionally, if significant pitching and rolling is expected during alignment, accelerometer scale factor errors may have to be modeled to account for the component of vertical specific force sensed by the nominally level accelerometers, and the tipping of the nominally vertical accelerometer (with its scale factor error) so that it has a horizontal component. These effects can be modeled as combined X, Y accelerometer scale factor error states.

The above error model approximations are based on the assumption that gyro scale factor errors and gyro bias errors are small (as in ring laser gyro (RLG) strapdown systems) so that their error effects in rotating environments are negligible (for the applications studied) compared to other sensor error effects and system accuracy requirements.

For the at-sea alignment scenario it is interesting to note that a modern day aircraft carrier is in a constant state of lateral low frequency horizontal dynamic acceleration, even under calm sea state conditions without intentional ship turning. The horizontal acceleration provides a coupling of the heading error into the integrated velocity measurement that has one less integration than the coupling of east gyro bias into the measurement (See previous error propagation chart entitled “Simplified Strapdown INS Short Term Error Characteristics”). Observability is thereby provided for the heading and east gyro bias error states that allows each to be estimated individually. This is the basis for the in-air “transfer alignment” concept in which large horizontal accelerations are intentionally created in an aircraft in the process of initially aligning a missile INS heading (and attitude) prior to launch (using the aircraft INS as a reference). For the at-sea alignment problem, the added observability aids the gimbaled system initial heading determination and gyro bias calibration process to compensate for conventional momentum wheel gyro long term bias instability. Little added benefit is afforded to RLG strapdown inertial systems in this scenario because the RLG long term bias stability is generally sufficiently accurate to not require calibration updates.

**NOTES**

**NOTES**

# **STRAPDOWN SYSTEM TESTING**

## **INS PERFORMANCE INDICES**

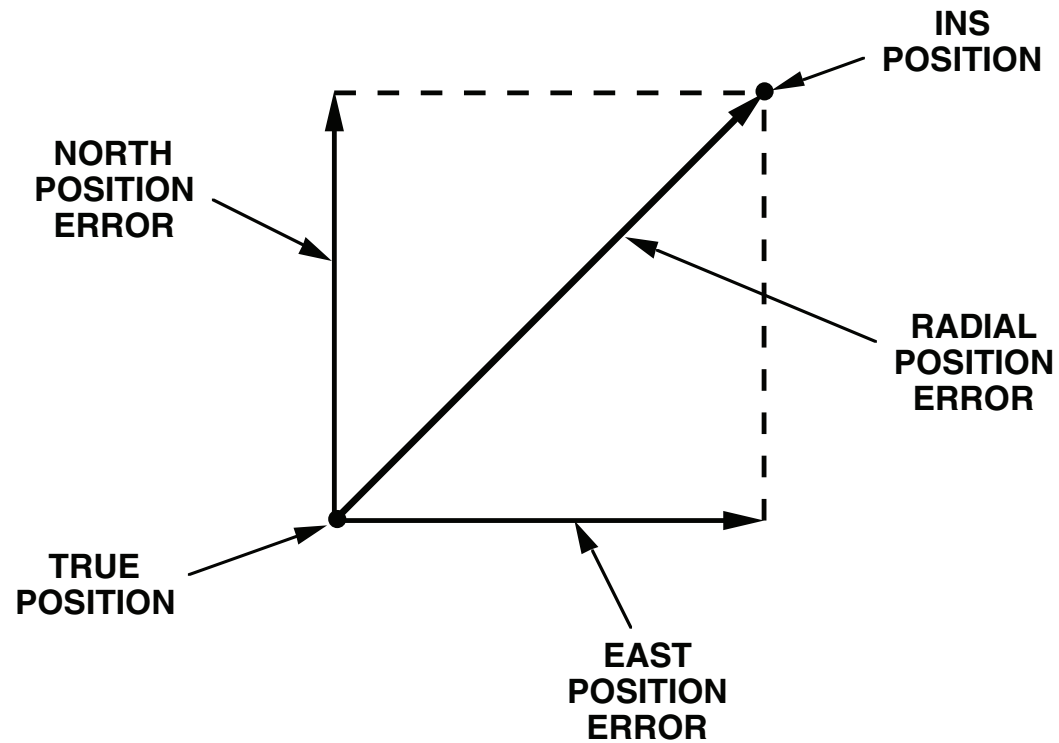
- **POSITION**
- **VELOCITY**

## **INS PERFORMANCE INDICES**

INS performance is generally evaluated during system testing in terms of position and velocity accuracy.

# POSITIONING PERFORMANCE

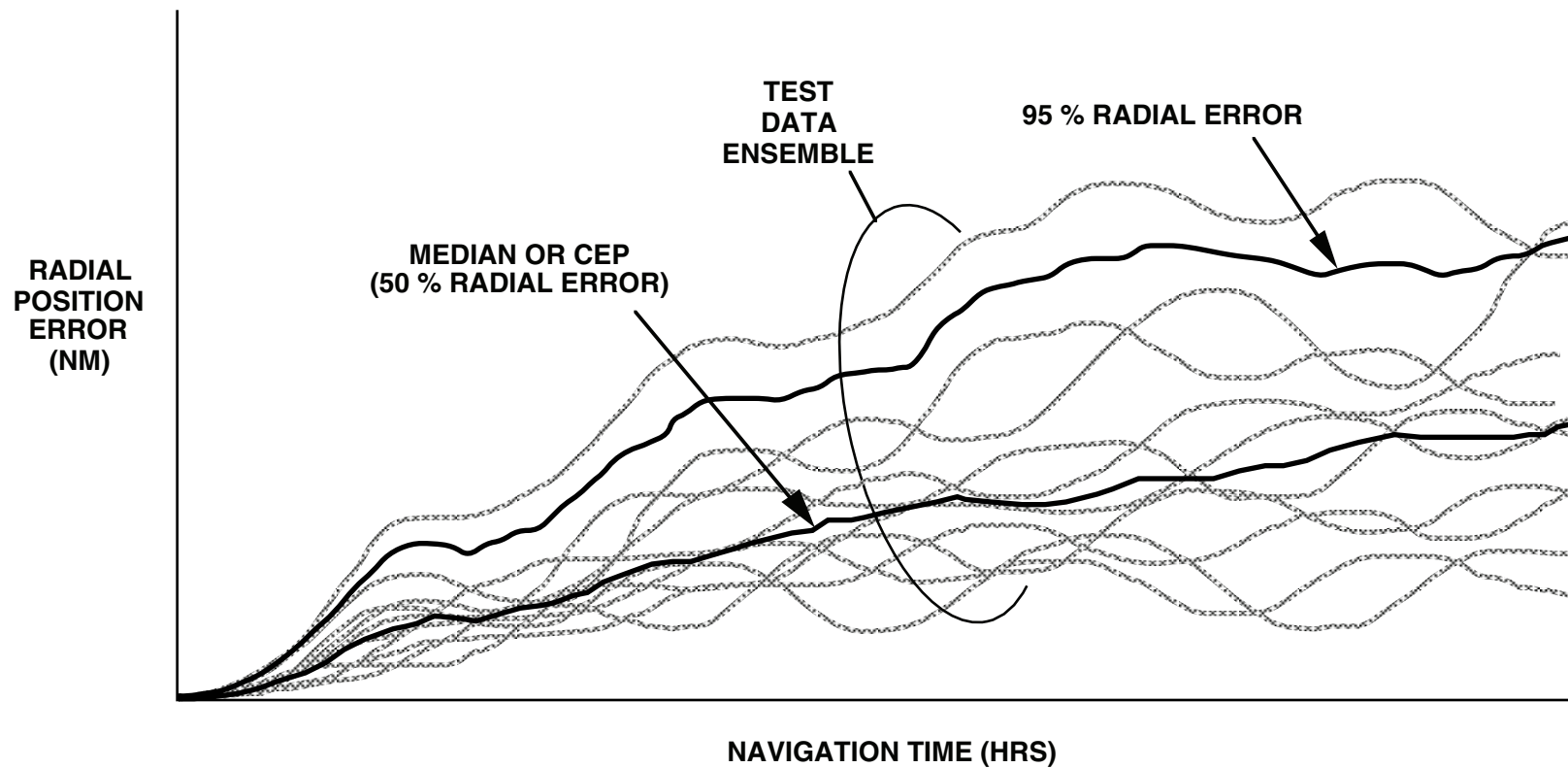
- PER AXIS - NORTH/EAST POSITION ERROR
- RADIAL POSITION ERROR
- HORIZONTAL PROJECTION
- STATISTICAL CRITERIA



## **POSITIONING PERFORMANCE**

Positioning accuracy in an INS generally refers to the horizontal component of the position error vector. This can be measured in terms of North/East components, but is generally measured as the magnitude of the total horizontal position error magnitude (denoted as the "radial position error"). Various statistical criteria have been established for specifying, evaluating, and rating inertial navigation systems in terms of these position error definitions.

# RADIAL POSITIONING ERROR

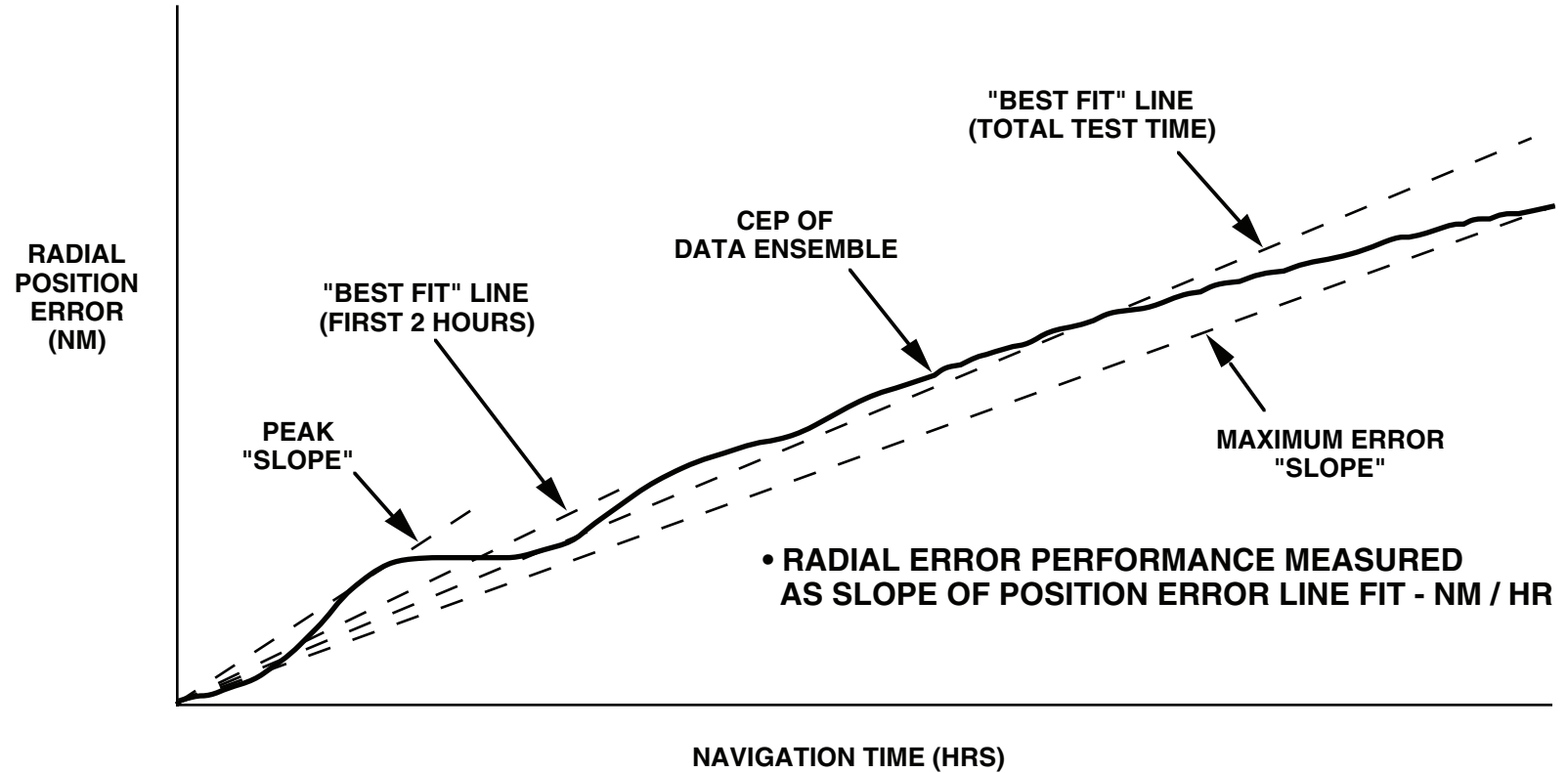


## **RADIAL POSITIONING ERROR**

The slide depicts a typical ensemble of radial position errors that one might obtain as a function of navigation time for a series of INS test runs (e.g., an ensemble of flight tests). Two of the commonly used position error criteria are shown superimposed on the data ensemble: the 50 percentile or median radial error (also known as the CEP or circle of equal probability), and the 95 percentile radial error.

The CEP is the radius of the circle within which the position error will lie 50 percent of the time. The 95 percentile radial error is the radius of the circle within which the position error will lie 95 percent of the time. For the ensemble shown in the slide, the CEP and 95 percentile error are calculated at each time point based on the statistics of the ensemble data at that time point. For a very large ensemble, the CEP (50 percentile) and 95 percentile points can be directly measured by ordering the radial errors from largest to smallest, and finding the radial error that divides the final ordered set into 95 percent members and 50 percent members. For a limited sample size, the equivalent statistical data can be calculated from a simple statistical measure of the ensemble average (e.g., the RMS), and using an analytical relationship between the calculated statistical parameter and the desired statistical parameter (assuming some standard form for the ensemble probability distribution; e.g., Gaussian with zero mean along each axis).

# TYPICAL RADIAL POSITIONING PERFORMANCE CRITERIA



## TYPICAL RADIAL POSITIONING PERFORMANCE CRITERIA

Due to the traditional concern with gyro error and its ramp-type impact on inertial navigation system performance (at least for the first few hours of navigation), inertial navigation system positioning accuracy has traditionally been measured in terms of nautical-miles-per-hour radial position error growth rate. From the slide, it is not altogether clear how such a performance parameter can be defined to represent the ensemble performance behavior of a particular INS.

The slide illustrates a typical CEP versus time plot for an INS. Note the Schuler oscillation effects, and reduction of the average growth rate with navigation time (4 to 8 hour period) due to earth loop effects.

Four "position error slopes" are shown on this figure; a "peak slope" line corresponding to the upper limit tangent to the CEP curve, a "best fit" line over the first two navigation hours, a "best fit" line for the total test time and a "maximum error slope" line passing through the latest time test point. Note that each of these performance figures provide a different numerical value for system performance based on the same data.

The above example illustrates the importance for clearly specifying the meaning of the nautical-miles-per-hour performance index used to specify or characterize an INS.

## **POSITION ERROR CRITERIA CONSIDERATIONS**

- **PERCENTAGE ERROR DEFINITION – 50%, 95%, ETC.**
- **RADIAL OR PER AXIS**
  - **NOTE: “ONE SIGMA” OR “TWO SIGMA” USUALLY REFERS TO THE “STANDARD DEVIATION” OF A SINGLE AXIS GAUSSIAN DISTRIBUTION BUT HAS NO SIGNIFICANCE FOR A RADIAL ERROR DISTRIBUTION. PERCENTAGE PROBABILITY DEFINITIONS APPLY TO ALL DISTRIBUTIONS.**
- **TEST DURATION**
  - **EARTH LOOP EFFECTS**
- **PEAK SLOPE OR LINE FIT**
  - **SCHULER OSCILLATIONS**
- **SLOPE OF STATISTICAL PARAMETER WITH TIME CURVE OR STATISTICAL EVALUATION OF LINE SLOPES OBTAINED FOR EACH TEST**

## POSITION ERROR CRITERIA CONSIDERATIONS

In specifying or characterizing the positioning accuracy of an INS, the percentile statistical figure of merit should be clearly defined (e.g., 50 percentile, 95 percentile, etc.), plus a clear definition of whether the specification is for radial error or per axis (e.g., North or East) performance. Performance requirements denoted as "one sigma" or "two sigma" for example are vague, because they imply error characteristics associated with a single axis Gaussian distribution (usually with implied zero mean). A radial error is a magnitude error (i.e., only has positive values) and is not Gaussian distributed (actually, it is usually closer to a Rayleigh distribution), hence, the single axis Gaussian terminology is just not applicable. Percentage probability definitions for device performance, on the other hand, are independent of distribution function and apply to single axis or radial error distributions.

In specifying performance, the navigation period should be clearly specified. In this manner, earth loop effects which tend to reduce position error growth in longer term flights, will not be used to benefit one INS over another during performance evaluation.

Schuler oscillations should also be considered in INS position error slope specifications or evaluation. A "peak slope" requirement is more difficult for the same system than a "best line" fit (see previous slide) due to Schuler effects. Moreover, the exact definition of the "best line fit" should also be clear (i.e., in a least squares sense, "equal area" mean line, through the origin, etc.)

Finally, the method for calculating the statistical ensemble line slope should be defined. Two commonly used but different methods are the slope of the statistical ensemble position versus time data, and the ensemble statistical average of the best line fit slopes to the radial position error versus time curves for each flight.

## **THEORETICAL ANALYTICAL RELATIONSHIPS BETWEEN RADIAL ERROR AND PER AXIS PERFORMANCE PARAMETERS (ASSUMING ZERO MEAN PER AXIS)**

$$\text{CEP} = R_{50} \approx 0.589 \Delta (\sigma_x + \sigma_y) = 1.178\sigma \text{ (FOR } \sigma_x = \sigma_y = \sigma \text{)}$$

$$R_{\text{RMS}} = (\sigma_x^2 + \sigma_y^2)^{1/2} = 1.414\sigma \text{ (FOR } \sigma_x = \sigma_y = \sigma \text{)}$$

$$R_{90} = 2.15\sigma \text{ (FOR } \sigma_x = \sigma_y = \sigma \text{)}$$

$$R_{95} = 2.45\sigma \text{ (FOR } \sigma_x = \sigma_y = \sigma \text{)}$$

$\sigma_x, \sigma_y$  = STANDARD DEVIATION OF X, Y POSITION ERROR COMPONENTS

CEP = CIRCLE OF EQUAL PROBABILITY

$R_{\text{RMS}}$  = ROOT-MEAN-SQUARE ENSEMBLE AVERAGE OF RADIAL POSITION ERROR

$R_{50}, R_{90}, R_{95}$  = 50, 90, 95 PERCENTILE RADIAL ERRORS

**THEORETICAL ANALYTICAL RELATIONSHIP BETWEEN RADIAL ERROR AND PER AXIS PERFORMANCE PARAMETERS (ASSUMING ZERO MEAN PER AXIS)**

The slide illustrates analytical relationships between popular navigation system error criteria. These expressions can be useful in relating the performance of one system to another when each is characterized using a different criteria.

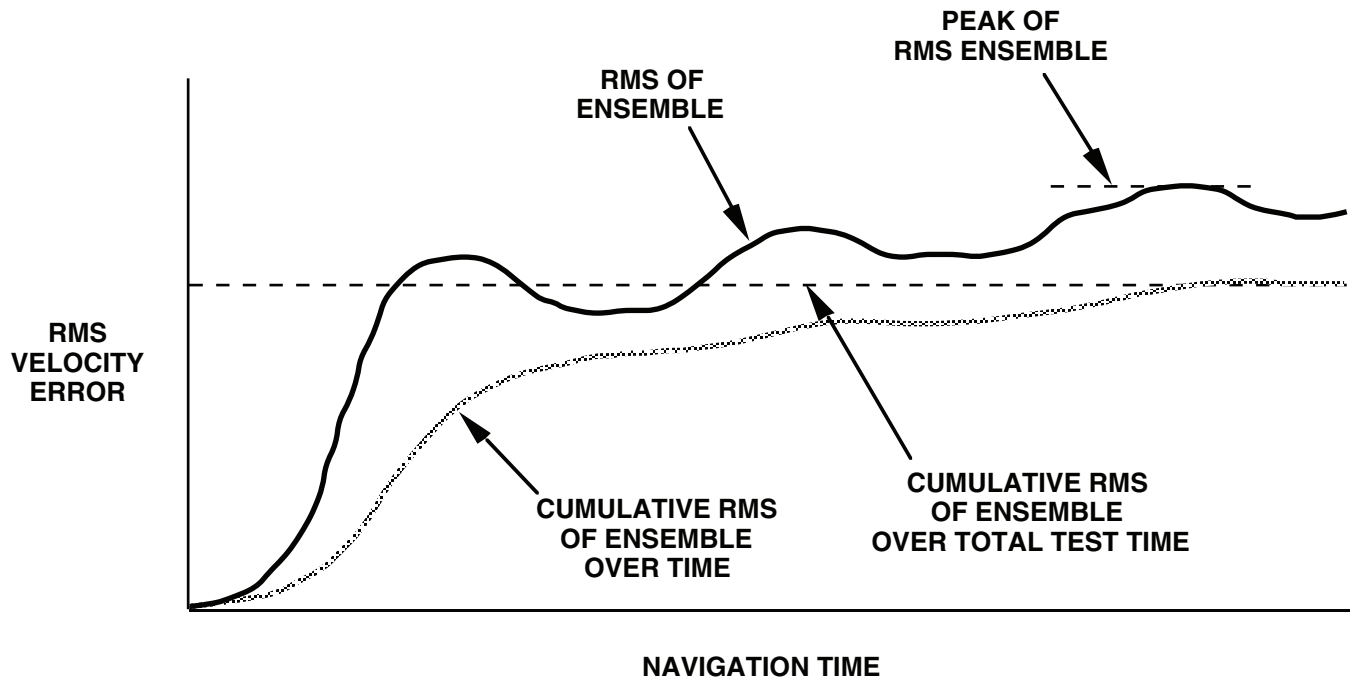
## **VELOCITY PERFORMANCE**

- **PER AXIS**
- **RADIAL**
- **STATISTICAL CRITERIA**

## **VELOCITY PERFORMANCE**

The velocity performance for inertial navigation systems is usually evaluated (and specified) on a per axis basis (i.e., North or East) although radial velocity error may sometimes be specified.

# TYPICAL VELOCITY ERROR PERFORMANCE CRITERIA



## TYPICAL VELOCITY ERROR PERFORMANCE CRITERIA

The slide illustrates the plot of a typical RMS ensemble average velocity error curve. Each point is calculated as the RMS of the data over an ensemble of tests (e.g., flight tests) at the same time during navigation.

The curve illustrates three commonly used definitions of INS velocity error based on this data. The peak of the RMS ensemble is the peak of the RMS data over the time for which the ensemble data was taken. The cumulative RMS of the ensemble over the total test time is the time RMS average of the RMS data over the total time for the data ensemble. The cumulative (or running) RMS of the ensemble over time is the RMS average in time of the RMS data up to the point in time where the cumulative figure is evaluated. The latter data is calculated as a function of navigation time (as shown in the slide), and at the last time point in the data set, is equal to the cumulative RMS over total test time datum value. Note that the cumulative RMS over time data shows a lower velocity error than any of the other criteria, even though it is based on the same test data results.

## **VELOCITY ERROR CRITERIA CONSIDERATIONS**

- **ERROR DEFINITION – 67%, 90%, 95%, “ONE-SIGMA”, “THREE-SIGMA”**
- **PER AXIS OR RADIAL**
- **FPS OR KNOTS**
- **“NORTH/EAST” PER AXIS ERROR DISTORTION AT HIGH LATITUDES**
  - **EARTH REFERENCE AXIS ALTERNATIVE**
- **RADIAL OR GROUND SPEED**
  - **ONLY EQUIVALENT ON GROUND**

## VELOCITY ERROR CRITERIA CONSIDERATIONS

In evaluating, specifying, or rating an INS velocity capability, the performance criteria should be clearly specified. Percentile probability figures (e.g., 67 percentile, 90 percentile, 95 percentile) are preferred over the commonly used "one-sigma", "three-sigma" type notation (which implies a one dimensional Gaussian error distribution which may not be the case). Additionally, it should be clearly stated whether the velocity accuracy is on a per axis basis (e.g., North or East), or whether it is a radial error (the magnitude of the horizontal component of the velocity error). Hopefully, the velocity performance figures will contain units (e.g., knots or fps). Note, one knot equals 1.69 fps).

Two particular peculiarities of velocity error parameters should be remembered when defining velocity performance; North/East velocity error distortion at high latitudes, and the difference between radial velocity error and ground speed error (they are only equivalent at zero true velocity).

At high latitude, the navigation reference heading relative to North becomes increasingly in error (due to the inability to clearly define North). Consequently, any parameters expressed in geographic North/East coordinates becomes in error at high latitudes due to the North heading uncertainty (including velocity). On the other hand, the velocity accuracy in earth reference axes (i.e., polar/equatorial) may be highly accurate at high latitudes. When specifying velocity accuracy on a "per axis" basis, the axis definition should be clearly specified (North/East, body, or whatever), because it can have a pronounced impact on the velocity error value at high (or low) latitudes.

The following slide illustrates that ground speed error is not synonymous with radial velocity error magnitude and should not be used to specify radial velocity error when ground speed accuracy is what is needed.

**NOTES**

**NOTES**

## **CLASSES OF SYSTEM TESTING**

- **LABORATORY TESTING**
- **VAN TESTING**
- **FLIGHT TESTING**

## **CLASSES OF SYSTEM TESTING**

Testing of an inertial navigation system can be generally grouped into three categories: laboratory testing, van testing, and flight testing. Aspects of each, particularly with regard to strapdown INS testing, are discussed in the following slides.

## **INS LABORATORY TESTING**

- **SENSOR CALIBRATION TESTING**
  - **CALIBRATION OVER ENVIRONMENTS**
  - **ERROR CHARACTERIZATION**
  
- **SYSTEM DEVELOPMENTAL TESTING**
  - **VERIFY FUNCTIONAL PERFORMANCE – HARDWARE, SOFTWARE, INTERFACES**
  - **VERIFY HARDWARE AND SOFTWARE ACCURACY – SENSOR CALIBRATION**
  - **VERIFY HARDWARE, SOFTWARE PERFORMANCE UNDER ENVIRONMENTAL EXPOSURES**
  
- **SYSTEM EVALUATION TESTING**
  - **VERIFY FUNCTIONAL PERFORMANCE – SYSTEM, EXTERNAL INTERFACES**
  - **VERIFY SYSTEM ACCURACY**
  - **VERIFY SYSTEM PERFORMANCE UNDER ENVIRONMENTAL EXPOSURES**

## INS LABORATORY TESTING

INS laboratory testing generally consists of sensor calibration testing, developmental testing, and evaluation testing.

Sensor calibration testing consists of performing the tests needed to measure the systematic (or compensatable) sensor errors (e.g., fixed gyro bias). Sensor error measurements obtained from the calibration testing are used to compensate the sensors, usually through INS computer software operations, in which sensor error model equations are applied to correct the sensor errors (based on the measured sensor error coefficients which have been stored in computer memory). For example, in a strapdown system, the fixed gyro bias coefficient (stored in memory) would be subtracted from the sensor output in the system computer software before it was used for attitude updating. If the compensatable sensor errors are environmentally sensitive (e.g., temperature sensitive for a heaterless sensor) the calibration process must extend over the environments as a function of measured environmental parameters used in the analytical calibration error model (e.g., sensor temperature measurements for the temperature sensitive coefficients). An important initial part of the sensor calibration process is the characterization of the sensor errors as a class for a particular sensor configuration. Characterization is the process of developing and verifying the sensor software analytical error model whose coefficients will then be determined for each individual sensor during calibration.

System developmental testing is performed by the engineering group designing the INS. Its purpose is to verify that system functional operations are being performed properly (including all hardware, software, and system interface functions), and that the system accuracy is meeting performance requirements in the laboratory environment and under anticipated user environments (e.g., temperature, vibration, altitude, etc.). The accuracy assessment during developmental testing must evaluate both hardware and software accuracy. Computational errors (due to programming flaws, round-off, or algorithm error) impact INS accuracy, and must be eliminated from the system before any meaningful hardware evaluation can begin. This generally entails a sophisticated software verification process during the INS engineering development cycle prior to software/hardware integration. Once the software has been conclusively verified, it need no longer be tested unless software changes are made during developmental testing which necessitate reverification. A commonly used technique during developmental testing to aid in verifying both hardware and software accuracy is to execute a system/sensor calibration procedure and verify that the system will perform accurately after calibration.

Where system developmental testing implies an iterative design correction process, system evaluation testing is used to verify overall system performance after developmental tests are completed. This includes verification of functional performance (within the system and the system external interface), and system accuracy in the laboratory environment and under environmental exposures. The evaluation testing may duplicate some of the tests performed during developmental testing. Nevertheless, these tests are important to conclusively demonstrate that the overall developmental process has been successfully completed.

## **CALIBRATION TESTING**

- **SENSORS**
  - **MEASURE AND COMPENSATE FIXED, G-SENSITIVE, THERMALLY SENSITIVE ERRORS (IF NO THERMAL CONTROLS)**
  - **REQUIRES ROTATION FIXTURES TO:**
    - > **SEPARATE EARTH RATE FROM GYRO BIAS ERRORS**
    - > **EXPOSE SENSORS TO G FROM DIFFERENT DIRECTIONS**
    - > **ROTATE GYROS TO MEASURE SCALE FACTOR AND MISALIGNMENT ERRORS**
  - **THERMAL COMPENSATION REQUIRES TESTING AT OVEN TEMPERATURES – SYSTEM OR SENSOR LEVEL**
  
- **PLATFORM**
  - **MEASURE AND COMPENSATE MISALIGNMENT BETWEEN SENSOR PLATFORM AND INS MOUNT**
    - > **REQUIRES LEVEL TABLE WITH PITCH-UP CAPABILITY**

## CALIBRATION TESTING

Calibration testing entails tests to measure (and compensate) sensor errors, and misalignment errors for the platform (strapdown or gimbaled) to which the sensors are mounted.

Sensor calibration testing must measure and compensate all significant error sources that are measurable, modelable (for compensation in system software), and repeatable (over the calibration interval for the device). Depending on the particular instruments used in the INS and their individual design characteristics, compensatable errors can include fixed (constant) errors, G-sensitive errors, and thermally sensitive errors. Compensation for G-sensitive and thermally sensitive errors is based on acceleration measurements (from the INS accelerometers) and temperature measurements using temperature sensors mounted near or to the inertial sensors. Note, that if sensor assembly thermal controls are used, temperature compensation may not be necessary (except possibly during initial warm-up to decrease the delay time before the sensor data is usable in the system computer).

Sensor calibration generally entails the use of rotation fixtures (i.e., test tables) to discriminate earth rate input (and gyro output) effects from gyro bias output errors, expose the sensors to vertical specific force acceleration (G) at different directions relative to sensor axes (to excite different G-sensitive errors), and to rotate the gyros so that scale factor and misalignment errors can be measured.

If thermal compensation is used with the sensors, sensor testing at different temperatures is required. This entails use of a thermal oven for tests of the sensors alone, or of the system containing the sensors (the former method is generally simpler and preferred if sensor level thermal performance calibration is repeatable at the system level). Note that thermal testing, particularly at the system level, may be complicated by the need for rotation fixturing as part of thermal calibration measurements, and the need for lengthy time periods required for the inertial sensors to reach thermal equilibrium while being thermally shielded by the system which was designed to retard system-into-sensor heat flow.

In addition to the above described sensor assembly calibration, the angular orientation of the sensor assembly relative to the INS mount must also be measured and calibrated so that the angular orientation of the mount (hence, aircraft) can be precisely calculated relative to the earth (i.e., by correcting the inertially computed angular orientation of the sensor assembly relative to the earth by the sensor-assembly-to-mount calibration correction angles). The sensor assembly-to-mount calibration is typically performed by mounting the mount and INS on a level table with a horizontal axis rotation pitch-up capability. When level, the INS readout angles following a static system self-alignment measure the sensor assembly-to-mount pitch/roll misalignments. If the pitch axis of the mount is aligned to the table pitch axis, and the table is pitched-up 90 degrees, the direction cosine between the table pitch axis and the pitched-up INS roll axis following a static system self-alignment measures the sensor assembly-to-mount yaw misalignment.

## **LABORATORY TEST DESIGN**

- **EXPOSE SYSTEM TO ENVIRONMENTS THAT EXCITE ALL IMPORTANT ERROR SOURCES**
- **DIAGNOSTIC CAPABILITIES – DESIGN TESTS SO THAT ERRORS OBSERVED CAN BE RELATED TO SOURCE ERRORS (e.g., PARTICULAR GYRO ERRORS)**

## **LABORATORY TEST DESIGN**

The design of laboratory tests for inertial navigation systems should have the goal of evaluating all aspects of the system that impacts performance. As such, the test design should assure that the system is exposed to all environments (including attitude, heading, rotation rate, acceleration, in all functional modes) to excite all error sources in the system. Additionally, for developmental tests, the tests should be designed so that test results can be used with a diagnostic procedure to relate anomalies observed to particular error sources in the system. It can be argued that the latter capability should be a goal for all tests, not only developmental tests.

## TYPICAL STRAPDOWN LABORATORY TESTS

- **STATIC NAVIGATION**
  - TESTS BIAS OF GYRO POINTING NORTH, RANDOM ERRORS IN LEVEL AXIS SENSORS, VERTICAL GYRO DRIFT, VERTICAL ACCELEROMETER SCALE FACTOR/BIAS
- **SCORSBY**
  - TESTS GIMBAL SERVOES IN GIMBALED SYSTEMS
  - TESTS STRAPDOWN GYRO MISALIGNMENT/SCALE FACTOR ERROR, LEVEL AXIS ACCELEROMETER SCALE FACTOR ASYMMETRY, ATTITUDE COMPUTATION SOFTWARE AND HARDWARE IN STRAPDOWN SYSTEMS
  - ALSO TESTS STRAPDOWN SENSOR PARAMETERS IDENTIFIED ABOVE UNDER "STATIC NAVIGATION" TESTS
- **HEADING ROTATION**
  - TESTS LEVEL AXIS GYRO BIAS/MISALIGNMENT, LEVEL AXIS ACCELEROMETER BIAS/MISALIGNMENT, VERTICAL GYRO AND ACCELEROMETER BIAS/SCALE FACTOR, LEVEL AXIS SENSOR RANDOM ERRORS
  - SCHULER PUMP OPTION (42 MINUTES 180 DEGREE ROTATION)
- **ACCELEROMETER POSITIONING**
  - TESTS X, Y, Z ACCELEROMETER SCALE FACTOR ERROR AND SCALE FACTOR ASYMMETRY
- **STRAPDOWN ROTATION TEST**
  - TESTS X, Y, Z GYRO/ACCELEROMETER SCALE FACTOR/MISALIGNMENT AND X, Y, Z ACCELEROMETER BIAS
- **DRIFT CALIBRATION TESTS**
  - TESTS GYRO BIAS

## TYPICAL STRAPDOWN LABORATORY TESTS

The slide lists several of the commonly used laboratory tests for strapdown systems.

The static navigation test consists of an alignment and navigation run at the same static attitude/heading condition in the laboratory (at room temperature, in the oven, on a vibration fixture, etc.). The slide lists the sensor errors excited by this test.

Scorsby testing has been popular for strapdown systems as a carry-over from gimbal system testing and from early technology strapdown system testing when inherent sensor performance capabilities were marginal. A Scorsby table is a device that imparts three-axis cyclic rotations to a system at the same frequency but out of phase so that coning type motion is generated (usually about two of the table axes). The physical construction of the table generates only oscillation motion so that no net attitude displacement takes place. Scorsby tables were traditionally used to test the gimbal servoes in gimballed inertial systems. Scorsby testing of strapdown systems rectifies gyro misalignment and scale factor errors, and "level" axis accelerometer scale factor asymmetry errors, so that they generate horizontal position/velocity errors. From a functional standpoint, Scorsby testing of strapdown systems is useful in verifying that the overall strapdown software/hardware functions are operating properly and accurately (e.g., coning algorithms and sensor/computer data interfaces). The Scorsby test also tests the sensor parameters evaluated under the static navigation test.

The heading rotation test is one of the simplest and most revealing tests for a strapdown system. The test consists of a static alignment, entry into the navigation mode, then an immediate 180 degree rotation in heading. The system is then allowed to navigate statically while monitoring horizontal velocity (and position) performance. The 180 degree rotation causes initial leveling and heading alignment errors (produced by accelerometer and gyro error) to add to (and effectively double) the effect of these error sources during navigation. Additionally, the 180 degree rotation exercises gyro misalignment and scale factor errors. The slide lists the sensor errors made visible by the heading rotation test.

As an option, the heading rotation test can include additional 180 degree azimuth rotations at half Schuler periods (42 minute intervals). The resulting Schuler pump further amplifies the level axis constant gyro bias and accelerometer errors.

The accelerometer positioning test measures the scale factor errors in all of the accelerometers in a strapdown system. The method is to position each accelerometer axis vertical (up and down) and measure system vertical velocity response. This test is used to make accelerometer scale factor error effects visible, particularly the "nominally level" X, Y axis instruments which only

## **TYPICAL STRAPDOWN LABORATORY TESTS (CONTINUED)**

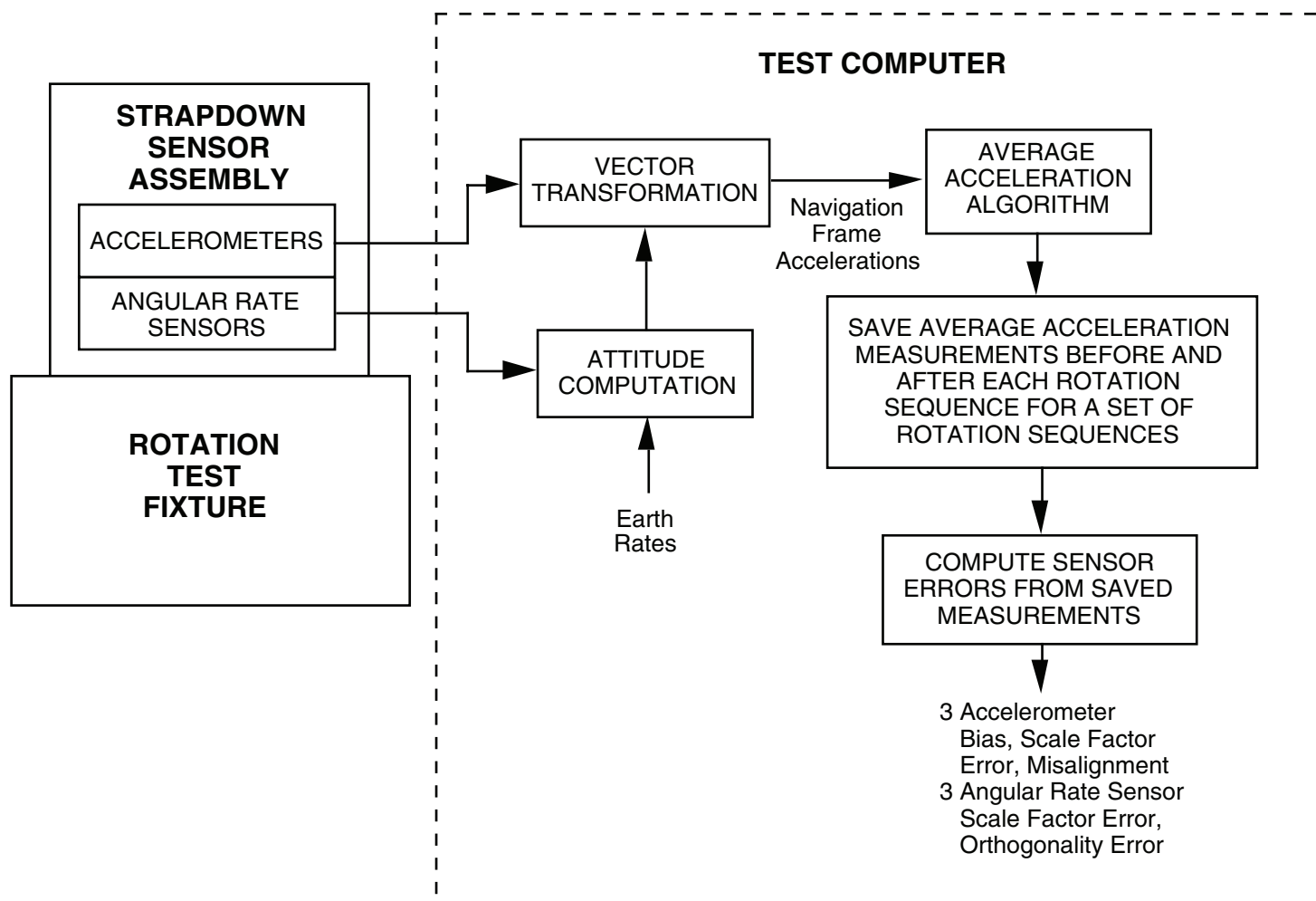
see a small component of specific force acceleration during most of the other nominally near level laboratory tests.

The Strapdown Rotation Test is used with strapdown inertial systems to measure the scale factor and misalignment errors in each sensor, and each accelerometer bias. A special software function is implemented for the test in which a strapdown analytical platform is created, initially aligned (as on page 120), and then set into a free inertial mode by in effect, setting the alignment gains to zero. A series of rotation sequences is then executed in which the analytic platform transformed acceleration is averaged while the system is stationary between rotations. The averaged accelerations are sampled before and after each rotation sequence for the test measurement. The measured data from all rotation sequences (typically 16) are then combined analytically to calculate the sensor errors.

The Strapdown Rotation Test does not measure gyro bias. Strapdown gyro bias is measured through static "drift" runs, either at the system or sensor level, with long term data (typically several hours for a high accuracy inertial system) used to calculate gyro bias effects.

**NOTES**

# STRAPDOWN SENSOR ASSEMBLY ROTATION TEST



## STRAPDOWN SENSOR ASSEMBLY ROTATION TEST

The slide depicts the setup for the Strapdown Rotation Test showing a strapdown sensor assembly mounted on a rotation test fixture (typically with two rotation axes, the outer axis horizontal with a perpendicular inner axis). The sensor assembly test mount is attached to the inner rotation axis. The intent of the fixture is to allow angular positioning of the sensor assembly at different orientations relative to vertical.

The chart shows the test computer containing software to implement a stabilized analytic platform that calculates sensor assembly attitude from the gyro outputs and transforms accelerometer outputs into the platform navigation frame (established to be nominally locally level at arbitrary orientation relative to north). Attitude initialization would be performed using test software that implements the standard strapdown INS initial alignment function as shown on page 120. The test software shown could also reside in the strapdown system under test.

When the sensor assembly is stationary, an averaging algorithm calculates the average navigation frame acceleration components. Measurements for the test are the acceleration averages immediately before executing a particular rotation sequence, and immediately following the rotation sequence. Such measurements are taken for several different rotation sequences. Following completion of the rotation sequences, the measurements are processed to determine misalignments between gyro input axes, accelerometer misalignments relative to "mean" gyro axes, gyro/accelerometer scale factor error, accelerometer scale factor asymmetry, accelerometer bias, and misalignment of the sensor assembly relative to the sensor assembly test mount.

The basic principle behind the Strapdown Rotation Test is that a sensor assembly without sensor error will output the same navigation frame specific-force acceleration at any stationary orientation (i.e. - 1 g up with horizontal components associated with misalignment of the analytic platform relative to vertical (a residual error produced from the initial alignment process). Consequently if the sensor assembly is rotated from one stationary orientation to another (via a particular rotation sequence), it should have the same measured average acceleration outputs before and after the rotations. Differences in before/after horizontal specific force measurements are produced by sensor assembly gyro/accelerometer errors; gyro scale-factor/misalignment errors produce attitude error during the rotation that change the transformed accelerometer signals; accelerometer errors will look differently in navigation coordinates after the rotation because the accelerometer error sources (the accelerometers) have changed their orientation (Note, if the sensor assembly attitude after the rotation sequence is the same as before the sequence, accelerometer errors will not change in navigation coordinates, and the before/after average acceleration comparison will measure only gyro error. This forms the basis for design of rotation sequences intended to measure only gyro error effects).

By designing the rotation sequences properly, all sensor errors noted above can be excited to produce a distinct signature on the measurements. Post-processing of the measurements then allows each individual sensor error to be determined and then used to update the strapdown system compensation coefficients.

## TYPICAL ROTATION TEST SEQUENCE SET

SEQUENCE NUMBER	ROTATION SEQUENCE (Degrees, B Frame Axis)	STARTING ATTITUDE (+Z Down, Axis Indicated Along Outer Rotation Fixture Axis)
1	+360 Y	+Y
2	+360 X	+X
3	+90 Y, +360 Z, -90 Y	+Y
4	+180 Y, +90 Z, +180 X, -90 Z	+Y
5	+180 X, +90 Z, +180 Y, -90 Z	+X
6	+90 Y, +90 Z, -90 X, -90 Z	+Y
7	+90 Y	+Y
8	-90 Y	+Y
9	+90 Y, +90 Z	+Y
10	+90 Y, -90 Z	+Y
11	-90 Y, -90 Z	+Y
12	+90 X, +90 Z	+X
13	+90 X, -90 Z	+X
14	+180 Z	+Y
15	+180 Y	+Y
16	+180 X	+X

## TYPICAL ROTATION TEST SEQUENCE SET

The chart depicts a typical Strapdown Rotation Test set of rotation sequences. The rotations shown are about strapdown sensor assembly (B Frame) axes. The rotation fixture has its outer axis horizontal. The starting attitude for each sequence has the B Frame Z axis down with the B Frame axis identified in the third table column being horizontal and parallel to the rotation fixture outer axis.

The first six rotation sequences return the sensor assembly to its starting attitude. Consequently (as noted in the previous chart), accelerometer errors for these sequences produce no change in the average before/after analytic platform navigation frame averaged transformed specific-force acceleration measurements. As such, measurements from these sequences are used to determine misalignment between gyro axes (non-orthogonality) and gyro scale factor error. Once gyro non-orthogonality/scale-factor errors are determined, the remaining ten sequences are used to calculate accelerometer scale factor error, scale factor asymmetry, and misalignment relative to "mean" gyro reference axes. Mean gyro reference axes (or MARS - Mean Angular Rate Sensor axes) are defined as the orthogonal coordinate frame that best fits the actual gyro input axes. This corresponds to the MARS Frame X and Y axes being symmetrically oriented relative to B Frame X/Y axes around the B Frame Z axis (and similarly by permutation for the MARS Frame Y/Z and Z/X axes).

Accelerometer scale factor and asymmetry errors are determined from vertical average acceleration measurement after removal of known vertical specific force reaction against local gravity. The remaining sensor errors are calculated from horizontal average acceleration before/after difference measurements as discussed on the previous chart. Misalignment of the sensor assembly relative to the test fixture mount are computed from measurements of the inertial calculated attitude orientation with corrections for previously determined sensor error effects.

## **PRECISE ROTATION TEST FIXTURE ANGLE POSITIONING AND READOUT ACCURACY IS NOT REQUIRED**

- **ROTATION TEST DIRECTLY MEASURES SENSOR ERROR EFFECTS**
  - **PRECISION ROTATION FIXTURE READOUT CAPABILITY NOT REQUIRED**
- **ERRORS IN ROTATION ANGLE EXECUTION HAVE SECOND ORDER IMPACT ON TRANSFORMED ACCELERATION OUTPUT MEASUREMENTS**
  - **E.G., FOR A  $\delta K_{\gamma\gamma}$  GYRO SCALE FACTOR ERROR, A 0.1 % ROTATION ERROR WILL GENERATE 0.001  $\delta K_{\gamma\gamma}$  ERROR IN DETERMINING  $\delta K_{\gamma\gamma}$ . FOR  $\delta K_{\gamma\gamma} = 0.1\%$  THE  $\delta K_{\gamma\gamma}$  DETERMINATION ERROR WILL BE 0.0001% OR 1 PPM (PARTS PER MILLION) - TYPICALLY NEGLIGIBLE IN THE SYSTEM ERROR BUDGET**
  - **A REPEATED TEST SEQUENCE CAN BE USED IF NEEDED TO CONVERGE LARGE INITIAL SENSOR ERRORS**
  - **CONCLUSION: 0.1 % ROTATION TEST FIXTURE POSITIONING ACCURACY IS ACCEPTABLE**

## **PRECISE ROTATION TEST FIXTURE ANGLE POSITIONING AND READOUT ACCURACY IS NOT REQUIRED**

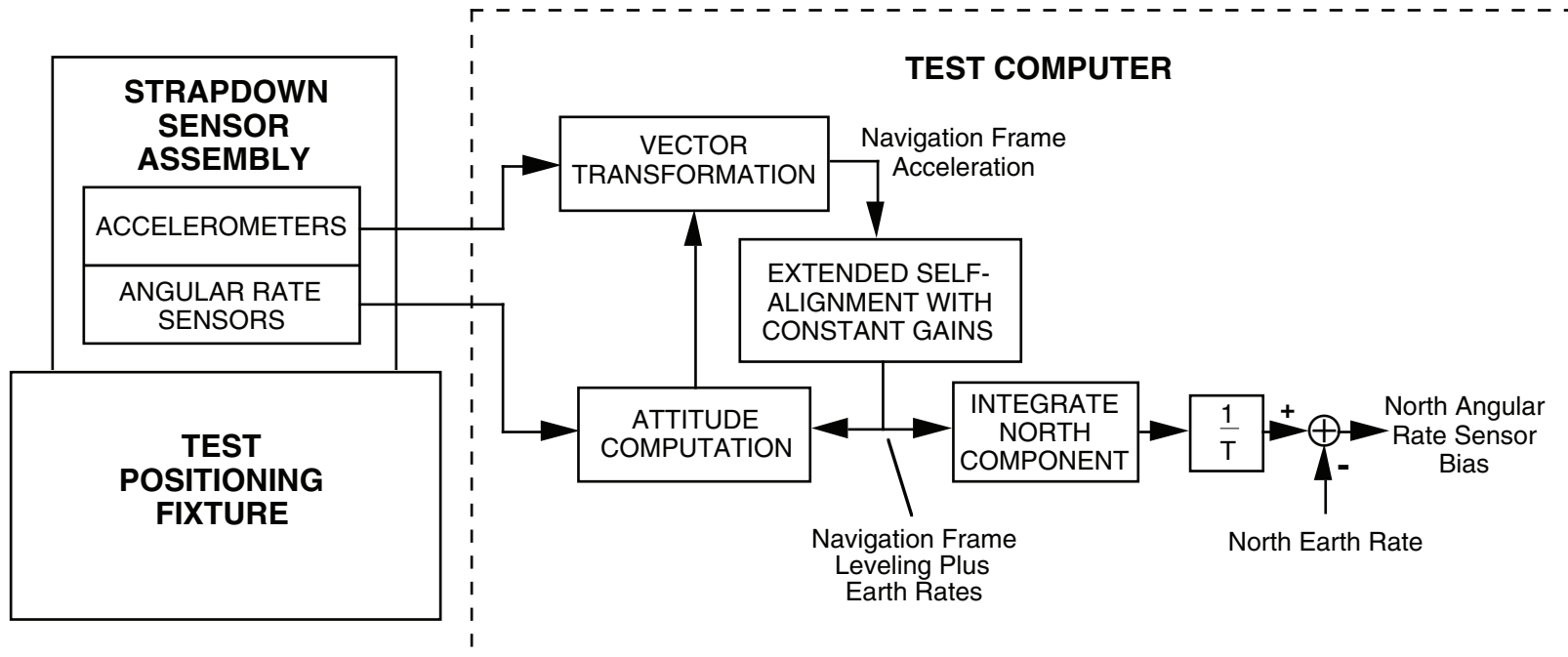
An important characteristic of the Strapdown Rotation Test concept is that it implicitly does not require precise rotation test fixturing for execution. Precision is not required in rotation angle execution and precision rotation-fixture angle read-outs are not required, even though the test is designed to measure sensor misalignment errors to better than one arc-second accuracy. This is because basic output measurements for the test (the change in averaged transformed specific force across each rotation sequence) provide direct measurements of the sensor errors being determined. Rotation angle measurements are not required to make the measurements and errors in executing the rotations only affect sensor determination accuracy to second order.

The chart provides an example of the impact of rotation error on rotation sequence Number 1 on page 521C (a 360 degree rotation about the horizontal Y axis) whose measurements are used to calculate Y axis gyro scale factor error. The difference in the before/after averaged transformed specific force measurements for this test is  $2 \pi g \delta K_{YY}$  where  $g$  is local gravity magnitude and  $\delta K_{YY}$  is the Y gyro scale factor error. The Y gyro scale factor error is calculated by dividing the before/after difference by  $2 \pi g$ . But if there is a 0.1% error in executing the 360 degree rotation, the before/after measurement will be  $(1 + 0.001) \times 2 \pi g \delta K_{YY}$ , not  $2 \pi g \delta K_{YY}$ . Division by  $2 \pi g$  will then produce a value for Y gyro scale factor error of  $\delta K_{YY} \times (1 + 0.001)$ , or a test measurement error of  $0.001 \delta K_{YY}$ . For a  $\delta K_{YY}$  of 0.1%, the error in the calculated  $\delta K_{YY}$  would be 0.0001% or 1 ppm (parts-per-million). A 1 ppm gyro scale factor determination error is generally negligible in a strapdown system error budget.

For cases where initial sensor errors are significantly larger than in the example above, the rotation test can be repeated, with the sensor errors corrected after each test for errors measured as a result of the previous test.

Based on the above analysis it can be concluded that 0.1% rotation test fixture angle positioning accuracy is acceptable (an easily achievable requirement for rotation fixturing) which has a major favorable impact on test fixture cost.

# STRAPDOWN SENSOR ASSEMBLY DRIFT TEST



## STRAPDOWN ASENSOR ASSEMBLY DRIFT TEST

The Strapdown Rotation Test described on page 521A provides an accurate determination of the principle sensor errors in a strapdown inertial system with two exceptions; gyro bias and gyro random output noise. These two error types can be evaluated using a "Strapdown System Drift Test" setup as depicted in the chart.

For the drift test setup illustrated in the chart, the sensor assembly (or strapdown system) is mounted to an angular positioning fixture that can orient the particular gyro being tested with its input axis along the horizontal north direction. An extended strapdown system alignment is then performed (as on page 120) in which the alignment gains are fixed after alignment initialization transients have dissipated. The estimated north earth rate component feedback into the attitude integration process is then averaged over a long enough time period to average out gyro noise effects (random output noise and pulse quantization). The averaging process is performed as the integrated north earth rate estimate divided by the integration time. For a long enough integration time (to attenuate sensor noise effects), the averaged north earth rate estimate will be in error primarily from north gyro bias (particularly if a rotation test is first used to measure and correct the other system sensor errors). Subtracting the true north rate component (earth rate magnitude multiplied by cosine latitude) from the averaged estimate then provides the desired measurement of north gyro bias.

The motivation behind a north orientation for the gyro under test is to minimize the sensitivity of gyro earth rate input to sensor assembly and test fixture heading misalignment. Heading misalignment of a sensor assembly couples cross-axis horizontal earth rate components into the gyro. Because horizontal earth rate is north (has no east component), heading misalignment of a north pointing gyro has only a second order effect on its earth rate component input. Because the sensor assembly test fixture may not be mechanically stable relative to the earth (e.g., when mounted in a thermal chamber to evaluate gyro bias at different temperatures), insensitivity to heading alignment can be an important factor for accurate evaluation of gyro bias.

Gyro random output noise can also be evaluated with the test setup in the chart by measuring the randomness on the horizontal earth rate estimates input to the attitude computation process. Alternatively, the estimated horizontal earth rates can be recorded for a series of standard duration strapdown system alignments. The variation about the mean for the measurements provides a measure of gyro random output noise along each horizontal earth rate estimation axis.

## **INS VAN TESTING**

- **PURPOSE – TEST INS IN A MOVING VEHICLE TO EVALUATE COMPOSITE SYSTEM PERFORMANCE**
  - **RESULTS INTERPRETABLE BY NON-ENGINEERS**
  - **EASILY CONTROLLED TEST**
  - **FAIRLY STRAIGHTFORWARD DATA EVALUATION**
  - **HIGH YIELD DATA OUTPUT**
    - > **POSITION ERROR**
    - > **VELOCITY ERROR BY STOPPING OR FROM POSITION ERROR RATE OF CHANGE**
  
- **SPECIAL REQUIREMENTS**
  - **TEST VAN WITH PROPER POWER INTERFACE**
  - **CHARTED ROAD TEST COURSE WITH IDENTIFIED LAND MARKS AND ASSOCIATED LATITUDE/LONGITUDE COORDINATES (e.g., HIGHWAY OVERPASSES) – NOTE: MODERN DAY TEST SYSTEMS CAN UTILIZE A GPS RECEIVER FOR POSITION REFERENCING**
  - **RECORDING SYSTEM WITH REFERENCE CLOCK – MANUAL OR AUTOMATED**

## INS VAN TESTING

INS van testing is the testing of an INS in a moving ground vehicle (e.g., a truck or van). Van tests are designed to evaluate the system in a moving vehicle where actual "point a to point b" navigational positioning accuracy can be assessed.

The advantage of van tests is that the test results are easily interpreted by non-engineers (i.e., the system has to be operating properly if it can accurately navigate by itself between two remote locations. In a laboratory, the system navigation outputs are stationary "in a perfect system", which is also the case for a system that is not functioning at all. Engineering personnel who "understand" the operating characteristics of an accurate INS must "interpret" laboratory test data to "assure" that the system is truly operational, and will indeed operate properly when in a moving vehicle).

Other advantages of van testing are that the tests are easily controlled (compared to flight testing in a aircraft), data evaluation is fairly straight forward (actual van position reference data is readily attainable), and the tests provide a high yield of data output points per unit test time (positioning error, and also velocity error through periodic stopping of the van where the velocity error then equals the INS velocity output, or by the rate of change of the high yield position error data using suitable smoothing filters).

To perform van tests, a test van must be outfitted with the proper power interface to operate the INS. This generally entails the need for a motor driven electrical generator (two if back-up capability is desired). A road test course must be established prior to the actual van tests with clearly identified landmarks and known latitude and longitude (e.g., highway overpasses with detailed maps). Modern day test systems can utilize a GPS receiver for position referencing. Finally, a recording system must be provided in the van to record the test data as a function of navigation time. This implies the use of a reference clock. The recording functions in the van can be performed with a set of automated test equipment, or can even be performed manually by the test operators (with pencil and paper) using a stop-watch (for example) as a time reference (between position measurements).

## **STRAPDOWN INS VAN TEST COURSE DESIGN CONSIDERATIONS**

- **ALIGN HEADING**
- **ALIGN VERSUS CRUISE HEADING**
- **CLOSED-COURSE VERSUS STRAIGHT RUN**
- **TIME PERIOD FOR CLOSED-COURSE TRAJECTORIES RELATIVE TO SCHULER PERIOD**
- **WARM-UP TIME AND ALIGNMENT TIME**
- **ALIGNMENT AREA ACCESS TO NAV COURSE**
- **TRAFFIC PATTERNS**
- **DRY RUN**

## **STRAPDOWN INS VAN TEST COURSE DESIGN CONSIDERATIONS**

The design of the particular road course to be driven for a strapdown INS van test should be based on the operating conditions that impact strapdown INS performance. The slide lists some of the pertinent factors that should be considered.

The alignment direction (North, East or otherwise) impacts the strapdown gyro error component along the East axis. Since the East gyro error during alignment determines heading alignment accuracy, the characteristics of particular gyros in the system will impact alignment accuracy differently, depending on their orientation with respect to East.

The navigation heading of the INS relative to the alignment heading has a pronounced influence on system performance (due to the potential canceling or amplification of accelerometer and gyro errors from initial alignment tilt and heading errors). Depending on whether the test course is straight or closed (circular), horizontal strapdown sensor error effects can propagate or cancel each other. For closed-course trajectories, the time period the course is traversed relative to the 84 minute Schuler period can have pronounced impact on system performance due to Schuler pumping.

If operational characteristics of the system are to be duplicated to the extent possible, system warm-up and alignment time allowances during van testing should be controlled. Too often, this point is overlooked, and the van test data reflects the result of a long alignment period (that reduces random gyro error effects) after a lengthy warm-up (which allows sensor turn-on transients to dissipate).

The area designated for the system initial alignment should be identified as part of the test plan to assure that desired alignment heading directions are easily obtained, and convenient access to the test course exists. Because the van test course must of necessity use existing highways, traffic patterns must also be taken into consideration in the test course design.

Finally, before actual system tests are performed, it pays to conduct a dry run of the test in the van to validate all test plans and data taking procedures.

# INS FLIGHT TESTING

- **PURPOSE – TEST INS IN OPERATIONAL ENVIRONMENT**
  - **RESULTS INTERPRETABLE BY NON-ENGINEERS**
  - **MEASURES PERFORMANCE EXPECTED IN OPERATIONAL ENVIRONMENT**
  - **FAIRLY COMPLICATED AND EXPENSIVE**
  - **DATA OUTPUT YIELD DEPENDS ON:**
    - > **COMPLEXITY OF TEST INSTRUMENTATION**
    - > **TEST AIRCRAFT FLIGHT HOUR AVAILABILITY**
    - > **WEATHER**
  
- **SPECIAL REQUIREMENTS**
  - **TEST AIRCRAFT WITH PROPER POWER INTERFACE**
  - **AUTOMATIC DATA RECORDING SYSTEM WITH REFERENCE CLOCK**
  - **ON-BOARD NAVIGATION REFERENCE**
    - > **RADIO OR GPS**
    - > **HIGHER ACCURACY INS**
    - > **VELOCITY PERFORMANCE GENERALLY DIFFICULT TO OBTAIN DIRECTLY (POSITION OR GPS AIDED INS PROVIDES CONTINUOUS HIGH ACCURACY POSITION/VELOCITY REFERENCE DATA)**
    - > **SYSTEM AND REFERENCE DATA SYNCHRONIZATION AND LEVER ARMS**
  - **TEST RANGE LIMITS**
    - > **INSTRUMENTATION**
    - > **FLIGHT PROFILES**
  - **ENSEMBLE STRUCTURE**
    - > **DIFFERENT PROFILES**
    - > **DUPLICATE PROFILES (TIME SEQUENCE)**

## INS FLIGHT TESTING

Flight testing of an inertial navigation system is the "ultimate proof" of its capability, short of operational deployment by the final user. The purpose of flight testing is to test the INS in as close to the actual operational environment as possible. The basic advantages of an INS flight test (as opposed to a laboratory test) is that the results are clearly interpretable by nonengineers and that system performance is measured in the actual expected operating environment. These benefits are costly. Flight testing is generally complicated and expensive, and test data yield can be limited by such factors as the complexity of the onboard test instrumentation, test aircraft flight hour availability, and weather conditions.

Special requirements for an INS test aircraft are to provide the required INS power interface, test data recording capability, and a navigation reference. Automatic test data recording equipment is (almost) a requirement for an INS flight test. Mechanization of an accurate in-flight navigation reference for comparison with INS data introduces complications not present on the ground. Radio navigation fixes (e.g., VOR/DME) or a "known" higher accuracy INS have been used for this purpose with varying degrees of success. Modern day test aircraft can utilize a GPS receiver for position referencing.

In-flight INS velocity accuracy measurements are generally more difficult to obtain than position accuracy measurements due to the difficulty in obtaining an accurate on-board velocity reference, and the limited number of position measurements (per unit time) for velocity inference from the position data. A position or GPS aided INS can be utilized as a continuous high accuracy position and velocity reference. An additional complication during flight testing is the need to accurately time synchronize the recorded INS and position/velocity reference data. During maneuvers, for example, synchronization errors can give rise to erroneously large velocity differences between an accurate INS and velocity reference. Finally, lever arm effects must be taken into account for velocity accuracy measurement during rotational maneuvers (i.e., distance between the INS being tested and the velocity reference).

Flight testing must live within the confines of the selected flight test range limits. Test instrumentation associated with a particular test site (ground tracking radar for example) may only have a limited range or field of view, hence, can only provide reference data over a limited portion of air space. Altitude restrictions in particular areas may not permit the more accurate low altitude radio aid fixes (e.g., VOR/DME). Flight test profiles must be designed to accommodate the test range limits encountered.

The flight test profiles must be structured with regard to eventual performance ensemble averaging on the data from each flight. These considerations must account for the number of identical flight profiles required for a valid statistical ensemble, as well as the number of different flight profiles needed to properly simulate the expected range of system application environments anticipated. With regard to duplicate profiles, it is important to recognize in flight testing that range and airport flight constraints may make it difficult to produce specified mission profiles in the planned time schedule from the start of navigation.

## **STRAPDOWN INS FLIGHT TEST PROFILE DESIGN CONSIDERATIONS**

- **ALIGN HEADING**
- **ALIGN VERSUS CRUISE HEADING**
- **TRANSPORT RATE HEADING ERROR COUPLING – WEST BEST, EAST WORST**
- **CLOSED-COURSE VERSUS STRAIGHT RUN**
- **TIME PERIOD FOR CLOSED-COURSE TRAJECTORIES RELATIVE TO SCHULER PERIOD**
- **HIGH BANK VERSUS FLAT TURNS**
- **MANEUVERS (e.g., JINKING, HOLDING PATTERN, SNAP ROLL)**
- **WARM-UP TIME AND ALIGNMENT TIME**
- **ALIGNMENT LATITUDE**
- **SCHULER ERROR RUN-OUT AFTER LAND – OBSERVE VELOCITY ERROR PEAK**
- **REALISM OF FLIGHT PROFILE FOR PERFORMANCE BEING EVALUATED**

## STRAPDOWN INS FLIGHT TEST PROFILE DESIGN CONSIDERATIONS

In addition to accommodating flight test range and instrumentation constraints, the flight test profile must be designed so that "all" INS performance capabilities (or limitations) are thoroughly exercised. The slide lists the flight test design considerations for a strapdown INS. As can be seen, many of the flight profile design considerations parallel those for the van test course design discussed in a previous slide. The considerations unique to flight testing are discussed below.

The principle difference between flight and ground testing is the large transport rates (velocity relative to the earth) that can be developed in the air as compared to on the ground (relative to earth rotation rates). Depending on whether the transport rate adds to or subtracts from earth rate, INS heading error coupling effects amplify differently. In general, Westerly flights benefit and Easterly flights degrade INS performance due to the subtraction of transport from earth rates when flying West, and addition when flying East.

Because strapdown INS gyro misalignment errors rectify for rotation axes that are skewed relative to orthogonal sensor axes, the bank angle held during lengthy continuous turns (e.g., holding patterns) will impact the degree of heading error build-up due to gyro misalignment errors. In general, flat continuous turns minimize gyro misalignment coupling effects.

Flight maneuvers simulating expected user aircraft mission segments should be performed to assure proper system operation. Classic maneuver patterns that excite particular strapdown INS sensor error effects are the jinking evasive maneuver, extended turn holding pattern, and snap roll.

The alignment latitude used for the flight tests should be considered since this can have a significant impact on system performance. If high latitude alignments are anticipated in the operational environment, it might be useful to demonstrate system accuracy after alignment at a high latitude airport, at least for some of the flight-tests.

Regarding velocity error performance, if possible, the test plan should include a recording of INS velocity after the aircraft has landed and been brought to a stop. Under this condition, a precise velocity error measurement can be taken which, is typically, the worst case for the flight. With regard to "close-out" velocity data measurements, it is helpful to provide up to 42 minutes on the ground for post-flight velocity data observation so that Schuler peaks can be clearly recorded.

Finally, the flight test profile should be constructed so that it realistically simulates the user missions for which particular performance parameters are to be evaluated. For example, strike type missions require high velocity accuracy at the target for weapons delivery (not at the return base), and strike missions prior to target engagement generally do not involve highly maneuvering air-to-air combat (which can introduce errors in strapdown systems.). On the other hand, air-to-air combat missions where high maneuvering is common, generally do not require high accuracy velocity data, but only accurate position data for navigation which is less vulnerable to maneuver induced error effects. It is common for INS flight testing, to utilize a

## **STRAPDOWN INS FLIGHT TEST PROFILE DESIGN CONSIDERATIONS (CONTINUED)**

"composite" mission profile which, during a single flight, exercises the INS over all expected mission maneuver profiles anticipated. If the INS displays high position and velocity accuracy during such a test, there is no question that it will be capable of performing in any of the missions used to construct the composite profile. On the other hand, if composite mission performance is marginal (or "out-of-spec"), this may lead to an erroneous conclusion that the system is not capable of performing accurately in the individual missions. It should also be recognized that an INS dedicated to performance testing is usually freshly calibrated using the "best" of the available sensors. Under these conditions, such an INS should perform better than a typical production unit, hence, should be stressed by more difficult flight test profiles than might be normally encountered, to uncover performance deficiencies.

**NOTES**

**NOTES**

# **SUMMARY**

# SUMMARY

- **MANY SIMILARITIES BETWEEN STRAPDOWN AND GIMBALED INERTIAL NAVIGATION SYSTEMS**
  - **INERTIAL POSITION/VELOCITY EQUATIONS**
  - **BASIC INITIAL ALIGNMENT EQUATIONS**
  - **BASIC ERROR BEHAVIOR**
  - **CRITICALITY OF SENSOR PERFORMANCE**
  - **THERMAL, PACKAGING DESIGN PHILOSOPHY**
  - **TESTING**
  
- **BASIC DISTINCTIONS BETWEEN STRAPDOWN AND GIMBALED INERTIAL NAVIGATION SYSTEMS**
  - **NO GIMBALS FOR STRAPDOWN**
  - **ADDITIONAL STRAPDOWN COMPUTATIONAL REQUIREMENTS FOR ATTITUDE REFERENCE FUNCTIONS**
    - > **NEGLECTIBLE PENALTY DUE TO COMPUTER TECHNOLOGY ADVANCES**
  - **UNIQUE STRAPDOWN SENSOR ERROR MECHANISMS CREATED BY BODY MOUNTED ENVIRONMENT**
    - > **IMPOSES MORE SEVERE ACCURACY REQUIREMENTS ON STRAPDOWN SENSORS (ERROR MECHANISMS, CALIBRATION INTERVAL)**
    - > **STRAPDOWN SYSTEM ACCURACY MORE SENSITIVE TO FLIGHT PROFILE (IMPORTANCE OF REALISTIC FLIGHT PROFILES AND ERROR CRITERIA IN EVALUATION)**

## SUMMARY

This and the next chart are an attempt to crystallize some of the more significant aspects of strapdown inertial navigation technology as it relates to gimbale systems, and with regard to its current limitations, capabilities, and growth potential.

Many similarities exist between strapdown and gimbale inertial navigation systems, hence, much of the design experience gained in the development of gimbale systems can be applied to strapdown system design. Some of the areas where design similarities exist are in the inertial position/velocity equations, the basic initial alignment equations, basic performance characteristics in response to sensor error (e.g., Schuler response and long term drift), the criticality of sensor performance to achieve navigational accuracy requirements (e.g., gyro bias accuracy), system thermal/packaging design philosophy, and several test techniques.

On the other hand, because of the fundamental difference in the mechanization concept for strapdown compared to gimbale systems, several distinctions clearly exist between the two inertial navigation concepts. The principle difference, of course, is the elimination of the gimbal assembly for the strapdown system, which reduces overall system costs and improves reliability. These benefits are achieved, however, for the penalty of requiring additional computer operations in strapdown systems (to analytically perform the accelerometer referencing function that is achieved mechanically in a gimbale system), and the need for more accurate strapdown sensors to meet overall system accuracy requirements when operating in a dynamic rotational body mounted rate environment.

The added computer burden for the strapdown system introduces no significant penalty today due to the advent of the low cost high speed microprocessor for flight computer operations. The strapdown performance issue is not as easily dismissed. Artificial maneuvers can be hypothesized for strapdown systems (e.g., continuous high speed rolling about a horizontal axis) that will eventually deteriorate the performance of the most accurate rate gyro type strapdown system. However, in realistic fighter aircraft maneuver profiles, the strapdown system of today is capable of providing required performance at an accuracy level comparable to traditional medium accuracy (e.g., 0.8 nmph CEP) gimbale systems.

## **SUMMARY (CONTINUED)**

- **RING LASER GYRO (RLG) HAS MADE MEDIUM ACCURACY (1 NMPH CEP) STRAPDOWN INERTIAL SYSTEMS PRACTICAL**
- **THE RLG AND RECENTLY, THE FIBER OPTIC GYRO (FOG), HAVE MADE MEDIUM AND LIMITED HIGHER ACCURACY GIMBALED SYSTEMS OBSOLETE**
  - **HIGH ACCURACY BALLISTIC MISSILE GUIDANCE SYSTEMS CONTINUE TO UTILIZE GIMBALED TECHNOLOGY**
- **MODERATE ACCURACY STRAPDOWN APPLICATIONS (<1 DEG/HR) HAVE TRANSITIONED FROM LOW COST CONVENTIONAL MOMENTUM WHEEL GYROS TO LOW COST RLGs, FOGs AND QUARTZ RATE SENSORS**
  - **MAJOR INVESTMENTS BY INERTIAL SENSOR GROUPS ARE MAKING SILICON BASED MEMS (MICRO ELECTRO-MECHANICAL SYSTEM) SENSOR TECHNOLOGY A SERIOUS COMPETITOR FOR FUTURE LOW COST STRAPDOWN SYSTEM APPLICATIONS**
- **SKEWED SENSOR REDUNDANCY HAS BEEN UTILIZED SUCCESSFULLY IN COMMERCIAL AIRCRAFT REDUNDANT INERTIAL SYSTEM APPLICATIONS**

## SUMMARY (CONTINUED)

The key factor that has made medium accuracy (1 nmph CEP) strapdown inertial navigation practical was the advent of the ring laser gyro (RLG) rate sensor. This unique instrument provides the long term accuracy required of a strapdown rate sensor for low cost and with high reliability due to its simple construction and absence of rotating friction producing parts. Strapdown inertial navigation systems using RLGs and recently, fiber optic gyros (FOGs), have made gimbalede medium and higher accuracy inertial systems obsolete. An exception is ballistic missile inertial guidance applications that continue to utilize high accuracy gimbalede inertial system technology.

Moderate accuracy (< 1 deg/hr) low cost strapdown systems (e.g., for tactical missiles and attitude / heading reference systems - AHRS) traditionally mechanized with low cost conventional momentum wheel gyros, have transitioned to low cost RLG, FOG and quartz rate sensor strapdown technology. Recent funding commitments by major inertial sensor manufacturing groups are making low cost silicon based MEMS (micro electro-mechanical system) inertial sensors a serious competitor for future low cost strapdown system applications.

Skewed sensor redundancy has been utilized successfully in some commercial aircraft redundant inertial system applications.

**NOTES**

# **SUPPLEMENTAL MATERIAL**

## **SUPPLEMENTAL MATERIAL TOPICS**

- **STRAPDOWN SYSTEM CONFIGURATIONS**
- **SCULLING AND CONING COMPUTER ALGORITHMS**
- **SENSOR COMPENSATION FOR CONING/SCULLING ALGORITHMS**
- **COVARIANCE PROPAGATION ALGORITHMS**
- **DIRECTION COSINE MATRIX ORTHONORMALITY PROPERTIES**
- **NAVIGATION ERROR EFFECTS AT HIGH / LOW LATITUDES**
- **RATE GYRO DIGITAL INTEGRATION ERROR UNDER VIBRATION**

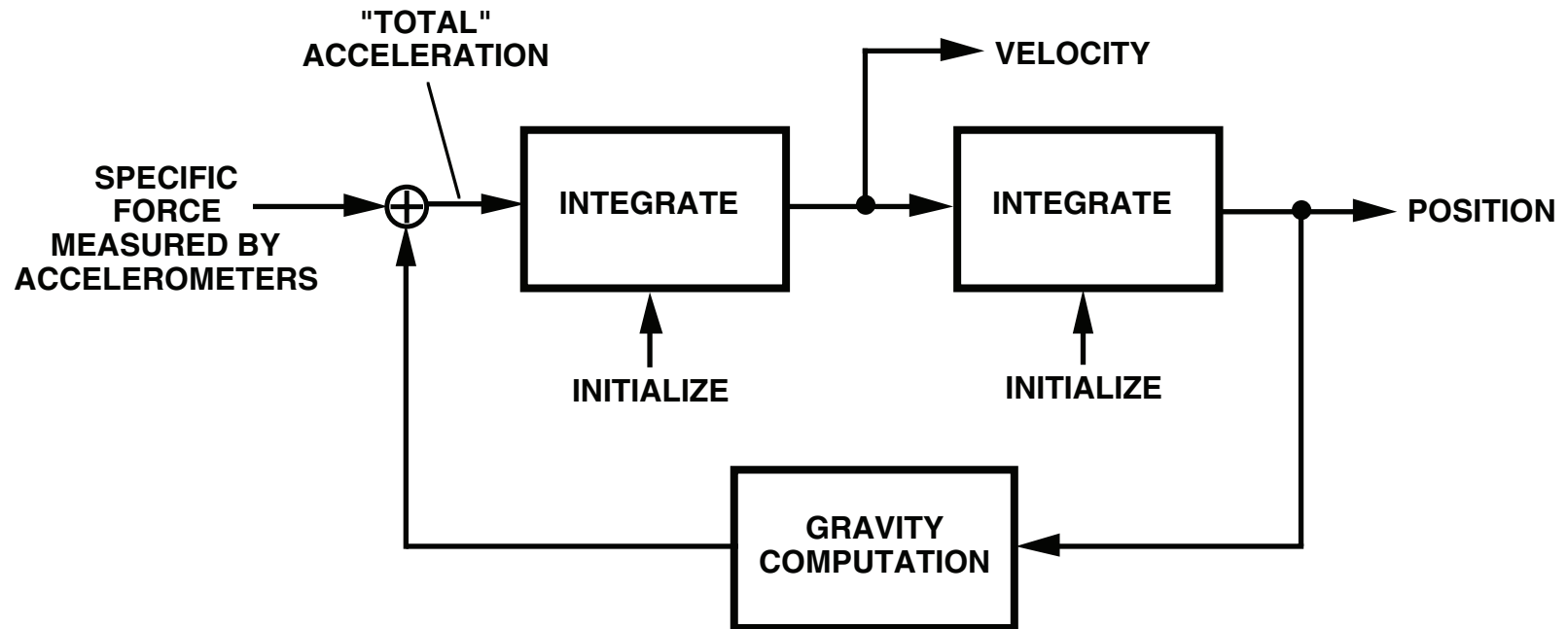
## SUPPLEMENTAL MATERIAL TOPICS

This section contains additional supplemental charts generated to expand upon particular topics covered during the basic course. Some of this material is presented as part the last half course day, the particular items selected being based on attendee interest. Following is a table of contents for the supplemental material that follows.

### TABLE OF CONTENTS

<u>TOPICS</u>	<u>PAGE NUMBER</u>
STRAPDOWN SYSTEM CONFIGURATIONS .....	542
SCULLING AND CONING COMPUTER ALGORITHMS.....	558
SENSOR COMPENSATION FOR CONING/SCULLING ALGORITHMS.....	574
COVARIANCE PROPAGATION ALGORITHMS .....	584
DIRECTION COSINE MATRIX ORTHONORMALITY PROPERTIES.....	590
NAVIGATION ERROR EFFECTS AT HIGH / LOW LATITUDES .....	594
RATE GYRO DIGITAL INTEGRATION ERROR UNDER VIBRATION .....	602

# FUNDAMENTAL INERTIAL NAVIGATION CONCEPT



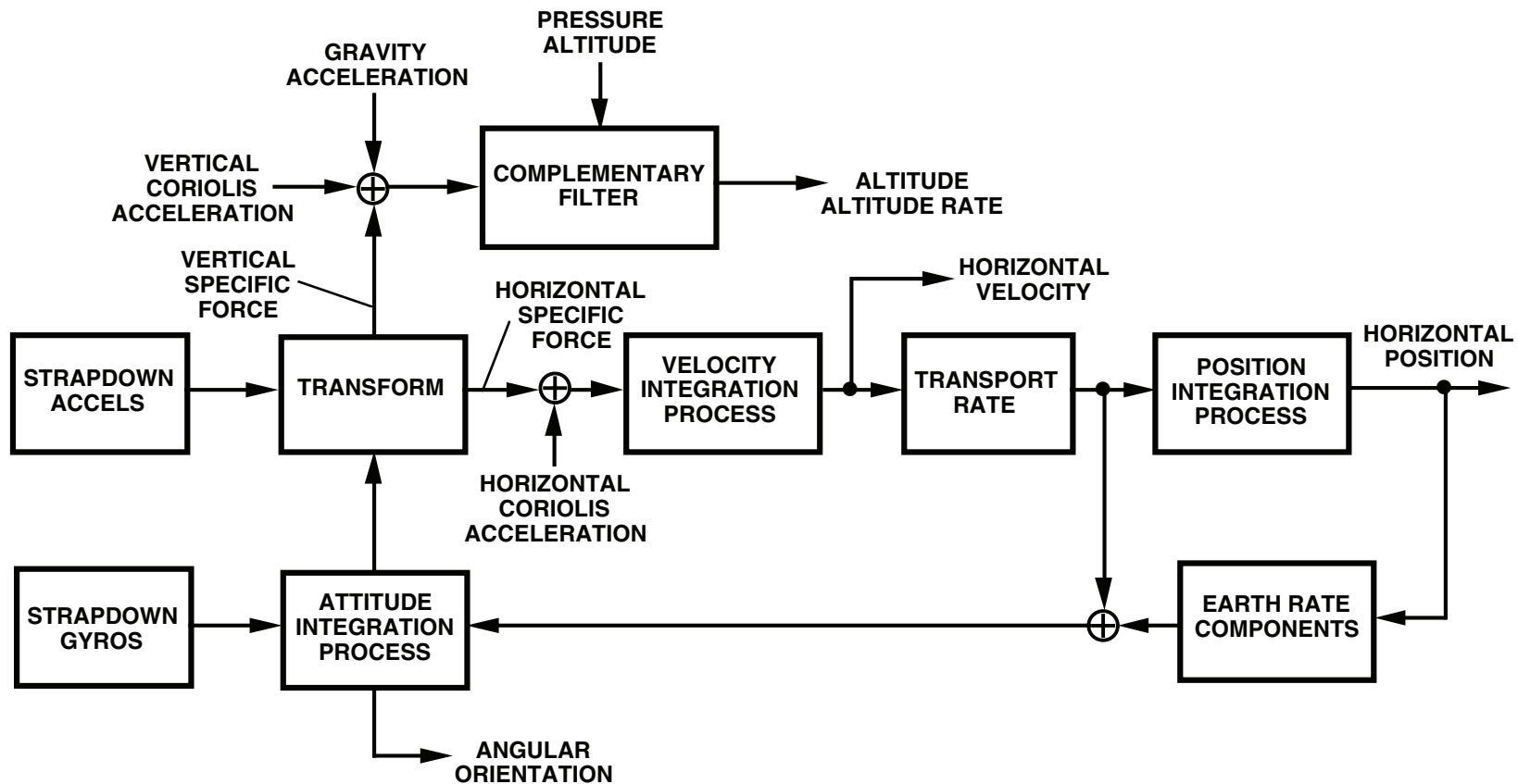
## FUNDAMENTAL INERTIAL NAVIGATION CONCEPT

Inertial navigation is the process of integrating acceleration to compute continuous outputs of current velocity and position. As for all integration processes, the velocity and position integrators must be initialized with starting velocity/position values prior to initiating the inertial navigation process. The acceleration input to the velocity integration (commonly referred to as "total acceleration") has two principle components; specific-force acceleration (measured by accelerometers) and gravitational acceleration (a property of local space). The gravity acceleration cannot be measured so instead, must be computed from a pre-determined gravity model as a function of the calculated position.

Inertial navigation systems implement the chart's concept in various forms (as illustrated in the subsequent charts). Gyros are also utilized in these system configurations that, through appropriate computational routines, determine the angular orientation of the accelerometers. Accelerometers only measure the specific-force component along their input axes. Their angular orientation is also required to determine the direction of the measured specific-force (implicit in the definition of terms in the chart as being vector quantities - i.e., having magnitude and angular direction).

The charts to follow also contain other smaller "Coriolis" acceleration terms input to the velocity integration. These terms typically account for angular rotation of the coordinate frame used for the velocity vector component description, and for the definition of velocity as being relative to a coordinate frame that may also be rotating (e.g., velocity relative to a coordinate frame fixed to the rotating earth).

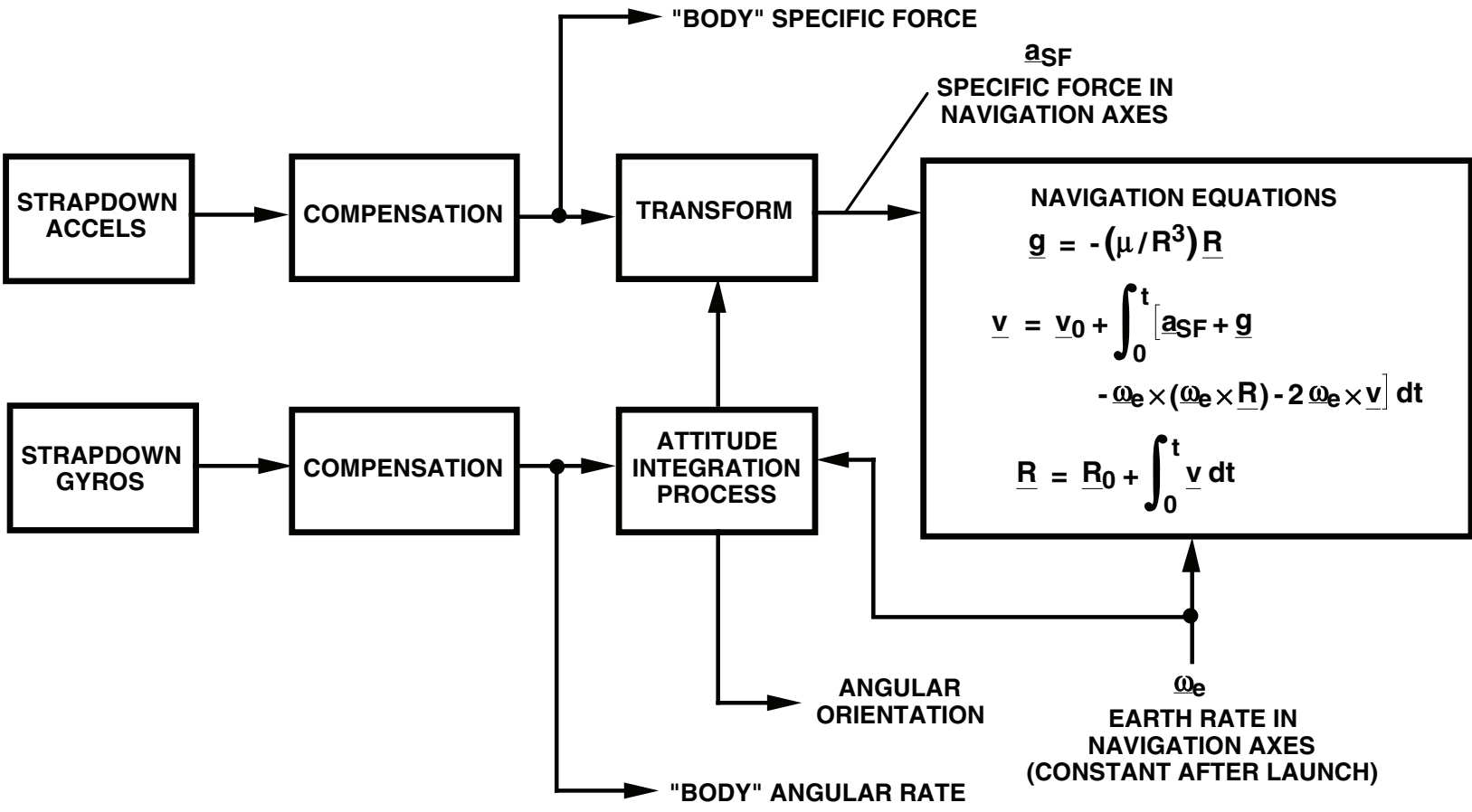
# STRAPDOWN INERTIAL NAVIGATION SYSTEM OPERATIONS



## **STRAPDOWN INERTIAL NAVIGATION SYSTEM OPERATIONS**

The chart describes the classical strapdown inertial navigation system configuration (summarized on page 61A). The chart shows the velocity/position integrations, the earth-rate/transport-rate feedbacks into the attitude integration to maintain a locally level navigation computation frame (for the velocity integration), and the pressure altitude stabilized vertical channel integration process (the complimentary filter) to calculate altitude/altitude-rate. The "strapdown platform" in this chart (strapdown sensors feeding the attitude-integration/specific-force-acceleration-transformation functions) is common to all the described system configurations that follow.

# TACTICAL MISSILE TANGENT PLANE NAVIGATION (NAVIGATION AXES TANGENT TO EARTH AT LAUNCH POINT)



## **TACTICAL MISSILE TANGENT PLANE NAVIGATION (NAVIGATION AXES TANGENT TO EARTH AT LAUNCH POINT)**

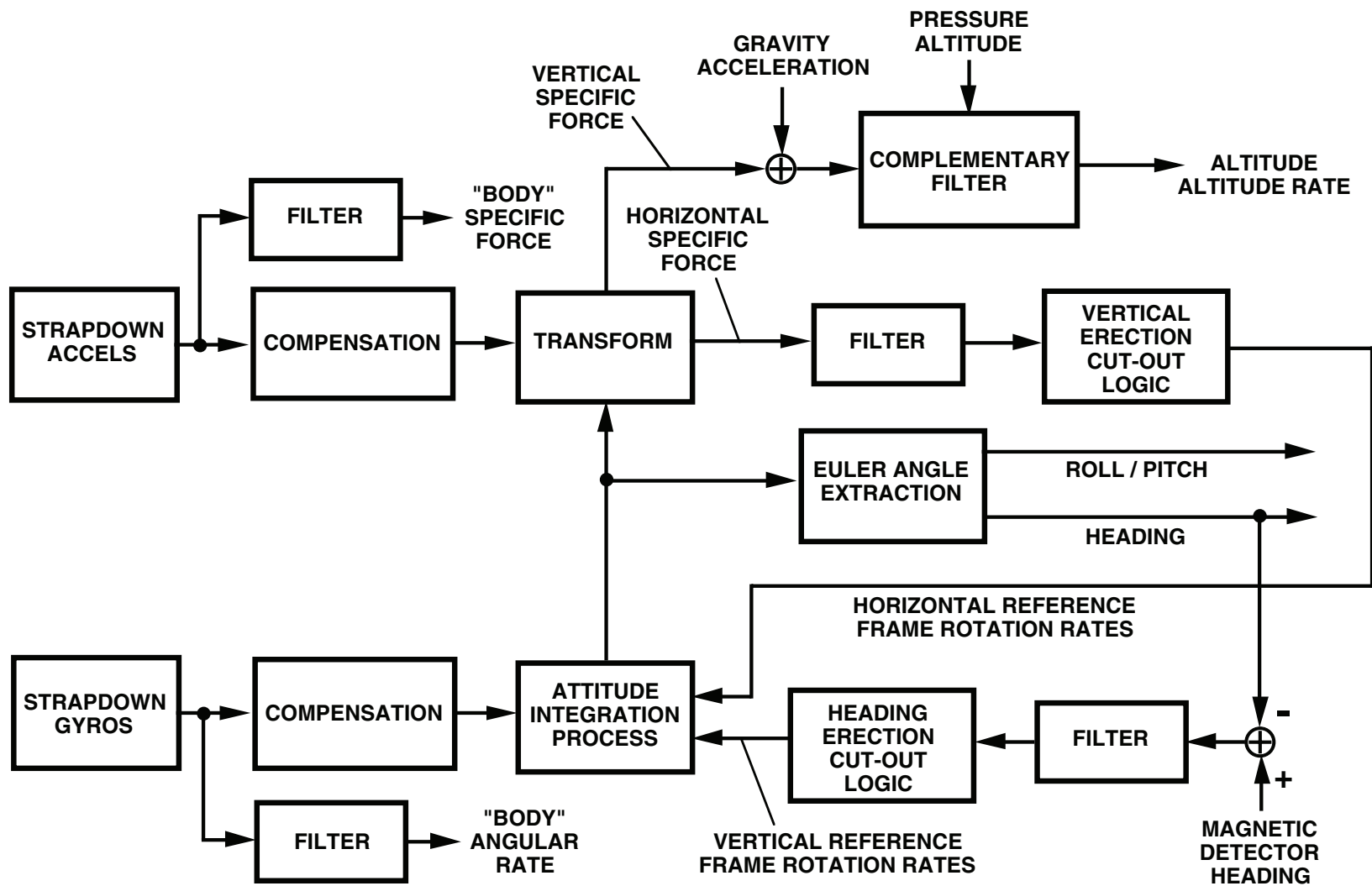
Tactical missile midcourse inertial guidance systems compute missile position inertially while out of range of the terminal seeker. Missile steering guidance toward its intended target is generated by steering the missile along a position vector to the target. The missile-to-target position vector is calculated by subtracting the inertially computed missile position from target position provided by electro-magnetic transmission uplink to the missile from the launching vehicle (e.g., an aircraft). Target position is identified by the launching vehicle by active missile tracking (e.g., by radar). When the missile-to-target vector magnitude is small enough, the target falls within the field-of-view and range of the terminal seeker. After target acquisition by the terminal seeker, guidance command authority is transferred to the missile seeker for the terminal homing guidance phase.

Target position data is provided on the uplink in a coordinate frame that is known in the missile and the launching vehicle (e.g., tangent plane coordinates). A tangent plane coordinate frame is defined to be fixed to and tangent to the earth at some specified earth referenced location. For a tangent plane tactical missile midcourse guidance configuration, the tangent plane is typically referenced to the missile launch point.

The chart illustrates a tactical missile midcourse guidance system using tangent plane coordinates for inertial navigation. Earth rate components (of  $\underline{\omega}_e$ ) in the tangent plane (TP) coordinate frame are used to bias the gyro rate data in the attitude computation, keeping the attitude reference frame parallel to TP coordinates. Specific-force from the accelerometers is transformed to the TP Frame using the computed attitude data, and then integrated with appropriate gravity/Coriolis additions to compute velocity ( $\underline{v}$ ) and position relative to earth's center ( $\underline{R}$ ) in TP coordinates. Position and velocity vectors are initialized at missile launch at  $\underline{v}_0$  and  $\underline{R}_0$ . Unlike the classical strapdown inertial navigation approach based on locally level navigation coordinates, because the TP Frame is not locally level, there is no velocity derived transport rate term in the Coriolis acceleration term (only earth rate  $\underline{\omega}_e$  appears corresponding to the TP Frame being fixed to the earth). Because the TP navigation frame is fixed to the earth, the components of  $\underline{\omega}_e$  are constant. Gravity is approximated as being along the negative of  $\underline{R}$  with magnitude inversely proportional to the magnitude of  $\underline{R}$  squared, the proportionality factor  $\mu$  being the mass of the earth times the universal gravity constant (i.e., Newton's law of gravitation).

Also shown in the chart is compensation for gyro/accelerometer error (present for all the system configurations described in this book but omitted in some system charts for simplicity). Compensated angular-rate/specific-force are also indicated as outputs for use in other non-navigation functions (e.g., autopilot stability augmentation and guidance steering turn coordination).

# STRAPDOWN ATTITUDE / HEADING REFERENCE SYSTEM (AHRS)



## STRAPDOWN ATTITUDE / HEADING REFERENCE SYSTEM (AHRS)

An important output from a strapdown inertial navigation system (INS) is the roll/pitch/heading data derived from the computed attitude information. These signals are used for vehicle steering control (either by manual pilot or by autopilot) and in military vehicles, for weapon systems initialization/control/launch/release. For the weapon systems function, attitude output accuracy requirements are equal to the capabilities of a standard accuracy INS (e.g., 2 - 3 arc minutes one sigma including sensor assembly mounting misalignment, under all vehicle dynamic conditions). Attitude accuracy requirements for vehicle steering are more relaxed, typically being on the order of 0.5 degrees in pitch/roll and 1.0 degrees in heading under non-maneuvering or short-term dynamic maneuvering conditions. For applications where inertial navigation is not required (at the redundancy level needed to support safety critical issues - e.g., attitude information for aircraft flight control), attitude outputs can be generated from a strapdown inertial system using lower accuracy (compared to INS requirements) inertial components. Such systems have had wide utilization in aircraft applications. This type of device has been designated as an Attitude / Heading Reference System (AHRS). The "attitude" in AHRS refers to traditional aircraft flight display terminology where "attitude" denotes aircraft orientation relative to the local vertical (i.e., pitch and roll).

Roll / pitch outputs from an INS provide a faithful indication of vehicle vertical orientation under all dynamic conditions. This is because the implementation of an INS creates a locally level reference "platform" by rotating the reference about the horizontal with the system determined values of horizontal earth rate plus transport rate (i.e., "Schuler tuning"). The design goal for an AHRS is to create a similar reference platform, but using lower accuracy inertial components. Achieving this goal for an AHRS by direct Schuler tuning is not practical because the larger sensor errors would create unacceptable Schuler amplitude oscillations (see page 352). For a Schuler tuned platform (i.e., in which horizontal specific-force is integrated into horizontal velocity, divided by the distance to earth center to generate transport rate, and then used with horizontal earth rate to rotate the platform), gyro bias errors on the order of 10 degrees per hour would generate platform tilt Schuler oscillations of 2.2 degrees. Gyros in a standard aircraft INS have bias errors on the order of 0.01 degrees per hour.

The chart illustrates the general configuration of a typical strapdown AHRS showing the strapdown platform (compensated gyro angular-rates integrated into attitude and compensated accelerometer specific-force transformed to horizontal reference platform axes), feedbacks into the attitude integration process to maintain a locally level north pointing analytic reference platform, and the roll / pitch (attitude) and heading outputs. Also shown is a vertical channel implemented to generate pressure altitude compensated altitude and altitude rate through vertical specific-force input to a complimentary filter (similar to the method used to generate these outputs in an INS on page 102).

The platform level maintenance function in an AHRS is based on the assumption that the dominant specific-force measured from the accelerometers will be upward to balance local downward gravity. Therefore, for a proper leveled analytical platform reference, the transformed specific-force measurements from the accelerometers would have zero horizontal components, and

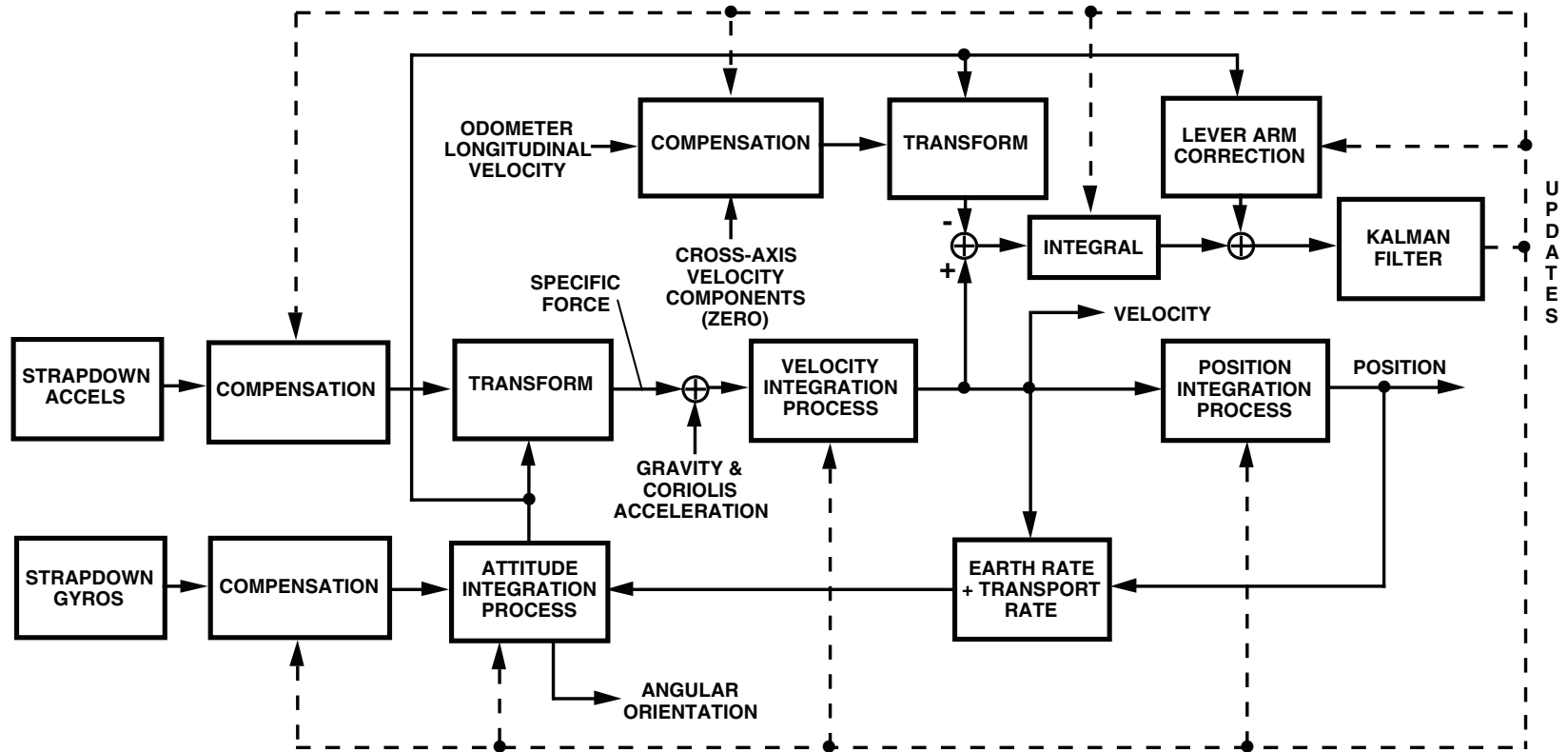
## **STRAPDOWN ATTITUDE / HEADING REFERENCE SYSTEM (AHRS) (CONTINUED)**

non-zero horizontal components would measure analytical platform tilt from horizontal. The AHRS feeds back the horizontal specific-force measurements (after filtering) to continuously correct the tilt error, thereby maintaining a level reference platform. The concept is similar to what was shown for initial leveling of an INS platform on page 115. The accuracy of such a leveling technique depends on the magnitude and characteristic of actual horizontal specific force present (i.e., variations from the assumption of only vertical specific-force). The filtering function is intended to average short term horizontal specific-force effects, hence, attenuate their impact on platform leveling. The vertical erection cut-out function interrupts leveling feed-back operations under particular vehicle maneuver conditions that indicate horizontal specific force generation (e.g., sustained angular rates, a sustained shift in horizontal specific force, or for an aircraft, a sustained moderate to large roll angle condition signifying a turn). If valid horizontal velocity is available to the AHRS from an external source (e.g., a GPS receiver/computer, or for an aircraft, true airspeed from the air data computer transformed from the longitudinal axis into the horizontal using AHRS attitude data), these signals can be differentiated and subtracted from the AHRS computed horizontal specific force to eliminate horizontal specific force as a leveling error source. For the true airspeed derived horizontal acceleration, wind variations would introduce an additional error source into leveling operations.

Due to the accuracy deficiency in AHRS gyros, the computed heading would drift at the vertical component of gyro bias unless restrained. The restraining function is provided by a magnetic heading detector input that is differenced with the computed AHRS heading to form an error signal. The heading error is fed back into the AHRS attitude integration process to continuously correct the AHRS heading. In this manner AHRS heading is maintained on the average to match measured local magnetic north referenced heading (typically accurate to within one degree of true heading). A heading erection cut-out function is included to regulate erection feed-back operations, disengaging the feed-back when the input magnetic heading is marked invalid. If the magnetic heading detector used by the AHRS was directly vehicle mounted and measuring the three orthogonal magnetic field components, these signals would be transformed to the horizontal using the computed AHRS attitude to form the magnetic detector heading input on the chart. For a magnetic detector implemented with a physical pendulum containing the magnetic sensor (e.g., similar to a classical fluid damped magnetic compass, but with an electronic output), the heading erection cut-out would also be used to disengage the feed-back under particular vehicle maneuver conditions indicating significant sustained horizontal specific force. The rationale is as follows. The horizontal component of earth's magnetic field is the signal used to indicate magnetic north. The magnetic sensor is mounted on a pendulum to keep it horizontal, hence, sensing the correct magnetic component. However, because of its pendulosity, the pendulum will shift from horizontal under sustained vehicle horizontal specific-force maneuvers, thereby sensing a portion of earth's vertical magnetic field and introducing a magnetic north heading measurement error. The filtering function in the chart would average short term horizontal specific-force effects, attenuating their impact on the heading erection process. The heading erection cut-out function would interrupt the heading control feed-back under sustained horizontal specific force.

**NOTES**

# STRAPDOWN LAND NAVIGATOR



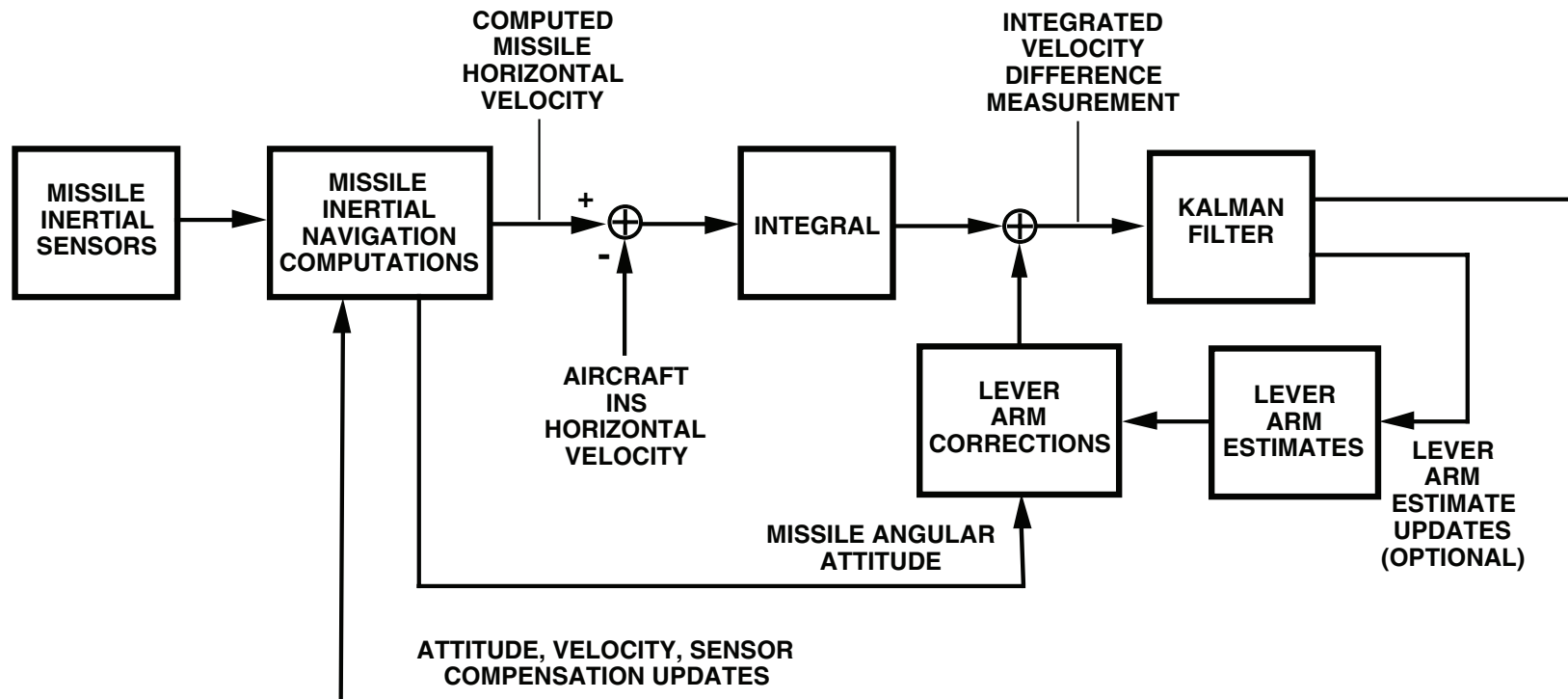
## STRAPDOWN LAND NAVIGATOR

A standard unaided inertial navigation system (INS) generally has insufficient positioning accuracy (i.e., 1 nautical mile per hour) for land-borne moving vehicle applications. A common method for increasing land-borne INS accuracy is through Kalman filter aiding using an odometer as the basic measurement input. The odometer provides velocity along the direction of vehicle travel. Assuming that this is the only velocity component (i.e., across-longitudinal-axis side-slip velocity components are zero), the odometer indicates total velocity (relative to the earth), can be transformed to locally level navigation coordinates, and compared with the equivalent INS velocity to form a velocity error signal. The concept is summarized in the chart for a classical strapdown INS (depicted on page 544), showing how the velocity error is formed, integrated, and corrected for lever arm displacement between the INS and odometer to form the measurement input to the Kalman filter (similar to the approach used on page 472 for the at-sea alignment Kalman filter).

Outputs from the Kalman filter are updates for INS attitude, velocity, position and sensor compensation errors, odometer derived velocity error sources (primarily scale factor and cross-axis misalignment), and if implemented, lever arm corrections. The Kalman filter in a land navigator is typically also configured to accept operator commanded "zero velocity update" measurements indicating that the vehicle is stationary, hence, the true velocity is identically zero. Under this condition, zero is substituted on the chart for the odometer input.

The ultimate accuracy of the odometer added INS land navigator is limited by INS heading error. INS heading error (caused by initialization error and the vertical component of gyro error) cannot be estimated by the odometer aiding measurement, hence, is limited in accuracy by the inherent capability of the unaided INS. Heading error produces cross-track velocity error in navigation coordinates equal to the product of velocity magnitude with the heading error, which then integrates into cross-track position error. Thus, the accuracy of the land navigator configuration shown is generally measured as a percentage of distance traveled (i.e., a percentage of the integral of velocity).

# IN-AIR TRANSFER ALIGNMENT KALMAN FILTER CONFIGURATION

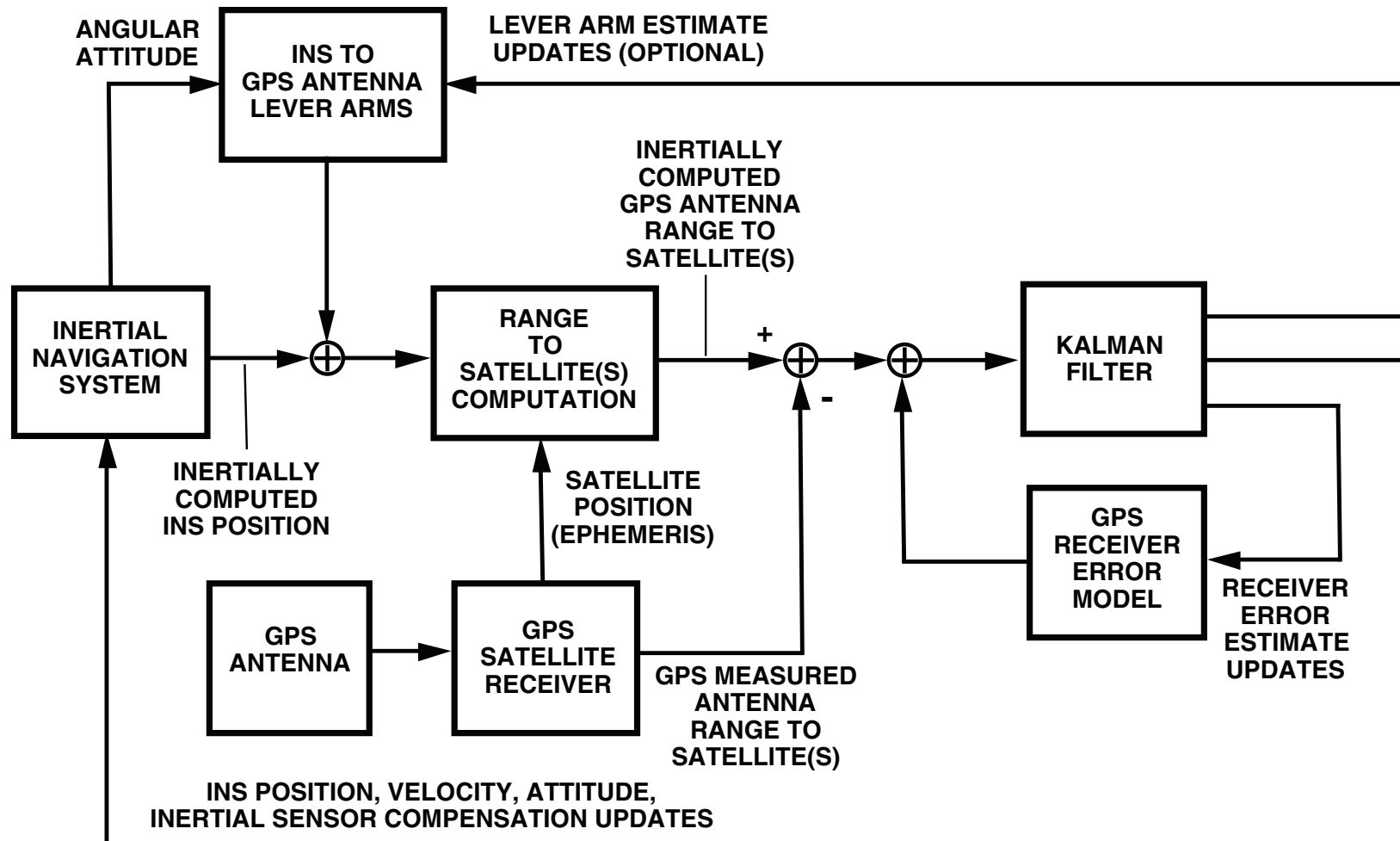


## IN-AIR TRANSFER ALIGNMENT KALMAN FILTER CONFIGURATION

An inertial navigation system (INS) in an air launched missile must be aligned prior to launch. The initial alignment function is of the classical moving vehicle type and can be executed properly with a Kalman filter similar in structure to the version illustrated on page 472 for at-sea alignment. The INS computed horizontal velocity is compared to a reference horizontal velocity input provided from the aircraft INS, integrated, corrected for lever arm displacement between the missile and aircraft INS locations, and input as the measurement to the Kalman filter. The Kalman filter performs missile INS attitude alignment together with velocity/sensor-compensation updates and, if implemented in the filter, lever arm uncertainty corrections.

Missile INS heading error propagates to the measurement through two primary paths (see page 352); through platform axis rotation rate (i.e., earth rate plus transport rate), and horizontal acceleration. In general, the missile launch sequence scenario does not permit sufficient time to depend on the generally slow earth rate path for heading error correction (particularly under wind buffeting effects which produce bending oscillations between the missile and aircraft INS, a large noise effect on the Kalman filter measurement input). In addition, if the missile INS inertial sensors have insufficient accuracy, earth rate coupled heading error measurements will be corrupted by large sensor errors, precluding accurate heading alignment. To assure good heading error observability, the acceleration/heading-error path to the measurement is amplified by intentionally generated horizontal aircraft maneuvers during the alignment period (e.g., classical repeated S-turn maneuvers consisting of sequences of roll right, turn right, roll left, turn left). The result is a rapid missile INS alignment, even with lower accuracy inertial sensors.

# GPS AIDED INS KALMAN FILTER CONFIGURATION



## **GPS AIDED INS KALMAN FILTER CONFIGURATION**

The most commonly used form of inertial navigation system (INS) aiding is with Global Positioning System (GPS) measurements. The chart depicts such an aided INS configuration based on comparing GPS receiver determined range measurements to GPS satellites with the equivalent signals generated using INS computed position.

Each GPS range measurement (called "pseudo-range" because it is not a direct range measurement) calculates the range from the vehicle-borne GPS antenna to one of several GPS satellites in view, as the measured time for an electromagnetic signal to travel from a satellite to the GPS antenna, divided by the speed of light. The GPS signal transmission time is computed as the time of arrival of the signal at the GPS antenna/receiver minus the time of signal transmission from the satellite. The signal arrival time is measured with a precision high frequency clock within the GPS receiver; the transmission time is the satellite generated time stamp on the transmitted/received signal. GPS satellite transmission time stamps are generated using precision reference clocks in each satellite that are regularly synchronized by earth based command/control to universal reference time.

The equivalent to the GPS pseudo-range measurements are also generated in the vehicle-borne GPS-aided-INS computer as the magnitude of the position vector from the center of the earth to a given satellite (obtained using satellite ephemeris data provided on the received satellite transmission signal) minus the calculated position vector from earth's center to the GPS antenna (obtained by adding the inertially computed INS position vector from earth's center to the lever arm vector distance from the INS to the GPS antenna).

The difference between the INS and GPS determined range measurements is corrected for GPS receiver errors and input as the measurement to a Kalman filter. The Kalman filter then calculates and applies corrections to the INS position, velocity, attitude, and inertial sensor compensation, to the GPS receiver error model and, if implemented, to the INS-to-GPS-antenna lever arms. The GPS receiver error model primarily accounts for GPS receiver clock time and frequency errors, both of which affect the pseudo-range measurements.

# SCULLING COMPUTER ALGORITHM

## COMPUTATION BETWEEN TRANSFORMATION CYCLES

CONTINUOUS FORM :

$$\Delta \underline{v}_{SCULLING}^B = \int_{t_m}^{t_{m+1}} \underline{\alpha}^B \times d\underline{v}^B \quad \underline{\alpha}^B = \int_{t_m}^t d\underline{\alpha}^B$$

INCREMENTAL COMPUTER ALGORITHM FORM :

$$\Delta \underline{v}_{SCULL_l}^B = \Delta \underline{v}_{SCULL_{l-1}}^B + \left( \underline{\alpha}_{l-1}^B + \frac{1}{2} \underline{\varepsilon}_{\alpha_l}^B \right) \times \underline{\varepsilon}_{v_l}^B + \frac{1}{12} \left( \underline{\varepsilon}_{\alpha_{l-1}}^B \times \underline{\varepsilon}_{v_l}^B + \underline{\varepsilon}_{v_{l-1}}^B \times \underline{\varepsilon}_{\alpha_l}^B \right)$$

$$\underline{\alpha}_l^B = \underline{\alpha}_{l-1}^B + \underline{\varepsilon}_{\alpha_l}^B$$

$$\Delta \underline{v}_{SCULLING}^B = \Delta \underline{v}_{SCULL}^B \quad (l = L)$$

$\underline{\varepsilon}_{v_l}^B$  = CUMULATIVE ACCELEROMETER PULSE COUNTS  
OVER HIGH SPEED SCULLING COMPUTATION CYCLE

$\underline{\varepsilon}_{\alpha_l}^B$  = CUMULATIVE GYRO PULSE COUNTS OVER  
HIGH SPEED SCULLING COMPUTATION CYCLE

## SCULLING COMPUTER ALGORITHM

The acceleration transformation computer algorithm configuration on page 184 is based on a two-speed approach whereby the basic transformation operation is performed at the velocity update rate and the input to the transformation operation is calculated using a high speed integration process during the time interval between velocity updates. The high speed integrals generate integrated specific-force and a sculling increment that are summed to form the input to the transformation operation. For simplicity, the high speed integration processes on page 184 are represented by continuous integrals. This chart illustrates repetitive digital algorithms that can be used to implement the high speed integration processes as high speed summing operations (at an  $l$  cycle rate) between transformation/velocity-updates (an  $m$  cycle rate).

The angular rate integral  $\alpha_l^B$  used in the sculling integration is obtained by summing integrated angular rate increments  $\epsilon_{\alpha_l}^B$ . The  $\epsilon_{\alpha_l}^B$  increments would be generated by summing integrated angular rate increment output pulses from the gyros over each  $l$  cycle. The sculling increment in the chart  $\Delta v_{SCULL_l}^B$  is generated by summing an analytical expression containing past values of  $\alpha_l^B$ , current and past values of  $\epsilon_{\alpha_l}^B$ , and current and past values of accelerometer integrated specific force increments  $\epsilon_{v_l}^B$ . The  $\epsilon_{v_l}^B$  increments would be generated by summing integrated specific force increment output pulses from the accelerometers over each  $l$  cycle. The  $\alpha_l^B$  and  $\Delta v_{SCULL_l}^B$  summing operations are executed at the  $l$  cycle rate and sampled when  $l = L$  (the number of  $l$  cycles in an  $m$  cycle) for use in the  $m$  cycle transformation routine. After sampling, the  $\alpha_l^B$  and  $\Delta v_{SCULL_l}^B$  sums would be reset to zero for initialization of  $l$  cycle summing over the next  $m$  cycle.

The analytical expression for  $\Delta v_{SCULL_l}^B$  is a second order updating algorithm (contains up to second order products in  $\epsilon_{\alpha_l}^B$  and  $\epsilon_{v_l}^B$ ) designed to provide the identical solution as the continuous integral under angular-rate/specific-force conditions modeled as a constant plus a linear ramp in time over each  $l$  cycle. The derivation for  $\Delta v_{SCULL_l}^B$  is similar to the first order algorithm development for  $S_1$  in section 4.4.1 of the Strapdown System Algorithm paper in the Strapdown Inertial Navigation Lecture Notes handout, but expanded to second order as in Section 3.3.2 of the Algorithm paper for the coning algorithm. Constant plus linear ramping angular-rate/specific-force is a reasonable approximation for actual motion during an  $l$  cycle. Structuring the algorithm to have an exact solution under particular easily modeled analytical inputs provides a simple method for validation; by assuring that the correct exact solution will be obtained under simulated angular-rate/specific-force design condition inputs. The correct exact solution is easily found by analytical integration of the continuous form integral under constant plus linear ramping angular-rate/specific-force input.

# SCULLING ALGORITHM FINITE ITERATION RATE ERROR

## BODY RATE

$$\dot{\underline{\alpha}}^B = 2\pi f \begin{bmatrix} \theta_0 \cos 2\pi f t \\ 0 \\ 0 \end{bmatrix}$$

## BODY ACCELERATION

$$\dot{\underline{v}}^B = \begin{bmatrix} 0 \\ A \sin(2\pi f t + \phi) \\ 0 \end{bmatrix}$$

## AVERAGE CONTINUOUS FORM SCULLING COMPENSATION

$$\dot{\Delta v}_z = \begin{array}{c} \text{CONSTANT ANGULAR} \\ \text{RATE APPROXIMATION} \\ \text{TERM} \end{array} + \frac{1}{2} \theta_0 A \cos \phi \left[ 1 - \frac{\sin 2\pi f T_m}{2\pi f T_m} \right]$$

$T_m =$  ACCELERATION TRANSFORMATION CYCLE PERIOD

## AVERAGE INCREMENTAL FORM SCULLING COMPENSATION

$$\dot{\Delta v}_z = \begin{array}{c} \text{CONSTANT ANGULAR} \\ \text{RATE APPROXIMATION} \\ \text{TERM} \end{array} + \frac{1}{2} \theta_0 A \cos \phi \left[ \left( 1 + \frac{1}{3} [1 - \cos 2\pi f T_l] \right) \frac{\sin 2\pi f T_l}{2\pi f T_l} - \frac{\sin 2\pi f T_m}{2\pi f T_m} \right]$$

$T_l =$  HIGH SPEED SCULLING ALGORITHM ITERATION PERIOD

## SCULLING ALGORITHM ITERATION RATE ERROR

$$e(\dot{\Delta v}_z) = \frac{1}{2} \theta_0 A \cos \phi \left[ \left( 1 + \frac{1}{3} [1 - \cos 2\pi f T_l] \right) \frac{\sin 2\pi f T_l}{2\pi f T_l} - 1 \right]$$

## SCULLING ALGORITHM FINITE ITERATION RATE ERROR

The accuracy of the sculling digital integration algorithm on the previous chart is measured by how closely it matches the continuous integral form under dynamic sculling conditions. This chart shows how the algorithm accuracy can be determined under classical X-Y axis angular-rate/specific-force sinusoidal sculling motion inputs (as defined on page 190). For the hypothesized motion, the chart provides the average Z axis sculling continuous integral solution (as on page 190). For comparison, this chart then provides the average Z axis solution for the incremental digital integration sculling algorithm on the previous chart under the same sculling input motion. Note that the incremental algorithm solution equals the continuous form solution under an infinitely fast algorithm processing rate (for which the algorithm update time interval  $T_l$  is zero), as it should.

The algorithm error  $e(\Delta v_z)$  is the difference between the continuous form and incremental algorithm solutions. Note that the algorithm error is proportional to the sculling amplitude function  $\frac{1}{2} \theta_0 A \cos \phi$  multiplied by an attenuation factor

$\left(1 + \frac{1}{3}(1 - \cos 2\pi f T_l)\right) \frac{\sin 2\pi f T_l}{2\pi f T_l} - 1$ . The attenuation factor is a function only of the angle parameter  $2\pi f T_l$  which can also be

expressed equivalently as  $2\pi f / f_l$ , where  $f$  is the sculling motion frequency and  $f_l$  is the algorithm update frequency (the reciprocal of the update period  $T_l$ ). It is easily verified that when  $f$  is large compared to  $f_l$ , the proportionality factor becomes minus 1, hence, the sculling error magnitude equals the sculling motion (i.e., the sculling algorithm is completely ineffective in calculating sculling and would output an average zero solution under these conditions). At the other extreme, when the algorithm update

frequency  $f_l$  is large compared to the sculling frequency  $f$ , the  $1 - \cos 2\pi f T_l$  term goes to zero, the  $\frac{\sin 2\pi f T_l}{2\pi f T_l}$  term goes to one, and

the attenuation factor goes to zero (i.e., the sculling algorithm is completely effective in calculating the sculling motion). In practice,  $f_l$  would be set large enough to assure that the sculling error  $e(\Delta v_z)$  is small (negligible) compared to accelerometer bias in the strapdown inertial system error budget.

# ALTERNATIVE SCULLING COMPUTER ALGORITHM

## CONTINUOUS FORM

### COMPUTATION BETWEEN TRANSFORMATION CYCLES

$$\Delta \underline{v}_{SCULL}^B(t) = \frac{1}{2} \int_{t_m}^t (\underline{\alpha}^B(t) \times d\underline{v}^B + \underline{u}^B(t) \times d\underline{\alpha}^B)$$

$$\underline{\alpha}^B(t) = \int_{t_m}^t d\underline{\alpha}^B \quad \underline{u}^B(t) = \int_{t_m}^t d\underline{v}^B$$

### COMPUTATION AT $t_m$ TRANSFORMATION CYCLE

$$\Delta \underline{v}_{SCULLING}^B = \Delta \underline{v}_{SCULL}^B(t_{m+1})$$

$$\Delta \underline{v}_{ROTATION}^B = \frac{1}{2} \underline{\alpha}^B(t_{m+1}) \times \underline{u}^B(t_{m+1})$$

$$\Delta \underline{v}_{TRANSFORM}^B = \underline{u}^B(t_{m+1}) + \Delta \underline{v}_{ROTATION}^B + \Delta \underline{v}_{SCULLING}^B$$

$$\Delta \underline{v}^L = C_{B(t_m)}^L \Delta \underline{v}_{TRANSFORM}^B$$

## ALTERNATIVE SCULLING COMPUTER ALGORITHM

The alternative acceleration transformation computer algorithm configuration on page 187A is based on a two-speed approach whereby the basic transformation operation is performed at the velocity update rate and the input to the transformation operation is calculated using a high speed integration process during the time interval between velocity updates. The high speed integrals generate integrated specific-force, a rotation compensation correction, and a sculling increment that are summed to form the input to the transformation operation. For simplicity, the high speed integration processes on page 187A are represented by continuous integrals. This chart and those following illustrate repetitive digital algorithms that can be used to implement the high speed integration processes as high speed summing operations (at an  $l$  cycle rate) between transformation/velocity-updates (an  $m$  cycle rate).

This chart analytically describes the transformation process on page 187A showing the continuous form integration operations to calculate the alternative sculling increment  $\Delta v_{SCULL}^B$ , the integrated specific-force increment  $\underline{u}^B$ , and the rotation compensation correction  $\Delta v_{ROTATION}^B$ , their sampling and summing to form  $\Delta v_{TRANSFORM}^B$  at the acceleration-transformation/velocity-update cycle  $m$ , and the transformation of  $\Delta v_{TRANSFORM}^B$  through  $C_{B(t_m)}^L$  (the direction cosine matrix at the start of the  $m$  cycle) from the body B Frame into the local level navigation L Frame to obtain the L Frame integrated specific force increment  $\Delta v^L$ . The L Frame velocity components would then be updated by adding  $\Delta v^L$  and gravity/Coriolis corrections to the previous  $m$  cycle value of L Frame velocity.

# ALTERNATIVE SCULLING COMPUTER ALGORITHM (Continued)

## INCREMENTAL COMPUTER ALGORITHM FORM

### COMPUTATION BETWEEN TRANSFORMATION CYCLES

$$\Delta \underline{v}_{SCULL_l}^B = \Delta \underline{v}_{SCULL_{l-1}}^B + \frac{1}{2} \left[ \left( \underline{\alpha}_{l-1}^B + \frac{1}{6} \underline{\varepsilon}_{\alpha_{l-1}}^B \right) \times \underline{\varepsilon}_{v_l} + \left( \underline{u}_{l-1}^B + \frac{1}{6} \underline{\varepsilon}_{v_{l-1}}^B \right) \times \underline{\varepsilon}_{\alpha_l} \right]$$

$$\underline{\alpha}_l^B = \underline{\alpha}_{l-1}^B + \underline{\varepsilon}_{\alpha_l}^B \quad \underline{u}_l^B = \underline{u}_{l-1}^B + \underline{\varepsilon}_{v_l}^B$$

### COMPUTATION AT $t_{m+1}$ TRANSFORMATION CYCLE

$$\Delta \underline{v}_{SCULLING}^B = \Delta \underline{v}_{SCULL}^B \quad (l = L)$$

$$\Delta \underline{v}_{ROTATION}^B = \frac{1}{2} \underline{\alpha}^B \quad (l = L) \times \underline{u}^B \quad (l = L)$$

$$\Delta \underline{v}_{TRANSFORM}^B = \underline{u}^B \quad (l = L) + \Delta \underline{v}_{ROTATION}^B + \Delta \underline{v}_{SCULLING}^B$$

$$\Delta \underline{v}^L = C_{B(t_m)}^L \Delta \underline{v}_{TRANSFORM}^B$$

### ALTERNATIVE SCULLING COMPUTER ALGORITHM (Continued)

This chart describes repetitive digital algorithms used to implement the high speed integration processes on the previous chart as high speed summing operations (at an  $l$  cycle rate) between transformation/velocity-updates (the  $m$  cycle rate).

The angular-rate/specific-force integrals  $\underline{\alpha}_l^B$  and  $\underline{u}^B$  used in the rotation compensation equation and sculling integration are obtained by summing integrated angular-rate/specific-force increments  $\underline{\epsilon}_{\alpha_l}^B$  and  $\underline{\epsilon}_{v_l}^B$ . The  $\underline{\epsilon}_{\alpha_l}^B$  and  $\underline{\epsilon}_{v_l}^B$  increments would be generated by summing integrated angular-rate/specific-force increment output pulses from the gyros and accelerometers over each  $l$  cycle. The sculling increment in the chart  $\Delta v_{SCULL_l}^B$  is generated by summing an analytical expression containing past values of  $\underline{\alpha}_l^B$  and  $\underline{u}^B$ , and current and past values of  $\underline{\epsilon}_{\alpha_l}^B$  and  $\underline{\epsilon}_{v_l}^B$ . The  $\underline{\alpha}_l^B$ ,  $\underline{u}^B$  and  $\Delta v_{SCULL_l}^B$  summing operations are executed at the  $l$  cycle rate and sampled when  $l = L$  (the number of  $l$  cycles in an  $m$  cycle) for use in the  $m$  cycle transformation routine. After sampling, the  $\underline{\alpha}_l^B$ ,  $\underline{u}^B$  and  $\Delta v_{SCULL_l}^B$  sums would be reset to zero for initialization of  $l$  cycle summing over the next  $m$  cycle.

The analytical expression for  $\Delta v_{SCULL_l}^B$  is a second order updating algorithm (contains up to second order products in  $\underline{\epsilon}_{\alpha_l}^B$  and  $\underline{\epsilon}_{v_l}^B$ ) designed to provide the identical solution as the continuous integral under angular-rate/specific-force conditions modeled as a constant plus a linear ramp in time over each  $l$  cycle. The derivation for  $\Delta v_{SCULL_l}^B$  is similar to the second order coning algorithm development in section 3.3.2 of the Strapdown System Algorithm paper in the Strapdown Inertial Navigation Lecture Notes handout.

Constant plus linear ramping angular-rate/specific-force is a reasonable approximation for actual motion during an  $l$  cycle. Structuring the algorithm to have an exact solution under particular easily modeled analytical inputs provides a simple method for validation; by assuring that the correct exact solution will be obtained under simulated angular-rate/specific-force design condition inputs. The correct exact solution is easily found by analytical integration of the continuous form integral under constant plus linear ramping angular-rate/specific-force input.

# ALTERNATIVE SCULLING ALGORITHM FINITE ITERATION RATE ERROR

## BODY RATE

$$\dot{\underline{\alpha}}^B = 2\pi f \begin{bmatrix} \theta_0 \cos 2\pi f t \\ 0 \\ 0 \end{bmatrix}$$

## BODY ACCELERATION

$$\dot{\underline{v}}^B = \begin{bmatrix} 0 \\ A \sin(2\pi f t + \phi) \\ 0 \end{bmatrix}$$

## AVERAGE CONTINUOUS FORM SCULLING INCREMENT

$$\Delta \dot{v}_{SCULLING_z}^B = \frac{1}{2} \theta_0 A \cos \phi \left[ 1 - \frac{\sin 2\pi f T_m}{2\pi f T_m} \right]$$

$T_m$  = ACCELERATION TRANSFORMATION CYCLE PERIOD

## AVERAGE INCREMENTAL FORM SCULLING INCREMENT

$$\Delta \dot{v}_{SCULLING_z}^B = \frac{1}{2} \theta_0 A \cos \phi \left[ \left( 1 + \frac{1}{3} [1 - \cos 2\pi f T_l] \right) \frac{\sin 2\pi f T_l}{2\pi f T_l} - \frac{\sin 2\pi f T_m}{2\pi f T_m} \right]$$

$T_l$  = HIGH SPEED SCULLING ALGORITHM ITERATION PERIOD

## SCULLING ALGORITHM ITERATION RATE ERROR

$$e(\Delta \dot{v}_{SCULLING_z}^B) = \frac{1}{2} \theta_0 A \cos \phi \left[ \left( 1 + \frac{1}{3} [1 - \cos 2\pi f T_l] \right) \frac{\sin 2\pi f T_l}{2\pi f T_l} - 1 \right]$$

## ALTERNATIVE SCULLING ALGORITHM FINITE ITERATION RATE ERROR

The accuracy of the alternative algorithm on the previous chart is measured by how closely it matches the continuous integral form under dynamic sculling conditions. This chart shows how the algorithm accuracy can be determined under classical X-Y axis angular-rate/specific-force sinusoidal sculling motion inputs (as defined on page 190). For the hypothesized motion, the chart provides the Z axis component of the continuous integral form for  $\Delta \dot{v}_{SCULLING_z}^B$  which is the same as on the page 190 chart, but excluding the "Constant Angular Rate Approximation Term" (the rotation compensation portion is handled separately for the alternative algorithm). For comparison, this chart then provides the Z axis solution for the incremental digital integration sculling algorithm on the previous chart under the same sculling input motion. Note that the incremental algorithm solution equals the continuous form solution under an infinitely fast algorithm processing rate (for which the algorithm update time interval  $T_I$  is zero), as it should.

The algorithm error rate  $e(\Delta \dot{v}_{SCULLING_z}^B)$  is the difference between the continuous form and incremental algorithm solutions and is identical to the algorithm error  $e(\Delta \dot{v}_z)$  presented for the original sculling algorithm. Note, however, that the original and alternative sculling algorithm (continuous forms on pages 184 and 187A) are based on using the page 186 first order accuracy approximation for rotation compensation in the acceleration transformation process (which neglects terms containing powers of  $\underline{\alpha}^B$  or  $\underline{u}^B$ ). For the original sculling algorithm, the first order rotation compensation approximation is embedded in the sculling integral; for the alternative sculling algorithm, rotation compensation is a separated part of the transformation process. The error associated with first order rotation compensation was not included in the sculling error for the original algorithm because the continuous form algorithm (the truth model) was also based on first order rotation compensation form. If higher order accuracy rotation compensation was used for the truth model, the error in the original sculling algorithm would include an additional first order rotation compensation approximation error implicit in the algorithm structure. Note, however, that because the rotation compensation term is separated from the sculling term in the alternative sculling approach, a higher order rotation compensation computation can be used (as discussed on page 187B) that eliminates the first order rotation approximation error source.

# CONING COMPUTER ALGORITHM

## COMPUTATION BETWEEN ATTITUDE UPDATE CYCLES

CONTINUOUS FORM :

$$\underline{\delta\phi}_{\text{CONING}}^{\text{B}} = \frac{1}{2} \int_{t_m}^{t_{m+1}} \underline{\alpha}^{\text{B}} \times d\underline{\alpha}^{\text{B}} \quad \underline{\alpha}^{\text{B}} = \int_{t_m}^t d\underline{\alpha}^{\text{B}}$$

INCREMENTAL COMPUTER ALGORITHM FORM :

$$\underline{\delta\phi}_{\text{CONE}_l}^{\text{B}} = \underline{\delta\phi}_{\text{CONE}_{l-1}}^{\text{B}} + \frac{1}{2} \left( \underline{\alpha}_{l-1}^{\text{B}} + \frac{1}{6} \underline{\varepsilon}_{\alpha_{l-1}}^{\text{B}} \right) \times \underline{\varepsilon}_{\alpha_l}^{\text{B}}$$

$$\underline{\alpha}_l^{\text{B}} = \underline{\alpha}_{l-1}^{\text{B}} + \underline{\varepsilon}_{\alpha_l}^{\text{B}}$$

$$\underline{\delta\phi}_{\text{CONING}}^{\text{B}} = \underline{\delta\phi}_{\text{CONE}}^{\text{B}} \quad (l = L)$$

$\underline{\varepsilon}_{\alpha_l}^{\text{B}}$  = CUMULATIVE GYRO PULSE COUNTS OVER  
HIGH SPEED SCULLING COMPUTATION CYCLE

## CONING COMPUTER ALGORITHM

The attitude update computer algorithm configurations on pages 204 and 205A are based on a two-speed approach whereby the basic attitude update operation is performed at an  $m$  cycle rate and the input to the update operation is calculated using a high speed integration process during the time interval between attitude updates. The high speed integrals generate integrated angular rate and a coning increment that are summed to form the input to the attitude update operation. For simplicity, the high speed integration processes are represented by continuous integrals. This chart illustrates repetitive digital algorithms that can be used to implement the high speed integration processes as high speed summing operations (at an  $l$  cycle rate) between attitude update cycles.

The angular rate integral  $\underline{\alpha}_l^B$  used in the coning integration is obtained by summing integrated angular rate increments  $\underline{\epsilon}_{\alpha_l}^B$ . The  $\underline{\epsilon}_{\alpha_l}^B$  increments would be generated by summing integrated angular rate increment output pulses from the gyros over each  $l$  cycle. The coning increment in the chart  $\underline{\delta\phi}_{\text{CONE}_l}^B$  is generated by summing an analytical expression containing past values of  $\underline{\alpha}_l^B$ , and current and past values of  $\underline{\epsilon}_{\alpha_l}^B$ . The  $\underline{\alpha}_l^B$  and  $\underline{\delta\phi}_{\text{CONE}_l}^B$  summing operations are executed at the  $l$  cycle rate and sampled when  $l = L$  (the number of  $l$  cycles in an  $m$  cycle) for use in the  $m$  cycle attitude update routine. After sampling, the  $\underline{\alpha}_l^B$  and  $\underline{\delta\phi}_{\text{CONE}_l}^B$  sums would be reset to zero for initialization of  $l$  cycle summing over the next  $m$  cycle.

The analytical expression for  $\underline{\delta\phi}_{\text{CONE}_l}^B$  is a second order updating algorithm (contains up to second order products in  $\underline{\epsilon}_{\alpha_l}^B$ ) designed to provide the identical solution as the continuous integral under angular rate conditions modeled as a constant plus a linear ramp in time over each  $l$  cycle. The derivation for  $\underline{\delta\phi}_{\text{CONE}_l}^B$  is provided in section 3.3.2 of the Strapdown System Algorithm paper in the Strapdown Inertial Navigation Lecture Notes handout. Constant plus linear ramping angular rate is a reasonable approximation for actual motion during an  $l$  cycle. Structuring the algorithm to have an exact solution under particular easily modeled analytical inputs provides a simple method for validation; by assuring that the correct exact solution will be obtained under simulated angular-rate/specific-force design condition inputs. The correct exact solution is easily found by analytical integration of the continuous form integral under constant plus linear ramping angular-rate/specific-force input.

Note the similarity of the second order coning algorithm in this chart and the second order alternative sculling algorithm on page 564.

# CONING ALGORITHM FINITE ITERATION RATE ERROR

**BODY RATE**  $\dot{\underline{\alpha}}^B = 2 \pi f \begin{bmatrix} \theta_X \cos 2 \pi f t \\ \theta_Y \cos (2 \pi f t - \phi) \\ 0 \end{bmatrix}$

## AVERAGE CONTINUOUS FORM CONING COMPENSATION

$$\dot{\delta\phi}_z = \pi f \theta_X \theta_Y \sin \phi \left[ 1 - \frac{\sin 2 \pi f T_m}{2 \pi f T_m} \right]$$

$T_m$  = TIME INTERVAL FOR ATTITUDE UPDATE CYCLE

## AVERAGE INCREMENTAL FORM CONING COMPENSATION

$$\dot{\delta\phi}_z = \pi f \theta_X \theta_Y \sin \phi \left[ \left( 1 + \frac{1}{3} [1 - \cos 2 \pi f T_l] \right) \frac{\sin 2 \pi f T_l}{2 \pi f T_l} - \frac{\sin 2 \pi f T_m}{2 \pi f T_m} \right]$$

$T_l$  = HIGH SPEED CONING ALGORITHM ITERATION PERIOD

## CONING ALGORITHM ITERATION RATE ERROR

$$e(\dot{\delta\phi}_z) = \pi f \theta_X \theta_Y \sin \phi \left[ \left( 1 + \frac{1}{3} [1 - \cos 2 \pi f T_l] \right) \frac{\sin 2 \pi f T_l}{2 \pi f T_l} - 1 \right]$$

## CONING ALGORITHM FINITE ITERATION RATE ERROR

The accuracy of the coning digital integration algorithm on the previous chart is measured by how closely it matches the continuous integral form under dynamic coning conditions. The chart shows how the algorithm accuracy can be determined under classical X-Y axis angular rate sinusoidal coning motion inputs (as defined on page 208). For the hypothesized motion, the chart provides the average Z axis coning continuous integral solution (as on the page 208 chart). For comparison, this chart then provides the average Z axis solution for the incremental digital integration coning algorithm on the previous chart under the same coning input motion. Note that the incremental algorithm solution equals the continuous form solution under an infinitely fast algorithm processing rate (for which the algorithm update time interval  $T_l$  is zero), as it should.

The algorithm error  $e(\dot{\delta\phi}_z)$  is the difference between the continuous form and incremental algorithm solutions. Note that the algorithm error is proportional to the coning amplitude function  $\pi f \theta_x \theta_y \sin \phi$  multiplied by an attenuation factor

$$\left(1 + \frac{1}{3}(1 - \cos 2\pi f T_l)\right) \frac{\sin 2\pi f T_l}{2\pi f T_l} - 1. \text{ Also note that the attenuation factor is identical to that for the sculling algorithm error on}$$

pages 560 and 566. The attenuation factor is a function only of the angle parameter  $2\pi f T_l$  which can also be expressed equivalently as  $2\pi f / f_l$ , where  $f$  is the coning motion frequency and  $f_l$  is the algorithm update frequency (the reciprocal of the update period  $T_l$ ). It is easily verified that when  $f$  is large compared to  $f_l$ , the proportionality factor becomes minus 1, hence, the coning error magnitude equals the coning motion (i.e., the coning algorithm is completely ineffective in calculating coning and would output an average zero solution under these conditions). At the other extreme, when the algorithm update frequency  $f_l$  is

large compared to the coning frequency  $f$ , the  $1 - \cos 2\pi f T_l$  term goes to zero, the  $\frac{\sin 2\pi f T_l}{2\pi f T_l}$  term goes to one, and the attenuation factor goes to zero (i.e., the coning algorithm is completely effective in calculating the coning motion). In practice,  $f_l$  would be set

large enough to assure that the coning error  $e(\dot{\delta\phi}_z)$  is small (negligible) compared to gyro bias in the strapdown inertial system error budget.

## CONING AND SCULLING EFFECTS UNDER VIBRATION

$$\text{MEAN CONING} \int_0^{\infty} \left(1 - \frac{\sin \omega T_m}{\omega T_m}\right) \omega A_1(\omega) A_2(\omega) \sin[\phi_{A2}(\omega) - \phi_{A1}(\omega)] P_{nn}(j\omega) d\omega$$

$$\begin{aligned} \text{MEAN CONING} \\ \text{ALGORITHM ERROR} \int_0^{\infty} \left\{ \left[ 1 + \frac{1}{3}(1 - \cos \omega T_l) \right] \frac{\sin \omega T_l}{\omega T_l} - 1 \right\} \omega A_1(\omega) A_2(\omega) \\ \sin[\phi_{A2}(\omega) - \phi_{A1}(\omega)] P_{nn}(j\omega) d\omega \end{aligned}$$

$$\begin{aligned} \text{MEAN SCULLING} \int_0^{\infty} \left(1 - \frac{\sin \omega T_m}{\omega T_m}\right) \{ A_2(\omega) B_1(\omega) \cos[\phi_{A2}(\omega) - \phi_{B1}(\omega)] \\ - A_1(\omega) B_2(\omega) \cos[\phi_{A1}(\omega) - \phi_{B2}(\omega)] \} P_{nn}(j\omega) d\omega \end{aligned}$$

$$\begin{aligned} \text{MEAN SCULLING} \\ \text{ALGORITHM ERROR} \int_0^{\infty} \left\{ \left[ 1 + \frac{1}{3}(1 - \cos \omega T_l) \right] \frac{\sin \omega T_l}{\omega T_l} - 1 \right\} \{ A_2(\omega) B_1(\omega) \cos[\phi_{A2}(\omega) - \phi_{B1}(\omega)] \\ - A_1(\omega) B_2(\omega) \cos[\phi_{A1}(\omega) - \phi_{B2}(\omega)] \} P_{nn}(j\omega) d\omega \end{aligned}$$

$A_i(\omega), \phi_{Ai}(\omega)$  = Amplitude And Phase Of Transfer Function Relating System Input Vibration Noise To Angular Attitude Response Of Sensor Assembly About Axis i

$B_i(\omega), \phi_{Bi}(\omega)$  = Amplitude And Phase Of Transfer Function Relating System Input Vibration Noise To Linear Acceleration Response Of Sensor Assembly Along Axis i

$P_{nn}(j\omega)$  = Power Spectral Density Of Input Vibration Noise

$$\text{Note : Mean Squared Vibration Energy} = \int_0^{\infty} P_{nn}(j\omega) d\omega$$

$\omega$  = Fourier Frequency (Radians Per Second)

$T_l$  = High Speed Coning / Sculling Algorithm Repetition Rate Time Period

$T_m$  = Time Period for Attitude - Update / Acceleration - Transformation Cycle

## CONING AND SCULLING EFFECTS UNDER VIBRATION

The equations for calculating average coning/sculling motion and algorithm errors were based on angular-rate/specific-force sinusoidal inputs at discrete amplitudes and the same frequency  $f$ . In actual vehicle use, a real inertial navigation system will in general experience a mixture of input angular-rate/specific-force sinusoidal inputs at different amplitudes and frequencies. The higher frequency components will have the dominant effect on coning/sculling algorithm error because the lower frequency inputs have a minor contribution to attitude updating error. The input frequency effect on attitude motion can be seen on page 208 which shows that the coning motion contains a  $1 - (\sin 2\pi f T_m) / 2\pi f T_m$  attenuation factor where  $f$  is the coning frequency and  $T_m$  is the time period for the attitude update  $m$  cycle. When  $f$  is low compared to the attitude update frequency (the reciprocal of  $T_m$ ), the  $2\pi f T_m$  angle term becomes small,  $\sin 2\pi f T_m$  approximately equals  $2\pi f T_m$ , and the attenuation factor goes to zero. In other words, the basic attitude update rate is fast enough to handle the low frequency coning, and the high speed coning algorithm measurement would be small, hence, not needed in the attitude update. To analyze coning/sculling error then, expected high frequency motion effects are the cause to be investigated. These are produced primarily by random vehicle linear vibration inputs that through mechanical coupling effects, produce strapdown sensor assembly high frequency linear/angular motion. The principle coupling mechanism is mechanical bending of the rigid strapdown sensor assembly relative to the vibration source (e.g., through sensor assembly mass imbalance and mechanical isolator compliance/mismatch). For most applications, the vehicle vibration input is represented by a power spectral density of vibration acceleration-squared (g-specific-force-squared) energy per frequency component.

The chart extends the discrete amplitude/frequency coning/sculling motion and error charts for random motion produced by input vibration with power spectral density  $P_{nn}$  as a function of vibration frequency component  $\omega$ . The mean coning, sculling and associated algorithm error terms are integrals over the full  $\omega$  frequency range of the input vibration  $P_{nn}$  multiplied by appropriate frequency dependent X-Y axis (1 and 2) amplitude transmission gains ( $A_1, A_2, B_1$  and  $B_2$ ), sine/cosine of relative phase angles the between X-Y axis transmitted vibrations ( $\phi_{A1}, \phi_{A2}, \phi_{B1}, \phi_{B2}$ ), and frequency dependent attenuation coefficients,

$$1 - (\sin \omega T_m) / \omega T_m \text{ for mean coning/sculling and } \left(1 + \frac{1}{3} (1 - \cos 2\pi f T_l)\right) \frac{\sin 2\pi f T_l}{2\pi f T_l} - 1 \text{ for mean coning/sculling algorithm error.}$$

If this chart is compared with the equivalent discrete frequency charts (e.g., pages 190, 208, 566 and 570) with  $2\pi f$  equated to  $\omega$ , the equivalency between the charts should be apparent.

# **SENSOR COMPENSATION BEFORE OR AFTER CONING/SCULLING HIGH SPEED PROCESSING**

**AFTER - ACCEPTABLE FOR BENIGN VIBRATION MEDIUM ACCURACY  
APPLICATIONS**

**E.G. - COMMERCIAL AIRCRAFT**

**BEFORE - REQUIRED FOR HIGH VIBRATION HIGH ACCURACY  
APPLICATIONS**

**E.G. - MILITARY AIRCRAFT**

## **SENSOR COMPENSATION BEFORE OR AFTER CONING/SCULLING HIGH SPEED PROCESSING**

This and the next few charts address the basic question of whether it is necessary to apply compensation for inertial sensor inputs to coning/sculling high speed algorithms and if so, is it possible to first perform the coning/sculling calculations with uncompensated data, and then compensate the result at the attitude/acceleration-transformation cycle time. The motivation is that sensor compensation might be throughput intensive when executed at high coning/sculling computation frequencies in which case, a less demanding alternative would be desirable.

For low vibration applications (e.g., commercial aircraft) coning/sculling effects are small, hence, calculating them with uncompensated sensor data does not add a significant error to the system error budget (e.g., for compensation corrections on the order of 0.1% for scale factor or 1 milli-radian for misalignments). For high vibration applications (e.g., military aircraft), sensor compensation may be required for coning/sculling inputs to meet accuracy requirements. Note that because coning and sculling computations involve products of angular-rate/specific-force effects each of which is proportional to vibration input magnitude, coning/sculling amplitudes increase as the square of the vibration input magnitude. Thus a 7 g vibration amplitude input would produce 49 times the coning/sculling value as a 1 g vibration magnitude input.

## CONING ALGORITHM CORRECTION FOR SENSOR ERROR

### COMPENSATED GYRO DATA

$$\begin{aligned}\mathbf{X - GYRO:} \quad \omega_{XC} &= [(1 - K_{XX}) \omega_X - K_{X0}] - K_{XY} [(1 - K_{YY}) \omega_Y - K_{Y0}] - K_{XZ} [(1 - K_{ZZ}) \omega_Z - K_{Z0}] \\ \mathbf{Y - GYRO:} \quad \omega_{YC} &= -K_{YX} [(1 - K_{XX}) \omega_X - K_{X0}] + [(1 - K_{YY}) \omega_Y - K_{Y0}] - K_{YZ} [(1 - K_{ZZ}) \omega_Z - K_{Z0}] \\ \mathbf{Z - GYRO:} \quad \omega_{ZC} &= -K_{ZX} [(1 - K_{XX}) \omega_X - K_{X0}] - K_{ZY} [(1 - K_{YY}) \omega_Y - K_{Y0}] + [(1 - K_{ZZ}) \omega_Z - K_{Z0}]\end{aligned}$$

### CONING ALGORITHM BASED ON UNCOMPENSATED GYRO DATA

$$\underline{\alpha} = [\alpha_X, \alpha_Y, \alpha_Z]^T = \int_0^t \underline{\omega} dt = \int_0^t [\omega_X, \omega_Y, \omega_Z]^T dt$$

$$\underline{C} = [C_X, C_Y, C_Z]^T = \int_0^t \frac{1}{2} (\alpha \times \omega) dt$$

### CONING ALGORITHM CORRECTED FOR GYRO ERROR

$$\begin{aligned}C_{XC} &= (1 - K_{YY} - K_{ZZ}) C_X + K_{YX} C_Y + K_{ZX} C_Z \\ C_{YC} &= K_{XY} C_X + (1 - K_{ZZ} - K_{XX}) C_Y + K_{ZY} C_Z \\ C_{ZC} &= K_{XZ} C_X + K_{YZ} C_Y + (1 - K_{XX} - K_{YY}) C_Z\end{aligned}$$

### COMPENSATED ANGULAR INCREMENT

$$\begin{aligned}\phi_X &= [(1 - K_{XX}) \alpha_X - K_{X0} \Delta t] - K_{XY} [(1 - K_{YY}) \alpha_Y - K_{Y0} \Delta t] - K_{XZ} [(1 - K_{ZZ}) \alpha_Z - K_{Z0} \Delta t] + C_{XC} \\ \phi_Y &= -K_{YX} [(1 - K_{XX}) \alpha_X - K_{X0} \Delta t] + [(1 - K_{YY}) \alpha_Y - K_{Y0} \Delta t] - K_{YZ} [(1 - K_{ZZ}) \alpha_Z - K_{Z0} \Delta t] + C_{YC} \\ \phi_Z &= -K_{ZX} [(1 - K_{XX}) \alpha_X - K_{X0} \Delta t] - K_{ZY} [(1 - K_{YY}) \alpha_Y - K_{Y0} \Delta t] + [(1 - K_{ZZ}) \alpha_Z - K_{Z0} \Delta t] + C_{ZC}\end{aligned}$$

## CONING ALGORITHM CORRECTION FOR SENSOR ERROR

This chart addresses the requirements for coning computation (pages 204 and 205A) correction for gyro input error. Two methods are shown; compensating the gyro data before input to the high speed coning computation algorithm, and compensating a coning computation result that was calculated with uncompensated gyro data. The gyro compensation shown corrects for scale factor ( $K_{ii}$ ), misalignment ( $K_{ij}$ ) and fixed bias ( $K_{i0}$ ). Uncompensated  $i$  axis gyro data is denoted as  $\omega_i$  and compensated  $i$  axis gyro data is denoted as  $\omega_{iC}$ .

The  $i$  axis coning computation outputs (integrals over an attitude update cycle) are denoted as  $C_i$  if computed with uncompensated gyro data. If computed with compensated gyro data they are denoted as  $C_{iC}$ . The chart shows how the  $C_{iC}$ s can be also be calculated from the uncompensated  $C_i$  data (The equations shown for the  $C_{iC}$ s are derived by substituting the compensated  $\omega_{iC}$ s into the coning integral equation, expanding the integrand, dropping second order  $K$  coefficient products, and re-grouping/separating terms). The advantage for the latter approach is that the compensation corrections need only be applied once per attitude update cycle rather than at the higher speed coning algorithm update rate if coning is computed with compensated gyro data.

Also shown is the total compensated angular  $\phi_i$  increments ( $i$  axis components of the rotation vector on pages 204 and 205A) that would be used for attitude updating. Included are integrated angular rate increments ( $\alpha_i$ ) compensated for gyro scale factor error, misalignment and bias plus the compensated coning data.

## SCULLING ALGORITHM CORRECTION FOR SENSOR ERROR

### COMPENSATED GYRO DATA

$$\begin{aligned} \text{X - GYRO: } \omega_{XC} &= [(1 - K_{XX}) \omega_X - K_{X0}] - K_{XY} [(1 - K_{YY}) \omega_Y - K_{Y0}] - K_{XZ} [(1 - K_{ZZ}) \omega_Z - K_{Z0}] \\ \text{Y - GYRO: } \omega_{YC} &= -K_{YX} [(1 - K_{XX}) \omega_X - K_{X0}] + [(1 - K_{YY}) \omega_Y - K_{Y0}] - K_{YZ} [(1 - K_{ZZ}) \omega_Z - K_{Z0}] \\ \text{Z - GYRO: } \omega_{ZC} &= -K_{ZX} [(1 - K_{XX}) \omega_X - K_{X0}] - K_{ZY} [(1 - K_{YY}) \omega_Y - K_{Y0}] + [(1 - K_{ZZ}) \omega_Z - K_{Z0}] \end{aligned}$$

### COMPENSATED ACCELEROMETER DATA

$$\begin{aligned} \text{X - ACCEL: } a_{XC} &= [(1 - L_{XX}) a_X - L_{X0}] - L_{XY} [(1 - L_{YY}) a_Y - L_{Y0}] - L_{XZ} [(1 - L_{ZZ}) a_Z - L_{Z0}] \\ \text{Y - ACCEL: } a_{YC} &= -K_{YX} [(1 - L_{XX}) a_X - L_{X0}] + [(1 - L_{YY}) a_Y - L_{Y0}] - L_{YZ} [(1 - L_{ZZ}) a_Z - L_{Z0}] \\ \text{Z - ACCEL: } a_{ZC} &= -K_{ZX} [(1 - L_{XX}) a_X - L_{X0}] - L_{ZY} [(1 - L_{YY}) a_Y - L_{Y0}] + [(1 - L_{ZZ}) a_Z - L_{Z0}] \end{aligned}$$

### SCULLING ALGORITHM BASED ON UNCOMPENSATED SENSOR DATA

$$\begin{aligned} \underline{\alpha} &= [\alpha_X, \alpha_Y, \alpha_Z]^T = \int_0^t \underline{\omega} dt & \underline{\omega} &= [\omega_X, \omega_Y, \omega_Z]^T \\ \underline{u} &= [u_X, u_Y, u_Z]^T = \int_0^t \underline{a} dt & \underline{a} &= [a_X, a_Y, a_Z]^T \end{aligned} \quad \underline{S} = \int_0^{t_1} \frac{1}{2} (\underline{\alpha} \times \underline{a} + \underline{u} \times \underline{\omega}) dt$$

OR

$$\underline{S} = \underline{S}_1 - \underline{S}_2 \quad \underline{S}_1 = \begin{bmatrix} S_{1X} \\ S_{1Y} \\ S_{1Z} \end{bmatrix} = \int_0^{t_1} \frac{1}{2} \begin{bmatrix} \alpha_Y a_Z - u_Z \omega_Y \\ \alpha_Z a_X - u_X \omega_Z \\ \alpha_X a_Y - u_Y \omega_X \end{bmatrix} dt \quad \underline{S}_2 = \begin{bmatrix} S_{2X} \\ S_{2Y} \\ S_{2Z} \end{bmatrix} = \int_0^{t_1} \frac{1}{2} \begin{bmatrix} \alpha_Z a_Y - u_Y \omega_Z \\ \alpha_X a_Z - u_Z \omega_X \\ \alpha_Y a_X - u_X \omega_Y \end{bmatrix} dt$$

## SCULLING ALGORITHM CORRECTION FOR SENSOR ERROR

This chart and the next two address the requirements for alternative sculling computation (page 187A) correction for gyro and accelerometer input error. Two methods are shown; compensating the gyro/accelerometer data before input to the high speed sculling computation algorithm, and compensating a sculling computation result that was calculated with uncompensated gyro/accelerometer data. The sensor compensation shown corrects for gyro/accelerometer scale factor ( $K_{ij}$ ,  $L_{ij}$ ) misalignment ( $K_{ij}$ ,  $L_{ij}$ ) and fixed bias ( $K_{i0}$ ,  $L_{i0}$ ). Uncompensated i axis gyro/accelerometer data are denoted as  $\omega_i$ ,  $a_i$  and compensated i axis gyro/accelerometer data are denoted as  $\omega_{iC}$ ,  $a_{iC}$ .

The i axis sculling computation outputs (integrals over an acceleration-transformation/velocity-update cycle) computed with uncompensated gyro/accelerometer data are denoted as  $S_i$ . In addition to the direct  $S_i$  computation approach, the chart also shows how the  $S_i$ s can be calculated as the difference between two partial sculling integrals ( $S_{1i}$ s and  $S_{2i}$ s) also shown calculated with uncompensated sensor data. The latter form is advantageous when applying compensation to the uncorrected sculling solution as shown on the next chart.

## CORRECTION TO SCULLING ALGORITHM (Continued)

### SCULLING SUPPLEMENT BASED ON UNCOMPENSATED SENSOR DATA

$$Q_X = \int_0^t \frac{1}{2} (\alpha_X a_X - u_X \omega_X) dt \quad Q_Y = \int_0^t \frac{1}{2} (\alpha_Y a_Y - u_Y \omega_Y) dt \quad Q_Z = \int_0^t \frac{1}{2} (\alpha_Z a_Z - u_Z \omega_Z) dt$$

### SCULLING ALGORITHM CORRECTED FOR SENSOR ERROR

$$S_{XC} = (1 - K_{YY} - L_{ZZ}) S_{1X} - (1 - K_{ZZ} - L_{YY}) S_{2X} + \frac{1}{2} (L_{YX} + K_{YX}) (S_{1Y} - S_{2Y}) + \frac{1}{2} (L_{ZX} + K_{ZX}) (S_{1Z} - S_{2Z}) \\ + \frac{1}{2} (L_{YX} - K_{YX}) (S_{1Y} + S_{2Y}) - \frac{1}{2} (L_{ZX} - K_{ZX}) (S_{1Z} + S_{2Z}) - (L_{ZY} - K_{ZY}) Q_Y + (L_{YZ} - K_{YZ}) Q_Z$$

$$S_{YC} = (1 - K_{ZZ} - L_{XX}) S_{1Y} - (1 - K_{XX} - L_{ZZ}) S_{2Y} + \frac{1}{2} (L_{ZY} + K_{ZY}) (S_{1Z} - S_{2Z}) + \frac{1}{2} (L_{XY} + K_{XY}) (S_{1X} - S_{2X}) \\ + \frac{1}{2} (L_{ZY} - K_{ZY}) (S_{1Z} + S_{2Z}) - \frac{1}{2} (L_{XY} - K_{XY}) (S_{1X} + S_{2X}) - (L_{XZ} - K_{XZ}) Q_Z + (L_{ZX} - K_{ZX}) Q_X$$

$$S_{ZC} = (1 - K_{XX} - L_{YY}) S_{1Z} - (1 - K_{YY} - L_{XX}) S_{2Z} + \frac{1}{2} (L_{XZ} + K_{XZ}) (S_{1X} - S_{2X}) + \frac{1}{2} (L_{YZ} + K_{YZ}) (S_{1Y} - S_{2Y}) \\ + \frac{1}{2} (L_{XZ} - K_{XZ}) (S_{1X} + S_{2X}) - \frac{1}{2} (L_{YZ} - K_{YZ}) (S_{1Y} + S_{2Y}) - (L_{YX} - K_{YX}) Q_X + (L_{XY} - K_{XY}) Q_Y$$

## CORRECTION TO SCULLING ALGORITHM (Continued)

If computed with compensated gyro/accelerometer data, the sculling  $S_i$  terms are denoted as  $S_{iC}$ . The chart shows how the  $S_{iC}$ s can be also be calculated from uncompensated  $S_{1i}$ ,  $S_{2i}$  and supplemental uncompensated  $Q_i$  data (The  $S_{iC}$  equations are derived by substituting the compensated  $\omega_{iC}$ s and  $a_{iC}$ s into the sculling integral equation, expanding the integrand, dropping second order  $K / L$  coefficient products, and re-grouping/separating terms). The advantage for the latter approach is that the compensation corrections need only be applied once per acceleration-transformation/velocity-update cycle rather than at the higher speed sculling algorithm update rate if sculling is computed with compensated sensor data.

Included in the  $S_{iC}$  calculations are the supplemental  $Q_i$  terms. Note that the  $Q_i$  terms only multiply sensor misalignment error effects, hence, are only required if sensor misalignment effects are large enough to significantly impact sculling computational accuracy requirements (i.e., compared to accelerometer bias error in the strapdown inertial system error budget). Similarly, if only sensor scale factor error effects have impact on sculling computation accuracy requirements (e.g., 5 % scale factor error versus 1 mill-radian for misalignments), only the leading two terms in the  $S_{iC}$ s need be included.

## CORRECTION TO SCULLING ALGORITHM (Continued)

### COMPENSATED VELOCITY INCREMENTS

$$u_{XC} = [(1 - L_{XX}) u_X - L_{X0} \Delta t] - L_{XY} [(1 - L_{YY}) u_Y - K_{Y0} \Delta t] - L_{XZ} [(1 - L_{ZZ}) u_Z - L_{Z0} \Delta t]$$

$$u_{YC} = -L_{YX} [(1 - L_{XX}) u_X - L_{X0} \Delta t] + [(1 - L_{YY}) u_Y - K_{Y0} \Delta t] - L_{YZ} [(1 - L_{ZZ}) u_Z - L_{Z0} \Delta t]$$

$$u_{ZC} = -L_{ZX} [(1 - L_{XX}) u_X - L_{X0} \Delta t] - L_{ZY} [(1 - L_{YY}) u_Y - L_{Y0} \Delta t] + [(1 - L_{ZZ}) u_Z - L_{Z0} \Delta t]$$

$$\alpha_{XC} = [(1 - K_{XX}) \alpha_X - K_{X0} \Delta t] - K_{XY} [(1 - K_{YY}) \alpha_Y - K_{Y0} \Delta t] - K_{XZ} [(1 - K_{ZZ}) \alpha_Z - K_{Z0} \Delta t]$$

$$\alpha_{YC} = -K_{YX} [(1 - K_{XX}) \alpha_X - K_{X0} \Delta t] + [(1 - K_{YY}) \alpha_Y - K_{Y0} \Delta t] - K_{YZ} [(1 - K_{ZZ}) \alpha_Z - K_{Z0} \Delta t]$$

$$\alpha_{ZC} = -K_{ZX} [(1 - K_{XX}) \alpha_X - K_{X0} \Delta t] - K_{ZY} [(1 - K_{YY}) \alpha_Y - K_{Y0} \Delta t] + [(1 - K_{ZZ}) \alpha_Z - K_{Z0} \Delta t]$$

$$\Delta v_{RotX} = \frac{1}{2} (\alpha_{YC} u_{ZC} - \alpha_{ZC} u_{YC})$$

$$\Delta v_{RotY} = \frac{1}{2} (\alpha_{ZC} u_{XC} - \alpha_{XC} u_{ZC})$$

$$\Delta v_{RotZ} = \frac{1}{2} (\alpha_{XC} u_{YC} - \alpha_{YC} u_{XC})$$

$$\Delta v_X = u_{XC} + \Delta v_{RotX} + S_{XC}$$

$$\Delta v_Y = u_{YC} + \Delta v_{RotY} + S_{YC}$$

$$\Delta v_Z = u_{ZC} + \Delta v_{RotZ} + S_{ZC}$$

## CORRECTION TO SCULLING ALGORITHM (Continued)

This chart shows the total computation for body frame velocity increments  $\Delta v_i$ s (i axis components of the vector input to the  $C_{B(m)}^L$  transformation matrix on pages 187A) that would be used for velocity updating. Included (as on page 187A) are integrated specific-force increments ( $u_i$ s) compensated for gyro/accelerometer scale factor error, misalignment and bias, rotation compensation ( $\Delta v_{Rot_i}$ s - first order accuracy version in this chart) computed with compensated gyro/accelerometer data, and the compensated sculling data.

## TYPICAL INTEGRATION ALGORITHM FOR CALCULATING ERROR STATE TRANSITION MATRIX

$$\Phi \triangleq \int_{t_{m-1}}^{t_m} A \, dt$$

$$F(t_m, t_{m-1}) \approx e^{\Phi} = I + \Phi + \frac{1}{2} \Phi^2 + \frac{1}{6} \Phi^3 + \dots$$

$$F(t_m, t_{n-1}) = F(t_m, t_{m-1}) F(t_{m-1}, t_{n-1})$$

$$\text{INITIAL CONDITION: } F(t_{n-1}, t_{n-1}) = I$$

$$F_n = F(t_n, t_{n-1}) = F(t_m, t_{n-1}) \quad \text{AT } t_m = t_n$$

$F(t_B, t_A)$  = ERROR STATE TRANSITION MATRIX THAT PROPAGATES  
ERROR STATE VECTOR FROM TIME  $t_A$  TO TIME  $t_B$

$n$  = KALMAN FILTER UPDATE CYCLE INDEX

$m$  = HIGHER SPEED CYCLE INDEX WITHIN KALMAN UPDATE CYCLE

## TYPICAL INTEGRATION ALGORITHM FOR CALCULATING ERROR STATE TRANSITION MATRIX

The slide illustrates a typical integration algorithm for calculating the state transition matrix. The integration operation is a two step process.

First, the error state dynamic matrix ( $A$ ) is integrated between times  $t_{m-1}$  and  $t_m$  within the Kalman filter update cycle (from  $t_{n-1}$  to  $t_n$ ). The integrated error state dynamic matrix ( $\Phi$ ) is used to calculate an error state transition matrix  $F(t_m, t_{m-1})$  that would propagate the error state vector from time  $t_{m-1}$  to time  $t_m$ . The calculation of  $F(t_m, t_{m-1})$  is based on the approximation that the time period  $t_{m-1}$  to  $t_m$  is short so that  $F(t_m, t_{m-1})$  is approximately equal to the identity matrix plus the integral of the error state dynamic matrix (See previous slide entitled "Relationship Between Discrete And Continuous Parameters"). The time interval is selected sufficiently small to make the error in the approximation negligible.

Second, the  $F(t_m, t_{m-1})$  matrix is used in an m cycle iteration algorithm to compute  $F(t_m, t_{n-1})$ , the error state transition matrix that would propagate the error state vector from the start of the current Kalman filter computation cycle ( $t_{n-1}$ ) to  $t_m$  within the filter cycle. The  $F(t_m, t_{n-1})$  matrix is initialized at identity ( $I$ ) at the start of the Kalman filter cycle ( $t_{n-1}$ ). The desired error state transition matrix  $F_n = F(t_n, t_{n-1})$  that would propagate the error state vector from  $t_{n-1}$  at the start to  $t_n$  at the end of the current Kalman cycle is the value of  $F(t_m, t_{n-1})$  at  $t_m = t_n$ .

The digital integration of  $A$  to obtain  $\Phi$  is typically performed individually on each element of  $A$  using a suitable algorithm at the iteration rate required to handle the expected dynamics of the particular element. Typically, many of the elements of  $A$  are zero, hence, the associated integral is also zero and need not be computed. Many of the elements of  $A$  have very little change over the integration interval (i.e., the Kalman cycle) and their integral can, therefore, be accurately approximated by the average of the value at the start and end of the interval multiplied by the Kalman cycle time. The overall result is that the computer throughput required to integrate  $A$  in obtaining  $\Phi$  can generally be reduced to a level where it has negligible penalty on overall computation time resources.

# ESTIMATED ERROR STATE VECTOR AND COVARIANCE PROPAGATION BY ITERATIVE ALGORITHM PROCESSING BETWEEN KALMAN ESTIMATION CYCLES

## CONTINUOUS FORM ESTIMATED ERROR STATE VECTOR AND COVARIANCE PROPAGATION EQUATIONS

$$\frac{d}{dt} \underline{\dot{X}}^* = A \underline{X}^* \quad \dot{P} = A P + P A^T + G_P Q_{PDN} G_P^T$$

## DISCRETE FORM ESTIMATED ERROR STATE VECTOR AND COVARIANCE PROPAGATION (INTEGRAL OF CONTINUOUS FORM)

$$\underline{X}_m^* = \Phi_m \underline{X}_{m-1}^* \quad P_m = \Phi_m P_{m-1} \Phi_m + Q_m$$

$m$  = HIGHER SPEED CYCLE INDEX WITHIN KALMAN ESTIMATION CYCLE

$\Phi_m$  = ERROR STATE TRANSITION MATRIX THAT PROPAGATES  
ERROR STATE VECTOR FROM  $t_{m-1}$  TO  $t_m$

$Q_m$  = INTEGRATED EFFECT OF PROCESS NOISE ON  $P$  FROM  $t_{m-1}$  TO  $t_m$

PROPAGATION CYCLE INITIALIZATION:  $\underline{X}_m^* = \underline{X}_{n-1}^*(+)$   $P_m = P_{n-1}(+)$  AT  $t = t_{n-1}$

READINGS FOR KALMAN ESTIMATION CYCLE:  $\underline{X}_n^*(-) = \underline{X}_m^*$   $P_n(-) = P_m$  AT  $t = t_n$

## ESTIMATED ERROR STATE VECTOR AND COVARIANCE PROPAGATION BY ITERATIVE ALGORITHM PROCESSING BETWEEN KALMAN ESTIMATION CYCLES

For high dynamic environments and/or situations where there is a lengthy time period between Kalman estimation/update cycles, it may be necessary to propagate the estimated error state vector  $\underline{\hat{x}}^*$  and covariance matrix  $P$  using an iterative discrete processing routine between Kalman cycles. The slide illustrates an example of such an iterative algorithm based on sequential  $\underline{\hat{x}}^*$  and  $P$  propagation between the cycle times of an  $m$  cycle computation loop between the basic  $n$  cycle Kalman estimation/update loop. The discrete propagation algorithm represents the integrated form of the continuous differential propagation equations shown from the  $m-1$  to  $m$  propagation cycle times. The  $\Phi_m$  matrix in the slide represents the error state dynamic matrix that would propagate the error state vector from the  $m-1$  to  $m$  cycle times. The  $Q_m$  matrix represents the integrated effect of  $G_P Q_{PDN} G_P^T$  on the covariance  $P$  from cycle  $m-1$  to cycle  $m$  (See pages 426 and 442 for the definitions of  $G_P$  and  $Q_{PDN}$ ).

The estimated error state vector and covariance matrix for the propagation algorithms is initialized at the computed  $\underline{\hat{x}}^*$  and  $P$  values following the last Kalman estimation/reset (i.e.,  $\underline{\hat{x}}_{n-1}^*(+)$  and  $P_{n-1}(+)$ ). The  $\underline{\hat{x}}^*$  and  $P$  values used for the next Kalman cycle estimation/reset cycle (i.e.,  $\underline{\hat{x}}_n^*(-)$  and  $P_n(-)$ ) are then set to the output of the  $m$  cycle propagation algorithms at the next Kalman cycle time  $t_n$ .

## COVARIANCE PROPAGATION BY ITERATIVE ALGORITHM PROCESSING BETWEEN KALMAN ESTIMATION CYCLES (CONTINUED)

HIGH SPEED CALCULATIONS  
WITHIN EACH m CYCLE

$$\Delta\Phi_{\lambda\lambda_m} \equiv \int_{t_{m-1}}^{t_m} \mathbf{A} dt \quad \Delta\Phi_{\lambda y_m} \equiv \int_{t_{m-1}}^{t_m} \mathbf{G}_p \mathbf{Q}_{PDN} \mathbf{G}_p^T dt$$

CALCULATIONS EACH m CYCLE TO DETERMINE  $\Phi_m$  AND  $\mathbf{Q}_m$

INITIALIZATION:  $\mathbf{M}_{\lambda y} = 0 \quad \mathbf{M}_{\lambda\lambda} = \mathbf{I} \quad \Phi_{\lambda y} = 0 \quad \Phi_{\lambda\lambda} = \mathbf{I} \quad \text{FACT} = \mathbf{I}$

COMPUTATIONS:

DO FOR  $i = 1$  TO SPECIFIED  $\Phi_m$  EXPANSION ORDER

$$\text{FACT} = \text{FACT} \times i$$

IF  $i$  IS LESS THAN OR EQUAL TO SPECIFIED  $\mathbf{Q}_m$  EXPANSION ORDER:

$$\mathbf{M}_{\lambda y} = -\mathbf{M}_{\lambda y} \Delta\Phi_{\lambda\lambda_m}^T + \mathbf{M}_{\lambda\lambda} \Delta\Phi_{\lambda y_m}$$

$$\Phi_{\lambda y} = \Phi_{\lambda y} + \frac{1}{\text{FACT}} \mathbf{M}_{\lambda y}$$

IF  $i$  IS EQUAL TO SPECIFIED  $\mathbf{Q}_m$  EXPANSION ORDER:  $\mathbf{B} = \Phi_{\lambda y} \Phi_{\lambda\lambda}^T$

$$\mathbf{M}_{\lambda\lambda} = \mathbf{M}_{\lambda\lambda} \Delta\Phi_{\lambda\lambda_m}$$

$$\Phi_{\lambda\lambda} = \Phi_{\lambda\lambda} + \frac{1}{\text{FACT}} \mathbf{M}_{\lambda\lambda}$$

END DO

$$\Phi_m = \Phi_{\lambda\lambda} \quad \mathbf{Q}_m = \frac{1}{2} (\mathbf{B} + \mathbf{B}^T)$$

## COVARIANCE PROPAGATION BY ITERATIVE ALGORITHM PROCESSING BETWEEN KALMAN ESTIMATION CYCLES (CONTINUED)

The slide illustrates an example of an algorithm for calculating  $\Phi_m$  and  $Q_m$  on the previous chart. The algorithm utilizes the direct integral of  $A$  and  $G_P Q_{PDN} G_P^T$  for its basic input parameters  $\Delta\Phi_{\lambda\lambda_m}$  and  $\Delta\Phi_{\lambda y_m}$ . The integration of  $A$  and  $G_P Q_{PDN} G_P^T$  to obtain  $\Delta\Phi_{\lambda\lambda_m}$  and  $\Delta\Phi_{\lambda y_m}$  is typically implemented on an element by element basis at an iteration rate sufficiently high to properly account for high frequency variations on the element being integrated. In most applications, many of the elements of  $A$  and  $G_P Q_{PDN} G_P^T$  are zero, hence, need not be integrated. Many of the elements are varying at a slow enough rate that their integral over an  $m$  cycle can be approximated by the average of their values at  $m-1$  and  $m$  multiplied by the  $m-1$  to  $m$  cycle time. Some of the elements, however, usually contain attitude and acceleration terms which generally require update rates for accurate digital integration on the order of the attitude and velocity update cycle rates.

Once  $\Delta\Phi_{\lambda\lambda_m}$  and  $\Delta\Phi_{\lambda y_m}$  are calculated, they are used in the chart to calculate  $\Phi_m$  and  $Q_m$  through series expansion routines. The number of terms carried in the expansion series depends on the  $m$  cycle time interval, the frequency content of the  $A$  and  $G_P Q_{PDN} G_P^T$  terms and the number of integrators linking each error state to the measurement. Simulation studies are required to verify that the series expansion order is sufficient for proper characterization of the  $\Phi_m$  and  $Q_m$  matrices. It should be noted that the approximate algorithm for calculating  $Q_n$  on page 442 can be derived from the  $Q_m$  algorithm (in this chart) using a second order expansion for  $Q_m$  with the covariance matrix propagated at the  $n$  cycle Kalman estimation rate.

The  $\Phi_m$  and  $Q_m$  algorithm shown is based on the exact integral solution to the continuous covariance propagation rate equation (previous chart) under conditions where  $A$  and  $G_P Q_{PDN} G_P^T$  are constant. The algorithm is obtained from the latter described integral solution by substituting  $\Delta\Phi_{\lambda\lambda_m}/T_m$  and  $\Delta\Phi_{\lambda y_m}/T_m$  for  $A$  and  $G_P Q_{PDN} G_P^T$ , where  $T_m$  is the  $m$  cycle covariance propagation time interval. Use of  $\Delta\Phi_{\lambda\lambda_m}/T_m$  and  $\Delta\Phi_{\lambda y_m}/T_m$  for  $A$  and  $G_P Q_{PDN} G_P^T$  makes the algorithm accurate to first order under dynamic conditions and accurate to the selected expansion order under slowly varying  $A$  and  $G_P Q_{PDN} G_P^T$  conditions. The final calculation of  $Q_m$  from  $B$  in the slide assures that  $Q_m$  obtained from the truncated expansion series is symmetric (as it would be, both theoretically, and for the infinite expansion series).

## DIRECTION COSINE MATRIX ORTHONORMALITY RELATIONSHIPS

$$\underline{v}^B = C_A^B \underline{v}^A \quad C_A^B = \begin{bmatrix} C_{11} & C_{12} & C_{13} \\ C_{21} & C_{22} & C_{23} \\ C_{31} & C_{32} & C_{33} \end{bmatrix}$$

$$\begin{bmatrix} C_{11} \\ C_{21} \\ C_{31} \end{bmatrix} = \begin{bmatrix} C_{11} & C_{12} & C_{13} \\ C_{21} & C_{22} & C_{23} \\ C_{31} & C_{32} & C_{33} \end{bmatrix} \begin{bmatrix} 1 \\ 0 \\ 0 \end{bmatrix} \quad \begin{bmatrix} C_{12} \\ C_{22} \\ C_{32} \end{bmatrix} = \begin{bmatrix} C_{11} & C_{12} & C_{13} \\ C_{21} & C_{22} & C_{23} \\ C_{31} & C_{32} & C_{33} \end{bmatrix} \begin{bmatrix} 0 \\ 1 \\ 0 \end{bmatrix} \quad \begin{bmatrix} C_{13} \\ C_{23} \\ C_{33} \end{bmatrix} = \begin{bmatrix} C_{11} & C_{12} & C_{13} \\ C_{21} & C_{22} & C_{23} \\ C_{31} & C_{32} & C_{33} \end{bmatrix} \begin{bmatrix} 0 \\ 0 \\ 1 \end{bmatrix}$$

$$\begin{bmatrix} 1 \\ 0 \\ 0 \end{bmatrix} \times \begin{bmatrix} 0 \\ 1 \\ 0 \end{bmatrix} = \begin{bmatrix} 0 \\ 0 \\ 1 \end{bmatrix} \quad \begin{bmatrix} 0 \\ 1 \\ 0 \end{bmatrix} \times \begin{bmatrix} 0 \\ 0 \\ 1 \end{bmatrix} = \begin{bmatrix} 1 \\ 0 \\ 0 \end{bmatrix} \quad \begin{bmatrix} 0 \\ 0 \\ 1 \end{bmatrix} \times \begin{bmatrix} 1 \\ 0 \\ 0 \end{bmatrix} = \begin{bmatrix} 0 \\ 1 \\ 0 \end{bmatrix}$$

$$\begin{bmatrix} C_{11} \\ C_{21} \\ C_{31} \end{bmatrix} \times \begin{bmatrix} C_{12} \\ C_{22} \\ C_{32} \end{bmatrix} = \begin{bmatrix} C_{13} \\ C_{23} \\ C_{33} \end{bmatrix} \quad \begin{bmatrix} C_{12} \\ C_{22} \\ C_{32} \end{bmatrix} \times \begin{bmatrix} C_{13} \\ C_{23} \\ C_{33} \end{bmatrix} = \begin{bmatrix} C_{11} \\ C_{21} \\ C_{31} \end{bmatrix} \quad \begin{bmatrix} C_{13} \\ C_{23} \\ C_{33} \end{bmatrix} \times \begin{bmatrix} C_{11} \\ C_{21} \\ C_{31} \end{bmatrix} = \begin{bmatrix} C_{12} \\ C_{22} \\ C_{32} \end{bmatrix}$$

## DIRECTION COSINE MATRIX ORTHONORMALITY RELATIONSHIPS

From the direction cosine matrix development on page 10, each element (say  $C_{ij}$ ) of a row (or column) of a direction matrix is the cosine of the angle between axis  $i$  of one coordinate frame and axis  $j$  of another. This is the equivalent of the projection onto axis  $j$  in one coordinate frame of a unit vector along axis  $i$  of the other (and visa versa). Thus a row (or column) of a direction matrix represents a unit vector along an axis of one coordinate frame as it projects along the axes of the other. The chart expands this concept for the three rows of the direction cosine matrix  $C_A^B$  that transforms vectors from one coordinate frame (Frame A) to another (Frame B).

The chart shows that the columns of the  $C_A^B$  matrix are the B Frame projections of unit vectors along X, Y and Z axes of the A Frame. Because the axes of the A Frame are mutually perpendicular, the cross product of unit vectors along any two A Frame axes equals a unit vector along the third A Frame axis. This equality holds whether the A Frame axis unit vector components are written in A Frame or B Frame coordinates. Hence, as shown in the chart, the cross-product of any two columns of the  $C_A^B$  matrix equals the third column. It is easily demonstrated by similar reasoning that the rows of  $C_A^B$  represent unit vectors along B Frame axes projected on axes of the A Frame, and that the cross-product of any two rows (in column vector format) of the  $C_A^B$  matrix equals the third row. The latter equality is the basis for the  $d_{33}$  expression on page 88 and computation of the third row of the  $C_B^L$  matrix on page 170.

## DIRECTION COSINE MATRIX ORTHONORMALITY RELATIONSHIPS (Continued)

$$\begin{bmatrix} 1 \\ 0 \\ 0 \end{bmatrix} \cdot \begin{bmatrix} 1 \\ 0 \\ 0 \end{bmatrix} = 1 \quad \begin{bmatrix} 0 \\ 1 \\ 0 \end{bmatrix} \cdot \begin{bmatrix} 0 \\ 1 \\ 0 \end{bmatrix} = 1 \quad \begin{bmatrix} 0 \\ 0 \\ 1 \end{bmatrix} \cdot \begin{bmatrix} 0 \\ 0 \\ 1 \end{bmatrix} = 1$$

$$\begin{bmatrix} C_{11} \\ C_{21} \\ C_{31} \end{bmatrix} \cdot \begin{bmatrix} C_{11} \\ C_{21} \\ C_{31} \end{bmatrix} = 1 \quad \begin{bmatrix} C_{12} \\ C_{22} \\ C_{32} \end{bmatrix} \cdot \begin{bmatrix} C_{12} \\ C_{22} \\ C_{32} \end{bmatrix} = 1 \quad \begin{bmatrix} C_{13} \\ C_{23} \\ C_{33} \end{bmatrix} \cdot \begin{bmatrix} C_{13} \\ C_{23} \\ C_{33} \end{bmatrix} = 1$$

$$\begin{bmatrix} 1 \\ 0 \\ 0 \end{bmatrix} \cdot \begin{bmatrix} 0 \\ 1 \\ 0 \end{bmatrix} = 0 \quad \begin{bmatrix} 0 \\ 1 \\ 0 \end{bmatrix} \cdot \begin{bmatrix} 0 \\ 0 \\ 1 \end{bmatrix} = 0 \quad \begin{bmatrix} 0 \\ 0 \\ 1 \end{bmatrix} \cdot \begin{bmatrix} 1 \\ 0 \\ 0 \end{bmatrix} = 0$$

$$\begin{bmatrix} C_{11} \\ C_{21} \\ C_{31} \end{bmatrix} \cdot \begin{bmatrix} C_{12} \\ C_{22} \\ C_{32} \end{bmatrix} = 0 \quad \begin{bmatrix} C_{12} \\ C_{22} \\ C_{32} \end{bmatrix} \cdot \begin{bmatrix} C_{13} \\ C_{23} \\ C_{33} \end{bmatrix} = 0 \quad \begin{bmatrix} C_{13} \\ C_{23} \\ C_{33} \end{bmatrix} \cdot \begin{bmatrix} C_{11} \\ C_{21} \\ C_{31} \end{bmatrix} = 0$$

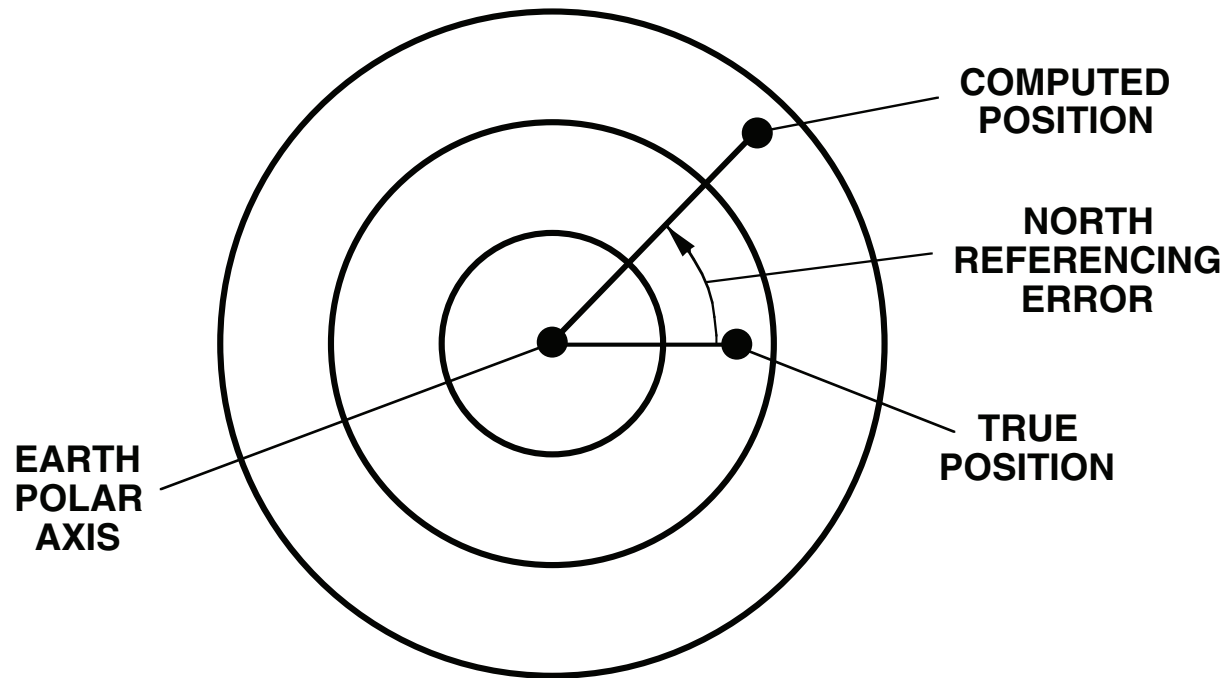
## DIRECTION COSINE MATRIX ORTHONORMALITY RELATIONSHIPS (Continued)

The previous chart discussed the cross-product properties of the columns and rows of a direction cosine matrix. This chart uses the unit vector principles on the previous chart to develop the dot-product properties of the direction cosine matrix columns and rows.

Unit vectors along the A Frame axes are mutually orthogonal and unity in magnitude, hence, the dot product of any axis unit vector with itself is unity and the dot product with any other axis unit vector is zero. This is true if the A Frame unit vectors are projected on A Frame axes (where each has a unity component along its respective axis), or if the A Frame unit vectors are projected on B Frame axes. For the latter case, the A Frame axis unit vectors are represented in the B Frame as columns of the  $C_A^B$  direction cosine matrix.

The dot product rules for the  $C_A^B$  direction cosine matrix also apply to its rows which (in column vector format) represent unit vectors along B Frame axes projected on A Frame axes. The dot product of any row with itself is unity and the dot product with any other row is zero. These properties for the rows of  $C_A^B$  form the basis for the orthogonality and normality correction algorithms on page 216.

# NORTH REFERENCING ERRORS AT HIGH / LOW LATITUDE



## **NORTH REFERENCING ERRORS AT HIGH / LOW LATITUDE**

The chart schematically depicts a view of the earth as projected on a plane perpendicular to earth's polar axis. The circles represent constant latitude loci spaced evenly over the polar axis by small intervals (e.g., one minute of arc indicating close proximity to the pole). Two position locations are shown on the chart, one representing the true position of an inertial navigation system (INS), the other representing the INS computed position (containing errors). The lines from the position points to the polar axis represent the direction to north (or south) from each point. The angular distance between the north reference lines represents a north angular referencing error in the INS computed position.

The chart illustrates that in the vicinity of the poles, even a small INS computed position error (e.g., one nautical mile which is equivalent to one arc minute of angle over earth's surface) can lead to significantly large errors in INS determination of the direction of true north. This is the same effect noted on page 86, and results in potentially large errors in INS north referenced output parameters (e.g., true heading, north/east velocity) when operating in polar regions.

# VELOCITY ERROR DEFINITIONS

$$\delta \underline{v}_1^E \equiv \hat{\underline{v}}^E - \underline{v}^E$$

$$\delta \underline{v}_2^{\text{Geo}} \equiv \hat{\underline{v}}^{\text{Geo}} - \underline{v}^{\text{Geo}}$$

$$\delta \underline{v}_3^E \equiv \hat{\underline{v}}^B - \underline{v}^B$$

**E = EARTH FIXED POLAR / EQUATORIAL COORDINATES**

**Geo = NORTH / EAST / DOWN LOCAL GEOGRAPHIC COORDINATES**

**B = INERTIAL SENSOR (BODY) COORDINATES**

**$\underline{v}$  = VEHICLE VELOCITY RELATIVE TO THE EARTH**

**$\hat{\underline{v}}$  = INS CALCULATED VALUE OF  $\underline{v}$  (I.E., CONTAINING ERRORS)**

**$\delta \underline{v}$  = ERROR IN  $\hat{\underline{v}}$**

**1, 2, 3 = THREE METHODS FOR DEFINING VELOCITY ERROR**

## VELOCITY ERROR DEFINITIONS

This and the next few charts compare error effects in INS velocity and attitude output signals as a function of output data coordinate frames used and, for the velocity error, the basic error definition itself. The differences increase with latitude magnitude, being maximum in the polar regions due to the north referencing error effect noted on the previous chart.

This chart shows three methods for defining velocity error. Each defines velocity error as the difference between the true velocity and INS computed velocity. They differ in the coordinate frame used for making the error evaluation. Method 1 uses an earth fixed (E) coordinate frame for calculating velocity error, method 2 used local geographic (north/east/down) coordinates, and method 3 uses the strapdown sensor body (B) coordinate frame which is fixed relative to vehicle axes.

## VELOCITY ERRORS IN GEOGRAPHIC COORDINATES

$$\delta \underline{v}_1^{\text{Geo}} = \mathbf{C}_E^{\text{Geo}} \delta \underline{v}_1^E$$

$$\delta \underline{v}_2^{\text{Geo}} = \delta \underline{v}_2^{\text{Geo}}$$

$$\delta \underline{v}_3^{\text{Geo}} = \mathbf{C}_B^{\text{Geo}} \delta \underline{v}_3^B$$

$\mathbf{C}_E^{\text{Geo}}$  = DIRECTION COSINE MATRIX THAT TRANSFORMS VECTORS FROM E TO Geo FRAME AXES

$\mathbf{C}_B^{\text{Geo}}$  = DIRECTION COSINE MATRIX THAT TRANSFORMS VECTORS FROM B TO Geo FRAME AXES

## VELOCITY ERRORS IN GEOGRAPHIC COORDINATES

The chart shows three ways for defining velocity error in Geo (geographic - north/east/down) coordinates. Each is a transformation of the velocity errors defined on the previous chart from the error evaluation coordinate frame (1, earth fixed - E, 2, geographic - Geo, or 3, sensor body - B). The  $\delta \underline{v}_2^{\text{Geo}}$  definition is the one commonly used for evaluating INS velocity accuracy.

## RELATIONSHIPS BETWEEN VELOCITY ERRORS

$$\delta \underline{v}_2^{\text{Geo}} = \delta \underline{v}_1^{\text{Geo}} - \underline{\varepsilon}^{\text{Geo}} \times \underline{v}^{\text{Geo}}$$

$$\delta \underline{v}_2^{\text{Geo}} = \delta \underline{v}_3^{\text{Geo}} - \underline{\phi}^{\text{Geo}} \times \underline{v}^{\text{Geo}}$$

$$\delta \underline{v}_3^{\text{Geo}} = \delta \underline{v}_1^{\text{Geo}} + \underline{\psi}^{\text{Geo}} \times \underline{v}^{\text{Geo}}$$

$$(\underline{\phi}^{\text{Geo}} \times) \equiv \mathbf{I} - \widehat{\mathbf{C}}_B^{\text{Geo}} \mathbf{C}_{\text{Geo}}^B$$

$$(\underline{\varepsilon}^{\text{Geo}} \times) \equiv \mathbf{I} - \widehat{\mathbf{C}}_E^{\text{Geo}} \mathbf{C}_{\text{Geo}}^E$$

$$\underline{\psi}^{\text{Geo}} = \mathbf{C}_E^{\text{Geo}} \underline{\psi}^E \quad (\underline{\psi}^E \times) \equiv \mathbf{I} - (\widehat{\mathbf{C}}_B^E \mathbf{C}_E^B) \rightarrow \underline{\psi}^{\text{Geo}} = \underline{\phi}^{\text{Geo}} - \underline{\varepsilon}^{\text{Geo}}$$

$$\widehat{\mathbf{C}}_B^E = (\widehat{\mathbf{C}}_E^{\text{Geo}})^T \widehat{\mathbf{C}}_B^{\text{Geo}} \quad \mathbf{C}_E^B = (\mathbf{C}_B^{\text{Geo}})^T \mathbf{C}_E^{\text{Geo}}$$

$$(\underline{\phi}^{\text{Geo}} \times) = \text{SKEW SYMMETRIC FORM OF } \underline{\phi}^{\text{Geo}}$$

$$(\underline{\varepsilon}^{\text{Geo}} \times) = \text{SKEW SYMMETRIC FORM OF } \underline{\varepsilon}^{\text{Geo}}$$

$$(\underline{\psi}^E \times) = \text{SKEW SYMMETRIC FORM OF } \underline{\psi}^E$$

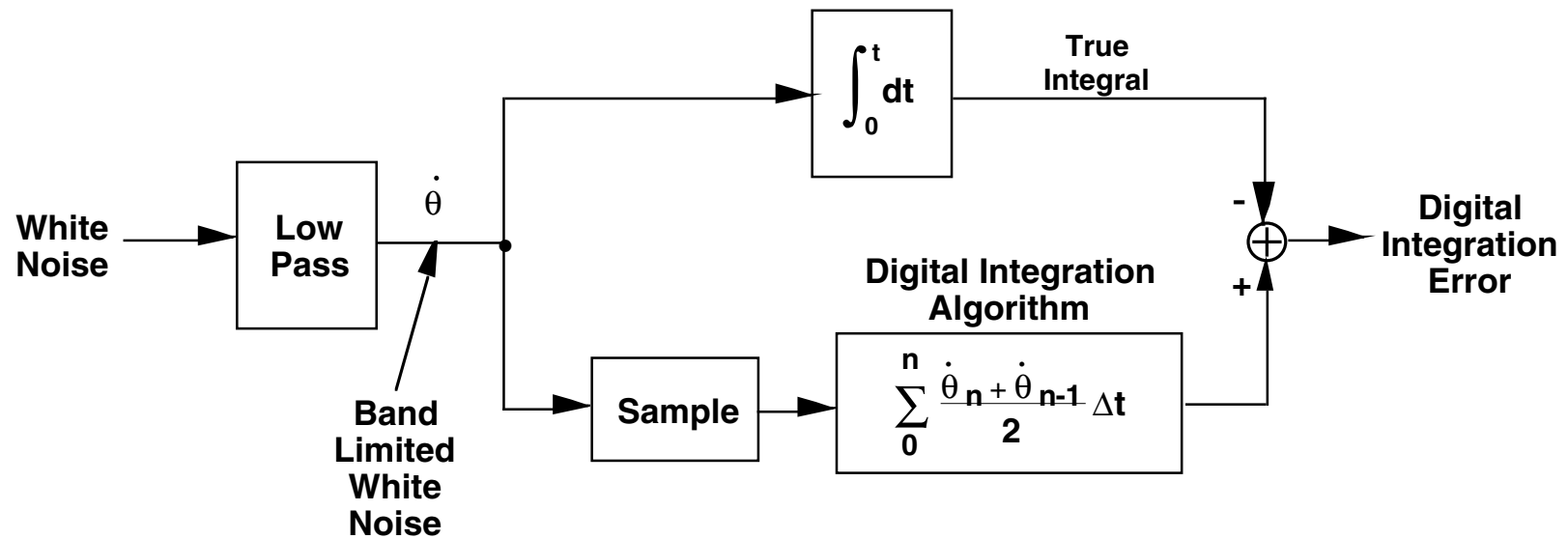
$$\widehat{\mathbf{C}}_B^{\text{Geo}}, \widehat{\mathbf{C}}_E^{\text{Geo}} = \text{INS CALCULATED VALUES OF } \mathbf{C}_B^{\text{Geo}}, \mathbf{C}_E^{\text{Geo}} \\ \text{(I.E., CONTAINING ERRORS)}$$

## RELATIONSHIPS BETWEEN VELOCITY ERRORS

This chart shows the analytical equivalency between the three velocity error types defined previously. Note that they are equivalent except for the direction cosine matrix angle error terms  $\underline{\varepsilon}^{\text{Geo}}$ ,  $\underline{\phi}^{\text{Geo}}$ ,  $\underline{\psi}^{\text{Geo}}$  multiplying  $\underline{v}^{\text{Geo}}$ . Because the  $\delta\underline{v}_1^{\text{Geo}}$  and  $\delta\underline{v}_3^{\text{Geo}}$  do not use north referencing in their definitions (see previous chart) they will not contain the potentially large angle error effect noted earlier at high latitudes. Also, because the  $\underline{\psi}^{\text{Geo}}$  error is in the  $\hat{\mathbf{C}}_B^E$  matrix that has no north angular dependency, its magnitude will be small at all latitudes. Consequently, from their equivalency relation,  $\delta\underline{v}_1^{\text{Geo}}$  and  $\delta\underline{v}_3^{\text{Geo}}$  type velocity errors will generally be approximately equal and latitude independent.

On the other hand, the  $\delta\underline{v}_2^{\text{Geo}}$  type error has direct north referencing dependency because it is evaluated in north pointing geographic coordinates. Consequently,  $\delta\underline{v}_2^{\text{Geo}}$  can be expected to exhibit large latitude dependent distortions that are not representative of the expected velocity error relative to the earth. Similarly, the  $\underline{\varepsilon}^{\text{Geo}}$  and  $\underline{\phi}^{\text{Geo}}$  angle errors associated with the geographic frame referenced  $\hat{\mathbf{C}}_E^{\text{Geo}}$  and  $\hat{\mathbf{C}}_B^{\text{Geo}}$  matrices may have the large heading error effects at high latitudes noted previously. The  $\delta\underline{v}_2^{\text{Geo}}$  error distortion effect at high latitude can be seen analytically in this chart as its variation from  $\delta\underline{v}_1^{\text{Geo}}$  and  $\delta\underline{v}_3^{\text{Geo}}$  by the  $\underline{\varepsilon}^{\text{Geo}}$ ,  $\underline{\phi}^{\text{Geo}}$  cross-product with velocity terms. Interestingly, the  $\delta\underline{v}_2^{\text{Geo}}$  definition is the method commonly used to evaluate INS velocity error even though the  $\delta\underline{v}_1^{\text{Geo}}$ ,  $\delta\underline{v}_3^{\text{Geo}}$  type definitions are more representative of accuracy requirements in velocity dependent applications (e.g., military aircraft weapons control and delivery).

## RATE SENSOR SAMPLE / INTEGRATION ERROR ANALYSIS MODEL



## **RATE SENSOR SAMPLE / INTEGRATION ERROR ANALYSIS MODEL**

The chart describes an analytical method for evaluating the error in a digital versus analog integration of a random angular rate signal. The random angular rate is defined analytically as white noise passed through a first order low pass filter. The digital integration process is structured using a classical trapezoidal integration algorithm. The analytical solution to the digital integration error can be obtained in closed form using covariance analysis techniques. The results can be used to determine the required update rate to minimize the digital integration error.

## RATE SENSOR DIGITAL INTEGRATION ALGORITHM RANDOM WALK ERROR BUILD-UP ANALYTICAL SOLUTION

$$\sigma_{\text{RAND}} = 61.4 \frac{F_{\text{BW}}^{1/2}}{F_{\text{S}}} \sigma_{\dot{\theta}}$$

WHERE

$\sigma_{\dot{\theta}}$  = INPUT RATE NOISE RMS AMPLITUDE (DEG/SEC)

$F_{\text{BW}}$  = INPUT RATE NOISE BANDWIDTH (Hz)

$F_{\text{S}}$  = DIGITAL INTEGRATION SAMPLE RATE (Hz)

$\sigma_{\text{RAND}}$  = DIGITAL INTEGRATION RANDOM WALK ERROR (DEG/RT-HR)

### NUMERICAL EXAMPLE

FOR:  $\sigma_{\dot{\theta}} = 1 \text{ DEG/SEC}$

$F_{\text{BW}} = 10 \text{ Hz}$

$F_{\text{S}} = 1 \text{ KHz}$

FIND:  $\sigma_{\text{RAND}} = 0.194 \text{ DEG/RT-HR}$

## **RATE SENSOR DIGITAL INTEGRATION ALGORITHM RANDOM WALK ERROR BUILD-UP ANALYTICAL SOLUTION**

The chart presents the analytical solution to the block diagram on the previous chart. The equation shown is an accurate approximation to the complete closed-form solution.

The result shows that the root-mean-square (rms) digital integration error  $\sigma_{\text{RAND}}$  is inversely proportional to the digital integration process update sample rate ( $F_S$ ), directly proportional to the rms input rate  $\sigma_{\dot{\theta}}$ , and directly proportional to the square root of the rate noise band-width  $F_{\text{BW}}$  (for the first order low pass filter model on the previous chart, the reciprocal of the filter time constant). This is the equivalent of a random walk process on attitude, i.e., the analytical equivalent of integrated white noise.

For a  $\sigma_{\dot{\theta}}$  value of 1 degree per second (e.g., typical value for random angular motion of an aircraft under random wind gusts), a noise bandwidth of 10 Hertz (Hz) and a digital sample/integration rate of 1 KHz (1,000 Hz), the digital integration error is 0.194 degrees per square-root-of hour (deg/rt-hr). An error of this magnitude would generate the equivalent attitude/velocity/position error from an inertial navigation system having gyros with 0.194 deg/rt-hr random walk error.

Strapdown gyros used in standard aircraft navigation quality inertial navigation have inherent random walk output error characteristics of typically 0.002 deg/rt-hr. The gyros in these systems are typically implemented as rate integrating gyros so that the samples taken into the system computer represent increments of analog integrated rate. Summing the increments in the computer generate the integrated rate without the accompanying digital integration random error effect noted in the slide.

**NOTES**

**NOTES**

**NOTES**